

# Rotorcraft Flight Dynamics and Control

## Modeling, Simulation, Stability, and Flight Control Design

Umberto Saetti

Joseph F. Horn



DEPARTMENT OF AEROSPACE ENGINEERING, UNIVERSITY OF MARYLAND

email: [saetti@umd.edu](mailto:saetti@umd.edu)

web: <https://umbertosaetti.com>



## Contents

|          |  |           |
|----------|--|-----------|
| <b>1</b> | <b>Introduction</b>                                | <b>9</b>  |
| 1.1      | Basic Concepts                                     | 9         |
| 1.2      | Overview of Rotorcraft Configurations              | 9         |
| 1.2.1    | Conventional Main-Tail Rotor Helicopter            | 9         |
| 1.2.2    | Counter-Rotating Coaxial Helicopter                | 10        |
| 1.2.3    | Tandem Rotor Helicopter                            | 10        |
| 1.2.4    | Synchropter  | 11        |
| 1.2.5    | Tiltrotor Aircraft                                 | 12        |
| 1.2.6    | Tilt-Wing Rotorcraft                               | 13        |
| 1.2.7    | Tip-Driven Rotorcraft                              | 13        |
| 1.2.8    | Compound Rotorcraft                                | 14        |
| 1.3      | Distributed Electric Propulsion Rotorcraft         | 15        |
| 1.4      | Modeling and Simulation Challenges                 | 15        |
| 1.4.1    | Contemporary Challenges                            | 17        |
| 1.4.2    | Rotor Interaction with Obstacles                   | 18        |
| 1.5      | Control Challenges                                 | 19        |
| 1.5.1    | Conventional Main-Tail Rotor Helicopter            | 20        |
| 1.5.2    | Tiltrotor Aircraft                                 | 21        |
| 1.5.3    | Counter-Rotating Coaxial Helicopter                | 22        |
| 1.5.4    | Tandem Rotor Helicopter                            | 22        |
| 1.5.5    | Compound Rotorcraft                                | 23        |
| 1.5.6    | Electric Powered Quad-Rotor                        | 23        |
| <b>2</b> | <b>Review of Kinematics and Dynamics</b>           | <b>29</b> |
| 2.1      | Reference Frames, Coordinate Systems, and Notation | 29        |
| 2.1.1    | Coordinate Systems and Reference Frames            | 29        |
| 2.1.2    | Key Reference Frames                               | 30        |
| 2.1.3    | Notation   | 30        |
| 2.1.4    | Vector Components and Cross Product                | 31        |

|   |           |
|---|-----------|
| <b>2.2 Rigid Body Kinematics</b>  | <b>31</b> |
| 2.2.1 Vector Derivatives . . . . .  | 31        |
| 2.2.2 Definition of Velocity and Acceleration . . . . .                       | 32        |
| 2.2.3 Rotation Transformations . . . . .                                      | 33        |
| 2.2.4 Composite Rotations . . . . .   | 34        |
| 2.2.5 Body-Fixed Rotation Sequence . . . . .                                  | 35        |
| 2.2.6 Angular Velocity Vector . . . . .                                       | 35        |
| 2.2.7 Vector Derivative Transport Theorem . . . . .                           | 37        |
| 2.2.8 Angular Velocity Addition Formula . . . . .                             | 38        |
| 2.2.9 Angular Momentum and Moment of Inertia . . . . .                        | 38        |
| 2.2.10 Moments of Inertia in Different Frames . . . . .                       | 40        |
| 2.2.11 Mass Moment of Inertia Matrix for a Composite Body . . . . .           | 40        |
| 2.2.12 Center of Mass . . . . .   | 41        |
| <b>2.3 Rigid Body Dynamics</b>  | <b>41</b> |
| 2.3.1 Translational Kinematics . . . . .                                      | 42        |
| 2.3.2 Rotational Kinematics . . . . .   | 43        |
| 2.3.3 Translational Dynamics . . . . .  | 44        |
| 2.3.4 Rotational Dynamics . . . . .   | 44        |
| 2.3.5 Acceleration of an Arbitrary Point on the Rotorcraft Body . . . . .     | 45        |
| 2.3.6 Motion Primitives . . . . .   | 47        |
| <b>3 Rotor Aerodynamics</b>   | <b>51</b> |
| <b>3.1 Review of Conservation Laws of Aerodynamics</b>                        | <b>51</b> |
| <b>3.2 Momentum Theory in Hover</b>   | <b>52</b> |
| <b>3.3 Disk Loading and Power Loading</b>                                     | <b>55</b> |
| <b>3.4 Non-dimensional Analysis</b>   | <b>56</b> |
| 3.4.1 Total Power Coefficient . . . . .                                       | 57        |
| 3.4.2 Figure of Merit . . . . .   | 58        |
| <b>3.5 Momentum Analysis in Axial Climb</b>                                   | <b>60</b> |
| <b>3.6 Momentum Analysis in Axial Descent</b>                                 | <b>62</b> |
| <b>3.7 Momentum Analysis in Forward Flight</b>                                | <b>63</b> |
| <b>3.8 Numerical Solution to the Inflow Equation in Forward Flight</b>        | <b>69</b> |
| 3.8.1 Fixed-Point Iteration . . . . .   | 70        |
| 3.8.2 Newton-Raphson . . . . .  | 70        |
| <b>3.9 Dynamic Inflow Modeling</b>  | <b>72</b> |
| 3.9.1 Pitt-Peters . . . . .   | 72        |
| 3.9.2 1-State Inflow Model . . . . .  | 74        |
| <b>3.10 Rotor-on-Rotor Interactions</b>                                       | <b>75</b> |
| 3.10.1 Induced Velocity Near a Lifting Rotor . . . . .                        | 75        |
| 3.10.2 State-Space CMTSVT . . . . .   | 76        |
| <b>4 Rotor Modeling for Flight Dynamics</b>                                   | <b>83</b> |
| <b>4.1 Useful Coordinate Transformations</b>                                  | <b>83</b> |
| 4.1.1 Body to Hub Frame Transformation . . . . .                              | 83        |
| 4.1.2 Hub to Blade Frame Transformation . . . . .                             | 85        |
| 4.1.3 Blade to Air Mass Frame Transformation . . . . .                        | 87        |
| 4.1.4 Blade to Radial-Tangential-Perpendicular Frame Transformation . . . . . | 87        |

|            |  |            |
|------------|--|------------|
| <b>4.2</b> | <b>Blade Kinematics</b>  | <b>88</b>  |
| 4.2.1      | Rotor Hub Position . . . . .                                   | 88         |
| 4.2.2      | Rotor Hub Velocity . . . . .                                   | 88         |
| 4.2.3      | Rotor Hub Acceleration . . . . .                               | 89         |
| 4.2.4      | Blade Element Velocity . . . . .                               | 89         |
| 4.2.5      | Blade Element Acceleration . . . . .                           | 90         |
| <b>4.3</b> | <b>Rotor Forces and Moments</b>                                | <b>90</b>  |
| 4.3.1      | Aerodynamic Loads on Blade Elements . . . . .                  | 90         |
| 4.3.2      | Aerodynamics Forces and Moments About the Flap Hinge . . . . . | 93         |
| <b>4.4</b> | <b>Flapping Dynamics</b>                                       | <b>94</b>  |
| 4.4.1      | Simplified Flapping Dynamics . . . . .                         | 95         |
| 4.4.2      | Equivalent Hinge Offset . . . . .                              | 97         |
| 4.4.3      | Inertial Forces and Moments About the Flap Hinge . . . . .     | 98         |
| 4.4.4      | Total Forces and Moments About the Flap Hinge . . . . .        | 99         |
| 4.4.5      | Rotor Hub Forces and Moments . . . . .                         | 99         |
| 4.4.6      | Multi-Blade Coordinates (MBC) . . . . .                        | 100        |
| 4.4.7      | Flapping Dynamics in Multi-Blade Coordinates . . . . .         | 104        |
| 4.4.8      | Center Spring Approximation . . . . .                          | 106        |
| 4.4.9      | Flapping Dynamics at Hover . . . . .                           | 108        |
| 4.4.10     | Quasi-Static Flapping . . . . .                                | 108        |
| 4.4.11     | Simplified Forces and Moments . . . . .                        | 111        |
| <b>4.5</b> | <b>Blade Discretization</b>                                    | <b>111</b> |
| 4.5.1      | Spanwise . . . . .   | 111        |
| 4.5.2      | Chordwise . . . . .  | 112        |
| 4.5.3      | Blade Surface Pressure . . . . .                               | 112        |
| <b>4.6</b> | <b>Computational Setup</b>                                     | <b>113</b> |
| 4.6.1      | Rotor Module . . . . .   | 113        |
| 4.6.2      | Simplified Rotor Module . . . . .                              | 116        |
| 4.6.3      | Quasi-Static Rotor Module . . . . .                            | 116        |
| <b>5</b>   | <b>Fuselage and Empennage Modeling</b> . . . . .               | <b>117</b> |
| <b>5.1</b> | <b>Fuselage</b>  | <b>118</b> |
| 5.1.1      | Body to Wind Frame Transformation . . . . .                    | 118        |
| 5.1.2      | Fuselage Forces and Moments . . . . .                          | 119        |
| <b>5.2</b> | <b>Empennage</b>   | <b>122</b> |
| 5.2.1      | Hub to Wing Frame Transformation . . . . .                     | 122        |
| 5.2.2      | Empennage Kinematics . . . . .                                 | 124        |
| 5.2.3      | Wing Aerodynamics . . . . .                                    | 125        |
| 5.2.4      | Simple Aerodynamic Modeling . . . . .                          | 126        |
| 5.2.5      | Wing Element Modeling . . . . .                                | 128        |
| 5.2.6      | Lifting Line - Linear . . . . .                                | 130        |
| 5.2.7      | Lifting Line - Nonlinear . . . . .                             | 133        |
| <b>6</b>   | <b>Trim, Linearization, and Simulation</b> . . . . .           | <b>135</b> |
| <b>6.1</b> | <b>Introduction</b>  | <b>135</b> |
| <b>6.2</b> | <b>Linearization</b>   | <b>135</b> |
| <b>6.3</b> | <b>Trim Algorithm</b>  | <b>138</b> |
| 6.3.1      | Trim with Zero Sideslip . . . . .                              | 140        |

|            |   |            |
|------------|---|------------|
| 6.3.2      | Trim with Zero Bank Angle .....                                       | 142        |
| 6.3.3      | Trim in Autorotation .....  | 143        |
| <b>6.4</b> | <b>Model Order Reduction</b>  | <b>144</b> |
| 6.4.1      | Truncation .....  | 145        |
| 6.4.2      | Singular Perturbation Theory .....                                    | 146        |
| 6.4.3      | Linear Models Verification .....                                      | 151        |
| <b>6.5</b> | <b>Review of Numerical Integration Methods</b>                        | <b>154</b> |
| 6.5.1      | Forward and Backward Euler .....                                      | 155        |
| 6.5.2      | Backward Euler .....  | 156        |
| 6.5.3      | Trapezoidal (or Crank-Nicholson) .....                                | 156        |
| 6.5.4      | Heun .....  | 156        |
| 6.5.5      | Runge-Kutta Fourth Order (RK4) .....                                  | 157        |
| 6.5.6      | Runge-Kutta Fifth Order (RK5) .....                                   | 157        |
| <b>7</b>   | <b>Stability and Response Analysis</b>                                | <b>159</b> |
| <b>7.1</b> | <b>Introduction</b>   | <b>159</b> |
| <b>7.2</b> | <b>Static Stability</b>   | <b>159</b> |
| 7.2.1      | Longitudinal Static Stability with Speed .....                        | 159        |
| 7.2.2      | Longitudinal Static Stability with Angle of Attack .....              | 160        |
| 7.2.3      | Lateral Static Stability or Dihedral Effect .....                     | 160        |
| 7.2.4      | Directional Stability or Weathercock Stability .....                  | 161        |
| <b>7.3</b> | <b>Dynamic Stability</b>  | <b>161</b> |
| 7.3.1      | Review of Linear Systems Analysis .....                               | 161        |
| 7.3.2      | Linear Systems Analysis Tools in MATLAB® .....                        | 167        |
| 7.3.3      | Decoupled Longitudinal and Lateral Dynamics .....                     | 168        |
| 7.3.4      | Hover .....   | 169        |
| 7.3.5      | Forward Flight .....  | 176        |
| 7.3.6      | Coupled Longitudinal-Lateral Dynamic Stability .....                  | 181        |
| 7.3.7      | Example 1: Longitudinal Dynamics of a UH-60 Helicopter in Hover ..... | 182        |
| 7.3.8      | Example 2: Quadrotor Flight Dynamics at Hover .....                   | 184        |
| <b>7.4</b> | <b>Stability with Feedback</b>  | <b>184</b> |
| 7.4.1      | Mathematical Overview .....   | 186        |
| 7.4.2      | Hover Stabilization .....   | 187        |
| <b>8</b>   | <b>Flight Control Design</b>  | <b>193</b> |
| <b>8.1</b> | <b>Introduction</b>   | <b>193</b> |
| <b>8.2</b> | <b>Types of Stability and Control Augmentation</b>                    | <b>193</b> |
| <b>8.3</b> | <b>Frequency Domain Analysis</b>                                      | <b>194</b> |
| 8.3.1      | Overview .....  | 194        |
| 8.3.2      | Stability Margins .....   | 195        |
| <b>8.4</b> | <b>Response Types</b>   | <b>196</b> |
| 8.4.1      | Angular Dynamics .....  | 197        |
| 8.4.2      | Translational Dynamics .....  | 198        |
| <b>8.5</b> | <b>Explicit Model Following</b>                                       | <b>200</b> |
| 8.5.1      | RCAH EMF Controller .....   | 200        |
| 8.5.2      | ACAH EMF Controller .....   | 203        |
| 8.5.3      | TRC EMF Controller .....  | 205        |

---

|  |            |
|--|------------|
| 8.5.4 Example 1: UH-60 EMF SCAS . . . . .  | 207        |
| 8.5.5 Example 2: Quadrotor EMF AFCS . . . . .  | 208        |
| <b>8.6 Dynamic Inversion</b>   | <b>209</b> |
| 8.6.1 RCAH DI Controller . . . . .   | 210        |
| 8.6.2 ACAH DI Controller . . . . .   | 213        |
| 8.6.3 TRC DI Controller . . . . .  | 215        |
| 8.6.4 Example 3: UH-60 DI AFCS . . . . .   | 216        |
| <b>8.7 Feed-Forward Compensation</b>   | <b>219</b> |
| 8.7.1 Turn Coordination . . . . .  | 219        |
| 8.7.2 Turn Compensation . . . . .  | 221        |
| <b>8.8 Redundant Control Allocation</b>  | <b>221</b> |
| 8.8.1 EMF Control Law with Redundant Control Allocation . . . . .                              | 222        |
| 8.8.2 DI Control Law with Redundant Control Allocation . . . . .                               | 223        |
| 8.8.3 Non-Minimum Phase Zeros . . . . .  | 223        |
| <b>9 Time-Periodic Systems Analysis . . . . .</b>  | <b>229</b> |
| <b>9.1 Introduction</b>  | <b>229</b> |
| <b>9.2 Overview of Linear Time-Periodic Systems</b>  | <b>230</b> |
| 9.2.1 State Space and Input-Output Representations . . . . .                                   | 230        |
| 9.2.2 Free Response and the Monodromy Matrix . . . . .   | 231        |
| 9.2.3 Stability of LTP Systems . . . . .   | 232        |
| 9.2.4 Floquet Theory . . . . .   | 233        |
| 9.2.5 Time-Invariant Reformulations . . . . .  | 234        |
| <b>9.3 Extraction of LTP/LTI Systems from Simulation Models</b>                                | <b>237</b> |
| 9.3.1 Overview of Periodic Trim Methods . . . . .  | 237        |
| 9.3.2 Early Efforts in the Approximation of the LTP Rotor Dynamics with High-Order LTI Models  | 239        |
| 9.3.3 $T$ -Matrix . . . . .  | 240        |
| 9.3.4 Frequency and Time Lifting of Helicopter Models with HHC . . . . .                       | 241        |
| 9.3.5 Direct Derivation of High-Order LTI Models . . . . .                                     | 242        |
| 9.3.6 Harmonic Decomposition: Second-Order Formulation . . . . .                               | 244        |
| 9.3.7 Harmonic Decomposition: First-Order Formulation . . . . .                                | 246        |
| 9.3.8 Recent Advancements in the Direct Derivation of High-Order LTI Models . . . . .          | 247        |
| <b>9.4 Deeper Dive into Harmonic Balance and Harmonic Decomposition</b>                        | <b>248</b> |
| 9.4.1 Periodic Trim Problem Definition . . . . .   | 248        |
| 9.4.2 Modified Harmonic Balance . . . . .  | 249        |
| 9.4.3 Modal Participation Factors . . . . .  | 252        |
| 9.4.4 Example 1: Vibrational Stabilization of an Inverted Pendulum . . . . .                   | 254        |
| 9.4.5 Example 2: Periodic Trim of the Vertical Dynamics of Flapping-Wing Vehicle . . . . .     | 258        |
| 9.4.6 Example 3: Periodic Trim of the Longitudinal Dynamics of Flapping-Wing Vehicle . . . . . | 261        |
| 9.4.7 Example 4: Periodic Trim of a Helicopter . . . . .                                       | 268        |
| 9.4.8 Example 5: Vibrational Stabilization Effects in Rotorcraft Flight Dynamics . . . . .     | 272        |





# 1. Introduction

## 1.1 Basic Concepts

A rotorcraft is a type of aircraft that uses one or more rotary wings (rotors) to provide lift and propulsion. Unlike fixed-wing aircraft, which rely on forward motion and airflow over their wings to generate lift, rotorcraft can hover in place and take off and land vertically. This book will treat those aspects of rotorcraft that pertain to their flight dynamics and control. To understand what this means, consider the following definitions:

- **Trim:** An equilibrium flight condition. The states defining the aircraft dynamics are constant with time.
- **Stability:** Tendency of an aircraft to return to equilibrium (trim) following a disturbance.
- **Control:** Ability of the aircraft to be maneuvered from one flight condition to another.
- **Static Stability:** Tendency of an aircraft to initially return to equilibrium following a disturbance (does not necessarily imply stability). Static stability is a necessary but not sufficient condition for stability.
- **Flight Dynamics:** The study of how an aircraft responds to control inputs and disturbances. Purely objective science based on aircraft aerodynamics and equations of motion.
- **Handling Qualities:** Those qualities that govern the ease and precision with which a pilot is able to perform the tasks required in support of an aircraft role. They are a combination of objective and subjective sciences, a function of a number of factors: (i) stability and control characteristics of aircraft, (ii) mission requirements, (iii) human factors considerations, (iv) environmental conditions.
- **Flying Qualities:** Includes handling qualities and ride qualities (aircraft qualities that impact passenger comfort and experience).

As such, rotorcraft flight dynamics is the study of the motion of the aircraft as it relates to handling qualities and maneuvering performance. Rotorcraft flight dynamics are not to be confused with rotorcraft dynamics, which usually refer to the study of the dynamics of the rotor system as it relates to loads, vibration, and rotor stability analysis. The differences between the two are articulated in Table 1.1

## 1.2 Overview of Rotorcraft Configurations

### 1.2.1 Conventional Main-Tail Rotor Helicopter

Conventional main-tail rotor helicopters are the most common type of helicopter in use today, and are often referred to simply as helicopters. They feature a main rotor mounted on the top of the aircraft and a smaller tail rotor mounted on the tail boom. The main rotor provides lift and propulsion, while the tail rotor is used to counteract the torque generated by the main rotor and provide directional control. The main rotor is made up of multiple rotor blades (typically from two, *e.g.*, the Bell UH-1, up to eight, *e.g.*, the Mil Mi-26), which

Table 1.1: Rotorcraft flight dynamics versus helicopter dynamics.

|                     | Rotorcraft Flight Dynamics  | Rotorcraft Dynamics   |
|---------------------|---|---|
| Dynamics            | Low frequency dynamics (steady-state to 1/rev)                    | High frequency dynamics (out to $N_b/\text{rev}$ and above)                                 |
| Blades              | Usually assume rigid blades                                       | Flexible blades models  |
| Fuselage            | Rigid   | Flexible (sometimes)  |
| Fuselage Aero       | Detailed modeling   | Simple modeling   |
| Rotor Inflow        | Finite-state inflow model ( <i>e.g.</i> , Pitt-Peters, Peters-He) | More complex wake models ( <i>e.g.</i> , free-vortex wake, viscous vortex particle methods) |
| Flight Controls     | Detailed model of automatic flight control system                 | Simple models of automatic flight control system  |
| Powerplant          | Detailed modeling   | Simple modeling   |
| Flight Conditions   | Can simulate large amplitude maneuvers                            | Normally used for analysis of trimmed (or quasi-steady) flight conditions only              |
| Real-Time Operation | Desirable   | Not normally feasible   |

are connected to the rotor hub and rotate around the main rotor mast. The blades can feather to provide lift and are controlled by the pilot through the use of the collective and cyclic controls. The collective control adjusts the pitch angle of all the rotor blades together, while the cyclic control adjusts the pitch of each blade individually to control the direction of flight. The tail rotor is typically located at the end of the tail boom and consists of two to four rotor blades mounted on a rotor hub. The tail rotor is used as an anti-torque mechanism in that it counteracts the torque generated by the main rotor and allows for directional control. The tail rotor is controlled by the pilot through the use of the foot pedals, which adjust the pitch of the rotor blades. Conventional main-tail rotor helicopters are known for their versatility and ability to hover and maneuver in tight spaces. They are widely used in a variety of applications, including search and rescue, medical transport, law enforcement, and military operations. In recent years, there has been growing interest in alternative rotorcraft designs that address some of the limitations of conventional helicopters, such as forward flight efficiency. These include tiltrotor aircraft, coaxial rotor helicopters, and other types of innovative rotorcraft designs. However, conventional main-tail rotor helicopters remain the most widely used type of helicopter in the world today. Examples are shown in Fig. 8.7.

### 1.2.2 Counter-Rotating Coaxial Helicopter

Counter-rotating coaxial helicopters feature two rotors mounted one on top of the other and rotating in opposite directions. This counter-rotation cancels out the torque generated by each rotor and eliminates the need for a tail rotor and provides improved footprint compared to conventional main-tail rotor helicopters. Directional control for this kind of design is provided by differential torque on the rotors, produced by differentially varying the collective input on the rotors, while still providing the same amount of thrust. Counter-rotating coaxial helicopters are used in a variety of applications, including military transport, search and rescue, and heavy lifting operations. One example of a counter-rotating coaxial helicopter is the Russian-built Kamov Ka-32 (Fig. 1.2a), another is the Sikorsky SB>1 Defiant (Fig. 1.2b).

### 1.2.3 Tandem Rotor Helicopter

Tandem rotor helicopters are a type of rotary-wing aircraft that utilize two sets of rotors placed one in front of the other along the longitudinal axis of the aircraft. The rotors are connected by a system of drive shafts and gearboxes, which allow the rotors to spin synchronously in opposite directions. Synchronous rotation is necessary to avoid blade strikes between the rotors in those flight conditions that yield significant blade flapping. The forward rotor is typically located slightly lower than the aft rotor, as shown in Fig. 1.3, to prevent reduce interference between the two rotors and to provide tip clearance. Because the front rotor acts



Figure 1.1: Conventional main-tail rotor helicopter examples.

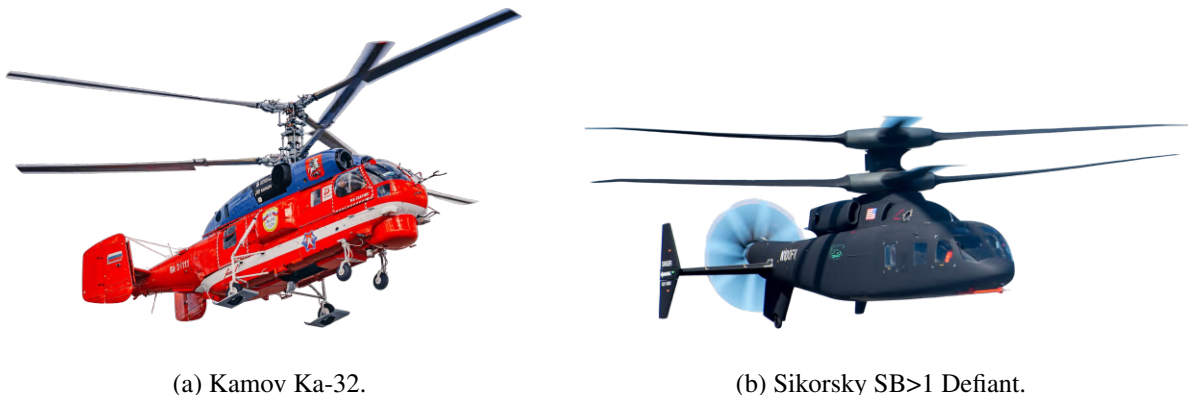


Figure 1.2: Counter-rotating coaxial helicopter examples.

partially in the wake of the aft rotor, the combined performance of the two rotors is less than that of the two rotors if they were isolated. Nonetheless, counter-rotation cancels out the torque generated by each rotor and eliminates the need for a tail rotor and the power losses associated to it. As such, both rotors are used to provide thrust and propulsive force making these platforms particularly disposed toward heavy lift.

#### 1.2.4 Synchropter

Intermeshing rotor helicopters, also known as synchropters, are a type of rotary-wing aircraft that use two rotors that are intermeshed and synchronized. Unlike tandem rotor helicopters, the rotors on synchropters are positioned side-by-side on separate masts that are angled with respect to each other. Examples are shown in Fig. 1.4. Because of the complex relative positioning of the rotors, rotor aerodynamic interactions are complex and difficult to model. Like for tandem rotor helicopters, counter rotation of the rotors cancels out the overall rotors torque and removes the need for an anti-torque mechanism like the tail rotor. It follows that



Figure 1.3: Tandem rotor helicopters.

both rotors are used to provide thrust and propulsive force making it an apt configuration for heavy lift.

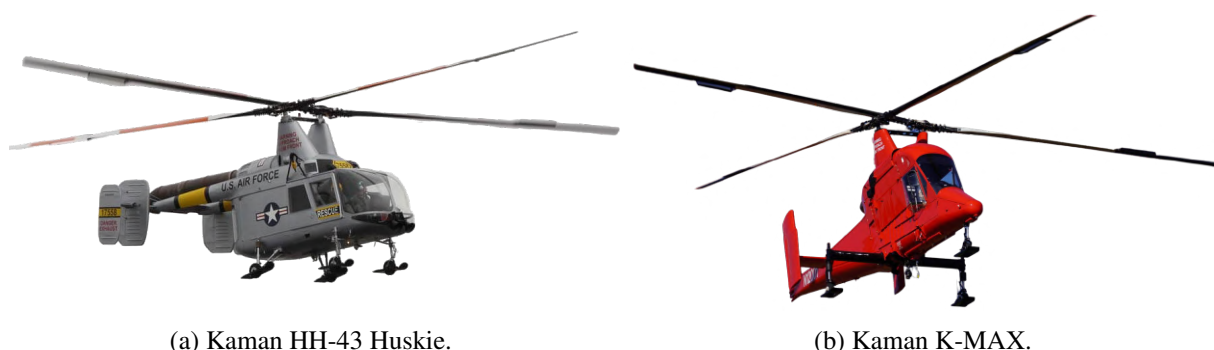


Figure 1.4: Synchropter examples.

### 1.2.5 Tiltrotor Aircraft

Tiltrotor aircraft are a type of vertical takeoff and landing (VTOL) aircraft that feature rotors that can be tilted from a vertical to a horizontal position, allowing them to take off and land like a helicopter and fly like a fixed-wing aircraft. Tiltrotor aircraft offer several advantages over traditional helicopters and fixed-wing aircraft, including increased speed and range which are a direct consequence of their forward flight efficiency. Tiltrotor aircraft are typically designed with two large rotors mounted on wings that are capable of tilting up to 90 degrees. In the vertical position, the rotors function like those on a helicopter, providing lift and propulsion. In the horizontal position, the rotors function like those on a fixed-wing aircraft, providing lift and forward propulsion. This allows tiltrotor aircraft to take off and land vertically like a helicopter, then tilt their rotors to fly like an airplane, offering faster speeds and longer ranges than traditional helicopters. One of the most well-known examples of a tiltrotor aircraft is the Bell Boeing V-22 Osprey, which is used by the United States military for a variety of missions, including troop transport, cargo transport, and special operations. The V-22 Osprey has a cruising speed of over 300 mph and a range of over 1,000 nautical miles, making it faster and more versatile than traditional helicopters. From an engineering perspective, designing a tiltrotor aircraft presents several unique challenges. One of the primary challenges is ensuring that the aircraft remains stable and controllable in both vertical and horizontal flight modes. This requires careful design and optimization of the wing and rotor systems, as well as advanced control systems to manage the transition between flight modes. Tiltrotor aircraft also require careful consideration of their aerodynamics, particularly during the transition between helicopter and airplane flight modes, as the tilting rotors and wings interfere in complex ways. Examples are shown in Fig. 1.5.

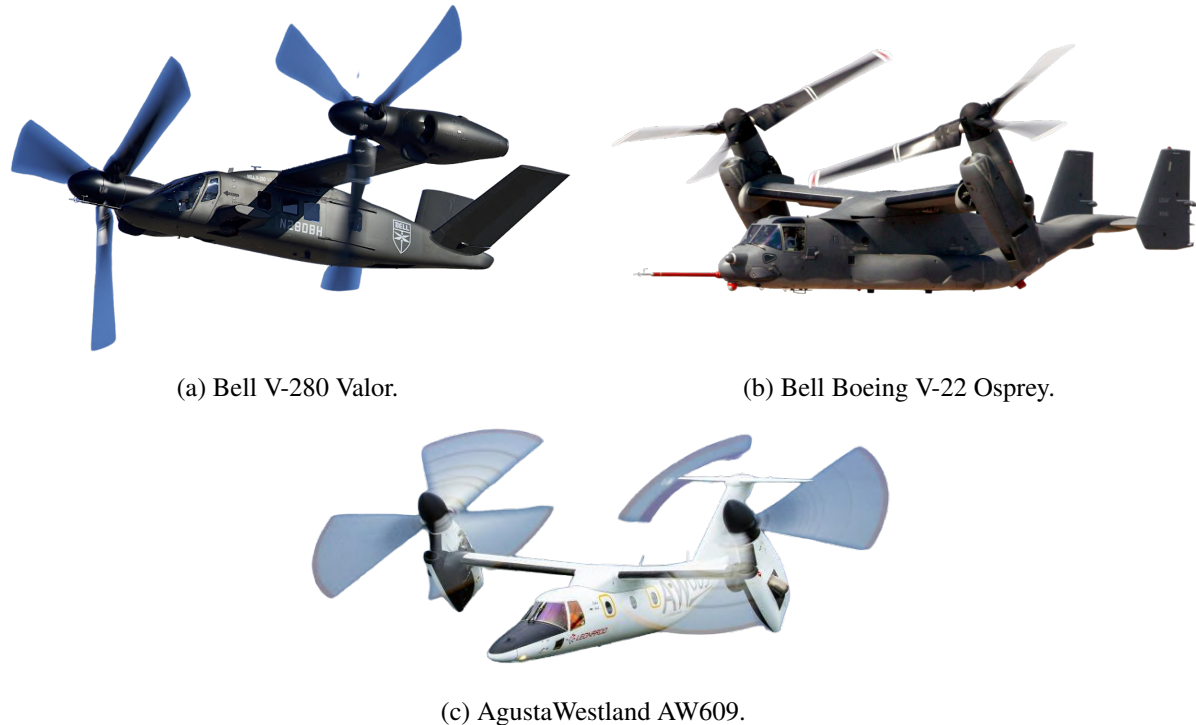


Figure 1.5: Tiltrotor aircraft examples.

### 1.2.6 Tilt-Wing Rotorcraft

Tilt-wing rotorcraft are a type of VTOL aircraft that use a combination of wings and rotor blades to achieve both vertical and horizontal flight. Unlike tiltrotors, tilt-wing aircraft achieve rotor tilting through the combined rotation of the rotor and wing, rather than the rotor alone. This leads to a reduced rotor-on-wing interference in helicopter mode as the flow past the wing due to the rotor downwash remains attached to the wing profile. This makes modeling of rotor-on-wing interference simpler. Unlike tiltrotors, tilt-wing rotorcraft historically featured multiple rotors per wing. However, this is changing with distributed electric propulsion (DEP) configurations proposed in recent years. Because the rotors typically counter rotate to cancel out the overall torque, no anti-torque mechanisms like tail rotors are necessary. Because rotors must be designed to operate both in helicopter mode and as propellers in forward flight, this introduced a trade-off that typically yields to a higher disk loading and twist distributions compared to conventional helicopter rotors. Examples are shown in Fig. 5.6b.

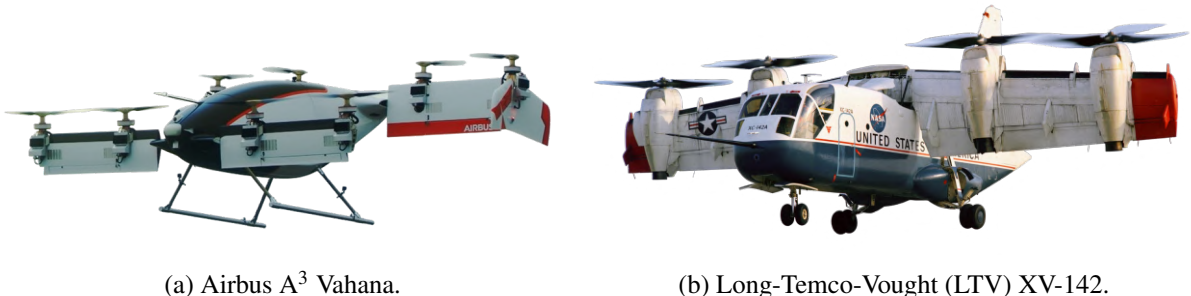


Figure 1.6: Tilt-wing rotorcraft examples.

### 1.2.7 Tip-Driven Rotorcraft

The use of tip-jets to provide the torque to power rotor blades has long been considered as an alternate approach to more traditional shaft-driven rotor systems. This is because the tip-driven rotor approach leads to

the elimination of the transmission and the anti-torque rotor, the latter of which allows to shorten the tail boom. The associated reduction in the overall mechanical complexity, moving parts, and empty weight of the aircraft results in decreased power requirements (or equivalently, in more payload capacity for the same gross weight) and decreased maintenance costs. Additionally, because the angular dynamics of the main rotor is no longer coupled with the directional dynamics of the rotorcraft, an increase or decrease in collective pitch will not result in an off-axis response about the yaw axis. This is a favorable response characteristic when comparing the tip-driven rotorcraft to conventional helicopters, for which the heave-yaw dynamics are strongly coupled. In fact, helicopter pilots typically need to counteract an increase or decrease in collective pitch with pedal input to keep the desired heading. However, it should be noted that, depending on the tip-driven propulsion system used, reduction in mechanical complexity in the anti-torque rotor and corresponding transmission may come at the cost of increased complexity from the introduction of the tip-driven propulsion system itself.

A summary of the various approaches to tip-driven rotors that were proposed and implemented over the years, including illustrious rotorcraft examples, is provided below:

- **Cold Tip Jets:** Compressed air is forced out of aft-facing nozzles at the blade tips. An engine-driven air compressor located in the fuselage pumps the air through a rotating seal and into hollow rotor blades. The FIAT 7002, an Italian helicopter which first flew in 1961 adopted this approach [Mor58].
- **Hot Tip Jets:** These jets are produced by burning fuel to heat the air for greater thrust. Two types of these jets exist, the first in which the fuel is added to the air and burnt at the blade tip, the second in which the exhaust gasses from a turbine engine located in the fuselage are expelled from nozzles at the blade tips. The Fairy Rotodyne, a British compound gyroplane, used hot tip jets and completed its first flight in 1957 [Hir58].
- **Ramjets:** Ramjet engines are mounted on the blade tips. These jet engines use the engine's forward motion to compress incoming air without axial or centrifugal compressors to then add fuel and ignite it. This solution was used on the Hiller YH-32 Hornet, an American ultralight helicopter that first flew in 1950 [Hol54].
- **Pulsejets:** Jet engines in which combustion occurs in pulses are mounted on the blade tips. This method was demonstrated on the American Helicopter XH-26 Jet Jeep, an experimental helicopter developed in 1951 [Loc50].

Although the use of tip-jets is appealing because of the advantages described above, it also comes with significant drawbacks that have prevented this approach to vertical flight to develop into a major commercial success. These drawbacks include the pressure losses and sealing challenges associated with transporting compressed air or exhaust gasses to the blade tips, the high centrifugal loads acting on the jet engines, and the relatively high noise levels produced by the tip-jet when compared to those of the usual sources of rotating blade noise [BML14]. Examples of tip-driven rotorcraft are shown in Fig. 1.7.

In recent years, distributed electric propulsion is actively being explored in the vertical flight community as a novel propulsion solution for electric Vertical Take-Off and Landing (eVTOL) vehicles intended for Urban Air Mobility (UAM). Attempts to categorize the various UAM eVTOL configurations are provided in [Sli+18; Str+20]. In these studies, configurations are differentiated between rotary-wing cruise and fixed-wing cruise. The rotary-wing cruise category includes rotary-wing and lift-fan aircraft, whereas the fixed-wing category includes lift+cruise, tilt-wing/rotor, and tailsitter aircraft. With regards to rotary-wing configurations, distributed electric propulsion offers new opportunities to revisit tip-driven rotor concepts. Recently, an eVTOL concept aircraft was proposed in which the main rotor is driven by rotor-mounted electric propellers rather than by tip-jets [SEH22] (Fig. 1.7d). While this design enjoys the same advantages of tip-driven rotors, it eliminates the difficulties related to transporting compressed air or exhaust gasses to the blade tips. Additionally, it may relax the disadvantages associated with the high noise levels of tip-jets. On the other hand, the increase in rotor and blade parts, electric components, and in the complexities of electrical power transmission from the fixed to the rotating frame constitute potential drawbacks.

## 1.2.8 Compound Rotorcraft

Compound rotorcraft are a type of rotorcraft that combine elements of both helicopters and fixed-wing aircraft to achieve enhanced performance and versatility. Compound rotorcraft typically feature one or more fixed



Figure 1.7: Tip-driven rotorcraft examples.

wings to provide lift, as well as one or more rotors to provide lift and propulsion. The rotors can be powered by an engine or electric motors, and may be mounted on the wings or on a separate pylon above the fuselage. There are several different types of compound rotorcraft, each with its own unique configuration and design. Some of the most common types include tiltrotors, coaxial helicopters, and more exotic configurations featuring wings, pusher propellers, and auxiliary control surfaces. With the introduction of these auxiliary control surfaces and rotors, the rotorcraft effectively becomes overactuated in that the number of control effectors exceeds the number of axes being controlled (*i.e.*, roll, pitch, yaw, and heave). As such, one major problem is how to reallocate the control signal to the redundant control effectors in such a way that can be beneficial to trimmed flight performance, maneuvering flight, and/or to minimize measures of interest such as rotor noise or rotor loads. While compound rotorcraft are generally more capable than conventional helicopters, they come with added mechanical and control complexity. Examples of compound rotorcraft are shown in Fig. 1.8.

### 1.3 Distributed Electric Propulsion Rotorcraft

Distributed electric propulsion (DEP) is an emerging technology that involves the use of multiple electric motors and propellers distributed throughout the aircraft, rather than a single power source driving a single main rotor or propeller. DEP rotorcraft can take many different forms, but generally, they feature multiple rotors or propellers distributed along the wings, fuselage, or other parts of the aircraft. The rotors or propellers are powered by electric motors, which are usually powered by batteries or other electrical sources. DEP rotorcraft are still in the early stages of development, and there are many challenges to be overcome before they become a practical and viable technology. These challenges include developing more efficient and reliable electric motors, batteries, and power systems, safety, and addressing regulatory and certification issues. Examples of DEP rotorcraft are shown in Fig. 1.9.

### 1.4 Modeling and Simulation Challenges

Rotorcraft are inherently interdisciplinary, in that their dynamics is governed by physics from wildly different engineering fields which are articulated as follows and illustrated in Fig. 1.10:

(a) Eurocopter X<sup>3</sup>.

(b) Piasecki 16H-1A Pathfinder II.



(c) Fairey Rotodyne.



(d) Sikorsky X2.

Figure 1.8: Compound helicopter examples.



(a) Joby S4 2.0.



(b) Archer Midnight.



(c) Wisk Cora Generation 4.



(d) Volocopter 2X.

Figure 1.9: Distributed electric propulsion rotorcraft examples.

- **Aerodynamics:** Governs the generation of forces and moments of the rotors, fuselage, and empennage of the helicopter.
- **Dynamics:** Concerns the motion of the blades and how this motion is affected by aerodynamics and inertial forces.
- **Stability and Control:** Involves the dynamics of the aircraft as a whole, that is, how the forces and moments from the rotors, fuselage, and empennage affect the motion of the fuselage and the handling of the rotorcraft.
- **Structures:** Particular emphasis on composite materials to save weight of rotor blades and fuselage.

- **Acoustics:** Involves understanding the aerodynamically-induced noise of the rotor (branch of CFD).
- **Propulsion and Drivetrains:** Turboprops that have to operate in hostile conditions (*e.g.*, sand, extreme heat and cold).
- **Autonomy:** With Urban Air Mobility and the rise of unmanned flight, demand is growing for automatic systems that are able to steer the rotorcraft within a network of aircraft, avoid collisions, and take decisions.



Figure 1.10: Interdisciplinarity of rotorcraft physics.

Because of their interdisciplinarity, the coupled dynamics, aerodynamics, and structural mechanics of rotorcraft are very difficult to accurately model. Particular challenges are associated with: (i) the complex aerodynamic interactions between different components on the aircraft, such that one cannot just use wind tunnel data to model aerodynamic forces; (ii) the dynamics being very high order in that each rotor adds additional degrees of freedom; and (iii) the difficulty of gathering comprehensive and accurate flight test data because of vibrations, downwash effects, rotating systems, and the fact that one cannot normally measure rotor loads or degrees of freedom.

#### 1.4.1 Contemporary Challenges

Simulations of rotorcraft flight dynamics have advanced significantly over the past decade. To provide rapid simulations of generalized maneuvering flight, flight dynamics models were once restricted to relatively low fidelity aeromechanics models, *e.g.*, finite-state inflow, rigid blade element models. On the other hand, comprehensive aeromechanics simulations historically used much higher fidelity aeromechanics, *e.g.*, free vortex-wake modeling or even CFD coupled with structural dynamics, at the cost of longer run times with analysis restricted to trim or very simple maneuvers. But in recent years, increasingly higher fidelity aeromechanics are making their way into flight dynamics simulations, and even real-time piloted simulations. Real-time time-accurate free wake modeling was implemented in the General Helicopter (GenHel) [How80] simulation and demonstrated using the CHARM Wake Module [Hor+06] in the early two-thousands. The CHARM Wake Module and was subsequently implemented in Navy training simulators coupled with ship airwake effects [KWH15]. FLIGHTLAB has the capability to use Viscous Vortex Particle Models (VVPM) [ZH10]. Both free wake and VVPM models have the capability to predict rotor inflow and rotor wake interference effects in generalized maneuvering flight, moving beyond simplified models and empirical

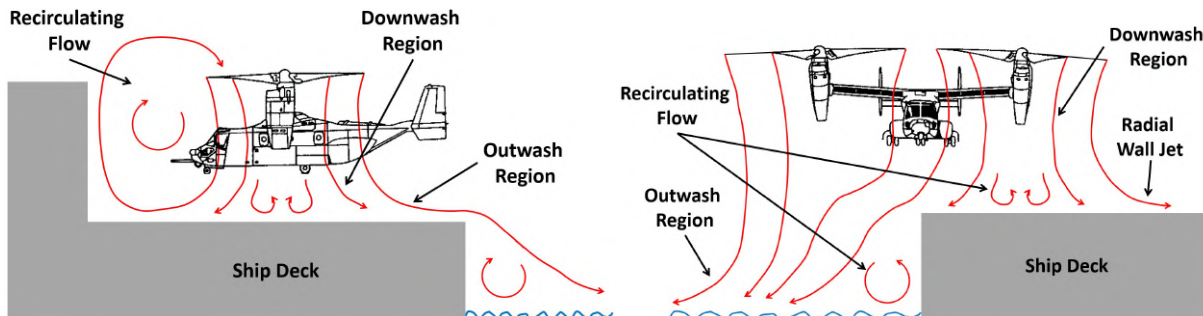
models that have been historically used in flight simulations. In 2017, [Oru+17] even investigated the feasibility of using Euler-based Computational Fluid Dynamics (CFD) methods in real-time simulation models. While those results indicated that such an approach is theoretically possible, the CFD would need to be greatly simplified and rely on massively parallelized computations. In any case, the gap between the fidelity of rotorcraft flight simulation models and rotorcraft comprehensive models is steadily closing.

In the meantime, new configurations have become more complex. Future Vertical Lift (FVL) and Urban Air Mobility (UAM) configurations feature multiple rotors, high levels of aerodynamic interactions, and in the case of UAM, high RPM / variable speed rotors. These features drive the need for advanced aeromechanics models while at the same time making real-time simulation (or even sufficiently fast execution speeds for routine design) much more difficult. For example, time steps in rotor models are driven by the minimum blade sweep per time step, so computational cost goes up with smaller, higher RPM rotors. Modeling aerodynamic interactions requires larger amounts of wake to be computed, and rigid rotor systems require more costly structural dynamics models of the blades. Thus, while more advanced aeromechanics models are feasible, it is likely that in many cases, execution speeds required for real-time simulations or routine design applications will remain elusive.

It is therefore critical that high-fidelity aeromechanics models are formulated in such a way that they can be readily linearized and/or simplified to extract more tractable and less expensive models. Linearized state space models are particularly attractive from the control designer's perspectives. Not only are linearized models used in a majority of practical control design methodologies, but linear model analysis provides many physical insights to system dynamics. To this end, a first-order state variable implementation of the aeromechanics (or state-space implementation) that can be efficiently linearized is a highly desirable feature for future advanced simulations.

#### 1.4.2 Rotor Interaction with Obstacles

In August 2017 an MV-22B Osprey crashed into the ship-deck of USS Green Bay off the coast of Queensland, Australia, killing three and injuring twenty-three. A similar occurrence in December 2015 saw a near-miss in which an Osprey landed short of the deck of an amphibious transport ship, and hung halfway off the back of the ship. Subsequent investigations attributed the cause of both mishaps to heavy rotor downwash which, in its interactions with the ship deck, ship hull, and water surface, recirculated into the rotor causing increased power demands and an uncontrolled response about the roll axis, ultimately leading to a tragic end [Eck18]. Examples of these shipboard interactions that include ground effect due to ship deck and sea surface, and recirculation due to vertical walls are shown qualitatively in Fig. 1.11 for a tilt-rotor aircraft.



(a) Side view of a tiltrotor experiencing ground effect and recirculation due to the ship deck and superstructures. (b) Front view of a tiltrotor in a ship deck crossing experiencing ground effect and recirculation due to the sea surface, ship deck, and ship hull.

Figure 1.11: Examples of rotor wake and ship-deck interactions in shipboard operations for a tiltrotor aircraft.

As such, modeling of the rotor downwash and its interactions with the sea surface, ship deck, and ship superstructures is key in understanding the adverse effect on the flight dynamics and performance of rotorcraft in shipboard operations. Moreover, the ability to replicate these interactions in real-time flight simulations could help supplement the creation of Launch and Recovery Envelopes (LREs) aboard naval vessels. In fact,

this virtual approach to LRE certification could be used to replace potentially unsafe live simulations during a Dynamic Interface (DI) period. Additionally, flight control laws designed to compensate for the adverse effect of shipboard interactions could lead to constructive simulations to further supplement and abate the cost of LRE certification, and to enabling fully-autonomous launch and recovery. Key to the development of flight control laws is the derivation of linear models of the coupled rotorcraft and wake dynamics that account for adverse shipboard interactions.

These features, like for FVL and UAM configurations modeling, drive the need for advanced aeromechanics models while at the same time making real-time speeds much more difficult. A number of free-wake solutions were developed over the years for modeling ground effect [GAL05; rW04; SM87], including partial ground effect and sloped surfaces [Xin99]. Interactions with more complex objects, such as naval ships, have been investigated using a variety of methods including free-vortex wake modeling [McKillip2002], Euler-based CFD methods [Alp+07; Oru+17], finite state inflow models [ZRH13], and grid-based models [FOH14]. However, none of these methods demonstrated real-time performance. Thus, also for modeling aerodynamic interactions with obstacles, it is important that high-fidelity aeromechanics models are formulated in such a way, that they can be readily linearized and/or simplified to extract more tractable and less expensive models.

There have been some recent efforts to extract linearized state-space models from free-wake and VVPM models using system identification methods [He+17; Kel+19]. These approaches perform frequency sweep excitations on the rotor wake model, then perform frequency domain system identification to extract a low-order linearized models. These are in the form of finite-state inflow models and thus can be readily employed in simulation models. The method has the advantage that it can be applied to almost any wake model, and the wake model does not need to be in state variable form. However, it is not a self-contained or automated process. Frequency sweeps need to be generated across the range of flight conditions of interest, and the system identification process needs to be performed and checked for each of these flight conditions.

In [Cel05], a state-space free-wake model is introduced in which the method of lines is used to express the partial differential equations (PDEs) constituting the University Maryland Free Wake Model [BL95; Bha01] into first order state variable form. The formulation of the Maryland Free Wake model is well-suited for state space implementation due to the introduction of the wake age parameter, such that a particular wake state represents the position of a free wake node of a given age. The wake age is an angular distance measured along the vortex starting from the vortex release point on the wing/blade trailing edge. The underlying PDEs are governed by the Biot-Savart law, which is the most expensive part of the free-wake computation. These PDEs are discretized with respect to the wake age using a fourth-order 5-point biased upwind (5PBU4) scheme. The discretized system becomes a set of first-order ODEs in time (*i.e.*, a state space system) which can be accurately integrated forward in time and linearized. This wake model consisted of only the wake node positions. The vortex strength was not considered in the systems state so presumably vortex strength is constant along the filament.

## 1.5 Control Challenges

Rotorcraft are difficult to fly due to their inherent unstable flight dynamics, high order dynamics, and inter-axis coupling. Because of their unstable flight dynamics, rotorcraft have no tendency to hold trim attitude at low and speeds so that the pilot must actively regulate all four control axes, effectively acting as a feedback control system. Further, rotocraft have a restrictive flight envelope due to complex power and structural limits that need to be monitored by the pilot, which greatly contributes to the pilot workload. This task is generally demanding and can be alleviated by the use of Automatic Flight Control Systems (AFCS), as shown in Fig. 1.12. The primary role of the flight control system is to improve the handling qualities of the aircraft, alleviate pilot workload, and to yield to a simple and predictable closed-loop dynamic response to a commanded output. One important concept is that of *response type*, which identifies which state exhibits proportional response to a control input (in the short term at least). The natural response type for a rotorcraft is angular rate command, meaning that a stick input will result in a proportional response in the angular rates or vertical speed.

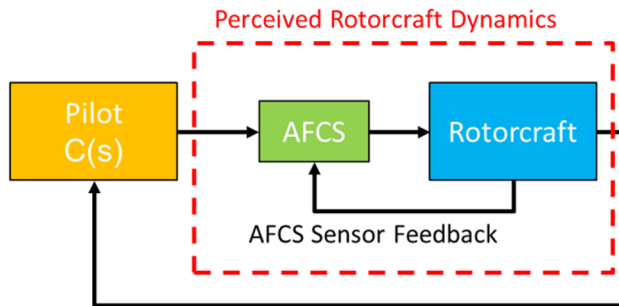


Figure 1.12: Automatic Flight Control System.

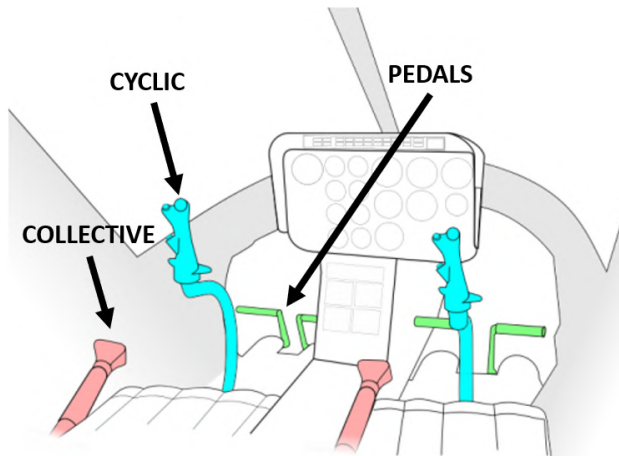


Figure 1.13: Helicopter primary controls.

### 1.5.1 Conventional Main-Tail Rotor Helicopter

For a conventional single rotor helicopter pilots have four primary controls, as shown in Fig. 1.13 and described as follows. Lateral cyclic is a left/right displacement of the center stick that provides bank angle control through lateral rotor disk tilt. Longitudinal cyclic is a fore/aft displacement of the center stick that provides pitch control through longitudinal rotor disk tilt. Collective corresponds to an up/down movement of the left hand lever that changes the main rotor thrust. Pedals provide yaw control through tail rotor collective pitch. Forward and lateral speed are indirectly controlled through the aircraft attitude. The same control axes are used for other rotorcraft configurations, but with different mechanisms to effect control (*e.g.*, differential lateral cyclic on a tandem for yaw axis control). The response type of a helicopter is rate command, meaning that pilot inputs are directly proportional to the angular rates response.

On the other hand, rotorcraft in forward flight are flown differently. Consider the case where a helicopter is flying in forward flight at a speed great than approximately 60 kts and the pilots wants to gain altitude. To increase the altitude, the pilot applied positive longitudinal stick to tilt the thrust vector aft and thus provide positive (*i.e.*, nose up) pitch rate (Fig. 1.15a). Then, the pilot releases the longitudinal stick once the helicopter has entered a steady climb (Fig. 1.15b). Once the target altitude is reached, to stop the climb, the pilot applies negative longitudinal stick to tilt the thrust vector forward and thus provide negative (*i.e.*, nose down) pitch rate (Fig. 1.15c). To return to level flight, the pilot releases the longitudinal stick (Fig. 1.15d). As such, in high-speed forward flight altitude is regulated with the longitudinal cyclic rather than with the collective, thus using the rotor almost like an horizontal stabilizer in a fixed-wing aircraft.

It is worth noting that not only primary flight controls provide desired effects like those described above, but also adverse effects like cross coupling. There are three major cross-coupling effects for conventional helicopter configurations:

- **Roll-to-Pitch and Pitch-to-Roll:** In forward flight the effective cyclic phasing changes such that longitudinal/lateral stick commands will produce a lateral/longitudinal off-axis response.

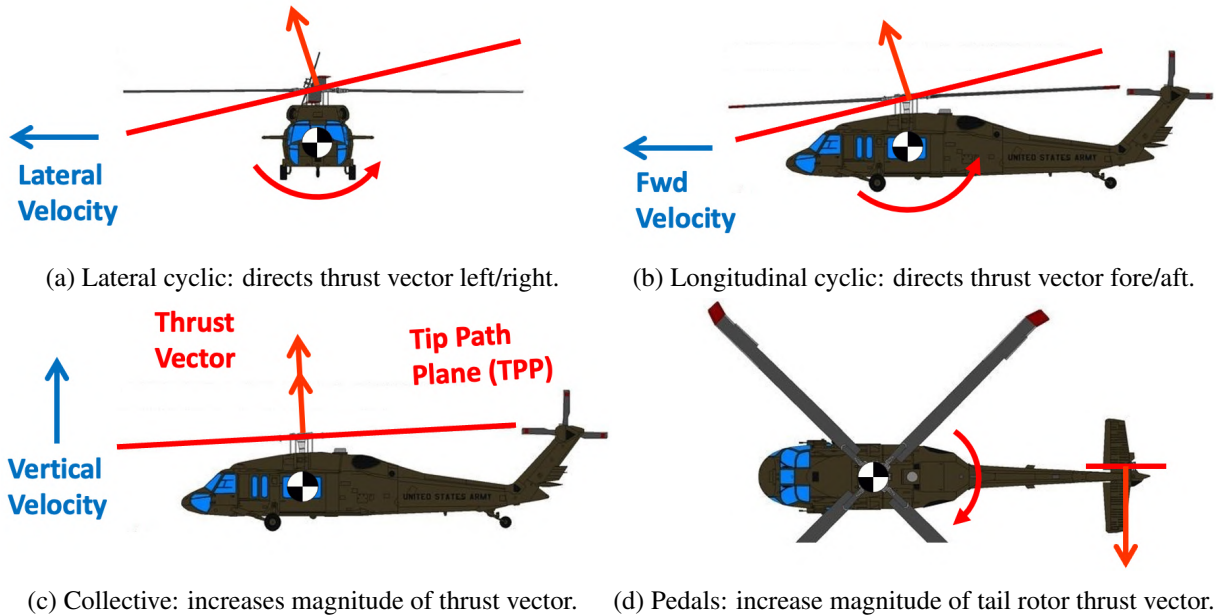


Figure 1.14: Primary helicopter controls.

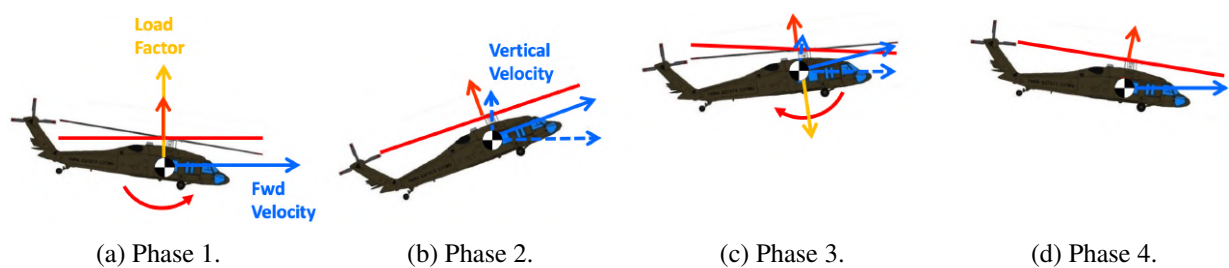


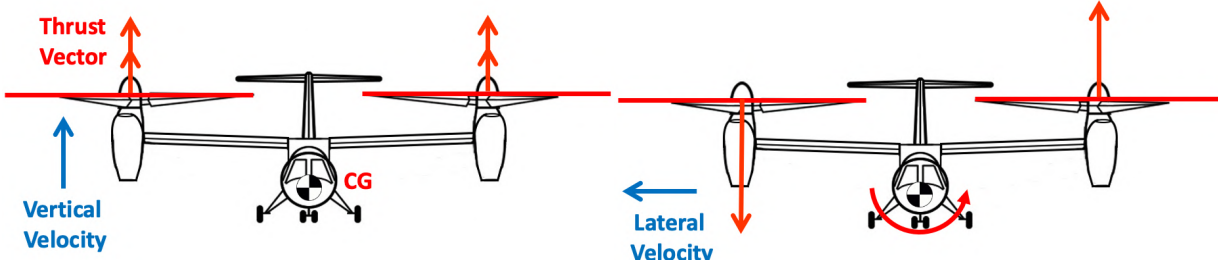
Figure 1.15: Use of helicopter primary controls in forward flight: climb sequence.

- **Thrust-to-Yaw:** Changes in collective pitch result in changes in main rotor torque reaction, such that these changes need to be compensated with pedal inputs.
- **Yaw-to-Roll:** Because the tail rotor is typically above the center of gravity (CG), changes in tail rotor thrust produce a rolling moment.

## 1.5.2 Tiltrotor Aircraft

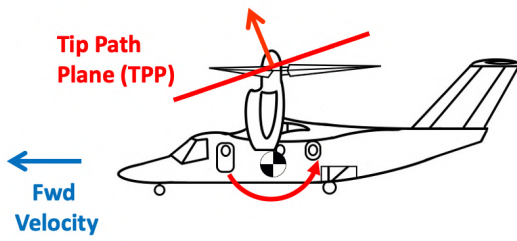
Compound rotorcraft and tiltrotors add another layer of complexity as these rotorcraft typically feature auxiliary control surfaces and/or rotors, making the number of control effectors greater than the axes being controlled (*i.e.*, four: roll, pitch, yaw, and heave). As such, these rotorcraft feature redundant control effectors. Either the pilot or the AFCS must appropriately redistribute the control signal across the control effectors depending on the flight condition. For instance, consider the control mixing of a tiltrotor aircraft in helicopter mode shown in Fig. 1.16. Collective pitch increases the magnitude of the thrust vector of both rotors to control vertical velocity and altitude (Fig. 1.16a). Differential collective pitch is used to increase/decrease the thrust vector magnitude on the left/right rotor and provide bank angle control. Lateral speed is indirectly controlled via the bank angle (Fig. 1.16b). It is worth noting that lateral speed control can be achieved somewhat independently of the bank angle by the use of lateral cyclic on both rotors. However, tiltrotors do not always feature lateral cyclic control. One example is the AgustaWestland AW609 where lateral cyclic was removed in the early stages of development due to weight saving measures. On the other hand, the Bell V-22 Osprey features lateral cyclic. Longitudinal cyclic is used to direct the thrust vector of the rotors fore/aft and thus to provide pitch angle control and indirectly longitudinal speed control (Fig. 1.16c). Lastly, differential longitudinal cyclic is used to direct the thrust vector of the left/right rotor fore/aft asymmetrically to provide

directional control (Ref. 1.16d).

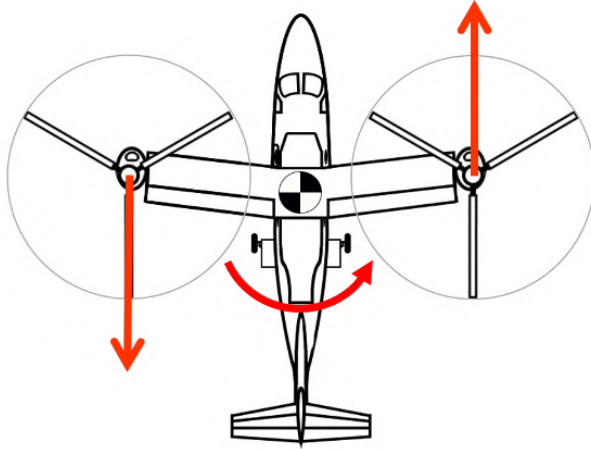


(a) Collective: increases magnitude of thrust vector.

(b) Longitudinal cyclic: directs thrust vector fore/aft.



(c) Differential collective: increases thrust vector magnitude of left/right side.



(d) Differential longitudinal cyclic: directs thrust vector fore/aft asymmetrically.

Figure 1.16: Primary tilt-rotor controls in helicopter mode.

Naturally, tiltrotors in high-speed forward flight are flown differently as their rotors are tilted 90 deg forward (Fig. 1.17). Collective pitch is used to increase the magnitude of the thrust vector of both rotors and thus to control forward speed (Fig. 1.17a). Flaperons are used to provide rolling moment and thus bank angle control (Fig. 1.17c). The elevator is used to provide pitching moment and to indirectly control vertical speed (Fig. 1.17b). The rudder is used to provide rolling moment and thus directional control (Fig. 1.17d).

Cross-coupling effects are present also in tilt-rotor aircraft, namely roll-to-yaw coupling. Differential collective pitch produces differential rotor torque that needs to be counteracted with pedal inputs. Otherwise, tiltrotor aircraft are very symmetric and have low cross coupling.

### 1.5.3 Counter-Rotating Coaxial Helicopter

Tandem rotor helicopters are controlled similarly to conventional, single main rotor helicopters in that roll, pitch, and vertical control are applied symmetrically to both rotors (Figs. 1.18a, 1.18b, and ??). The only major difference lies in the use of differential collective pitch for directional control. In fact, differential collective pitch is used to induce a differential change in torque reaction of the counter-rotating rotors and thus a yaw moment imbalance (Fig. 1.18d). Most cross-coupling effects are reduced compared to single main rotor helicopters, although some cross coupling can still occur since the lower rotor operates in the downwash of the upper rotor.

### 1.5.4 Tandem Rotor Helicopter

Control mixing for tandem rotor helicopters is typically set up such that symmetric collective pitch changes the thrust on both rotors to produce vertical force and to control vertical velocity and altitude (Fig. 1.19a). Symmetric lateral cyclic pitch is used to tilt the rotor planes laterally and produce a roll moment (Fig. 1.19b). This provides bank angle control, which is used to indirectly control lateral speed. Differential collective

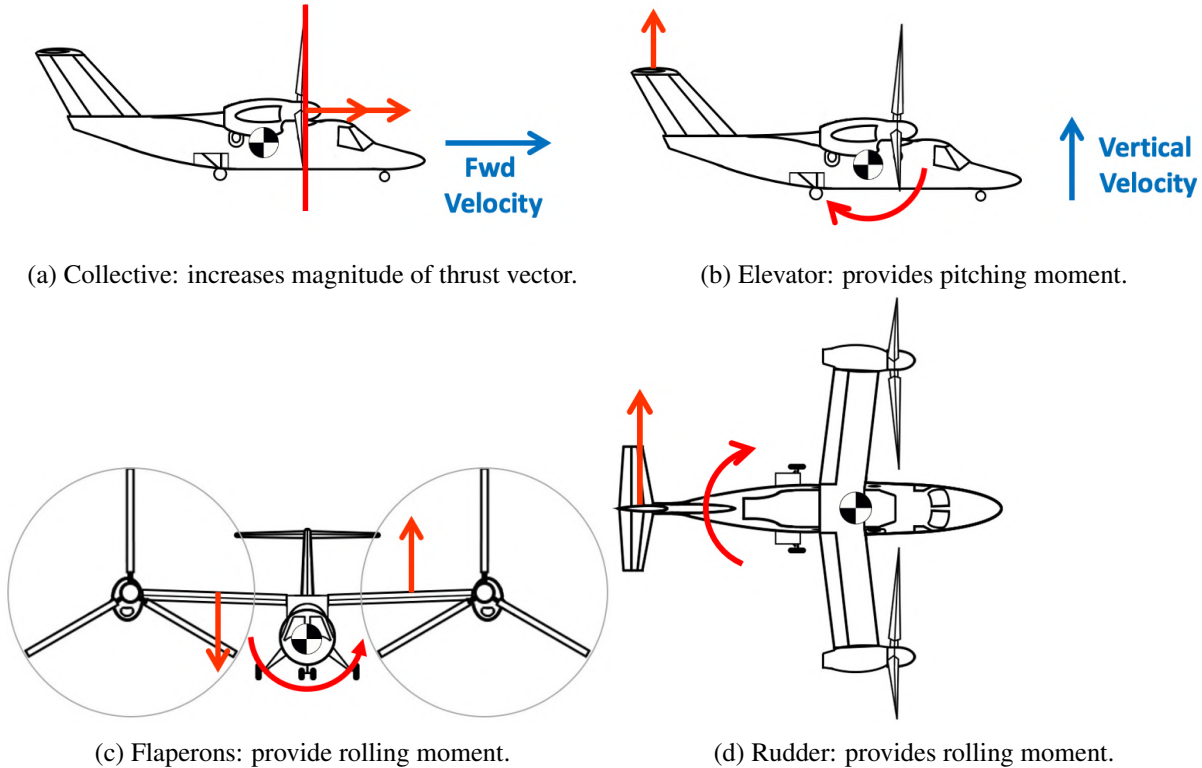


Figure 1.17: Primary tilt-rotor controls in airplane mode.

pitch results in differential rotor thrust to produce pitching moment and provide pitch angle control (Fig. 1.19c). Pitch angle control is used to indirectly control longitudinal speed. Lastly, differential lateral cyclic pitch is used to tilt the front and aft rotors differentially to produce opposite lateral forces on each rotor, which in turns results in a yawing moment and thus directional control (Fig. 1.19d). One can also use longitudinal cyclic pitch to adjust trim attitude in forward flight and optimize performance. Major cross-coupling effects involve pitch-to-yaw coupling, where differential collective pitch produces differential torque. Roll-to-pitch, pitch-to-roll, and thrust-to-yaw couplings are mostly eliminated due to opposite reaction on counter-rotating rotors.

### 1.5.5 Compound Rotorcraft

Consider now another example involving variations of the H-60 platform employing various kinds of redundant control surfaces. The Piasecki X-49A, shown in Fig. 1.20a features wings equipped with flaperons. Flaperons can be actuated symmetrically and/or differentially to provide additional load factor and/or rolling moment, respectively. Each of these actuators offload the main rotor loads depending on the flight condition/maneuver performed. While the horizontal stabilizer incidence of the H-60, shown in Fig. 1.20b is linked with flight speed, it could in theory be actuated independently to provide pitching moment in push-up/pull-over maneuvers to offload the main rotor. This has been the subject of recent studies on load alleviation flight control design [Sae+20].

### 1.5.6 Electric Powered Quad-Rotor

Differently from full-scale rotorcraft, small- and medium-scale electric powered quad-rotors use fixed-pitch rotor blades, but variable rotor speed. Rotors across from one another typically rotate in the same direction, while rotors adjacent to one another rotate in the opposite direction. Vertical force is controlled by varying all rotor speeds together (Fig. 1.21a). Increasing the angular speed of rotors adjacent to one another while decreasing angular speed of rotors on the other side creates either a rolling or a pitching moment (Figs. 1.21b and 1.21c). On the other hand, increasing the angular speed of two rotors across from one another creates

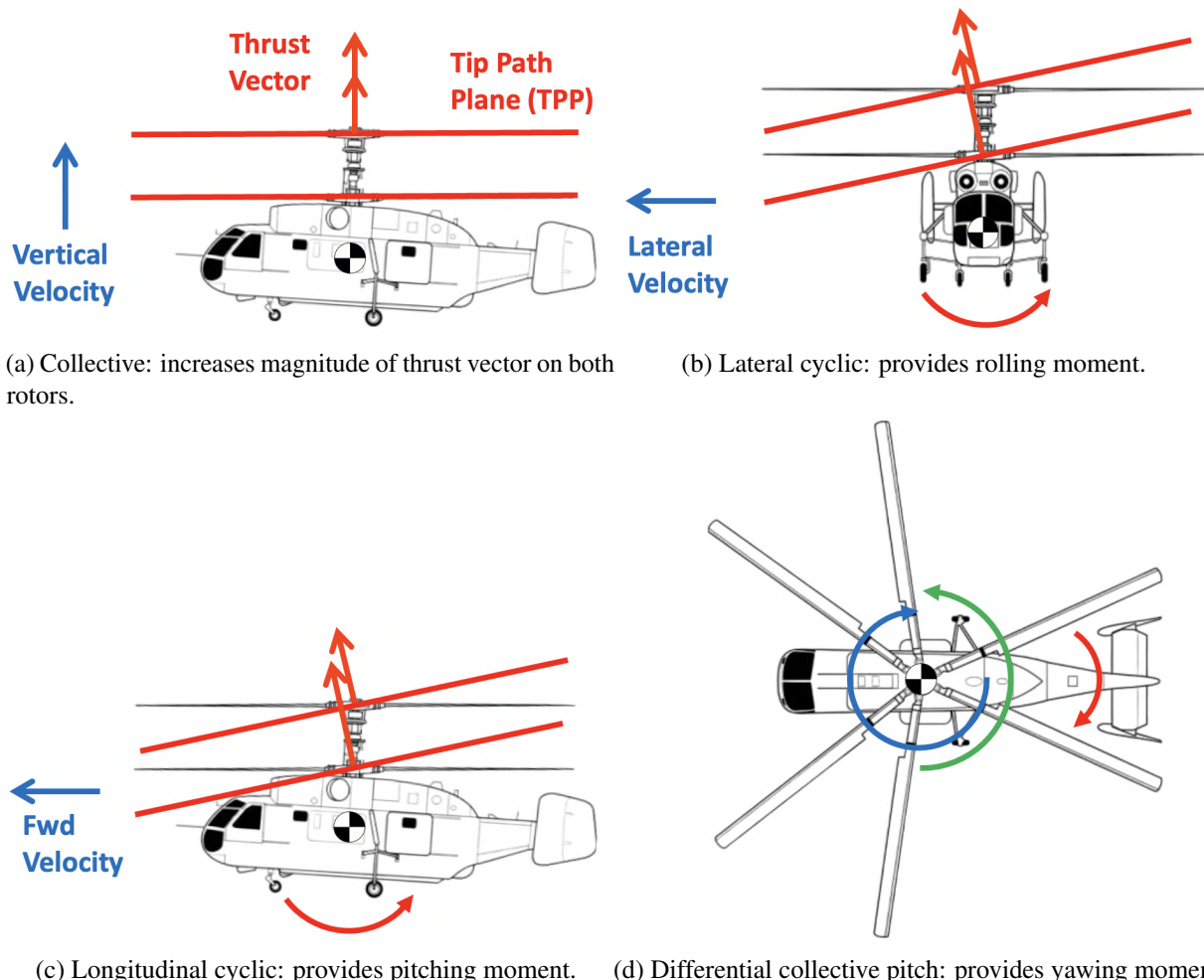
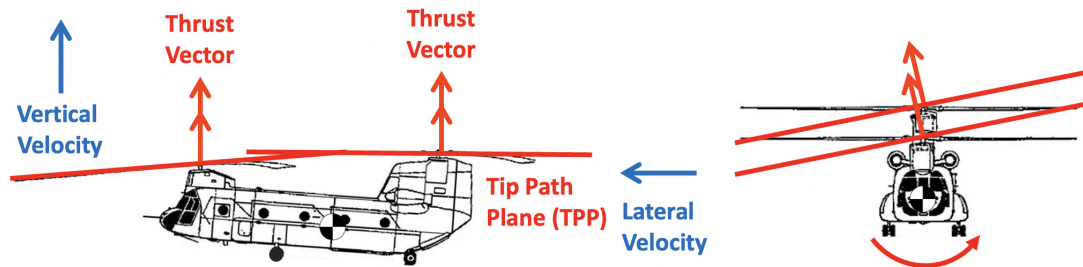


Figure 1.18: Primary controls counter-rotating coaxial helicopter.

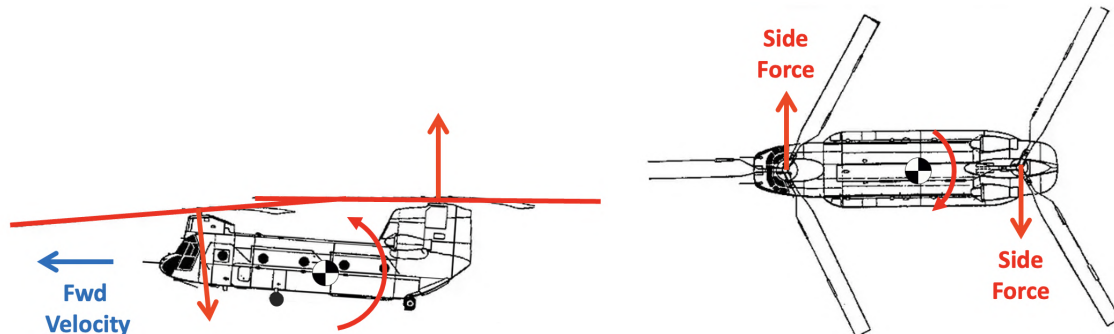
a yawing moment (Fig. 1.21d). The yawing moment can also be enhanced by lateral canting of the rotors. Cross-coupling effects for these configurations are typically small, especially in hover.

## Bibliography

- [Alp+07] E. Alpman et al. “Fully-Coupled Simulations of the Rotorcraft/Ship Dynamic Interface”. In: *Proceedings of the 63<sup>rd</sup> Annual Forum of the American Helicopter Society*. Virginia Beach, VA, May 2007 (cited on page 19).
- [BL95] A. Bagai and G. J. Leishman. “Rotor Free-Wake Modeling Using a Pseudo-Implicit Technique—Including Comparison with Experimental Data”. In: *Journal of the American Helicopter Society* 40.3 (July 1995), pages 29–41. DOI: <https://doi.org/10.4050/JAHS.40.29> (cited on page 19).
- [Bha01] M. J. Bhagwat. “Transient Dynamics of Helicopter Rotor Wakes Using a Time-Accurate Free-Vortex Method”. PhD thesis. College Park, MD: University of Maryland, 2001 (cited on page 19).
- [BML14] K. S. Brentner, P. J. Morris, and L. V. Lopes. “A Method for Predicting the Noise of a Tip-Jet Driven Rotor”. In: *Journal of the American Helicopter Society* (59, 032004 (2014)). DOI: <https://doi.org/10.4050/JAHS.59.032004> (cited on page 14).



(a) Symmetric collective: increases magnitude of thrust (b) Symmetric lateral cyclic: provides rolling moment. vector of both rotors.



(c) Differential collective: provides pitching moment. (d) Differential lateral cyclic: provides yawing moment.

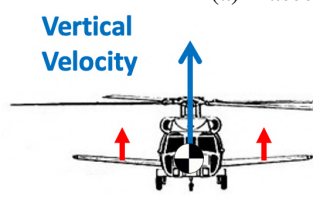
Figure 1.19: Primary controls for a tandem-rotor helicopter.



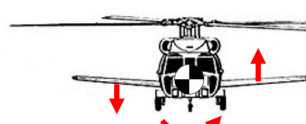
(a) Piasecki X-49A flaperons.



(b) Sikorsky UH-60 stabilator.



(c) Symmetric flaperons: provide load factor.



(d) Differential flaperons: provide rolling moment.



(e) Stabilator: provides pitching moment.

Figure 1.20: Auxiliary control surfaces.

- [Cel05] R. Celi. "State-Space Representation of Vortex Wakes by the Method of Lines". In: *Journal of the American Helicopter Society* 50.2 (Apr. 2005), pages 195–205. DOI: [https://doi.org/1-3092855](https://doi.org/10.4050/1-3092855) (cited on page 19).
- [Eck18] M. Eckstein. "Investigation: 2017 Osprey Crash Due to Heavy Downwash; Excessive Aircraft Weight May Have Contributed". In: *USNI News* (May 21, 2018.). URL: <https://news.usni.org/2018/05/21/investigation-2017-osprey-crash-due-heavy-downwash-excessive-aircraft-weight-may-contributed> (cited on page 18).

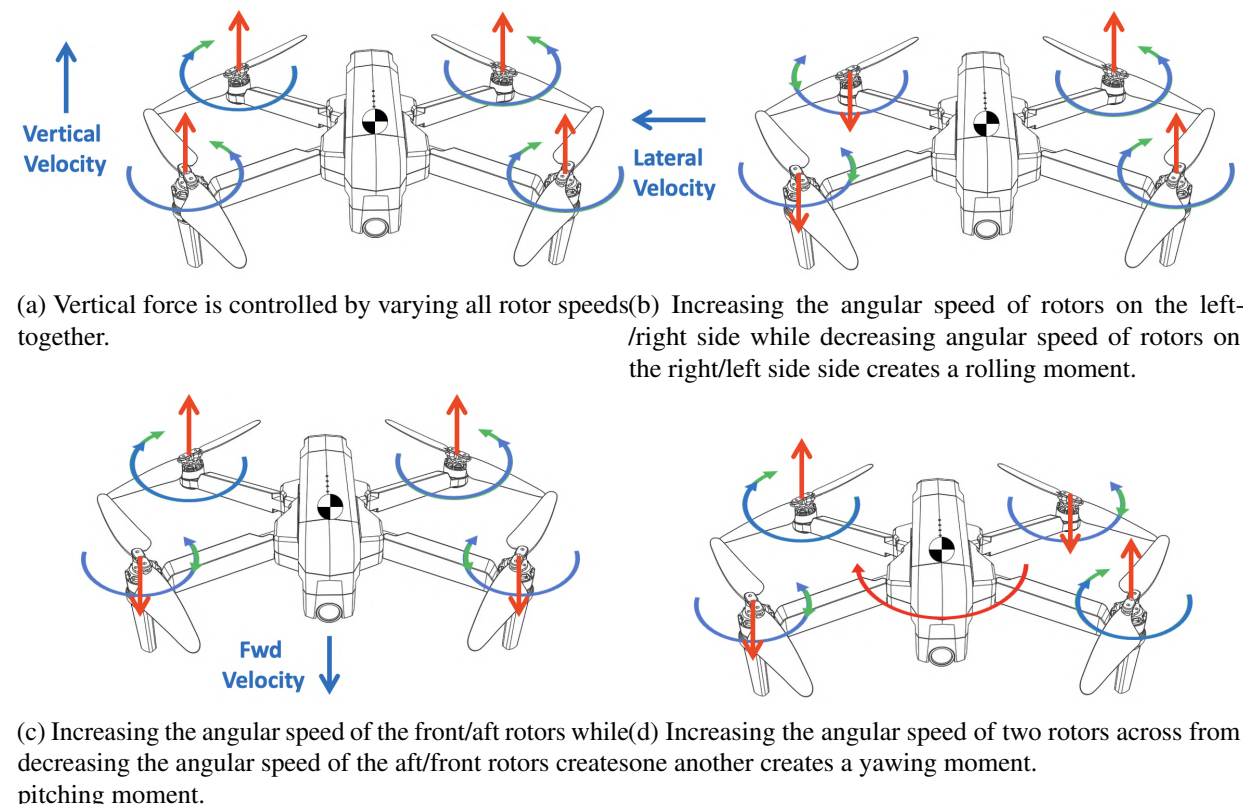


Figure 1.21: Primary tilt-rotor controls in airplane mode.

- [FOH14] L. Friedmann, P. Ohmer, and M. Hajek. “Real-Time Simulation of Rotorcraft Downwash in Proximity of Complex Obstacles Using Grid-Based Approaches”. In: *Proceedings of the 70<sup>th</sup> Annual Forum of the American Helicopter Society*. Montreal, Canada, June 2014 (cited on page 19).
- [GAL05] D. A. Griffiths, S. Ananthan, and J. G. Leishman. “Predictions of Rotor Performance in Ground Effect Using a Free-Vortex Wake Model”. In: *Journal of the American Helicopter Society* 50.4 (Oct. 2005), pages 302–314. DOI: 10.4050/jahs.62.012006 (cited on page 19).
- [He+17] C. He et al. “State-Space Inflow Model Identification from Viscous Vortex Particle Method for Advanced Rotorcraft Configurations”. In: *Proceedings of the 73<sup>rd</sup> Annual Forum of the Vertical Flight Society*. Fort Worth, TX, May 9-11, 2017. (Cited on page 19).
- [Hir58] H. B. Hirsch. “The Hot Cycle Jet Helicopter”. In: *Proceedings of the 14<sup>th</sup> Annual Forum of the American Helicopter Society*. Washington, DC, Apr. 1958 (cited on page 14).
- [Hol54] K. H. Holm. “The Technical Aspects of the Transfer of Fuel to a Tip Mounted Ramjet Engine Combustion Chamber”. In: *Proceedings of the 10<sup>th</sup> Annual Forum of the American Helicopter Society*. Washington, DC, May 1954 (cited on page 14).
- [Hor+06] J. F. Horn et al. “Implementation of a Free-Vortex Wake Model in Real-Time Simulation of Rotorcraft”. In: *AIAA Journal of Computing, Information, and Communications* 3.3 (Mar. 2006), pages 93–107. DOI: <https://doi.org/10.2514/1.18273> (cited on page 17).
- [How80] J. J. Howlett. *UH-60A Black Hawk Engineering Simulation Program. Volume 1: Mathematical Model*. Technical report. NASA-CR-166309, 1980. (Cited on page 17).
- [Kel+19] J. Keller et al. “Linearized Inflow and Interference Models from High Fidelity Free Wake Analysis for Modern Rotorcraft Configurations”. In: *Proceedings of the 75<sup>th</sup> Annual Forum of the Vertical Flight Society*. Philadelphia, PA, May 14-15, 2019. (Cited on page 19).

- [KWH15] J. D. Keller, D. A. Wachspress, and J. C. Hoffler. “Real Time Free Wake and Ship Airwake Model for Rotorcraft Flight Training Applications”. In: *Proceedings of the 71<sup>st</sup> Annual Forum of the American Helicopter Society*. Virginia Beach, VA, May 2015 (cited on page 17).
- [Loc50] R. M. Lockwood. “DESIGN OF A HELICOPTER WITH A JET-PROPELLED ROTOR”. Master’s thesis. Corvallis, OR: Oregon State University, 1950 (cited on page 14).
- [Mor58] P. H. L. Morain. “Cold Jet Cycle Helicopters”. In: *Proceedings of the 14<sup>th</sup> Annual Forum of the American Helicopter Society*. Washington, DC, Apr. 1958 (cited on page 14).
- [Oru+17] I. Oruc et al. “Towards real-time pilot-in-the-loop CFD simulations of helicopter/ship dynamic interface”. In: *International Journal of Modeling, Simulation, and Scientific Computing* 8.4 (Jan. 2017). DOI: <https://doi.org/10.1142/S179396231743005X> (cited on pages 18, 19).
- [rW04] R. E. rown and G. R. Whitehouse. “Modeling Rotor Wakes in Ground Effect”. In: *Journal of the American Helicopter Society* 49.3 (2004), pages 238–249. DOI: 10.4050/JAHS.49.238 (cited on page 19).
- [SM87] H. A. Saberi and M. D. Maisel. “A Free Wake Rotor Analysis Including Ground Effect”. In: *Proceedings of the 43<sup>rd</sup> Annual Forum of the American Helicopter Society*. Saint Louis, MO, May 1987 (cited on page 19).
- [SEH22] U. Saetti, J. Enciu, and J. F. Horn. “Flight Dynamics and Control of an eVTOL Concept Aircraft with a Propeller-Driven Rotor”. In: *Journal of the American Helicopter Society* 67.3 (2022), pages 153–166. DOI: <https://doi.org/10.4050/JAHS.67.032012> (cited on page 14).
- [Sae+20] U. Saetti et al. “Handling-Qualities Perspective on Rotorcraft Load Alleviation Control”. In: *Journal of Guidance, Control, and Dynamics* (2020), pages 1–13. DOI: <https://doi.org/10.2514/1.G004965> (cited on page 23).
- [Sli+18] C. Sliva et al. “VTOL Urban Air Mobility Concept Vehicles for Technology Development”. In: *Paper AIAA 2018-3847, Proceedings of the 2018 Aviation Technology, Integration, and Operations Conference*. Atlanta, GA, June 2018. DOI: <https://doi.org/10.2514/6.2018-3847> (cited on page 14).
- [Str+20] A. Straubinger et al. “An overview of current research and developments in urban air mobility – Setting the scene for UAM introduction”. In: *Journal of Air Transport Management* 87 (2020), page 101852. DOI: <https://doi.org/10.1016/j.jairtraman.2020.101852> (cited on page 14).
- [Xin99] H. Xin. “Development and Validation of a Generalized Ground Effect Model for Lifting Rotors”. PhD thesis. Atlanta, GA: Georgia Institute of Technology, 1999 (cited on page 19).
- [ZH10] J. Zhao and C. He. “A Viscous Vortex Particle Model for Rotor Wake and Interference Analysis”. In: *Journal of the American Helicopter Society* 55.1 (Jan. 2010). DOI: <https://doi.org/10.4050/JAHS.55.012007> (cited on page 17).
- [ZRH13] J. Zhao, N. Rajmoham, and C. He. “Physics-Based Rotorcraft/Ship Aerodynamic Interaction Modeling in Support of Real Time Flight Simulation”. In: *Proceedings of the 51<sup>st</sup> AIAA Aerospace Science Meeting*. Grapevine, TX, Jan. 2013. DOI: 10.2514/6.2013-227 (cited on page 19).

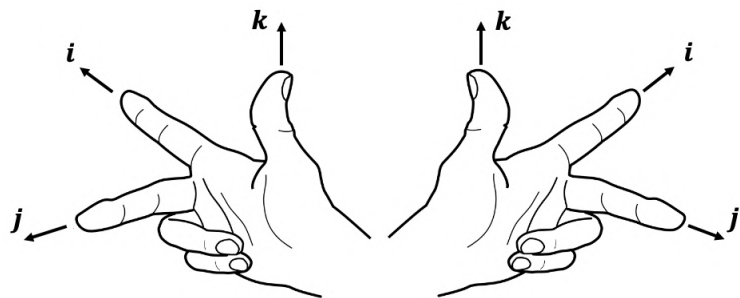




## 2. Review of Kinematics and Dynamics

### 2.1 Reference Frames, Coordinate Systems, and Notation

#### 2.1.1 Coordinate Systems and Reference Frames



(a) Right-handed coordinate system (b) Left-handed coordinate system.

Figure 2.1: Coordinate systems.

Reference frames are a fundamental concept in the field of flight mechanics. A reference frame can be thought of as a rigid body with no mass or inertia. A complementary concept to a reference frame is a coordinate system. To characterize a coordinate system, define a set of three vectors  $\mathbf{i}$ ,  $\mathbf{j}$ ,  $\mathbf{k}$  with the following properties:

1. Unit length:

$$\|\mathbf{i}\| = \|\mathbf{j}\| = \|\mathbf{k}\| = 1 \quad (2.1)$$

2. Orthonormal to one another such that  $\mathbf{i}$ ,  $\mathbf{j}$ ,  $\mathbf{k}$  form an orthonormal basis:

$$\mathbf{i} \cdot \mathbf{j} = \mathbf{j} \cdot \mathbf{k} = \mathbf{k} \cdot \mathbf{i} = 0 \quad (2.2)$$

3. Are right handed (Fig. 2.1a), such that:

$$\mathbf{i} = \mathbf{j} \times \mathbf{k} \quad (2.3a)$$

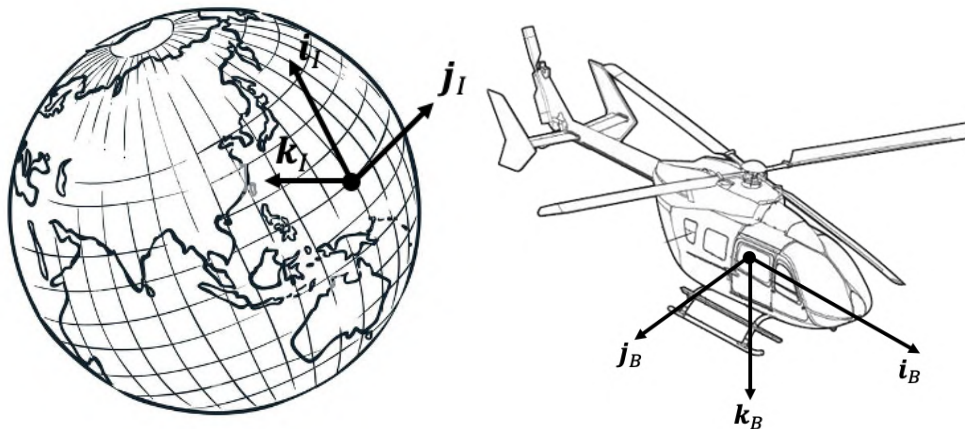
$$\mathbf{j} = \mathbf{k} \times \mathbf{i} \quad (2.3b)$$

$$\mathbf{k} = \mathbf{i} \times \mathbf{j} \quad (2.3c)$$

Note that, for a left-handed system (Fig. 2.1b), Eq. (2.3c) changes to  $-\mathbf{k} = \mathbf{i} \times \mathbf{j}$ . In general, only right-handed frames will be used in this book.

A coordinate system is defined by the  $\mathbf{i}$ ,  $\mathbf{j}$ ,  $\mathbf{k}$  vectors and is rigidly attached to a reference frame.

### 2.1.2 Key Reference Frames



(a) Inertial frame, also known as North-East-Down (NED) frame.

(b) Body frame.

Figure 2.2: Coordinate systems.

Although rotorcraft feature several reference frames of importance to their flight dynamics, only the most two important reference frames are introduced here.

1. **Inertial Frame (I)**: Defined as a frame attached to any body which is not being acted upon by an outside net force. By Newton's second law, this frame is either at rest or moves at a constant speed.

$$\mathbf{F}' = \mathbf{0} \quad = m\mathbf{a} \quad \Rightarrow \quad \mathbf{a} = \mathbf{0} \quad \Rightarrow \quad \mathbf{v} = \text{const.} \quad (2.4)$$

Not only the inertial frame is a non-accelerating frame, it is also a non-rotating frame. In fact, frame rotation results in the velocity of its unit vector basis to not be constant in time. A frame fixed to the surface of the Earth has sufficiently low acceleration for the purpose of rotorcraft flight dynamics analysis. As such, this frame can be pragmatically considered as the inertial frame. This frame is also known as North-East-Down (NED) frame, where  $\mathbf{i}_I$  identifies the North direction,  $\mathbf{j}_I$  identifies the East direction,  $\mathbf{k}_I$  identifies the Down (toward center of the Earth) direction (Fig. 2.2a).

2. **Body Frame (B)**: This frame is typically centered at the rotorcraft center of mass. The axes are defined such that  $\mathbf{i}_B$  points out of the nose,  $\mathbf{j}_B$  points out of the right wing (imagining the rotorcraft is equipped with one), and  $\mathbf{k}_B$  points out of the bottom of the aircraft (Fig. 2.2b).

### 2.1.3 Notation

The following notation will be used throughout the book:

- $\mathbf{a}$   $\equiv$  “vector”  $\mathbf{a}$ ,
- $\mathbf{i}_C, \mathbf{j}_C, \mathbf{k}_C$  are unit vectors where the subscript denotes the reference frame (in this case, the reference frame is  $(C)$ ),
- $\mathbf{r}_{O \rightarrow P} \equiv$  position vector from point O to point P,
- $\mathbf{v}_{B/I} \equiv$  velocity vector of point B with respect to frame  $(I)$ ,
- $\mathbf{a}_{B/I} \equiv$  acceleration vector of point B with respect to frame  $(I)$ ,
- $\boldsymbol{\omega}_{C/I} \equiv$  angular velocity vector of body  $(C)$  with respect to frame  $(I)$ ,
- $\boldsymbol{\alpha}_{C/I} \equiv$  angular acceleration vector of body  $(C)$  with respect to frame  $(I)$ ,
- $\mathbf{H}_{C/I}^D \equiv$  angular momentum vector of body  $(C)$  with respect to frame  $(I)$  about point D,

- $\mathbf{T}_{I \rightarrow A} \equiv$  transformation matrix relating the (I) and (A) frames unit vectors such that:

$$\begin{bmatrix} \mathbf{i}_A \\ \mathbf{j}_A \\ \mathbf{k}_A \end{bmatrix} = \mathbf{T}_{I \rightarrow A} \begin{bmatrix} \mathbf{i}_I \\ \mathbf{j}_I \\ \mathbf{k}_I \end{bmatrix} \quad (2.5)$$

- $\textcircled{B} \frac{ds}{dt} \equiv$  time derivative of vector  $s$  taken in the (B) frame. Note that, in general,

$$\textcircled{B} \frac{ds}{dt} \neq \textcircled{C} \frac{ds}{dt} \quad (2.6)$$

#### 2.1.4 Vector Components and Cross Product

Consider some vector components in the reference frame (I):

$$\mathbf{f} = f_1 \mathbf{i}_I + f_2 \mathbf{j}_I + f_3 \mathbf{k}_I \quad (2.7)$$

where  $\mathbf{f}_1, \mathbf{f}_2, \mathbf{f}_3$  are the projections of  $\mathbf{f}$  onto the orthogonal axes of frame (I). We can equivalently express  $\mathbf{f}$  in a different coordinate system (e.g., frame (C)) as:

$$\mathbf{f} = g_1 \mathbf{i}_C + g_2 \mathbf{j}_C + g_3 \mathbf{k}_C \quad (2.8)$$

Hence, the same vector has different components when expressed in a different coordinate system. Sometimes, the following notation will be used to express the coordinates of a vector:

$$\mathbf{f} = \begin{bmatrix} f_1 \\ f_2 \\ f_3 \end{bmatrix} \quad (2.9)$$

When doing this, one needs to be very careful about the coordinate system it is being used to express these components, as the coordinate system is not explicitly expressed. Consider now two vectors:

$$\mathbf{b} = b_1 \mathbf{i}_A + b_2 \mathbf{j}_A + b_3 \mathbf{k}_A \quad (2.10a)$$

$$\mathbf{c} = c_1 \mathbf{i}_A + c_2 \mathbf{j}_A + c_3 \mathbf{k}_A \quad (2.10b)$$

$$(2.10c)$$

The cross product between these two vectors is given by:

$$\mathbf{d} = \mathbf{b} \times \mathbf{c} = \begin{vmatrix} \mathbf{i}_A & \mathbf{j}_A & \mathbf{k}_A \\ b_1 & b_2 & b_3 \\ c_1 & c_2 & c_3 \end{vmatrix} = \dots = \underbrace{\begin{bmatrix} 0 & -b_3 & b_2 \\ b_3 & 0 - b_1 & \\ -b_2 & b_1 & 0 \end{bmatrix}}_{\text{Skew-symmetric matrix}} \begin{bmatrix} c_1 \\ c_2 \\ c_3 \end{bmatrix} = \begin{bmatrix} b_2 c_3 - b_3 c_2 \\ b_3 c_1 - b_1 c_3 \\ b_1 c_2 - b_2 c_1 \end{bmatrix} \quad (2.11)$$

## 2.2 Rigid Body Kinematics

### 2.2.1 Vector Derivatives

Consider a point P rotating with constant height  $a$  from the  $\mathbf{i}_I - \mathbf{k}_I$  plane about the  $\mathbf{j}_I$  axis with a distance  $l$  from it, and an angular velocity  $\omega$  (Fig. 2.3). The axes  $\mathbf{i}_R, \mathbf{j}_R, \mathbf{k}_R$  form a right-handed orthonormal frame where P lies in the  $\mathbf{i}_I - \mathbf{k}_I$  plane. Consider a position vector from the origin of the (I) frame O to point P:

$$\begin{aligned} \mathbf{r}_{O \rightarrow P} &= l \mathbf{i}_R + a \mathbf{j}_R \\ &= (l \cos \theta) \mathbf{i}_I + a \mathbf{j}_I + (-l \sin \theta) \mathbf{k}_I \end{aligned} \quad (2.12)$$

Differentiating with respect to time yields to the following two expressions:

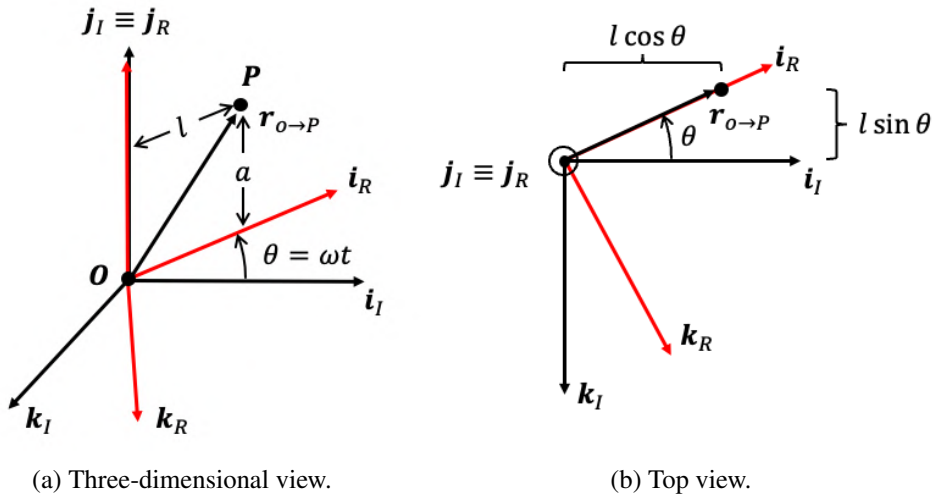


Figure 2.3: point P rotating with constant height  $a$  from the  $i_I - k_I$  plane about the  $j_I$  axis with a distance  $l$  from it, and an angular velocity  $\omega$ .

1. Expression 1:

$$\frac{d}{dt}(\mathbf{r}_{O \rightarrow P}) = \frac{d}{dt}(li_R + aj_R) = 0 \quad (2.13)$$

2. Expression 2:

$$\begin{aligned} \frac{d}{dt}(\mathbf{r}_{O \rightarrow P}) &= \frac{d}{dt}[(l \cos \theta) \mathbf{i}_I + a \mathbf{j}_I + (-l \sin \theta) \mathbf{k}_I] \\ &= -l\omega \sin(\omega t) \mathbf{i}_I - l\omega \cos(\omega t) \mathbf{j}_I \end{aligned} \quad (2.14)$$

It is clear that these two expressions are not equal. Thus, we can conclude that:

$$\textcircled{(R)} \frac{d}{dt}(\mathbf{r}_{O \rightarrow P}) \neq \textcircled{(I)} \frac{d}{dt}(\mathbf{r}_{O \rightarrow P}) \quad (2.15)$$

The reason for this is that in the first expression a time derivative is taken in the  $\textcircled{(R)}$  frame, whereas in the second expression the same derivative is performed in the  $\textcircled{(I)}$  frame. In fact, to an observer in the  $\textcircled{(R)}$  frame P looks like it is not moving, whereas to an observer in the  $\textcircled{(I)}$  frame, indeed, P will appear as in motion. As such, one must specify the reference frame in which the derivative is observed. Note that derivatives of scalars are frame-independent. In general,

$$\textcircled{(A)} \frac{ds}{dt} \neq \textcircled{(B)} \frac{ds}{dt} \quad (2.16)$$

## 2.2.2 Definition of Velocity and Acceleration

Consider a point P moving with respect to frame  $\textcircled{(I)}$ , where  $\textcircled{(I)}$  may or may not be an inertial frame (Fig. 2.4). The definition of velocity of a point P with respect to frame  $\textcircled{(I)}$  is:

$$\mathbf{v}_{P/I} = \textcircled{(R)} \frac{d}{dt}(\mathbf{r}_{O \rightarrow P}) \quad (2.17)$$

The definition of acceleration of a point P with respect to frame  $\textcircled{(I)}$  is:

$$\mathbf{a}_{P/I} = \textcircled{(I)} \frac{d}{dt} \mathbf{v}_{P/I} = \textcircled{(I)} \frac{d}{dt} \left[ \textcircled{(I)} \frac{d}{dt}(\mathbf{r}_{O \rightarrow P}) \right] \quad (2.18)$$

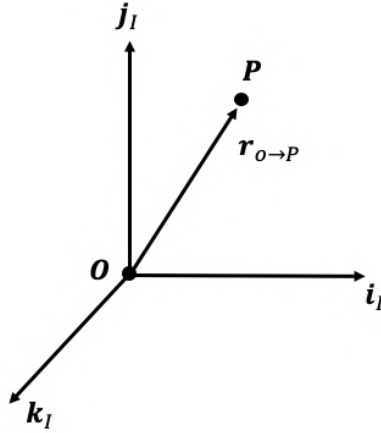


Figure 2.4: Point moving with respect its parent frame.

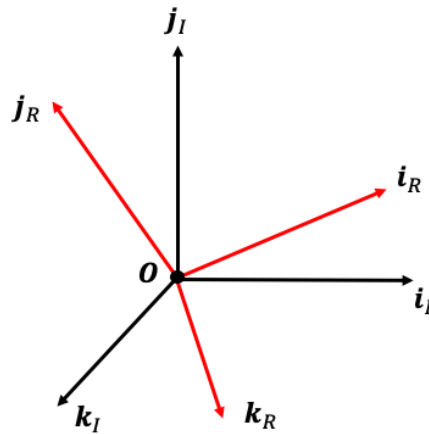


Figure 2.5: Two reference frames sharing the same origin but rotated with respect to each other.

### 2.2.3 Rotation Transformations

Consider two reference frames which share the same origin but are rotated relative to each other (Fig. 2.5). From definition of the dot product, it can be shown that:

$$\begin{aligned}\mathbf{i}_R &= (\mathbf{i}_R \cdot \mathbf{i}_I)\mathbf{i}_I + (\mathbf{i}_R \cdot \mathbf{j}_I)\mathbf{j}_I + (\mathbf{i}_R \cdot \mathbf{k}_I)\mathbf{k}_I \\ \mathbf{j}_R &= (\mathbf{j}_R \cdot \mathbf{i}_I)\mathbf{i}_I + (\mathbf{j}_R \cdot \mathbf{j}_I)\mathbf{j}_I + (\mathbf{j}_R \cdot \mathbf{k}_I)\mathbf{k}_I \\ \mathbf{k}_R &= (\mathbf{k}_R \cdot \mathbf{i}_I)\mathbf{i}_I + (\mathbf{k}_R \cdot \mathbf{j}_I)\mathbf{j}_I + (\mathbf{k}_R \cdot \mathbf{k}_I)\mathbf{k}_I\end{aligned}\tag{2.19}$$

Reformulating into matrix form yields:

$$\begin{bmatrix} \mathbf{i}_R \\ \mathbf{j}_R \\ \mathbf{k}_R \end{bmatrix} = \underbrace{\begin{bmatrix} \mathbf{i}_R \cdot \mathbf{i}_I & \mathbf{i}_R \cdot \mathbf{j}_I & \mathbf{i}_R \cdot \mathbf{k}_I \\ \mathbf{j}_R \cdot \mathbf{i}_I & \mathbf{j}_R \cdot \mathbf{j}_I & \mathbf{j}_R \cdot \mathbf{k}_I \\ \mathbf{k}_R \cdot \mathbf{i}_I & \mathbf{k}_R \cdot \mathbf{j}_I & \mathbf{k}_R \cdot \mathbf{k}_I \end{bmatrix}}_{\text{Direction Cosine Matrix (DCM)}} \begin{bmatrix} \mathbf{i}_I \\ \mathbf{j}_I \\ \mathbf{k}_I \end{bmatrix} = \mathbf{T}_{I \rightarrow R} \begin{bmatrix} \mathbf{i}_I \\ \mathbf{j}_I \\ \mathbf{k}_I \end{bmatrix}\tag{2.20}$$

The opposite analysis can also be performed (*i.e.*, expressing the  $\textcircled{I}$  frame unit vectors in terms of  $\textcircled{R}$  frame unit vectors) which yields:

$$\begin{bmatrix} \mathbf{i}_I \\ \mathbf{j}_I \\ \mathbf{k}_I \end{bmatrix} = \begin{bmatrix} \mathbf{i}_I \cdot \mathbf{i}_R & \mathbf{i}_I \cdot \mathbf{j}_R & \mathbf{i}_I \cdot \mathbf{k}_R \\ \mathbf{j}_I \cdot \mathbf{i}_R & \mathbf{j}_I \cdot \mathbf{j}_R & \mathbf{j}_I \cdot \mathbf{k}_R \\ \mathbf{k}_I \cdot \mathbf{i}_R & \mathbf{k}_I \cdot \mathbf{j}_R & \mathbf{k}_I \cdot \mathbf{k}_R \end{bmatrix} \begin{bmatrix} \mathbf{i}_R \\ \mathbf{j}_R \\ \mathbf{k}_R \end{bmatrix} = \mathbf{T}_{R \rightarrow I} \begin{bmatrix} \mathbf{i}_R \\ \mathbf{j}_R \\ \mathbf{k}_R \end{bmatrix}\tag{2.21}$$

It follows that:

$$\mathbf{T}_{R \rightarrow I} = \mathbf{T}_{I \rightarrow R}^{-1} = \mathbf{T}_{I \rightarrow R}^T \quad (2.22)$$

The fact that the inverse of the DCM is equal to its transpose is a direct consequence of the dot product being cumulative (*i.e.*,  $\mathbf{a} \cdot \mathbf{b} = \mathbf{b} \cdot \mathbf{a}$ ). This is a particularly important property of DCMs in that it avoids the calculation of the inverse at each time step of flight simulations, which is significantly computationally more expensive than calculating the transpose. Consider a generic rotation transformation  $\mathbf{T}$ . Other useful properties DCMs are summarized below:

1. Orthonormality, *i.e.*,  $\mathbf{T}^{-1} = \mathbf{T}^T$ .
2. The length of any vector operated on by  $\mathbf{T}$  remains unchanged in that the vector is only rotated but not stretched.
3. Volume is preserved, *i.e.*,  $\det(\mathbf{T}) = 1$  for a transformation from a right-handed to a right-handed (or left-handed to a left-handed) frame and  $\det(\mathbf{T}) = -1$  for a transformation from a right-handed to a left-handed frame (and vice versa).
4. All components of  $\mathbf{T}$  lie between  $-1$  and  $1$ , which is a direct consequence of these components being formed by dot products of unit vectors such that the maximum possible absolute value is  $1$ .
5. The Product of orthogonal matrices is still an orthogonal matrix. As such, multiple rotations at a time can be seen as one single rotation.

## 2.2.4 Composite Rotations

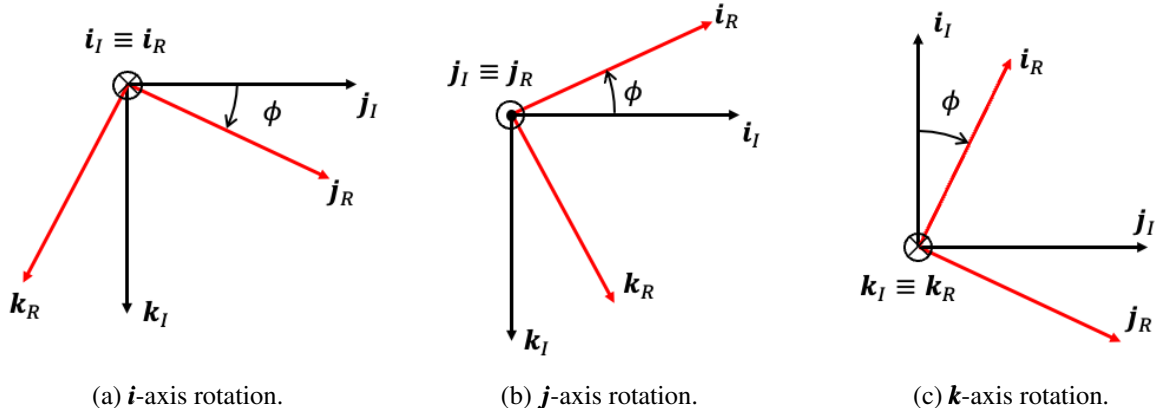


Figure 2.6: Single-axis rotations.

When defining the orientation of an aircraft body frame (B) with respect to the inertial frame (I), a specific rotation sequence must be defined. This rotation sequence is formed by composite rotations. The building block for composite rotations are single-axis rotation transformation matrices.

1.  **$i$ -axis single axis rotation** (Fig. 2.6a):

$$\begin{bmatrix} i_R \\ j_R \\ k_R \end{bmatrix} = \begin{bmatrix} 1 & 0 & 0 \\ 0 & \cos \phi & \sin \phi \\ 0 & -\sin \phi & \cos \phi \end{bmatrix} \begin{bmatrix} i_I \\ j_I \\ k_I \end{bmatrix} = \mathbf{T}_i(\phi) \begin{bmatrix} i_I \\ j_I \\ k_I \end{bmatrix} \quad (2.23)$$

2.  **$j$ -axis single axis rotation** (Fig. 2.6b):

$$\begin{bmatrix} i_R \\ j_R \\ k_R \end{bmatrix} = \begin{bmatrix} \cos \phi & 0 & -\sin \phi \\ 0 & 1 & 0 \\ \sin \phi & 0 & \cos \phi \end{bmatrix} \begin{bmatrix} i_I \\ j_I \\ k_I \end{bmatrix} = \mathbf{T}_j(\phi) \begin{bmatrix} i_I \\ j_I \\ k_I \end{bmatrix} \quad (2.24)$$

3.  **$k$ -axis single axis rotation** (Fig. 2.6c):

$$\begin{bmatrix} i_R \\ j_R \\ k_R \end{bmatrix} = \begin{bmatrix} \cos \phi & \sin \phi & 0 \\ -\sin \phi & \cos \phi & 0 \\ 0 & 0 & 1 \end{bmatrix} \begin{bmatrix} i_I \\ j_I \\ k_I \end{bmatrix} = \mathbf{T}_k(\phi) \begin{bmatrix} i_I \\ j_I \\ k_I \end{bmatrix} \quad (2.25)$$

### 2.2.5 Body-Fixed Rotation Sequence

The rotorcraft body frame  $\textcircled{B}$  can be obtained through three rotations about successively rotated axes. Starting from the inertial frame  $\textcircled{I}$ , the sequence of rotations is:

1. Rotation about  $\mathbf{k}_I$  axis by an angle  $\psi$  (results in  $\textcircled{A}$  frame),
2. Rotation about  $\mathbf{j}_A$  axis by an angle  $\theta$  (results in  $\textcircled{N}$  frame), and
3. Rotation about  $\mathbf{i}_N$  axis by an angle  $\phi$  (results in  $\textcircled{B}$  frame).

The resulting reference frame relationships are:

$$\begin{bmatrix} \mathbf{i}_A \\ \mathbf{j}_A \\ \mathbf{k}_A \end{bmatrix} = \mathbf{T}_k(\psi) \begin{bmatrix} \mathbf{i}_I \\ \mathbf{j}_I \\ \mathbf{k}_I \end{bmatrix}, \quad \begin{bmatrix} \mathbf{i}_N \\ \mathbf{j}_N \\ \mathbf{k}_N \end{bmatrix} = \mathbf{T}_j(\theta) \begin{bmatrix} \mathbf{i}_A \\ \mathbf{j}_A \\ \mathbf{k}_A \end{bmatrix}, \quad \begin{bmatrix} \mathbf{i}_B \\ \mathbf{j}_B \\ \mathbf{k}_B \end{bmatrix} = \mathbf{T}_i(\phi) \begin{bmatrix} \mathbf{i}_N \\ \mathbf{j}_N \\ \mathbf{k}_N \end{bmatrix} \quad (2.26)$$

Substituting these relationships into one another leads to:

$$\begin{bmatrix} \mathbf{i}_B \\ \mathbf{j}_B \\ \mathbf{k}_B \end{bmatrix} = \underbrace{\mathbf{T}_i(\phi) \mathbf{T}_j(\theta) \mathbf{T}_k(\psi)}_{\mathbf{T}_{I \rightarrow B}} \begin{bmatrix} \mathbf{i}_I \\ \mathbf{j}_I \\ \mathbf{k}_I \end{bmatrix} \quad (2.27)$$

where:

$$\mathbf{T}_{I \rightarrow B} = \begin{bmatrix} \cos \theta \cos \psi & \cos \theta \sin \psi & -\sin \theta \\ \sin \phi \sin \theta \cos \psi - \cos \phi \sin \psi & \sin \phi \sin \theta \sin \psi + \cos \phi \cos \psi & \sin \phi \cos \theta \\ \cos \phi \sin \theta \cos \psi + \sin \phi \sin \psi & \cos \phi \sin \theta \sin \psi - \sin \phi \cos \psi & \cos \phi \cos \theta \end{bmatrix} \quad (2.28)$$

The angles  $\phi$ ,  $\theta$ , and  $\psi$  are called Euler angles and identify, respectively, the roll, pitch, and yaw attitude of the rotorcraft. Euler angles are defined for a 3-2-1 rotation sequence, which represents the industry standard for aircraft and rotorcraft. Because this sequence gives a singularity in the rotational kinematics equations of motion for  $\theta = 90$  deg (to be derived later on in the chapter), it is not necessarily suitable for vehicles flying at such pitch attitudes (e.g., fighter jets, space launch vehicles). For these kinds of vehicles, a 3-1-3 rotation sequence is more commonly adopted. In general, any sequence of three rotations can be used as long as the same axis is not used for successive rotations. It follows that the total combinations of unique three-rotation sequences are 12. It is worth noting that the Euler angles are defined about three non orthogonal axes (*i.e.*,  $\mathbf{k}_I$ ,  $\mathbf{j}_A$ , and  $\mathbf{i}_N$ ). This fact will become important when developing the rotational kinematics equations of motion for a rigid body.

### 2.2.6 Angular Velocity Vector

Consider the geometry of Fig. 2.7 where frames  $\textcircled{I}$  and  $\textcircled{B}$  rotate with respect to each other. Point O is fixed in, and the origin of, both frames. Point P is fixed in the  $\textcircled{B}$  frame. Let

$$\begin{aligned} \mathbf{r}_{O \rightarrow P} &= x\mathbf{i}_I + y\mathbf{j}_I + z\mathbf{k}_I \\ &= x^*\mathbf{i}_B + y^*\mathbf{j}_B + z^*\mathbf{k}_B \end{aligned} \quad (2.29)$$

where  $x, y, z$  change with time and  $x^*, y^*, z^*$  are constant with time. Differentiating in the  $\textcircled{I}$  frame yields:

$$\textcircled{I} \frac{d}{dt} (\mathbf{r}_{O \rightarrow P}) = \dot{x}\mathbf{i}_I + \dot{y}\mathbf{j}_I + \dot{z}\mathbf{k}_I \quad (2.30)$$

Also recall that the components of  $\mathbf{r}_{O \rightarrow P}$  in the  $\textcircled{B}$  and  $\textcircled{I}$  frames are related through the following:

$$\begin{bmatrix} x^* \\ y^* \\ z^* \end{bmatrix} = \mathbf{T} \begin{bmatrix} x \\ y \\ z \end{bmatrix} \quad (2.31)$$

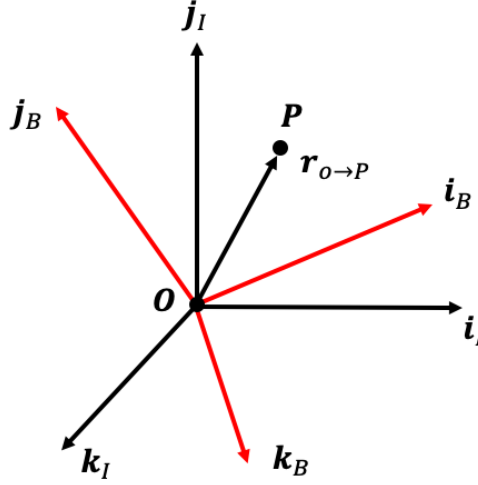


Figure 2.7: Two frames rotating with respect to each other about their shared origin, with a point P fixed in one of the frames.

where  $\mathbf{T} = \mathbf{T}_{I \rightarrow B}$  for simplicity. Taking the time derivative of each scalar quantity yields:

$$\frac{d}{dt} \begin{bmatrix} x^* \\ y^* \\ z^* \end{bmatrix} = \frac{d}{dt} \left( \mathbf{T} \begin{bmatrix} x \\ y \\ z \end{bmatrix} \right) = \frac{d}{dt} (\mathbf{T}) \begin{bmatrix} x \\ y \\ z \end{bmatrix} + \mathbf{T} \frac{d}{dt} \begin{bmatrix} x \\ y \\ z \end{bmatrix} \quad (2.32)$$

By rearranging, one obtains:

$$\begin{bmatrix} \dot{x} \\ \dot{y} \\ \dot{z} \end{bmatrix} = -\mathbf{T}^T \dot{\mathbf{T}} \begin{bmatrix} x \\ y \\ z \end{bmatrix} \quad (2.33)$$

where the property  $\mathbf{T}^{-1} = \mathbf{T}^T$  was used to obtain this equation. Matrix  $-\mathbf{T}^T \dot{\mathbf{T}}$  has a very specific structure. To uncover this structure, recall that:

$$\mathbf{T} \mathbf{T}^T = \mathbf{T}^T \mathbf{T} = \mathbf{I} \Leftrightarrow \mathbf{T}^{-1} = \mathbf{T}^T \quad (2.34)$$

where  $\mathbf{I}$  is the identity matrix. Differentiation leads to the following two expressions:

$$\frac{d}{dt} (\mathbf{T} \mathbf{T}^T) = \dot{\mathbf{T}} \mathbf{T}^T + \mathbf{T} \dot{\mathbf{T}}^T = \mathbf{0} \quad (2.35a)$$

$$\frac{d}{dt} (\mathbf{T}^T \mathbf{T}) = \dot{\mathbf{T}}^T \mathbf{T} + \mathbf{T}^T \dot{\mathbf{T}} = \mathbf{0} \quad (2.35b)$$

Reformulate Eq. (2.35b) to obtain:

$$-\mathbf{T}^T \dot{\mathbf{T}} = \dot{\mathbf{T}}^T \mathbf{T} \quad (2.36)$$

Also recognize that:

$$(-\mathbf{T}^T \dot{\mathbf{T}})^T = -\dot{\mathbf{T}}^T \mathbf{T} \quad (2.37)$$

As such, the right hand sides of these two equations are negatives of each other, such that  $-\dot{\mathbf{T}}^T \mathbf{T} = -(-\dot{\mathbf{T}}^T \mathbf{T})$ , which is the definition of a skew-symmetric matrix (*i.e.*,  $\mathbf{A} = -\mathbf{A}^T$ ). Thus, matrix  $-\mathbf{T}^T \dot{\mathbf{T}}$  must

always be a skew-symmetric matrix. If the elements populating the skew-symmetric matrix are defined as the components of the angular velocity vector, then:

$$-\mathbf{T}^T \dot{\mathbf{T}} = \begin{bmatrix} 0 & -\Omega_z & \Omega_y \\ \Omega_z & 0 & -\Omega_x \\ -\Omega_y & \Omega_x & 0 \end{bmatrix} \quad (2.38)$$

where the angular velocity vector is:

$$\begin{aligned} \boldsymbol{\omega}_{B/I} &= \Omega_x \mathbf{i}_I + \Omega_y \mathbf{j}_I + \Omega_z \mathbf{k}_I \\ &= \omega_x \mathbf{i}_B + \omega_y \mathbf{j}_B + \omega_z \mathbf{k}_B \end{aligned} \quad (2.39)$$

The first expression identified the angular velocity vector of the  $\textcircled{B}$  frame with respect to the  $\textcircled{I}$  frame expressed in the  $\textcircled{I}$  frame unit vectors. The second expression represents the same angular velocity vector but expressed in the  $\textcircled{B}$  frame unit vectors. The angular velocity vector components expressed in the inertial and body frame are related through the transformation matrix between the two frames.

$$\begin{bmatrix} \omega_x \\ \omega_y \\ \omega_z \end{bmatrix} = \mathbf{T} \begin{bmatrix} \Omega_x \\ \Omega_y \\ \Omega_z \end{bmatrix} \quad (2.40)$$

Given the relationships above, Eq. (2.33) can be rewritten as:

$$\begin{bmatrix} \dot{x} \\ \dot{y} \\ \dot{z} \end{bmatrix} = -\mathbf{T}^T \dot{\mathbf{T}} \begin{bmatrix} x \\ y \\ z \end{bmatrix} = \begin{bmatrix} 0 & -\Omega_z & \Omega_y \\ \Omega_z & 0 & -\Omega_x \\ -\Omega_y & \Omega_x & 0 \end{bmatrix} \begin{bmatrix} x \\ y \\ z \end{bmatrix} = \boldsymbol{\omega}_{B/I} \times \mathbf{r}_{O \rightarrow P} \quad (2.41)$$

Thus,

$$\textcircled{I} \frac{d}{dt} (\mathbf{r}_{O \rightarrow P}) = \boldsymbol{\omega}_{B/I} \times \mathbf{r}_{O \rightarrow P} \quad (2.42)$$

This is a general equation that applies to any vector fixed in the  $\textcircled{B}$  frame. For instance, it can be used to differentiate the unit vectors of the  $\textcircled{B}$  frame, such that:

$$\textcircled{I} \frac{d\mathbf{i}_B}{dt} = \boldsymbol{\omega}_{B/I} \times \mathbf{i}_B \quad (2.43a)$$

$$\textcircled{I} \frac{d\mathbf{j}_B}{dt} = \boldsymbol{\omega}_{B/I} \times \mathbf{j}_B \quad (2.43b)$$

$$\textcircled{I} \frac{d\mathbf{k}_B}{dt} = \boldsymbol{\omega}_{B/I} \times \mathbf{k}_B \quad (2.43c)$$

$$(2.43d)$$

However, this equation only reflects vector rotation but not stretching. As such, we will have to seek for an even more general expression.

## 2.2.7 Vector Derivative Transport Theorem

Consider a general vector  $\boldsymbol{\beta}$ :

$$\boldsymbol{\beta} = \beta_x \mathbf{i}_B + \beta_y \mathbf{j}_B + \beta_z \mathbf{k}_B \quad (2.44)$$

Taking its time derivative in the  $\textcircled{I}$  frame yields:

$$\begin{aligned} \textcircled{I} \frac{d\boldsymbol{\beta}}{dt} &= \dot{\beta}_x \mathbf{i}_B + \beta_x \textcircled{I} \frac{d\mathbf{i}_B}{dt} + \dot{\beta}_y \mathbf{j}_B + \beta_y \textcircled{I} \frac{d\mathbf{j}_B}{dt} + \dot{\beta}_z \mathbf{k}_B + \beta_z \textcircled{I} \frac{d\mathbf{k}_B}{dt} \\ &= \dot{\beta}_x \mathbf{i}_B + \dot{\beta}_y \mathbf{j}_B + \dot{\beta}_z \mathbf{k}_B + \beta_x (\boldsymbol{\omega}_{B/I} \times \mathbf{i}_B) + \beta_y (\boldsymbol{\omega}_{B/I} \times \mathbf{j}_B) + \beta_z (\boldsymbol{\omega}_{B/I} \times \mathbf{k}_B) \\ &= \underbrace{\dot{\beta}_x \mathbf{i}_B + \dot{\beta}_y \mathbf{j}_B + \dot{\beta}_z \mathbf{k}_B}_{\textcircled{I} \frac{d\boldsymbol{\beta}}{dt}} + \underbrace{\boldsymbol{\omega}_{B/I} \times (\beta_x \mathbf{i}_B + \beta_y \mathbf{j}_B + \beta_z \mathbf{k}_B)}_{\boldsymbol{\beta}} \end{aligned} \quad (2.45)$$

Thus,

$$\boxed{\textcircled{I} \frac{d\beta}{dt} = \textcircled{B} \frac{d\beta}{dt} + \omega_{B/I} \times \beta} \quad (2.46)$$

This formula is known as the *vector derivative transport theorem*. It relates the  $\textcircled{I}$  and  $\textcircled{B}$  frame time derivatives of a vector where the link between the two is the angular velocity between the frames.

### 2.2.8 Angular Velocity Addition Formula

Consider three different frames  $\textcircled{A}$ ,  $\textcircled{B}$ , and  $\textcircled{C}$ . Then, their angular velocity is rotated as follows:

$$\boxed{\omega_{C/A} = \omega_{C/B} + \omega_{B/A}} \quad (2.47)$$

This relationship generalizes to  $N$  reference frames  $\textcircled{1}, \textcircled{2}, \dots, \textcircled{N}$  such that:

$$\omega_{N/1} = \omega_{N/N-1} + \dots + \omega_{2/1} \quad (2.48)$$

If the frames are related by a series of single-axis rotations, then the angular velocity of one frame with respect to the other is given by;

$$\omega_{B/I} = \sum_{i=1}^N \omega_i e_i \quad (2.49)$$

where  $\omega_i$  is the angular speed about the  $i^{\text{th}}$  axis and  $e_i$  is the axis of the  $i^{\text{th}}$  rotation.

### 2.2.9 Angular Momentum and Moment of Inertia

Consider a set of  $N$  particles and an arbitrary point P, which may be moving or stationary, as shown in Fig. 2.8.

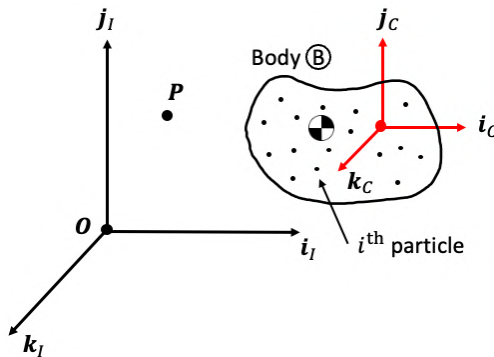


Figure 2.8:  $N$  particles and an arbitrary point P, which may be moving or stationary.

The angular momentum of body  $\textcircled{B}$  with respect to frame  $\textcircled{I}$  about point P is:

$$\hat{H}_{B/I}^P = \sum_{i=1}^N \mathbf{r}_{P \rightarrow i} \times m_i \textcircled{I} \frac{d}{dt} (\mathbf{r}_{P \rightarrow i}) \quad (2.50)$$

By selecting the point P as the center of mass  $\bullet$ , the equation above changes to:

$$\hat{H}_{B/I}^\bullet = \sum_{i=1}^N \mathbf{r}_{\bullet \rightarrow i} \times m_i \textcircled{I} \frac{d}{dt} (\mathbf{r}_{\bullet \rightarrow i}) \quad (2.51)$$

Let us now assume body (B) to be a rigid body, such that:

$$\textcircled{I} \frac{d}{dt} (\mathbf{r}_{\bullet \rightarrow i}) = \cancel{\textcircled{B} \frac{d}{dt} (\mathbf{r}_{\bullet \rightarrow i})}^{\rightarrow = \mathbf{0}} + \boldsymbol{\omega}_{B/I} \times \mathbf{r}_{\bullet \rightarrow i} \quad (2.52)$$

Thus, the angular momentum equation simplifies to:

$$\begin{aligned} \hat{\mathbf{H}}_{B/I}^{\bullet} &= \sum_{i=1}^N m_i \mathbf{r}_{\bullet \rightarrow i} \times (\boldsymbol{\omega}_{B/I} \times \mathbf{r}_{\bullet \rightarrow i}) \\ &= - \sum_{i=1}^N m_i \mathbf{r}_{\bullet \rightarrow i} \times (\mathbf{r}_{\bullet \rightarrow i} \times \boldsymbol{\omega}_{B/I}) \end{aligned} \quad (2.53)$$

where the cross product property  $\mathbf{u} \times \mathbf{v} = -\mathbf{v} \times \mathbf{u}$  was used. To explore this formula further, define the following vectors:

$$\mathbf{r}_{\bullet \rightarrow i} = x_i \mathbf{i}_C + y_i \mathbf{j}_C + z_i \mathbf{k}_C \quad (2.54a)$$

$$\boldsymbol{\omega}_{B/I} = \omega_x \mathbf{i}_C + \omega_y \mathbf{j}_C + \omega_z \mathbf{k}_C \quad (2.54b)$$

$$\hat{\mathbf{H}}_{B/I}^{\bullet} = h_x \mathbf{i}_C + h_y \mathbf{j}_C + h_z \mathbf{k}_C \quad (2.54c)$$

Then, this expression becomes, after some algebraic manipulations, the following:

$$\begin{bmatrix} h_x \\ h_y \\ h_z \end{bmatrix} = \underbrace{\left( \sum_{i=1}^N m_i \begin{bmatrix} y_i^2 + z_i^2 & -x_i y_i & -x_i z_i \\ -x_i y_i & x_i^2 + z_i^2 & -y_i z_i \\ -x_i z_i & -y_i z_i & x_i^2 + y_i^2 \end{bmatrix} \right)}_{\mathbf{I}_{B/C}} \begin{bmatrix} \omega_x \\ \omega_y \\ \omega_z \end{bmatrix} \quad (2.55)$$

where  $\mathbf{I}_{B/C}$  is the mass moment of inertia of body (B) about (C) with respect to frame (C). If the rigid body (B) is constituted of an infinite number of particles, each with an infinitesimal mass  $dm$ , the summation turns into a volume integral such that:

$$\mathbf{I}_{B/C} = \begin{bmatrix} I_{xx} & I_{xy} & I_{xz} \\ I_{xy} & I_{yy} & I_{yz} \\ I_{xz} & I_{yz} & I_{zz} \end{bmatrix} \quad (2.56)$$

where the elements of mass moment of inertia matrix are given by:

$$I_{xx} = \int_{\textcircled{B}} (y^2 + z^2) dm \quad (2.57a)$$

$$I_{yy} = \int_{\textcircled{B}} (x^2 + z^2) dm \quad (2.57b)$$

$$I_{zz} = \int_{\textcircled{B}} (x^2 + y^2) dm \quad (2.57c)$$

$$I_{xy} = \int_{\textcircled{B}} -xy dm \quad (2.57d)$$

$$I_{xz} = \int_{\textcircled{B}} -xz dm \quad (2.57e)$$

$$I_{yz} = \int_{\textcircled{B}} -yz dm \quad (2.57f)$$

$$(2.57g)$$

with

$$\mathbf{r}_{O \rightarrow dm} = x\mathbf{i}_C + y\mathbf{j}_C + z\mathbf{k}_C \quad (2.58)$$

$I_{xx}$ ,  $I_{yy}$ , and  $I_{zz}$  are known as *moments of inertia* whereas  $I_{xy}$ ,  $I_{xz}$ , and  $I_{yz}$  are known as *products of inertia*. Typically, for fixed-wing aircraft and rotorcraft  $I_{xy} \approx I_{yz} \approx 0$ , such that:

$$\mathbf{I}_{B/C} = \begin{bmatrix} I_{xx} & 0 & I_{xz} \\ 0 & I_{yy} & 0 \\ I_{xz} & 0 & I_{zz} \end{bmatrix} \quad (2.59)$$

### 2.2.10 Moments of Inertia in Different Frames

Consider a body (B) with two reference frames, (C) and (P), rigidly attached to it, as shown in Fig. 2.9. Frames (C) and (P) may be rotated and/or translated with respect to each other.

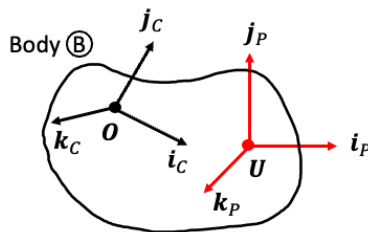


Figure 2.9: Two reference frames rigidly attached to a rigid body which may be rotated and/or translated with respect to each other.

Let  $\mathbf{r}_{O \rightarrow U}$  be the distance vector from the origin of frame (C) to that of frame (P), such that:

$$\mathbf{r}_{O \rightarrow U} = x_T \mathbf{i}_P + y_T \mathbf{j}_P + z_T \mathbf{k}_P \quad (2.60)$$

Also, let  $\mathbf{T}_{C \rightarrow P}$  be the transformation matrix from frame (C) to frame (P). Then, given  $\mathbf{I}_{B/C}$ , we can compute  $\mathbf{I}_{B/P}$  according to:

$$\boxed{\mathbf{I}_{B/P} = \mathbf{T}_{C \rightarrow P} \mathbf{I}_{B/C} \mathbf{T}_{C \rightarrow P}^T - m \begin{bmatrix} y_T^2 + z_T^2 & -x_T y_T & -x_T z_T \\ -x_T y_T & x_T^2 + z_T^2 & -y_T z_T \\ -x_T z_T & -y_T z_T & x_T^2 + y_T^2 \end{bmatrix}} \quad (2.61)$$

This is known as the *parallel axis theorem*. Note that if the frames share the same origin,

$$\mathbf{I}_{B/P} = \mathbf{T}_{C \rightarrow P} \mathbf{I}_{B/C} \mathbf{T}_{C \rightarrow P}^T \quad (2.62)$$

### 2.2.11 Mass Moment of Inertia Matrix for a Composite Body

Consider the case where one has inertia matrices for  $N$  components of a rotorcraft (e.g., fuselage, horizontal and vertical stabilizers, etc.), each given in the natural reference frame of that component. The mass moment of inertia can be found for the entire body by summing the mass moment of inertia matrices of all components transformed into a common parent frame:

$$\mathbf{I}_{B/R} = \sum_{i=1}^N \left( \mathbf{T}_i \mathbf{I}_{B_i/U_i} \mathbf{T}_i^T + m_i \begin{bmatrix} y_i^2 + z_i^2 & -x_i y_i & -x_i z_i \\ -x_i y_i & x_i^2 + z_i^2 & -y_i z_i \\ -x_i z_i & -y_i z_i & x_i^2 + y_i^2 \end{bmatrix} \right) \quad (2.63)$$

where:

$m_i$  is the mass of component body (B<sub>i</sub>),

(R) is the parent frame with origin O,

$\textcircled{U}_i$  is the natural reference frame of component  $i$ ,

$\mathbf{T}_i$  is the transformation matrix from frame the  $\textcircled{U}_i$  to the  $\textcircled{R}$  frame, and

$x_i, y_i, z_i$  are the  $\textcircled{R}$  frame components of  $\mathbf{r}_{O \rightarrow i}$ .

## 2.2.12 Center of Mass

Consider  $N$  particles which comprise body  $\textcircled{B}$ , as shown in Fig. 2.8. The center of mass (also known as center of gravity, or CG) of body  $\textcircled{B}$  (point  $\textcircled{\Theta}$ ) is defined as:

$$\mathbf{r}_{O \rightarrow \Theta} = \frac{1}{m} \sum_{i=1}^N m_i \mathbf{r}_{O \rightarrow i} \quad (2.64)$$

where  $m_i$  is the mass of the  $i^{\text{th}}$  particle and  $m = \sum_{i=1}^N m_i$  is the total mass of body  $\textcircled{B}$ . As  $N \rightarrow \infty$ , the summation over the number of discrete particles turns into a volume integral such that:

$$\mathbf{r}_{O \rightarrow \Theta} = \frac{1}{m} \int_{\textcircled{B}} \mathbf{r}_{O \rightarrow dm} dm \quad (2.65)$$

## 2.3 Rigid Body Dynamics

To derive the rigid-body equations of motion of a rotorcraft, consider making the following assumptions: (i) the rotorcraft fuselage is a rigid body, (ii) the body frame is centered at the rotorcraft center of mass, and (iii) an inertial frame is fixed to the flat and non-rotating Earth. This setup is shown in Fig. 2.10.

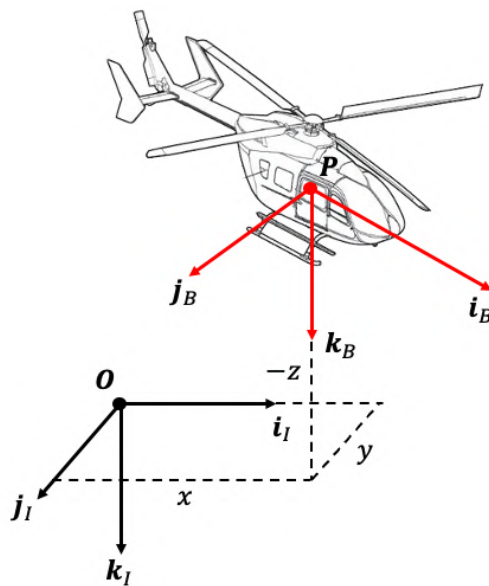


Figure 2.10: Geometry for the equations of motion of a rigid body.

The rigid-body state vector is defined as follows:

$$\boldsymbol{x} = \begin{bmatrix} u \\ v \\ w \\ p \\ q \\ r \\ \phi \\ \theta \\ \psi \\ x \\ y \\ z \end{bmatrix} \quad \left\{ \begin{array}{l} \boldsymbol{v}_{\bullet/I} = ui_B + vj_B + wk_B \\ \boldsymbol{\omega}_{B/I} = pi_B + qj_B + rk_B \\ \text{Euler Angles} \\ \boldsymbol{r}_{O \rightarrow \bullet} = xi_I + yj_I + zk_I \end{array} \right. \quad (2.66)$$

where:

$u, v, w$  are the body-frame components of the velocity of the CG with respect to the inertial frame,

$p, q, r$  are the body-frame components of the angular velocity with respect to the inertial frame,

$\phi, \theta, \psi$  are the Euler angles, and

$x, y, z$  are the inertial-frame components of the CG position.

The rigid body has 6 degrees of freedom: 3 translational and 3 rotational. To model these degrees of freedom, one needs 12 equations of motion and thus 12 states. Typically, the linear and angular velocity vector components are expressed in the body frame as it is convenient for the calculation and/or measurement of aerodynamic forces and moments acting on the rotorcraft. On the other hand, the position vector generally expressed in NED frame components as it is convenient to know the how the rotorcraft is positioned with respect to the world. Note that the Euler angles are expressed neither in the body frame nor in the inertial frame. In fact, the Euler angles represent rotations about successively rotated axes (*i.e.*,  $\mathbf{k}_I, \mathbf{j}_A$ , and  $\mathbf{i}_N$ ), such that these angles are expressed using a non-orthogonal basis.

### 2.3.1 Translational Kinematics

The translational kinematic equations relate the time derivatives of the position states to the velocity states. Typically, position coordinates are expressed in the inertial frame:

$$\boldsymbol{r}_{O \rightarrow \bullet} = xi_I + yj_I + zk_I \quad (2.67)$$

whereas velocity components are expressed in the body frame:

$$\boldsymbol{v}_{\bullet/I} = ui_B + vj_B + wk_B \quad (2.68)$$

Recall the definition of velocity:

$$\begin{aligned} \textcircled{I} \frac{d}{dt} (\boldsymbol{r}_{O \rightarrow P}) &= \boldsymbol{v}_{\bullet/I} \\ &= \dot{x}\mathbf{i}_I + \dot{y}\mathbf{j}_I + \dot{z}\mathbf{k}_I \\ &= ui_B + vj_B + wk_B \end{aligned} \quad (2.69)$$

Therefore,

$$\begin{bmatrix} \dot{x} \\ \dot{y} \\ \dot{z} \end{bmatrix} = \boldsymbol{T}_{I \rightarrow B} \begin{bmatrix} u \\ v \\ w \end{bmatrix} \quad (2.70)$$

Substituting for the transformation matrix from the inertial to the body frame yields the translational kinematics equations of motion:

$$\begin{bmatrix} \dot{x} \\ \dot{y} \\ \dot{z} \end{bmatrix} = \begin{bmatrix} \cos \theta \cos \psi & \cos \theta \sin \psi & -\sin \theta \\ \sin \phi \sin \theta \cos \psi - \cos \phi \sin \psi & \sin \phi \sin \theta \sin \psi + \cos \phi \cos \psi & \sin \phi \cos \theta \\ \cos \phi \sin \theta \cos \psi + \sin \phi \sin \psi & \cos \phi \sin \theta \sin \psi - \sin \phi \cos \psi & \cos \phi \cos \theta \end{bmatrix} \begin{bmatrix} u \\ v \\ w \end{bmatrix} \quad (2.71)$$

These are the translational kinematics equations of motion.

### 2.3.2 Rotational Kinematics

Recall from the angular velocity addition formula that the angular velocity of the body frame with respect to the inertial frame may be written as a summation of single-axis rotations such that:

$$\boldsymbol{\omega}_{B/I} = \dot{\phi}\mathbf{i}_N + \dot{\theta}\mathbf{j}_A + \dot{\psi}\mathbf{k}_I \quad (2.72)$$

Equivalently,  $\boldsymbol{\omega}_{B/I}$  can be expressed in the body frame as:

$$\boldsymbol{\omega}_{B/I} = p\mathbf{i}_B + q\mathbf{j}_B + r\mathbf{k}_B \quad (2.73)$$

where  $p$ ,  $q$ , and  $r$  are the roll, pitch, and yaw rate, respectively. Consider now relating  $\dot{\phi}$ ,  $\dot{\theta}$ ,  $\dot{\psi}$  and  $p$ ,  $q$ ,  $r$  by using unit vector relationships:

$$\begin{bmatrix} \mathbf{i}_B \\ \mathbf{j}_B \\ \mathbf{k}_B \end{bmatrix} = \begin{bmatrix} 1 & 0 & 0 \\ 0 & \cos \phi & \sin \phi \\ 0 & -\sin \phi & \cos \phi \end{bmatrix} \begin{bmatrix} \mathbf{i}_N \\ \mathbf{j}_N \\ \mathbf{k}_N \end{bmatrix} \rightarrow \begin{bmatrix} \mathbf{i}_N \\ \mathbf{j}_N \\ \mathbf{k}_N \end{bmatrix} = \begin{bmatrix} 1 & 0 & 0 \\ 0 & \cos \phi & -\sin \phi \\ 0 & \sin \phi & \cos \phi \end{bmatrix} \begin{bmatrix} \mathbf{i}_B \\ \mathbf{j}_B \\ \mathbf{k}_B \end{bmatrix} \quad (2.74a)$$

$$\begin{bmatrix} \mathbf{i}_N \\ \mathbf{j}_N \\ \mathbf{k}_N \end{bmatrix} = \begin{bmatrix} \cos \theta & 0 & -\sin \theta \\ 0 & 1 & 0 \\ \sin \theta & 0 & \cos \theta \end{bmatrix} \begin{bmatrix} \mathbf{i}_A \\ \mathbf{j}_A \\ \mathbf{k}_A \end{bmatrix} \rightarrow \begin{bmatrix} \mathbf{i}_A \\ \mathbf{j}_A \\ \mathbf{k}_A \end{bmatrix} = \begin{bmatrix} \cos \theta & 0 & \sin \theta \\ 0 & 1 & 0 \\ -\sin \theta & 0 & \cos \theta \end{bmatrix} \begin{bmatrix} \mathbf{i}_N \\ \mathbf{j}_N \\ \mathbf{k}_N \end{bmatrix} \quad (2.74b)$$

$$\begin{bmatrix} \mathbf{i}_A \\ \mathbf{j}_A \\ \mathbf{k}_A \end{bmatrix} = \begin{bmatrix} \cos \psi & \sin \psi & 0 \\ -\sin \psi & \cos \psi & 0 \\ 0 & 0 & 1 \end{bmatrix} \begin{bmatrix} \mathbf{i}_I \\ \mathbf{j}_I \\ \mathbf{k}_I \end{bmatrix} \rightarrow \begin{bmatrix} \mathbf{i}_I \\ \mathbf{j}_I \\ \mathbf{k}_I \end{bmatrix} = \begin{bmatrix} \cos \psi & -\sin \psi & 0 \\ \sin \psi & \cos \psi & 0 \\ 0 & 0 & 1 \end{bmatrix} \begin{bmatrix} \mathbf{i}_A \\ \mathbf{j}_A \\ \mathbf{k}_A \end{bmatrix} \quad (2.74c)$$

Then,

$$\mathbf{i}_N = \mathbf{i}_B \quad (2.75a)$$

$$\mathbf{j}_A = \mathbf{j}_N = \cos \phi \mathbf{j}_B - \sin \phi \mathbf{k}_B \quad (2.75b)$$

$$\mathbf{k}_I = \mathbf{k}_A = -\sin \theta \mathbf{i}_N + \cos \theta \mathbf{k}_N = -\sin \theta \mathbf{i}_B + \cos \theta \sin \phi \mathbf{j}_B + \cos \theta \cos \phi \mathbf{k}_B \quad (2.75c)$$

Substituting for  $\mathbf{i}_N$ ,  $\mathbf{j}_A$ , and  $\mathbf{k}_I$  in Eq. (2.72) yields:

$$\begin{aligned} \boldsymbol{\omega}_{B/I} &= \dot{\phi}\mathbf{i}_B + \dot{\theta}(\cos \theta \mathbf{j}_B - \sin \theta \mathbf{k}_B) + \dot{\psi}(-\sin \theta \mathbf{i}_B + \cos \theta \sin \phi \mathbf{j}_B + \cos \theta \cos \phi \mathbf{k}_B) \\ &= \underbrace{(\dot{\phi} - \dot{\psi} \sin \theta)}_p \mathbf{i}_B + \underbrace{(\dot{\theta} \cos \phi + \dot{\psi} \cos \theta \sin \phi)}_q \mathbf{j}_B + \underbrace{(-\dot{\theta} \sin \phi + \dot{\psi} \cos \theta \cos \phi)}_r \mathbf{k}_B \end{aligned} \quad (2.76)$$

Thus,

$$p = \dot{\phi} - \dot{\psi} \sin \theta \quad (2.77a)$$

$$q = \dot{\theta} \cos \phi + \dot{\psi} \cos \theta \sin \phi \quad (2.77b)$$

$$r = -\dot{\theta} \sin \phi + \dot{\psi} \cos \theta \cos \phi \quad (2.77c)$$

In matrix form,

$$\begin{bmatrix} p \\ q \\ r \end{bmatrix} = \begin{bmatrix} 1 & 0 & -\sin \theta \\ 0 & \cos \phi & \cos \theta \sin \phi \\ 0 & -\sin \phi & \cos \theta \cos \phi \end{bmatrix} \begin{bmatrix} \dot{\phi} \\ \dot{\theta} \\ \dot{\psi} \end{bmatrix} \quad (2.78)$$

Inverting this relationship yields the rotational kinematics equations (also known as gimbal or strapdown equations):

$$\begin{bmatrix} \dot{\phi} \\ \dot{\theta} \\ \dot{\psi} \end{bmatrix} = \begin{bmatrix} 1 & \sin \phi \tan \theta & \cos \phi \tan \theta \\ 0 & \cos \phi & -\sin \phi \\ 0 & \sin \phi & \cos \phi \end{bmatrix} \begin{bmatrix} p \\ q \\ r \end{bmatrix} \quad (2.79)$$

Note that this is not a rotation matrix in that it is not orthonormal. In fact, it relates non-orthogonal components (*i.e.*,  $\dot{\phi}$ ,  $\dot{\theta}$ ,  $\dot{\psi}$ ) with orthogonal components (*i.e.*,  $p$ ,  $q$ ,  $r$ ). It is also worth noting that this matrix is undefined for  $\theta = 90$  deg (*i.e.*, one would need  $p = q = r = \infty$  to have finite  $\dot{\phi}$ ,  $\dot{\theta}$ ,  $\dot{\psi}$ ).

### 2.3.3 Translational Dynamics

From the definition of Newton's second law, it can be shown that the net force acting on a rigid body is proportional to the acceleration of its mass center with respect to an inertial frame:

$$\mathbf{F} = m\mathbf{a}_{\bullet/I} = m \bigcirc \frac{d}{dt} (\mathbf{v}_{\bullet/I}) \quad (2.80)$$

where  $\mathbf{a}_{\bullet/I}$  is the acceleration of the center of mass with respect to the inertial frame and  $\frac{d}{dt} (\mathbf{v}_{\bullet/I})$  is the time rate of change of the velocity of the center of mass with respect to the inertial frame, calculated in the inertial frame. Let  $\mathbf{F}$  denote the net forces acting on the rotorcraft CG:

$$\mathbf{F} = X\mathbf{i}_B + Y\mathbf{j}_B + Z\mathbf{k}_B \quad (2.81)$$

where  $X$ ,  $Y$ , and  $Z$  are the longitudinal, lateral, and vertical forces at the CG, respectively. Because it is convenient to formulate the translational dynamics equations in the body frame, consider converting the equation above to the body frame:

$$\mathbf{F} = m \left[ \bigcirc \frac{d}{dt} (\mathbf{v}_{\bullet/I}) + \boldsymbol{\omega}_{B/I} \times \mathbf{v}_{\bullet/I} \right] \quad (2.82)$$

where:

$$\bigcirc \frac{d}{dt} (\mathbf{v}_{\bullet/I}) = \dot{u}\mathbf{i}_B + \dot{v}\mathbf{j}_B + \dot{w}\mathbf{k}_B \quad (2.83)$$

Rearranging leads to:

$$\begin{bmatrix} X \\ Y \\ Z \end{bmatrix} = m \begin{bmatrix} \dot{u} \\ \dot{v} \\ \dot{w} \end{bmatrix} + m \begin{bmatrix} 0 & -r & q \\ r & 0 & -p \\ -q & p & 0 \end{bmatrix} \begin{bmatrix} u \\ v \\ w \end{bmatrix} \quad (2.84)$$

Solving for the time rate of change of the velocity of the center of mass yields the translational dynamics equations of motion:

$$\begin{bmatrix} \dot{u} \\ \dot{v} \\ \dot{w} \end{bmatrix} = \frac{1}{m} \begin{bmatrix} X \\ Y \\ Z \end{bmatrix} - \begin{bmatrix} qw - rv \\ ru - pw \\ pv - qu \end{bmatrix} \quad (2.85)$$

### 2.3.4 Rotational Dynamics

Euler's rotational dynamics equations relate the rate of change of a body's angular momentum to the external moments applied to it:

$$\bigcirc \frac{d}{dt} \left( \hat{\mathbf{H}}_{B/I}^P \right) = \mathbf{M}_P - m(\mathbf{r}_{P \rightarrow \bullet}) \times \mathbf{a}_{P/I} \quad (2.86)$$

where  $\hat{\mathbf{H}}_{B/I}^P$  is the angular momentum of body  $\bigcirc$  with respect to the inertial frame about an arbitrary point P and  $\mathbf{M}_P$  is the net external moment on body  $\bigcirc$  about point P. If one selects P coincident with the CG (*i.e.*,  $\mathbf{r}_{P \rightarrow \bullet} = \mathbf{0}$ ), then the formula above reduces to:

$$\bigcirc \frac{d}{dt} \left( \hat{\mathbf{H}}_{B/I}^\bullet \right) = \mathbf{M}_\bullet \quad (2.87)$$

Because it is convenient to formulate the rotational dynamics equations in the body frame, consider converting the equation above to the body frame:

$$\bigcirc \frac{d}{dt} \left( \hat{\mathbf{H}}_{B/I}^\bullet \right) = \bigcirc \frac{d}{dt} \left( \hat{\mathbf{H}}_{B/I}^\bullet \right) + \underbrace{\boldsymbol{\omega}_{B/I} \times \hat{\mathbf{H}}_{B/I}^\bullet}_{\text{Gyroscopic moment}} = \mathbf{M}_\bullet \quad (2.88)$$

Define the components of the net moment acting on the CG as:

$$\mathbf{M}_{\bullet} = L\mathbf{i}_B + M\mathbf{j}_B + N\mathbf{k}_B \quad (2.89)$$

where  $L$ ,  $M$ , and  $N$  are the rolling, pitching, and yawing moments, respectively. Recall that:

$$\hat{\mathbf{H}}_{B/I}^{\bullet} = \begin{bmatrix} h_x \\ h_y \\ h_z \end{bmatrix} = \mathbf{I}_{B/I} \begin{bmatrix} p \\ q \\ r \end{bmatrix} \quad (2.90)$$

Then, Eq. (2.88) can be rewritten as:

$$\begin{bmatrix} L \\ M \\ N \end{bmatrix} = \underbrace{\mathbf{I}_{B/I} \begin{bmatrix} \dot{p} \\ \dot{q} \\ \dot{r} \end{bmatrix}}_{\textcircled{B} \frac{d}{dt}(\hat{\mathbf{H}}_{B/I}^{\bullet})} + \underbrace{\begin{bmatrix} 0 & -r & q \\ r & 0 & -p \\ -q & p & 0 \end{bmatrix} \mathbf{I}_{B/I} \begin{bmatrix} p \\ q \\ r \end{bmatrix}}_{\boldsymbol{\omega}_{B/I} \times \hat{\mathbf{H}}_{B/I}^{\bullet}} \quad (2.91)$$

Solving for the time rate of change of the angular rates yields the rotational dynamics equations of motion:

$$\begin{bmatrix} \dot{p} \\ \dot{q} \\ \dot{r} \end{bmatrix} = \mathbf{I}_{B/I}^{-1} \left( \begin{bmatrix} L \\ M \\ N \end{bmatrix} - \begin{bmatrix} 0 & -r & q \\ r & 0 & -p \\ -q & p & 0 \end{bmatrix} \mathbf{I}_{B/I} \begin{bmatrix} p \\ q \\ r \end{bmatrix} \right) \quad (2.92)$$

Write out rot dynamics eqs. of motion with  $\mathbf{I}_{xz}$ .

### 2.3.5 Acceleration of an Arbitrary Point on the Rotorcraft Body

Acceleration at an arbitrary point on the rotorcraft body can be of interest for multiple reasons, including assessing the accelerations perceived by the pilot and/or passengers at their seat for comfort purposes, or for motion cueing in a simulated environment. Consider the geometry shown in Fig. 2.11, where:

$$\mathbf{r}_{\bullet \rightarrow P} = l_x \mathbf{i}_B + l_y \mathbf{j}_B + l_z \mathbf{k}_B \quad (2.93)$$

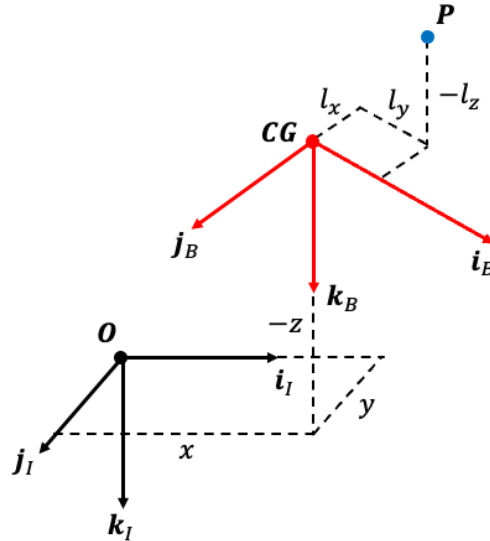


Figure 2.11: Geometry for the acceleration at an arbitrary point  $P$  on the rotorcraft body.

To obtain the acceleration at point P, one can start by differentiating the velocity vector at that point with respect to time:

$$\begin{aligned}
 \mathbf{a}_{P/I} &= \textcircled{I} \frac{d}{dt} (\mathbf{v}_{P/I}) \\
 &= \textcircled{I} \frac{d}{dt} (\mathbf{v}_{\bullet/I} + \boldsymbol{\omega}_{B/I} \times \mathbf{r}_{\bullet \rightarrow P}) \\
 &= \textcircled{I} \frac{d}{dt} (\mathbf{v}_{\bullet/I}) + \textcircled{I} \frac{d}{dt} (\boldsymbol{\omega}_{B/I} \times \mathbf{r}_{\bullet \rightarrow P}) \\
 &= \textcircled{B} \frac{d}{dt} (\mathbf{v}_{\bullet/I}) + \boldsymbol{\omega}_{B/I} \times \mathbf{v}_{\bullet/I} + \textcircled{I} \frac{d}{dt} (\boldsymbol{\omega}_{B/I}) \times \mathbf{r}_{\bullet \rightarrow P} + \boldsymbol{\omega}_{B/I} \times \textcircled{I} \frac{d}{dt} (\mathbf{r}_{\bullet \rightarrow P}) \\
 &= \textcircled{B} \frac{d}{dt} (\mathbf{v}_{\bullet/I}) + \boldsymbol{\omega}_{B/I} \times \mathbf{v}_{\bullet/I} + \left[ \textcircled{B} \frac{d}{dt} (\boldsymbol{\omega}_{B/I}) + \cancel{\boldsymbol{\omega}_{B/I} \times \boldsymbol{\omega}_{B/I}} = \mathbf{0} \right] \times \mathbf{r}_{\bullet \rightarrow P} + \\
 &\quad + \boldsymbol{\omega}_{B/I} \left[ \textcircled{B} \frac{d}{dt} (\mathbf{r}_{\bullet \rightarrow P}) + \boldsymbol{\omega}_{B/I} \times \mathbf{r}_{\bullet \rightarrow P} \right] \\
 &= \underbrace{\textcircled{B} \frac{d}{dt} (\mathbf{v}_{\bullet/I}) + \boldsymbol{\omega}_{B/I} \times \mathbf{v}_{\bullet/I}}_{\text{Term 1}} + \underbrace{\textcircled{B} \frac{d}{dt} (\boldsymbol{\omega}_{B/I}) \times \mathbf{r}_{\bullet \rightarrow P}}_{\text{Term 2}} + \underbrace{\boldsymbol{\omega}_{B/I} \times (\boldsymbol{\omega}_{B/I} \times \mathbf{r}_{\bullet \rightarrow P})}_{\text{Term 3}}
 \end{aligned} \tag{2.94}$$

Let us analyze the various terms:

1. **Term 1:** It was previously shown that:

$$\textcircled{B} \frac{d}{dt} (\mathbf{v}_{\bullet/I}) + \boldsymbol{\omega}_{B/I} \times \mathbf{v}_{\bullet/I} = \begin{bmatrix} \dot{u} \\ \dot{v} \\ \dot{w} \end{bmatrix} + \begin{bmatrix} 0 & -r & q \\ r & 0 & -p \\ -q & p & 0 \end{bmatrix} \begin{bmatrix} u \\ v \\ w \end{bmatrix} = \begin{bmatrix} \dot{u} - rv + qw \\ \dot{v} + ru - pw \\ \dot{w} - qu + pv \end{bmatrix} \tag{2.95}$$

2. **Term 2:**

$$\textcircled{B} \frac{d}{dt} (\boldsymbol{\omega}_{B/I}) \times \mathbf{r}_{\bullet \rightarrow P} = \begin{bmatrix} \dot{p} \\ \dot{q} \\ \dot{r} \end{bmatrix} \times \begin{bmatrix} l_x \\ l_y \\ l_z \end{bmatrix} = \begin{bmatrix} 0 & -\dot{r} & \dot{q} \\ \dot{r} & 0 & -\dot{p} \\ -\dot{q} & \dot{p} & 0 \end{bmatrix} \begin{bmatrix} l_x \\ l_y \\ l_z \end{bmatrix} = \begin{bmatrix} -\dot{r}l_y + \dot{q}l_z \\ \dot{r}l_x - \dot{p}l_z \\ -\dot{q}l_x + \dot{p}l_y \end{bmatrix} \tag{2.96}$$

3. **Term 3:**

$$\begin{aligned}
 \boldsymbol{\omega}_{B/I} \times (\boldsymbol{\omega}_{B/I} \times \mathbf{r}_{\bullet \rightarrow P}) &= \begin{bmatrix} p \\ q \\ r \end{bmatrix} \times \left( \begin{bmatrix} p \\ q \\ r \end{bmatrix} \times \begin{bmatrix} l_x \\ l_y \\ l_z \end{bmatrix} \right) = \begin{bmatrix} 0 & -r & q \\ r & 0 & -p \\ -q & p & 0 \end{bmatrix} \begin{bmatrix} -rl_y + ql_z \\ rl_x - pl_z \\ -ql_x + pl_y \end{bmatrix} \\
 &= \begin{bmatrix} -(q^2 + r^2)l_x + pql_y + prl_z \\ pql_x - (p^2 + r^2)l_y + qrl_z \\ prl_x + qrl_y - (p^2 + q^2)l_z \end{bmatrix}
 \end{aligned} \tag{2.97}$$

Thus,

$$\begin{aligned}
 \begin{bmatrix} a_x \\ a_y \\ a_z \end{bmatrix} &= \begin{bmatrix} \ddot{u} - rv + qw - \dot{r}l_y + \dot{q}l_z - (q^2 + r^2)l_x + pql_y + prl_z \\ \ddot{v} + ru - pw + \dot{r}l_x - \dot{p}l_z + pql_x - (p^2 + r^2)l_y + qrl_z \\ \ddot{w} - qu + pv - \dot{q}l_x + \dot{p}l_y + prl_x + qrl_y - (p^2 + q^2)l_z \end{bmatrix} \\
 &= \begin{bmatrix} \ddot{u} - rv + qw \\ \ddot{v} + ru - pw \\ \ddot{w} - qu + pv \end{bmatrix} + \begin{bmatrix} -(q^2 + r^2) & -\dot{r} + pq & \dot{q} + pr \\ \dot{r} + pq & -(p^2 + r^2) & -\dot{p} + qr \\ -\dot{q} + pr & \dot{p} + qr & -(p^2 + q^2) \end{bmatrix} \begin{bmatrix} l_x \\ l_y \\ l_z \end{bmatrix}
 \end{aligned} \tag{2.98}$$

Note that not only the inertial forces act on the point P but also gravitational forces. Gravitational forces are

transformed to the body frame as follows:

$$\begin{aligned}
 (\mathbf{a}_{P/I})_{\text{grav}} &= \mathbf{T}_{I \rightarrow B} \begin{bmatrix} 0 \\ 0 \\ g \end{bmatrix} \\
 &= \begin{bmatrix} \cos \theta \cos \psi & \cos \theta \sin \psi & -\sin \theta \\ \sin \phi \sin \theta \cos \psi - \cos \phi \sin \psi & \sin \phi \sin \theta \sin \psi + \cos \phi \cos \psi & \sin \phi \cos \theta \\ \cos \phi \sin \theta \cos \psi + \sin \phi \sin \psi & \cos \phi \sin \theta \sin \psi - \sin \phi \cos \psi & \cos \phi \cos \theta \end{bmatrix} \begin{bmatrix} 0 \\ 0 \\ g \end{bmatrix} \quad (2.99) \\
 &= \begin{bmatrix} -g \sin \phi \\ g \sin \phi \cos \theta \\ g \cos \phi \cos \theta \end{bmatrix}
 \end{aligned}$$

where  $g$  is the gravitational acceleration. Thus,

$$\boxed{\mathbf{a}_{P/I} = \begin{bmatrix} a_x \\ a_y \\ a_z \end{bmatrix} = \begin{bmatrix} \dot{u} - rv + qw \\ \dot{v} + ru - pw \\ \dot{w} - qu + pv \end{bmatrix} + \begin{bmatrix} -(q^2 + r^2) & -\dot{r} + pq & \dot{q} + pr \\ \dot{r} + pq & -(p^2 + r^2) & -\dot{p} + qr \\ -\dot{q} + pr & \dot{p} + qr & -(p^2 + q^2) \end{bmatrix} \begin{bmatrix} l_x \\ l_y \\ l_z \end{bmatrix} + \begin{bmatrix} -g \sin \phi \\ g \sin \phi \cos \theta \\ g \cos \phi \cos \theta \end{bmatrix}} \quad (2.100)$$

### 2.3.6 Motion Primitives

As shown above, the rigid-body dynamics of the rotorcraft can be described as a nonlinear time-invariant system of the form:

$$\dot{\mathbf{x}} = \mathbf{f}(\mathbf{x}, \mathbf{u}) \quad (2.101)$$

where  $\mathbf{x} \in \mathcal{X} \subseteq \mathbb{R}^n$  is the state vector belonging to an  $n$ -dimensional manifold  $\mathcal{X}$  and  $\mathbf{u} \in \mathcal{U} \subseteq \mathbb{R}^m$  is the control input vector belonging to an  $m$ -dimensional manifold  $\mathcal{U}$ . The state space  $\mathcal{X}$  can be decomposed into the product  $\mathcal{C} \times \mathcal{Y}$ , where  $\mathcal{C}$  is the space defined by the so-called *cyclic coordinates* and  $\mathcal{Y}$  is the space defined by the *non-cyclic coordinates* [FDF05]. The system dynamics are invariant with respect to group actions (e.g., translations or rotations) on  $\mathcal{C}$ . The space  $\mathcal{C}$  is called a reduced configuration space and is defined by a subset of the state vector with respect to which the system has certain symmetry properties. Consider the following state and control input vectors relative to the rigid-body dynamics of the conventional helicopter of Eq. (9.141):

$$\mathbf{x}^T = [u \ v \ w \ p \ q \ r \ \phi \ \theta \ \psi \ x \ y \ z] \quad (2.102a)$$

$$\mathbf{u}^T = [\delta_{\text{lat}} \ \delta_{\text{lon}} \ \delta_{\text{col}} \ \delta_{\text{ped}}] \quad (2.102b)$$

where  $\delta_{\text{lat}}$  and  $\delta_{\text{lon}}$  are the lateral and longitudinal stick pilot inputs,  $\delta_{\text{col}}$  is the collective stick input, and  $\delta_{\text{ped}}$  are the pedal inputs. If one assumes the air density to be constant with the vertical position  $z$ , such that the aerodynamic forces and moments do not change with altitude, then helicopter dynamics do not depend on the helicopter's position ( $x$ ,  $y$ , and  $z$ ) or on its heading  $\psi$ . As such, the space  $\mathcal{C}$  corresponds to the space of translations in the position space and rotations about the NED frame vertical axis. Specifically, the space  $\mathcal{C}$  is invariant with respect to actions of the group  $\mathcal{G}$ , defined as the space of  $4 \times 4$  matrices of the form:

$$\mathcal{G}(\psi, x, y, z) = \begin{bmatrix} \cos \psi & -\sin \psi & 0 & x \\ \sin \psi & \cos \psi & 0 & y \\ 0 & 0 & 1 & z \\ 0 & 0 & 0 & 1 \end{bmatrix} \quad (2.103)$$

where the air density change with respect to the vertical position  $z$  is assumed as negligible. In light of this, it is convenient to partition the state vector into invariant and non-invariant parts with respect to the group action  $\mathcal{G}$ , given respectively by:

$$\mathbf{x}_C^T = [\psi \ x \ y \ z] \quad (2.104a)$$

$$\mathbf{x}_Y^T = [u \ v \ w \ p \ q \ r \ \phi \ \theta] \quad (2.104b)$$

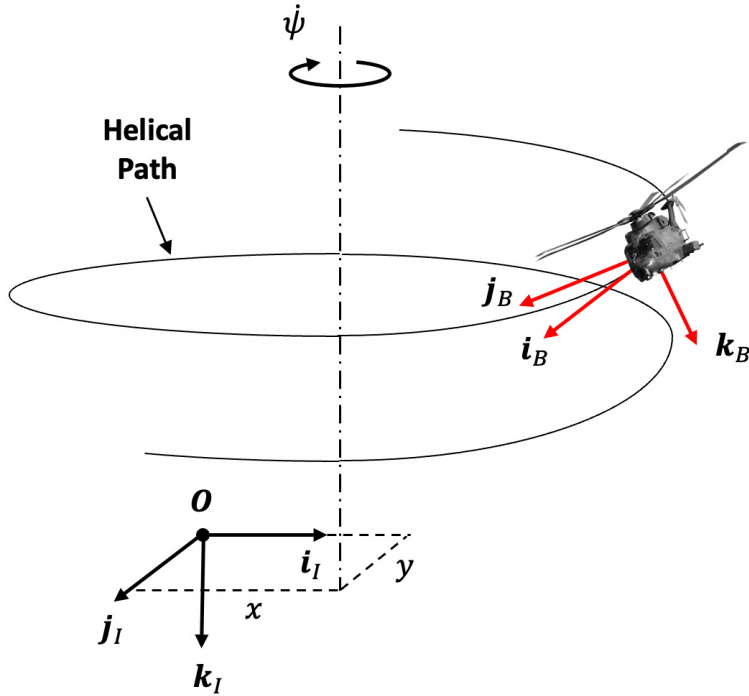


Figure 2.12: Trim primitives: arcs of helical flight paths with a vertical axis.

The invariance with respect to a group action leads to the definition of a notion of equivalent trajectories, and to the concept of motion primitives. Two state and control trajectories are said to be equivalent if they can be exactly superimposed through time translation and the action of the symmetry group  $\mathcal{G}$ . Consider a state and control trajectory  $\pi : [0, T] \rightarrow \mathcal{X} \times \mathcal{U}$ , where  $T$  is the duration of the trajectory. A motion primitive is the class of trajectories equivalent to  $\pi$ .

Once motion primitives are defined, it is convenient to classify them into two groups: trim primitives and maneuver primitives. Trim primitives correspond to steady-state motions, or trim trajectories, where the controls and non-invariant part of the state vector are constant (or trimmed). This means that their time derivative is zero:

$$\frac{d}{dt} [\mathbf{x}_Y^T \mathbf{u}^T]^T = \mathbf{0} \quad (2.105)$$

On the other hand, maneuver primitives are defined as unsteady trajectories that begin and end at a steady-state condition. This means that maneuver primitives are those trajectories that connect subsequent trim primitives. It follows that two different trim primitives must be connected by at least one maneuver primitive [FDF05]. In the context of flight dynamics, these concepts help define the notions of trim flight and maneuvering flight for a helicopter in a mathematically rigorous way. Specifically, trim primitives correspond to arcs of helical flight paths with a vertical axis, including degenerate ones such as straight lines and horizontal circles which are flown at constant speed, constant roll and pitch angles, and constant control settings (Fig. 2.12). In terms of typical helicopter maneuvers, these trim trajectories correspond to hover, steady level flight, steady turns, steady climbs and descents, and their combinations (*i.e.*, steady climbing or descending turns, *etc.*).

Maneuvers are defined as those trajectories that connect the above trim conditions. An example may be pull-up or push-over maneuvers that connect trim conditions including, but not limited to, steady level flight and steady climbing or descending flight. Another example may be roll-in or roll-out maneuvers that connect trim conditions such as steady level flight and steady turns. This concept is illustrated in Fig. 2.13.

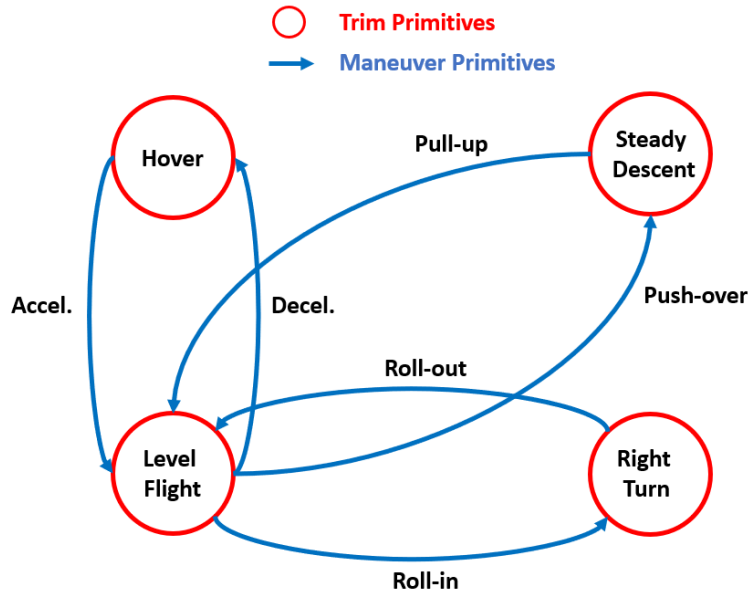


Figure 2.13: Transition diagram between trim and maneuver primitives.

## Bibliography

- [FDF05] E. Frazzoli, M. A. Dahleh, and E. Feron. “Maneuver-Based Motion Planning for Nonlinear Systems With Symmetries”. In: *IEEE Transactions on Robotics* 21.6 (Dec. 2005), pages 1077–1091. DOI: <https://doi.org/10.1109/TR0.2005.852260> (cited on pages 47, 48).





## 3. Rotor Aerodynamics

### 3.1 Review of Conservation Laws of Aerodynamics

Consider a fluid flow with the following characteristics: (i) 1-dimensional, (ii) quasi-steady, (iii) incompressible, (iv) inviscid, and (v) unconstrained. Additionally, consider the control volume  $V$  fixed with respect to the reference frame  $x, y, z$  (*i.e.*, Eulerian control volume). The control volume is enclosed by the surface  $S$ . This setup is shown in Fig. 3.1. Then, the dynamics of the fluid flow is fully described by the equations that follow.

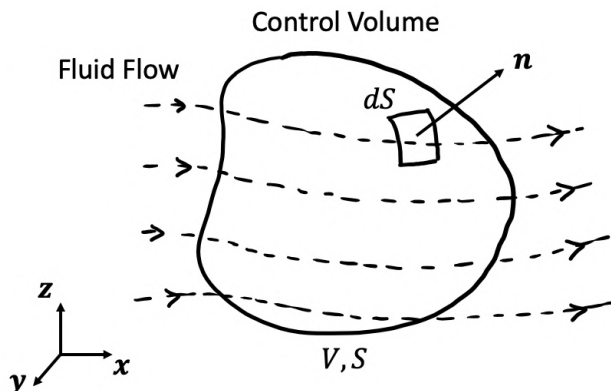


Figure 3.1: Fluid flow over a control volume fixed with respect to the reference frame.

- 1. Conservation of Mass (or Continuity Equation):** Mass flow rate into the control volume must be equal to the mass flow rate out of the control volume.

$$\iint_S \rho (\mathbf{v} \cdot \mathbf{n}) dS = 0 \quad (3.1)$$

where  $\rho$  is the density of the fluid,  $\mathbf{v}$  is the local velocity of the fluid, and  $\mathbf{n}$  is the unity vector normal to the elemental area  $dS$  enclosing the control volume  $V$ . Note that, by convention,  $dS$  points outward of the enclosed control volume. This equation is a scalar equation.

- 2. Conservation of Momentum:** Net force  $\mathbf{F}$  on the fluid flow is equal to the time rate of change of the fluid momentum across the control surface.

$$\mathbf{F} = \underbrace{\iint_S p \mathbf{n} dS}_{=0} + \iint_S (\rho \mathbf{v} \cdot \mathbf{n}) \mathbf{v} dS \quad (3.2)$$

where  $p$  is the local pressure and  $\mathbf{F}$  is the net force on the fluid flow. This equation is a vector equation. Note that the first term on the right-hand side, which describes the net pressure on the fluid flow, is zero for an unconstrained flow.

3. **Conservation of Energy:** Work done on the fluid per unit time is equal to the time rate of change of the kinetic energy of the fluid.

$$W = \iint_S \frac{1}{2} (\rho \mathbf{v} \cdot \mathbf{n}) |\mathbf{v}|^2 dS \quad (3.3)$$

where  $W$  is the work done on the fluid. This equation is a scalar equation.

4. **Bernoulli's Principle:** A re-arrangement of the conservation of energy and, as such, an alternative to it. Bernoulli's principle states that an increase in speed of fluid occurs simultaneously with a decrease in static pressure.

$$p + \frac{1}{2} \rho |\mathbf{v}|^2 + \rho g z \approx 0 = \text{const.} \quad (3.4)$$

where  $p$  is the static pressure,  $g$  is the gravitational acceleration,  $z$  is the height of the fluid, and  $\frac{1}{2} \rho |\mathbf{v}|^2$  is the dynamic pressure. Note that the second term on the right-hand side, which describes the gravitational potential, can typically be neglected. Like the conservation of energy, this equation is scalar.

## 3.2 Momentum Theory in Hover

Consider the case of a hovering (*i.e.*, fixed with respect to the ground) helicopter rotor, as shown in Fig. 3.2. The cross sections in this figure indicate the following regions in the rotor wake:

- 0: plane *far upstream* the rotor
- 1: plane just above rotor disk
- 2: plane just below rotor disk
- $\infty$ : *far wake*

The objective of this analysis is to apply the conservation laws to derive useful equations relating the rotor thrust, rotor area, induced velocity at the rotor disk, and velocity in the far wake.

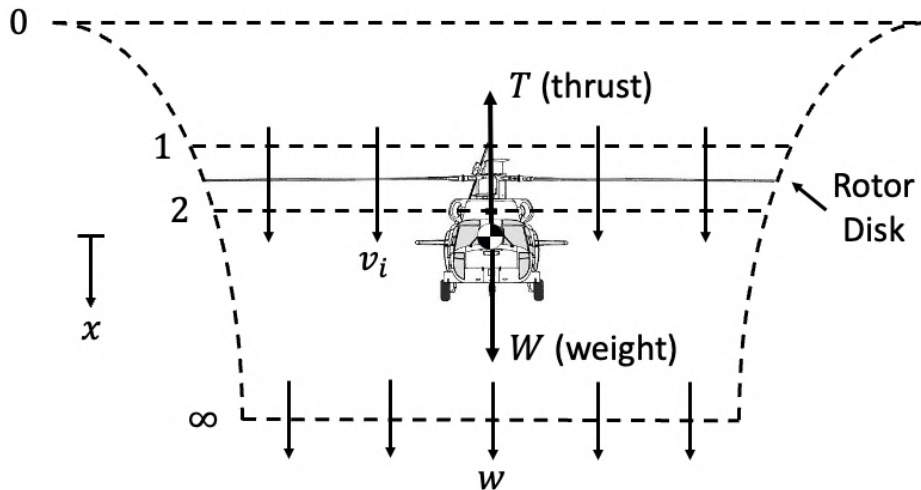


Figure 3.2: Hovering helicopter rotor.

Recall that the principle of the conservation of mass states that the mass flow rate  $\dot{m}$  must be constant within the boundaries of the control volume. In this case, the control volume is chosen as the rotor wake. By

applying the conservation of mass between 2 and  $\infty$ , as shown in Fig. 3.3a, one obtains:

$$\begin{aligned} 0 &= \iint_{\infty} \rho (\mathbf{v} \cdot \mathbf{n}_{\infty}) dS + \iint_2 \rho (\mathbf{v} \cdot \mathbf{n}_2) dS \\ &= \iint_{\infty} \rho w dS - \iint_2 \rho v_i dS \\ &= \rho A_{\infty} w - \rho A v_i \end{aligned} \quad (3.5)$$

where:

$v_i$  is the *induced velocity* at the rotor disk (in ft/s),

$w$  is the *far wake velocity* (in ft/s),

$\dot{m}$  is the mass flow rate (in lb/s), and

$A_2 = A_1 = A$  is the rotor disk area (in  $\text{ft}^2$ ).

It follows that the mass flow rate is given by:

$$\dot{m} = \rho A_{\infty} w = \rho A v_i \quad (3.6)$$

Next, by using conservation of momentum one can relate the rotor thrust,  $T$ , to the net time rate of change of the fluid momentum out of the control volume. Note that the rotor thrust has the same magnitude but opposite sign with respect to aircraft weight,  $W$ . By applying conservation of momentum between 0 and  $\infty$ , as shown in Fig. 3.3b, one obtains:

$$\begin{aligned} -F = -W = T &= \iint_{\infty} \rho (\mathbf{v} \cdot \mathbf{n}_{\infty}) \mathbf{v} dS + \iint_0 \rho (\mathbf{v} \cdot \mathbf{n}_0) \mathbf{v} dS \\ &= (\rho A_{\infty} w) w \\ &= \dot{m} w \end{aligned} \quad (3.7)$$

Note that the integral taken at cross section 0 is zero as the velocity of the fluid far upstream of the rotor is zero.

From the principle of conservation of energy, the work done on the rotor per unit time is equal to the gain in energy of the fluid per unit time. The work done by the rotor per unit time (*i.e.*, the power consumed by the rotor) is found by applying the conservation of energy between 0 and  $\infty$ , as shown in Fig. 3.3b:

$$\begin{aligned} T v_i &= \iint_{\infty} \frac{1}{2} \rho (\mathbf{v} \cdot \mathbf{n}_{\infty}) |\mathbf{v}|^2 dS + \iint_0 \frac{1}{2} \rho (\mathbf{v} \cdot \mathbf{n}_0) |\mathbf{v}|^2 dS \\ &= \frac{1}{2} (\rho A_{\infty} w) w^2 \\ &= \frac{1}{2} \dot{m} w^2 \end{aligned} \quad (3.8)$$

Again, note that the integral taken at cross section 0 is zero as the velocity of the fluid far upstream of the rotor is zero. The result of Eq. (3.8) can be re-arranged to yield to:

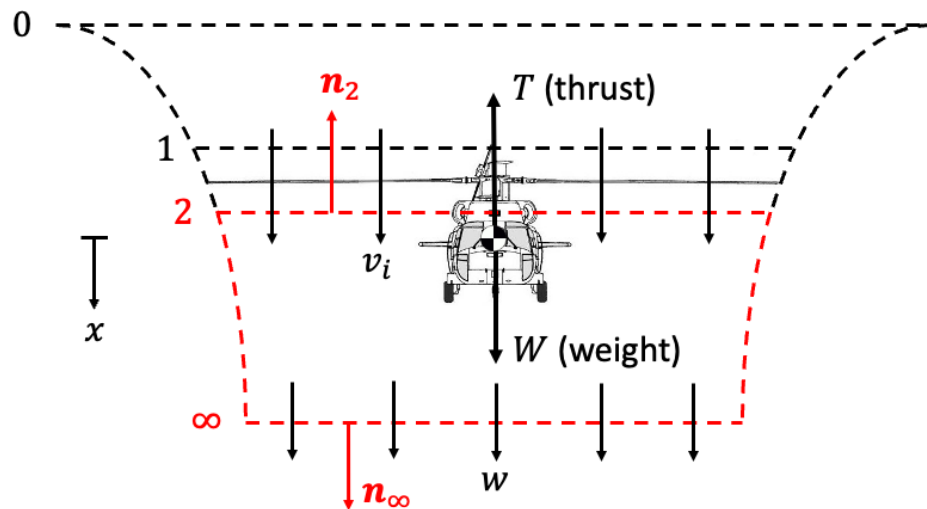
$$T = \frac{1}{2} \dot{m} \frac{w^2}{v_i} \quad (3.9)$$

By now equating Eqs. (3.7) and (3.9) and rearranging, one obtains the following relation between the induced velocity at the rotor disk and the velocity in the far wake:

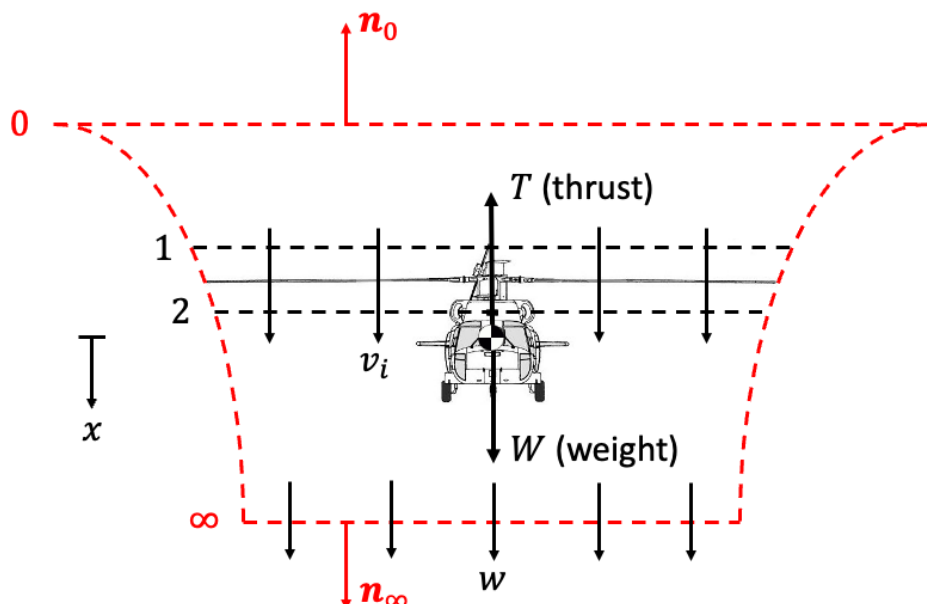
$$v_i = \frac{1}{2} w \quad (3.10)$$

It is clear that the far wake velocity is twice the induced velocity at the rotor disk. This result can substituted in Eq. (3.6) to yield:

$$\boxed{\frac{A_{\infty}}{A} = \frac{1}{2}} \quad (3.11)$$



(a) Conservation of mass.



(b) Conservation of momentum and energy.

Figure 3.3: Control volumes used for the application of momentum theory in hover.

Or, equivalently,

$$\frac{R_\infty}{R} = 0.707 \quad (3.12)$$

This means that the area of the fluid flow in the far wake is half of the main rotor area. This is why the fluid flow in the far wake is called *vena contracta* (Latin etymology: *vena*: vein, *contracta*: contracted; used for the first time by Evangelista Torricelli, an Italian mathematician student of Galileo Galilei circa 1643 to describe where the cross-section of a fluid flow is minimum). Check out the wake contraction of a Sikorsky S-92 in the video at the following link: <https://www.youtube.com/watch?v=lslarZiRJhg>.

### 3.3 Disk Loading and Power Loading

Consider the results from the application of conservation of momentum and substitute  $w = 2v_i$  in the thrust equation:

$$T = \dot{m}w = \dot{m}(wv_i) = (\rho Av_i)(2v_i) = 2\rho Av_i^2 \quad (3.13)$$

Solving for  $v_i$  leads to:

$$v_i = \sqrt{\left(\frac{T}{A}\right) \frac{1}{2\rho}} = v_h \quad (3.14)$$

where  $v_h$  is the induced velocity in hover (*i.e.*, stationary flight) and  $T/A = DL$  is the *disk loading* (in lb/ft<sup>2</sup>). Note that for multi-rotor aircraft, it should be assumed that each rotor carries an equal proportion of the aircraft weight such that the disk loading is given by:

$$DL = \frac{(T/n)}{A_n} = \frac{(W/n)}{A_n} \quad (3.15)$$

where  $n$  is the number of rotors.

Consider now the results from the application of conservation of energy. The ideal power required to hover is:

$$\begin{aligned} P &= T v_i = T v_h = T \sqrt{\left(\frac{T}{A}\right) \frac{1}{2\rho}} = \frac{T^{3/2}}{\sqrt{2\rho A}} \\ &= 2\rho Av_i^3 \end{aligned} \quad (3.16)$$

It is best to have low disk loading to minimize power required. Note that the power grows with the cube of the induced velocity and, as such, is best to have low induced velocity to minimize power required.

Define *power loading* as:

$$PL = \frac{T}{P} = \frac{T}{Tv_i} = \frac{1}{v_i} = \sqrt{\frac{2\rho}{T/A}} \quad (3.17)$$

Power loading is a measure of hovering efficiency. It can be thought about as the amount of power needed to hover per unit thrust (in lb/hp). The power loading decreases with increasing disk loading. It follows that it is best to have low disk loading to achieve high power loading (*i.e.*, hovering efficiency). Additionally, power loading is inversely proportional to the induced velocity at the rotor disk,  $v_i$ , which indicates that low induced velocities are necessary for high hovering efficiency. General trends for power loading vs. disk loading across different rotorcraft designs are shown in Fig.. 3.4a, whereas examples from specific rotorcraft are shown in Fig. 3.4b.

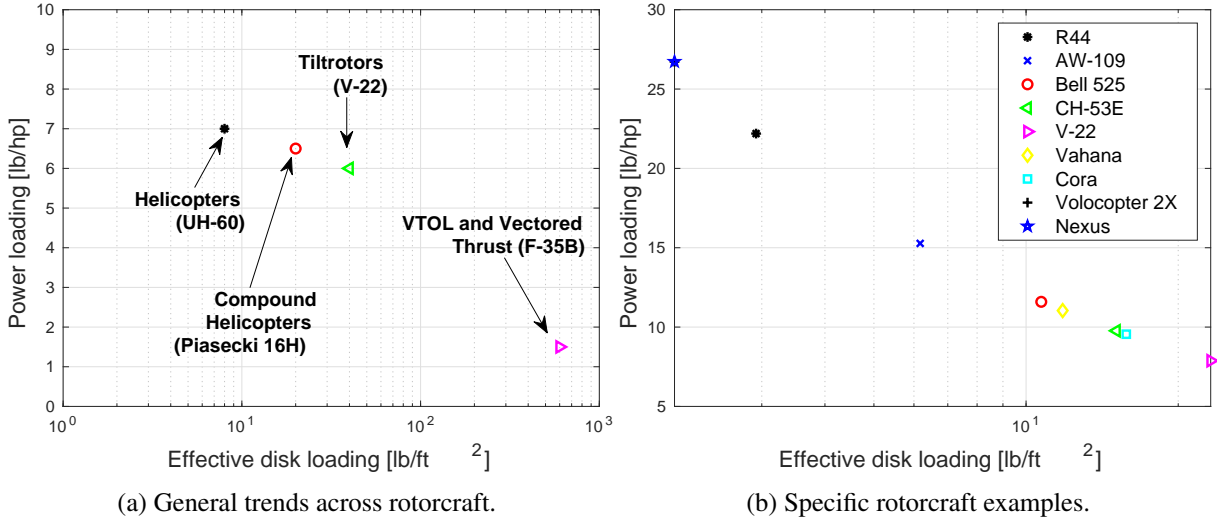


Figure 3.4: Power loading vs. disk loading.

### 3.4 Non-dimensional Analysis

It is convenient to define non-dimensional quantities to be able to compare different rotors. Consider non-dimensionalizing the induced velocity at the rotor disk by dividing by the rotor blade tip speed:

$$\lambda_i = \frac{v_i}{v_{\text{tip}}} = \frac{v_i}{R\Omega} \quad (3.18)$$

where:

$\lambda_i$  is the *induced inflow ratio*,

$R$  is the radius of the rotor,

$\omega$  is the angular speed of the rotor in rad/s, and

$v_{\text{tip}} = \Omega R$  is the tangential speed of the rotor blade tip in ft/s.

Following Buckingham's  $\Pi$  method, one can define other non-dimensional quantities:

$$\text{Thrust Coefficient : } C_T = \frac{T}{\rho A v_{\text{tip}}^2} = \boxed{\frac{T}{\rho A \Omega^2 R^2}} \quad (3.19a)$$

$$\text{Torque Coefficient : } C_Q = \frac{Q}{\rho A v_{\text{tip}}^2 R} = \boxed{\frac{Q}{\rho A \Omega^2 R^3}} \quad (3.19b)$$

$$\text{Power Coefficient : } C_P = \frac{P}{\rho A v_{\text{tip}}^3} = \frac{P}{\rho A \Omega^3 R^3} = \frac{Q \lambda_i}{\rho A \Omega^2 R^3} = \boxed{\frac{Q}{\rho A \Omega^2 R^3} = C_Q} \quad (3.19c)$$

(3.19d)

where  $v_{\text{tip}}$  is the reference speed (in ft/s),  $A$  is the reference area (*i.e.*, the rotor disk area, in ft<sup>2</sup>), and  $\rho$  is the reference air density (in slug/ft<sup>3</sup>). In addition, relations between non-dimensional coefficients can be derived:

$$\lambda_i = \frac{v_i}{\Omega R} = \frac{1}{\Omega R} \sqrt{\left(\frac{T}{A}\right) \frac{1}{2\rho}} = \sqrt{\frac{T}{2\rho A (\Omega R)^2}} = \boxed{\sqrt{\frac{C_T}{2}}} \quad (3.20a)$$

$$C_P = \frac{T v_i}{\rho A (\Omega R)^3} = \left( \frac{T}{\rho A (\Omega R)^2} \right) \left( \frac{v_i}{\Omega R} \right) = \boxed{C_T \lambda_i = \frac{C_T^{3/2}}{\sqrt{2}}} \quad (3.20b)$$

Consider now the relationship  $C_P = \frac{C_T^{3/2}}{\sqrt{2}}$  derived with momentum theory. There is a mismatch between momentum theory and experimental data, as shown in Fig. 3.5. This is because momentum theory does not include the following:

- Non-uniform inflow
- Tip losses
- Wake swirl
- Less-than-ideal wake contraction
- Finite number of blades
- Blade drag

How to include these sources in power estimate?

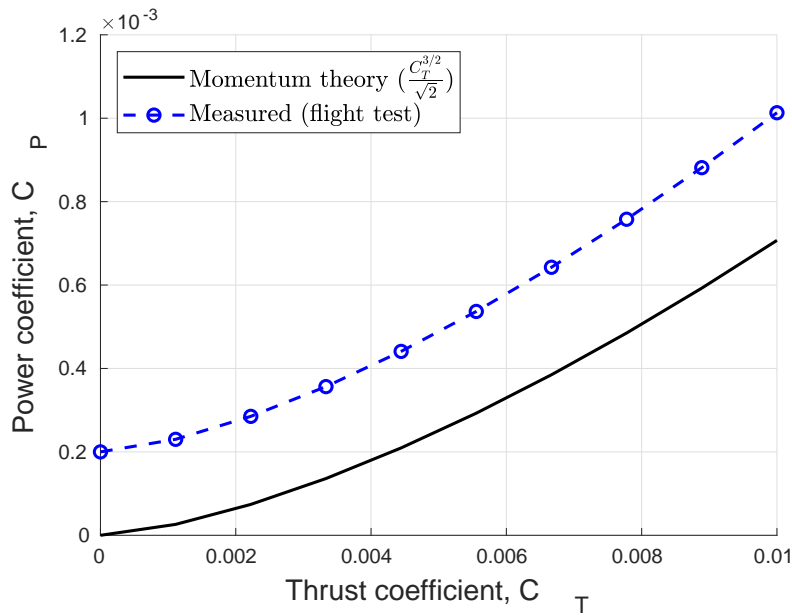


Figure 3.5: Comparison between the power coefficient measured from flight-test data and that derived with momentum theory.

### 3.4.1 Total Power Coefficient

Let us start by analyzing the mismatch between the theoretical and experimental curves in Fig. 3.5. It appears that the two curves differ because of two major reasons: (i) a constant bias and (ii) a constant factor multiplying  $\frac{C_T^{3/2}}{\sqrt{2}}$ . In fact, with regards to the latter, the experimental curve is shown to be steeper than that obtained with momentum theory for increasing  $C_T$ . As such, make the assumption that the total power coefficient is the summation of two contributions:

$$C_P = C_{P_i} + C_{P_0} \quad (3.21)$$

where  $C_{P_i}$  is the *induced power coefficient* and  $C_{P_0}$  is the *profile power coefficient*. The mathematical description of these two contributions is articulated as follows.

The induced power coefficient is given by an empirical modification of the results from momentum theory:

$$C_{P_i} = k \frac{C_T^{3/2}}{\sqrt{2}} \quad (3.22)$$

where  $k$  is known as the *induced power factor* (typically  $k = 1.15$ ). The induced power factor accounts for non-uniform inflow, tip losses, wake swirl, less-than-ideal wake contraction, and finite number of blades.

The profile power coefficient accounts for the power losses associated to the profile drag of the rotor blades. Consider an element-by-element analysis of the rotor blade sectional drag force to define the power dissipated by aerodynamic drag:

$$\begin{aligned}
 P_0 &= \Omega N_b \int_0^R D y dy \\
 &= \Omega N_b \int_0^R \left( \frac{1}{2} \rho u^2 c C_D \right) y dy \approx C_{D0} \\
 &= \Omega N_b \int_0^R \left( \frac{1}{2} \rho (\Omega y)^2 c D_0 \right) y dy \\
 &= \frac{1}{8} \rho N_b \Omega^3 c C_{D0} R^4
 \end{aligned} \tag{3.23}$$

where:

- $D$  is the drag of the infinitesimal blade element in lb,
- $y$  is the coordinate along the blade element in ft,
- $u$  is the blade element tangential speed in ft/s,
- $c$  is the blade chord in ft,
- $C_D$  is the drag coefficient of the rotor blade, and
- $N_b$  is the number of blades.

Converting to non-dimensional form yields:

$$C_{P0} = \frac{P_0}{\rho A V_{tip}^3} = \frac{P_0}{\rho A \Omega^3 R^3} = \frac{1}{8} \left( \frac{N_b c R}{A} \right) C_{D0} = \frac{1}{8} \left( \frac{N_b c R}{\pi R^2} \right) C_{D0} = \underbrace{\frac{1}{8} \left( \frac{N_b c}{\pi R} \right)}_{\sigma} C_{D0} = \boxed{\frac{1}{8} \sigma C_{D0}} \tag{3.24}$$

where  $\sigma$  is defined as the *rotor solidity*. The rotor solidity is the ratio of the blade area to the rotor disk area:

$$\boxed{\sigma = \frac{N_b c}{\pi R}} \tag{3.25}$$

and is typically within the range  $0.05 < \sigma < 0.12$  for conventional rotors. As such, the total power coefficient is:

$$\boxed{C_P = k \frac{C_T^{3/2}}{\sqrt{2}} + \frac{1}{8} \sigma C_{D0}} \tag{3.26}$$

where  $k \approx 1.15$  and  $C_{D0} \approx 0.01$ .

### 3.4.2 Figure of Merit

Although power loading is a very useful quantity, it is dimensional. As a result, a non-dimensional quantity became more popular over the years to evaluate and compare rotor efficiency. This measure is the *figure of merit* (FM).

$$\begin{aligned}
 FM &= \frac{\text{Ideal Power Required to Hover}}{\text{Actual Power Required to Hover}} < 1 \\
 &= \frac{P_{ideal}}{P_{meas}} = \frac{C_{Tmeas}^{3/2} / \sqrt{2}}{C_{Pmeas}}
 \end{aligned} \tag{3.27}$$

The measured power can be approximated with the estimate obtained from modified momentum theory to yield:

$$\boxed{FM = \frac{\frac{C_{T_{\text{meas}}}^{3/2}}{\sqrt{2}}}{k \frac{C_{T_{\text{meas}}}^{3/2}}{\sqrt{2}} + \frac{1}{8} \sigma C_{D_0}}} \quad (3.28)$$

Consider the following observations:

1. At low operating thrust, the FM is low. This is because the profile drag term in the denominator is large compared to the induced power term in the numerator.
2. As  $C_T$  increases, the FM increases approaching an asymptote given by  $y = 1/k$ , as shown in Fig. 3.6. Formally:

$$\lim_{C_T \rightarrow \infty} FM = \frac{1}{k} \approx 0.87, \quad k = 1.15 \quad (3.29)$$

3. In practice, the FM reaches a lesser value than  $FM = 1/k$  because high rotor thrust coefficients are associated with higher profile drag coefficients. In fact, for high rotor thrust coefficients, the approximation  $C_D \approx C_{D_0}$  is no longer valid. Rather, for these conditions, a more effective approximation may be the following:

$$C_D \approx C_{D_0} + aC_L^2 = C_{D_0} + a(C_{L_\alpha})^2 \quad (3.30)$$

4. Typical rotors have  $0.7 < FM < 0.8$ . State of the art rotors may have  $FM \approx 0.82$  (e.g., Blue Edge rotor on the Airbus H160, or the BERP rotor on the AgustaWestland AW101).

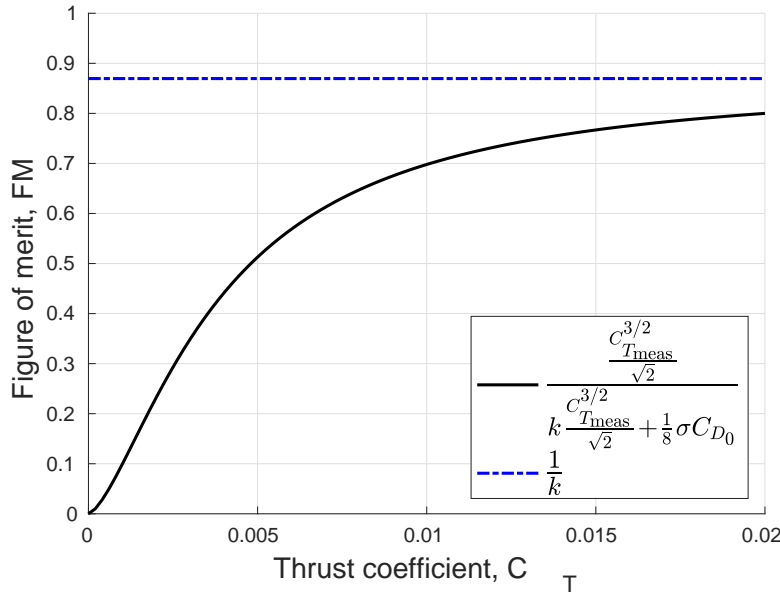


Figure 3.6: FM with increasing thrust coefficients for a rotor with  $k = 1.15$ ,  $\sigma = 0.1$ , and  $C_{D_0} = 0.01$ .

It is also worth noting that the FM shall be used to compare only rotors with the same disk loading. Consider re-writing the FM in terms of disk loading (*i.e.*,  $DL = T/A$ ):

$$FM = \frac{P_{\text{ideal}}}{kP_{\text{ideal}} + P_0} = \frac{1}{k + \frac{P_0}{P_{\text{ideal}}}} = \frac{1}{k + \frac{\sqrt{2\rho}}{T} \frac{P_0}{\sqrt{DL}}} \quad (3.31)$$

Increasing disk loading increases ideal power associated to profile power, producing a higher FM (with all other factors being equal). It follows that rotors with higher disk loading always have higher FM.

### 3.5 Momentum Analysis in Axial Climb

Consider the case of a helicopter in axial climb with climb velocity  $V_c > 0$ , as shown in Fig. 3.7. Note that this is a steady condition such that thrust equals the weight (*i.e.*,  $T = W$ ). Note that, differently from the hover case,

- The relative velocity far upstream the main rotor is  $V_c$  (*i.e.*, climb velocity).
- The velocity at the rotor disk (cross sections 1 and 2) is  $V_c + v_i$ .
- The velocity far downstream the main rotor (at cross section  $\infty$ ) is  $w + V_c$ .

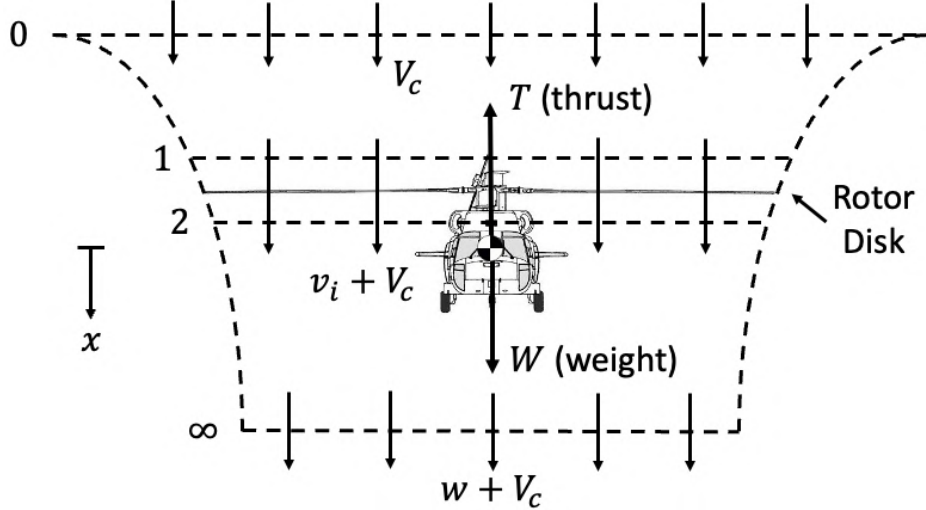


Figure 3.7: Helicopter rotor in an axial climb.

Let us follow the same steps taken for the analysis of the hover case. Consider applying conservation of mass between cross sections 2 and  $\infty$ :

$$\begin{aligned} 0 &= \iint_{\infty} \rho (\mathbf{v} \cdot \mathbf{n}_{\infty}) dS + \iint_2 \rho (\mathbf{v} \cdot \mathbf{n}_2) dS \\ &= \iint_{\infty} \rho (w + V_c) dS - \iint_2 \rho (v_i + V_c) dS \\ &= \rho A_{\infty} (w + V_c) - \rho A (v_i + V_c) \end{aligned} \quad (3.32)$$

It follows that the mass flow rate is given by:

$$\dot{m} = \rho A_{\infty} (w + V_c) = \rho A (v_i + V_c) \quad (3.33)$$

Next, conservation of momentum is used to relate the rotor thrust,  $T$ , to the net time rate of change of the fluid momentum out of the control volume. By applying conservation of momentum between 0 and  $\infty$  one obtains:

$$\begin{aligned} T &= \iint_{\infty} \rho (\mathbf{v} \cdot \mathbf{n}_{\infty}) \mathbf{v} dS + \iint_0 \rho (\mathbf{v} \cdot \mathbf{n}_0) \mathbf{v} dS \\ &= \iint_{\infty} \rho (w + V_c)^2 dS - \iint_0 \rho V_c^2 dS \\ &= \dot{m} (w + V_c) - \dot{m} V_c \\ &= \dot{m} w \end{aligned} \quad (3.34)$$

Knowing that the work per unit time done by the climbing rotor is  $T (v_i + V_c)$ , apply conservation of energy

between 0 and  $\infty$ :

$$\begin{aligned}
 T(v_i + V_c) &= \iint_{\infty} \frac{1}{2} \rho (\mathbf{v} \cdot \mathbf{n}_{\infty}) |\mathbf{v}|^2 dS + \iint_0 \frac{1}{2} \rho (\mathbf{v} \cdot \mathbf{n}_0) |\mathbf{v}|^2 dS \\
 &= \iint_{\infty} \frac{1}{2} \rho (w + V_c)^3 dS - \iint_0 \frac{1}{2} \rho V_c^3 dS \\
 &= \frac{1}{2} \dot{m} (w + V_c)^2 - \frac{1}{2} \dot{m} V_c^2 \\
 &= \frac{1}{2} \dot{m} w (2V_c + w)
 \end{aligned} \tag{3.35}$$

Now, re-arrange Eq. (3.35) to obtain:

$$T = \frac{1}{2} \dot{m} w \frac{(2V_c + w)}{(V_c + v_i)} \tag{3.36}$$

By equating Eqs. (3.34) and (3.36), one can find the relationship between the far wake and the induced velocities:

$$\cancel{\dot{m} w} = \frac{1}{2} \cancel{\dot{m} w} \frac{(2V_c + w)}{(V_c + v_i)} \rightarrow v_i = \frac{1}{2} w \tag{3.37}$$

It is clear that in the case of an axial climb, like for the hover case, the far wake velocity is twice the induced velocity at the rotor disk. However, the induced velocity at the rotor disk differs between the axial climb and the hover case.

To find the relationship between the induced velocity in axial climb and that in hover consider substituting Eq. (3.33) into Eq. (3.34):

$$T = \dot{m} w = [\rho A (v_i + V_c)] 2V_i = 2\rho A (v_i + V_c) v_i \tag{3.38}$$

Now divide Eq. (3.38) by  $2\rho A$  to obtain:

$$\frac{T}{2\rho A} = v_h^2 = V_c v_i + v_i^2 \tag{3.39}$$

Rearranging yields the following quadratic equation in  $\frac{v_i}{v_h}$ :

$$\left( \frac{v_i}{v_h} \right)^2 + \frac{V_c}{v_h} \left( \frac{v_i}{v_h} \right) - 1 = 0 \tag{3.40}$$

which has two possible solutions:

$$\frac{v_i}{v_h} = \begin{cases} -\left(\frac{V_c}{2v_h}\right) + \sqrt{\left(\frac{V_c}{2v_h}\right)^2 + 1} > 0 & \text{Induced velocity decreases with increasing climb speed} \\ -\left(\frac{V_c}{2v_h}\right) - \sqrt{\left(\frac{V_c}{2v_h}\right)^2 + 1} < 0 & \text{Physically invalid since } \frac{v_i}{v_h} > 0 \text{ for axial climb} \end{cases} \tag{3.41}$$

Because the climb velocity changes the induced velocity at the rotor disk, the induced power will also be affected:

$$\begin{aligned}
 \frac{P}{P_h} &= \frac{\mathcal{X}(v_i + V_c)}{\mathcal{X}v_h} = \frac{V_c}{v_h} + \frac{v_i}{v_h} = \frac{V_c}{v_h} - \frac{V_c}{2v_h} + \sqrt{\left(\frac{V_c}{2v_h}\right)^2 + 1} \\
 &= \boxed{\frac{V_c}{2v_h} + \sqrt{\left(\frac{V_c}{2v_h}\right)^2 + 1}, \quad V_c > 0}
 \end{aligned} \tag{3.42}$$

Consider the following observations:

1. The *power ratio*,  $\frac{P}{P_h}$ , increases monotonically with increasing *climb ratio*,  $\frac{V_c}{v_h}$  in axial climb (*i.e.*,  $V_c > 0$ ).
2. The power required to climb is always greater than the power required to hover.

### 3.6 Momentum Analysis in Axial Descent

Consider the case of an axial descent, as shown in Fig. 3.8, for which the climb velocity is  $V_c < 0$ . Note that for  $-2v_h \leq V_c < 0$  the axial climb model cannot be used since the velocity at any cross section of the assumed control volume, including the plane of the rotor, could either be positive or negative. As a consequence, momentum theory cannot be used as no definite control volume surrounding the main rotor and its wake can be established. As such, a key assumption that is required for the axial descent case is that  $|V_c| > 2v_h$ . Also note that, like the axial climb case, this is a steady condition such that thrust equals the weight (*i.e.*,  $T = W$ ).

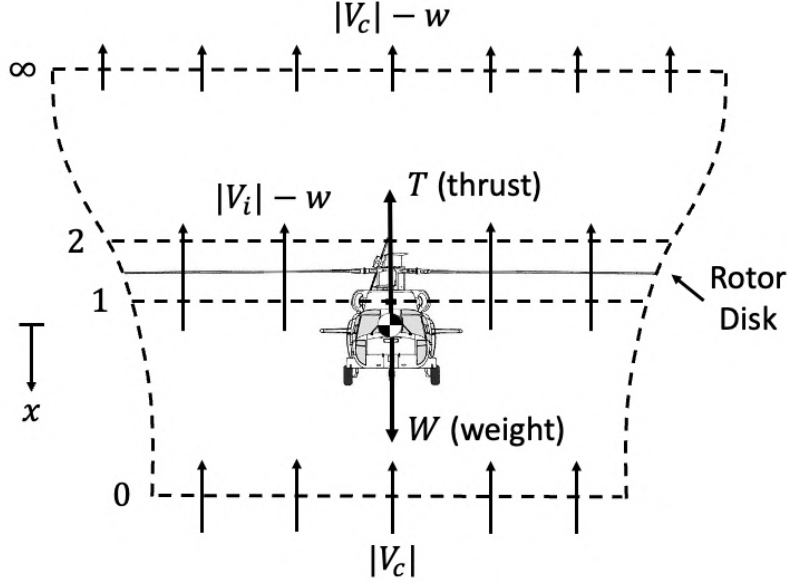


Figure 3.8: Helicopter rotor in an axial descent.

The flow velocities at the cross sections are the following:

- 0: far upstream (now below the rotor):  $|V_c|$
- 1, 2: planes respectively just below and above rotor disk:  $|V_c| - v_i$
- $\infty$ : far downstream (now above the rotor):  $|V_c| - w$  (note that the air decelerates through the rotor)

Let us follow the same steps taken for the analysis of the hover and axial climb cases. Consider applying conservation of mass between cross sections 2 and  $\infty$ , as shown in Fig. 3.9a, to obtain:

$$\begin{aligned} 0 &= \iint_{\infty} \rho (\mathbf{v} \cdot \mathbf{n}_{\infty}) dS + \iint_2 \rho (\mathbf{v} \cdot \mathbf{n}_2) dS \\ &= \iint_{\infty} \rho (V_c + w) dS - \iint_2 \rho (V_c + v_i) dS \\ &= \rho A_{\infty} (V_c + w) - \rho A (V_c + v_i) \end{aligned} \quad (3.43)$$

It follows that the mass flow rate is given by:

$$\dot{m} = \rho A_{\infty} (V_c + w) = \rho A \underbrace{(V_c + v_i)}_{<0} < 0 \quad (3.44)$$

Next, apply conservation of momentum between 0 and  $\infty$  as shown in Fig. 3.9b:

$$\begin{aligned} T &= \iint_{\infty} \rho (\mathbf{v} \cdot \mathbf{n}_{\infty}) \mathbf{v} dS + \iint_0 \rho (\mathbf{v} \cdot \mathbf{n}_0) \mathbf{v} dS \\ &= - \iint_{\infty} \rho (w + V_c)^2 dS + \iint_0 \rho V_c^2 dS \\ &= - \dot{m} (Y_c + w) + \dot{m} Y_c \\ &= - \dot{m} w \end{aligned} \quad (3.45)$$

Note that  $\dot{m} < 0$  such that  $T > 0$ . Knowing that the work per unit time done by the climbing rotor is  $T(v_i + V_c)$ , apply conservation of energy between 0 and  $\infty$  as shown in Fig. 3.9b:

$$\begin{aligned} T(v_i + V_c) &= \iint_{\infty} \frac{1}{2} \rho (\mathbf{v} \cdot \mathbf{n}_{\infty}) |\mathbf{v}|^2 dS + \iint_0 \frac{1}{2} \rho (\mathbf{v} \cdot \mathbf{n}_0) |\mathbf{v}|^2 dS \\ &= - \iint_{\infty} \frac{1}{2} \rho (w + V_c)^3 dS + \iint_0 \frac{1}{2} \rho V_c^3 dS \\ &= - \frac{1}{2} \dot{m} (w + V_c)^2 + \frac{1}{2} \dot{m} V_c^2 \\ &= - \frac{1}{2} \dot{m} w (2V_c + w) < 0 \end{aligned} \quad (3.46)$$

Because the power differential between 0 and  $\infty$  is less than zero, as shown in Eq. (3.46), the rotor is effectively extracting power from the airstream. This operating condition is called *windmill state* and is shown in Fig. 3.10a.

Similarly to the axial climb case, the relationship between the induced velocity in axial descent and the induced velocity in hover is found by substituting Eq. (3.44) into Eq. (3.45) and by rearranging, yielding two possible solutions:

$$\frac{v_i}{v_h} = \begin{cases} -\left(\frac{V_c}{2v_h}\right) + \sqrt{\left(\frac{V_c}{2v_h}\right)^2 - 1} > 1 & \text{Contradicts assumption that } v_i < v_h \Leftrightarrow v_i > \frac{1}{2}|V_c| \\ -\left(\frac{V_c}{2v_h}\right) - \sqrt{\left(\frac{V_c}{2v_h}\right)^2 - 1} < 1 & \text{In accord with assumptions} \end{cases} \quad (3.47)$$

The ratio between power required in an axial descent and that in hover is:

$$\begin{aligned} \frac{P}{P_h} &= \frac{\mathcal{I}(v_i + V_c)}{\mathcal{I}v_h} = \frac{V_c}{v_h} + \frac{v_i}{v_h} = \frac{V_c}{v_h} - \frac{V_c}{2v_h} - \sqrt{\left(\frac{V_c}{2v_h}\right)^2 - 1} \\ &= \boxed{\frac{V_c}{2v_h} - \sqrt{\left(\frac{V_c}{2v_h}\right)^2 - 1}, \quad \frac{V_c}{v_h} \leq -2} \end{aligned} \quad (3.48)$$

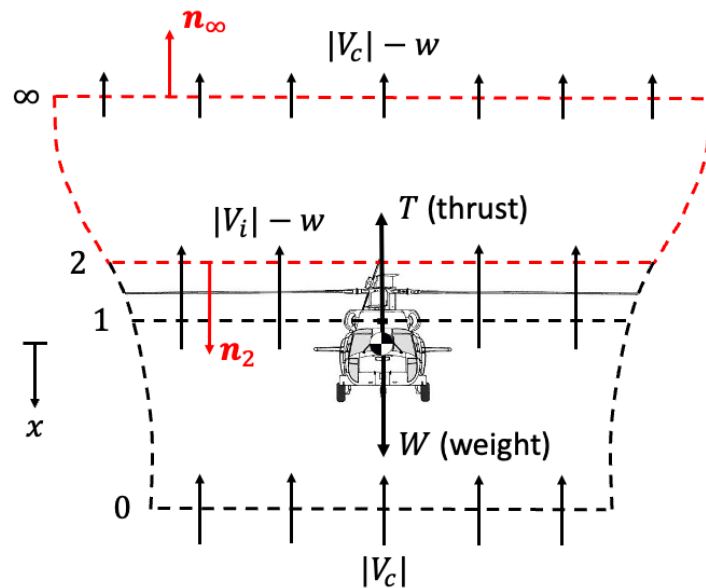
It is worth noting that no analytical treatment exists for the operating condition occurring between  $-2v_h \leq V_c < 0$ . This operating condition is known as the *vortex ring state* (Fig. 3.10b) and requires the velocity and power curves to be defined empirically. Check out a video on the vortex ring state at the following link: <https://www.youtube.com/watch?v=HjeRSDsy-nE&t=115s>.

Based on the analyses conducted for the case of axial climb and descent, the induced velocity and power ratios for varying climb ratio are reported respectively in Figs. 3.11a and 3.11b, including those derived empirically for the vortex ring state. Note that the climb ratio which results in zero power required (*i.e.*,  $\frac{V_c}{v_h} \approx 1.8$ ) corresponds to the point for ideal autorotation. In an ideal autorotation, the energy used to drive the rotor comes from potential energy converted to kinetic energy by the descent velocity of the rotor with respect to the airflow. The climb ratio for ideal autorotation corresponds to an induced velocity ratio of about  $\frac{v_i}{v_h} \approx 1.8$ .

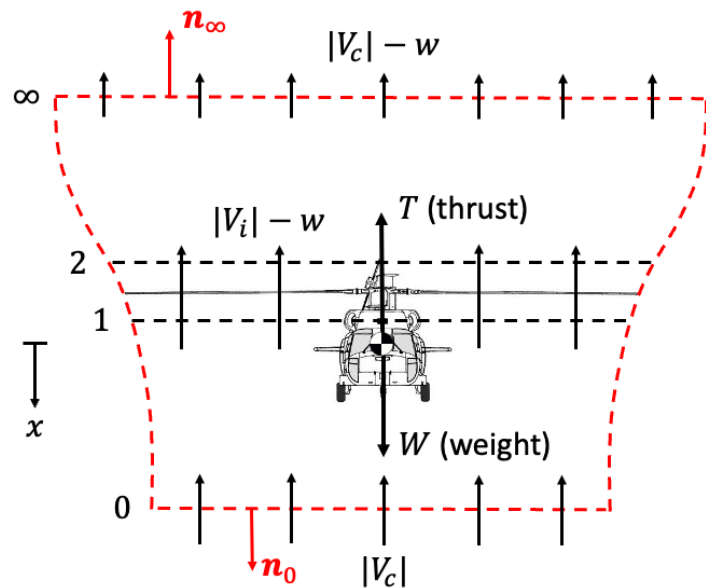
### 3.7 Momentum Analysis in Forward Flight

Consider the case of a helicopter in forward flight. Note that:

- The rotor moves with an edgewise component of velocity that is parallel to the plane of the rotor disk (*i.e.*,  $V_{\infty} \cos \alpha$ )
- Because the rotor is required to produce both lifting force,  $L$ , to overcome the weight of the helicopter, and a propulsive force equal and opposite to the drag,  $D$ , to propel the helicopter forward, the rotor disk must be tilted forward at an angle of attack  $\alpha$  relative to the oncoming flow.



(a) Conservation of mass.



(b) Conservation of momentum and energy.

Figure 3.9: Control volumes used for the application of momentum theory in axial descent.

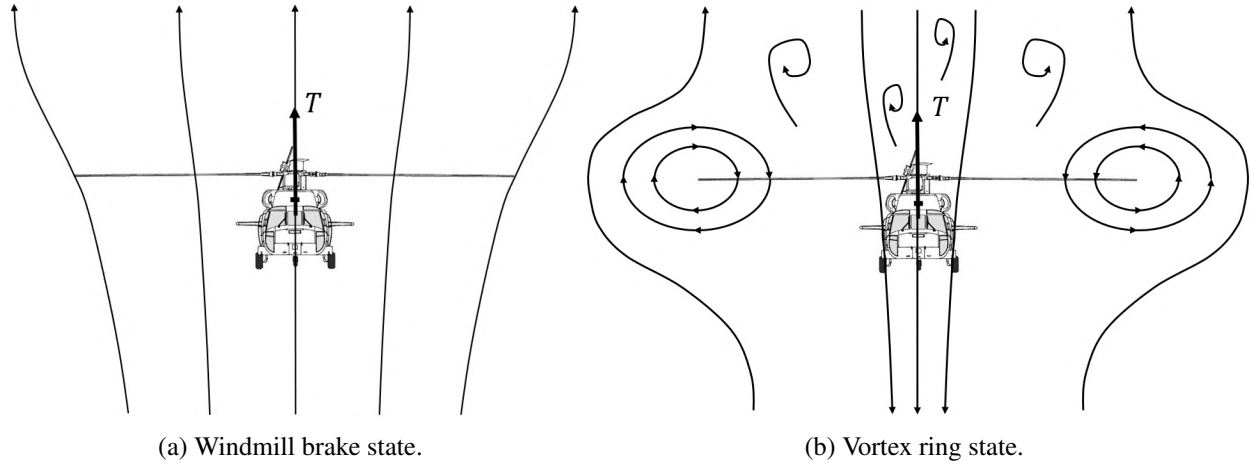


Figure 3.10: Rotor operating conditions in axial descent.

The mass flow rate through the actuator disk is  $\dot{m} = \rho A u$ , where:

$$u = \sqrt{(V_\infty \cos \alpha)^2 + (V_\infty \sin \alpha + v_i)^2} = \sqrt{V_\infty^2 + 2V_\infty v_i \sin \alpha + v_i^2} \quad (3.49)$$

Note that there is no rigor in this assumption, but it works. As done for the axial flight cases, consider applying conservation of momentum between cross sections 0 and  $\infty$ :

$$\begin{aligned} T &= \iint_{\infty} \rho (\mathbf{v} \cdot \mathbf{n}_\infty) \mathbf{v} dS + \iint_0 \rho (\mathbf{v} \cdot \mathbf{n}_0) \mathbf{v} dS \\ &= \dot{m} (w + V_\infty \sin \alpha) - \dot{m} V_\infty \sin \alpha \\ &= \dot{m} w \end{aligned} \quad (3.50)$$

Next, apply conservation of energy between 0 and  $\infty$ :

$$\begin{aligned} T(v_i + V_\infty \sin \alpha) &= \iint_{\infty} \frac{1}{2} \rho (\mathbf{v} \cdot \mathbf{n}_\infty) |\mathbf{v}|^2 dS + \iint_0 \frac{1}{2} \rho (\mathbf{v} \cdot \mathbf{n}_0) |\mathbf{v}|^2 dS \\ &= \frac{1}{2} \dot{m} (w + V_\infty \sin \alpha)^2 - \frac{1}{2} \dot{m} (V_\infty \sin \alpha)^2 \\ &= \frac{1}{2} \dot{m} (2V_\infty w \sin \alpha + w^2) \end{aligned} \quad (3.51)$$

By substituting Eq. (3.50) into Eq. (3.51) one obtains:

$$\cancel{\dot{m} w} (v_i + V_\infty \sin \alpha) = \frac{1}{2} \cancel{\dot{m}} (2V_\infty w \sin \alpha + w^2) \rightarrow v_i = \frac{1}{2} w \quad (3.52)$$

Like for the axial flight cases, the far wake velocity is twice the induced velocity at the rotor disk. Check out a video on the rotor wake in forward flight at: <https://www.youtube.com/watch?v=Mh-tRy2bE14>.

In light of this result, Eq. (3.50) can be re-written as:

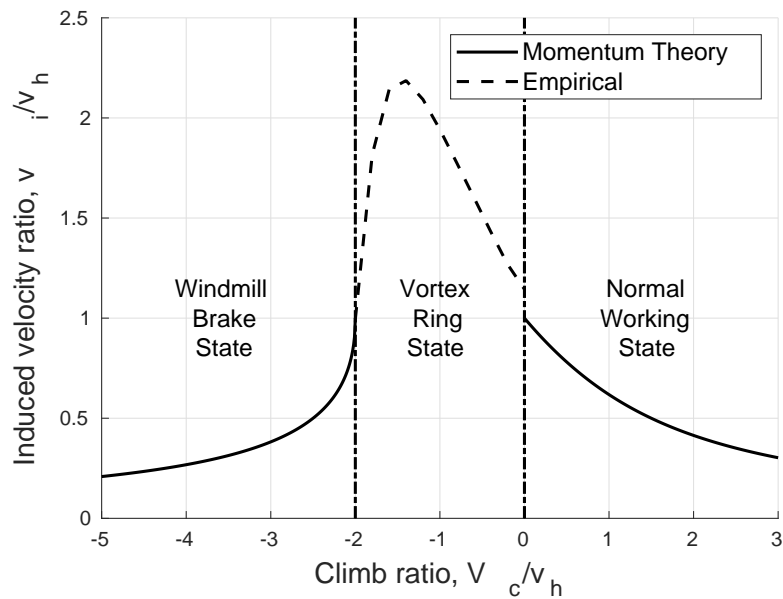
$$T = \dot{m} w = (\rho A u) (2v_i) = \boxed{2\rho A v_i \sqrt{V_\infty^2 + 2V_\infty v_i \sin \alpha + v_i^2}} \quad (3.53)$$

Note that:

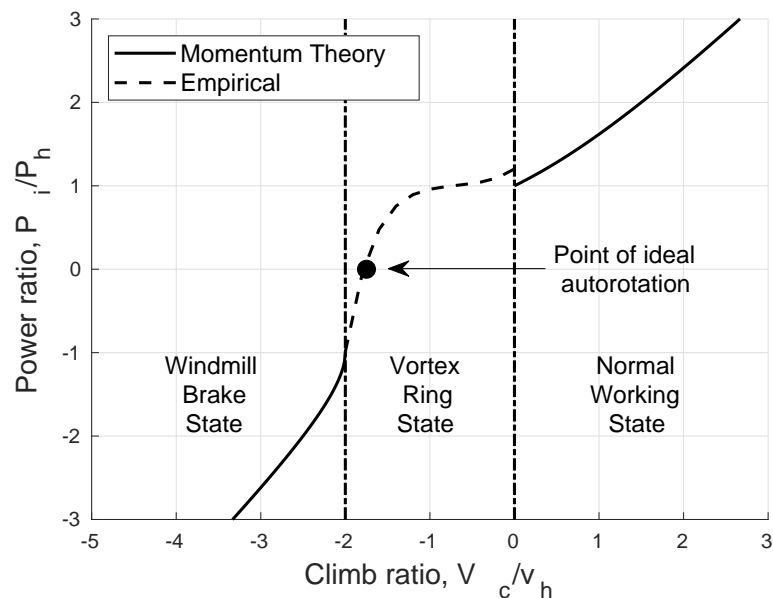
- For hovering flight ( $V_\infty = 0$ ), Eq. (3.53) reduces to:

$$T = 2\rho A v_i^2 = 2\rho A v_h^2 \quad (3.54)$$

which is in accord to the results from the momentum analysis in hovering flight.



(a) Induced velocity ratio.



(b) Induced power ratio.

Figure 3.11: Induced velocity and power ratios for varying climb ratio.

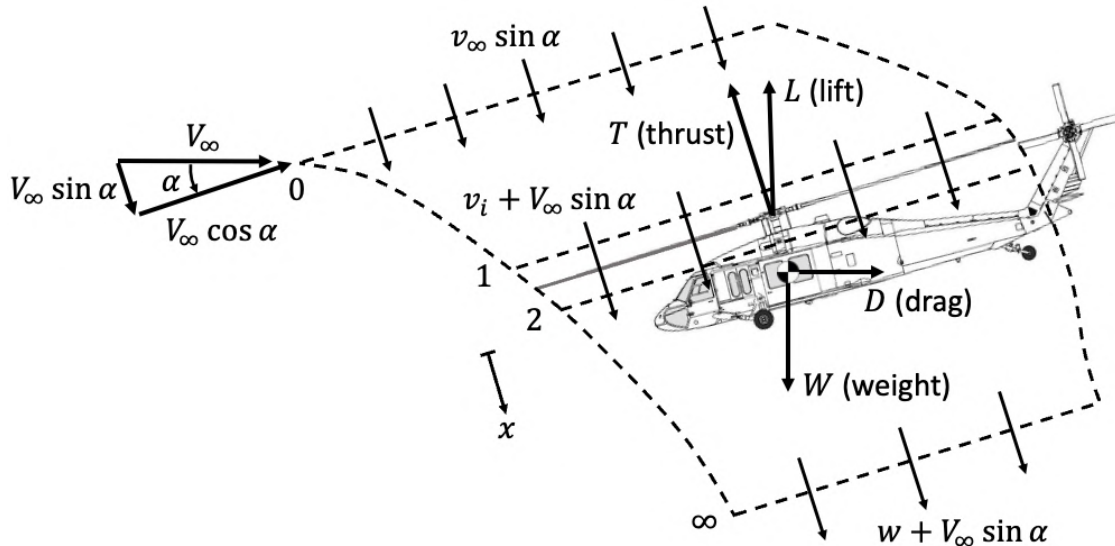


Figure 3.12: Helicopter rotor in forward flight.

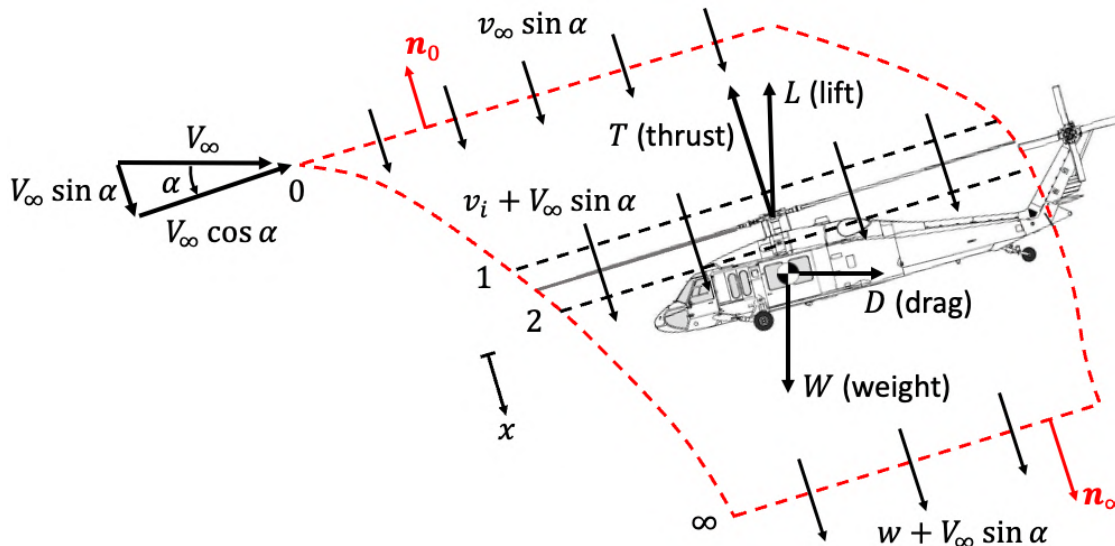


Figure 3.13: Helicopter rotor in forward flight.

- For  $V_\infty \gg v_i$ , Eq. (3.53) reduces to:

$$T \approx 2\rho A v_i v_\infty \quad \text{Glauert's high speed approximation} \quad (3.55)$$

By dividing Eq. (3.55) by  $2\rho A$  and noting that  $v_h = T / (2\rho A)$ , a second form of Glauert's high-speed approximation can be found:

$$\frac{v_i}{v_h} \approx \frac{1}{v_\infty} \quad (3.56)$$

To understand the relationship between the induced velocity at the rotor disk in forward flight and that in hover, consider rearranging Eq. (3.53) as follows:

$$\frac{T}{2\rho A} = v_i \sqrt{V_\infty^2 + 2V_\infty v_i \sin \alpha + v_i^2} \quad (3.57)$$

Recall that  $v_h = T / (2\rho A)$ . In light of this, Eq. (3.57) becomes:

$$v_i = \frac{v_h}{\sqrt{V_\infty^2 + 2V_\infty v_i \sin \alpha + v_i^2}} \quad (3.58)$$

Define the *advance ratio* as the ratio between the velocity parallel to the plane of the rotor and the tip speed:

$$\boxed{\mu = \frac{v_\infty \cos \alpha}{\Omega R}} \quad \rightarrow \quad \frac{v_\infty}{\Omega R} = \frac{\mu}{\cos \alpha} \quad (3.59)$$

Using Eq. (3.59), the inflow ratio can be written as:

$$\lambda = \frac{v_\infty \sin \alpha + v_i}{\Omega R} = \frac{v_\infty \sin \alpha}{\Omega R} + \frac{v_i}{\Omega R} = \mu \frac{\sin \alpha}{\cos \alpha} + \lambda_i = \mu \tan \alpha + \lambda_i \quad (3.60)$$

Consider now re-writing Eq. (3.58) in non-dimensional form (*i.e.*, divide by  $\Omega R$ ):

$$\lambda_i = \frac{\lambda_h^2}{\sqrt{\mu^2 + \lambda^2}} = \frac{\lambda_h = \sqrt{\frac{C_T}{2}}}{2\sqrt{\mu^2 + \lambda^2}} = \frac{C_T}{2\sqrt{\mu^2 + \lambda^2}} \quad (3.61)$$

Finally, Eq. (3.61) can be substituted in Eq. (3.60) to yield:

$$\boxed{\lambda = \mu \tan \alpha + \frac{C_T}{2\sqrt{\mu^2 + \lambda^2}}} \quad (3.62)$$

This equation describes the change in inflow with advance ratio, angle of attack, and thrust coefficient. Closed-form solution for  $\lambda$  can be found only for special cases (*e.g.*,  $\alpha = 0$ ) but generally simple numerical procedures are used to solve for  $\lambda$ .

Consider the special case where the angle of attack of the rotor is zero (*i.e.*,  $\alpha = 0$ ). Notice that, from Eq. (3.60),  $\lambda = \lambda_i$  for  $\alpha = 0$ . In this case, Eq. (3.62) reduces to:

$$\lambda_i = \frac{C_T}{2\sqrt{\mu^2 + \lambda^2}} = \frac{\lambda_h^2}{\sqrt{\mu^2 + \lambda^2}} \quad (3.63)$$

Squaring both sides of the equation above and rearranging leads to:

$$\lambda_i^4 + \mu^2 \lambda_i^2 - \lambda_h^4 = 0 \quad (3.64)$$

Dividing by  $\lambda_h^4$  leads to:

$$\left(\frac{\lambda_i}{\lambda_h}\right)^4 + \left(\frac{\mu}{\lambda_h}\right)^2 \left(\frac{\lambda_i}{\lambda_h}\right)^2 - 1 = 0 \quad (3.65)$$

This is a quadratic equation in  $(\lambda_i/\lambda_h)^2$  with the following closed-form solution:

$$\frac{\lambda_i}{\lambda_h} = \left[ -\frac{1}{2} \left( \frac{\mu}{\lambda_h} \right)^2 + \sqrt{\frac{1}{4} \left( \frac{\mu}{\lambda_h} \right)^4 + 1} \right]^{1/2}, \quad \alpha = 0 \quad (3.66)$$

This solution is shown in Fig. 3.14 and compared to Glauert's high-speed approximation. In this figure, it is shown that Glauert's approximation matches the exact solution obtained by assuming  $\alpha = 0$  for forward speed ratios equal or greater than 2 (*i.e.*, for  $\mu/\lambda_h > 2$ ). This approximation may reasonable for those compound rotorcraft with a pusher propeller and a single main rotor such as the Eurocopter X<sup>3</sup>, or the Lockheed AH-56. This is because these rotorcraft rely on the pusher propeller for propulsive force such the main rotor typically operates at angles of attack close to zero.

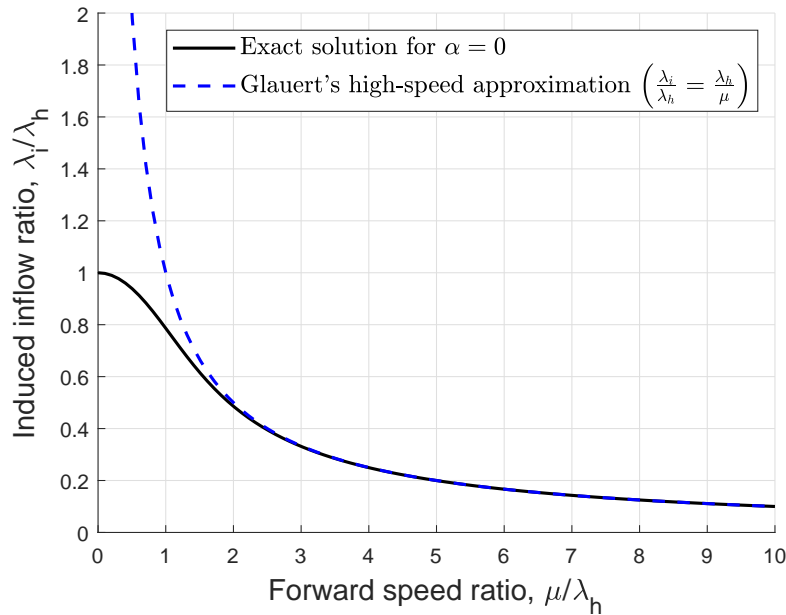


Figure 3.14: Induced inflow ratio as a function of forward speed ratio for  $\alpha = 0$ .

From Eq. (3.50), the power required in forward flight is:

$$P = T(v_\infty \sin \alpha + v_i) = \underbrace{T v_\infty \sin \alpha}_{\text{Power required to propel the rotor forward (and climb)}} + \underbrace{T v_i}_{\text{Induced power}} \quad (3.67)$$

The power ratio between the power required in forward flight and that in hover is:

$$\begin{aligned} \frac{P}{P_h} &= \frac{P}{T v_h} = \frac{\cancel{T}(v_\infty \sin \alpha + v_i)}{\cancel{T} v_h} = \frac{\frac{v_\infty \sin \alpha + v_i}{\Omega R}}{\frac{v_h}{\Omega R}} = \frac{\lambda}{\lambda_h} = \frac{\mu \tan \alpha + \frac{\lambda_h^2}{\sqrt{\mu^2 + \lambda^2}}}{\lambda_h} \\ &= \underbrace{\frac{\mu}{\lambda_h} \tan \alpha}_{\text{Power required to propel the rotor forward (and climb)}} + \underbrace{\frac{\lambda_h^2}{\sqrt{\mu^2 + \lambda^2}}}_{\text{Induced power}} \end{aligned} \quad (3.68)$$

As such, the power ratio coincides with the inflow ratio. General trends in inflow/power ratio are shown in Fig. 3.15. It is important to notice that the power required decreases to a minimum value at a certain forward speed ratio, and then increases again as the forward speed ratio grows. This result indicates that helicopters typically require less power to operate in hover than in forward flight.

### 3.8 Numerical Solution to the Inflow Equation in Forward Flight

Consider the inflow equation for forward flight, *i.e.*, Eq. (3.62):

$$\lambda = \mu \tan \alpha + \frac{C_T}{2\sqrt{\mu^2 + \lambda^2}}$$

Since in practice  $\alpha \neq 0$ , this equation is usually solved numerically. Two main numerical schemes are typically adopted for its solution: (i) fixed-point iteration or (ii) Newton-Raphson.

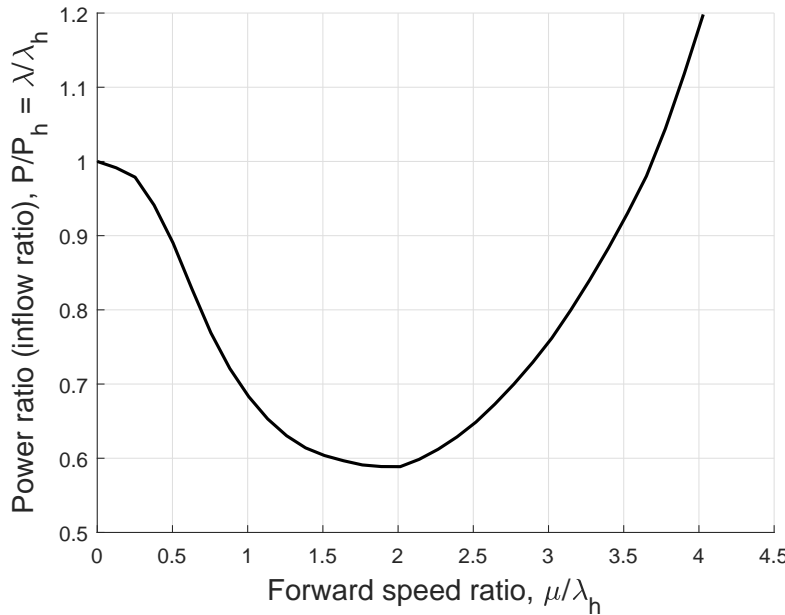


Figure 3.15: Inflow ratio/power ratio as a function of forward speed ratio.

### 3.8.1 Fixed-Point Iteration

Consider re-writing the inflow equation as an iteration equation:

$$\lambda_{n+1} = \mu \tan \alpha + \frac{C_T}{2\sqrt{\mu^2 + \lambda_n^2}} \quad (3.69)$$

where  $n$  is the iteration number. Then, new estimates of  $\lambda$  are iteratively computed until a termination criteria is met. The algorithm steps are articulated as follows:

1. Choose initial guess as:

$$\lambda_0 = \lambda_h = \sqrt{\frac{C_T}{2}} \quad (3.70)$$

2. Iteratively compute  $\lambda_{n+1}$  using Eq.(3.69).

3. Stop the algorithm when the convergence error, as defined below, is less than an arbitrary tolerance (e.g.,  $1e^{-5}$ ):

$$\varepsilon = \left| \frac{\lambda_{n+1} - \lambda_n}{\lambda_{n+1}} \right| < 1e^{-5} \quad (3.71)$$

Note that fixed-point iteration always converges from any initial guess. A typical number of iterations for convergence when applied to this problem is about 5 to 10. The fixed-point iteration scheme is of first order of convergence, as shown in Fig. 3.17. Example solutions to the inflow equation computed with this algorithm are shown in Fig. 3.16.

### 3.8.2 Newton-Raphson

The iteration scheme for Newoton-Raphson [Ypm95] is:

$$\lambda_{n+1} = \lambda_n - \gamma \frac{f(\lambda_n)}{f'(\lambda_n)} \quad (3.72)$$

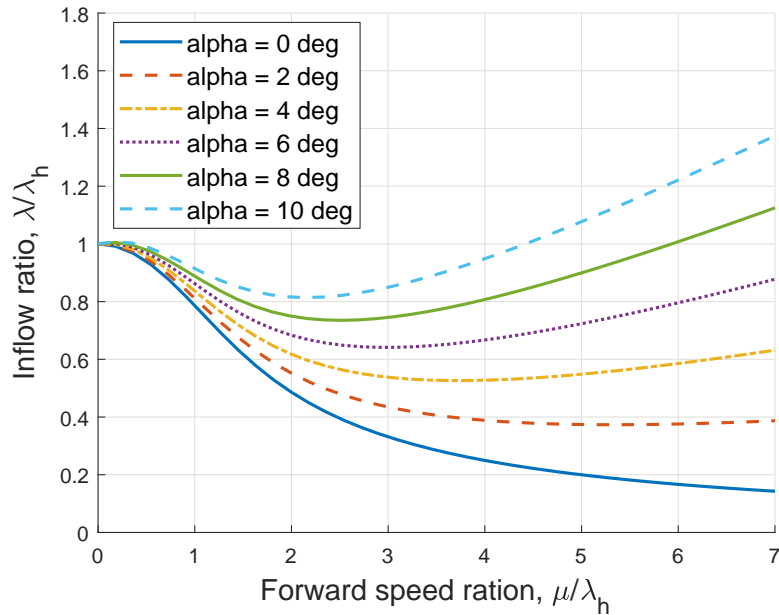


Figure 3.16: Inflow ratio as a function of forward speed ratio for varying rotor disk angles of attack.

where  $n$  is the iteration number and  $\gamma$  is a relaxation parameter that increases convergence stability at the cost of convergence speed. Typically,  $\gamma = 1$  for faster convergence and  $\gamma = 0.5$  for increased convergence stability. The function  $f(\lambda_n)$  is obtained by rearranging the inflow equation such that:

$$f(\lambda_n) = \lambda_n - \mu \tan \alpha - \frac{C_T}{2\sqrt{\mu^2 + \lambda_n^2}} \quad (3.73)$$

Differentiating with respect to  $\lambda$  yields:

$$f'(\lambda_n) = 1 + \frac{C_T}{2} (\mu^2 + \lambda_n^2)^{-3/2} \lambda_n \quad (3.74)$$

which is used in the Newton-Raphson update equation. New estimates of  $\lambda$  are iteratively computed until a termination criteria is met. The algorithm steps are articulated as follows:

1. Choose initial guess as:

$$\lambda_0 = \lambda_h = \sqrt{\frac{C_T}{2}} \quad (3.75)$$

2. Iteratively compute  $\lambda_{n+1}$  using Eq.(3.72).
3. Stop the algorithm when the convergence error, as defined below, is less than an arbitrary tolerance (e.g.,  $1e^{-5}$ ):

$$\varepsilon = \left| \frac{\lambda_{n+1} - \lambda_n}{\lambda_{n+1}} \right| < 1e^{-5} \quad (3.76)$$

Note that Newton-Raphson is sensitive to the first guess and, unlike fixed-point iteration, may not converge if the first guess is too far from the solution. However, it takes less iterations than the fixed-point scheme to converge as it is of second order of convergence (Fig. 3.17).

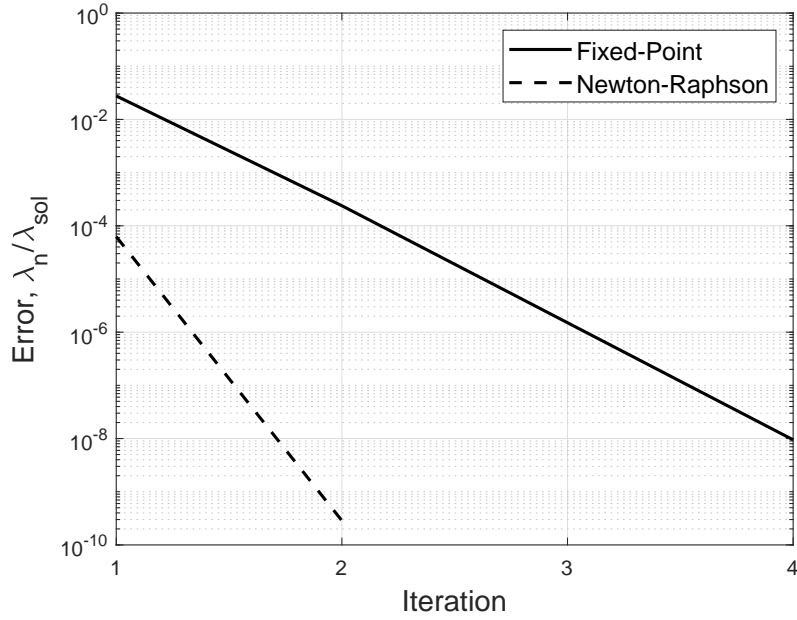


Figure 3.17: Convergence properties of numerical solution of inflow equation.

### 3.9 Dynamic Inflow Modeling

Solving iteratively for the inflow distribution at each iteration step may not be desirable as it can be computationally expensive. Moreover, this approach does not account for the inflow dynamics, which also include delays in the inflow response to pilot inputs. In fact, the methods described above rely on the assumption that the inflow is quasi static. While this may be a good enough approximation for trimmed flight, it may not necessarily be so for maneuvering flight and, in general, for unsteady flight conditions. Thus, it is often desirable in rotorcraft flight dynamics modeling to express the inflow distribution as a dynamic state (or multiple states) that augments the vehicle dynamics.

#### 3.9.1 Pitt-Peters

According to generalized dynamic inflow theory [Pet09; PBH89; PH91], the induced inflow distribution at the rotor disk can be approximated by a finite summation of radial and harmonic expansion functions:

$$v_i(\hat{r}, \psi, t) = \sum_{r=0}^{\infty} \sum_{j=r+1, r+3, \dots}^{\infty} \underbrace{\phi_j^r(\hat{r})}_{\begin{array}{c} \text{Radial} \\ \text{expansion} \\ \text{functions} \end{array}} \underbrace{[\alpha_j^r(t) \cos(r\psi) + \beta_j^r \sin(r\psi)]}_{\begin{array}{c} \text{Harmonic} \\ \text{expansion} \\ \text{functions} \end{array}} \quad (3.77)$$

where:

- $\hat{r} = \frac{r}{R}$  is the non-dimensional radial coordinate,
- $\psi$  is the azimuth angle of a reference rotor blade, and
- $\phi_j^r$ ,  $\alpha_j^r$ ,  $\beta_j^r$  are coefficients.

These coefficients can be driven by state equations based on the theory of Peters and He:

$$\mathbf{M} \begin{bmatrix} \dot{\alpha}_j^r \\ \dot{\beta}_j^r \end{bmatrix} + \mathbf{L}^{-1} \begin{bmatrix} \alpha_j^r \\ \beta_j^r \end{bmatrix} = \frac{1}{2} \begin{bmatrix} \tau_n^{mc} \\ \tau_n^{ms} \end{bmatrix} \quad (3.78)$$

where  $\mathbf{M}$  and  $\mathbf{L}^{-1}$  are the apparent mass and inflow static gain matrices, respectively. It is worth noting that the Peter-He inflow model can be scaled to include any number of states. The simplest form of this model is

the Pitt-Peters model [PP80], which is a 3-state inflow model. In this model, the induced inflow is assumed to have the following linear form:

$$\lambda(\hat{r}, \psi) = \lambda_0 + \lambda_{1c}\hat{r}\cos\psi + \lambda_{1s}\hat{r}\sin\psi \quad (3.79)$$

where  $\lambda_0$ ,  $\lambda_{1s}$ ,  $\lambda_{1c}$  are the uniform, lateral, and longitudinal rotor inflow components in the rotor hub frame and  $\psi$  is the azimuth angle of a reference blade. Because the apparent mass and inflow static gain matrices are typically given in the wind frame, it is convenient to introduce the transformation from the rotor hub to the wind frame. Consider the geometry in Fig. 3.18.

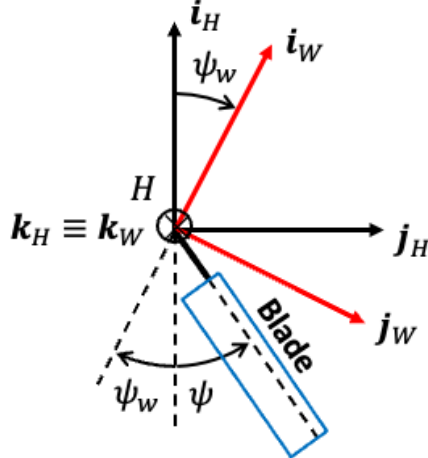


Figure 3.18: Rotor hub to wind frame transformation.

The wind frame consists of a positive rotation about the  $\mathbf{k}_H$  axis by the wind azimuth angle  $\psi_w$  given by:

$$\psi_w = \begin{cases} \tan^{-1}\left(\frac{v_H}{u_H}\right), & \text{counterclockwise rotor} \\ \tan^{-1}\left(-\frac{v_H}{u_H}\right), & \text{clockwise rotor} \end{cases} \quad (3.80)$$

where  $u_H$  and  $v_H$  are the longitudinal and lateral velocity components in the rotor hub frame (to be introduced in the next chapter). Then, the transformation matrix from the hub to wind frame is the following:

$$\begin{bmatrix} \mathbf{k}_W \\ \mathbf{i}_W \\ \mathbf{j}_W \end{bmatrix} = \underbrace{\begin{bmatrix} 1 & 0 & 0 \\ 0 & \cos\psi_w & \sin\psi_w \\ 0 & -\sin\psi_w & \cos\psi_w \end{bmatrix}}_{\mathbf{T}_{H \rightarrow W}} \begin{bmatrix} \mathbf{k}_H \\ \mathbf{i}_H \\ \mathbf{j}_H \end{bmatrix} \quad (3.81)$$

Note that the order of the axes in this transformation has been modified to be in agreement with the ordering of the inflow harmonic coefficients. The inflow harmonic coefficients are the solution of the following differential equation:

$$\begin{bmatrix} \dot{\lambda}_0 \\ \dot{\lambda}_{1s} \\ \dot{\lambda}_{1c} \end{bmatrix} = \Omega \mathbf{T}_{W \rightarrow H} \mathbf{M}^{-1} \left\{ -\mathbf{L}^{-1} \left( \mathbf{T}_{H \rightarrow W} \begin{bmatrix} \lambda_0 \\ \lambda_{1s} \\ \lambda_{1c} \end{bmatrix} \right) + \left( \mathbf{T}_{H \rightarrow W} \begin{bmatrix} C_T \\ -C_L \\ -C_M \end{bmatrix} \right) \right\} \quad (3.82)$$

where  $\Omega$  is the rotor angular speed,  $C_T$ ,  $C_L$ , and  $C_M$  are the rotor thrust, roll, and pitching moment coefficients in the hub frame, and  $\mathbf{T}_{W \rightarrow H} = \mathbf{T}_{H \rightarrow W}^T$ . The apparent mass matrix is given by:

$$\mathbf{M} = \begin{bmatrix} \frac{128}{75\pi} & 0 & 0 \\ 0 & \frac{16}{45\pi} & 0 \\ 0 & 0 & \frac{16}{45\pi} \end{bmatrix} \quad (3.83)$$

whereas the inflow static gain matrix is:

$$\mathbf{L} = \begin{bmatrix} \frac{0.5}{V_T} & 0 & -\frac{15\pi}{64V} \sqrt{\frac{1-\sin\alpha}{1+\sin\alpha}} \\ 0 & \frac{4}{V(1+\sin\alpha)} & 0 \\ \frac{15\pi}{64V_T} \sqrt{\frac{1-\sin\alpha}{1+\sin\alpha}} & 0 & \frac{4\sin\alpha}{V(1+\sin\alpha)} \end{bmatrix} \quad (3.84)$$

To define the variables used in the static gain matrix, it is convenient to introduce the following quantities:

$$\mu = \frac{\sqrt{u_H^2 + v_H^2}}{\Omega R} \quad (3.85a)$$

$$\mu_z = \frac{w_H}{\Omega R} \quad (3.85b)$$

$$V_T = \sqrt{\mu^2 + (\mu_z - \lambda_0)^2} \quad (3.85c)$$

where  $\mu$  is the rotor in-plane advance ratio of the rotor,  $\mu_z$  is the rotor climb ratio, and  $V_T$  is the total rotor advance ratio. The variables  $u_H$ ,  $v_H$ , and  $w_H$  are the rotor hub longitudinal, lateral, and vertical velocity components in the hub frame, respectively, and will be defined in the next chapter. The rotor angle of attack  $\alpha$  is defined as:

$$\alpha = \tan^{-1} \left( \frac{\lambda_0 - \mu_z}{\mu} \right) \quad (3.86)$$

The mass flow parameter is defined as:

$$V = \frac{\mu^2 + (\lambda_0 - \mu_z)(2\lambda_0 - \mu_z)}{V_T} \quad (3.87)$$

### 3.9.2 1-State Inflow Model

The Pitt-Peters inflow model can be reduced to a 1-state model, which is still somewhat of an improvement with respect to quasi-static modeling. The first step is to find  $\mathbf{L}^{-1}$ :

$$\mathbf{L}^{-1} = \begin{bmatrix} \frac{16384V_T \sin\alpha}{8192 \sin\alpha + 225\pi^2 - 225\pi^2 \sin\alpha} & 0 & \frac{960V_T \pi (\sin\alpha + 1) \sqrt{1 - \frac{\sin\alpha - 1}{\sin\alpha + 1}}}{8192 \sin\alpha + 225\pi^2 - 225\pi^2 \sin\alpha} \\ 0 & \frac{V(\sin\alpha + 1)}{4} & 0 \\ -\frac{960V\pi (\sin\alpha + 1) \sqrt{1 - \frac{\sin\alpha - 1}{\sin\alpha + 1}}}{8192 \sin\alpha + 225\pi^2 - 225\pi^2 \sin\alpha} & 0 & \frac{2048V(\sin\alpha + 1)}{8192 \sin\alpha + 225\pi^2 - 225\pi^2 \sin\alpha} \end{bmatrix} \quad (3.88)$$

By assuming uniform inflow only such that  $\lambda_{1s} = \lambda_{1c} = 0$ , Eq. (3.82) becomes:

$$\frac{1}{\Omega} \frac{128}{75\pi} \dot{\lambda}_0 + \frac{16384V_T \sin\alpha}{8192 \sin\alpha + 225\pi^2 - 225\pi^2 \sin\alpha} \lambda_0 = C_T \quad (3.89)$$

Thus, the uniform inflow dynamics becomes:

$$\dot{\lambda}_0 = -9600\pi\Omega \frac{V_T \sin\alpha}{8192 \sin\alpha + 225\pi^2 - 225\pi^2 \sin\alpha} \lambda_0 + \frac{75\pi}{128} \Omega C_T \quad (3.90)$$

For low advance ratios (*i.e.*,  $\mu \ll \lambda_0 - \mu_z$ ) such that  $\sin\alpha \approx 1$  and for low climb ratios (*i.e.*,  $|\mu_z| \ll \lambda_0$ ), then:

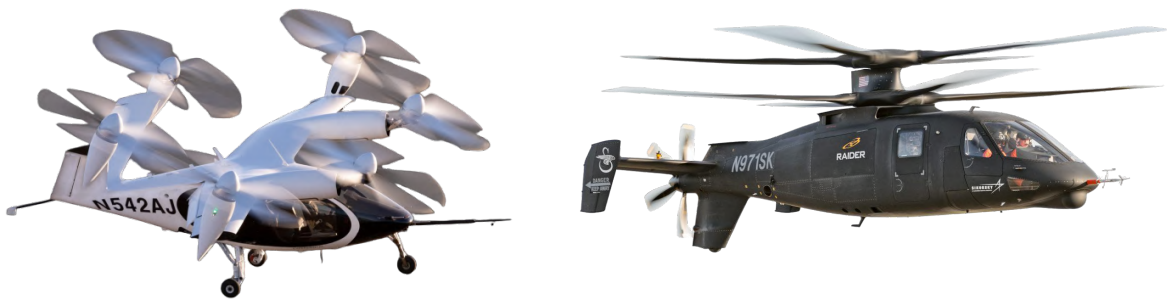
$$\begin{aligned} \dot{\lambda}_0 &= -\frac{150\pi}{128} \Omega \lambda_0^2 + \frac{75\pi}{128} \Omega C_T \\ &\approx -3.6816\Omega \lambda_0^2 + 1.8408\Omega C_T \end{aligned} \quad (3.91)$$

Note that if one makes a quasi-static assumption such that  $\dot{\lambda}_0 = 0$ , then this equation reduces to the induced inflow equation at hover derived analytically earlier in the chapter:

$$\lambda_0 = \sqrt{\frac{C_T}{2}} \quad (3.92)$$

### 3.10 Rotor-on-Rotor Interactions

Modeling of rotor-on-rotor interactions is particularly important for future-generation rotorcraft such as electric Vertical Take-Off and Landing (eVTOL) vehicles intended for applications including Urban Air Mobility (UAM) and drone delivery, and for U.S. Army Future Vertical Lift (FVL) vehicles. Examples are shown in Fig. 3.19. more specifically, Fig. 3.19a shows the Joby Aviation S4, an eVTOL intended for UAM with a tiltrotor configuration, whereas 3.19b shows the Sikorsky S-97 Raider, competing as the Future Attack Reconnaissance Aircraft (FARA) for the U.S. Army Future Vertical Lift (FVL) initiative. All of these vehicles feature multiple rotors with a high degree of aerodynamic interactions, not only between the rotors, but also between the rotors and auxiliary aerodynamic surfaces which are typically used to increase both trimmed flight performance as well as agility in maneuvers. Rotor-on-rotor interactions can severely affect the inflow dynamics in such a way that, in turns, the performance characteristics and handling qualities of the vehicle are also affected.



(a) Joby Aviation S4, eVTOL vehicle intended for UAM. (b) Sikorsky S-97 Raider, competing as the U.S. Army Future Attack Reconnaissance Aircraft (FARA).

Figure 3.19: Examples of future-generation vehicles featuring multiple rotors with a high degree of aerodynamic interaction.

#### 3.10.1 Induced Velocity Near a Lifting Rotor

The first step toward rotor-on-rotor interaction modeling is being able to compute the induced velocity of a lifting rotor at an arbitrary point in space. Not only this is useful for rotor-on-rotor interaction modeling, but also for Consider the geometry shown in Fig. 3.21 featuring a lifting rotor and a point P arbitrarily located in space.

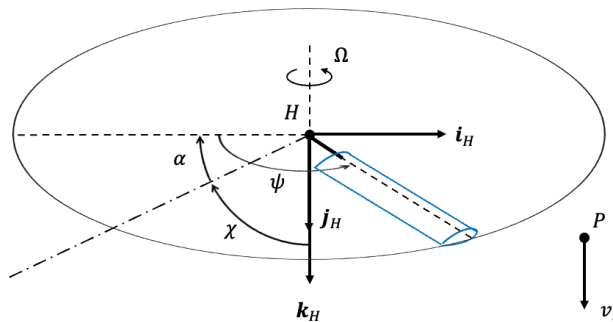


Figure 3.20: Induced velocity at a point P near a lifting rotor.

The point P has the following distance from the center of the rotor:

$$\mathbf{r}_{O \rightarrow P} = x\mathbf{i}_H + y\mathbf{j}_H + z\mathbf{k}_H \quad (3.93)$$

To generalize the problem, it is convenient to normalize this distance by the rotor radius, such that:

$$\hat{\mathbf{r}}_{O \rightarrow P} = \hat{x}\mathbf{i}_H + \hat{y}\mathbf{j}_H + \hat{z}\mathbf{k}_H \quad (3.94)$$

where  $\hat{x} = x/R$ ,  $\hat{y} = y/R$ , and  $\hat{z} = z/R$ . Heyson [Hey60] showed that by using the Biot-Savart law, the induced velocities non-dimensionalized by the rotor tip speed  $\lambda_i = v_i/v_{\text{tip}}$  (where  $v_{\text{tip}} = \Omega R$ ) near a lifting rotor can be calculated as:

$$\lambda_i = \frac{1}{4\pi} \int_0^{2\pi} F(\psi) \frac{1 - (-\hat{x}\cos\psi + \hat{y}\sin\psi) + R_c \sin\chi \cos\psi}{[R_c + (\cos\psi + \hat{x})\sin\chi - \hat{z}\cos\chi]R_c} d\psi \quad (3.95)$$

where  $F(\psi)$  is the vorticity variation around the azimuth:

$$F(\psi) = \gamma_0 + \gamma_{1c} \cos\psi + \gamma_{1s} \sin\psi \quad (3.96)$$

and

$$R_c = \sqrt{1 + (-\hat{x})^2 + \hat{y}^2 + (-\hat{z})^2 - 2(-\hat{x}\cos\psi + \hat{y}\sin\psi)} \quad (3.97)$$

Uniform ( $\gamma_0$ ), cosine ( $\gamma_{1c}$ ), and sine ( $\gamma_{1s}$ ) portions of the vorticity are related to the coefficients of thrust, pitching moment, and rolling moment in the hub frame as follows:

$$\gamma_0 = \frac{C_T}{V_T(1 - 1.5\mu^2)} + \frac{3\mu C_L}{V_T(1 - 1.5\mu^2)} \quad (3.98a)$$

$$\gamma_{1c} = -\frac{3C_M}{V_T} \quad (3.98b)$$

$$\gamma_{1s} = \frac{3C_L}{V_T(1 - 1.5\mu^2)} + \frac{1.5\mu C_T}{V_T(1 - 1.5\mu^2)} \quad (3.98c)$$

The wake skew angle is:

$$\begin{aligned} \chi &= \frac{\pi}{2} - \tan^{-1} \left( \frac{\lambda_0 - \mu_z}{\mu} \right) \\ &= \frac{\pi}{2} - \alpha \end{aligned} \quad (3.99)$$

Note that the  $\mathbf{i}_H$  and  $\mathbf{k}_H$  axes are opposite with respect to those in the original formulation (*i.e.*,  $\mathbf{i}_H$  positive pointing forward and  $\mathbf{k}_H$  pointing up). Also note that this induced velocity is parallel to the  $\mathbf{k}_H$  axis. Figure 3.21 shows the induced velocities near a lifting rotor in the rotor  $\mathbf{i}_H$ - $\mathbf{k}_H$  and  $\mathbf{i}_H$ - $\mathbf{j}_H$  planes for thrust coefficient  $C_T = 0.005$  and advance ratios of  $\mu = 0$  and  $\mu = 0.02$ , respectively.

### 3.10.2 State-Space CMTSVT

This subsection will discuss rotor-on-rotor interactions modeled with the Combined Momentum Theory and Simple Vortex Theory (CMTSVT) by Guner and Prasad [Gun22; GP22]. Consider the case where an arbitrary number  $N$  of rotors are sufficiently close such that their inflow dynamics is mutually interacting. For simplicity, consider two mutually-interacting rotors that are arbitrarily positioned and oriented in space and have radii that are not necessarily equal. This setup is shown in Fig. 3.22.

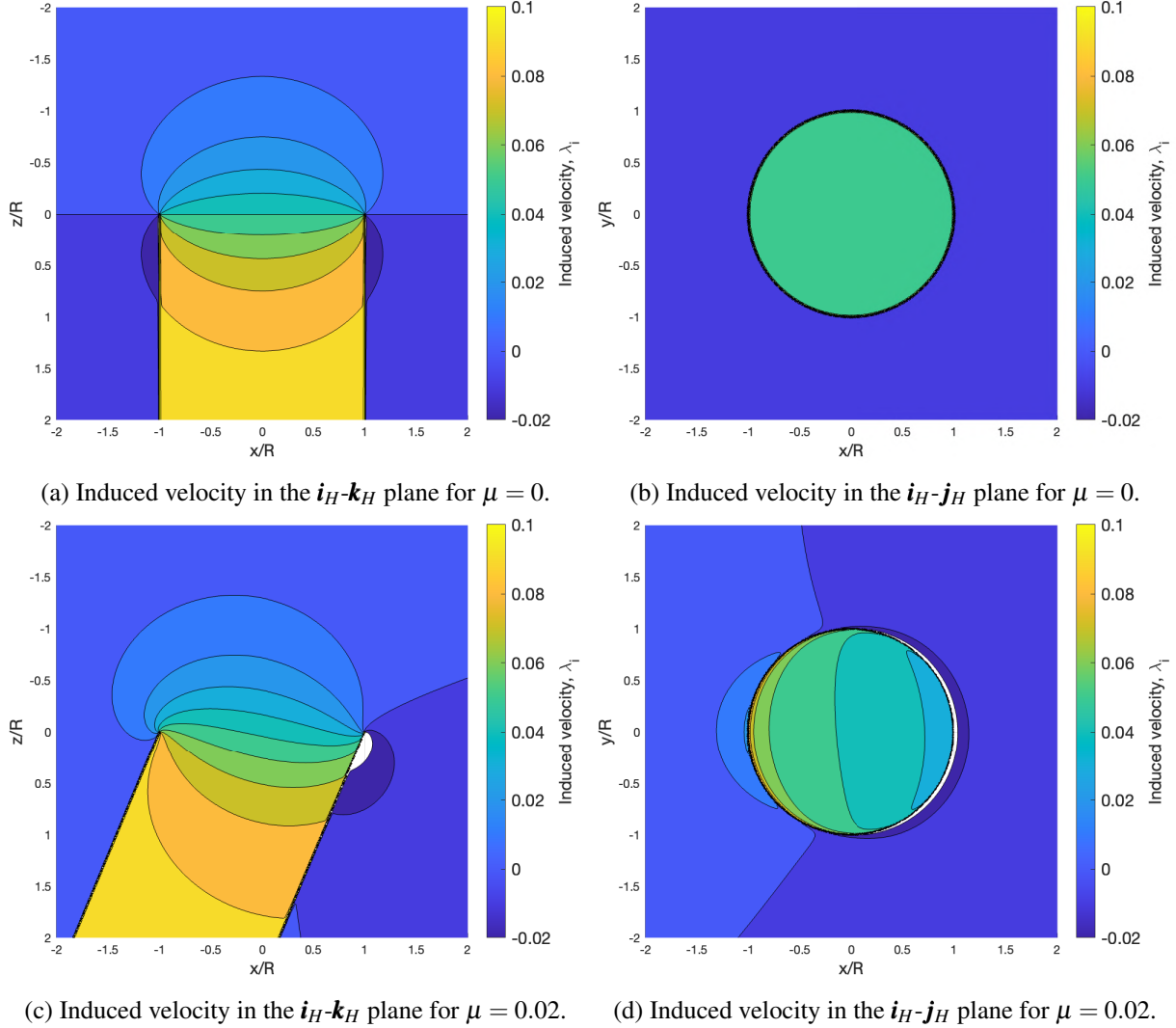
Then, the inflow of the  $i^{\text{th}}$  rotor can be expressed as the summation between the self-induced inflow of that rotor and the interference inflow from all other rotors:

$$\boldsymbol{\lambda}_i = \boldsymbol{\lambda}_{s_i} + \sum_{j=1, j \neq i}^N \boldsymbol{\lambda}_{\text{int}_{ij}} \quad (3.100)$$

where:

$\boldsymbol{\lambda}_i^T = [\lambda_{i_0} \ \lambda_{i_{1s}} \ \lambda_{i_{1c}}]$  is the total inflow of the  $i^{\text{th}}$  rotor in the local hub frame,

$\boldsymbol{\lambda}_{s_i}^T = [\lambda_{s_{i_0}} \ \lambda_{s_{i_{1s}}} \ \lambda_{s_{i_{1c}}}]$  is the self-induced inflow of the  $i^{\text{th}}$  rotor in the local hub frame, and

Figure 3.21: Induced velocity near a lifting rotor for  $C_T = 0.005$  and varying advance ratio.

$\boldsymbol{\lambda}_{\text{int}_{ij}}^T = [\lambda_{\text{int}_{j_0}}, \lambda_{\text{int}_{j_1s}}, \lambda_{\text{int}_{j_1c}}]$  is the interference inflow on the  $i^{\text{th}}$  from the  $j^{\text{th}}$  rotor in the  $i^{\text{th}}$  rotor hub frame.

The self-induced inflow dynamics of the  $i^{\text{th}}$  rotor are given by:

$$\dot{\boldsymbol{\lambda}}_{s_i} = \Omega \mathbf{T}_{W_i \rightarrow H_i} \mathbf{M}_{ii}^{-1} [ -\mathbf{L}_{ii}^{-1} (\mathbf{T}_{H_i \rightarrow W_i} \boldsymbol{\lambda}_{s_i}) + (\mathbf{T}_{H_i \rightarrow W_i} \mathbf{F}_{ii}) ] \quad (3.101)$$

where  $\mathbf{M}_{ii}$  is the apparent mass matrix given in Eq. (3.83) and the static gain inflow matrix is given by:

$$\mathbf{L}_{ii} = \begin{bmatrix} \frac{0.5}{V_{T_i}} & 0 & -\frac{15\pi}{64V_i} \sqrt{\frac{1-\sin\alpha_i}{1+\sin\alpha_i}} \\ 0 & \frac{4}{V_i(1+\sin\alpha_i)} & 0 \\ \frac{15\pi}{64V_i} \sqrt{\frac{1-\sin\alpha_i}{1+\sin\alpha_i}} & 0 & \frac{4\sin\alpha_i}{V_i(1+\sin\alpha_i)} \end{bmatrix} \quad (3.102)$$

Additionally,  $\mathbf{F}_{ii}^T = [C_{T_i} - C_{L_i} - C_{M_i}]$ , where  $C_{T_i}$ ,  $C_{L_i}$ , and  $C_{M_i}$  are the thrust, rolling moments, and pitching moment coefficients of the  $i^{\text{th}}$  rotor in the local hub frame. The transformation from the  $i^{\text{th}}$  rotor hub frame to

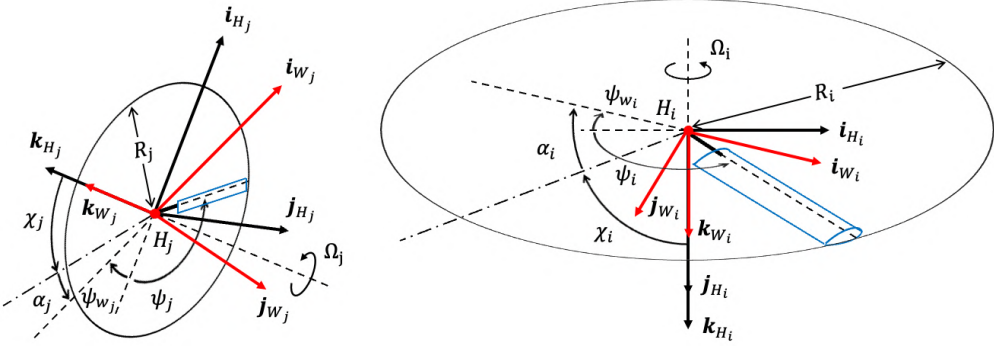


Figure 3.22: Two mutually-interacting rotors that are arbitrarily positioned and oriented in space.

the  $i^{\text{th}}$  rotor wind frame is:

$$\begin{bmatrix} \mathbf{k}_{W_i} \\ \mathbf{i}_{W_i} \\ \mathbf{j}_{W_i} \end{bmatrix} = \underbrace{\begin{bmatrix} 1 & 0 & 0 \\ 0 & \cos \psi_{w_i} & \sin \psi_{w_i} \\ 0 & -\sin \psi_{w_i} & \cos \psi_{w_i} \end{bmatrix}}_{T_{H_i \rightarrow W_i}} \begin{bmatrix} \mathbf{k}_{H_i} \\ \mathbf{i}_{H_i} \\ \mathbf{j}_{z_{H_i}} \end{bmatrix} \quad (3.103)$$

where:

$$\psi_{w_i} = \begin{cases} \tan^{-1} \left( \frac{v_{H_i}}{u_{H_i}} \right), & \text{counterclockwise rotor} \\ \tan^{-1} \left( -\frac{v_{H_i}}{u_{H_i}} \right), & \text{clockwise rotor} \end{cases} \quad (3.104)$$

The total inflow and advance ratios of the  $i^{\text{th}}$  rotor are given by:

$$\mu_i = \frac{\sqrt{u_{H_i}^2 + v_{H_i}^2}}{\Omega_i R_i} \quad (3.105a)$$

$$\mu_{z_i} = \frac{w_{H_i}}{\Omega_i R_i} \quad (3.105b)$$

$$V_{T_i} = \sqrt{\mu_i^2 + (\mu_{z_i} - \lambda_{i_0})^2} \quad (3.105c)$$

where  $u_{H_i}$ ,  $v_{H_i}$ , and  $w_{H_i}$  are the longitudinal, lateral, and vertical velocity components of the  $i^{\text{th}}$  rotor hub. The angle of attack and skew angle of the  $i^{\text{th}}$  rotor is:

$$\alpha_{R_i} = \tan^{-1} \left( \frac{\lambda_{i_0} - \mu_{z_i}}{\mu_i} \right) \quad (3.106a)$$

$$\chi_i = \frac{\pi}{2} - \alpha_{R_i} \quad (3.106b)$$

The mass flow parameter is defined as:

$$V_i = \frac{\mu_i^2 + (\lambda_{i_0} - \mu_{z_i})(2\lambda_{i_0} - \mu_{z_i})}{V_{T_i}} \quad (3.107)$$

The interference inflow on the  $i^{\text{th}}$  from the  $j^{\text{th}}$  rotor is given by:

$$\boldsymbol{\lambda}_{\text{int}_{ij}} = \mathbf{L}_{ij} (\eta_{ij} \boldsymbol{\lambda}_{s_j}) \quad (3.108)$$

where  $\eta_{ij}$  is a parameter that scales the non-dimensional quantities of the  $j^{\text{th}}$  rotor to non-dimensional quantities of the  $i^{\text{th}}$  rotor:

$$\eta_{ij} = \frac{\Omega_j R_j}{\Omega_i R_i} \quad (3.109)$$

The interference matrix  $\mathbf{L}_{ij}$  is given by the multiplication of three matrices:

$$\mathbf{L}_{ij} = \mathbf{G}_{ij} \mathbf{R}_{\gamma_j} \mathbf{L}_{jj} \quad (3.110)$$

where:

$$\mathbf{R}_{\gamma_j} = \frac{1}{\eta_{ij} V_{T_j} (1 - 1.5\eta_{ij}^2 \mu_j^2)} \begin{bmatrix} 1 & 0 & -3\eta_{ij}\mu_j \\ 0 & 3(1 - 1.5\eta_{ij}^2 \mu_j^2) & 0 \\ -1.5\eta_{ij}\mu_j & 0 & 3 \end{bmatrix} \quad (3.111a)$$

$$\mathbf{G}_{ij} = \begin{bmatrix} g_{00ij} & g_{01sij} & g_{01cij} \\ g_{1s0ij} & g_{1s1sij} & g_{1s1cij} \\ g_{1c0ij} & g_{1c1sij} & g_{1c1cij} \end{bmatrix} \quad (3.111b)$$

and where  $\mathbf{L}_{jj}$  is the static inflow gain matrix defined above. The elements of the  $\mathbf{G}_{ij}$  matrix are given by the following integrals:

$$g_{00ij} = -\frac{1}{4\pi^2} \int_{-\psi_{wi}}^{2\pi-\psi_{wi}} \left[ \int_0^{R_i/R_j} \left( \int_{-\psi_{wj}}^{2\pi-\psi_{wj}} K_{ij} d\psi_j \right) \hat{r}_i d\hat{r}_i \right] d\psi_i \quad (3.112a)$$

$$g_{01sij} = -\frac{1}{4\pi^2} \int_{-\psi_{wi}}^{2\pi-\psi_{wi}} \left[ \int_0^{R_i/R_j} \left( \int_{-\psi_{wj}}^{2\pi-\psi_{wj}} K_{ij} \sin \psi_j d\psi_j \right) \hat{r}_i d\hat{r}_i \right] d\psi_i \quad (3.112b)$$

$$g_{01cij} = -\frac{1}{4\pi^2} \int_{-\psi_{wi}}^{2\pi-\psi_{wi}} \left[ \int_0^{R_i/R_j} \left( \int_{-\psi_{wj}}^{2\pi-\psi_{wj}} K_{ij} \cos \psi_j d\psi_j \right) \hat{r}_i d\hat{r}_i \right] d\psi_i \quad (3.112c)$$

$$g_{1s0ij} = -\frac{1}{\pi^2} \int_{-\psi_{wi}}^{2\pi-\psi_{wi}} \left[ \int_0^{R_i/R_j} \left( \int_{-\psi_{wj}}^{2\pi-\psi_{wj}} K_{ij} d\psi_j \right) \hat{r}_i^2 \sin \psi_i d\hat{r}_i \right] d\psi_i \quad (3.112d)$$

$$g_{1s1sij} = -\frac{1}{\pi^2} \int_{-\psi_{wi}}^{2\pi-\psi_{wi}} \left[ \int_0^{R_i/R_j} \left( \int_{-\psi_{wj}}^{2\pi-\psi_{wj}} K_{ij} \sin \psi_j d\psi_j \right) \hat{r}_i^2 \sin \psi_i d\hat{r}_i \right] d\psi_i \quad (3.112e)$$

$$g_{1s1cij} = -\frac{1}{\pi^2} \int_{-\psi_{wi}}^{2\pi-\psi_{wi}} \left[ \int_0^{R_i/R_j} \left( \int_{-\psi_{wj}}^{2\pi-\psi_{wj}} K_{ij} \cos \psi_j d\psi_j \right) \hat{r}_i^2 \sin \psi_i d\hat{r}_i \right] d\psi_i \quad (3.112f)$$

$$g_{1c0ij} = -\frac{1}{\pi^2} \int_{-\psi_{wi}}^{2\pi-\psi_{wi}} \left[ \int_0^{R_i/R_j} \left( \int_{-\psi_{wj}}^{2\pi-\psi_{wj}} K_{ij} d\psi_j \right) \hat{r}_i^2 \cos \psi_i d\hat{r}_i \right] d\psi_i \quad (3.112g)$$

$$g_{1c1sij} = -\frac{1}{\pi^2} \int_{-\psi_{wi}}^{2\pi-\psi_{wi}} \left[ \int_0^{R_i/R_j} \left( \int_{-\psi_{wj}}^{2\pi-\psi_{wj}} K_{ij} \sin \psi_j d\psi_j \right) \hat{r}_i^2 \cos \psi_i d\hat{r}_i \right] d\psi_i \quad (3.112h)$$

$$g_{1c1cij} = -\frac{1}{\pi^2} \int_{-\psi_{wi}}^{2\pi-\psi_{wi}} \left[ \int_0^{R_i/R_j} \left( \int_{-\psi_{wj}}^{2\pi-\psi_{wj}} K_{ij} \cos \psi_j d\psi_j \right) \hat{r}_i^2 \cos \psi_i d\hat{r}_i \right] d\psi_i \quad (3.112i)$$

where  $j$  identifies the acting rotor whereas  $i$  represents the receiving rotor. To find the integrand function  $K_{ij}$ , one must first define the relative position of the rotors. Assume that the  $i^{\text{th}}$  rotor hub has the following coordinates in the body frame:

$$\mathbf{r}_{\bullet \rightarrow H_i} = x_i \mathbf{i}_B + y_i \mathbf{j}_B + z_i \mathbf{k}_B \quad (3.113)$$

whereas the  $j^{\text{th}}$  rotor body-frame coordinates are:

$$\mathbf{r}_{\bullet \rightarrow H_j} = x_j \mathbf{i}_B + y_j \mathbf{j}_B + z_j \mathbf{k}_B \quad (3.114)$$

Then, the position of the  $i^{\text{th}}$  rotor with respect to the  $j^{\text{th}}$  rotor is:

$$\begin{aligned} \mathbf{r}_{H_j \rightarrow H_i} &= \mathbf{r}_{\bullet \rightarrow H_i} - \mathbf{r}_{\bullet \rightarrow H_j} \\ &= \mathbf{T}_{B \rightarrow H_j} \left( \begin{bmatrix} x_i \\ y_i \\ z_i \end{bmatrix} - \begin{bmatrix} x_j \\ y_j \\ z_j \end{bmatrix} \right) \\ &= x_{ij} \mathbf{i}_{H_j} + y_{ij} \mathbf{j}_{H_j} + z_{ij} \mathbf{k}_{H_j} \end{aligned} \quad (3.115)$$

where the transformation  $\mathbf{T}_{B \rightarrow H_j}$  will be defined in the next chapter. The aerodynamic calculation points of the  $i^{\text{th}}$  rotor expressed in the  $j^{\text{th}}$  rotor hub coordinates are:

$$\begin{bmatrix} x_{AC_i} \\ y_{AC_i} \\ z_{AC_i} \end{bmatrix} = \begin{bmatrix} x_{ij} \\ y_{ij} \\ z_{ij} \end{bmatrix} + \underbrace{\mathbf{T}_{B \rightarrow H_j} \mathbf{T}_{H_i \rightarrow B}}_{\mathbf{T}_{H_i \rightarrow H_j}} \begin{bmatrix} -r_i \cos \psi_i \\ r_i \sin \psi_i \\ 0 \end{bmatrix} \quad (3.116)$$

where  $r_i$  is the dimensional radial coordinate  $0 \leq r_i \leq R_i$ . The aerodynamic calculation points are non-dimensionalized with respect to the  $j^{\text{th}}$  rotor radius, such that:

$$\begin{bmatrix} \hat{x}_{AC_i} \\ \hat{y}_{AC_i} \\ \hat{z}_{AC_i} \end{bmatrix} = \frac{1}{R_j} \begin{bmatrix} x_{AC_i} \\ y_{AC_i} \\ z_{AC_i} \end{bmatrix} \quad (3.117)$$

Then, the interference of the  $j^{\text{th}}$  rotor on the  $i^{\text{th}}$  rotor can be computed according to Heyson, such that:

$$J_{ij} = \frac{1 - (-\hat{x}_{AC_i} \cos \psi_j + \hat{y}_{AC_i} \sin \psi_j) + R_c \sin \chi_j \cos \psi_j}{[R_c + (\cos \psi_j + \hat{x}_{AC_i}) \sin \chi_j - \hat{z}_{AC_i} \cos \chi_j] R_c} \quad (3.118)$$

where:

$$R_c = \sqrt{1 + (-\hat{x}_{AC_i})^2 + \hat{y}_{AC_i}^2 + (-\hat{z}_{AC_i})^2 - 2(-\hat{x}_{AC_i} \cos \psi_j + \hat{y}_{AC_i} \sin \psi_j)} \quad (3.119)$$

Finally, the integrand function  $K_{ij}$  can be found as  $K_{ij} = J_{ij} (\mathbf{k}_{H_j} \cdot \mathbf{k}_{H_i})$  or, equivalently:

$$\begin{bmatrix} \cdot \\ \cdot \\ K_{ij} \end{bmatrix} = \mathbf{T}_{H_j \rightarrow H_i} \begin{bmatrix} 0 \\ 0 \\ J_{ij} \end{bmatrix} \quad (3.120)$$

where  $\mathbf{T}_{H_j \rightarrow H_i} = \mathbf{T}_{H_i \rightarrow H_j}^T$ . It is worth noting that the total inflow harmonic coefficients  $\boldsymbol{\lambda}_i$  are in fact an output of the system of dynamic inflow equations rather than states. Because these quantities are typically used to calculate the thrust coefficient and other variables before being computed in the inflow calculations, it is desirable to express them as states. This avoids algebraic loops in the rotor simulation. As such, the dynamics of the total inflow is expressed as a first-order filter with the following form:

$$\dot{\bar{\boldsymbol{\lambda}}}_i = \frac{1}{\tau_\lambda} (\bar{\boldsymbol{\lambda}}_i - \boldsymbol{\lambda}_i) \quad (3.121)$$

where  $\bar{\boldsymbol{\lambda}}_i$  is the total inflow calculated at each time step using Eq. (3.100), and  $\tau_\lambda$  is the filter time constant which should be chosen as at least one order of magnitude faster than the fastest inflow dynamics. Based on this setup, the inflow dynamics has the following state vector:

$$\mathbf{x}_{\text{inflow}}^T = [\boldsymbol{\lambda}_{s_1} \dots \boldsymbol{\lambda}_{s_N} \boldsymbol{\lambda}_1 \dots \boldsymbol{\lambda}_N] \quad (3.122)$$

### Computational Setup

The computational steps of the CMTSVT algorithm are as follows.

- **Offline Computations**

Prior to running the simulation, compute and store the following:

1. Transformation matrices from each rotor hub to that of all other rotors (*i.e.*,  $\mathbf{T}_{H_i \rightarrow H_j}$ ), as well as the transformation matrices from the body frame to each rotor (*i.e.*,  $\mathbf{T}_{B \rightarrow H_i}$ ).
2. Relative position vector of the  $i^{\text{th}}$  rotor hub with respect to the  $j^{\text{th}}$  rotor hub expressed in the  $j^{\text{th}}$  rotor hub frame and non-dimensionalized by the  $j^{\text{th}}$  rotor tip speed by using Eq. (3.115).
3. Elements of the  $\mathbf{G}_{ij}$  matrix for varying wake skew angles  $\chi_i$ ,  $\chi_j$  and wind azimuth angles  $\psi_{w_i}$ ,  $\psi_{w_j}$  using Eq. (3.111b), such that  $\mathbf{G}_{ij} = \mathbf{G}_{ij}(\chi_i, \chi_j, \psi_{w_i}, \psi_{w_j})$ .

- **Online Computations**

The following are the steps to be performed at each time step of the simulation:

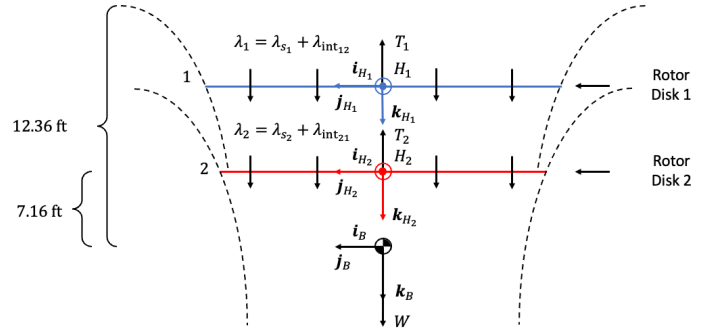
1. If not provided, compute the rotor thrust coefficients  $C_{T_i}$ , rolling moment coefficients  $C_{L_i}$ , and pitching moment coefficients  $C_{M_i}$  based on the current total inflow ratios  $\lambda_i$ .
2. Compute the current mass flow parameter  $V_i$ , advance ratio  $\mu_i$ , total advance ratio  $V_{T_i}$ , wake skew angle  $\chi_i$ , rotor angle of attack  $\alpha_i$ , and wind azimuth angle  $\psi_{w_i}$  based on Eqs. (3.107), (3.105a), (3.105c), (3.106b), (3.106a), and (3.104), respectively.
3. Compute the inflow gain matrices  $L_{ii}$  based on the current  $V_i$ ,  $V_{T_i}$ , and  $\alpha_i$  using Eq. (3.102).
4. Interpolate the  $G_{ij}$  matrices based on  $\chi_j$  and  $\psi_{w_j}$ .
5. Compute the  $R_{\gamma_j}$  matrices based on  $\mu_j$  and  $V_{T_j}$  using Eq. (3.111a).
6. Compute the interference matrices  $L_{ij}$  using Eq. (3.110).
7. Compute the interference inflow  $\lambda_{int_{ij}}$  using Eq. (3.108).
8. Compute the total inflow  $\bar{\lambda}_i$  using Eq. (3.100).
9. Compute the self-induced inflow dynamics  $\lambda_{s_i}$  using Eq. (3.101).
10. Compute the total inflow dynamics  $\lambda_i$  using Eq. (3.121).

**Example: Rotor-on-Rotor Interactions for a Coaxial Helicopter**

Consider an example involving the Kamov Ka-32 (Fig. 3.23a) at hover. This helicopter features two counter-rotating coaxial rotors with a radius of  $R_1 = R_2 = 26.08$  ft and an angular speed of  $\Omega_1 = \Omega_2 = 28.48$  rad/s. The position of the rotors with respect to the CG (in ft) is approximately given by  $r_{\bullet \rightarrow H_1} = -12.36\mathbf{k}_B$  and  $r_{\bullet \rightarrow H_2} = -7.16\mathbf{k}_B$ . The CMTSVT schematics are shown in Fig. 3.23b).



(a) Kamov Ka-32.



(b) CMTSVT schematics.

Figure 3.23: CMTSVT applied to a coaxial helicopter.

Then, based on this setup, the inflow interference of rotor 2 on rotor 1, and vice versa, is given by:

$$\mathbf{G}_{12} = \begin{bmatrix} 0.3286 & 0 & 0 \\ 0 & 0.0578 & 0 \\ 0 & 0 & 0.0578 \end{bmatrix}, \quad \mathbf{G}_{21} = \begin{bmatrix} 0.6718 & 0 & 0 \\ 0 & 0.4433 & 0 \\ 0 & 0 & 0.4426 \end{bmatrix} \quad (3.123)$$

**Example: Rotor-on-Rotor Interactions for a Conventional Main-Tail Rotor Helicopter**

Consider an example involving the Sikorsky UH-60 (Fig. 3.24) at hover. The main rotor has a tilt angle of  $\beta_{m1} = -3$  deg, a radius  $R_1 = 26.83$  ft, and an angular velocity  $\Omega_1 = 27$  rad/s. The tail rotor has a cant angle of  $\phi_{m1} = 70$  deg, a radius  $R_2 = 5.5$  ft, and an angular velocity  $\Omega_2 = 124.62$  rad/s. The position of the rotors with respect to the CG (in ft) is  $r_{\bullet \rightarrow H_1} = 1.2196\mathbf{i}_B - 5.9248\mathbf{k}_B$  and  $r_{\bullet \rightarrow H_2} = -31.3429\mathbf{i}_B + 1.1667\mathbf{j}_B - 6.7331\mathbf{k}_B$ . The inflow interference of rotor 2 on rotor 1, and vice versa, is given by:

$$\mathbf{G}_{12} = \begin{bmatrix} ? & 0 & 0 \\ 0 & ? & 0 \\ 0 & 0 & ? \end{bmatrix}, \quad \mathbf{G}_{21} = \begin{bmatrix} ? & 0 & 0 \\ 0 & ? & 0 \\ 0 & 0 & ? \end{bmatrix} \quad (3.124)$$



Figure 3.24: Sikorsky UH-60.

## Bibliography

- [Gun22] F. Guner. “A Multirotor Inflow Model Based on Combined Momentum Theory and Simple Vortex Theory (CMTSVT) for Flight Simulations”. In: *Proceedings of the 78<sup>th</sup> Forum of the Vertical Flight Society*. Fort Worth, TX, May 10-12, 2022. (Cited on page 76).
- [GP22] F. Guner and J. V. R. Prasad. “Combined Momentum Theory and Simple Vortex Theory Inflow Model for Multirotor Configurations”. In: *Journal of the American Helicopter Society* 67.2 (Jan. 2022), pages 1–15. DOI: <https://doi.org/10.4050/JAHS.67.022007> (cited on page 76).
- [Hey60] H. H. Heyson. *Equations for the Induced Velocities Near a Lifting Rotor with Nonuniform Azimuthwise Vorticity Distribution*. Technical report. NASA TN D394, August 1960. (Cited on page 76).
- [Pet09] D. A. Peters. “How Dynamic Inflow Survives in the Competitive World of Rotorcraft Aerodynamics”. In: *Journal of the American Helicopter Society* 54.1 (Jan. 2009), page 11001. DOI: <https://doi.org/10.4050/JAHS.54.011001> (cited on page 72).
- [PBH89] D. A. Peters, D. D. Boyd, and C. J. He. “Finite-State Induced-Flow Model for Rotors in Hover and Forward Flight”. In: *Journal of the American Helicopter Society* 34.4 (Oct. 1989), pages 5–17. DOI: <https://doi.org/10.4050/JAHS.34.5> (cited on page 72).
- [PH91] D. A. Peters and C. J. He. “Correlation of Measured Induced Velocities with a Finite-State Wake Model”. In: *Journal of the American Helicopter Society* 36.3 (July 1991), pages 59–70. DOI: <https://doi.org/10.4050/JAHS.36.59> (cited on page 72).
- [PP80] D. M. Pitt and D. A. Peters. “Theoretical Prediction of Dynamic-Inflow Derivatives”. In: *Proceedings of the 6<sup>th</sup> European Rotorcraft and Powered Lift Aircraft Forum*. Bristol, England, September 16-19, 1980. (Cited on page 73).
- [Ypm95] T. J. Ypma. “Historical Development of the Newton–Raphson Method”. In: *SIAM Review* 37.4 (1995), pages 531–551. DOI: <https://doi.org/10.1137/1037125> (cited on page 70).



## 4. Rotor Modeling for Flight Dynamics

### 4.1 Useful Coordinate Transformations

Before beginning the analysis object of this chapter, it is convenient to introduce commonly-used transformations between reference frames.

#### 4.1.1 Body to Hub Frame Transformation



(a) Sikorsky UH-60 with 3 deg forward tilt of the main rotor and 70 deg canting of the tail rotor.  
(b) Kaman K-MAX with 12.5 deg outboard cant of the intermeshing rotors.

Figure 4.1: Rotor hub cant and tilt on example rotorcraft.

Rotor hubs may be tilted forward or aft, canted starboard or port, or both at the same time. For instance, the Sikorsky UH-60 features a 3 deg forward tilt of the main rotor and a 70 deg cant of the tail rotor (Fig. 4.1a), whereas the Kaman K-MAX has a 12.5 deg outboard tilt on both rotors (Fig. 4.1b). Tiltrotors typically have varying tilt and cant, where tilt is adjusted for conversion from helicopter to airplane mode and vice versa, and where outward cant is sometimes provided in hover to account for the wing flexibility. The latter is done not to have rotor thrust pointing inboard. For instance, the Bell XV-15 has a 1 deg outboard cant of the rotor hubs at hover. In the present analysis, rotor hub tilt is assumed positive aft, whereas positive hub cant is assumed right wing down. The rotor hub frame, labelled as  $H$ , is related to the body frame through two successive transformations. Consider Fig. 4.2. The first transformation is about the  $i_B$  axis by an angle  $\phi_m$  and yields to the intermediate frame  $T$  (Fig. 4.3a).

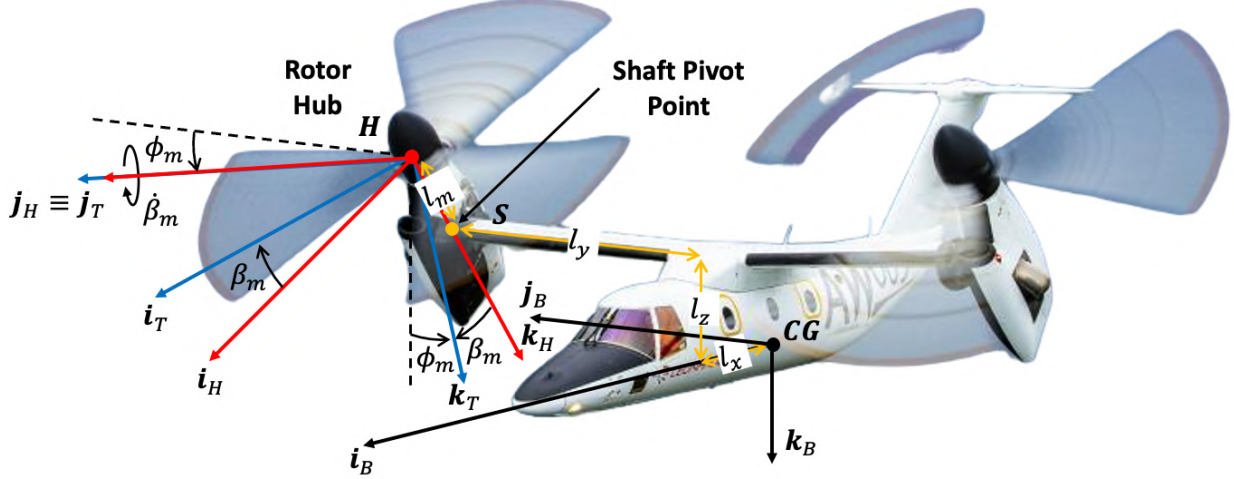


Figure 4.2: Rotor hub cant and tilt angles on a AW609.

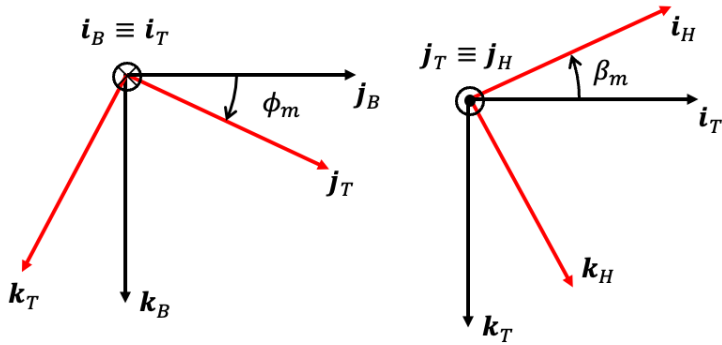
(a) Rotation about the  $i_B$  axis by an angle  $\phi_m$ .  
(b) Rotation about the  $j_T$  axis by an angle  $\beta_m$ .

Figure 4.3: Body to hub frame rotations.

$$\begin{bmatrix} \mathbf{i}_T \\ \mathbf{j}_T \\ \mathbf{k}_T \end{bmatrix} = \underbrace{\begin{bmatrix} 1 & 0 & 0 \\ 0 & \cos \phi_m & \sin \phi_m \\ 0 & -\sin \phi_m & \cos \phi_m \end{bmatrix}}_{T_{B \rightarrow T}} \begin{bmatrix} \mathbf{i}_B \\ \mathbf{j}_B \\ \mathbf{k}_B \end{bmatrix} \quad (4.1)$$

Note that, according to this definition, main rotors with a rotation axis in the direction of the  $\mathbf{k}_B$  axis will have a cant of  $\phi_m = 0$  deg. Conversely, tail rotors with a rotation axis in the direction of the  $\mathbf{j}_B$  axis will have a cant of  $\phi_m = 90$  deg. The second transformation is about the  $\mathbf{j}_T$  axis by an angle  $\beta_m$ , yielding the hub frame H.

$$\begin{bmatrix} \mathbf{i}_H \\ \mathbf{j}_H \\ \mathbf{k}_H \end{bmatrix} = \underbrace{\begin{bmatrix} \cos \beta_m & 0 & -\sin \beta_m \\ 0 & 1 & 0 \\ \sin \beta_m & 0 & \cos \beta_m \end{bmatrix}}_{T_{T \rightarrow H}} \begin{bmatrix} \mathbf{i}_T \\ \mathbf{j}_T \\ \mathbf{k}_T \end{bmatrix} \quad (4.2)$$

According to this definition, the tilt angle of either rotors of a tiltrotor aircraft in helicopter mode will be  $\beta_m = 0$  deg. Conversely, the tilt angle of either rotors of tiltrotor aircraft in helicopter mode will be  $\beta_m = -90$  deg. Similarly, the forward tilt of the UH-60 main rotor is expressed as  $\beta_m = -3$  deg. The transformation from the body to the hub frame is obtained by substituting Eq. (4.2) into Eq. (4.1).

$$\begin{aligned}
\begin{bmatrix} \mathbf{i}_H \\ \mathbf{j}_H \\ \mathbf{k}_H \end{bmatrix} &= \mathbf{T}_{T \rightarrow H} \mathbf{T}_{B \rightarrow T} \begin{bmatrix} \mathbf{i}_B \\ \mathbf{j}_B \\ \mathbf{k}_B \end{bmatrix} \\
&= \underbrace{\begin{bmatrix} \cos \beta_m & 0 & -\sin \beta_m \\ 0 & 1 & 0 \\ \sin \beta_m & 0 & -\cos \beta_m \end{bmatrix}}_{\mathbf{T}_{B \rightarrow H}} \underbrace{\begin{bmatrix} 1 & 0 & 0 \\ 0 & \cos \phi_m & \sin \phi_m \\ 0 & -\sin \phi_m & \cos \phi_m \end{bmatrix}}_{\mathbf{T}_{T \rightarrow H}} \begin{bmatrix} \mathbf{i}_B \\ \mathbf{j}_B \\ \mathbf{k}_B \end{bmatrix} \\
&= \underbrace{\begin{bmatrix} \cos \beta_m & \sin \beta_m \sin \phi_m & -\sin \beta_m \cos \phi_m \\ 0 & \cos \phi_m & \sin \phi_m \\ \sin \beta_m & -\cos \beta_m \sin \phi_m & \cos \beta_m \cos \phi_m \end{bmatrix}}_{\mathbf{T}_{B \rightarrow H}} \begin{bmatrix} \mathbf{i}_B \\ \mathbf{j}_B \\ \mathbf{k}_B \end{bmatrix}
\end{aligned} \tag{4.3}$$

The inverse transformation, *i.e.*, that from the hub to the body frame, is:

$$\begin{bmatrix} \mathbf{i}_B \\ \mathbf{j}_B \\ \mathbf{k}_B \end{bmatrix} = \mathbf{T}_{B \rightarrow H}^T \begin{bmatrix} \mathbf{i}_H \\ \mathbf{j}_H \\ \mathbf{k}_H \end{bmatrix} = \underbrace{\begin{bmatrix} \cos \beta_m & 0 & \sin \beta_m \\ \sin \beta_m \sin \phi_m & \cos \phi_m & -\cos \beta_m \sin \phi_m \\ -\sin \beta_m \cos \phi_m & \sin \phi_m & \cos \beta_m \cos \phi_m \end{bmatrix}}_{\mathbf{T}_{H \rightarrow B}} \begin{bmatrix} \mathbf{i}_H \\ \mathbf{j}_H \\ \mathbf{k}_H \end{bmatrix} \tag{4.4}$$

#### 4.1.2 Hub to Blade Frame Transformation

Consider a rotor blade with co-located flap and lag hinges as shown in Fig. 4.4.

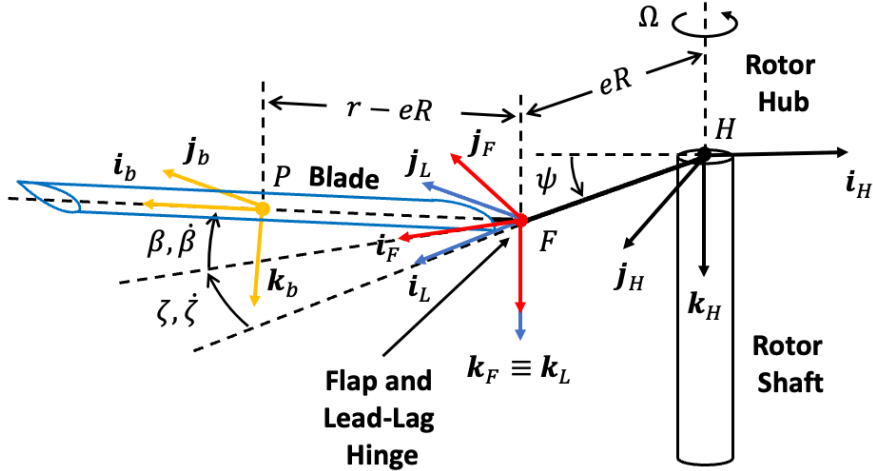


Figure 4.4: Rotor blade rigid flap and lead-lag degrees of freedom.

The blade undergoes the following motion (successive single-axis rotations), shown in Fig 4.5:

1. Rotation with an angular speed  $-\Omega$  about the vertical axis of the rotor hub frame  $\mathbf{k}_H$ . The degree of freedom associated to this rotation is the azimuth angle  $\psi$ . The transformation from the hub to the lead-lag frame is:

$$\begin{bmatrix} \mathbf{i}_L \\ \mathbf{j}_L \\ \mathbf{k}_L \end{bmatrix} = \underbrace{\begin{bmatrix} \cos(\pi - \psi) & \sin(\pi - \psi) & 0 \\ -\sin(\pi - \psi) & \cos(\pi - \psi) & 0 \\ 0 & 0 & 1 \end{bmatrix}}_{\mathbf{T}_{H \rightarrow L}} \begin{bmatrix} \mathbf{i}_H \\ \mathbf{j}_H \\ \mathbf{k}_H \end{bmatrix} = \begin{bmatrix} -\cos \psi & \sin \psi & 0 \\ -\sin \psi & -\cos \psi & 0 \\ 0 & 0 & 1 \end{bmatrix} \begin{bmatrix} \mathbf{i}_H \\ \mathbf{j}_H \\ \mathbf{k}_H \end{bmatrix} \tag{4.5}$$

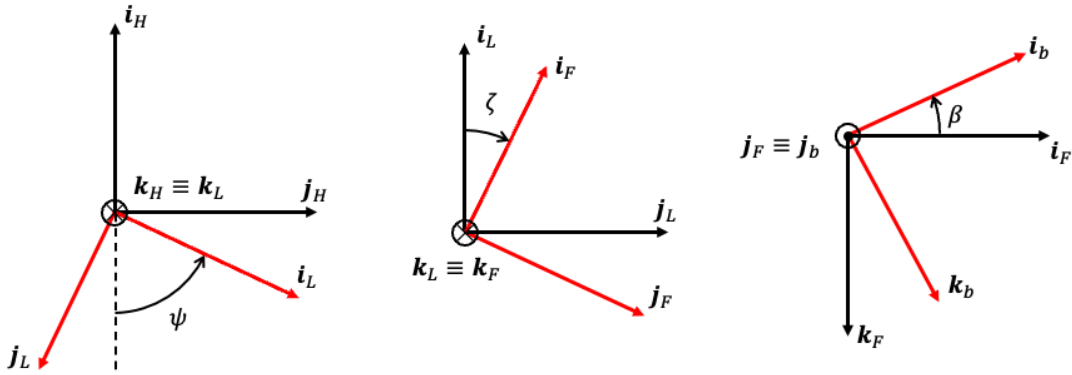
2. Rotation about its lead-lag hinge ( $\mathbf{k}_F$  axis), located at a distance  $eR$  from the origin of the hub frame,

of an angle  $\zeta$  and with a lag rate  $\dot{\zeta}$ . The transformation from the lead-lag to the flap frame is:

$$\begin{bmatrix} \mathbf{i}_F \\ \mathbf{j}_F \\ \mathbf{k}_F \end{bmatrix} = \underbrace{\begin{bmatrix} \cos \zeta & \sin \zeta & 0 \\ -\sin \zeta & \cos \zeta & 0 \\ 0 & 0 & 1 \end{bmatrix}}_{\mathbf{T}_{L \rightarrow F}} \begin{bmatrix} \mathbf{i}_L \\ \mathbf{j}_L \\ \mathbf{k}_L \end{bmatrix} \quad (4.6)$$

3. Rotation about its flapping hinge ( $\mathbf{j}_F$  axis), located at a distance  $eR$  from the origin of the hub frame, of an angle  $\beta$  and with a flap rate  $\dot{\beta}$ . The transformation from the flap to the blade frame is:

$$\begin{bmatrix} \mathbf{i}_b \\ \mathbf{j}_b \\ \mathbf{k}_b \end{bmatrix} = \underbrace{\begin{bmatrix} \cos \beta & 0 & -\sin \beta \\ 0 & 1 & 0 \\ \sin \beta & 0 & \cos \beta \end{bmatrix}}_{\mathbf{T}_{F \rightarrow b}} \begin{bmatrix} \mathbf{i}_F \\ \mathbf{j}_F \\ \mathbf{k}_F \end{bmatrix} \quad (4.7)$$



- (a) Rotation about the  $-k_H$  axis by an angle  $\psi$ .  
 (b) Rotation about the  $k_L$  axis by an angle  $\zeta$ .  
 (c) Rotation about the  $j_F$  axis by an angle  $\beta$ .

Figure 4.5: Rotor hub to blade frame rotations.

Because the first two transformations are conducted about parallel axes  $\mathbf{k}_H$  and  $\mathbf{k}_L$ , it is often convenient to express these rotations as a single transformation. As such, the transformation between the hub and the flap frame can be found by substituting Eq. (4.5) into Eq. (4.6):

$$\begin{aligned} \begin{bmatrix} \mathbf{i}_F \\ \mathbf{j}_F \\ \mathbf{k}_F \end{bmatrix} &= \mathbf{T}_{L \rightarrow F} \mathbf{T}_{H \rightarrow L} \begin{bmatrix} \mathbf{i}_H \\ \mathbf{j}_H \\ \mathbf{k}_H \end{bmatrix} \\ &= \begin{bmatrix} \cos \zeta & \sin \zeta & 0 \\ -\sin \zeta & \cos \zeta & 0 \\ 0 & 0 & 1 \end{bmatrix} \begin{bmatrix} -\cos \psi & \sin \psi & 0 \\ -\sin \psi & -\cos \psi & 0 \\ 0 & 0 & 1 \end{bmatrix} \begin{bmatrix} \mathbf{i}_H \\ \mathbf{j}_H \\ \mathbf{k}_H \end{bmatrix} \\ &= \begin{bmatrix} -\cos \zeta \cos \psi - \sin \zeta \sin \psi & \cos \zeta \sin \psi - \sin \zeta \cos \psi & 0 \\ -\sin \zeta \cos \psi - \cos \zeta \sin \psi & -\sin \zeta \sin \psi - \cos \zeta \cos \psi & 0 \\ 0 & 0 & 1 \end{bmatrix} \begin{bmatrix} \mathbf{i}_H \\ \mathbf{j}_H \\ \mathbf{k}_H \end{bmatrix} \\ &= \underbrace{\begin{bmatrix} -\cos(\psi - \zeta) & \sin(\psi - \zeta) & 0 \\ -\sin(\psi - \zeta) & -\cos(\psi - \zeta) & 0 \\ 0 & 0 & 1 \end{bmatrix}}_{\mathbf{T}_{H \rightarrow F}} \begin{bmatrix} \mathbf{i}_H \\ \mathbf{j}_H \\ \mathbf{k}_H \end{bmatrix} \end{aligned} \quad (4.8)$$

The transformation from the hub to the blade frame is found by substituting Eq. (4.8) into Eq. (4.7):

$$\begin{aligned} \begin{bmatrix} \mathbf{i}_b \\ \mathbf{j}_b \\ \mathbf{k}_b \end{bmatrix} &= \mathbf{T}_{F \rightarrow b} \mathbf{T}_{H \rightarrow F} \begin{bmatrix} \mathbf{i}_H \\ \mathbf{j}_H \\ \mathbf{k}_H \end{bmatrix} \\ &= \underbrace{\begin{bmatrix} \cos \beta & 0 & -\sin \beta \\ 0 & 1 & 0 \\ \sin \beta & 0 & \cos \beta \end{bmatrix}}_{\mathbf{T}_{H \rightarrow b}} \begin{bmatrix} -\cos(\psi - \zeta) & \sin(\psi - \zeta) & 0 \\ -\sin(\psi - \zeta) & -\cos(\psi - \zeta) & 0 \\ 0 & 0 & 1 \end{bmatrix} \begin{bmatrix} \mathbf{i}_H \\ \mathbf{j}_H \\ \mathbf{k}_H \end{bmatrix} \\ &= \underbrace{\begin{bmatrix} -\cos \beta \cos(\psi - \zeta) & \cos \beta \sin(\psi - \zeta) & -\sin \beta \\ -\sin(\psi - \zeta) & -\cos(\psi - \zeta) & 0 \\ -\sin \beta \cos(\psi - \zeta) & \sin \beta \sin(\psi - \zeta) & \cos \beta \end{bmatrix}}_{\mathbf{T}_{H \rightarrow b}} \begin{bmatrix} \mathbf{i}_H \\ \mathbf{j}_H \\ \mathbf{k}_H \end{bmatrix} \end{aligned} \quad (4.9)$$

The inverse transformation, *i.e.*, that from the blade to the hub frame, is:

$$\begin{bmatrix} \mathbf{i}_H \\ \mathbf{j}_H \\ \mathbf{k}_H \end{bmatrix} = \mathbf{T}_{H \rightarrow b}^T \begin{bmatrix} \mathbf{i}_b \\ \mathbf{j}_b \\ \mathbf{k}_b \end{bmatrix} = \underbrace{\begin{bmatrix} -\cos \beta \cos(\psi - \zeta) & -\sin(\psi - \zeta) & -\sin \beta \cos(\psi - \zeta) \\ \cos \beta \sin(\psi - \zeta) & -\cos(\psi - \zeta) & \sin \beta \sin(\psi - \zeta) \\ -\sin \beta & 0 & \cos \beta \end{bmatrix}}_{\mathbf{T}_{b \rightarrow H}} \begin{bmatrix} \mathbf{i}_b \\ \mathbf{j}_b \\ \mathbf{k}_b \end{bmatrix} \quad (4.10)$$

### 4.1.3 Blade to Air Mass Frame Transformation

When calculating lift and drag of an airfoil section, lift and drag are defined as perpendicular and parallel, respectively, to the velocity vector of the air mass the blade section is moving through. The air mass frame is found through a positive rotation about the radial axis  $\mathbf{i}_a$  about an angle  $\pi - \phi$ , where  $\phi$  is known as the inflow angle, and which will be defined later in the chapter. The transformation from the blade to the air mass frame is:

$$\begin{bmatrix} \mathbf{i}_a \\ \mathbf{j}_a \\ \mathbf{k}_a \end{bmatrix} = \underbrace{\begin{bmatrix} 1 & 0 & 0 \\ 0 & \cos(\pi - \phi) & \sin(\pi - \phi) \\ 0 & -\sin(\pi - \phi) & \cos(\pi - \phi) \end{bmatrix}}_{\mathbf{T}_{b \rightarrow a}} \begin{bmatrix} \mathbf{i}_b \\ \mathbf{j}_b \\ \mathbf{k}_b \end{bmatrix} = \underbrace{\begin{bmatrix} 1 & 0 & 0 \\ 0 & -\cos \phi & \sin \phi \\ 0 & -\sin \phi & -\cos \phi \end{bmatrix}}_{\mathbf{T}_{b \rightarrow a}} \begin{bmatrix} \mathbf{i}_b \\ \mathbf{j}_b \\ \mathbf{k}_b \end{bmatrix} \quad (4.11)$$

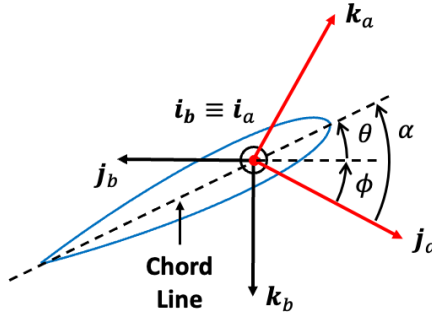


Figure 4.6: Transformation from the blade to the air mass frame.

### 4.1.4 Blade to Radial-Tangential-Perpendicular Frame Transformation

For aerodynamic calculations, it is convenient to flip the verse of the  $\mathbf{j}_b$  axis of the blade frame to obtain the radial-tangential-perpendicular (RTP) frame. Note that the RTP frame is a left-handed frame. The transformation from the blade to the RTP frame, shown in Fig. 4.7 is:

$$\begin{bmatrix} \mathbf{R} \\ \mathbf{T} \\ \mathbf{P} \end{bmatrix} = \underbrace{\begin{bmatrix} 1 & 0 & 0 \\ 0 & -1 & 0 \\ 0 & 0 & 1 \end{bmatrix}}_{\mathbf{T}_{b \rightarrow RTP}} \begin{bmatrix} \mathbf{i}_b \\ \mathbf{j}_b \\ \mathbf{k}_b \end{bmatrix} = \begin{bmatrix} \mathbf{i}_b \\ -\mathbf{j}_b \\ \mathbf{k}_b \end{bmatrix} \quad (4.12)$$

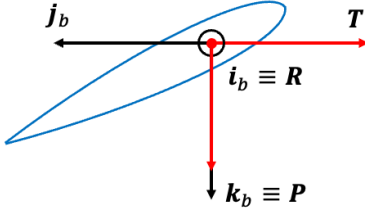


Figure 4.7: Transformation from the blade to the RTP frame.

## 4.2 Blade Kinematics

To ease the understanding of the calculations in this section, vectors expressed in a certain frame, will have the letter representing that frame as a superscript. For instance, the position vector from the center of mass  $\bullet$  to the shaft pivot point S, expressed in body-frame coordinates, will be written as  $\mathbf{r}_{\bullet \rightarrow S}^B$ .

### 4.2.1 Rotor Hub Position

Assume that the position vector from the center of mass to the shaft pivot point S, as shown in Fig. 4.2, is:

$$\mathbf{r}_{\bullet \rightarrow S}^B = x_s \mathbf{i}_B + y_s \mathbf{j}_B + z_s \mathbf{k}_B \quad (4.13)$$

Also, assume the position vector from the shaft pivot point S to the the rotor hub H to be  $\mathbf{r}_{S \rightarrow H}^H = -l_m \mathbf{k}_H$ . Then, the position vector from the center of mass to the rotor hub, expressed in body-frame components, is:

$$\begin{aligned} \mathbf{r}_{\bullet \rightarrow H}^B &= \mathbf{r}_{\bullet \rightarrow S}^B + \mathbf{T}_{H \rightarrow B} \mathbf{r}_{S \rightarrow H}^H \\ &= \begin{bmatrix} x_s \\ y_s \\ z_s \end{bmatrix} + \begin{bmatrix} \cos \beta_m & 0 & \sin \beta_m \\ \sin \beta_m \sin \phi_m & \cos \phi_m & -\cos \beta_m \sin \phi_m \\ -\sin \beta_m \cos \phi_m & \sin \phi_m & \cos \beta_m \cos \phi_m \end{bmatrix} \begin{bmatrix} 0 \\ 0 \\ -l_m \end{bmatrix} \\ &= \begin{bmatrix} x_s - l_m \sin \beta_m \\ y_s + l_m \cos \beta_m \sin \phi_m \\ z_s - l_m \cos \beta_m \cos \phi_m \end{bmatrix} = \begin{bmatrix} x_H \\ y_H \\ z_H \end{bmatrix} \end{aligned} \quad (4.14)$$

### 4.2.2 Rotor Hub Velocity

The translational velocity vector of the rotor hub with respect to the inertial frame, expressed in body-frame components, is:

$$\begin{aligned} \mathbf{v}_{H/I}^B &= \mathbf{v}_{\bullet/I}^B + \boldsymbol{\omega}_{B/I}^B \times \mathbf{r}_{\bullet \rightarrow H}^B \\ &= \begin{bmatrix} u \\ v \\ w \end{bmatrix} + \begin{bmatrix} 0 & -r & q \\ r & 0 & -p \\ -q & p & 0 \end{bmatrix} \begin{bmatrix} x_H \\ y_H \\ z_H \end{bmatrix} = \begin{bmatrix} u - ry_H + qz_H \\ v + rx_H - pz_H \\ w - qx_H + py_H \end{bmatrix} \end{aligned} \quad (4.15)$$

Then, the translational velocity vector of the rotor hub with respect to the inertial frame, expressed in hub-frame components, is:

$$\begin{aligned} \mathbf{v}_{H/I}^H &= \mathbf{T}_{B \rightarrow H} \mathbf{v}_{H/I}^B \\ &= \begin{bmatrix} \cos \beta_m & \sin \beta_m \sin \phi_m & -\sin \beta_m \cos \phi_m \\ 0 & \cos \phi_m & \sin \phi_m \\ \sin \beta_m & -\cos \beta_m \sin \phi_m & \cos \beta_m \cos \phi_m \end{bmatrix} \begin{bmatrix} u - ry_H + qz_H \\ v + rx_H - pz_H \\ w - qx_H + py_H \end{bmatrix} = \begin{bmatrix} u_H \\ v_H \\ w_H \end{bmatrix} \end{aligned} \quad (4.16)$$

The angular velocity vector of the rotor hub with respect to the inertial frame, expressed in hub frame

components, is:

$$\begin{aligned}\boldsymbol{\omega}_{H/I}^H &= \mathbf{T}_{B \rightarrow H} \boldsymbol{\omega}_{H/I}^B \\ &= \begin{bmatrix} \cos \beta_m & \sin \beta_m \sin \phi_m & -\sin \beta_m \cos \phi_m \\ 0 & \cos \phi_m & \sin \phi_m \\ \sin \beta_m & -\cos \beta_m \sin \phi_m & \cos \beta_m \cos \phi_m \end{bmatrix} \begin{bmatrix} p \\ q \\ r \end{bmatrix} = \begin{bmatrix} p_H \\ q_H \\ r_H \end{bmatrix}\end{aligned}\quad (4.17)$$

### 4.2.3 Rotor Hub Acceleration

The acceleration of the rotor hub, expressed in the body frame, is given by Eq. (2.100):

$$\boldsymbol{a}_{H/I}^B = \begin{bmatrix} a_x \\ a_y \\ a_z \end{bmatrix} = \begin{bmatrix} \dot{u} - rv + qw \\ \dot{v} + ru - pw \\ \dot{w} - qu + pv \end{bmatrix} + \begin{bmatrix} -(q^2 + r^2) & -\dot{r} + pq & \dot{q} + pr \\ \dot{r} + pq & -(p^2 + r^2) & -\dot{p} + qr \\ -\dot{q} + pr & \dot{p} + qr & -(p^2 + q^2) \end{bmatrix} \begin{bmatrix} x_H \\ y_H \\ z_H \end{bmatrix} + \begin{bmatrix} -g \sin \phi \\ g \sin \phi \cos \theta \\ g \cos \phi \cos \theta \end{bmatrix} \quad (4.18)$$

The acceleration of the rotor hub, expressed in the body frame, is:

$$\begin{aligned}\boldsymbol{a}_{H/I}^H &= \mathbf{T}_{B \rightarrow H} \boldsymbol{a}_{H/I}^B \\ &= \begin{bmatrix} \cos \beta_m & \sin \beta_m \sin \phi_m & -\sin \beta_m \cos \phi_m \\ 0 & \cos \phi_m & \sin \phi_m \\ \sin \beta_m & -\cos \beta_m \sin \phi_m & \cos \beta_m \cos \phi_m \end{bmatrix} \begin{bmatrix} a_x \\ a_y \\ a_z \end{bmatrix} = \begin{bmatrix} \dot{u}_H \\ \dot{v}_H \\ \dot{w}_H \end{bmatrix}\end{aligned}\quad (4.19)$$

### 4.2.4 Blade Element Velocity

Assume the position vector from the rotor hub to the flapping hinge to be  $\mathbf{r}_{H \rightarrow F} = eR\mathbf{i}_L$ , where  $e$  is the flapping hinge offset non-dimensionalized by the rotor radius  $R$ . Then, the velocity of the flapping hinge with respect to the inertial frame, expressed in the hub frame, is:

$$\begin{aligned}\boldsymbol{v}_{F/I}^H &= \boldsymbol{v}_{H/I}^H + \boldsymbol{\omega}_{L/I}^H \times \mathbf{r}_{H \rightarrow F}^H \\ &= \boldsymbol{v}_{H/I}^H + (\boldsymbol{\omega}_{L/H}^H + \boldsymbol{\omega}_{H/I}^H) \times (\mathbf{T}_{L \rightarrow H} \mathbf{r}_{H \rightarrow F}^L) \\ &= \begin{bmatrix} u_H \\ v_H \\ w_H \end{bmatrix} + \left( \begin{bmatrix} 0 \\ 0 \\ -\Omega \end{bmatrix} + \begin{bmatrix} p_H \\ q_H \\ r_H \end{bmatrix} \right) \times \left( \begin{bmatrix} -\cos \psi & -\sin \psi & 0 \\ \sin \psi & -\cos \psi & 0 \\ 0 & 0 & 1 \end{bmatrix} \begin{bmatrix} eR \\ 0 \\ 0 \end{bmatrix} \right) \\ &= \begin{bmatrix} u_H + (\Omega - r_H)eR \sin \psi \\ v_H + (\Omega - r_H)eR \cos \psi \\ w_H + q_H eR \cos \psi + p_H eR \sin \psi \end{bmatrix} = \begin{bmatrix} u_F \\ v_F \\ w_F \end{bmatrix}\end{aligned}\quad (4.20)$$

Assume the position vector from the flap hinge F to an arbitrary point P on the blade to be  $\mathbf{r}_{F \rightarrow P}^b = (r - eR)\mathbf{i}_b$ , where  $r$  is the blade radial coordinate. The velocity of the blade element with respect to the inertial frame, expressed in blade-frame components, is:

$$\begin{aligned}\boldsymbol{v}_{P/I}^b &= \boldsymbol{v}_{F/I}^b + \boldsymbol{\omega}_{b/I}^b \times \mathbf{r}_{F \rightarrow P}^b \\ &= \mathbf{T}_{H \rightarrow b} \boldsymbol{v}_{F/I}^H + (\boldsymbol{\omega}_{b/L}^H + \mathbf{T}_{H \rightarrow b} \boldsymbol{\omega}_{L/I}^H) \times \mathbf{r}_{F \rightarrow P}^b \\ &= \mathbf{T}_{H \rightarrow b} \begin{bmatrix} u_F \\ v_F \\ w_F \end{bmatrix} + \left( \begin{bmatrix} 0 \\ \dot{\beta} \\ \dot{\zeta} \end{bmatrix} + \mathbf{T}_{H \rightarrow b} \begin{bmatrix} p_H \\ q_H \\ r_H - \Omega \end{bmatrix} \right) \times \begin{bmatrix} r - eR \\ 0 \\ 0 \end{bmatrix} = \begin{bmatrix} u_b \\ v_b \\ w_b \end{bmatrix}\end{aligned}\quad (4.21)$$

where:

$$\begin{aligned} u_b = & -u_H \cos(\psi - \zeta) \cos \beta + v_H \sin(\psi - \zeta) \cos \beta - w_H \sin \beta \\ & - eR [q_H \cos(\psi - \zeta) + p_H \sin(\psi - \zeta)] \sin \beta \end{aligned} \quad (4.22a)$$

$$\begin{aligned} v_b = & -u_H \sin(\psi - \zeta) - v_H \cos(\psi - \zeta) \\ & - eR (\Omega - r_H) [\cos(\psi - \zeta) \cos \psi + \sin(\psi - \zeta) \sin \psi] \\ & + (r - eR) \left\{ \dot{\zeta} - (\Omega - r_H) \cos \beta + \sin \beta [-p_H \cos(\psi - \zeta) + q_H \sin(\psi - \zeta)] \right\} \end{aligned} \quad (4.22b)$$

$$\begin{aligned} w_b = & -u_H \cos(\psi - \zeta) \sin \beta + v_H \sin(\psi - \zeta) \sin \beta + w_H \cos \beta \\ & + eR (p_H \sin \psi + q_H \cos \psi) \cos \beta \\ & + eR (\Omega - r_H) [-\cos(\psi - \zeta) \sin \psi + \sin(\psi - \zeta) \cos \psi] \sin \beta \\ & + (r - eR) [-\dot{\beta} + q_H \cos(\psi - \zeta) + p_H \sin(\psi - \zeta)] \end{aligned} \quad (4.22c)$$

#### 4.2.5 Blade Element Acceleration

Need to do this. Get from GenHel.

### 4.3 Rotor Forces and Moments

#### 4.3.1 Aerodynamic Loads on Blade Elements

Consider the geometry in Fig. 4.8, showing a section of a representative rotor blade moving through the air.

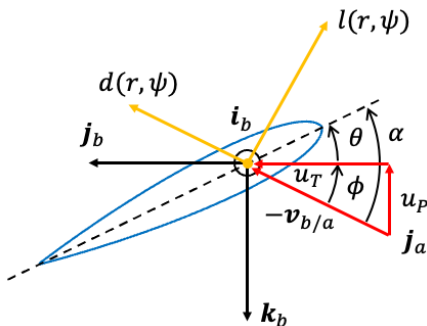


Figure 4.8: Section of a representative rotor blade element moving through the air.

Define the following quantities:

- $\theta = \theta(r)$  is the geometric pitch of the blade,
- $\phi = \phi(r)$  is the aerodynamic incidence angle,
- $\alpha$  is the blade section angle of attach,
- $v_{b/a}$  is the velocity of the blade with respect to the air mass,
- $u_T$  is the velocity tangent to the blade leading edge ( $-j_b$  verse),
- $u_p$  is the velocity perpendicular to the  $i_b - j_b$  plane ( $-k_b$  verse), and
- $u_R$  is the velocity in the radial blade direction ( $i_b$  verse).

Note that:

- $u_p$  arises from the blade flapping motion, as well as from the rotorcraft vertical and angular motions,
- $u_T$  arises mainly from the rotorcraft rotation and forward motion, and
- $u_R$  arises mainly from the rotorcraft forward and lateral motion.

The velocity of the blade with respect to the air mass, expressed in blade-frame coordinates, is:

$$\begin{aligned}
\mathbf{v}_{b/a}^b &= \mathbf{v}_{b/I}^b - \mathbf{v}_{a/I}^b \\
&= \mathbf{v}_{b/I}^b - \mathbf{T}_{H \rightarrow b} \mathbf{v}_{a/I}^H \\
&= \begin{bmatrix} u_b \\ v_b \\ w_b \end{bmatrix} - \mathbf{T}_{L \rightarrow b} \begin{bmatrix} 0 \\ 0 \\ v_i \end{bmatrix} = \begin{bmatrix} u_b \\ v_b \\ w_b \end{bmatrix} - \mathbf{T}_{F \rightarrow b} \mathbf{T}_{L \rightarrow F} \begin{bmatrix} 0 \\ 0 \\ v_i \end{bmatrix} \\
&= \begin{bmatrix} u_b \\ v_b \\ w_b \end{bmatrix} - \begin{bmatrix} \cos \beta & 0 & -\sin \beta \\ 0 & 1 & 0 \\ \sin \beta & 0 & \cos \beta \end{bmatrix} \begin{bmatrix} \cos \zeta & \sin \zeta & 0 \\ -\sin \zeta & \cos \zeta & 0 \\ 0 & 0 & 1 \end{bmatrix} \begin{bmatrix} 0 \\ 0 \\ v_i \end{bmatrix} \\
&= \begin{bmatrix} u_b \\ v_b \\ w_b \end{bmatrix} - \begin{bmatrix} \cos \beta \cos \zeta & \cos \beta \sin \zeta & -\sin \beta \\ -\sin \zeta & \cos \zeta & 0 \\ \sin \beta \cos \psi & \sin \beta \sin \zeta & \cos \beta \end{bmatrix} \begin{bmatrix} 0 \\ 0 \\ v_i \end{bmatrix} \\
&= \begin{bmatrix} u_b + v_i \sin \beta \\ v_b \\ w_b - v_i \cos \beta \end{bmatrix} = \begin{bmatrix} u_R \\ -u_T \\ u_P \end{bmatrix}
\end{aligned} \tag{4.23}$$

where  $v_i = v_i(r, \psi) = \Omega R \lambda_i(r, \psi)$  is the induced velocity at the blade element. The geometric pitch of the blade is given by:

$$\theta(r) = \theta_P(\psi) + \theta_{tw}(r) + \beta \tan \delta_3 \tag{4.24}$$

where  $\delta_3$  is the pitch-flap coupling,  $\theta_P$  represents the prescribed blade pitch at the root (from the control system), and  $\theta_{tw}$  is the twist angle distribution. Typically,  $\theta_{tw} = 0$  at the root  $r = 0$  and  $\theta_{tw} < 0$  for  $0 < r \leq R$ . The blade pitch at the root is:

$$\theta_P(\psi) = \theta_0 + \theta_{1c} \cos(\psi - \Delta_{sp}) + \theta_{1s} \sin(\psi - \Delta_{sp}) \tag{4.25}$$

where  $\theta_0$  is collective pitch,  $\theta_{1c}$  is lateral cyclic, and  $\theta_{1s}$  is longitudinal cyclic. These are the angles of the swashplate and come from the control system. Additionally,  $\Delta_{sp}$  is the swashplate phasing angle which will be discussed later in the chapter. This is typically a constant. The total speed at the blade element is:

$$U_{\text{tot}} = \sqrt{u_R^2 + u_T^2 + u_P^2} \tag{4.26}$$

The velocity component in the plane of the blade section is:

$$U = \sqrt{u_T^2 + u_P^2} = \sqrt{u_T^2 \left( 1 + \frac{u_P^2}{u_T^2} \right)} \tag{4.27}$$

The local angle of attack is:

$$\alpha = \theta + \phi = \theta + \tan^{-1} \left( \frac{u_P}{u_T} \right) \approx \theta + \frac{u_P}{u_T} \tag{4.28}$$

The local Mach number is:

$$M = \frac{U_{\text{tot}}}{v_{\text{sound}}} \tag{4.29}$$

where  $v_{\text{sound}}$  is the speed of sound. The local lift and drag coefficients are typically calculated in one of two ways. The first way is by using lookup tables of the airfoil section (Fig. 4.9) such that:

$$C_l = f(\alpha, M) \tag{4.30a}$$

$$C_d = f(\alpha, M) \tag{4.30b}$$

where  $C_l$  and  $C_d$  are the lift and drag coefficients. The second way is to assume linear lift variation of the angle of attack and constant drag coefficient, that is:

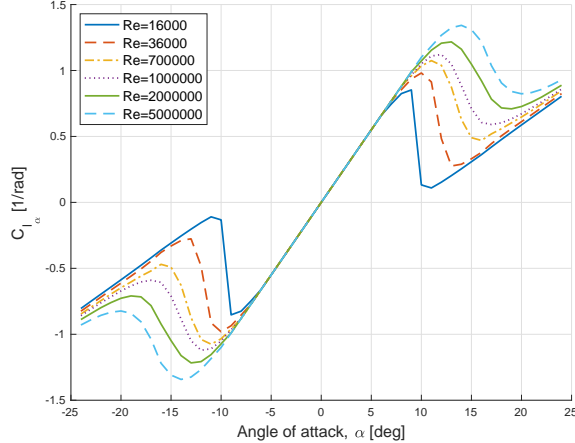
$$C_l \approx a_0 \alpha \quad (4.31a)$$

$$C_d \approx \delta \quad (4.31b)$$

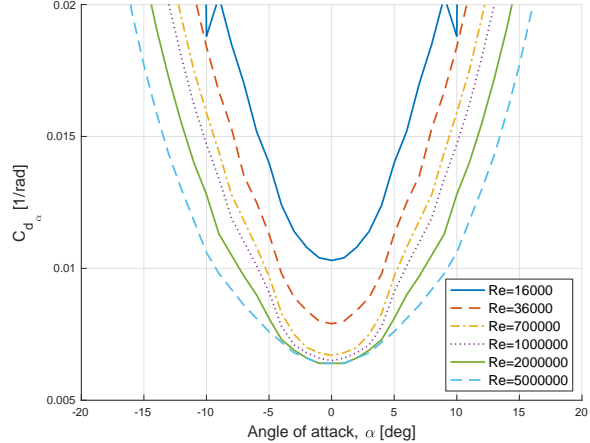
where  $a_0$  is the lift-curve slope (for a NACA 0012 airfoil at representative Mach numbers of  $10^6$ ,  $a_0 \approx 5.72$  1/rad) and  $\delta \approx 0.01$ . For NACA airfoils of the symmetric series, it can be shown [AV59] that:

$$\delta \approx 0.007 + 0.025 \left( \frac{t}{c} \right) \quad (4.32)$$

where  $t/c$  is the airfoil thickness-to-chord ratio.



(a) Coefficient of lift with angle of attack.



(b) Coefficient of drag with angle of attack.

Figure 4.9: Lookup tables for a NACA 0012 airfoil.

The sectional blade lift and drag are, expressed in the air mass frame, are:

$$l(r, \psi) = \frac{1}{2} \rho c(r) U^2 C_l \quad (4.33a)$$

$$d(r, \psi) = \frac{1}{2} \rho c(r) U^2 C_d \quad (4.33b)$$

where  $\rho$  is the air density and  $c(r)$  is the blade chord. The blade segment forces, expressed in the RTP frame, are:

$$\begin{aligned} \begin{bmatrix} f_R \\ f_T \\ f_P \end{bmatrix} &= \mathbf{T}_{a \rightarrow RTP} \begin{bmatrix} 0 \\ -\frac{1}{2} \rho c(r) U^2 C_d \\ \frac{1}{2} \rho c(r) U^2 C_l \end{bmatrix} = \mathbf{T}_{b \rightarrow RTP} \mathbf{T}_{a \rightarrow b} \begin{bmatrix} 0 \\ -\frac{1}{2} \rho c(r) U^2 C_d \\ \frac{1}{2} \rho c(r) U^2 C_l \end{bmatrix} \\ &= \begin{bmatrix} 1 & 0 & 0 \\ 0 & -1 & 0 \\ 0 & 0 & 1 \end{bmatrix} \begin{bmatrix} 1 & 0 & 0 \\ 0 & -\cos \phi & -\sin \phi \\ 0 & \sin \phi & -\cos \phi \end{bmatrix} \begin{bmatrix} 0 \\ -\frac{1}{2} \rho c(r) U^2 C_d \\ \frac{1}{2} \rho c(r) U^2 C_l \end{bmatrix} \\ &= \begin{bmatrix} 0 \\ \frac{1}{2} \rho c(r) U^2 (C_l \sin \phi - C_d \cos \phi) \\ \frac{1}{2} \rho c(r) U^2 (-C_l \cos \phi - C_d \sin \phi) \end{bmatrix} \end{aligned} \quad (4.34)$$

Assuming  $u_P \ll u_T$  such that  $U \approx u_T$  and  $\tan^{-1} \left( \frac{u_P}{u_T} \right) \approx \frac{u_P}{u_T}$ , the blade segment forces become:

$$f_R = 0 \quad (4.35a)$$

$$f_T = \frac{1}{2} \rho c(r) u_T^2 \left[ a_0 \left( \theta + \frac{u_P}{u_T} \right) \frac{u_P}{u_T} - \delta \right] = \frac{1}{2} \rho c(r) [a_0 (u_T \theta + u_P) u_P - u_T^2 \delta] \quad (4.35b)$$

$$f_P = \frac{1}{2} \rho c(r) u_T^2 \left[ -a_0 \left( \theta + \frac{u_P}{u_T} \right) - \delta \frac{u_P}{u_T} \right] \stackrel{\approx 0}{\rightarrow} -\frac{1}{2} \rho c(r) a_0 (u_T^2 \theta + u_P u_T) \quad (4.35c)$$

### 4.3.2 Aerodynamics Forces and Moments About the Flap Hinge

The total blade aerodynamic loads, expressed in the RTP frame, are:

$$F_R = \int_{eR}^R f_R(r) dr = 0 \quad (4.36a)$$

$$F_T = \int_{eR}^R f_T(r) dr = \frac{1}{2} \rho a_0 \int_{eR}^R c(r) [(\theta u_T - u_P) u_P - u_T^2 \delta] dr \quad (4.36b)$$

$$F_P = \int_{eR}^R f_P(r) dr = -\frac{1}{2} \rho a_0 \int_{eR}^R c(r) (u_T^2 \theta + u_P u_T) dr \quad (4.36c)$$

The total blade aerodynamic loads, expressed in the lead-lag frame, are:

$$\begin{aligned} \begin{bmatrix} (F_x)_{\text{aero}} \\ (F_y)_{\text{aero}} \\ (F_z)_{\text{aero}} \end{bmatrix} &= \mathbf{T}_{b \rightarrow L} \mathbf{T}_{RTP \rightarrow b} \begin{bmatrix} F_R \\ F_T \\ F_P \end{bmatrix} = \mathbf{T}_{F \rightarrow L} \mathbf{T}_{b \rightarrow F} \mathbf{T}_{RTP \rightarrow b} \begin{bmatrix} F_R \\ F_T \\ F_P \end{bmatrix} \\ &= \begin{bmatrix} \cos \zeta & -\sin \zeta & 0 \\ \sin \zeta & \cos \zeta & 0 \\ 0 & 0 & 1 \end{bmatrix} \begin{bmatrix} \cos \beta & 0 & \sin \beta \\ 0 & 1 & 0 \\ -\sin \beta & 0 & \cos \beta \end{bmatrix} \begin{bmatrix} 1 & 0 & 0 \\ 0 & -1 & 0 \\ 0 & 0 & 1 \end{bmatrix} \begin{bmatrix} F_R \\ F_T \\ F_P \end{bmatrix} \\ &= \begin{bmatrix} \cos \zeta \cos \beta & -\sin \zeta & \cos \zeta \sin \beta \\ \sin \zeta \cos \beta & \cos \zeta & \sin \zeta \sin \beta \\ -\sin \beta & 0 & \cos \beta \end{bmatrix} \begin{bmatrix} F_R \\ -F_T \\ F_P \end{bmatrix} \\ &= \begin{bmatrix} F_R \cos \zeta \cos \beta + F_T \sin \zeta + F_P \cos \zeta \sin \beta \\ F_R \sin \zeta \cos \beta - F_T \cos \zeta + F_P \sin \zeta \sin \beta \\ -F_R \sin \beta + F_P \cos \beta \end{bmatrix} \end{aligned} \quad (4.37)$$

The total aerodynamic moments about the flapping hinge, expressed in the flap frame, are:

$$(M_x)_{\text{aero}} = 0 \quad (4.38a)$$

$$(M_y)_{\text{aero}} = \int_{eR}^R f_P(r) (r - eR) dr \quad (4.38b)$$

$$= -\frac{1}{2} \rho a_0 \int_{eR}^R c(r) (u_T^2 \theta + u_P u_T) (r - eR) dr = (M_{\text{flap}})_{\text{aero}}$$

$$(M_z)_{\text{aero}} = \int_{eR}^R -f_T(r) (r - eR) dr \quad (4.38c)$$

$$= -\frac{1}{2} \rho a_0 \int_{eR}^R c(r) [(\theta u_T - u_P) u_P - u_T^2 \delta] (r - eR) dr = (M_{\text{lag}})_{\text{aero}}$$

where  $(M_{\text{flap}})_{\text{aero}}$  and  $(M_{\text{lag}})_{\text{aero}}$  are the aerodynamic flap and lead-lag moments about the flapping hinge. The total aerodynamic moments about the flapping hinge, expressed in the hub frame, are:

$$\begin{aligned} \left( \mathbf{M}_{b/H}^H \right)_{\text{aero}} &= \mathbf{T}_{L \rightarrow H} \left( \mathbf{M}_{b/H}^L \right)_{\text{aero}} = \begin{bmatrix} -\cos \psi & -\sin \psi & 0 \\ \sin \psi & -\cos \psi & 0 \\ 0 & 0 & 1 \end{bmatrix} \begin{bmatrix} (M_{\text{flap}})_{\text{aero}} \\ (M_{\text{lag}})_{\text{aero}} \end{bmatrix} \\ &= \begin{bmatrix} -(M_{\text{flap}})_{\text{aero}} \sin \psi \\ -(M_{\text{flap}})_{\text{aero}} \cos \psi \\ (M_{\text{lag}})_{\text{aero}} \end{bmatrix} = \begin{bmatrix} L_{\text{aero}} \\ M_{\text{aero}} \\ N_{\text{aero}} \end{bmatrix} \end{aligned} \quad (4.39)$$

(Need to sum up the aero forces and moments of individual blades before using in Pitt Peters. Also need to define what thrust is.) Then, the aerodynamic forces and moments coefficients are:

$$C_T = \frac{T_{\text{aero}}}{\pi \rho \Omega^2 R^4} \quad (4.40\text{a})$$

$$C_L = \frac{L_{\text{aero}}}{\pi \rho \Omega^2 R^5} \quad (4.40\text{b})$$

$$C_M = \frac{M_{\text{aero}}}{\pi \rho \Omega^2 R^5} \quad (4.40\text{c})$$

where these quantities are used in Eq. (3.82) to drive the inflow dynamics.

## 4.4 Flapping Dynamics

Consider the geometry shown in Fig. 4.10, representative of a flapping blade with a flapping hinge offset  $eR$  and a root spring with constant  $k_\beta$ .

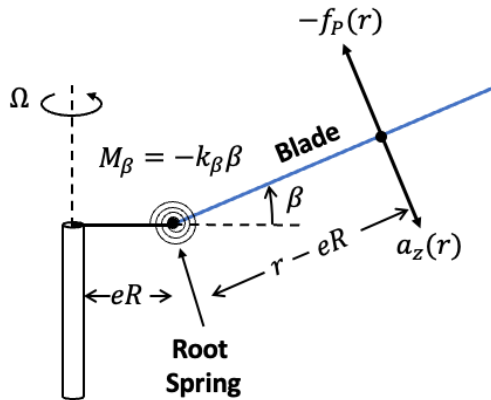


Figure 4.10: Flapping blade with a hinge offset and a root spring.

By applying Newton's second law, that is, by performing a summation of the moments across the span of the blade about the flapping hinge, one obtains:

$$\mathbf{M}_{\text{aero}} + \mathbf{M}_{\text{inertial}} = 0 \quad (4.41)$$

This is equivalent to:

$$\underbrace{\int_{eR}^R (r - eR)}_{\text{Moment arm}} \underbrace{[f_P(r) - m(r)a_z(r)]dr}_{\text{Aero load}} \underbrace{-k_\beta \beta}_{\text{Flapping spring moment}} = 0 \quad (4.42)$$

where  $m(r)$  is the blade mass per unit span. The inertial acceleration is:

$$a_z(r) = \underbrace{-(r - eR)\ddot{\beta}}_{\text{Flapping acceleration}} + \underbrace{\dot{w}_H \cos \beta + \dot{v}_H \sin \beta \sin \psi - \dot{u}_H \sin \beta \cos \psi}_{\text{Hub acceleration}} + \underbrace{[(r - eR) \cos \beta + eR]}_{\text{Radial distance to hub}} + \left\{ \cos \beta \underbrace{[2\Omega(p_H \cos \psi - q_H \sin \psi) + \dot{p}_H \sin \psi + \dot{q}_H \cos \psi]}_{\text{Gyroscopic forces}} - \underbrace{\sin \beta (\Omega - r_H)^2}_{\text{Centripetal acceleration along normal axis of blade}} \right\} \quad (4.43)$$

Define:

$$M_\beta = \int_{er}^R (r - eR) m(r) dr \quad (4.44a)$$

$$I_\beta = \int_{er}^R (r - eR)^2 m(r) dr \quad (4.44b)$$

where  $M_\beta$  is the first mass moment about the flapping hinge and  $I_\beta$  the second mass moment (moment of inertia) about the flapping hinge. For a blade with uniform mass distribution, such that  $m = \text{const.}$ , one has:

$$M_\beta = \frac{m}{2} R(1 - e)^2 \quad (4.45a)$$

$$I_\beta = \frac{m}{3} R(1 - e)^3 \quad (4.45b)$$

Substituting these quantities into Eq. (4.43) yields:

$$\ddot{\beta} = -\frac{k_\beta}{I_\beta} \beta - \sin \beta \cos \beta \left( 1 + \frac{M_\beta e R}{I_\beta \cos \beta} \right) (\Omega - r_H)^2$$

$$+ \cos^2 \beta \left( 1 + \frac{M_\beta e R}{I_\beta \cos \beta} \right) [2\Omega(p_H \cos \psi - q_H \sin \psi) + \dot{p}_H \sin \psi + \dot{q}_H \cos \psi]$$

$$+ \frac{M_\beta}{I_\beta} (\dot{w}_H \cos \beta + \dot{v}_H \sin \beta \sin \psi - \dot{u}_H \sin \beta \cos \psi) - \underbrace{\frac{1}{I_\beta} \int_{er}^R (r - eR) f_P(r) dr}_{\text{Aero moment}}$$

(4.46)

Check out the blade flapping motion seen from an observer in the flapping frame in the video at the following link: <https://www.youtube.com/watch?v=Pu48f7s5Ru8>.

#### 4.4.1 Simplified Flapping Dynamics

If one assumes  $\dot{u}_H = \dot{v}_H = \dot{w}_H = 0$  and  $\beta$  small such that  $\cos \beta \approx 1$  and  $\sin \beta \approx \beta$ , the equation above can be simplified to:

$$\ddot{\beta} = -\frac{k_\beta}{I_\beta} \beta - \left( 1 + \frac{M_\beta e R}{I_\beta \cos \beta} \right) (\Omega - r_H)^2 \beta$$

$$+ \left( 1 + \frac{M_\beta e R}{I_\beta \cos \beta} \right) [2\Omega(p_H \cos \psi + q_H \sin \psi) + \dot{p}_H \sin \psi + \dot{q}_H \cos \psi]$$

$$- \frac{1}{I_\beta} \int_{er}^R (r - eR) f_P(r) dr$$
(4.47)

By assuming  $r_H \ll \Omega$  such that  $(\Omega - r_H)^2 \approx \Omega^2$ , the equation further simplifies to:

$$\ddot{\beta} = -\Omega^2 \lambda_\beta^2 \beta + \sqrt{\lambda_\beta^2 - \frac{k_\beta}{I_\beta \Omega^2}} [2\Omega(p_H \cos \psi + q_H \sin \psi) + \dot{p}_H \sin \psi + \dot{q}_H \cos \psi]$$

$$- \frac{1}{I_\beta} \int_{er}^R (r - eR) f_P(r) dr$$

(4.48)

where:

$$\lambda_\beta = \sqrt{1 + \frac{k_\beta}{I_\beta \Omega^2} + \frac{M_\beta e R}{I_\beta}}$$

(4.49)

The quantity  $\lambda_\beta$  is the flapping frequency ratio, *i.e.*, the ratio between the blade flapping natural frequency and the rotor speed. It is worth noting that this quantity is also known as  $v_\beta$ . If the flapping hinge offset is

greater than zero (*i.e.*,  $e > 0$ ) or if the rotor has a root spring (*i.e.*,  $k_\beta > 0$ ), then  $\lambda_\beta > 1$ . A centrally-hinged rotor (*i.e.*,  $e = 0$ ) with a root spring (*i.e.*,  $k_\beta > 0$ ) will still have  $\lambda_\beta > 1$ , whereas a centrally-hinged rotor with no root spring (*i.e.*,  $k_\beta = 0$ ) will have  $\lambda_\beta = 1$ . For the latter case, the natural frequency of the rotor blade coincides with the angular speed of the rotor  $\Omega$ . As such, the rotor blade effectively operates in a resonance state. Typically, rotors have  $1 \leq \lambda_\beta < 1.2$  and are referred to as soft out-of-plane rotors. This is the case of most articulated rotor systems. Rigid rotor blades may have a flapping frequency ratio up to  $\lambda_\beta \approx 1.5$ . Rotors mounting these kind of blades are known as stiff out-of-plane rotors, which are typically hingeless rotor systems, often mounted on coaxial helicopters to avoid blade strikes across rotors.

An additional simplification involves assuming the blade chord distribution as constant, such that Eq. (4.35c) becomes:

$$f_P = -\frac{1}{2}\rho c a_0 (u_T^2 \theta + u_P u_T) \quad (4.50)$$

Substituting this expression into Eq. (4.48) yields:

$$\ddot{\beta} = -\Omega^2 \lambda_\beta^2 \beta + \sqrt{\lambda_\beta^2 - \frac{k_\beta}{I_\beta \Omega^2}} [2\Omega(p_H \cos \psi + q_H \sin \psi) + \dot{p}_H \sin \psi + \dot{q}_H \cos \psi] + \frac{\rho c a_0}{2I_\beta} \int_{eR}^R [(u_T^2 \theta + u_P u_T)(r - eR)] dr \quad (4.51)$$

An equivalent non-dimensional version of this equation is:

$$\beta'' = -\lambda_\beta^2 \beta + \sqrt{\lambda_\beta^2 - \frac{k_\beta}{I_\beta \Omega^2}} [2(\bar{p}_H + \bar{q}'_H) \cos \psi - (2\bar{q}_H - \bar{p}'_H) \sin \psi] + \frac{\gamma}{2} \int_e^1 [(\bar{u}_T^2 \theta + \bar{u}_P \bar{u}_T)(\bar{r} - e)] d\bar{r} \quad (4.52)$$

where:

$$\bar{r} = \frac{r}{R}, \quad \bar{u}_T = \frac{u_T}{\Omega R}, \quad \bar{u}_P = \frac{u_P}{\Omega R}, \quad \bar{p}_H = \frac{p_H}{\Omega}, \quad \bar{q}_H = \frac{q_H}{\Omega}, \quad \bar{p}'_H = \frac{\dot{p}_H}{\Omega^2}, \quad \bar{q}'_H = \frac{\dot{q}_H}{\Omega^2} \quad (4.53)$$

Additionally,

$$\beta' = \frac{d\beta}{d\psi} = \frac{d\beta}{dt} \frac{dt}{d\psi} = \frac{\dot{\beta}}{\Omega} \quad (4.54a)$$

$$\beta'' = \frac{d^2\beta}{d\psi^2} = \frac{d^2\beta}{dt^2} \frac{dt^2}{d\psi^2} = \frac{\ddot{\beta}}{\Omega^2} \quad (4.54b)$$

where  $\psi$  is non-dimensional time (and also the blade azimuth angle). The quantity  $\gamma$  is known as Lock number and is defined as:

$$\gamma = \frac{\text{aerodynamic flap forces}}{\text{inertial flap forces}} = \frac{\rho a_0 c R^4}{I_\beta} \quad (4.55)$$

Typical rotors have  $3 < \gamma < 15$ , where the low Lock numbers correspond to heavy blades and high Lock numbers are representative of light blades with a wide surface area.

By dropping the higher-order terms and performing the integrations, Eq. (4.52) becomes:

$$\underbrace{\beta''}_{\text{Inertia}} = -\underbrace{\gamma f_{\beta'} \beta'}_{\text{Damper}} - \underbrace{(\lambda_\beta^2 + \gamma f_\beta) \beta}_{\text{Spring}} + \underbrace{k_g [(2\bar{p}_H + \bar{q}'_H) \cos \psi - (2\bar{q}_H - \bar{p}'_H) \sin \psi]}_{\text{Gyroscopic forcing terms}} + \underbrace{\gamma \{f_\theta \theta_P + f_{\theta_{tw}} \theta_{tw} + f_\lambda (\mu_z - \lambda_0) + f_\omega [(\bar{p}_H - \lambda_{1s}) \sin \psi + (\bar{q}_H - \lambda_{1c}) \cos \psi]\}}_{\text{Aero forcing terms}} \quad (4.56)$$

where:

$$f_\theta = \frac{k_3}{2} + \frac{k_2}{2}\mu \sin \psi + \frac{k_1}{2}\mu^2 \sin^2 \psi \quad (4.57a)$$

$$f_{\theta_{tw}} = \frac{k_4}{2} + k_3\mu \sin \psi + \frac{k_2}{2}\mu^2 \sin^2 \psi \quad (4.57b)$$

$$f_\lambda = \frac{k_2}{2} + \frac{k_1}{2}\mu \sin \psi \quad (4.57c)$$

$$f_\beta = f_\lambda \mu \cos \beta \quad (4.57d)$$

$$f'_\beta = \frac{k_3}{2} + \frac{k_2}{2}(\mu \sin \psi - e) \quad (4.57e)$$

$$f_\omega = \frac{k_3}{2} + \frac{k_2}{2}\mu \sin \psi \quad (4.57f)$$

$$k_g = \sqrt{\lambda_\beta^2 - \frac{k_\beta}{\Omega_\beta^2}} \quad (4.57g)$$

$$k_1 = \frac{1 - 2e + e^2}{2} \quad (4.57h)$$

$$k_2 = \frac{2 - 3e + e^2}{6} \quad (4.57i)$$

$$k_3 = \frac{3 - 4e + e^2}{12} \quad (4.57j)$$

$$k_4 = \frac{4 - 5e + e^2}{20} \quad (4.57k)$$

#### 4.4.2 Equivalent Hinge Offset

Hingless rotor blades can be approximated as rigidly flapping about a virtual flapping hinge, as shown in Fig. 4.11.

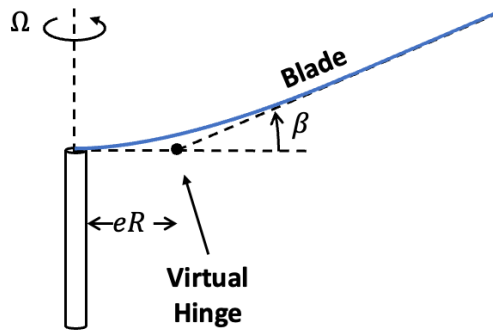


Figure 4.11: Hingless blade with a virtual hinge offset.

The equivalent hinge offset can be found by assuming  $k_\beta = 0$  and by solving for  $e$  in Eq. (4.49), yielding:

$$e_{\text{equiv}} = \frac{I_\beta}{M_\beta R} (\lambda_\beta^2 - 1) \quad (4.58)$$

Table 4.1: Flapping frequency and actual/equivalent hinge offset values for different rotors.

| Rotorcraft          | Rotor Type  | $\lambda_\beta$ | $e$   |
|---------------------|-------------|-----------------|-------|
| Sikorsky UH-60      | Articulated | 1.037           | 0.047 |
| MBB/Kawasaki BK 117 | Hingless    | 1.08            | 0.11  |
| MBB BO 105          | Hingless    | 1.1             | 0.14  |

#### 4.4.3 Inertial Forces and Moments About the Flap Hinge

The inertial forces at the flapping hinge, expressed in the lead-lag frame, are:

$$(F_x)_{\text{inertial}} = M_\beta \left\{ \left[ (\dot{\beta} - \omega_y)^2 + (\Omega - r_H)^2 \right] \cos \beta + \ddot{\beta} \sin \beta \right\} + m_b [\dot{u}_H \cos \psi + \dot{v}_H \sin \psi + eR(\Omega - r_H)^2] \quad (4.59a)$$

$$(F_y)_{\text{inertial}} = M_\beta \left[ (\dot{\Omega} - \dot{r}_H) \cos \beta - 2\dot{\beta}(\Omega - r_H) \sin \beta - 2\dot{\beta}\omega_x \cos \beta \right] + m_b (\dot{u}_H \sin \psi + \dot{v}_H \cos \psi) \quad (4.59b)$$

$$(F_z)_{\text{inertial}} = M_\beta \left[ \ddot{\beta} \cos \beta - \dot{\beta}^2 \sin \beta + 2\dot{\beta}\omega_y \sin \beta - (2\Omega\omega_x + \dot{p}_H \sin \psi + \dot{q}_H \cos \psi) \cos \beta \right] - m_b [\dot{w}_H + eR(2\Omega\omega_x + \dot{p}_H \sin \psi + \dot{q}_H \cos \psi) \cos \beta] \quad (4.59c)$$

where:

$$\omega_x = p_H \cos \psi - q_H \sin \psi \quad (4.60a)$$

$$\omega_y = p_H \sin \psi + q_H \cos \psi \quad (4.60b)$$

$$(4.60c)$$

Additionally,

$$m_b = \int_{eR}^R m(r) dr \quad (4.61)$$

where  $m_b$  is the mass of a single blade. The inertial moments about the lead-lag hinge, expressed in the lead-lag frame, are:

$$(M_x)_{\text{inertial}} = I_\beta \sin \beta \left[ (\dot{\Omega} - \dot{r}_H) \cos \beta - 2\dot{\beta}(\Omega - r_H) \sin \beta - 2\dot{\beta}p_H \cos \beta \right] + M_\beta \sin \beta (\dot{u}_H \sin \psi + \dot{v}_H \cos \psi) \quad (4.62a)$$

$$(M_y)_{\text{inertial}} = k_\beta \beta \quad (4.62b)$$

$$(M_z)_{\text{inertial}} = I_\beta \cos \beta \left[ (\dot{\Omega} - \dot{r}_H) \cos \beta - 2\dot{\beta}(\Omega - r_H) \sin \beta - 2\dot{\beta}p_H \cos \beta \right] + M_\beta \cos \beta (\dot{u}_H \sin \psi + \dot{v}_H \cos \psi) \quad (4.62c)$$

Make the following assumptions:

1.  $\beta$  is small such that  $\cos \beta \approx 1$  and  $\sin \beta \approx \beta$ .
  2.  $r_H \ll \Omega$  such that  $(\Omega - r_H)^2 \approx \Omega^2$ .
  3. The products of terms that are small is negligible such that  $\beta'^2 \approx \beta''\beta \approx \beta'\beta \approx \beta'\omega_x \approx \beta'\omega_y \approx \text{etc.} \approx 0$
- Then, the inertial forces at the flapping hinge simplify to:

$$(F_x)_{\text{inertial}} \approx \Omega^2 M_\beta + m_b (\dot{u}_H \cos \psi + \dot{v}_H \sin \psi + eR\Omega^2) \quad (4.63a)$$

$$(F_y)_{\text{inertial}} \approx \dot{\Omega} M_\beta + m_b (\dot{u}_H \sin \psi + \dot{v}_H \cos \psi) \quad (4.63b)$$

$$(F_z)_{\text{inertial}} \approx M_\beta \dot{\beta} - M_\beta (\dot{p}_H \sin \psi + \dot{q}_H \cos \psi) - m_b [\dot{w}_H + eR(\dot{p}_H \sin \psi + \dot{q}_H \cos \psi)] \quad (4.63c)$$

The inertial moments simplify to:

$$(M_x)_{\text{inertial}} \approx I_\beta \dot{\Omega} \beta \quad (4.64a)$$

$$(M_y)_{\text{inertial}} \approx k_\beta \beta \quad (4.64b)$$

$$(M_z)_{\text{inertial}} \approx I_\beta \dot{\Omega} + M_\beta (\dot{u}_H \sin \psi + \dot{v}_H \cos \psi) \quad (4.64c)$$

#### 4.4.4 Total Forces and Moments About the Flap Hinge

The total forces at the blade flapping hinge, expressed in the lead-lag frame, are:

$$\mathbf{F}^L = \mathbf{F}_{\text{aero}}^L + \mathbf{F}_{\text{inertial}}^L = \begin{bmatrix} (F_x)_{\text{aero}} \\ (F_y)_{\text{aero}} \\ (F_z)_{\text{aero}} \end{bmatrix} + \begin{bmatrix} (F_x)_{\text{inertial}} \\ (F_y)_{\text{inertial}} \\ (F_z)_{\text{inertial}} \end{bmatrix} = \begin{bmatrix} F_x \\ F_y \\ F_z \end{bmatrix} \quad (4.65)$$

where  $F_x$ ,  $F_y$ , and  $F_z$  are the radial, in-plane, and vertical shear forces. The total moments about the blade flapping hinge, expressed in the lead-lag frame, are:

$$\mathbf{M}^L = \mathbf{M}_{\text{aero}}^L + \mathbf{M}_{\text{inertial}}^L = \begin{bmatrix} (M_x)_{\text{aero}} \\ (M_y)_{\text{aero}} \\ (M_z)_{\text{aero}} \end{bmatrix} + \begin{bmatrix} (M_x)_{\text{inertial}} \\ (M_y)_{\text{inertial}} \\ (M_z)_{\text{inertial}} \end{bmatrix} = \begin{bmatrix} M_x \\ M_y \\ M_z \end{bmatrix} \quad (4.66)$$

where  $M_x$  is the torsional moment,  $M_y$  is moment through the flapping hinge, and  $M_z$  is the in-plane moment. Note that  $M_y \neq 0$  only exists if there is a flapping spring (*i.e.*,  $k_\beta \neq 0$ ).

#### 4.4.5 Rotor Hub Forces and Moments

The total forces acting at the flapping hinge of each blade can be summed to form the resultant forces at the rotor hub. These forces, expressed in the rotor hub frame, are:

$$X_H = \sum_{i=1}^{N_b} (-F_{x_i} \cos \psi_i - F_{y_i} \sin \psi_i) \quad (4.67a)$$

$$Y_H = \sum_{i=1}^{N_b} (F_{x_i} \sin \psi_i - F_{y_i} \cos \psi_i) \quad (4.67b)$$

$$Z_H = \sum_{i=1}^{N_b} F_{z_i} \quad (4.67c)$$

The same can be done with the moments about each flapping hinge, such that the hub moments, expressed in the rotor hub frame, are:

$$L_H = \sum_{i=1}^{N_b} [-M_{x_i} \cos \psi_i - (M_{y_i} - eRF_{z_i}) \sin \psi_i] \quad (4.68a)$$

$$M_H = \sum_{i=1}^{N_b} [M_{x_i} \sin \psi_i - (M_{y_i} - eRF_{z_i}) \cos \psi_i] \quad (4.68b)$$

$$N_H = \sum_{i=1}^{N_b} (M_{z_i} + eRF_{y_i}) \quad (4.68c)$$

$$(4.68d)$$

The ultimate goal is to find the forces and moments acting on the CG of the rotorcraft, such that these quantities can be used to drive the fuselage equations of motion. As such, the hub forces are transformed to body-frame components as follows:

$$\begin{bmatrix} X_R \\ Y_R \\ Z_R \end{bmatrix} = \mathbf{T}_{H \rightarrow B} \begin{bmatrix} X_H \\ Y_H \\ Z_H \end{bmatrix} \quad (4.69)$$

The rotor hub moments about the CG, expressed in body-frame coordinates, are:

$$\begin{aligned} \begin{bmatrix} L_R \\ M_R \\ N_R \end{bmatrix} &= \mathbf{T}_{H \rightarrow B} \begin{bmatrix} L_H \\ M_H \\ N_H \end{bmatrix} + \begin{bmatrix} X_R \\ Y_R \\ Z_R \end{bmatrix} \times \mathbf{r}_{\bullet \rightarrow H} \\ &= \mathbf{T}_{H \rightarrow B} \begin{bmatrix} L_H \\ M_H \\ N_H \end{bmatrix} + \begin{bmatrix} 0 & -Z_R & Y_R \\ Z_R & 0 & -X_R \\ -Y_R & X_R & 0 \end{bmatrix} \begin{bmatrix} x_H \\ y_H \\ z_H \end{bmatrix} \end{aligned} \quad (4.70)$$

#### 4.4.6 Multi-Blade Coordinates (MBC)

Multi-blade coordinates transform degrees of freedom from a rotating coordinate system (such as the flap or lead-lag frames) to a non-rotating coordinate system (such as the rotor hub frame). Consider the flap degree of freedom and let  $\beta_i$  be the flap angle of the  $i^{\text{th}}$  blade of an  $N_b$ -bladed rotor. Then, multi-blade coordinates are defined as follows:

$$\beta_0 = \frac{1}{N_b} \sum_{i=1}^{N_b} \beta_i \quad (4.71a)$$

$$\beta_{nc} = \frac{2}{N_b} \sum_{i=1}^{N_b} \beta_i \cos(n\psi_i) \quad (4.71b)$$

$$\beta_{ns} = \frac{2}{N_b} \sum_{i=1}^{N_b} \beta_i \sin(n\psi_i) \quad (4.71c)$$

$$\beta_{0D} = \frac{1}{N_b} \sum_{i=1}^{N_b} \beta_i (-1)^i \quad (4.71d)$$

where  $\beta_0$  is known as coning angle,  $\beta_{nc}$  and  $\beta_{ns}$  are longitudinal and lateral flapping angle harmonics, respectively, and  $\beta_{0D}$  is the differential coning angle. The azimuth angle  $\psi_i$  is that of the  $i^{\text{th}}$  blade. If the azimuth of the (arbitrarily) first blade is taken as the reference, then the azimuth of the  $i^{\text{th}}$  blade is:

$$\psi_i = \psi - \frac{2\pi}{N_b} (i-1), \quad i = 1, \dots, N_b \quad (4.72)$$

Conversely, given the multi-blade coordinates, the flap angle of each blade can be reconstructed from:

$$\beta_i = \beta_0 + \sum_{n=1}^{N_{\max}} [\beta_{nc} \cos n\psi_i + \beta_{ns} \sin n\psi_i] + \beta_{0D} (-1)^i \quad (4.73)$$

where the upper limit for the summation is:

$$N_{\max} = \begin{cases} \frac{N_b - 1}{2}, & N_b \text{ odd} \\ \frac{N_b - 2}{2}, & N_b \text{ even} \end{cases} \quad (4.74)$$

Examples for varying rotor blades are as follows:

- 2 blades:  $\beta_i = \beta_{1c} \cos \psi_i + \beta_{1s} \sin \psi_i$
- 3 blades:  $\beta_i = \beta_0 \beta_{1c} \cos \psi_i + \beta_{1s} \sin \psi_i$
- 4 blades:  $\beta_i = \beta_0 + \beta_{1c} \cos \psi_i + \beta_{1s} \sin \psi_i + \beta_{0D} (-1)^i$
- 5 blades:  $\beta_i = \beta_0 + \beta_{1c} \cos \psi_i + \beta_{1s} \sin \psi_i + \beta_{2c} \cos 2\psi_i + \beta_{2s} \sin 2\psi_i$

- 6 blades:  $\beta_i = \beta_0 + \beta_{1c} \cos \psi_i + \beta_{1s} \sin \psi_i + \beta_{2c} \cos 2\psi_i + \beta_{2s} \sin 2\psi_i + \beta_{0D} (-1)^i$

- 7 blades:  $\beta_i = \beta_0 + \beta_{1c} \cos \psi_i + \beta_{1s} \sin \psi_i + \beta_{2c} \cos 2\psi_i + \beta_{2s} \sin 2\psi_i + \beta_{3c} \cos 3\psi_i + \beta_{3s} \sin 3\psi_i$

Multi-blade coordinates are shown qualitatively in Fig. 4.12 for a four-bladed rotor. The MBC associated with this rotor are the coning angle  $\beta_0$  (Fig. 4.12a), the differential coning angle  $\beta_{0D}$  (Fig. 4.12b), the longitudinal cyclic flapping angle  $\beta_{1c}$  (Fig. 4.12c), and the lateral cyclic flapping angle  $\beta_{1s}$  (Fig. 4.12d).

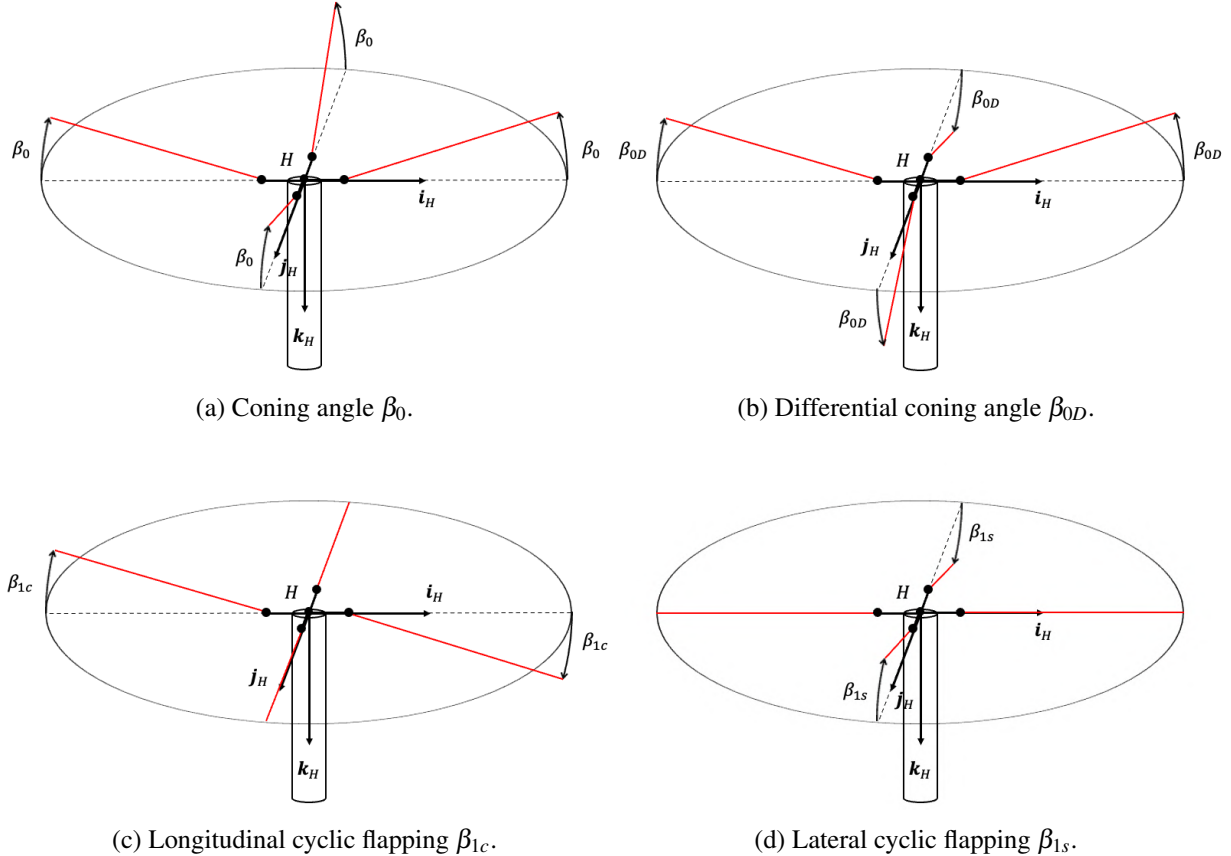


Figure 4.12: Multi-blade coordinates for a four-bladed rotor.

Let us know express MBCs in matrix form. The MBC matrices will be derived here for the special case of a four-bladed rotor. The relationship between individual blade coordinates (IBC) and MBC is:

$$\underbrace{\begin{bmatrix} \beta_1 \\ \beta_2 \\ \beta_3 \\ \beta_4 \end{bmatrix}}_{\boldsymbol{\beta}_I} = \underbrace{\begin{bmatrix} 1 & -1 & \cos \psi_1 & \sin \psi_1 \\ 1 & 1 & \cos \psi_2 & \sin \psi_2 \\ 1 & -1 & \cos \psi_3 & \sin \psi_3 \\ 1 & 1 & \cos \psi_4 & \sin \psi_4 \end{bmatrix}}_{L_\beta} \underbrace{\begin{bmatrix} \beta_0 \\ \beta_{0D} \\ \beta_{1c} \\ \beta_{1s} \end{bmatrix}}_{\boldsymbol{\beta}_M} \quad (4.75)$$

The inverse transformation (*i.e.*, from IBC to MBC) is given by:

$$\underbrace{\begin{bmatrix} \beta_0 \\ \beta_{0D} \\ \beta_{1c} \\ \beta_{1s} \end{bmatrix}}_{\boldsymbol{\beta}_M} = \frac{1}{N_b} \underbrace{\begin{bmatrix} 1 & 1 & 1 & 1 \\ -1 & 1 & -1 & 1 \\ 2 \cos \psi_1 & 2 \cos \psi_2 & 2 \cos \psi_3 & 2 \cos \psi_4 \\ 2 \sin \psi_1 & 2 \sin \psi_2 & 2 \sin \psi_3 & 2 \sin \psi_4 \end{bmatrix}}_{L_\beta^{-1}} \underbrace{\begin{bmatrix} \beta_1 \\ \beta_2 \\ \beta_3 \\ \beta_4 \end{bmatrix}}_{\boldsymbol{\beta}_I} \quad (4.76)$$

Consider now differentiating the MBC to IBC transformation with respect to time:

$$\begin{aligned} \frac{d}{dt} \dot{\boldsymbol{\beta}}_I &= \frac{d}{dt} (\mathbf{L}_\beta \boldsymbol{\beta}_M) = \frac{d}{dt} \mathbf{L}_\beta \boldsymbol{\beta}_M + \mathbf{L}_\beta \frac{d}{dt} \boldsymbol{\beta}_M = \\ &= \Omega \underbrace{\begin{bmatrix} 0 & 0 & -\sin \psi_1 & \cos \psi_1 \\ 0 & 0 & -\sin \psi_2 & \cos \psi_2 \\ 0 & 0 & -\sin \psi_3 & \cos \psi_3 \\ 0 & 0 & -\sin \psi_4 & \cos \psi_4 \end{bmatrix}}_{\dot{\mathbf{L}}_\beta} \underbrace{\begin{bmatrix} \beta_0 \\ \beta_{0D} \\ \beta_{1c} \\ \beta_{1s} \end{bmatrix}}_{\boldsymbol{\beta}_M} + \underbrace{\begin{bmatrix} 1 & -1 & \cos \psi_1 & \sin \psi_1 \\ 1 & 1 & \cos \psi_2 & \sin \psi_2 \\ 1 & -1 & \cos \psi_3 & \sin \psi_3 \\ 1 & 1 & \cos \psi_4 & \sin \psi_4 \end{bmatrix}}_{\mathbf{L}_\beta} \underbrace{\begin{bmatrix} \dot{\beta}_0 \\ \dot{\beta}_{0D} \\ \dot{\beta}_{1c} \\ \dot{\beta}_{1s} \end{bmatrix}}_{\dot{\boldsymbol{\beta}}_M} \end{aligned} \quad (4.77)$$

Let us now differentiate one more time with respect to time:

$$\begin{aligned} \frac{d}{dt} \ddot{\boldsymbol{\beta}}_I &= \frac{d}{dt} (\ddot{\mathbf{L}}_\beta \boldsymbol{\beta}_M + \mathbf{L}_\beta \dot{\boldsymbol{\beta}}_M) = \frac{d}{dt} \ddot{\mathbf{L}}_\beta \boldsymbol{\beta}_M + \ddot{\mathbf{L}}_\beta \frac{d}{dt} \boldsymbol{\beta}_M + \frac{d}{dt} \mathbf{L}_\beta \dot{\boldsymbol{\beta}}_M + \mathbf{L}_\beta \frac{d}{dt} \dot{\boldsymbol{\beta}}_M = \\ &= \Omega^2 \underbrace{\begin{bmatrix} 0 & 0 & -\cos \psi_1 & -\sin \psi_1 \\ 0 & 0 & -\cos \psi_2 & -\sin \psi_2 \\ 0 & 0 & -\cos \psi_3 & -\sin \psi_3 \\ 0 & 0 & -\cos \psi_4 & -\sin \psi_4 \end{bmatrix}}_{\ddot{\mathbf{L}}_\beta} \underbrace{\begin{bmatrix} \beta_0 \\ \beta_{0D} \\ \beta_{1c} \\ \beta_{1s} \end{bmatrix}}_{\boldsymbol{\beta}_M} + 2\Omega \underbrace{\begin{bmatrix} 0 & 0 & -\sin \psi_1 & \cos \psi_1 \\ 0 & 0 & -\sin \psi_2 & \cos \psi_2 \\ 0 & 0 & -\sin \psi_3 & \cos \psi_3 \\ 0 & 0 & -\sin \psi_4 & \cos \psi_4 \end{bmatrix}}_{\mathbf{L}_\beta} \underbrace{\begin{bmatrix} \dot{\beta}_0 \\ \dot{\beta}_{0D} \\ \dot{\beta}_{1c} \\ \dot{\beta}_{1s} \end{bmatrix}}_{\dot{\boldsymbol{\beta}}_M} \\ &\quad + \underbrace{\begin{bmatrix} 1 & -1 & \cos \psi_1 & \sin \psi_1 \\ 1 & 1 & \cos \psi_2 & \sin \psi_2 \\ 1 & -1 & \cos \psi_3 & \sin \psi_3 \\ 1 & 1 & \cos \psi_4 & \sin \psi_4 \end{bmatrix}}_{\mathbf{L}_\beta} \underbrace{\begin{bmatrix} \ddot{\beta}_0 \\ \ddot{\beta}_{0D} \\ \ddot{\beta}_{1c} \\ \ddot{\beta}_{1s} \end{bmatrix}}_{\ddot{\boldsymbol{\beta}}_M} + \dot{\Omega} \underbrace{\begin{bmatrix} 0 & 0 & -\sin \psi_1 & \cos \psi_1 \\ 0 & 0 & -\sin \psi_2 & \cos \psi_2 \\ 0 & 0 & -\sin \psi_3 & \cos \psi_3 \\ 0 & 0 & -\sin \psi_4 & \cos \psi_4 \end{bmatrix}}_{\frac{1}{2} \frac{\Omega}{\dot{\Omega}} \dot{\mathbf{L}}_\beta} \underbrace{\begin{bmatrix} \dot{\beta}_0 \\ \dot{\beta}_{0D} \\ \dot{\beta}_{1c} \\ \dot{\beta}_{1s} \end{bmatrix}}_{\dot{\boldsymbol{\beta}}_M} \end{aligned} \quad (4.78)$$

Writing these three equations more compactly:

$$\boldsymbol{\beta}_I = \mathbf{L}_\beta \boldsymbol{\beta}_M \quad (4.79a)$$

$$\dot{\boldsymbol{\beta}}_I = \dot{\mathbf{L}}_\beta \boldsymbol{\beta}_M + \mathbf{L}_\beta \dot{\boldsymbol{\beta}}_M \quad (4.79b)$$

$$\ddot{\boldsymbol{\beta}}_I = \ddot{\mathbf{L}}_\beta \boldsymbol{\beta}_M + 2\dot{\mathbf{L}}_\beta \dot{\boldsymbol{\beta}}_M + \mathbf{L}_\beta \ddot{\boldsymbol{\beta}}_M + \frac{\Omega}{\dot{\Omega}} \dot{\mathbf{L}}_\beta \boldsymbol{\beta}_M \quad (4.79c)$$

In non-dimensional form:

$$\boldsymbol{\beta}_I = \mathbf{L}_\beta \boldsymbol{\beta}_M \quad (4.80a)$$

$$\boldsymbol{\beta}'_I = \mathbf{L}'_\beta \boldsymbol{\beta}_M + \mathbf{L}_\beta \boldsymbol{\beta}'_M \quad (4.80b)$$

$$\boldsymbol{\beta}''_I = \mathbf{L}''_\beta \boldsymbol{\beta}_M + 2\mathbf{L}'_\beta \boldsymbol{\beta}'_M + \mathbf{L}_\beta \boldsymbol{\beta}''_M + \frac{1}{\dot{\Omega}} \mathbf{L}'_\beta \boldsymbol{\beta}_M \quad (4.80c)$$

where:

$$\mathbf{L}'_\beta = \frac{1}{\Omega} \dot{\mathbf{L}}_\beta \quad (4.81a)$$

$$\mathbf{L}''_\beta = \frac{1}{\Omega^2} \ddot{\mathbf{L}}_\beta \quad (4.81b)$$

Let us now differentiate the IBC to MBC transformation with respect to time:

$$\begin{aligned} \frac{d}{dt} \boldsymbol{\beta}_M &= \frac{d}{dt} (\mathbf{L}_\beta^{-1} \boldsymbol{\beta}_I) = \frac{d}{dt} \mathbf{L}_\beta^{-1} \boldsymbol{\beta}_I + \mathbf{L}_\beta^{-1} \frac{d}{dt} \boldsymbol{\beta}_I \\ &= \underbrace{\frac{\Omega}{N_b} \begin{bmatrix} 0 & 0 & 0 & 0 \\ 0 & 0 & 0 & 0 \\ -2 \sin \psi_1 & -2 \sin \psi_2 & -2 \sin \psi_3 & -2 \sin \psi_4 \\ 2 \cos \psi_1 & 2 \cos \psi_2 & 2 \cos \psi_3 & 2 \cos \psi_4 \end{bmatrix}}_{\dot{\mathbf{L}}_\beta^{-1}} \underbrace{\begin{bmatrix} \beta_1 \\ \beta_2 \\ \beta_3 \\ \beta_4 \end{bmatrix}}_{\boldsymbol{\beta}_I} \\ &\quad + \underbrace{\frac{1}{N_b} \begin{bmatrix} 1 & 1 & 1 & 1 \\ -1 & 1 & -1 & 1 \\ 2 \cos \psi_1 & 2 \cos \psi_2 & 2 \cos \psi_3 & 2 \cos \psi_4 \\ 2 \sin \psi_1 & 2 \sin \psi_2 & 2 \sin \psi_3 & 2 \sin \psi_4 \end{bmatrix}}_{\mathbf{L}_\beta^{-1}} \underbrace{\begin{bmatrix} \dot{\beta}_1 \\ \dot{\beta}_2 \\ \dot{\beta}_3 \\ \dot{\beta}_4 \end{bmatrix}}_{\dot{\boldsymbol{\beta}}_I} \end{aligned} \quad (4.82)$$

Let us differentiate one more time with respect to time:

$$\begin{aligned} \frac{d}{dt} \dot{\boldsymbol{\beta}}_M &= \frac{d}{dt} (\dot{\mathbf{L}}_\beta^{-1} \boldsymbol{\beta}_I + \mathbf{L}_\beta^{-1} \dot{\boldsymbol{\beta}}_I) = \frac{d}{dt} \dot{\mathbf{L}}_\beta^{-1} \boldsymbol{\beta}_I + \dot{\mathbf{L}}_\beta^{-1} \frac{d}{dt} \boldsymbol{\beta}_I + \frac{d}{dt} \mathbf{L}_\beta^{-1} \dot{\boldsymbol{\beta}}_I + \mathbf{L}_\beta^{-1} \frac{d}{dt} \dot{\boldsymbol{\beta}}_I \\ &= \underbrace{\frac{\Omega^2}{N_b} \begin{bmatrix} 0 & 0 & 0 & 0 \\ 0 & 0 & 0 & 0 \\ -2 \cos \psi_1 & -2 \cos \psi_2 & -2 \cos \psi_3 & -2 \cos \psi_4 \\ -2 \sin \psi_1 & -2 \sin \psi_2 & -2 \sin \psi_3 & -2 \sin \psi_4 \end{bmatrix}}_{\ddot{\mathbf{L}}_\beta^{-1}} \underbrace{\begin{bmatrix} \beta_1 \\ \beta_2 \\ \beta_3 \\ \beta_4 \end{bmatrix}}_{\boldsymbol{\beta}_I} \\ &\quad + \underbrace{\frac{\dot{\Omega}}{N_b} \begin{bmatrix} 0 & 0 & 0 & 0 \\ 0 & 0 & 0 & 0 \\ -2 \sin \psi_1 & -2 \sin \psi_2 & -2 \sin \psi_3 & -2 \sin \psi_4 \\ 2 \cos \psi_1 & 2 \cos \psi_2 & 2 \cos \psi_3 & 2 \cos \psi_4 \end{bmatrix}}_{\frac{\Omega}{\dot{\Omega}} \dot{\mathbf{L}}_\beta^{-1}} \underbrace{\begin{bmatrix} \dot{\beta}_1 \\ \dot{\beta}_2 \\ \dot{\beta}_3 \\ \dot{\beta}_4 \end{bmatrix}}_{\dot{\boldsymbol{\beta}}_I} \\ &\quad + \underbrace{\frac{2\Omega}{N_b} \begin{bmatrix} 0 & 0 & 0 & 0 \\ 0 & 0 & 0 & 0 \\ -2 \sin \psi_1 & -2 \sin \psi_2 & -2 \sin \psi_3 & -2 \sin \psi_4 \\ 2 \cos \psi_1 & 2 \cos \psi_2 & 2 \cos \psi_3 & 2 \cos \psi_4 \end{bmatrix}}_{\mathbf{L}_\beta^{-1}} \underbrace{\begin{bmatrix} \ddot{\beta}_1 \\ \ddot{\beta}_2 \\ \ddot{\beta}_3 \\ \ddot{\beta}_4 \end{bmatrix}}_{\ddot{\boldsymbol{\beta}}_I} \\ &\quad + \underbrace{\frac{1}{N_b} \begin{bmatrix} 1 & 1 & 1 & 1 \\ -1 & 1 & -1 & 1 \\ 2 \cos \psi_1 & 2 \cos \psi_2 & 2 \cos \psi_3 & 2 \cos \psi_4 \\ 2 \sin \psi_1 & 2 \sin \psi_2 & 2 \sin \psi_3 & 2 \sin \psi_4 \end{bmatrix}}_{\mathbf{L}_\beta^{-1}} \underbrace{\begin{bmatrix} \ddot{\beta}_1 \\ \ddot{\beta}_2 \\ \ddot{\beta}_3 \\ \ddot{\beta}_4 \end{bmatrix}}_{\ddot{\boldsymbol{\beta}}_I} \end{aligned} \quad (4.83)$$

Writing these three equations more compactly yields:

$$\boldsymbol{\beta}_M = \mathbf{L}_\beta^{-1} \boldsymbol{\beta}_I \quad (4.84a)$$

$$\dot{\boldsymbol{\beta}}_M = \dot{\mathbf{L}}_\beta^{-1} \boldsymbol{\beta}_I + \mathbf{L}_\beta^{-1} \dot{\boldsymbol{\beta}}_I \quad (4.84b)$$

$$\ddot{\boldsymbol{\beta}}_M = \ddot{\mathbf{L}}_\beta^{-1} \boldsymbol{\beta}_I + 2\dot{\mathbf{L}}_\beta^{-1} \dot{\boldsymbol{\beta}}_I + \mathbf{L}_\beta^{-1} \ddot{\boldsymbol{\beta}}_I + \frac{\Omega}{\dot{\Omega}} \dot{\mathbf{L}}_\beta^{-1} \boldsymbol{\beta}_I \quad (4.84c)$$

In non-dimensional form:

$$\boldsymbol{\beta}_M = \mathbf{L}_\beta^{-1} \boldsymbol{\beta}_I \quad (4.85a)$$

$$\boldsymbol{\beta}'_M = \mathbf{L}'_\beta^{-1} \boldsymbol{\beta}_I + \mathbf{L}_\beta^{-1} \boldsymbol{\beta}'_I \quad (4.85b)$$

$$\boldsymbol{\beta}''_M = \mathbf{L}''_\beta^{-1} \boldsymbol{\beta}_I + 2\mathbf{L}'_\beta^{-1} \boldsymbol{\beta}'_I + \mathbf{L}_\beta^{-1} \boldsymbol{\beta}''_I + \frac{1}{\dot{\Omega}} \mathbf{L}'_\beta^{-1} \boldsymbol{\beta}_I \quad (4.85c)$$

where:

$$\mathbf{L}'_\beta^{-1} = \frac{1}{\Omega} \dot{\mathbf{L}}_\beta^{-1} \quad (4.86a)$$

$$\mathbf{L}''_\beta^{-1} = \frac{1}{\Omega^2} \ddot{\mathbf{L}}_\beta^{-1} \quad (4.86b)$$

#### 4.4.7 Flapping Dynamics in Multi-Blade Coordinates

Consider writing the flapping dynamics of Eq. (4.56) for an  $n$ -bladed rotor, such that:

$$\boldsymbol{\beta}''_I = -\mathbf{C}_I(\psi) \boldsymbol{\beta}'_I - \mathbf{D}_I(\psi) \boldsymbol{\beta}_I + \mathbf{H}_I(\psi) \quad (4.87)$$

For a four-bladed rotor where all the rotor blades have the same properties, then:

$$\boldsymbol{\beta}_I^T = [\beta_1 \ \beta_2 \ \beta_3 \ \beta_4] \quad (4.88a)$$

$$\mathbf{C}_I(\psi) = \begin{bmatrix} \gamma_{f_{\beta'_1}} & 0 & 0 & 0 \\ 0 & \gamma_{f_{\beta'_2}} & 0 & 0 \\ 0 & 0 & \gamma_{f_{\beta'_3}} & 0 \\ 0 & 0 & 0 & \gamma_{f_{\beta'_4}} \end{bmatrix} \quad (4.88b)$$

$$\mathbf{D}_I(\psi) = \begin{bmatrix} (\lambda_\beta^2 + \gamma f_{\beta_1}) & 0 & 0 & 0 \\ 0 & (\lambda_\beta^2 + \gamma f_{\beta_2}) & 0 & 0 \\ 0 & 0 & (\lambda_\beta^2 + \gamma f_{\beta_3}) & 0 \\ 0 & 0 & 0 & (\lambda_\beta^2 + \gamma f_{\beta_4}) \end{bmatrix} \quad (4.88c)$$

$$\mathbf{H}_I(\psi) = \begin{bmatrix} k_g [(2\bar{p}_H + \bar{q}'_H) \cos \psi - (2\bar{q}_H - \bar{p}'_H) \sin \psi_1] \\ + \gamma \left\{ f_{\theta_1} \theta_P + f_{\theta_{tw_1}} \theta_{tw} + f_{\lambda_1} (\mu_z - \lambda_0) + f_{\omega_1} [(\bar{p}_H - \lambda_{1s}) \sin \psi_1 + (\bar{q}_H - \lambda_{1c}) \cos \psi_1] \right\} \\ k_g [(2\bar{p}_H + \bar{q}'_H) \cos \psi - (2\bar{q}_H - \bar{p}'_H) \sin \psi_2] \\ + \gamma \left\{ f_{\theta_2} \theta_P + f_{\theta_{tw_2}} \theta_{tw} + f_{\lambda_2} (\mu_z - \lambda_0) + f_{\omega_2} [(\bar{p}_H - \lambda_{1s}) \sin \psi_2 + (\bar{q}_H - \lambda_{1c}) \cos \psi_2] \right\} \\ k_g [(2\bar{p}_H + \bar{q}'_H) \cos \psi - (2\bar{q}_H - \bar{p}'_H) \sin \psi_3] \\ + \gamma \left\{ f_{\theta_3} \theta_P + f_{\theta_{tw_3}} \theta_{tw} + f_{\lambda_3} (\mu_z - \lambda_0) + f_{\omega_3} [(\bar{p}_H - \lambda_{1s}) \sin \psi_3 + (\bar{q}_H - \lambda_{1c}) \cos \psi_3] \right\} \\ k_g [(2\bar{p}_H + \bar{q}'_H) \cos \psi - (2\bar{q}_H - \bar{p}'_H) \sin \psi_4] \\ + \gamma \left\{ f_{\theta_4} \theta_P + f_{\theta_{tw_4}} \theta_{tw} + f_{\lambda_4} (\mu_z - \lambda_0) + f_{\omega_4} [(\bar{p}_H - \lambda_{1s}) \sin \psi_4 + (\bar{q}_H - \lambda_{1c}) \cos \psi_4] \right\} \end{bmatrix} \quad (4.88d)$$

By now substituting Eq. (4.80) into Eq. (4.87), one gets:

$$\underbrace{\left( \mathbf{L}''_\beta \boldsymbol{\beta}_M + 2\mathbf{L}'_\beta \boldsymbol{\beta}'_M + \mathbf{L}_\beta \boldsymbol{\beta}''_M + \frac{1}{\dot{\Omega}} \mathbf{L}'_\beta \boldsymbol{\beta}_M \right)}_{\boldsymbol{\beta}''_I} = -\mathbf{C}_I(\psi) \underbrace{\left( \mathbf{L}'_\beta \boldsymbol{\beta}_M + \mathbf{L}_\beta \boldsymbol{\beta}'_M \right)}_{\boldsymbol{\beta}'_I} - \mathbf{D}_I(\psi) \underbrace{\left( \mathbf{L}_\beta \boldsymbol{\beta}_M \right)}_{\boldsymbol{\beta}_I} + \mathbf{H}_I(\psi) \quad (4.89)$$

Re-organizing and assuming  $\Omega = \text{const.}$ , such that  $\dot{\Omega} = 0$ , yields:

$$\boldsymbol{\beta}''_M = -\mathbf{L}_\beta^{-1} \underbrace{\left[ \mathbf{C}_I(\psi) \mathbf{L}_\beta + 2\mathbf{L}'_\beta \right]}_{\mathbf{C}_M(\psi)} \boldsymbol{\beta}'_M - \mathbf{L}_\beta^{-1} \underbrace{\left[ \mathbf{L}''_\beta + \mathbf{C}_I(\psi) \mathbf{L}'_\beta + \mathbf{D}_I(\psi) \mathbf{L}_\beta \right]}_{\mathbf{D}_M(\psi)} \boldsymbol{\beta}_M + \underbrace{\mathbf{L}_\beta^{-1} \mathbf{H}_I(\psi)}_{\mathbf{H}_M(\psi)} \quad (4.90)$$

where  $\boldsymbol{\beta}_M^T = [\beta_0 \ \beta_{0D} \ \beta_{1c} \ \beta_{1s}]$ . The matrices  $\mathbf{C}_M$ ,  $\mathbf{D}_M$ , and  $\mathbf{H}_M$  can now be evaluated. Note that many terms cancel, but the matrices will still be a function of the azimuth angle  $\psi$ , including several trigonometric functions in  $\psi$ . This implies that these matrices are time-varying, *i.e.*, their values varies over one rotor revolution. However, at a first approximation, the time-varying terms can be neglected as they do not affect the flight dynamics significantly, but typically only contribute to vibrations. For instance, consider:

$$\begin{aligned}\mathbf{C}_M(\psi) &= \mathbf{L}_\beta^{-1} \left[ \mathbf{C}_I(\psi) \mathbf{L}_\beta + 2\mathbf{L}'_\beta \right] \\ &= \frac{1}{4} \begin{bmatrix} 0 & 0 & 0 & 0 \\ 0 & 0 & 0 & 0 \\ -2s_{\psi_1} & -2s_{\psi_2} & -2s_{\psi_3} & -2s_{\psi_4} \\ 2s_{\psi_1} & 2s_{\psi_2} & 2s_{\psi_3} & 2s_{\psi_4} \end{bmatrix} \begin{bmatrix} \gamma_{f_{\beta'_1}} & 0 & 0 & 0 \\ 0 & \gamma_{f_{\beta'_2}} & 0 & 0 \\ 0 & 0 & \gamma_{f_{\beta'_3}} & 0 \\ 0 & 0 & 0 & \gamma_{f_{\beta'_4}} \end{bmatrix} \begin{bmatrix} 1 & -1 & c_{\psi_1} & s_{\psi_1} \\ 1 & 1 & c_{\psi_2} & s_{\psi_2} \\ 1 & -1 & c_{\psi_3} & s_{\psi_3} \\ 1 & 1 & c_{\psi_4} & s_{\psi_4} \end{bmatrix} \quad (4.91) \\ &\quad + \frac{2}{4} \begin{bmatrix} 0 & 0 & 0 & 0 \\ 0 & 0 & 0 & 0 \\ -2s_{\psi_1} & -2s_{\psi_2} & -2s_{\psi_3} & -2s_{\psi_4} \\ 2s_{\psi_1} & 2s_{\psi_2} & 2s_{\psi_3} & 2s_{\psi_4} \end{bmatrix} \begin{bmatrix} 0 & 0 & -s_{\psi_1} & c_{\psi_1} \\ 0 & 0 & -s_{\psi_2} & c_{\psi_2} \\ 0 & 0 & -s_{\psi_3} & c_{\psi_3} \\ 0 & 0 & -s_{\psi_4} & c_{\psi_4} \end{bmatrix}\end{aligned}$$

where  $s_{\psi_i} = \sin \psi_i$  and  $c_{\psi_i} = \cos \psi_i$ . By using  $\psi_i = \psi - \frac{\pi}{2}(i-1)$ , the trigonometric identities in the equation above become:

$$\begin{aligned}\sin \psi_1 &= \sin \psi \\ \cos \psi_1 &= \cos \psi \\ \sin \psi_2 &= \sin \left( \psi - \frac{\pi}{2} \right) = -\cos \psi \\ \cos \psi_2 &= \cos \left( \psi - \frac{\pi}{2} \right) = \sin \psi \\ \sin \psi_3 &= \sin (\psi - \pi) = -\sin \psi \\ \cos \psi_3 &= \cos (\psi - \pi) = -\cos \psi \\ \sin \psi_4 &= \sin \left( \psi - \frac{3\pi}{2} \right) = \cos \psi \\ \cos \psi_4 &= \cos \left( \psi - \frac{3\pi}{2} \right) = -\sin \psi \quad (4.92)\end{aligned}$$

Then,

$$\begin{aligned}\mathbf{C}_M(\psi) &= \frac{1}{4} \begin{bmatrix} 0 & 0 & 0 & 0 \\ 0 & 0 & 0 & 0 \\ 2c_\psi & 2s_\psi & -2c_\psi & -2s_\psi \\ 2s_\psi & -2c_\psi & -2s_\psi & 2c_\psi \end{bmatrix} \begin{bmatrix} \gamma_{f_{\beta'_1}} & 0 & 0 & 0 \\ 0 & \gamma_{f_{\beta'_2}} & 0 & 0 \\ 0 & 0 & \gamma_{f_{\beta'_3}} & 0 \\ 0 & 0 & 0 & \gamma_{f_{\beta'_4}} \end{bmatrix} \begin{bmatrix} 1 & -1 & c_\psi & s_\psi \\ 1 & 1 & s_\psi & -c_\psi \\ 1 & -1 & -c_\psi & -s_\psi \\ 1 & 1 & -s_\psi & c_\psi \end{bmatrix} \quad (4.93) \\ &\quad + \frac{2}{4} \begin{bmatrix} 0 & 0 & 0 & 0 \\ 0 & 0 & 0 & 0 \\ 2c_\psi & 2s_\psi & -2c_\psi & -2s_\psi \\ 2s_\psi & -2c_\psi & -2s_\psi & 2c_\psi \end{bmatrix} \begin{bmatrix} 0 & 0 & -s_\psi & c_\psi \\ 0 & 0 & c_\psi & s_\psi \\ 0 & 0 & s_\psi & -c_\psi \\ 0 & 0 & -c_\psi & -s_\psi \end{bmatrix}\end{aligned}$$

Evaluating this expression and using the following trigonometric identities:

$$\begin{aligned}2 \sin \psi \cos \psi &= \sin (2\psi) \\ \cos^2 \psi - \sin^2 \psi &= \cos (2\psi) \quad (4.94)\end{aligned}$$

yields:

$$\mathbf{C}_M(\psi) = \underbrace{\frac{\gamma}{2}(k_3 - k_2e) \begin{bmatrix} 1 & 0 & 0 & 0 \\ 0 & 1 & 0 & 0 \\ 0 & 0 & 1 & 0 \\ 0 & 0 & 0 & 1 \end{bmatrix}}_{\text{Time invariant}} + \underbrace{\frac{\gamma}{2}(k_2 - k_1e)\mu \begin{bmatrix} 0 & 0 & 0 & \frac{1}{2} \\ 0 & 0 & -\sin(2\psi) & \cos(2\psi) \\ 0 & -\sin(2\psi) & 0 & 0 \\ 1 & \cos(2\psi) & 0 & 0 \end{bmatrix}}_{\text{Time varying}} \quad (4.95)$$

Thus, four terms have a periodicity of two-times-per-revolution (2/rev) and come into play in forward flight, that is, for  $\mu > 0$ . These are typically not important for flight dynamics and/or handling qualities as the average of these terms is zero over one rotor revolution. Neglecting these terms gives the following time-invariant approximation of the  $\mathbf{C}_M$  matrix:

$$\mathbf{C}_M(\psi) \approx \mathbf{C}_{M_0} = \frac{\gamma}{2} \begin{bmatrix} (k_3 - k_2e) & 0 & 0 & \frac{\mu}{2}(k_2 - k_1e) \\ 0 & (k_3 - k_2e) & 0 & 0 \\ 0 & 0 & (k_3 - k_2e) & \frac{4}{\gamma} \\ \mu(k_2 - k_1e) & 0 & -\frac{4}{\gamma} & (k_3 - k_2e) \end{bmatrix} \quad (4.96)$$

A similar analysis can be carried out for  $\mathbf{D}_M$  and  $\mathbf{H}_M$ , where these matrices turn out to be:

$$\mathbf{D}_{M_0} = \frac{\gamma}{2} \begin{bmatrix} \frac{2\lambda_\beta^2}{\gamma} & 0 & -k_1e\mu & 0 \\ 0 & \frac{2\lambda_\beta^2}{\gamma} & 0 & 0 \\ k_2\mu & 0 & \frac{2(\lambda_\beta^2 - 1)}{\gamma} & \left[(k_3 - k_2e) + \frac{\mu^2}{8} + \frac{2\Omega'}{\gamma}\right] \\ 0 & 0 & -\left[(k_3 - k_2e) + \frac{\mu^2}{8} + \frac{2\Omega'}{\gamma}\right] & \frac{2\lambda_\beta^2}{\gamma} \end{bmatrix} \quad (4.97a)$$

$$\mathbf{H}_{M_0} = \frac{\gamma}{2} \begin{bmatrix} \left(k_3 + \frac{k_1}{2}\mu^2\right)\theta_0 + \left(k_4 + \frac{k_2}{2}\mu^2\right)\theta_{tw} + k_2\mu\theta_{1s} + k_2(\mu_z - \lambda_0) + \frac{k_2}{2}\mu(\bar{p}_H - \lambda_{1s}) & 0 \\ \left(k_3 + \frac{k_1}{4}\mu^2\right)\theta_{1c} + k_3(\bar{q}_H - \lambda_{1c}) + \frac{2}{\gamma}k_g(2\bar{p}_H + \bar{q}'_H) & \\ 2k_2\mu\theta_0 + 2k_3\mu\theta_{tw} + \left(k_3 + \frac{3}{4}k_1\mu^2\right)\theta_{1s} + k_1\mu(\mu_z\lambda_0) + k_3(\bar{p}_H - \lambda_{1s}) - \frac{2}{\gamma}k_g(2\bar{q}_H - \bar{p}'_H) & \end{bmatrix} \quad (4.97b)$$

Note that the inflow harmonics (*i.e.*,  $\lambda_{1s}$  and  $\lambda_{1c}$ ), the swashplate harmonics (*i.e.*,  $\theta_{1s}$  and  $\theta_{1c}$ ), and the hub angular rates and accelerations (*i.e.*,  $\bar{p}_H$ ,  $\bar{q}_H$ ,  $\bar{p}'_H$ , and  $\bar{q}'_H$ ) used in this equation are those expressed in the rotor hub frame. One could use those expressed in the wind frame however, the flapping dynamics equations would then be in the wind frame as well. It is also worth noting that the differential coning state is decoupled from the rest of the flapping dynamics and the corresponding forcing term is zero. This applies to any rotor with an even number of blades (*e.g.*,  $N_b = 4, 6, 8, \text{etc.}$ ). This is the reason why the mode of motion associated to the differential coning state is called *reactionless* mode, since it produces no steady force or moment of the aircraft. As such, the differential coning state can be dropped from the flight dynamics analysis.

#### 4.4.8 Center Spring Approximation

The effect of the flapping hinge offset can be approximated by adopting a centrally-hinged blade with a center spring that produces the same flapping frequency as the hinge offset model, as shown in Fig. 4.13.

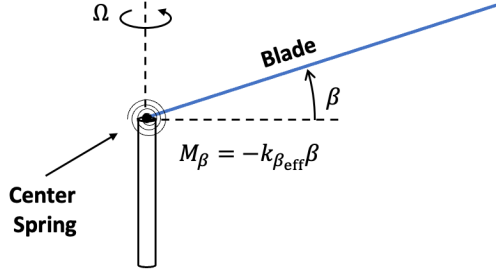


Figure 4.13: Rotor blade with center spring that produces the same flapping frequency as a blade with a hinge offset.

Recall Eq. (4.49):

$$\lambda_\beta = \sqrt{1 + \frac{k_\beta}{I_\beta \Omega^2} + \frac{M_\beta e R}{I_\beta}} \quad (4.98)$$

Then, the equation for an equivalent center spring constant can be found by setting  $e = 0$ :

$$\begin{aligned} k_{\beta_{\text{eff}}} &= I_\beta \Omega^2 (\lambda_\beta^2 - 1) \\ &= k_\beta + \Omega^2 M_\beta e R \end{aligned} \quad (4.99)$$

With this approximation, the constants  $k_g$ ,  $k_1$ ,  $k_2$ ,  $k_3$ , and  $k_4$  in the flapping equation simplify to:

$$k_g = \sqrt{\lambda_\beta^2 - \frac{k_\beta}{I_\beta \Omega^2}} \approx 1, \quad k_1 = \frac{1}{2}, \quad k_2 = \frac{1}{3}, \quad k_3 = \frac{1}{4}, \quad k_4 = \frac{1}{5} \quad (4.100)$$

By neglecting  $e$ , the flapping equations coefficient matrices become:

$$\mathbf{C}_{M_0} = \frac{\gamma}{8} \begin{bmatrix} 1 & 0 & 0 & \frac{2}{3}\mu \\ 0 & 1 & 0 & 0 \\ 0 & 0 & 1 & \frac{16}{\gamma} \\ \frac{4}{3}\mu & 0 & -\frac{16}{\gamma} & 1 \end{bmatrix} \quad (4.101a)$$

$$\mathbf{D}_{M_0} = \frac{\gamma}{8} \begin{bmatrix} \frac{8\lambda_\beta^2}{\gamma} & 0 & 0 & 0 \\ 0 & \frac{8\lambda_\beta^2}{\gamma} & 0 & 0 \\ \frac{4}{3}\mu & 0 & \frac{8(\lambda_\beta^2 - 1)}{\gamma} & \left(1 + \frac{\mu^2}{2} + \frac{8\Omega'}{\gamma}\right) \\ 0 & 0 & -\left(1 + \frac{\mu^2}{2} + \frac{8\Omega'}{\gamma}\right) & \frac{8(\lambda_\beta^2 - 1)}{\gamma} \end{bmatrix} \quad (4.101b)$$

$$\mathbf{H}_{M_0} = \frac{\gamma}{8} \begin{bmatrix} (1 + \mu^2)\theta_0 + \left(\frac{4}{5} + \frac{2}{3}\mu^2\right)\theta_{tw} + \frac{4}{3}\mu\theta_{ls} + \frac{4}{3}(\mu_z - \lambda_0) + \frac{2}{3}\mu(\bar{p}_H - \lambda_{ls}) & 0 \\ \left(1 + \frac{\mu^2}{2}\right)\theta_{lc} + (\bar{q}_H - \lambda_{lc}) + \frac{8}{\gamma}(2\bar{p}_H + \bar{q}'_H) & \\ \frac{8}{3}\mu\theta_0 + 2\mu\theta_{tw} + \left(1 + \frac{3}{2}\mu^2\right)\theta_{ls} + 2\mu(\mu_z - 0) + (\bar{p}_H - \lambda_{ls}) - \frac{8}{\gamma}(2\bar{q}_H - \bar{p}'_H) & \end{bmatrix} \quad (4.101c)$$

Note that the matrices  $\mathbf{C}_{M_0}$  and  $\mathbf{D}_{M_0}$  are function of the advance ratio and thus of the airspeed of the aircraft such that  $\mathbf{C}_{M_0} = \mathbf{C}_{M_0}(\mu)$  and  $\mathbf{D}_{M_0} = \mathbf{D}_{M_0}(\mu)$ . On the other hand, the forcing terms in the vector  $\mathbf{H}_{M_0}$  are a function of the swashplate inputs, inflow, and the motion of the aircraft such that  $\mathbf{H}_{M_0} = \mathbf{H}_{M_0}(\theta_0, \theta_{1s}, \theta_{1c}, \mu, \mu_z, \lambda_0, \lambda_{1s}, \lambda_{1c}, \bar{p}_H, \bar{q}_H, \bar{p}'_H, \bar{q}'_H)$ .

#### 4.4.9 Flapping Dynamics at Hover

Let us investigate the flapping dynamics at hover. By setting  $\mu = 0$  and neglecting the differential coning dynamics, then the simplified flapping equations become:

$$\beta''_0 = -\frac{\gamma}{8}\beta'_0 - \lambda_\beta^2\beta_0 + \frac{\gamma}{8}\left[\theta_0 + \frac{4}{5}\theta_{tw} + \frac{4}{3}(\mu_z - \lambda_0)\right] \quad (4.102a)$$

$$\beta''_{1c} = -\frac{\gamma}{8}\beta'_{1c} - (\lambda_\beta^2 - 1)\beta_{1c} - 2\beta'_{1s} - \frac{\gamma}{8}\beta_{1s} + \frac{\gamma}{8}(\theta_{1c} + \bar{q}_H - \lambda_{1c}) + (2\bar{p}_H + \bar{q}'_H) \quad (4.102b)$$

$$\beta''_{1s} = -\frac{\gamma}{8}\beta'_{1s} - (\lambda_\beta^2 - 1)\beta_{1s} + 2\beta'_{1c} + \frac{\gamma}{8}\beta_{1c} + \frac{\gamma}{8}(\theta_{1s} + \bar{p}_H - \lambda_{1s}) + (2\bar{q}_H - \bar{p}'_H) \quad (4.102c)$$

Note that the first equation (*i.e.*, the coning angle dynamics) is decoupled from the other two (*i.e.*, longitudinal and lateral flapping dynamics), which are coupled. These equations can be used for finding an approximation to the flapping dynamic modes as well as to investigate the quasi-steady flapping response to control inputs and angular rates and inflow. Consider the flapping dynamics characteristic equation, found by setting the forcing terms in Eq. (4.103) to zero:

$$\beta''_0 + \frac{\gamma}{8}\beta'_0 + \lambda_\beta^2\beta_0 = 0 \quad (4.103a)$$

$$\beta''_{1c} + \frac{\gamma}{8}\beta'_{1c} + (\lambda_\beta^2 - 1)\beta_{1c} + 2\beta'_{1s} + \frac{\gamma}{8}\beta_{1s} = 0 \quad (4.103b)$$

$$\beta''_{1s} + \frac{\gamma}{8}\beta'_{1s} + (\lambda_\beta^2 - 1)\beta_{1s} - 2\beta'_{1c} - \frac{\gamma}{8}\beta_{1c} = 0 \quad (4.103c)$$

Then, the roots of the first equation, which correspond to the eigenvalues associated to the coning mode, is:

$$\lambda_{1,2} = -\frac{\gamma}{16} \pm i\sqrt{\lambda_\beta^2 - \left(\frac{\gamma}{16}\right)^2} \quad (4.104)$$

The roots for the second and third equation can be found by solving the following equation:

$$\left(\lambda^2 + \frac{\gamma}{8}\lambda + \lambda_\beta^2 - 1\right)^2 + \left(2\lambda + \frac{\gamma}{8}\right)^2 = 0 \quad (4.105)$$

which does not have a closed-form solution, but its real part is  $\text{Re}\{\lambda_{3,4,5,6}\} = -\gamma/16$ . The modes associated with the longitudinal and lateral flapping motion are known as *regressive* and *progressive* flap modes. The regressive flap mode is associated with lower natural frequencies with respect to those of the progressive flap mode. Note that all of these roots are normalized by the rotor angular speed  $\Omega$ . To recover the actual value of the eigenvalues, one must multiply by  $\Omega$ . The flapping dynamics eigenvalues are shown in Fig. 4.14.

#### 4.4.10 Quasi-Static Flapping

If the rotor tip patch plane reaches a quasi-steady-state, then MBC are approximately constant such that  $\beta''_M \approx \beta'_M \approx \mathbf{0}$ . Then, the flapping dynamics equations of Eq. (4.90) simplify to algebraic equations:

$$(\boldsymbol{\beta}_M)_{qs} = \mathbf{D}_{M_0}^{-1}\mathbf{H}_{M_0} \quad (4.106)$$

This a minimum-fidelity approximation to rotorcraft flapping for use in flight dynamics. The quasi-static coning angle is:

$$(\beta_0)_{qs} = \frac{\gamma}{8\lambda_\beta^2} \left[ \theta_0 + \frac{4}{5}\theta_{tw} + \frac{4}{3}(\mu_z - \lambda_0) \right] \quad (4.107)$$

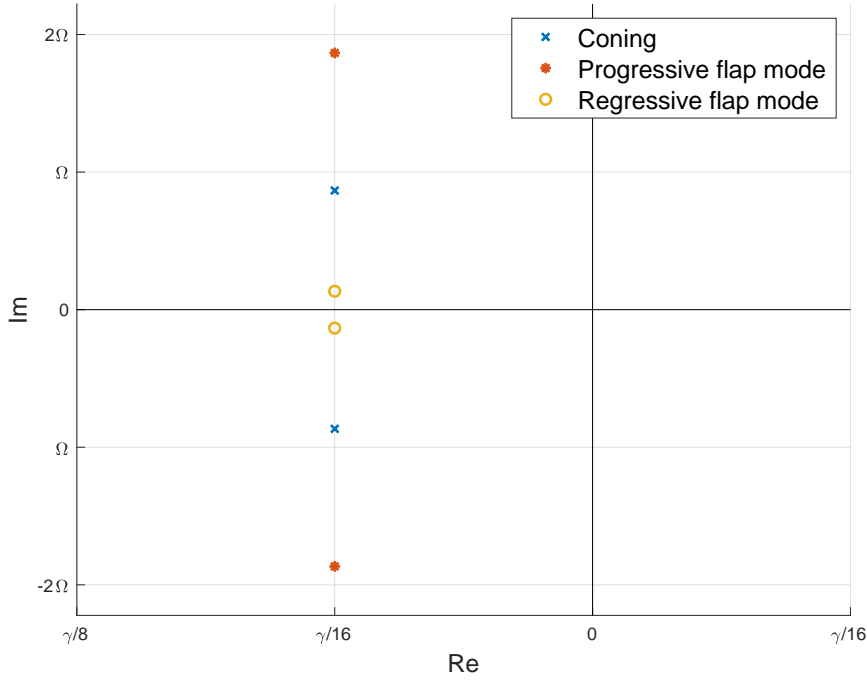


Figure 4.14: Flapping dynamics eigenvalues for a rotor with flap frequency ratio of  $\lambda_\beta = 1.037$  and Lock number of  $\gamma = 8$ .

Let us introduce the rotor stiffness number:

$$S_\beta = \frac{8(\lambda_\beta^2 - 1)}{\gamma} \quad (4.108)$$

This is an important parameter to determine the on- and off-axis flapping response of the rotor to control inputs and angular rates. Note that the  $S_\beta = 0$  for  $\lambda_\beta = 1$  (*i.e.*, for a centrally-hinged rotor with no root spring) whereas  $S_\beta \neq 0$  for  $\lambda_\beta > 1$  (*i.e.*, for a rotor with a flapping hinge offset and/or a root spring). Consider the quasi-static longitudinal flapping response to swashplate inputs and angular rates and neglect the response to the aircraft speed, rotor inflow ratio harmonics, and angular accelerations:

$$(\beta_{1c})_{qs} = \underbrace{-\left(\frac{1}{1+S_\beta^2}\right)\theta_{1s} + \left(\frac{S_\beta + \frac{16}{\gamma}}{1+S_\beta^2}\right)\bar{q}_H}_{\text{On-axis response}} + \underbrace{\left(\frac{S_\beta}{1+S_\beta^2}\right)\theta_{1c} + \left(\frac{S_\beta \frac{16}{\gamma} - 1}{1+S_\beta^2}\right)\bar{p}_H}_{\text{Off-axis response (or cross-coupling)}} \quad (4.109)$$

Similarly, the quasi-static lateral flapping response to swashplate inputs and angular rates is given by:

$$(\beta_{1s})_{qs} = \underbrace{\left(\frac{1}{1+S_\beta^2}\right)\theta_{1c} + \left(\frac{S_\beta + \frac{16}{\gamma}}{1+S_\beta^2}\right)\bar{p}_H}_{\text{On-axis response}} + \underbrace{\left(\frac{S_\beta}{1+S_\beta^2}\right)\theta_{1s} - \left(\frac{S_\beta \frac{16}{\gamma} - 1}{1+S_\beta^2}\right)\bar{q}_H}_{\text{Off-axis response (or cross-coupling)}} \quad (4.110)$$

For  $S_\beta = 0$ , the quasi-static longitudinal and lateral flapping responses simplify to:

$$(\beta_{1c})_{qs} = -\theta_{1s} + \frac{16}{\gamma}\bar{q}_H - \bar{p}_H \quad (4.111a)$$

$$(\beta_{1s})_{qs} = \theta_{1c} + \frac{16}{\gamma}\bar{p}_H + \bar{q}_H \quad (4.111b)$$

Note that the rotor provides an on-axis damping effect in that rotor flapping produces thrust tilt that opposes the angular motion. As for cross-coupling effects, a rolling moment will produce a longitudinal flapping response which, in turns, will produce a pitching moment from the aerodynamic forces on the blades. Similarly, a pitching moment will produce a lateral flapping response which, in turns, will produce a rolling moment. Recall that blade pitch is controlled by the swashplate and is governed by:

$$\theta_P(\psi) = \theta_0 + \theta_{1c} \cos \psi + \theta_{1s} \sin \psi \quad (4.112)$$

Also, recall that the flapping angle for a representative rotor blade of a four-bladed rotor in steady state is given by:

$$(\beta)_{qs} = (\beta_0)_{qs} + (\beta_{1c})_{qs} \cos \psi + (\beta_{1s})_{qs} \sin \psi \quad (4.113)$$

It is apparent that the flapping response for  $S_\beta = 0$  is 90 deg out of phase with the cyclic pitch control input. Because a 90 deg phase between input and output is representative of a system in resonance, a rotor with zero stiffness number is indeed a resonant system. This means that the control excitation frequency (*i.e.*, the rotor angular speed  $\Omega$ ) is equal to the flapping natural frequency. For instance, if the pilot/control system applies maximum pitch blade pitch at  $\psi = 90$  deg, then the rotor will respond with maximum flap at  $\psi = 90$  deg. For a rotor system with  $S_\beta > 0$ , the on-axis response terms are:

$$\frac{\partial(\beta_{1c})_{qs}}{\partial \theta_{1s}} = -\underbrace{\frac{1}{1+S_\beta^2}}_{<1} \quad \frac{\partial(\beta_{1s})_{qs}}{\partial \theta_{1c}} = \underbrace{\frac{1}{1+S_\beta^2}}_{<1} \quad (4.114)$$

(4.115)

where their magnitude will be slightly less than 1. The off-axis response terms are:

$$\frac{\partial(\beta_{1s})_{qs}}{\partial \theta_{1s}} = \underbrace{\frac{S_\beta}{1+S_\beta^2}}_{\ll 1} \quad \frac{\partial(\beta_{1c})_{qs}}{\partial \theta_{1c}} = \underbrace{\frac{S_\beta}{1+S_\beta^2}}_{\ll 1} \quad (4.116)$$

(4.117)

where their magnitude will be significantly smaller than 1. Thus, the cross-coupling response will be small compared to the on-axis response for  $0 < S_\beta \ll 1$ . The phase lag angle can be found as:

$$\phi_{lag} = \frac{\pi}{2} - \Delta_{sp} \quad (4.118)$$

where:

$$\Delta_{sp} = \tan^{-1} S_\beta \quad (4.119)$$

For instance, for a rotor with  $\gamma = 3.53$  and  $\lambda_\beta = 1.037$  (representative of a Sikorsky UH-60 rotor), the phasing angle  $\Delta_{sp}$  will be approximately equal to 9.7 deg. The phasing angle can be used to reduce/eliminate cross-coupling in hover via the swashplate:

$$\theta_P(\psi) = \theta_0 + \theta_{1c} \cos(\psi - \Delta_{sp}) + \theta_{1s} \sin(\psi - \Delta_{sp}) \quad (4.120)$$

However, coupling effects will change in forward flight, so it is not possible to eliminate cross-coupling across the flight envelope with swashplate phasing. It can also be shown that a rotor translation relative to the air induces rotor flapping. Consider the case of an increase in advance ratio  $\mu$ , which results in increased blade velocity on the advancing side of the rotor (*i.e.*,  $0 < \psi \leq 180$  deg). Then, the increased velocity on the advancing blade causes lift to increase, which will translate to a maximum flapping angle approximately 90 deg after (depending on  $S_\beta$ ), that is, at the front of the rotor. As such, the rotor will respond by flapping aft similar to an increase in longitudinal cyclic  $\theta_{1s}$ . This is known as rotor *blow back* effect.

#### 4.4.11 Simplified Forces and Moments

Need to add.

## 4.5 Blade Discretization

### 4.5.1 Spanwise

To be able to implement the rotor model shown in this chapter, discretization of the blade into spanwise elements is necessary. Two kinds of discretizations are typically used: (i) uniform and (ii) equal annuli area.

#### Uniform

Uniform distribution divides the rotor blade into  $n_{\text{seg}}$  number of segments in the interval  $[(e + e')R, R] \mathbf{i}_b$  where  $e'$  is the spar length (*i.e.*, the distance between the flap/lag hinge and the blade root). The length of each segment is the same and is given by:

$$\Delta r = \frac{(1 - e - e')}{n_{\text{seg}}} \quad (4.121)$$

The midpoint of the  $i^{\text{th}}$  blade element, *i.e.*, the aerodynamic calculation point, in non-dimensional form is:

$$r_i = e + e' + \left( \frac{\Delta r_{\text{seg}}}{2} \right) i, \quad i = 1, \dots, n_{\text{seg}} \quad (4.122)$$

#### Equal Annuli Area

Equal annuli area discretization is a technique used in the design and analysis of helicopter rotor blades to divide the blade's span into sections of equal annular areas. The annular area refers to the area between two consecutive blade stations, which are essentially cross-sectional slices of the rotor blade taken along the span. The purpose of using equal annuli area discretization is to ensure that each section of the rotor blade spans an equal area, regardless of its radial position. This approach helps to distribute the aerodynamic loads more evenly along the length of the blade and facilitates blade load calculations. As shown in [How80], the normalized segment midpoint for the first segment is:

$$r_1 = \sqrt{\frac{1 - (e + e')^2}{2n_{\text{seg}}} + (e + e')^2 - e} \quad (4.123)$$

Subsequent midpoints are given by:

$$r_i = \sqrt{\frac{1 - (e + e')^2}{n_{\text{seg}}} + (e + r_{i-1})^2 - e}, \quad i = 2, \dots, n_{\text{seg}} \quad (4.124)$$

The width of each segment is:

$$\Delta r_i = r_{\text{outb}_i} - r_{\text{inbb}_i} \quad (4.125)$$

where:

$$r_{\text{outb}_i} = \sqrt{(r_i + e)^2 + \frac{1 - (e + e')^2}{2n_{\text{seg}}}} \quad (4.126a)$$

$$r_{\text{inbb}_i} = \sqrt{(r_i + e)^2 - \frac{1 - (e + e')^2}{2n_{\text{seg}}}} \quad (4.126b)$$

### 4.5.2 Chordwise

While for flight dynamics predictions it is sufficient to calculate the blade loads based on a discretization of the blade in the sole spanwise direction, aeroacoustic calculations require increased resolution of the blade loads distribution over the blade surface. In addition, a detailed blade geometry is required to calculate the unit vectors perpendicular to the blade surface, as well as the velocity vector of each blade surface panel, which are all needed for aeroacoustics. As such, the upper and lower blade surfaces can be modeled with a discrete number of panels both in the spanwise and chordwise directions. Note that this approach is used solely for aeroacoustic calculations and does not directly affect any calculation used for the flight dynamics.

Consider a NACA 0012 airfoil section. The thickness distribution is described by the following equation [AV59]:

$$z_t(x_c) = \frac{\bar{t}}{0.2} (0.2969\sqrt{x_c} - 0.3516x_c^2 + 0.2843x_c^3 - 0.1015x_c^4) \quad (4.127)$$

where  $\bar{t}$  is the maximum thickness of the blade section expressed as a fraction of the chord, and  $x_c$  is the non-dimensional chordwise coordinate. Note that  $x_c = 0$  corresponds to the leading edge and  $x_c = 1$  corresponds to the trailing edge. For a NACA 0012 airfoil, the maximum thickness of the blade section is assumed to be 12% of the blade chord. Since the airfoil in consideration is symmetric, Eq. (4.127) can be used for describing the sectional geometry of both the upper and lower blade surfaces. The chordwise panels are distributed unevenly across the blade chord. In fact, the chordwise panels distribution is proportional to the square of the non-dimensional chordwise coordinate, such that the chordwise panels are concentrated toward the leading edge of the section. Consider a twist angle  $\theta(y, t)$  function of the spanwise location  $y$  and of time  $t$ , given by the summation of inherent blade twist distribution and blade pitch input. Then, the longitudinal and vertical position of an arbitrary blade surface element in blade frame axes is given by the following equation:

$$\begin{bmatrix} x \\ z \end{bmatrix} = \begin{bmatrix} \cos \theta & \sin \theta \\ -\sin \theta & \cos \theta \end{bmatrix} \left( \begin{bmatrix} x_c \\ \pm t z_t(x_c) \end{bmatrix} - \begin{bmatrix} 1/4 \\ 0 \end{bmatrix} \right) c \quad (4.128)$$

where  $t$  is the maximum thickness of the blade section and  $c$  is the blade chord. The blade frame axes are defined such that their origin lies at the intersection of the quarter-chord line, the mean line, and the blade root. The  $x$  axis is along the chordwise direction, pointing from the leading to the trailing edge; the  $y$  axis along in the spanwise direction, pointing from the blade root to the blade tip; and the  $z$  axis is perpendicular to  $x$  and  $y$ , pointing from the lower to the upper surface (for zero twist). It is worth noting that the following relation exists between the blade frame convention used in this analysis and that used in the rest of the notes:

$$\begin{bmatrix} x_b \\ y_b \\ z_b \end{bmatrix} = \begin{bmatrix} y + e' \\ -x \\ -z \end{bmatrix} \quad (4.129)$$

where  $e'$  is the spar length (*i.e.*, the distance between the flap/lag hinge and the blade root). The convention is such that the origin lies at the intersection of the quarter-chord line, the mean line, and the flap/lag hinge. Figure 4.15 shows the discretized geometry of different rotor blades with 10 spanwise panels and 10 chordwise panels. Fig. 4.15a shows a blade similar to that of a UH-60 helicopter, whereas 4.15b shows an XV-15 tiltrotor blade. Based on this geometry, the unit vectors normal to each blade element can be calculate and stored for the undeformed blade geometry, and rotated according to the transformation matrix in Eq. (4.128) at each time step based on the current blade pitch at each spanwise location. For aeroacoustic calculations, the blade surface locations, velocities, and unit vectors normal to the surface can then be transformed from the blade to the inertial frame via the transformations defined above.

### 4.5.3 Blade Surface Pressure

The surface pressure distribution for each blade spanwise segment is calculated based on the local lift coefficient, and on NACA 0012 lookup tables based on thin airfoil theory. These lookup tables provide the velocity ratio  $v/V$  and velocity increment ratio  $\Delta v_\alpha/V$  as functions of the normalized chordwise coordinate.

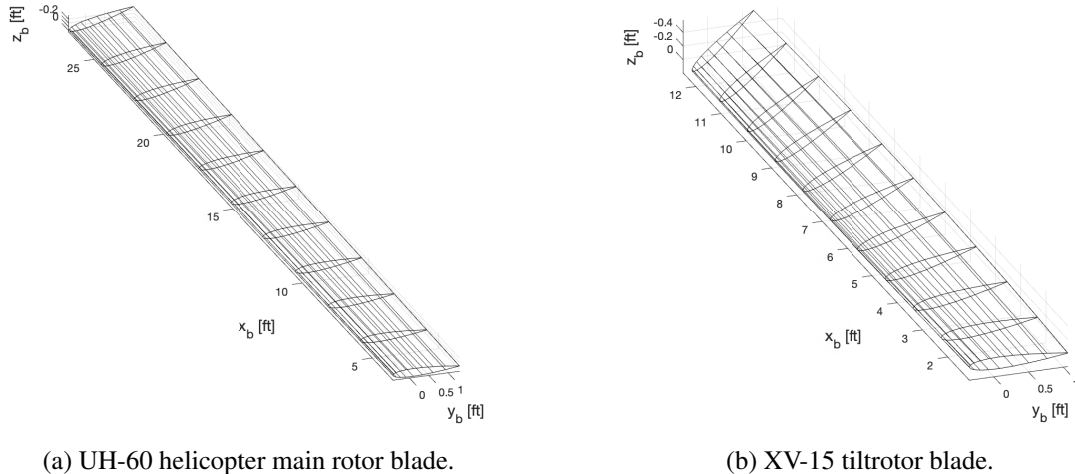


Figure 4.15: Blade geometry for different rotor blades.

The lookup tables for a symmetric NACA 0012 airfoil are shown quantitatively in Table 4.2 and are taken from Ref. Abbott. The pressure coefficient chordwise distribution on each spanwise segment is given by the following equation:

$$C_P = \begin{cases} 1 - \left( \frac{v}{V} + \frac{\Delta v_\alpha}{V} C_L \right)^2 & \text{upper surface} \\ 1 - \left( \frac{v}{V} - \frac{\Delta v_\alpha}{V} C_L \right)^2 & \text{lower surface} \end{cases} \quad (4.130)$$

where  $C_L$  is the lift coefficient of the spanwise segment. The blade gauge pressure chordwise distribution at each spanwise segment is then found by:

$$\tilde{p} = \frac{1}{2} \rho (u_T^2 + u_P^2) C_P \quad (4.131)$$

where  $u_T$  and  $u_P$  are respectively the tangential and perpendicular velocities of the oncoming flow to the blade spanwise segment in consideration. Figure 4.16 shows the blade surface pressure distribution for different rotorcraft and flight conditions. Figure 4.16a shows the blade surface pressure distribution for a utility helicopter similar to a UH-60 trimmed at 80 kts forward flight, whereas Fig. 4.16b corresponds to a XV-15 tiltrotor in forward flight at 120 kts during conversion from helicopter to airplane mode (45 deg nacelle angle).

## 4.6 Computational Setup

This section will focus on the implementation aspects of rotor modules based on the theory presented in the chapter for varying fidelity levels.

### 4.6.1 Rotor Module

The rotor module presented herein adopts a 3-state Pitt-Peters inflow model, a blade-element model, and rigid flap dynamics. Suppose the rotor module is a function that has access to state vector of the rotorcraft, where the state vector is given by:

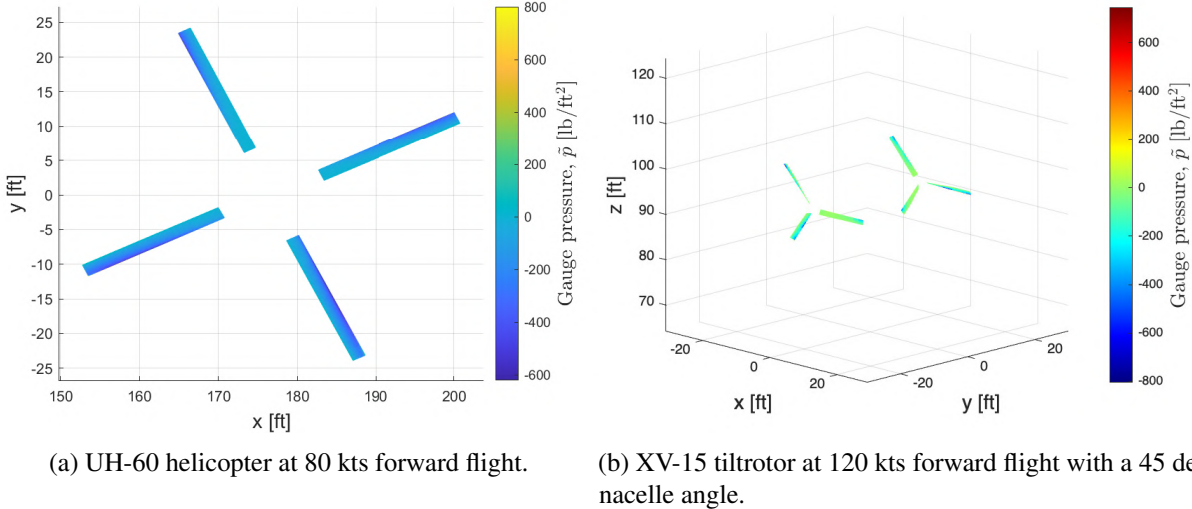
$$\mathbf{x}^T = [\mathbf{x}_F^T \ \mathbf{x}_{R_1}^T \ \dots \ \mathbf{x}_{R_N}^T] \quad (4.132)$$

where  $\mathbf{x}_F$  are the fuselage states and  $\mathbf{x}_{R_i}$  are the states of the  $i^{\text{th}}$  rotor. The fuselage states are given by:

$$\mathbf{x}_F^T = [u \ v \ w \ p \ q \ r \ \phi \ \theta \ \psi \ x \ y \ z] \quad (4.133)$$

Table 4.2: NACA 0012 velocity and velocity increment ratios vs. normalized chordwise location.

| Normalized Chordwise Location, $x_c$ | $v/V$ | $\Delta v_\alpha/V$ |
|--------------------------------------|-------|---------------------|
| 0                                    | 0     | 1.988               |
| 0.5                                  | 0.800 | 1.475               |
| 1.25                                 | 1.005 | 1.199               |
| 2.5                                  | 1.114 | 0.934               |
| 5.0                                  | 1.174 | 0.685               |
| 7.5                                  | 1.184 | 0.558               |
| 10                                   | 1.188 | 0.479               |
| 15                                   | 1.188 | 0.381               |
| 20                                   | 1.183 | 0.319               |
| 25                                   | 1.174 | 0.273               |
| 30                                   | 1.162 | 0.239               |
| 40                                   | 1.135 | 0.187               |
| 50                                   | 1.108 | 0.149               |
| 60                                   | 1.080 | 0.118               |
| 70                                   | 1.053 | 0.092               |
| 80                                   | 1.022 | 0.068               |
| 90                                   | 0.978 | 0.044               |
| 95                                   | 0.952 | 0.029               |
| 100                                  | 0.900 | 0                   |



(a) UH-60 helicopter at 80 kts forward flight.

(b) XV-15 tiltrotor at 120 kts forward flight with a 45 deg nacelle angle.

Figure 4.16: Blade surface pressure distribution.

whereas the states of the  $i^{\text{th}_i}$  rotor are given by:

$$\mathbf{x}_{\mathbf{R}_i}^T = \left[ \boldsymbol{\beta}_M^T \dot{\boldsymbol{\beta}}_M^T \lambda_0 \lambda_{1s} \lambda_{1c} \psi \right] \quad (4.134)$$

Assume also that the rotor module has access to the control inputs to the  $i^{\text{th}_i}$  rotor:

$$\mathbf{u}_{\mathbf{R}_i}^T = [\theta_0 \theta_{1c} \theta_{1s}] \quad (4.135)$$

Then, the rotor state dynamics, as well as the rotor forces and moments, can be computed as follows at each time step of the simulation:

1. Pre-compute the transformation matrix from the body to the rotor hub frame  $\mathbf{T}_{B \rightarrow H}$  and its inverse  $\mathbf{T}_{B \rightarrow H}^T$  using Eqs. (4.3) and (4.4).
2. Compute the azimuth angle of each blade by using Eq. (4.72).
3. Assemble the transformation matrices from IBC to MBC (*i.e.*,  $\mathbf{L}_\beta$  and  $\mathbf{L}_\beta^{-1}$ ) and vice versa, and their derivatives.
4. Convert the flapping states  $\boldsymbol{\beta}_M$  and  $\dot{\boldsymbol{\beta}}_M$  from MBC to IBC using Eqs. 4.79a and 4.79b.
5. Find the blade pitch at the root using Eq. (4.25). Subsequently, find the blade segment pitch using Eq. (4.24). This last step assumes a spanwise discretization of the blade in  $N$  segments, such that the center point of each segment is given by:

$$r_i = eR + (i-1)\Delta r + \frac{\Delta r}{2}, \quad i = 1, \dots, N \quad (4.136)$$

where:

$$\Delta r = \frac{R(1-e)}{N} \quad (4.137)$$

6. Compute the translational and angular velocity components of the rotor hub, expressed in the rotor hub frame, using Eqs. (4.16) and (4.17). Note that if the rotor is a clockwise-rotating rotor, then the sign of the hub lateral speed and roll rate must be switched such that  $(v_H)_{CW} = -v_H$  and  $(p_H)_{CW} = -p_H$ .
7. Compute the wind azimuth angle using Eq. (3.80). Subsequently, compute the transformation matrix from the hub to the wind frame using Eq. (3.81).
8. Compute the velocity at each blade element of each blade using Eq. (4.22). Note that, for a clockwise-rotating rotor, one shall use  $\Omega + r_H$  in place of  $\Omega - r_H$ .
9. Compute the induced inflow at the blade elements of each blade using Eq. (3.79).
10. Compute the velocity of the blade elements of each blade with respect to the air mass using Eq. (4.23).
11. Compute the sectional angle of attack of each blade element using Eq. (4.28). Subsequently, calculate the coefficient of lift and drag for each blade element either using lookup tables as in Eq. (4.30), or by assuming a linear lift variation with the angle of attack and a constant drag coefficient as in Eq. (4.31).
12. Compute the sectional lift and drag at each blade element using Eq. (4.33).
13. Compute the blade segment forces using Eq. (4.35).
14. Compute the total blade aerodynamic loads expressed in the RTP frame using Eq. (4.36) and subsequently transform to the lead-lag frame using Eq. (4.37).
15. Find the total aerodynamic moments about the flapping hinge, expressed in flap frame using Eq. (4.38) and subsequently transform to hub-frame components using Eq. (4.39).
16. Compute the aerodynamic forces and moments coefficients for use in the inflow dynamics equations using Eq. (4.40).
17. Compute the flapping acceleration in IBC using Eq. (4.43).
18. Compute the inertial shear forces and moments at the flapping hinge using Eqs. (4.59) and (4.62).
19. Compute the total forces and moments at each flapping hinge, expressed in the lead-lag frame, using Eqs. (4.65) and (4.66).
20. Compute the total forces and moments at each flapping hinge, expressed in the hub frame, using Eqs. (4.67) and (4.68). Subsequently, transform the rotor hub forces and moments to body-frame coordinates using Eqs. (4.69) and (4.70), respectively.
21. Transform the flapping angles, velocity, and accelerations from IBC (*i.e.*,  $\boldsymbol{\beta}_I$ ,  $\dot{\boldsymbol{\beta}}_I$ , and  $\ddot{\boldsymbol{\beta}}_I$ ) to MBC (*i.e.*,  $\boldsymbol{\beta}_M$ ,  $\dot{\boldsymbol{\beta}}_M$ , and  $\ddot{\boldsymbol{\beta}}_M$ ) using Eq. (4.84).
22. Compute the induced inflow dynamics using Eq. (3.82).
23. Assemble the state dynamics vector:

$$\dot{\mathbf{x}}_{R_i}^T = [\dot{\boldsymbol{\beta}}_M^T \ddot{\boldsymbol{\beta}}_M^T \dot{\lambda}_0 \dot{\lambda}_{ls} \dot{\lambda}_{lc} \Omega] \quad (4.138)$$

24. Assemble the output vector:

$$\mathbf{y}_{R_i}^T = [X_R \ Y_R \ Z_R \ L_R \ M_R \ N_R] \quad (4.139)$$

#### **4.6.2 Simplified Rotor Module**

The rotor module presented herein adopts a 3-state Pitt-Peters inflow model, and rigid flap dynamics. **To be finished.**

#### **4.6.3 Quasi-Static Rotor Module**

The rotor module presented herein is a minimum-fidelity rotor that adopts quasi-static rotor flapping and uniform inflow. **To be finished.**

### **Bibliography**

- [AV59] I. H. Abbott and A. E. Von Doenhoff. "Theory of Wing Sections: Including a Summary of Airfoil Data". In: New York, NY: Dover Publications, 1959 (cited on pages 92, 112).
- [How80] J. J. Howlett. *UH-60A Black Hawk Engineering Simulation Program. Volume 1: Mathematical Model*. Technical report. NASA-CR-166309, 1980. (Cited on page 111).



## 5. Fuselage and Empennage Modeling

Fuselage and empennage play a key role in the performance and stability properties of the rotorcraft. Fuselage drag dominates power requirements in high speed flight and to some extent in climbs while its major contribution to flight dynamics is a generally destabilizing yawing and pitching moment. Conventional empennage (*i.e.*, horizontal and vertical stabilizers) is employed to provide a stabilizing moments about the pitch and yawing axes and counteract the destabilizing moment contributions from the fuselage and rotor. Other empennage such as wings of various nature are used as redundant control effectors and/or to offload the main rotor in high-speed flight. This section will analyze fuselage and empennage modeling with varying fidelity levels, although the methods presented are still arguably simple to provide real-time capability and thus be suitable for flight dynamics.

It is worth noting that the velocity induced by one or multiple rotors on the fuselage/empennage may have a significant impact on the rotorcraft performance, trim, and stability. In this regard, not only Heyson's formulation introduced earlier can be used to calculate the velocity induced by a rotor on another rotor, but it can also be used for computing the velocity induced by a rotor on the rotorcraft empennage and/or fuselage. One significant example is the computation of the velocity induced by the main rotor on the horizontal stabilizer. This can affect trim performance and attitudes across the flight envelope. Consider two helicopter configurations: (i) with the horizontal stabilizer located under, or partially under, the footprint of the main rotor (typical of Bell helicopters, with examples including the Bell UH-1 and the Bell 505), and (ii) with the horizontal stabilizer located outside of the footprint of the main rotor (this solution is more commonly adopted). At hover, depending on the horizontal tail configuration, the tail may or may not be in the wake of the main rotor. For instance, for the configuration with the horizontal tail closer to the main rotor, the tail may be in the wake of the main rotor (Fig. 5.1c). This will not happen for the configuration with the tail further back (Fig. 5.1a). If the tail is indeed in the wake of the main rotor, the rotor downwash will cause comparatively higher pitch attitudes and poorer hover performance for the configuration with the tail located (partially) under the main rotor. If one considers high-speed forward flight, the opposite scenario may happen. For the configuration with the horizontal tail closer to the main rotor, in high-speed forward flight the skewed wake will pass higher than the tail such that the tail does not operate in the downwash of the main rotor (Fig. 5.1d). To the contrary, for the configuration with the horizontal tail located further back from the main rotor, the tail will operate in the downwash of the main rotor (Fig. 5.1b). This will likely result in higher trim pitch attitudes in forward flight for the configuration with the tail further from the main rotor. A direct consequence of this may be higher fuselage drag due to the higher pitch attitudes and thus higher power required in forward flight. As such, it is desirable to model the velocity induced by the main rotor on the empennage (possibly, using Heyson's) to avoid erroneous trim performance predictions. Because the wake skew angle may change abruptly during maneuvering flight, such that the horizontal stabilizer may transition from in to out (and vice versa) of rotor wake during the maneuver, it is also important to model

rotor-on-empennage interactions to accurately predict unsteady behaviours. Another significant example is the downwash of side-by-side rotors in the wings of a tiltrotor aircraft.



Figure 5.1: Rotor-on-empennage interactions.

## 5.1 Fuselage

### 5.1.1 Body to Wind Frame Transformation

Aerodynamic calculations for the fuselage are typically performed in the wind frame. The wind frame is obtained via the following two single-axis successive rotations:

1. Rotation about the  $-j_B$  axis by an angle  $\alpha_F$  (*i.e.*, the fuselage angle of attack), resulting in the temporary frame  $(\mathbf{\hat{T}})$  (Fig. 5.2a). The transformation from the body to the  $(\mathbf{\hat{T}})$  frame is:

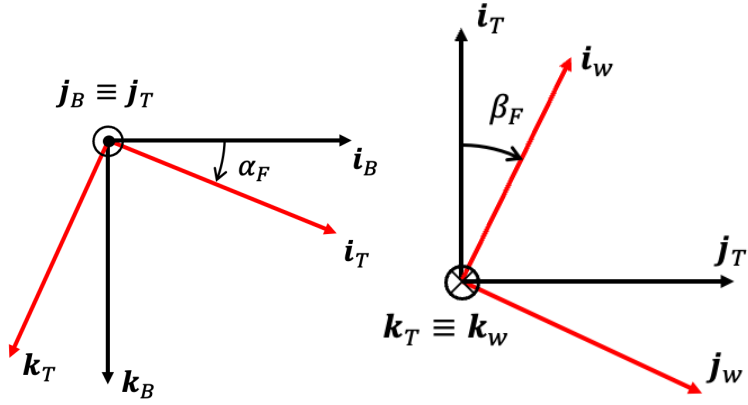
$$\begin{bmatrix} \mathbf{i}_T \\ \mathbf{j}_T \\ \mathbf{k}_T \end{bmatrix} = \underbrace{\begin{bmatrix} \cos \alpha_F & 0 & \sin \alpha_F \\ 0 & 1 & 0 \\ -\sin \alpha_F & 0 & \cos \alpha_F \end{bmatrix}}_{\mathbf{T}_{B \rightarrow T}} \begin{bmatrix} \mathbf{i}_B \\ \mathbf{j}_B \\ \mathbf{k}_B \end{bmatrix} \quad (5.1)$$

2. Rotation about the  $k_T$  axis by an angle  $\beta_F$  (*i.e.*, the fuselage sideslip angle), resulting in the wind frame  $(\mathbf{\hat{w}})$  (Fig. 5.2b). The transformation from the body to the  $(\mathbf{\hat{w}})$  frame is:

$$\begin{bmatrix} \mathbf{i}_w \\ \mathbf{j}_w \\ \mathbf{k}_w \end{bmatrix} = \underbrace{\begin{bmatrix} \cos \beta_F & \sin \beta_F & 0 \\ -\sin \beta_F & \cos \beta_F & 0 \\ 0 & 0 & 1 \end{bmatrix}}_{\mathbf{T}_{T \rightarrow w}} \begin{bmatrix} \mathbf{i}_T \\ \mathbf{j}_T \\ \mathbf{k}_T \end{bmatrix} \quad (5.2)$$

The transformation matrix from the body to the wind frame is:

$$\begin{aligned}
 \begin{bmatrix} \mathbf{i}_w \\ \mathbf{j}_w \\ \mathbf{k}_w \end{bmatrix} &= \mathbf{T}_{T \rightarrow w} \mathbf{T}_{B \rightarrow T} \begin{bmatrix} \mathbf{i}_B \\ \mathbf{j}_B \\ \mathbf{k}_B \end{bmatrix} \\
 &= \underbrace{\begin{bmatrix} \cos \beta_F & \sin \beta_F & 0 \\ -\sin \beta_F & \cos \beta_F & 0 \\ 0 & 0 & 1 \end{bmatrix}}_{\mathbf{T}_{B \rightarrow w}} \begin{bmatrix} \cos \alpha_F & 0 & \sin \alpha_F \\ 0 & 1 & 0 \\ -\sin \alpha_F & 0 & \cos \alpha_F \end{bmatrix} \begin{bmatrix} \mathbf{i}_B \\ \mathbf{j}_B \\ \mathbf{k}_B \end{bmatrix} \\
 &= \underbrace{\begin{bmatrix} \cos \alpha_F \cos \beta_F & \sin \beta_F & \sin \alpha_F \cos \beta_F \\ -\cos \alpha_F \sin \beta_F & \cos \beta_F & -\sin \alpha_F \sin \beta_F \\ -\sin \alpha_F & 0 & \cos \alpha_F \end{bmatrix}}_{\mathbf{T}_{B \rightarrow w}} \begin{bmatrix} \mathbf{i}_B \\ \mathbf{j}_B \\ \mathbf{k}_B \end{bmatrix}
 \end{aligned} \tag{5.3}$$



(a) Rotation about the  $-\mathbf{j}_B$  axis by an angle  $\alpha_F$ . (b) Rotation about the  $\mathbf{k}_T$  axis by an angle  $\beta_F$ .

Figure 5.2: Body to wind frame rotations.

The inverse transformation, *i.e.*, that from the wind to the body frame, is:

$$\begin{bmatrix} \mathbf{i}_B \\ \mathbf{j}_B \\ \mathbf{k}_B \end{bmatrix} = \mathbf{T}_{B \rightarrow w}^T \begin{bmatrix} \mathbf{i}_w \\ \mathbf{j}_w \\ \mathbf{k}_w \end{bmatrix} = \underbrace{\begin{bmatrix} \cos \alpha_F \cos \beta_F & -\cos \alpha_F \sin \beta_F & -\sin \alpha_F \\ \sin \beta_F & \cos \beta_F & 0 \\ \sin \alpha_F \cos \beta_F & -\sin \alpha_F \sin \beta_F & \cos \alpha_F \end{bmatrix}}_{\mathbf{T}_{w \rightarrow B}} \begin{bmatrix} \mathbf{i}_w \\ \mathbf{j}_w \\ \mathbf{k}_w \end{bmatrix} \tag{5.4}$$

### 5.1.2 Fuselage Forces and Moments

Assume the position vector from the center of mass to the center of pressure of the fuselage to be:

$$\mathbf{r}_{C \rightarrow C}^B = x_C \mathbf{i}_B + y_C \mathbf{j}_B + z_C \mathbf{k}_B \tag{5.5}$$

Then, the aerodynamic forces and moments generated by the fuselage will act about this point. Typically, for conventional helicopters, the center of pressure lies ahead of the center of mass as because of the distribution of the fuselage planform and side area. As a direct consequence, fuselage moments are generally destabilizing. Herein, it is assumed that the forces and moment coefficients are given about the center of pressure of the fuselage. It is also assumed that the fuselage frame axes are parallel to those of the body frame, but is centered

at point C. The velocity of the fuselage with respect to the inertial frame, expressed in the body frame, is:

$$\begin{aligned}
 \mathbf{v}_{C/I}^B &= \mathbf{v}_{C/I}^B + \boldsymbol{\omega}_{F/I}^B \times \mathbf{r}_{\bullet \rightarrow C}^B \\
 &= \begin{bmatrix} u \\ v \\ w \end{bmatrix} + \begin{bmatrix} p \\ q \\ r \end{bmatrix} \times \begin{bmatrix} x_C \\ y_C \\ z_C \end{bmatrix} \\
 &= \begin{bmatrix} u \\ v \\ w \end{bmatrix} + \begin{bmatrix} 0 & -r & q \\ r & 0 & -p \\ -q & p & 0 \end{bmatrix} \begin{bmatrix} x_C \\ y_C \\ z_C \end{bmatrix} \\
 &= \begin{bmatrix} u - ry_C + qz_C \\ v + rx_C - pz_C \\ w - qx_C + py_C \end{bmatrix} = \begin{bmatrix} u_F \\ v_F \\ w_F \end{bmatrix}
 \end{aligned} \tag{5.6}$$

Consider now the fuselage geometry in Fig. 5.3. The fuselage velocity with respect to the air mass, expressed in the body frame, is:

$$\begin{aligned}
 \mathbf{v}_{C/a}^B &= \mathbf{v}_{C/I}^B - \mathbf{v}_{a/I}^B \\
 &= \mathbf{v}_{C/I}^B - \sum_{j=1}^{N_{\text{rot}}} \left( \mathbf{T}_{H_j \rightarrow B} \mathbf{v}_{a/I}^{H_j} \right) \\
 &= \begin{bmatrix} u_F \\ v_F \\ w_F \end{bmatrix} - \sum_{j=1}^{N_{\text{rot}}} \left( \mathbf{T}_{H_j \rightarrow B} \begin{bmatrix} 0 \\ 0 \\ w_{\lambda_j} \end{bmatrix} \right) = \begin{bmatrix} u_R \\ u_T \\ u_P \end{bmatrix}
 \end{aligned} \tag{5.7}$$

where  $w_{\lambda_j} = \Omega_j R_j \lambda_i$  is the induced velocity at the fuselage center of pressure induced by the  $j^{\text{th}}$  rotor expressed in that rotor's hub frame. This velocity can be calculated using Eq. (3.95), *i.e.*, the formula for the induced velocity near a lifting rotor. At a first approximation, the rotor downwash on the fuselage may not necessarily be included.

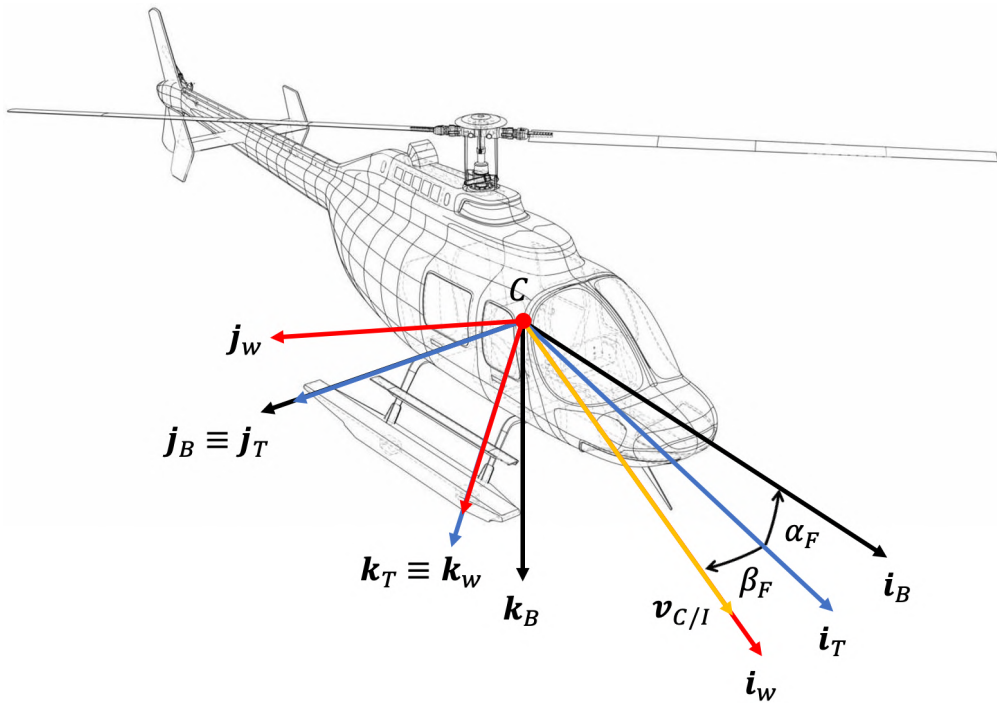


Figure 5.3: Fuselage angle of attack and sideslip angles.

The total fuselage speed is:

$$U_{\text{tot}} = \sqrt{u_R^2 + u_T^2 + u_P^2} \tag{5.8}$$

The velocity component in the plane of symmetry of the fuselage (*i.e.*, the  $\mathbf{i}_B - \mathbf{k}_B$  plane) is:

$$U = \sqrt{u_T^2 + u_P^2} = \sqrt{u_T^2 \left( 1 + \frac{u_P^2}{u_T^2} \right)} \approx u_T \quad (5.9)$$

The fuselage angle of attack is defined as:

$$\alpha_F = \tan^{-1} \left( \frac{u_p}{U} \right) \quad (5.10)$$

The fuselage sideslip angle is given by:

$$\beta_F = \sin^{-1} \left( \frac{u_R}{U_{\text{tot}}} \right) \quad (5.11)$$

The fuselage forces expressed in wind axes may now be written in generalized form as:

$$\begin{bmatrix} F_x \\ F_y \\ F_z \end{bmatrix} = \frac{1}{2} \rho U_{\text{tot}}^2 \begin{bmatrix} S_x C_x(\alpha_F, \beta_F) \\ S_y C_y(\alpha_F, \beta_F) \\ S_z C_z(\alpha_F, \beta_F) \end{bmatrix} \approx \frac{1}{2} \rho U_{\text{tot}}^2 \begin{bmatrix} D_1 \\ D_2 \\ D_3 \end{bmatrix} \quad (5.12)$$

where  $S_x$ ,  $S_y$ , and  $S_z$  are the front, side, and vertical areas of the fuselage. Additionally,  $C_x$ ,  $C_y$ , and  $C_z$  are the longitudinal, lateral, and vertical force coefficients. These coefficients are typically a function of the fuselage angle of attack and sideslip, and are obtained either through wind tunnel testing or computational fluid dynamics (CFD). To yield a simpler formulation, the areas and respective coefficients can be combined in a single term, *e.g.*,  $D_1 = S_x C_x(\alpha_F, \beta_F)$ , which gives the *equivalent wetted area* or *equivalent flat-plate area*. Similarly, the fuselage moments in generalized form about the center of pressure are given by:

$$\begin{bmatrix} M_x \\ M_y \\ M_z \end{bmatrix} = \frac{1}{2} \rho U_{\text{tot}}^2 \begin{bmatrix} S_x C_{l_x}(\alpha_F, \beta_F) \\ S_y C_{M_y}(\alpha_F, \beta_F) \\ S_z C_{N_y}(\alpha_F, \beta_F) \end{bmatrix} \approx \frac{1}{2} \rho U_{\text{tot}}^2 \begin{bmatrix} D_4 \\ D_5 \\ D_6 \end{bmatrix} \quad (5.13)$$

Figures 5.4 and 5.5 show the fuselage force and moment coefficients for varying angle of attack and sideslip angle for a Sikorsky UH-60 helicopter. The fuselage forces are then transformed from the wind to the body frame:

$$\begin{bmatrix} X_F \\ Y_R \\ Z_R \end{bmatrix} = \mathbf{T}_{w \rightarrow B} \begin{bmatrix} F_x \\ F_y \\ F_z \end{bmatrix} = \begin{bmatrix} \cos \alpha_F \cos \beta_F & -\cos \alpha_F \sin \beta_F & -\sin \alpha_F \\ \sin \beta_F & \cos \beta_F & 0 \\ \sin \alpha_F \cos \beta_F & -\sin \alpha_F \sin \beta_F & \cos \alpha_F \end{bmatrix} \begin{bmatrix} F_x \\ F_y \\ F_z \end{bmatrix} \quad (5.14)$$

The fuselage moments about the CG, expressed in body-frame coordinates, are:

$$\begin{aligned} \begin{bmatrix} L_F \\ M_F \\ N_F \end{bmatrix} &= \mathbf{T}_{w \rightarrow B} \begin{bmatrix} M_x \\ M_y \\ M_z \end{bmatrix} + \begin{bmatrix} X_F \\ Y_F \\ Z_F \end{bmatrix} \times \mathbf{r}_{\bullet \rightarrow C} \\ &= \mathbf{T}_{w \rightarrow B} \begin{bmatrix} M_x \\ M_y \\ M_z \end{bmatrix} + \begin{bmatrix} 0 & -Z_F & Y_F \\ Z_F & 0 & -X_F \\ -Y_F & X_F & 0 \end{bmatrix} \begin{bmatrix} x_C \\ y_C \\ z_C \end{bmatrix} \end{aligned} \quad (5.15)$$

The fuselage forces and moments about the center of mass shall be summed with those from the other rotorcraft components (*e.g.*, main rotor, tail rotor, empennage) and plugged into the rigid-body equations of motion to drive the fuselage dynamics. At a first approximation, all forces and moments from the fuselage can be set to zero except fuselage drag  $D_1$ . It is found that values of  $D_1$  range from about 10 ft<sup>2</sup> on smaller helicopters (*e.g.*, Robinson R-22) to as much as 50 ft<sup>2</sup> on large utility helicopters (*e.g.*, Sikorsky CH-53) [Lei06].

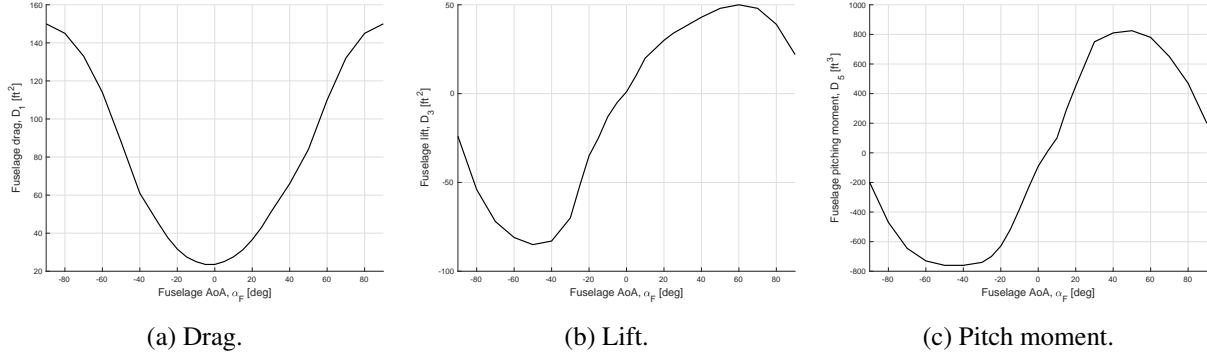


Figure 5.4: Sikorsky UH-60 fuselage force and moment coefficients for varying angle of attack [How80].

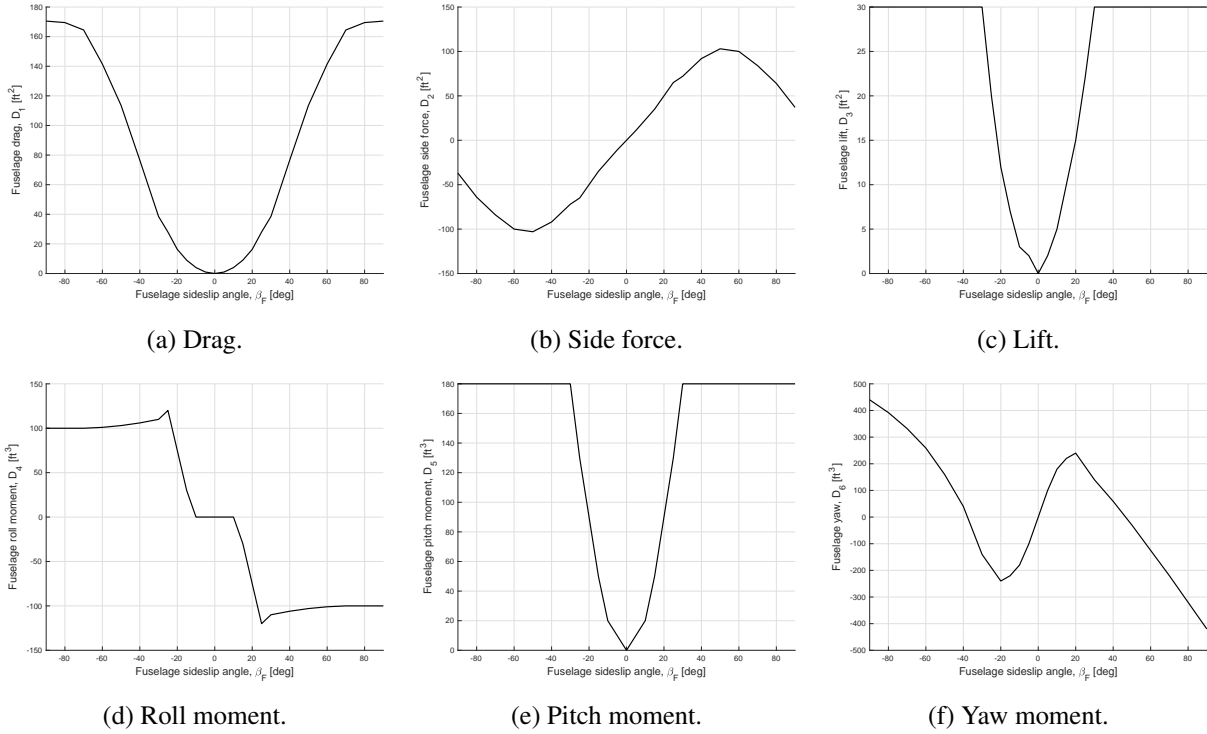


Figure 5.5: Sikorsky UH-60 fuselage force and moment coefficients for varying sideslip angle [How80].

## 5.2 Empennage

### 5.2.1 Hub to Wing Frame Transformation

Like for rotor hubs, aerodynamic appendices may be canted (Fig. 5.6a) and tilted (Fig. 5.6b). Additionally, these appendices may also be swiveled (Fig. 5.6c).

As such, the orientation of aerodynamic appendices, herein modeled as wings, can be described with a series of the following three successive single-axis rotations:

1. Rotation about the  $i_B$  axis by an angle  $\phi_a$  (i.e., canting), resulting in the intermediate frame  $(T)$  (Fig. 5.7a). The transformation from the body to the  $(T)$  frame is:

$$\begin{bmatrix} i_T \\ j_T \\ k_T \end{bmatrix} = \underbrace{\begin{bmatrix} 1 & 0 & 0 \\ 0 & \cos \phi_a & \sin \phi_a \\ 0 & -\sin \phi_a & \cos \phi_a \end{bmatrix}}_{T_{B \rightarrow T}} \begin{bmatrix} i_B \\ j_B \\ k_B \end{bmatrix} \quad (5.16)$$

2. Rotation about the  $j_T$  axis by an angle  $\beta_a$  (i.e., tilting), yielding a second intermediate frame  $(N)$  (Fig.

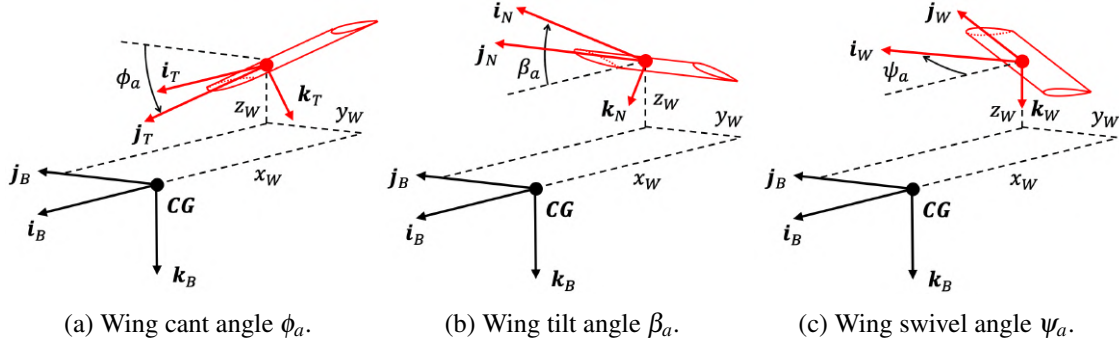


Figure 5.6: Empennage cant, tilt, and swivel.

5.7b). The transformation from intermediate frames  $\textcircled{T}$  to  $\textcircled{N}$  is:

$$\begin{bmatrix} \mathbf{i}_N \\ \mathbf{j}_N \\ \mathbf{k}_N \end{bmatrix} = \underbrace{\begin{bmatrix} \cos \beta_a & 0 & -\sin \beta_a \\ 0 & 1 & 0 \\ \sin \beta_a & 0 & \cos \beta_a \end{bmatrix}}_{T_{T \rightarrow N}} \begin{bmatrix} \mathbf{i}_T \\ \mathbf{j}_T \\ \mathbf{k}_T \end{bmatrix} \quad (5.17)$$

3. Rotation about the  $\mathbf{k}_N$  axis by an angle  $\psi_a$  (i.e., swiveling), yielding the wing frame  $\textcircled{W}$  (Fig. 5.7c).  
The transformation from frame  $\textcircled{N}$  to the wing frame is:

$$\begin{bmatrix} \mathbf{i}_W \\ \mathbf{j}_W \\ \mathbf{k}_W \end{bmatrix} = \begin{bmatrix} \cos \psi_a & \sin \psi_a & 0 \\ -\sin \psi_a & \cos \psi_a & 0 \\ 0 & 0 & 1 \end{bmatrix} \begin{bmatrix} \mathbf{i}_N \\ \mathbf{j}_N \\ \mathbf{k}_N \end{bmatrix} \quad (5.18)$$

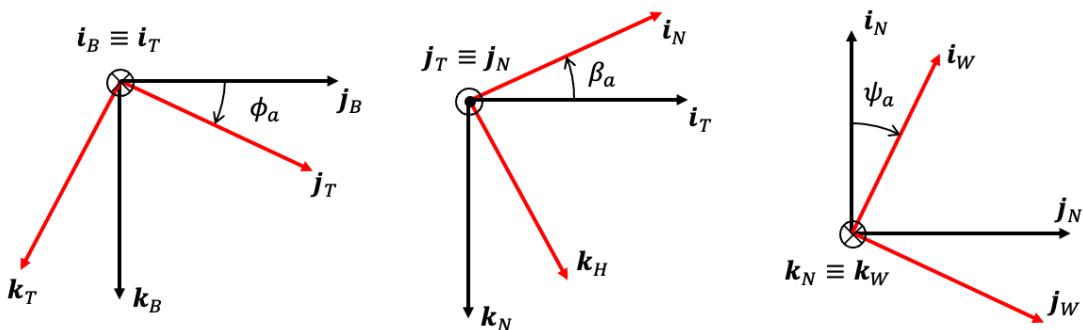


Figure 5.7: Body to wing frame rotations.

The transformation from the body to the wing frame is:

$$\begin{aligned}
 \begin{bmatrix} \mathbf{i}_W \\ \mathbf{j}_W \\ \mathbf{k}_W \end{bmatrix} &= \mathbf{T}_{N \rightarrow W} \mathbf{T}_{T \rightarrow N} \mathbf{T}_{B \rightarrow T} \begin{bmatrix} \mathbf{i}_B \\ \mathbf{j}_B \\ \mathbf{k}_B \end{bmatrix} \\
 &= \underbrace{\begin{bmatrix} \cos \psi_a & \sin \psi_a & 0 \\ -\sin \psi_a & \cos \psi_a & 0 \\ 0 & 0 & 1 \end{bmatrix} \begin{bmatrix} \cos \beta_a & 0 & -\sin \beta_a \\ 0 & 1 & 0 \\ \sin \beta_a & 0 & \cos \beta_a \end{bmatrix} \begin{bmatrix} 1 & 0 & 0 \\ 0 & \cos \phi_a & \sin \phi_a \\ 0 & -\sin \phi_a & \cos \phi_a \end{bmatrix}}_{\mathbf{T}_{B \rightarrow H}} \begin{bmatrix} \mathbf{i}_B \\ \mathbf{j}_B \\ \mathbf{k}_B \end{bmatrix} \\
 &= \underbrace{\begin{bmatrix} \cos \beta_a \cos \psi_a & \cos \phi_a \sin \psi_a + \sin \phi_a \sin \beta_a \cos \psi_a & \sin \phi_a \sin \psi_a - \cos \phi_a \sin \beta_a \cos \psi_a \\ -\cos \beta_a \sin \psi_a & \cos \phi_a \cos \psi_a - \sin \phi_a \sin \beta_a \sin \psi_a & \sin \phi_a \cos \psi_a + \cos \phi_a \sin \beta_a \sin \psi_a \\ \sin \beta_a & -\sin \phi_a \cos \beta_a & \cos \phi_a \cos \beta_a \end{bmatrix}}_{\mathbf{T}_{B \rightarrow H}} \begin{bmatrix} \mathbf{i}_B \\ \mathbf{j}_B \\ \mathbf{k}_B \end{bmatrix}
 \end{aligned} \tag{5.19}$$

The inverse transformation, *i.e.*, that from the hub to the body frame, is:

$$\begin{aligned}
 \begin{bmatrix} \mathbf{i}_B \\ \mathbf{j}_B \\ \mathbf{k}_B \end{bmatrix} &= \mathbf{T}_{B \rightarrow W}^T \begin{bmatrix} \mathbf{i}_W \\ \mathbf{j}_W \\ \mathbf{k}_W \end{bmatrix} \\
 &= \underbrace{\begin{bmatrix} \cos \beta_a \cos \psi_a & -\cos \beta_a \sin \psi_a & \sin \beta_a \\ \cos \phi_a \sin \psi_a + \sin \phi_a \sin \beta_a \cos \psi_a & \cos \phi_a \cos \psi_a - \sin \phi_a \sin \beta_a \sin \psi_a & -\sin \phi_a \cos \beta_a \\ \sin \phi_a \sin \psi_a - \cos \phi_a \sin \beta_a \cos \psi_a & \sin \phi_a \cos \psi_a + \cos \phi_a \sin \beta_a \sin \psi_a & \cos \phi_a \cos \beta_a \end{bmatrix}}_{\mathbf{T}_{W \rightarrow B}} \begin{bmatrix} \mathbf{i}_H \\ \mathbf{j}_H \\ \mathbf{k}_H \end{bmatrix}
 \end{aligned} \tag{5.20}$$

### 5.2.2 Empennage Kinematics

Assume that the position vector from the center of mass to the wing aerodynamic center (located at half of the wing span and 1/4 chord), expressed in body-frame components (Fig. 5.6), is:

$$\mathbf{r}_{\bullet \rightarrow W}^B = x_W \mathbf{i}_B + y_W \mathbf{j}_B + z_W \mathbf{k}_B \tag{5.21}$$

The translational velocity vector of the wing with respect to the inertial frame, expressed in body-frame components, is:

$$\begin{aligned}
 \mathbf{v}_{W/I}^B &= \mathbf{v}_{\bullet/I}^B + \boldsymbol{\omega}_{B/I}^B \times \mathbf{r}_{\bullet \rightarrow W}^B \\
 &= \begin{bmatrix} u \\ v \\ w \end{bmatrix} + \begin{bmatrix} 0 & -r & q \\ r & 0 & -p \\ -q & p & 0 \end{bmatrix} \begin{bmatrix} x_W \\ y_W \\ z_W \end{bmatrix} = \begin{bmatrix} u - ry_W + qz_W \\ v + rx_W - pz_W \\ w - qx_W + py_W \end{bmatrix}
 \end{aligned} \tag{5.22}$$

Then, the translational velocity vector of the wing with respect to the inertial frame, expressed in wing-frame components, is:

$$\begin{aligned}
 \mathbf{v}_{W/I}^W &= \mathbf{T}_{B \rightarrow W} \mathbf{v}_{W/I}^B \\
 &= \mathbf{T}_{B \rightarrow W} \begin{bmatrix} u - ry_W + qz_W \\ v + rx_W - pz_W \\ w - qx_W + py_W \end{bmatrix} = \begin{bmatrix} u_W \\ v_W \\ w_W \end{bmatrix}
 \end{aligned} \tag{5.23}$$

The angular velocity vector of the wing with respect to the inertial frame, expressed in hub frame components, is:

$$\begin{aligned}
 \boldsymbol{\omega}_{W/I}^W &= \mathbf{T}_{B \rightarrow W} \boldsymbol{\omega}_{W/I}^B \\
 &= \mathbf{T}_{B \rightarrow W} \begin{bmatrix} p \\ q \\ r \end{bmatrix} = \begin{bmatrix} p_W \\ q_W \\ r_W \end{bmatrix}
 \end{aligned} \tag{5.24}$$

### 5.2.3 Wing Aerodynamics

Consider the geometry shown in Fig. 5.8, showing a generic wing planform. The word planform refers to the shape of the wing when viewing it face down.

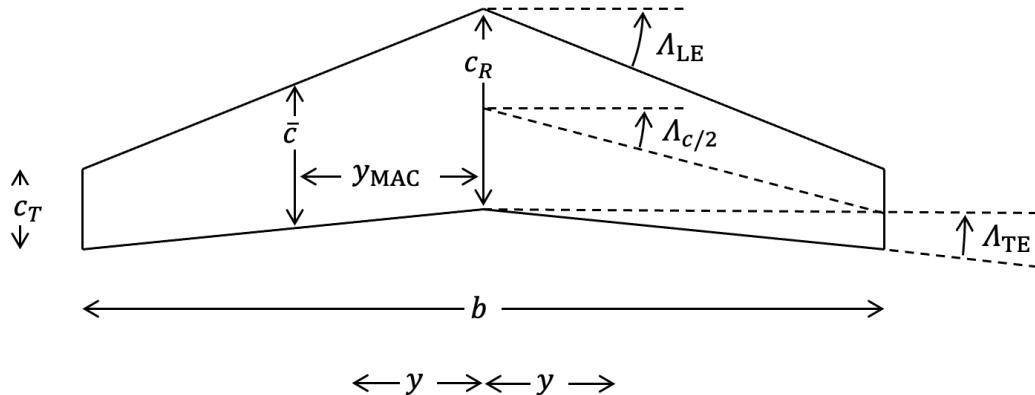


Figure 5.8: Wing planform.

Define the following quantities:

$b$  is the wing span,

$S$  is the wing surface area,

$\Lambda_{LE}$ : sweep angle at the leading edge,

$\Lambda_{TE}$ : sweep angle at the trailing edge,

$\Lambda_{c/2}$ : sweep angle at mid chord,

$c_R$ : chord at root,

$c_T$ : chord at tip, and

$y$  the spanwise coordinate.

Based of these quantities, it is possible to define other quantities:

$$S = 2 \int_0^{b/2} c dy \quad \text{Wing Area} \quad (5.25a)$$

$$\bar{c} = \frac{2}{S} \int_0^{b/2} c^2 dy \quad \text{Mean Aerodynamic Chord} \quad (5.25b)$$

$$y_{MAC} = \frac{2}{S} \int_0^{b/2} cy dy \quad \text{Location of Mean Aerodynamic Chord} \quad (5.25c)$$

$$A = \frac{b^2}{S} \quad \text{Aspect Ratio} \quad (5.25d)$$

$$(5.25e)$$

The total wing lift-curve slope can be defined through lifting-line theory at subsonic speeds:

$$C_{L\alpha} = \frac{2\pi A}{2 + \sqrt{\frac{A^2 \beta^2}{k^2} \left( \frac{\tan^2 \Lambda_{c/2}}{\beta^2} \right) + 4}} \quad (5.26)$$

where  $\beta = \sqrt{1 - M_\infty^2}$  with  $M_\infty$  being the Mach number of the free-stream flow, and  $k = C_{l\alpha}/2\pi$  where  $C_{l\alpha}$  is the sectional lift-curve slope. To obtain the zero-lift angle of attack, note that the angle of attack can change between the root and the tip due to twist  $\epsilon(y)$ . The twist angle is typically such that the tip is more leading-edge down than the root. On fixed-wing aircraft, twist is used to improve the stall characteristics of the aircraft in that the wing tip will be the last to stall so that the ailerons can remain effective. Define the wing angle of attack to be the angle of attack at the root. Then, lift on the wing is found by integrating the sectional lift over the span of the wing:

$$L = 2 \int_0^{b/2} C_{l\alpha}(y) [\alpha_{wing} + \epsilon(y) - \alpha_0(y)] q(y) c(y) dy \quad (5.27)$$

where  $q(y)$  is the spanwise dynamic pressure distribution. Setting the lift to zero and solving for the angle of attack yields the zero-lift angle for the entire wing:

$$\alpha_{0\text{wing}} = \frac{2}{S} \int_0^{b/2} [\alpha_0(y) - \varepsilon(y)] c(y) dy \quad (5.28)$$

### 5.2.4 Simple Aerodynamic Modeling

Consider now the geometry in Fig. 5.9, showing a section of a wing moving through the air.

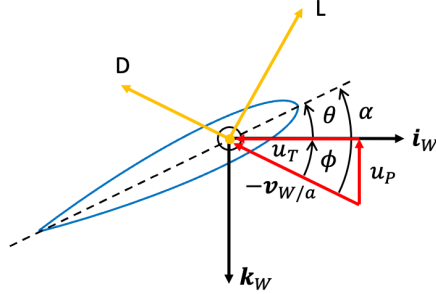


Figure 5.9: Wing section moving through the air.

Define the following quantities:

- $\theta = \theta(r)$  is the geometric pitch of the wing,
- $\phi = \phi(r)$  is the aerodynamic incidence angle,
- $\alpha$  is the wing angle of attack,
- $\mathbf{v}_{W/a}$  is the velocity of the wing with respect to the air mass,
- $u_T$  is the velocity tangent to the wing leading edge ( $-i_w$  verse),
- $u_P$  is the velocity perpendicular to the  $i_w - j_w$  plane ( $-k_w$  verse), and
- $u_R$  is the velocity in the wing spanwise direction ( $j_w$  verse).

The velocity of the  $i^{\text{th}}$  wing with respect to the air mass, expressed in the  $i^{\text{th}}$  wing-frame coordinates, is:

$$\begin{aligned} \mathbf{v}_{W/a}^{W_i} &= \mathbf{v}_{W/I}^{W_i} - \mathbf{v}_{a/I}^{W_i} \\ &= \mathbf{v}_{W/I}^{W_i} - \sum_{j=1}^{N_{\text{rot}}} (\mathbf{T}_{H_j \rightarrow W_i} \mathbf{v}_{a/I}^{H_j}) \\ &= \begin{bmatrix} u_E \\ v_E \\ w_E \end{bmatrix} - \sum_{j=1}^{N_{\text{rot}}} \left( \mathbf{T}_{B \rightarrow W_i} \mathbf{T}_{H_j \rightarrow B} \begin{bmatrix} 0 \\ 0 \\ w_{\lambda_j} \end{bmatrix} \right) = \begin{bmatrix} u_R \\ -u_T \\ u_P \end{bmatrix} \end{aligned} \quad (5.29)$$

where  $w_{\lambda_j} = \Omega_j R_j \lambda_j$  is the induced velocity at the wing element induced by the  $j^{\text{th}}$  rotor expressed in that rotor's hub frame. This velocity can be calculated using Eq. (3.95), *i.e.*, the formula for the induced velocity near a lifting rotor. At a first approximation, the rotor downwash on the wing may not necessarily be included. The geometric pitch of the wing  $\theta$  is to be considered an input from either the pilot or the rotorcraft flight control system (FCS). Sometimes, the horizontal stabilizer geometric pitch is scheduled with speed, like for the Sikorsky UH-60, such that the incidence of the tail is approximately parallel to the wake skew angle of the main rotor. However, the incidence of the horizontal stabilizer may also actively be controlled to provide additional pitching moment for pull-up/push-over maneuvers. The total speed at the wing is:

$$U_{\text{tot}} = \sqrt{u_R^2 + u_T^2 + u_P^2} \quad (5.30)$$

The velocity component in the plane of the blade section is:

$$U = \sqrt{u_T^2 + u_P^2} = \sqrt{u_T^2 \left( 1 + \frac{u_P^2}{u_T^2} \right)} \quad (5.31)$$

The local angle of attack is:

$$\alpha = \theta + \phi = \theta + \tan^{-1} \left( \frac{u_P}{u_T} \right) \approx \theta + \frac{u_P}{u_T} \quad (5.32)$$

The local Mach number is:

$$M = \frac{U_{\text{tot}}}{v_{\text{sound}}} \quad (5.33)$$

where  $v_{\text{sound}}$  is the speed of sound. The local lift and drag coefficients are typically calculated in one of two ways. The first way is by using lookup tables of the airfoil section such that:

$$C_L = f(\alpha, M) \quad (5.34a)$$

$$C_D = f(\alpha, M) \quad (5.34b)$$

where  $C_L$  and  $C_D$  are the wing lift and drag coefficients. The second way is to assume linear lift variation of the angle of attack and constant drag coefficient, that is:

$$C_L \approx a_0 \alpha \quad (5.35a)$$

$$C_D \approx \delta \quad (5.35b)$$

where  $a_0$  is the lift-curve slope and  $\delta$  is the wing profile drag coefficient (also known as zero-lift drag coefficient). The wing lift and drag are, expressed in the air mass frame, are:

$$L = \frac{1}{2} \rho S_W U^2 C_L \quad (5.36a)$$

$$D = \frac{1}{2} \rho S_W U^2 C_D \quad (5.36b)$$

where  $\rho$  is the air density and  $S_W$  is the surface area of the  $i^{\text{th}}$  wing. The wing forces, expressed in the RTP frame, are:

$$\begin{aligned} \begin{bmatrix} F_R \\ F_T \\ F_P \end{bmatrix} &= \mathbf{T}_{a \rightarrow RTP} \begin{bmatrix} 0 \\ -\frac{1}{2} \rho S_W U^2 C_D \\ \frac{1}{2} \rho S_W U^2 C_L \end{bmatrix} = \mathbf{T}_{W \rightarrow RTP} \mathbf{T}_{a \rightarrow W} \begin{bmatrix} 0 \\ -\frac{1}{2} \rho S_W U^2 C_D \\ \frac{1}{2} \rho S_W U^2 C_L \end{bmatrix} \\ &= \begin{bmatrix} 1 & 0 & 0 \\ 0 & -1 & 0 \\ 0 & 0 & 1 \end{bmatrix} \begin{bmatrix} 1 & 0 & 0 \\ 0 & -\cos \phi & -\sin \phi \\ 0 & \sin \phi & -\cos \phi \end{bmatrix} \begin{bmatrix} 0 \\ -\frac{1}{2} \rho S_W U^2 C_D \\ \frac{1}{2} \rho S_W U^2 C_L \end{bmatrix} \\ &= \begin{bmatrix} 0 \\ \frac{1}{2} \rho S_W U^2 (C_L \sin \phi - C_D \cos \phi) \\ \frac{1}{2} \rho S_W U^2 (-C_L \cos \phi - C_D \sin \phi) \end{bmatrix} \end{aligned} \quad (5.37)$$

The wing forces are transformed into the body frame as follows:

$$\begin{bmatrix} X_W \\ Y_W \\ Z_W \end{bmatrix} = \mathbf{T}_{W \rightarrow B} \begin{bmatrix} F_R \\ -F_T \\ F_P \end{bmatrix} \quad (5.38)$$

The wing moments about the CG, expressed in body-frame components, are:

$$\begin{bmatrix} L_W \\ M_W \\ N_W \end{bmatrix} = \begin{bmatrix} X_W \\ Y_W \\ Z_W \end{bmatrix} \times \mathbf{r}_{\bullet \rightarrow W} = \begin{bmatrix} 0 & -Z_W & Y_W \\ Z_W & 0 & -X_W \\ -Y_W & X_W & 0 \end{bmatrix} \begin{bmatrix} x_W \\ y_W \\ z_W \end{bmatrix} \quad (5.39)$$

The wing forces and moments about the CG shall be summed with those from the other rotorcraft components (*e.g.*, fuselage, main rotor, tail rotor, other empennage) and plugged into the rigid-body equations of motion to drive the fuselage dynamics.

### 5.2.5 Wing Element Modeling

Assume the position vector from the rotor hub to the wing element to be  $\mathbf{r}_{W \rightarrow E} = y\mathbf{j}_W$ , where  $y$  is the spanwise wing coordinate  $-b/2 \leq y \leq b/2$  and where  $b$  is the wing span. Then, the velocity of the wing element with respect to the inertial frame, expressed in the wing frame, is:

$$\begin{aligned}
 \mathbf{v}_{E/I}^W &= \mathbf{v}_{W/I}^W + \boldsymbol{\omega}_{W/I}^W \times \mathbf{r}_{W \rightarrow E}^W \\
 &= \begin{bmatrix} u_W \\ v_W \\ w_W \end{bmatrix} + \begin{bmatrix} p_W \\ q_W \\ r_W \end{bmatrix} \times \begin{bmatrix} 0 \\ y \\ 0 \end{bmatrix} \\
 &= \begin{bmatrix} u_W \\ v_W \\ w_W \end{bmatrix} + \begin{bmatrix} 0 & -r_W & q_W \\ r_W & 0 & -p_W \\ -q_W & p_W & 0 \end{bmatrix} \begin{bmatrix} 0 \\ y \\ 0 \end{bmatrix} \\
 &= \begin{bmatrix} u_W - r_W y \\ v_W \\ w_W + p_W y \end{bmatrix} = \begin{bmatrix} u_W \\ v_W \\ w_W \end{bmatrix}
 \end{aligned} \tag{5.40}$$

Consider now the geometry in Fig. 5.10, showing a section of a representative wing moving through the air.

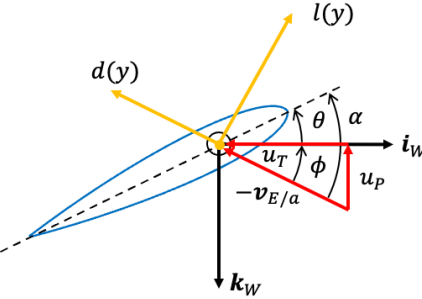


Figure 5.10: Section of a representative wing element moving through the air.

Define the following quantities:

- $\theta = \theta(y)$  is the geometric pitch of the wing element,
- $\phi = \phi(y)$  is the wing element aerodynamic incidence angle,
- $\alpha$  is the wing element angle of attach,
- $\mathbf{v}_{E/a}$  is the velocity of the wing element with respect to the air mass,
- $u_T$  is the velocity tangent to the wing leading edge ( $-\mathbf{i}_w$  verse),
- $u_P$  is the velocity perpendicular to the  $\mathbf{i}_w - \mathbf{j}_w$  plane ( $-\mathbf{k}_w$  verse), and
- $u_R$  is the velocity in the wing spanwise direction ( $\mathbf{j}_w$  verse).

The wing element velocity of the  $i^{th}$  wing with respect to the air mass, expressed in the  $i^{th}$  wing-frame coordinates, is:

$$\begin{aligned}
 \mathbf{v}_{E/a}^{W_i} &= \mathbf{v}_{E/I}^{W_i} - \mathbf{v}_{a/I}^{W_i} \\
 &= \mathbf{v}_{E/I}^{W_i} - \sum_{j=1}^{N_{\text{rot}}} \left( \mathbf{T}_{H_j \rightarrow W_i} \mathbf{v}_{a/I}^{H_j} \right) \\
 &= \begin{bmatrix} u_E \\ v_E \\ w_E \end{bmatrix} - \sum_{j=1}^{N_{\text{rot}}} \left( \mathbf{T}_{B \rightarrow W_i} \mathbf{T}_{H_j \rightarrow B} \begin{bmatrix} 0 \\ 0 \\ w_{\lambda_j} \end{bmatrix} \right) = \begin{bmatrix} u_R \\ -u_T \\ u_P \end{bmatrix}
 \end{aligned} \tag{5.41}$$

where  $w_{\lambda_j} = \Omega_j R_j \lambda_i$  is the induced velocity at the wing element induced by the  $j^{th}$  rotor expressed in that rotor's hub frame. This velocity can be calculated using Eq. (3.95), *i.e.*, the formula for the induced velocity near a lifting rotor. At a first approximation, the rotor downwash on the wing may not necessarily be included.

The geometric pitch of the wing element is given by:

$$\theta(y) = \theta_W + \varepsilon(y) \quad (5.42)$$

where  $\theta_W$  represents the prescribed blade pitch at the wing root (from the control system) and  $\varepsilon(y)$  is the twist angle distribution. Typically,  $\theta_{tw} = 0$  at the root  $y = 0$  and  $\theta_{tw} < 0$  for  $0 < |y| \leq b/2$ , where  $b$  is the wing span. The total speed at the wing element is:

$$U_{\text{tot}} = \sqrt{u_R^2 + u_T^2 + u_P^2} \quad (5.43)$$

The velocity component in the plane of the wing section is:

$$U = \sqrt{u_T^2 + u_P^2} = \sqrt{u_T^2 \left( 1 + \frac{u_P^2}{u_T^2} \right)} \quad (5.44)$$

The local angle of attack is:

$$\alpha = \theta + \phi = \theta + \tan^{-1} \left( \frac{u_P}{u_T} \right) \approx \theta + \frac{u_P}{u_T} \quad (5.45)$$

The local Mach number is:

$$M = \frac{U_{\text{tot}}}{v_{\text{sound}}} \quad (5.46)$$

where  $v_{\text{sound}}$  is the speed of sound. The local lift and drag coefficients are typically calculated in one of two ways. The first way is by using lookup tables of the airfoil section such that:

$$C_l = f(\alpha, M) \quad (5.47a)$$

$$C_d = f(\alpha, M) \quad (5.47b)$$

where  $C_l$  and  $C_d$  are the airfoil lift and drag coefficients. The second way is to assume linear lift variation of the angle of attack and constant drag coefficient, that is:

$$C_l \approx a_0 \alpha \quad (5.48a)$$

$$C_d \approx \delta \quad (5.48b)$$

where  $a_0$  is the lift-curve slope and  $\delta$  is the zero-lift drag coefficient. The sectional wing lift and drag are, expressed in the air mass frame, are:

$$l(y) = \frac{1}{2} \rho c(y) U^2 C_l \quad (5.49a)$$

$$d(y) = \frac{1}{2} \rho c(y) U^2 C_d \quad (5.49b)$$

where  $\rho$  is the air density and  $c(y)$  is the wing element chord. The wing segment forces, expressed in the RTP frame, are:

$$\begin{aligned} \begin{bmatrix} f_R \\ f_T \\ f_P \end{bmatrix} &= \mathbf{T}_{a \rightarrow RTP} \begin{bmatrix} 0 \\ -\frac{1}{2} \rho c(y) U^2 C_d \\ \frac{1}{2} \rho c(y) U^2 C_l \end{bmatrix} = \mathbf{T}_{W \rightarrow RTP} \mathbf{T}_{a \rightarrow W} \begin{bmatrix} 0 \\ -\frac{1}{2} \rho c(r) U^2 C_d \\ \frac{1}{2} \rho c(r) U^2 C_l \end{bmatrix} \\ &= \begin{bmatrix} 1 & 0 & 0 \\ 0 & -1 & 0 \\ 0 & 0 & 1 \end{bmatrix} \begin{bmatrix} 1 & 0 & 0 \\ 0 & -\cos \phi & -\sin \phi \\ 0 & \sin \phi & -\cos \phi \end{bmatrix} \begin{bmatrix} 0 \\ -\frac{1}{2} \rho c(r) U^2 C_d \\ \frac{1}{2} \rho c(r) U^2 C_l \end{bmatrix} \\ &= \begin{bmatrix} 0 \\ \frac{1}{2} \rho c(r) U^2 (C_l \sin \phi - C_d \cos \phi) \\ \frac{1}{2} \rho c(r) U^2 (-C_l \cos \phi - C_d \sin \phi) \end{bmatrix} \end{aligned} \quad (5.50)$$

The wing aerodynamic loads, expressed in the RTP frame, are:

$$F_R = \int_{-b/2}^{b/2} f_R(y) dy \quad (5.51a)$$

$$F_T = \int_{-b/2}^{b/2} f_T(y) dy \quad (5.51b)$$

$$F_P = \int_{-b/2}^{b/2} f_P(y) dy \quad (5.51c)$$

The transformation of these forces to forces and moments about the CG expressed in body-frame components is performed in the same way as in the section above.

### 5.2.6 Lifting Line - Linear

Consider an unswept, high aspect ration wing in an incompressible, inviscid flow. Then, the lift distribution on the wing can be found using Prandt's lifting line model [Hou+13]. The wing is modeled as a single bound vortex line at the quarter chord position and an associated vortex sheet as shown in Fig. 5.11.

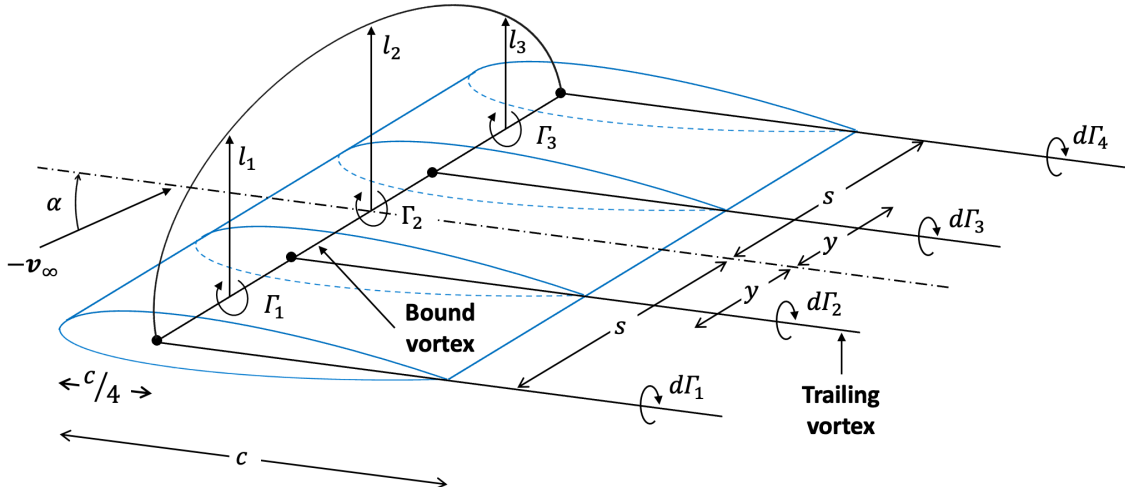


Figure 5.11: Unswept, high aspect ratio wing in an incompressible, inviscid flow.

The wing can be discretized into spanwise elements, each with a circulation (vortex strength  $\Gamma_i$ ). Each wing element is associated with a free-stream velocity  $v_\infty$ . The free-stream velocity is given by the summation of the velocity at the wing element  $v_{E/I}^W$  given in Eq. (5.40) and the velocity induced by the trailing vortex sheet  $w_i$ , such that:

$$\mathbf{v}_\infty^W = \mathbf{v}_{E/I}^W + \begin{bmatrix} 0 \\ 0 \\ w_i \end{bmatrix} = \begin{bmatrix} u_R \\ -u_T \\ u_P \end{bmatrix} \quad (5.52)$$

The total speed at the wing element is:

$$U_{\text{tot}} = \sqrt{u_R^2 + u_T^2 + u_P^2} \quad (5.53)$$

The velocity component in the plane of the wing section is:

$$U = \sqrt{u_T^2 + u_P^2} = \sqrt{u_T^2 \left( 1 + \frac{u_P^2}{u_T^2} \right)} \quad (5.54)$$

The wing semi-span is defines as  $s = b/2$ . The mapping of angle  $\theta$  to semi-span position is done by using a Fourier series (Fig. 5.12) and allows variation of the model to suit different wing geometries:

$$y = s \cos \theta \quad (5.55)$$

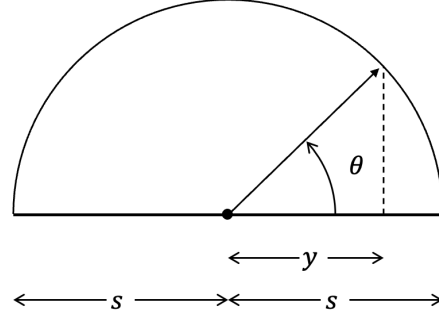


Figure 5.12: Mapping of angle  $\theta$  to semi-span position.

Spanwise lift distribution is assumed to be approximately elliptical, with small modifications to wing planform geometry. The vortex line strength is modeled using the following Fourier series approximation:

$$\begin{aligned}\Gamma(y) &= \Gamma(\theta) = 4sU \sum_{n=1}^{\infty} A_n \sin(n\theta) \\ &\approx 4sU \sum_{n=1}^N A_n \sin(n\theta)\end{aligned}\quad (5.56)$$

where  $N$  is the number of spanwise elements. The required strength of distribution coefficients  $A_n$  for a given geometry can be calculated applying a surface flow boundary condition. In this case, the condition of zero flow normal to the surface  $\mathbf{v}_n = \mathbf{0}$  is applied at each spanwise element. Consider now the geometry shown in Fig. 5.13.

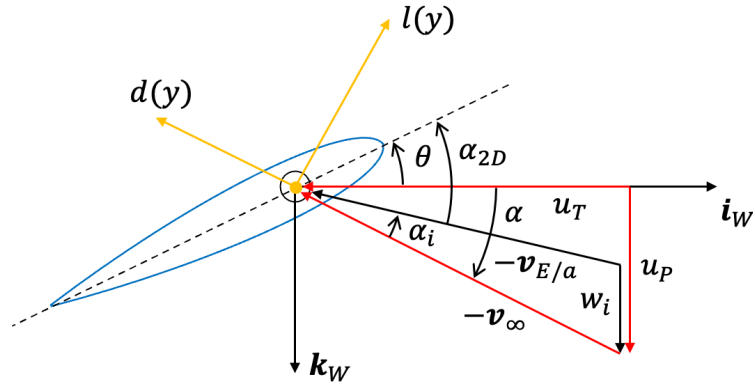


Figure 5.13: Section of a representative wing element modeled with lifting line theory.

According to this geometry, the wing element 2-D angle of attack is defined as:

$$\alpha_{2D} = \alpha - \alpha_i + \theta_W \quad (5.57)$$

where  $\alpha$  is the wing angle of attack,  $\theta = \theta(y)$  is the geometric pitch of the wing, and  $\alpha_i$  is the induced inflow angle. The wing angle of attack is:

$$\alpha = \tan^{-1} \left( \frac{u_P}{u_T} \right) \approx \frac{u_P}{u_T} \quad (5.58)$$

The geometric pitch of the wing element is given by Eq. (5.42). The induced inflow angle is given by:

$$\alpha_i = \tan^{-1} \left( \frac{w_i}{U} \right) \approx \frac{w_i}{U} \quad (5.59)$$

The vortex strength in the vortex sheet is a function of the changes in vortex strength along the wing span and is obtained by differentiating the bound vortex distribution of Eq. (5.56):

$$\frac{d\Gamma}{d\theta} = 4sU \sum_{n=1}^N nA_n \cos(n\theta) \quad (5.60)$$

The downwash at any span location can be found by integrating the influence of individual elements of the trailing sheet. Each sheet behaves like 1/2 of an infinite vortex line such that:

$$dw_i = \frac{\Gamma}{4\pi r} \quad (5.61)$$

where  $r = y - y_i$  is the distance across the span between the vortex element and the point at which the downwash is being calculated (*i.e.*, the control point). The full downwash at a the  $i^{\text{th}}$  control point is given by:

$$\begin{aligned} w_i &= \frac{1}{4\pi} \int_{-s}^s \frac{1}{y - y_i} d\Gamma \\ &= \frac{U}{\pi} \int_0^\pi \frac{1}{\cos \theta_i - \cos \theta} \sum_{n=1}^N nA_n \cos(n\theta) d\theta \\ &= U \sum_{n=1}^N nA_n \frac{\sin(n\theta_i)}{\sin \theta_i} \end{aligned} \quad (5.62)$$

Assume linear sectional coefficient of lift with the angle of attack such that:

$$C_{l2D} = a_0 (\alpha_{2D} - \alpha_0) = \frac{\Gamma_0}{Uc} \quad (5.63)$$

where  $a_0$  is the lift curve slope and  $\alpha_0$  is the section zero-lift angle of attack. This can be re-arranged in terms of vortex strength:

$$\Gamma = \frac{1}{2} a_0 U c [\alpha - \alpha_i + \theta(y) - \alpha_0] \quad (5.64)$$

Substituting for vortex strength and induced inflow angle produces the following boundary condition at a point  $\theta = \theta_i$ :

$$4sU \sum_{n=1}^N A_n \sin(n\theta) = \frac{1}{2} a_0 U c \left[ \alpha - \sum_{n=1}^N \frac{nA_n \sin(n\theta)}{\sin \theta} + \theta(y) - \alpha_0 \right] \quad (5.65)$$

Re-arranging yields:

$$\sum_{n=1}^N A_n \sin(n\theta) \left( \sin \theta + n \frac{a_0 c}{8s} \right) = \frac{a_0 c}{8s} \sin \theta [\alpha + \theta(y) - \alpha_0] \quad (5.66)$$

where:

$$\frac{a_0 c}{8s} = \mu \quad (5.67)$$

By applying the boundary condition at  $N$  spanwise locations, *i.e.*,  $\theta_i = 1, \dots, N$ , a set of simultaneous linear equations can be constructed. In matrix form, this system is:

$$\begin{bmatrix} \sin \theta_1 (\sin \theta_1 + \mu) & \cdots & \sin(N\theta_1) (\sin \theta_1 + N\mu) \\ \vdots & \ddots & \vdots \\ \sin \theta_N (\sin \theta_N + \mu) & \cdots & \sin(N\theta_N) (\sin \theta_N + N\mu) \end{bmatrix} \begin{bmatrix} A_1 \\ \vdots \\ A_N \end{bmatrix} = \begin{bmatrix} \mu \sin \theta_1 (\alpha - \alpha_0) \\ \vdots \\ \mu \sin \theta_N (\alpha - \alpha_0) \end{bmatrix} \quad (5.68)$$

Once the coefficients of the load distribution are known, the total lift of the wing can be found as:

$$\begin{aligned} L &= \rho U \int_{-s}^s \Gamma dy = \rho U \int_{-s}^s 4sU \sum_{n=1}^N A_n \sin(n\theta) s \sin \theta d\theta \\ &= \rho s^2 U 2\pi A_1 \end{aligned} \quad (5.69)$$

The wing coefficient of lift is:

$$C_L = \pi \left( \frac{b^2}{S} \right) A_1 \quad (5.70)$$

where  $S$  is the wing surface area. By integrating the components of the sectional lift coefficient that acts parallel to the free-stream velocity across the span, the induced drag coefficient is found as:

$$D_i = \rho U \int_{-s}^s \Gamma \sin \alpha_i dy \quad (5.71)$$

Using the small angle approximation such that  $\sin \alpha_i \approx \alpha_i$  and recalling that  $\alpha_i \approx w_i/U$ , the wing induced drag coefficient is:

$$C_{D_i} = \pi \frac{b^2}{S} \sum_{n=1}^N n A_n^2 \quad (5.72)$$

The total wing drag coefficient is:

$$C_D = \delta + C_{D_i} \quad (5.73)$$

where  $\delta$  is the zero-lift drag coefficient. These aerodynamic forces can be transformed to forces and moments about the CG and expressed in body-frame coordinates by following the same process as in the sections above.

### 5.2.7 Lifting Line - Nonlinear

Consider the lifting line theory from the section above. If the section lift coefficient is given by a (non-linear) lookup table such that  $C_l = f(\alpha, M)$  rather than being assumed as linearly-varying with the angle of attack, then:

$$C_l = f(\alpha_{2D} - \alpha_0, M) = \frac{\Gamma}{U c} \quad (5.74)$$

where  $M$  is the Mach number and is given in Eq. (4.29). Recall that:

$$\alpha_{2D} - \alpha_0 = \alpha - \sum_{n=1}^N \frac{n A_n \sin(n\theta)}{\sin \theta} + \theta(y) - \alpha_0 \quad (5.75)$$

Re-arranged in terms of vortex strength yields:

$$\Gamma = \frac{1}{2} U c f \left[ \alpha - \sum_{n=1}^N \frac{n A_n \sin(n\theta)}{\sin \theta} + \theta(y) - \alpha_0, M \right] \quad (5.76)$$

Thus,

$$4sU \sum_{n=1}^N A_n \sin(n\theta) = \frac{c}{8s} U f \left[ \alpha - \sum_{n=1}^N \frac{n A_n \sin(n\theta)}{\sin \theta} + \theta(y) - \alpha_0, M \right] \quad (5.77)$$

This set of equations must be solved numerically. To do so, re-write in matrix form:

$$\underbrace{\begin{bmatrix} \sin \theta_1 \\ \ddots \\ \sin(N\theta_N) \end{bmatrix}}_A \underbrace{\begin{bmatrix} A_1 \\ \vdots \\ A_N \end{bmatrix}}_x = \underbrace{\begin{bmatrix} f \left[ \alpha - \sum_{n=1}^N \frac{nA_n \sin(n\theta_1)}{\sin \theta_1} + \theta(y) - \alpha_0, M \right] \\ \vdots \\ f \left[ \alpha - \sum_{n=1}^N \frac{nA_n \sin(n\theta_N)}{\sin \theta_N} + \theta(y) - \alpha_0, M \right] \end{bmatrix}}_B \quad (5.78)$$

Using fixed-point iteration:

$$\begin{bmatrix} A_1^{k+1} \\ \vdots \\ A_N^{k+1} \end{bmatrix} = \underbrace{\begin{bmatrix} \sin \theta_1 & & \\ & \ddots & \\ & & \sin(N\theta_N) \end{bmatrix}}^{-1} \underbrace{\begin{bmatrix} f \left[ \alpha_1 - \sum_{n=1}^N \frac{nA_n^k \sin(n\theta_1)}{\sin \theta_1} + \theta(y_1) - \alpha_0, M \right] \\ \vdots \\ f \left[ \alpha_N - \sum_{n=1}^N \frac{nA_n^k \sin(n\theta_N)}{\sin \theta_N} + \theta(y_N) - \alpha_0, M \right] \end{bmatrix}} \quad (5.79)$$

where  $k$  is the iteration number. In MATLAB® one can use the command  $x=A\b$ .

## Bibliography

- [Hou+13] E. L. Houghton et al. “Aerodynamics for Engineering Students”. In: Oxford, UK: Butterworth-Heinemann, 2013 (cited on page 130).
- [How80] J. J. Howlett. *UH-60A Black Hawk Engineering Simulation Program. Volume 1: Mathematical Model*. Technical report. NASA-CR-166309, 1980. (Cited on page 122).
- [Lei06] J. G. Leishman. “Principles of Helicopter Aerodynamics”. In: New York, New York: Cambridge University Press, 2006 (cited on page 121).



## 6. Trim, Linearization, and Simulation

### 6.1 Introduction

The flight dynamics of helicopters are effectively time-periodic, where time-periodicity is due to multiple sources including rotor blade imbalances, lift asymmetry in forward flight, and retreating blade stall. It was shown that the relative importance of the time-periodic dynamics (*i.e.*, those dynamics with natural frequencies that are multiples of the fundamental frequency of the system) and the overall dynamics of the system (*i.e.*, averaged + time-periodic dynamics) is approximately 7% for a UH-60 helicopter flying at moderate to high speeds (80 kts) [Sae+19]. However, for general flight dynamics considerations, the flight dynamics can be assumed as time-invariant.

### 6.2 Linearization

This section describes the theoretical and implementation aspects of the linearization of the rotorcraft flight dynamics. Consider the non-linear time-invariant (NLTI) dynamics of a rotorcraft at equilibrium:

$$\dot{\mathbf{x}}_e = \mathbf{f}(\mathbf{x}_e, \mathbf{u}_e) \quad (6.1a)$$

$$\mathbf{y}_e = \mathbf{g}(\mathbf{x}_e, \mathbf{u}_e) \quad (6.1b)$$

where  $\mathbf{x}_e \in \mathcal{R}^n$ ,  $\mathbf{u}_e \in \mathcal{R}^m$ , and  $\mathbf{y}_e \in \mathcal{R}^l$  are the trim state, control input, and output vectors such that the state dynamics  $\dot{\mathbf{x}}_e$  and output  $\mathbf{y}_e$  are constant. Consider the case where small disturbances are applied to the state, control input, and output vectors:

$$\mathbf{x} = \mathbf{x}_e + \Delta\mathbf{x} \quad (6.2a)$$

$$\mathbf{u} = \mathbf{u}_e + \Delta\mathbf{u} \quad (6.2b)$$

$$\mathbf{y} = \mathbf{y}_e + \Delta\mathbf{y} \quad (6.2c)$$

Then, a Taylor series expansion is performed on the state dynamics:

$$\mathbf{f}(\mathbf{x}_e + \Delta\mathbf{x}, \mathbf{u}_e + \Delta\mathbf{u}) = \mathbf{f}(\mathbf{x}_e, \mathbf{u}_e) + \frac{\partial \mathbf{f}(\mathbf{x}, \mathbf{u})}{\partial \mathbf{x}} \Big|_{\mathbf{x}_e, \mathbf{u}_e} \Delta\mathbf{x} + \frac{\partial \mathbf{f}(\mathbf{x}, \mathbf{u})}{\partial \mathbf{u}} \Big|_{\mathbf{x}_e, \mathbf{u}_e} \Delta\mathbf{u} + O(\Delta\mathbf{x}^2, \Delta\mathbf{u}^2) \quad (6.3)$$

By neglecting those terms with order higher than first, and by re-organizing one obtains:

$$\Delta\dot{\mathbf{x}} = \frac{\partial \mathbf{f}(\mathbf{x}, \mathbf{u})}{\partial \mathbf{x}} \Big|_{\mathbf{x}_e, \mathbf{u}_e} \Delta\mathbf{x} + \frac{\partial \mathbf{f}(\mathbf{x}, \mathbf{u})}{\partial \mathbf{u}} \Big|_{\mathbf{x}_e, \mathbf{u}_e} \Delta\mathbf{u} \quad (6.4)$$

where:

$$\frac{\partial \mathbf{f}(\mathbf{x}, \mathbf{u})}{\partial \mathbf{x}} \Big|_{\mathbf{x}_e, \mathbf{u}_e} = \begin{bmatrix} \frac{\partial f_1(\mathbf{x}, \mathbf{u})}{\partial x_1} & \dots & \frac{\partial f_1(\mathbf{x}, \mathbf{u})}{\partial x_n} \\ \vdots & \ddots & \vdots \\ \frac{\partial f_n(\mathbf{x}, \mathbf{u})}{\partial x_1} & \dots & \frac{\partial f_n(\mathbf{x}, \mathbf{u})}{\partial x_n} \end{bmatrix}_{\mathbf{x}_e, \mathbf{u}_e} = \mathbf{A} \quad (6.5a)$$

$$\frac{\partial \mathbf{f}(\mathbf{x}, \mathbf{u})}{\partial \mathbf{u}} \Big|_{\mathbf{x}_e, \mathbf{u}_e} = \begin{bmatrix} \frac{\partial f_1(\mathbf{x}, \mathbf{u})}{\partial u_1} & \dots & \frac{\partial f_1(\mathbf{x}, \mathbf{u})}{\partial u_m} \\ \vdots & \ddots & \vdots \\ \frac{\partial f_n(\mathbf{x}, \mathbf{u})}{\partial u_1} & \dots & \frac{\partial f_n(\mathbf{x}, \mathbf{u})}{\partial u_m} \end{bmatrix}_{\mathbf{x}_e, \mathbf{u}_e} = \mathbf{B} \quad (6.5b)$$

Similarly, a Taylor series expansion is performed on the output equation:

$$\mathbf{g}(\mathbf{x}_e + \Delta \mathbf{x}, \mathbf{u}_e + \Delta \mathbf{u}) = \mathbf{g}(\mathbf{x}_e, \mathbf{u}_e) + \frac{\partial \mathbf{g}(\mathbf{x}, \mathbf{u})}{\partial \mathbf{x}} \Big|_{\mathbf{x}_e, \mathbf{u}_e} \Delta \mathbf{x} + \frac{\partial \mathbf{g}(\mathbf{x}, \mathbf{u})}{\partial \mathbf{u}} \Big|_{\mathbf{x}_e, \mathbf{u}_e} \Delta \mathbf{u} + O(\Delta \mathbf{x}^2, \Delta \mathbf{u}^2) \quad (6.6)$$

By neglecting those terms with order higher than first, and by re-organizing one obtains:

$$\Delta \mathbf{y} = \frac{\partial \mathbf{g}(\mathbf{x}, \mathbf{u})}{\partial \mathbf{x}} \Big|_{\mathbf{x}_e, \mathbf{u}_e} \Delta \mathbf{x} + \frac{\partial \mathbf{g}(\mathbf{x}, \mathbf{u})}{\partial \mathbf{u}} \Big|_{\mathbf{x}_e, \mathbf{u}_e} \Delta \mathbf{u} \quad (6.7)$$

where:

$$\frac{\partial \mathbf{g}(\mathbf{x}, \mathbf{u})}{\partial \mathbf{x}} \Big|_{\mathbf{x}_e, \mathbf{u}_e} = \begin{bmatrix} \frac{\partial g_1(\mathbf{x}_e, \mathbf{u}_e)}{\partial x_1} & \dots & \frac{\partial g_1(\mathbf{x}_e, \mathbf{u}_e)}{\partial x_n} \\ \vdots & \ddots & \vdots \\ \frac{\partial g_p(\mathbf{x}_e, \mathbf{u}_e)}{\partial x_1} & \dots & \frac{\partial g_p(\mathbf{x}_e, \mathbf{u}_e)}{\partial x_n} \end{bmatrix}_{\mathbf{x}_e, \mathbf{u}_e} = \mathbf{C} \quad (6.8a)$$

$$\frac{\partial \mathbf{g}(\mathbf{x}, \mathbf{u})}{\partial \mathbf{u}} \Big|_{\mathbf{x}_e, \mathbf{u}_e} = \begin{bmatrix} \frac{\partial g_1(\mathbf{x}_e, \mathbf{u}_e)}{\partial u_1} & \dots & \frac{\partial g_1(\mathbf{x}_e, \mathbf{u}_e)}{\partial u_m} \\ \vdots & \ddots & \vdots \\ \frac{\partial g_p(\mathbf{x}_e, \mathbf{u}_e)}{\partial u_1} & \dots & \frac{\partial g_p(\mathbf{x}_e, \mathbf{u}_e)}{\partial u_m} \end{bmatrix}_{\mathbf{x}_e, \mathbf{u}_e} = \mathbf{D} \quad (6.8b)$$

Then, the linearized system can be written as:

$$\Delta \dot{\mathbf{x}} = \mathbf{A} \Delta \mathbf{x} + \mathbf{B} \Delta \mathbf{u} \quad (6.9a)$$

$$\Delta \mathbf{y} = \mathbf{C} \Delta \mathbf{x} + \mathbf{D} \Delta \mathbf{u} \quad (6.9b)$$

In practice, the partial derivatives are computed numerically using a central difference scheme. For instance, the elements of the  $\mathbf{A}$  matrix are found as follows:

$$A_{ij} = \frac{\partial f_i(\mathbf{x}, \mathbf{u})}{\partial x_j} \approx \frac{f_i(\mathbf{x}_e + \Delta x_j, \mathbf{u}) - f_i(\mathbf{x}_e - \Delta x_j, \mathbf{u})}{2 \Delta x_j} \quad (6.10)$$

where the perturbations are performed one by one for each state, such that:

$$\Delta \mathbf{x}_j^T = [x_{e_1} \dots x_{e_j} + \Delta x_j \dots x_{e_n}] \quad (6.11)$$

A similar procedure is adopted for finding the elements of the  $\mathbf{B}$ ,  $\mathbf{C}$ , and  $\mathbf{D}$  coefficient matrices. An implementation of this algorithm in MATLAB® is shown in Listing 6.1.

Listing 6.1: Linearization routine.

```
function [A, B, C, D]=linearize(acfunction, x0, u0, constants)
% DESCRIPTION
```

```
% This module is used to linearize the dynamic equations.  
%  
% INPUT  
% - acfunction: name of function containing system dynamics (e.g.,  
%   'SimModel')  
% - x0: trim state vector  
% - u0: trim control vector  
% - const: data structure with helicopter parameters  
  
% number of states  
ns=length(x0);  
% number of controls  
nc=length(u0);  
% evaluate dynamics at given state and control vectors  
[xdot0,y0]=feval(acfunction,0,x0,u0,constants);  
% number of state dynamics elements  
nsd=length(xdot0);  
% number of outputs  
no=length(y0);  
% initialize state-space matrices  
A=zeros(nsd,ns);  
B=zeros(nsd,nc);  
C=zeros(no,ns);  
D=zeros(no,nc);  
% compute system and output matrices  
for k=1:ns  
    % init state perturbation  
    x_p=x0;  
    % positive state perturbation  
    x_p(k)=x_p(k)+constants.DELXLIN(k);  
    % effect of positive perturbation on dynamics  
    [xdot_p1,y_p1]=feval(acfunction,0.,x_p,u0,constants);  
    % negative state perturbation  
    x_p(k)=x_p(k)-2*constants.DELXLIN(k);  
    % effect of negative perturbation on dynamics  
    [xdot_p2,y_p2]=feval(acfunction,0.,x_p,u0,constants);  
    % coefficient matrices  
    A(:,k)=(xdot_p1-xdot_p2)/(2*constants.DELXLIN(k));  
    C(:,k)=(y_p1-y_p2)/(2*constants.DELXLIN(k));  
end  
% compute control and feed-through matrices  
for k=1:nc  
    % init control input perturbation  
    u_p=u0;  
    % positive control input perturbation  
    u_p(k)=u_p(k)+constants.DELCLIN(k);  
    % effect of positive perturbation on dynamics  
    [xdot_p1,y_p1]=feval(acfunction,0.,x0,u_p,constants);  
    % negative control input perturbation  
    u_p(k)=u_p(k)-2*constants.DELCLIN(k);
```

```
% effect of negative perturbation on dynamics
[xdot_p2,y_p2]=feval(acfunction,0.,x0,u_p,constants);
% coefficient matrices
B(:,k)=(xdot_p1-xdot_p2)/(2*constants.DELCLIN(k));
D(:,k)=(y_p1-y_p2)/(2*constants.DELCLIN(k));
end

return
```

### 6.3 Trim Algorithm

This section describes the theoretical and implementation aspects of an algorithm to trim the rotorcraft flight dynamics. In aircraft and rotorcraft flight dynamics and control, it is desirable to be able to obtain the trim condition of a simulated aircraft so that linearized models of the dynamics can be derived at that condition, and used stability analysis and flight control design. The trim problem can be stated as follows. Given a prescribed function in time  $\dot{\mathbf{x}}_e$ , the goal is to solve for a subset of the state vector  $\mathbf{x}_s \in \mathcal{R}^p$ , with  $p \leq n$  and for a subset of the control vector  $\mathbf{u}_s \in \mathcal{R}^q$ , with  $q \leq m$  subject to Eq. (6.1a). The trim variables for this problem are thus given by augmenting the subset of the state vector with the control vector:

$$\Theta^T = [\mathbf{x}_s^T \ \mathbf{u}_s^T] \quad (6.12)$$

which leads to  $l+o$  trim variables. The constraints are given by the  $n$  state derivatives and  $l$  outputs, which can be set to arbitrary quantities known as trim targets:

$$\dot{\mathbf{x}}_e^T = [\dot{x}_1 \ \dot{x}_2 \ \dots \ \dot{x}_n] \quad (6.13)$$

Then, the trim problem to be solved is given by:

$$\mathbf{e}(\Theta) = \dot{\mathbf{x}}_e - \mathbf{f}(\mathbf{x}_s, \mathbf{u}_s) = \mathbf{0} \quad (6.14)$$

where  $\mathbf{e}(\Theta)$  is the error vector. It is clear that, to make the problem square such that a unique solution exists, the number of trim variables must be equal to that of the constraints (*i.e.*,  $l+o=n$ ). It follows that  $n-l-o$  conditions still need to be specified. Note that if the  $m$  inputs are given and the corresponding equilibrium solution is required, then the problem in consideration becomes a closed system as  $o=0$  and  $l=n$ . On the other hand, in the case where one or more (possibly all) of the  $m$  control inputs are unknown, then each input is used to ensure some desired condition. For aerospace vehicles such as conventional fixed-wing aircraft and helicopters, for which the vehicle dynamics are invariant with respect to position and heading [FDF05], the position and heading can be arbitrarily assigned and removed from the vector of unknowns. Since these vehicles typically employ control about four axes (*i.e.*, roll, pitch, yaw, and heave) leading to four control inputs, fixing the three components of the zeroth harmonic of the position ( $x, y, z$ ) and heading ( $\psi$ ) at equilibrium leads to a square problem.

In practice this problem is solved iteratively, in that a candidate solution is refined over a series of computational steps until a convergence criteria is reached. Consider the candidate solution at iteration  $k$  of the algorithm,  $\Theta_k$ . One iteration of the algorithm begins with evaluating the cost function in Eq. (6.14). If the infinity norm of the cost function is less than an arbitrary tolerance (*i.e.*,  $\|\mathbf{e}_k\|_\infty$ ), then a solution is found. If not, the algorithm proceeds with linearizing the system about the candidate solution. More specifically, the function in Listing 6.1 is used to compute the system and control matrices at iteration  $k$  (*i.e.*,  $\mathbf{A}_k$  and  $\mathbf{B}_k$ ). These matrices are used to define the Jacobian matrix of the trimming algorithm:

$$\mathbf{J}_k = [\mathbf{A}_k \ \mathbf{B}_k] \quad (6.15)$$

where  $\mathbf{J}_k \in \mathbb{R}^{n \times (n+m)}$ . The  $m$  columns corresponding to those states and/or controls that are specified are truncated from the Jacobian matrix, leading to a modified Jacobian matrix  $\hat{\mathbf{J}}_k \in \mathbb{R}^{n \times n}$ . Next, the solution is updated using the Newton-Raphson method [Ben66]:

$$\hat{\Theta}_{k+1} = \Theta_k - \hat{\mathbf{J}}_k^{-1} \mathbf{e}_k \quad (6.16)$$

The next iteration of the algorithm then proceeds with this new candidate solution until the stopping criteria is met. An implementation of this algorithm in MATLAB® is shown in Listing 6.2.

Listing 6.2: Trimming routine.

```

function [x0trim,u0trim,itrim]=trimmer(aircraft,x0,u0,targ_des,
const)

% DESCRIPTION
% Trims simulation model.
%
% INPUT
% - aircraft: name of aircraft dynamic model
% - x0: guess to trim state vector
% - u0: guess to trim control input vector
% - targ_des: desired trim target vector
% - const: data structure with aircraft and trim properties
%
% OUTPUT
% - x0trim: trim state vector
% - u0trim: trim control input vector
% - itrim: flag for successful completion of trim
%           - 0: trim not achieved
%           - 1: trim achieved

% state scaling factors
XSCALE=const.XSCALE;
% indices of trim variables
TRIMVARS=const.TRIMVARS;
% indices of trim targets
TRIMTARG=const.TRIMTARG;
% number of states
NSTATES=const.NSTATES;
% number of controls
NCTRLS=const.NCTRLS;
% trim tolerance
trim_tol=const.trim_tol;
% maximum number of iterations
itmax=const.itmax;
% relaxation parameter for Newton-Raphson update
gamma=const.gamma_NR;
% initial state and control input guess
x0trim=x0;
u0trim=u0;

```

```
% initialize number of iterations
it=0;
% initialize error
err=100;
% trim aircraft
fprintf ('\nITERATION      TRIM ERROR\n')
while ((it<itmax)&&(err>trim_tol))
    % increment counter
    it=it+1;
    % aircfract fynamics
    xdot0=feval(aircraft,x0trim,u0trim,const);
    % target vector
    targvec=xdot0(TRIMTARG);
    % error on trim targets
    targ_err=targvec-targ_des;
    % norm infinity of error scaled by number of states
    err=max(abs(targ_err)./XSCALE(TRIMTARG))/NSTATES;
    % print iteration and error to screen
    fprintf ('\n%2.0f      %5.4f',it,err)
    % check whether error satisfies trim tolerance
    if (err>trim_tol)
        % linearize dynamics
        [A,B,C,D]=LinSim(aircraft,x0trim,u0trim,const);
        % compose Jacobian matrix
        Jac=[A B; C D];
        % evaluate only for trim targets and variables
        Jac=Jac(TRIMTARG,TRIMVARS);
        % vector of trim variables
        trimvec=[x0trim;u0trim];
        % Newton-Raphson update
        trimvec(TRIMVARS)=trimvec(TRIMVARS)-gamma*pinv(Jac)*
            targ_err;
        % state and control vectors update
        x0trim=trimvec(1:NSTATES);
        u0trim=trimvec(NSTATES+1:NSTATES+NCTRLS);
    end
end
% store info on whether trim was achieved or not
if err>trim_tol
    itrim=0;
else
    itrim=1;
end

return
```

### 6.3.1 Trim with Zero Sideslip

Let us first consider the case of trimmed flight in conditions including hover, forward flight, and coordinated turns, all of which with zero sideslip angle. Assume the nonlinear helicopter dynamics to have the following

states and control inputs:

$$\mathbf{x}^T = [\mathbf{x}_F^T \mathbf{x}_R^T \mathbf{x}_{TR}^T] \quad (6.17a)$$

$$\mathbf{u}^T = [\delta_{lat} \delta_{lon} \delta_{col} \delta_{ped}] \quad (6.17b)$$

where the fuselage and rotor states are given by:

$$\mathbf{x}_F^T = [u \ v \ w \ p \ q \ r \ \phi \ \theta \ \psi \ x \ y \ z] \quad (6.18a)$$

$$\mathbf{x}_R^T = [\boldsymbol{\beta}_M^T \dot{\boldsymbol{\beta}}_M^T \lambda_0 \ \lambda_{1s} \ \lambda_{1c} \ \psi_{MR}] \quad (6.18b)$$

$$\mathbf{x}_{TR} = \lambda_{0_{TR}} \quad (6.18c)$$

As such, the state vector has a dimension of  $n = 25$  whereas the control input vector has a dimension of  $m = 4$ . Suppose that the desired trim velocities in the heading frame are given by  $V_{x_{des}}$ ,  $V_{y_{des}}$ , and  $V_{z_{des}}$ . The heading frame is a vehicle-carried frame where the  $\mathbf{i}_h$  axis is aligned with the current aircraft heading, the  $\mathbf{j}_h$  axis points to the right, and the  $\mathbf{k}_h$  axis is positive up, and forming a left-handed orthogonal coordinate system. The following equation shows the rotation from body to the heading frame:

$$\begin{bmatrix} V_x \\ V_y \\ V_z \end{bmatrix} = \underbrace{\begin{bmatrix} \cos \theta & \sin \phi \sin \theta & \cos \phi \sin \theta \\ 0 & \cos \phi & -\sin \phi \\ \sin \theta & -\sin \phi \cos \theta & -\cos \phi \cos \theta \end{bmatrix}}_{\mathbf{T}_{b \rightarrow h}} \begin{bmatrix} u \\ v \\ w \end{bmatrix} \quad (6.19)$$

Additionally, suppose that the desired turn rate are is  $\dot{\psi}_{des}$ . Then, the trim targets shall be chosen as:

$$\dot{\mathbf{x}}_e^T = [\dot{u}_e \ \dot{v}_e \ \dot{w}_e \ \dot{p}_e \ \dot{q}_e \ \dot{r}_e \ \dot{\phi}_e \ \dot{\theta}_e \ \dot{\psi}_e \ \dot{x}_e \ \dot{y}_e \ \dot{z}_e \ \dot{\boldsymbol{\beta}}_{M_e}^T \ddot{\boldsymbol{\beta}}_{M_e}^T \dot{\lambda}_{0_e} \ \dot{\lambda}_{1c_e} \ \dot{\lambda}_{1s_e} \ \dot{\lambda}_{0_{TR_e}}] \quad (6.20)$$

Note that the time derivative of the blade azimuth angle  $\dot{\psi}_e$  is removed from the trim targets, yielding a total of  $n - 1 = 24$  trim targets. The trim targets shall be set as:

$$\dot{\psi}_e = \dot{\psi}_{des} \quad (6.21a)$$

$$\dot{x}_e = V_{x_{des}} \cos \psi_{des} - V_{y_{des}} \sin \psi_{des} \quad (6.21b)$$

$$\dot{y}_e = V_{x_{des}} \sin \psi_{des} + V_{y_{des}} \cos \psi_{des} \quad (6.21c)$$

$$\dot{z}_e = -V_{z_{des}} \quad (6.21d)$$

where the desired heading is given by:

$$\psi_{des} = \tan^{-1} \left( \frac{V_y}{V_x} \right) \quad (6.22)$$

All other trim targets shall be set to zero. The trim variables are chosen as:

$$\Theta^T = [u \ v \ w \ p \ q \ r \ \phi \ \theta \ \boldsymbol{\beta}_M^T \dot{\boldsymbol{\beta}}_M^T \lambda_0 \ \lambda_{1s} \ \lambda_{1c} \ \lambda_{0_{TR}} \ \delta_{lat} \ \delta_{lon} \ \delta_{col} \ \delta_{ped}] \quad (6.23)$$

Note that because the dynamics of the rotorcraft are invariant with respect to position and heading ( $x_e$ ,  $y_e$ ,  $z_e$ , and  $\psi_e$ ), these variables are prescribed and not included in the trim variables. Additionally, the rotor speed is set to the desired value (*i.e.*,  $\Omega_e = \Omega_{des}$ ) and also not included in the trim variables. This way, there are  $n - 1 = 24$  trim variable and  $n - 1 = 24$  constraints. It is important for the initial guess for the states and controls to be as accurate as possible to maximize the likelihood of convergence of the trim algorithm and to minimize the iterations needed for trim. As such, the initial guess for the state vector can be chosen as

follows:

$$u_0 = V_{x_{\text{des}}} \quad (6.24a)$$

$$v_0 = V_{y_{\text{des}}} \quad (6.24b)$$

$$w_0 = V_{z_{\text{des}}} \quad (6.24c)$$

$$q_0 = r_0 \tan \phi_0 \quad (6.24d)$$

$$r_0 = \frac{g}{V} \sin \phi_0 \quad (6.24e)$$

$$\phi_0 = \tan^{-1} \left( \frac{V}{g} \psi_{\text{des}} \right) \quad (6.24f)$$

$$\lambda_0 = \sqrt{\frac{C_T}{2}} \quad (6.24g)$$

$$\lambda_{0_{\text{TR}}} \approx 0.05 \quad (6.24h)$$

where  $V = \sqrt{V_{x_{\text{des}}}^2 + V_{y_{\text{des}}}^2 + V_{z_{\text{des}}}^2}$  is the desired absolute speed of the aircraft and where the initial guess for the pitch rate, yaw rate, and bank angle stem from turn compensation and turn compensation, which are discussed in a later chapter. All other states present in the trim variables shall be initialized to zero.

### 6.3.2 Trim with Zero Bank Angle

Typically, rotorcraft are trimmed with zero sideslip in low-speed flight and can be trimmed with either zero sideslip or zero bank angle in high-speed flight (*i.e.*, above approximately 40 to 60 kts). An example of this is clearly shown in the 1993 film Jurassic Park, in the “Journey to the Island” scene (<https://www.youtube.com/watch?v=vZZN9AVBS1I>). This scene depicts an Agusta A109 flying in high-speed forward flight with zero bank angle and some sideslip. Frames from the scene are shown in Fig. 6.1.



(a) Frame 1.



(b) Frame 2.



(c) Frame 3.



(d) Frame 4.

Figure 6.1: Agusta A109 in the “Journey to the Island” scene from the 1993 film Jurassic Park in trimmed flight with zero bank angle and some sideslip.

Differently from the trim with zero sideslip, the bank angle is prescribed (*i.e.*,  $\phi_e = 0$ ) and excluded from the trim variables, whereas the heading angle  $\psi_e$  is included in the trim variables. As such, the trim variables

become:

$$\Theta^T = [u \ v \ w \ p \ q \ r \ \theta \ \psi \ \boldsymbol{\beta}_M^T \ \dot{\boldsymbol{\beta}}_M^T \ \lambda_0 \ \lambda_{1s} \ \lambda_{1c} \ \lambda_{0_{TR}} \ \delta_{lat} \ \delta_{lon} \ \delta_{col} \ \delta_{ped}] \quad (6.25)$$

Note that the trim variables still have a size of  $n - 1 = 24$ . The trim targets remain the same as the case for zero sideslip ((6.26)). Figure 6.2 shows the trim attitude and pilot controls for a UH-60 helicopter at incremental speeds (from hover to 140 kts rectilinear flight) obtained with two trim strategies: zero sideslip and zero bank angle. It is worth noting that when trimming with zero bank angle at low speeds, the sideslip becomes large (Fig. 6.2a). In fact, trimming with zero bank angle at hover results in an infinite sideslip angle, which indicates that the sideslip angle is not effective as trim variable at low speed. This is why helicopters are trimmed with zero bank angle only above a certain speed. For a counterclockwise (CCW) rotor, the trim roll attitude at hover and low speed will be a left roll attitude. Conversely, helicopters with clockwise (CW) rotors (e.g., German helicopters) will have a right roll attitude at hover and low speed. It is also worth noting that the collective stick mimics the power/torque curve (Fig. 6.2b). These considerations are valid for conventional helicopter configurations with a main rotor and a tail rotor. However, counter-rotating coaxial or tiltrotor configurations are typically always trimmed with zero sideslip and zero bank angle, unless in presence of cross wind.

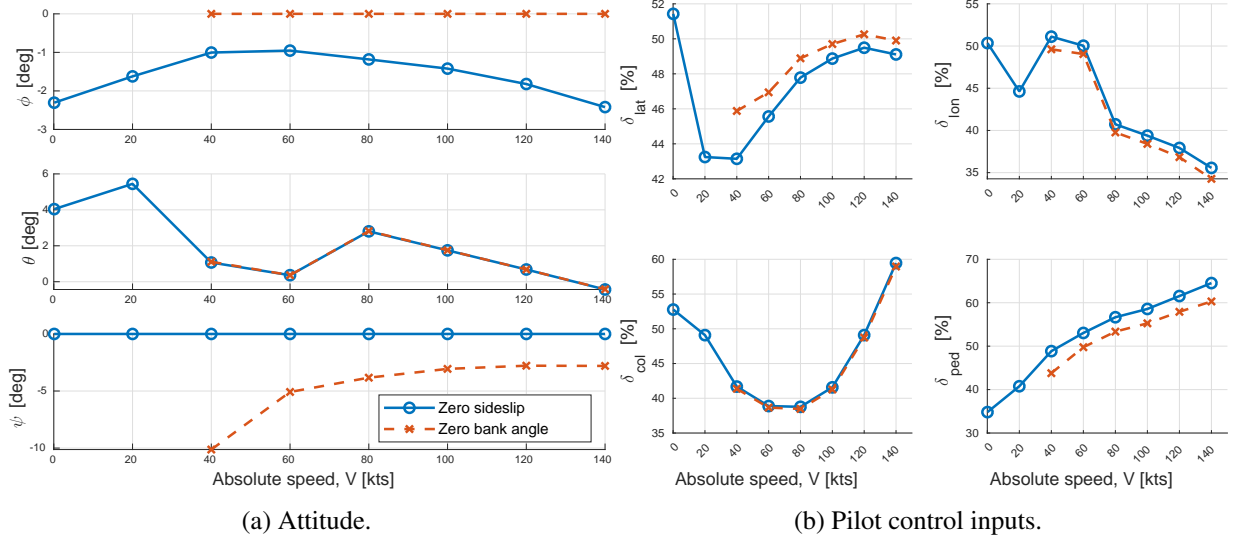


Figure 6.2: Trim variables for varying trim speed and trim strategy.

### 6.3.3 Trim in Autorotation

In autorotation, the desired vertical speed in the NED frame, *i.e.*,  $\dot{z}_e$  is removed from the trim targets. This is because the vertical speed is defined by the longitudinal speed  $V_x$  and main rotor angular speed  $\Omega$  that are assigned to the helicopter in autorotation. In autorotation, the main rotor angular speed is chosen as the nominal main rotor speed (*e.g.*, for a UH-60, the nominal rotor speed is  $\Omega = 27$  rad/s). Because the constraint on the vertical speed is dropped, another constraint must be added to keep the number of variables and constraints equal (*i.e.*,  $n - 1 = 24$ ). As such, the trim targets are chosen as follows:

$$\dot{\mathbf{x}}_e^T = [\dot{u}_e \ \dot{v}_e \ \dot{w}_e \ \dot{p}_e \ \dot{q}_e \ \dot{r}_e \ \dot{\phi}_e \ \dot{\theta}_e \ \dot{\psi}_e \ \dot{x}_e \ \dot{y}_e \ \dot{z}_e \ \dot{\boldsymbol{\beta}}_{M_e}^T \ \dot{\boldsymbol{\beta}}_{M_e}^T \ \dot{\lambda}_{0_e} \ \dot{\lambda}_{1c_e} \ \dot{\lambda}_{1s_e} \ \dot{\psi}_{MR_e} \ \dot{\lambda}_{0_{TR_e}}] \quad (6.26)$$

The trim targets are set to the following values:

$$\psi_e = \psi_{des} \quad (6.27a)$$

$$\dot{x}_e = V_{x_{des}} \cos \psi_{des} - V_{y_{des}} \sin \psi_{des} \quad (6.27b)$$

$$\dot{y}_e = V_{x_{des}} \sin \psi_{des} + V_{y_{des}} \cos \psi_{des} \quad (6.27c)$$

$$\dot{\psi}_{MR_e} = \Omega_{des} \quad (6.27d)$$

The trim variables are chosen as those for the trim with zero sideslip in Eq. (6.23). Figure 6.3 shows the trim variables for a UH-60 simulation trimmed at incremental speeds ranging from 0 to 100 kts at intervals of 20 kts. The aircraft weight chosen for this analysis is 17,000 lb. The trim attitude across this range of speeds is shown in Fig. 6.3a. Note that if the aircraft is trimmed with zero sideslip angle in powered level flight this would result in a non-zero bank angle. However, the trim bank angle in autorotation is zero because there is no torque exchanged between the main rotor and fuselage. Figure 6.3b shows the trim controls across the range of speeds in consideration. Notably, autorotation at low longitudinal speeds requires high aft longitudinal stick inputs. Finally, Fig. 6.3c shows the trim vertical speed with varying longitudinal speed. The vertical speed is shown to be minimum for a longitudinal speed equal to 60 kts. This minimum vertical speed is 37.5 ft/s, equivalent to about 2,250 ft/min.

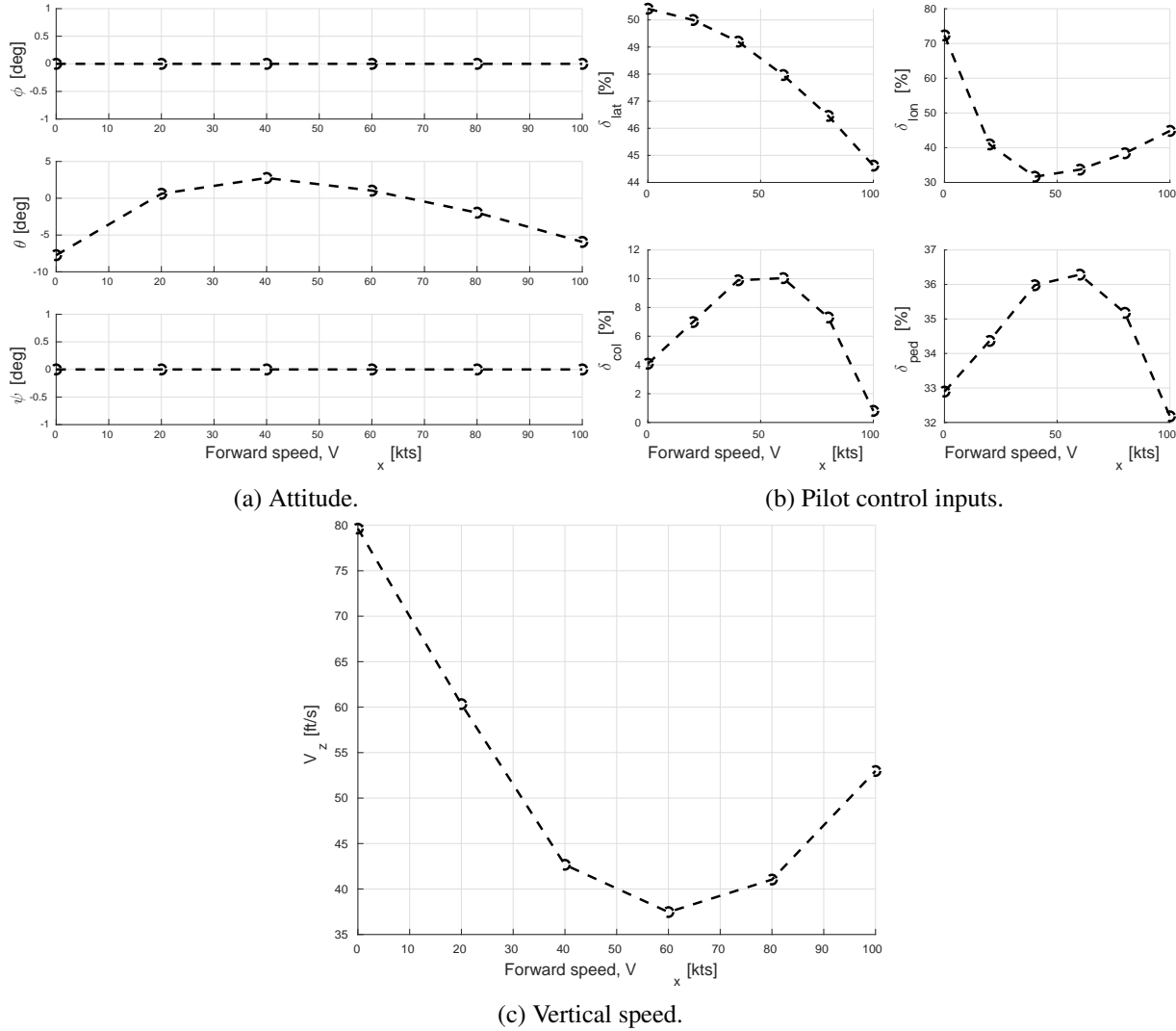


Figure 6.3: Trim variables for varying longitudinal speed in autorotation.

## 6.4 Model Order Reduction

Consider the rotorcraft model used in this chapter, with state and control vectors given in Eq. (6.17). If one linearizes this model, then the number of eigenvalues and eigenvectors would be equal to the number of states, *i.e.*,  $n = 25$ . To understand the dynamic properties of the rotorcraft, one must classify these modes. While the experienced rotorcraft flight dynamicist may be able to classify the modes based on the location of the eigenvalues in the complex plane, modes are typically classified by performing eigenvector analysis to see which states are most involved in each mode. Note that this requires particular care as states

have different units and must be scaled to comparable units across all states (*e.g.*, 1 deg is approximately equivalent to 1 ft, 1 deg/s to 1 ft/s, *etc.*). However, eigenvector analysis is challenging with 25 states. To gain a better understanding, the order of the model is typically reduced. Additionally, the full-order model cannot be used for control design, as this would require feeding back the entire state vector. This is because the measurement or estimation of states associated with the higher-order flap, lead-lag, torsion and inflow dynamics is impractical in real applications. To reduce the order of the linearized dynamics, a variety of methodology can be used. One approach is balanced realization and optimal Hankel norm methods (*balreal* function in MATLAB®). However, the method requires that a state transformation be applied, such that the states lose their physical meaning. This is not desirable in aerospace flight dynamics and control. Instead the analysis that follows will exploit some known properties of the rotorcraft system and apply some physical insight to the system. Two basic approaches will be used to reduce the number of states: truncation and residualization.

#### 6.4.1 Truncation

Truncation simply removes undesired states. The undesired states are removed by eliminating the corresponding rows and columns in the system matrix  $\mathbf{A}$ , and the corresponding rows in the control matrix  $\mathbf{B}$ . Truncation is justified in two cases: (i) when the states are completely or approximately decoupled from the states of interest in the system (*e.g.*, the position and heading states  $x$ ,  $y$ ,  $z$ , and  $\psi$ ); and (ii) when the states are approximately constant (*e.g.*, engine states once the rotor speed is assumed as constant). Because, as previously seen, the rotorcraft flight dynamics are invariant with respect to the position and heading states [FDF05] (*i.e.*, these states are decoupled). As such, these states are truncated yielding a linear system of  $n - 4 = 22$  states. Truncation is explained more in detail below through two examples.

##### Example 1: Truncation of a Decoupled Mode

Consider an example involving the following linear system:

$$\begin{bmatrix} \dot{x}_1 \\ \dot{x}_2 \\ \dot{x}_3 \end{bmatrix} = \begin{bmatrix} 0 & 1 & 0 \\ 0 & -2 & 1 \\ 0 & 1 & 3 \end{bmatrix} \begin{bmatrix} x_1 \\ x_2 \\ x_3 \end{bmatrix} + \begin{bmatrix} 0 \\ 0 \\ 1 \end{bmatrix} u \quad (6.28)$$

with eigenvalues  $\lambda_1 = -3.62$ ,  $\lambda_2 = -1.38$ , and  $\lambda_3 = 0$ . In this system, state  $x_1$  can be truncated because it is decoupled from the rest of the system. This is because  $\dot{x}_1 = x_2$  and, therefore,  $x_1 = \int x_2 dt$ , which results in eigenvalue  $\lambda_3 = 0$ . Truncating this state results in the following reduced-order system:

$$\begin{bmatrix} \dot{x}_2 \\ \dot{x}_3 \end{bmatrix} = \begin{bmatrix} -2 & 1 \\ 1 & 3 \end{bmatrix} \begin{bmatrix} x_2 \\ x_3 \end{bmatrix} + \begin{bmatrix} 0 \\ 1 \end{bmatrix} u \quad (6.29)$$

with eigenvalues  $\lambda_1 = -3.62$  and  $\lambda_2 = -1.38$ . These two decoupled systems are an exact approximation of the full-order system in that the eigenvalues are identical.

##### Example 2: Truncation of a Fast State

Consider another example where the system dynamics are given by:

$$\begin{bmatrix} \dot{x}_1 \\ \dot{x}_2 \\ \dot{x}_3 \end{bmatrix} = \begin{bmatrix} -5 & 0 & 0 \\ 1 & -2 & 1 \\ 1 & 1 & 3 \end{bmatrix} \begin{bmatrix} x_1 \\ x_2 \\ x_3 \end{bmatrix} + \begin{bmatrix} 0 \\ 0 \\ 1 \end{bmatrix} u \quad (6.30)$$

with eigenvalues  $\lambda_1 = -3.62$ ,  $\lambda_2 = -1.38$ , and  $\lambda_3 = -5$ . State  $x_1$  can be truncated in that it is a stable state that will converge to zero regardless of input or initial condition. In fact,  $\dot{x}_1 = -5x_1$  such that  $\lim_{t \rightarrow \infty} x_1 = 0$ . The corresponding eigenvalue is  $\lambda_3 = -5$ . In the long term response, the other state dynamics no longer depend on  $x_1$ , such that these dynamics can be expressed as:

$$\begin{bmatrix} \dot{x}_2 \\ \dot{x}_3 \end{bmatrix} = \begin{bmatrix} -2 & 1 \\ 1 & 3 \end{bmatrix} \begin{bmatrix} x_2 \\ x_3 \end{bmatrix} + \begin{bmatrix} 0 \\ 1 \end{bmatrix} u \quad (6.31)$$

where the eigenvalues are  $\lambda_1 = -3.62$  and  $\lambda_2 = -1.38$ . Again, these decoupled dynamics are an exact representation of the full order system as their eigenvalues are identical.

### 6.4.2 Singular Perturbation Theory

Singular perturbation theory assumes that some “fast” and stable states reach steady-state quicker than some other “slow” states, such that the derivative of the fast states is approximately zero while still these states change in time. Compared to balanced realization, singular perturbation theory is particularly convenient because it allows to retain the physical meaning of the states after the reduction. Consider the following set of differential equations:

$$\dot{\mathbf{x}} = \mathbf{f}(\mathbf{x}, \mathbf{z}, \mathbf{u}, t, \mu) \quad (6.32a)$$

$$\mu \dot{\mathbf{z}} = \mathbf{g}(\mathbf{x}, \mathbf{z}, \mathbf{u}, t, \mu) \quad (6.32b)$$

where:

$\mu > 0$  is a scalar,

$\mathbf{x}$  is a subset of the state vector of dimension  $n$ ,

$\mathbf{z}$  is a subset of the state vector of dimension  $m$ , and

$\mathbf{u}$  is the input vector of dimension  $r$ .

For  $0 < \mu \ll 1$  the dynamics of the second set of differential equations is substantially faster than that of the first set. Under this condition, one can assume that the dynamics of the second set of differential equations, when stable, reach steady-state quicker than the first set. Formally:

$$\mathbf{0} \approx \mathbf{g}(\bar{\mathbf{x}}, \bar{\mathbf{z}}, \bar{\mathbf{u}}, t, 0) \quad (6.33)$$

The substitution of a root of Eq. (6.33):

$$\bar{\mathbf{z}} = \phi(\bar{\mathbf{x}}, \bar{\mathbf{z}}, t) \quad (6.34)$$

into Eq. (6.32a) yields to a reduced-order model of order  $n$ :

$$\bar{\mathbf{x}} = \mathbf{f}[\bar{\mathbf{x}}, \phi(\bar{\mathbf{x}}, \bar{\mathbf{z}}, t), \bar{\mathbf{u}}, t, \mu] \equiv \tilde{\mathbf{f}}(\bar{\mathbf{x}}, \bar{\mathbf{u}}, t) \quad (6.35)$$

The reduced-order model represents slow and neglects fast phenomena of the system in Eq. 6.32. A more detailed derivation is found in [KOS76]. When this method is applied to a linear system, it is referred to as *residualization*. Because the rotorcraft dynamics typically features some stable states that are comparatively faster than other slower (and not necessarily stable) states (*e.g.*, flap, lead-lag, inflow states versus rigid-body states), the method above can be applied to the dynamic analysis of rotorcraft. In light of these results, the state vector of the rotorcraft dynamics can be partitioned into slow and fast components:

$$\mathbf{x} = \begin{bmatrix} \mathbf{x}_s \\ \mathbf{x}_f \end{bmatrix} \quad (6.36a)$$

Then, the linearized rotorcraft dynamics can be written as:

$$\begin{bmatrix} \dot{\mathbf{x}}_s \\ \dot{\mathbf{x}}_f \end{bmatrix} = \begin{bmatrix} \mathbf{A}_s & \mathbf{A}_{sf} \\ \mathbf{A}_{fs} & \mathbf{A}_f \end{bmatrix} \begin{bmatrix} \mathbf{x}_s \\ \mathbf{x}_f \end{bmatrix} + \begin{bmatrix} \mathbf{B}_s \\ \mathbf{B}_f \end{bmatrix} \mathbf{u} \quad (6.36b)$$

$$\mathbf{y} = [\mathbf{C}_s \quad \mathbf{C}_f] \begin{bmatrix} \mathbf{x}_s \\ \mathbf{x}_f \end{bmatrix} + \mathbf{D}\mathbf{u} \quad (6.36c)$$

Similarly to above, because the fast and stable states reach steady state more quickly than the slow states, the algebraic constraint  $\dot{\mathbf{x}}_f \approx 0$  is imposed. It follows that:

$$\mathbf{A}_{fs}\mathbf{x}_s + \mathbf{A}_{fs}\mathbf{x}_f + \mathbf{B}_f\mathbf{u} = \mathbf{0} \quad (6.37)$$

Solving for the fast states yields:

$$\mathbf{x}_f = \mathbf{A}_f^{-1}(-\mathbf{A}_{fs}\mathbf{x}_s - \mathbf{B}_f\mathbf{u}) \quad (6.38)$$

By substituting Eq. (6.38) into Eq. (6.36b), the slow states approximate dynamics is obtained:

$$\dot{\mathbf{x}}_s = \hat{\mathbf{A}}\mathbf{x}_s + \hat{\mathbf{B}}\mathbf{u} \quad (6.39)$$

where:

$$\hat{\mathbf{A}} = \mathbf{A}_s - \mathbf{A}_{sf}\mathbf{A}_f^{-1}\mathbf{A}_{fs} \quad (6.40a)$$

$$\hat{\mathbf{B}} = \mathbf{B}_s - \mathbf{A}_{sf}\mathbf{A}_f^{-1}\mathbf{B}_f \quad (6.40b)$$

By substituting Eq. (6.38) into Eq. (6.36c), the output equations as a function of the slow states are obtained:

$$\mathbf{y}_s = \hat{\mathbf{C}}\mathbf{x}_s + \hat{\mathbf{D}}\mathbf{u} \quad (6.41)$$

where:

$$\hat{\mathbf{C}} = \mathbf{C}_s - \mathbf{C}_f\mathbf{A}_f^{-1}\mathbf{A}_{fs} \quad (6.42a)$$

$$\hat{\mathbf{D}} = \mathbf{D} - \mathbf{C}_f\mathbf{A}_f^{-1}\mathbf{B}_f \quad (6.42b)$$

These are the dynamic equation of the reduced-order system obtained with residualization. Note that the  $\mathbf{A}_f$  matrix must be invertible. This is guaranteed if  $A_f$  is asymptotically stable, *i.e.*, all eigenvalues have their real part that is strictly negative. These concepts are illustrated through the example below.

### Code for residualization.

#### Example 3: Residualization

Consider an example involving the following linear system:

$$\begin{bmatrix} \dot{x}_1 \\ \dot{x}_2 \\ \dot{x}_3 \end{bmatrix} = \begin{bmatrix} -30 & 1 & 0 \\ 6 & -2 & 1 \\ 6 & 1 & -3 \end{bmatrix} \begin{bmatrix} x_1 \\ x_2 \\ x_3 \end{bmatrix} + \begin{bmatrix} 1 \\ 0 \\ 0 \end{bmatrix} u \quad (6.43)$$

with eigenvalues  $\lambda_1 = -30.4$ ,  $\lambda_2 = -3.6$ , and  $\lambda_3 = -0.987$ . In this system,  $x_1$  can be eliminated via residualization. This is because there is a significant time scale difference in the eigenvalues. Note that the dynamics of state  $x_1$  are dominated by the diagonal term  $-30$ , which is substantiated by the fact that one of the eigenvalues is very close to this value. Thus,  $x_1$  can be assumed to reach steady-state quicker than the other system dynamics following any perturbation on the system:

$$\dot{x}_1 = -30x_1 + x_2 + x_3 + u \approx 0 \quad (6.44)$$

Solving for state  $x_1$  yields the following algebraic constraint:

$$x_1 = \frac{1}{30} (x_2 + x_3 + 30u) \quad (6.45)$$

Substituting the equation above in the remaining system dynamics yields (after some algebraic manipulations):

$$\begin{bmatrix} \dot{x}_1 \\ \dot{x}_2 \end{bmatrix} = \begin{bmatrix} -1.8 & 1.2 \\ 1.2 & -2.8 \end{bmatrix} \begin{bmatrix} x_1 \\ x_2 \end{bmatrix} + \begin{bmatrix} 1 \\ 1 \end{bmatrix} u \quad (6.46)$$

The eigenvalues of this reduced-order approximate system are  $\lambda_1 = -1$  and  $\lambda_2 = -3.6$ . These eigenvalues are close to those of the full-order system but without the fast dynamics.

### 8-State Model

Consider now an example involving the dynamics of a helicopter model similar to the General Helicopter (GenHel) model [Hor19; How80]. This model is representative of a utility helicopter similar to a UH-60. The model contains a 6-DoF rigid-body dynamic model of the fuselage, nonlinear aerodynamic lookup tables for the fuselage, rotor blades, and empennage, rigid flap and lead-lag rotor blade dynamics, a three-state Pitt-Peters inflow model [PP80], and a Bailey tail rotor model [Bai41]. The state and control vectors are:

$$\mathbf{x}^T = \left[ u \ v \ w \ p \ q \ r \ \phi \ \theta \ \psi \ x \ y \ z \ \boldsymbol{\beta}_M^T \ \dot{\boldsymbol{\beta}}_M^T \ \boldsymbol{\zeta}_M^T \ \dot{\boldsymbol{\zeta}}_M^T \ \lambda_0 \ \lambda_{1c} \ \lambda_{1s} \ \psi_{MR} \ \lambda_{0T} \right] \quad (6.47a)$$

$$\mathbf{u}^T = \left[ \delta_{lat} \ \delta_{lon} \ \delta_{col} \ \delta_{ped} \right] \quad (6.47b)$$

The state vector has dimension of  $n = 33$  whereas the control input vector has dimension  $m = 4$ . The states can be conveniently partitioned in fuselage, rotor, and tail rotor states as follows:

$$\mathbf{x}_F^T = \left[ u \ v \ w \ p \ q \ r \ \phi \ \theta \ \psi \ x \ y \ z \right] \quad (6.48a)$$

$$\mathbf{x}_R^T = \left[ \boldsymbol{\beta}_M^T \ \dot{\boldsymbol{\beta}}_M^T \ \boldsymbol{\zeta}_M^T \ \dot{\boldsymbol{\zeta}}_M^T \ \lambda_0 \ \lambda_{1c} \ \lambda_{1s} \ \psi_{MR} \right] \quad (6.48b)$$

$$\mathbf{x}_{TR}^T = \left[ \lambda_{0T} \right] \quad (6.48c)$$

$$(6.48d)$$

The rotor and tail rotor states are all stable and significantly faster than the fuselage states. Thus, an 8-state reduced order model is found by applying residualization:

$$\mathbf{A}_8 = \mathbf{A}_s - \mathbf{A}_{sf} \mathbf{A}_f^{-1} \mathbf{A}_{fs} \quad (6.49a)$$

$$\mathbf{B}_8 = \mathbf{B}_s - \mathbf{A}_{sf} \mathbf{A}_f^{-1} \mathbf{B}_f \quad (6.49b)$$

where the slow states are chosen as the rigid-body states whereas the fast states can be chosen as the main rotor and tail rotor states:

$$\mathbf{x}_s^T = \left[ u \ v \ w \ p \ q \ r \ \phi \ \theta \right] \quad (6.50a)$$

$$\mathbf{x}_f^T = \left[ \mathbf{x}_R^T \ \mathbf{x}_{TR}^T \right] \quad (6.50b)$$

Note that the position and heading states were truncated from the slow state vector as these are decoupled from the rest of the rotorcraft dynamics. The general form of the 8-state model is the following:

$$\mathbf{A}_8 = \begin{bmatrix} X_u & X_v + r_e & X_w - q_e & X_p & X_q - w_e \\ Y_u - r_e & Y_v & Y_w + p_e & Y_p + w_e & Y_q \\ Z_u + q_e & Z_v - p_e & Z_w & Z_p - v_e & Z_q + u_e \\ L'_u & L'_v & L'_w & L'_p + k_1 q_e & L'_q + k_1 p_e - k_2 r_e \\ M_u & M_v & M_w & M_p - 2p_e \frac{I_{xz}}{I_{yy}} - r_e \frac{(I_{xx} - I_{zz})}{I_{yy}} & M_q \\ N'_u & N'_v & N'_w & N'_p + k_3 q_e & N'_q - k_1 r_e + k_3 p_e \\ 0 & 0 & 0 & 1 & \sin \phi_e \tan \theta_e \\ 0 & 0 & 0 & 0 & \cos \phi_e \end{bmatrix} \quad (6.51a)$$

$$\mathbf{B}_8 = \begin{bmatrix} X_{\delta_{\text{lat}}} & X_{\delta_{\text{ion}}} & X_{\delta_{\text{col}}} & X_{\delta_{\text{ped}}} \\ Y_{\delta_{\text{lat}}} & Y_{\delta_{\text{ion}}} & Y_{\delta_{\text{col}}} & Y_{\delta_{\text{ped}}} \\ Z_{\delta_{\text{lat}}} & Z_{\delta_{\text{ion}}} & Z_{\delta_{\text{col}}} & Z_{\delta_{\text{ped}}} \\ L'_{\delta_{\text{lat}}} & L'_{\delta_{\text{ion}}} & L'_{\delta_{\text{col}}} & L'_{\delta_{\text{ped}}} \\ M_{\delta_{\text{lat}}} & M_{\delta_{\text{ion}}} & M_{\delta_{\text{col}}} & M_{\delta_{\text{ped}}} \\ N'_{\delta_{\text{lat}}} & N'_{\delta_{\text{ion}}} & N'_{\delta_{\text{col}}} & N'_{\delta_{\text{ped}}} \\ 0 & 0 & 0 & 0 \\ 0 & 0 & 0 & 0 \end{bmatrix} \quad (6.51b)$$

where:

$$L'_p = \frac{I_{zz}}{I_{xx}I_{zz} - I_{xz}^2} L_p + \frac{I_{xz}}{I_{xx}I_{zz} - I_{xz}^2} N_p \quad (6.52a)$$

$$N'_r = \frac{I_{xz}}{I_{xx}I_{zz} - I_{xz}^2} L_r + \frac{I_{xx}}{I_{xx}I_{zz} - I_{xz}^2} N_r \quad (6.52b)$$

Similar equations can be derived for the roll and yaw moment stability and control derivatives with respect to other translational and rotational velocities (e.g.,  $L'_v$ ,  $L'_q$ ,  $L'_{\theta_0}$  etc.). The constants  $k_1$ ,  $k_2$ , and  $k_3$  are given by:

$$k_1 = \frac{I_{xz}(I_{zz} + I_{xx} - I_{yy})}{I_{xx}I_{zz} - I_{xz}^2} \quad (6.53a)$$

$$k_2 = \frac{I_{zz}(I_{zz} - I_{yy})}{I_{xx}I_{zz} - I_{xz}^2} \quad (6.53b)$$

$$k_3 = \frac{I_{xx}(I_{yy} - I_{xx})}{I_{xx}I_{zz} - I_{xz}^2} \quad (6.53c)$$

### 10-State Model

In the next section, we will see that the 8-state model is only accurate up to about 3 rad/s. For basic flight control design and handling qualities analysis, the interest is mainly in the frequency range of 0.2 to 2 Hz (approximately 1 to 12.5 rad/s). Thus, the 8-state model may not be accurate enough for this kind of analysis. To improve the high-frequency matching at least up to 12.5 rad/s, consider deriving a reduced-order model

that accounts for the coupled roll and regressive flap model. Note that this pair of eigenvalues was eliminated with the 8-state model. To do so, one needs to retain at least two more states to add additional eigenvalues for the regressive flap mode. This can only be done by retaining both the lateral and longitudinal flapping states, *i.e.*, these states become part of the slow dynamics. As such, the 10-state model is obtained by applying residualization:

$$\mathbf{A}_{10} = \mathbf{A}_s - \mathbf{A}_{sf}\mathbf{A}_f^{-1}\mathbf{A}_{fs} \quad (6.54a)$$

$$\mathbf{B}_{10} = \mathbf{B}_s - \mathbf{A}_{sf}\mathbf{A}_f^{-1}\mathbf{B}_f \quad (6.54b)$$

with the slow and fast states chosen as follows:

$$\mathbf{x}_s^T = [u \ v \ w \ p \ q \ r \ \phi \ \theta \ \beta_{1c} \ \beta_{1s}] \quad (6.55a)$$

$$\mathbf{x}_f^T = [\beta_0 \ \beta_{0d} \ \dot{\beta}_M^T \ \zeta_M^T \ \dot{\zeta}_M^T \ \lambda_0 \ \lambda_{1c} \ \lambda_{1s} \ \psi_{MR} \ \lambda_{0T}] \quad (6.55b)$$

The structure of the 10-state model is the following:

$$\mathbf{A}_{10} = \left[ \begin{array}{cccccc|cc|cc} & & & & & & & X_{\beta_{1c}} & X_{\beta_{1s}} \\ & & & & & & & Y_{\beta_{1c}} & Y_{\beta_{1s}} \\ & & & & & & & Z_{\beta_{1c}} & Z_{\beta_{1s}} \\ & & & & & & & L_{\beta_{1c}} & L_{\beta_{1s}} \\ & & & & & & & M_{\beta_{1c}} & M_{\beta_{1s}} \\ & & & & & & & N_{\beta_{1c}} & N_{\beta_{1s}} \\ \text{These terms will look very different from the 8-state model} & & & & & & & 0 & 0 \\ 0 & 0 & 0 & 1 & \sin \phi_e \tan \phi_e & \cos \phi_e \tan \phi_e & 0 & 0 & 0 & 0 \\ 0 & 0 & 0 & 0 & \cos \phi_e & -\sin \phi_e & 0 & 0 & 0 & 0 \\ \hline & & & \approx 1 & & & & 0 & 0 & -\frac{1}{\tau_f} \\ & & & & & & & 0 & 0 & -\frac{1}{\tau_f} \\ \end{array} \right] \quad (6.56a)$$

$$\mathbf{B}_{10} = \left[ \begin{array}{cccc} & & & \\ & & & \\ & & & \\ & & & \\ & & & \\ \text{These terms will look very different from the 8-state model} & & & \\ 0 & 0 & 0 & 0 \\ 0 & 0 & 0 & 0 \\ \hline R_{\delta_{ion}} \\ R_{\delta_{lat}} \end{array} \right] \quad (6.56b)$$

The 10-state model is quite accurate for modeling the roll and pitch rate responses out to 20 rad/s. The 10-state model is effectively representing the lateral and longitudinal flapping as first order. Note that many of the terms were the stability and control derivatives will be very different from the 8-state model. In the full-order model, the second-order lateral and longitudinal flapping dynamics are inherently coupled. But when the first-order approximation for the flapping dynamics is used, lateral and longitudinal flapping are approximately decoupled. Let us focus on the roll dynamics and assume that the roll rate and lateral flapping can be decoupled from the rest of the model:

$$\dot{p} = L_p p + L_{\beta_{1s}} \beta_{1s} \quad (6.57a)$$

$$\dot{\beta}_{1s} = p - \frac{1}{\tau_f} \beta_{1s} + R_{\delta_{lat}} \delta_{lat} \quad (6.57b)$$

The lateral flapping state can be thought of as lateral tilt of the rotor disk, where the effect of roll rate on lateral tilt of the rotor disk is purely gyroscopic precession. This is why there is a coefficient of 1 in front of roll rate in the flapping equation. The lateral tilt is well-damped, where the damping is described by the flapping time constant  $\tau_f$ . Note that roll control is only generated indirectly through tilting of the rotor disk (so there is no roll control derivative  $L_{\delta_{lat}}$ ). The roll damping term  $L_p$  is only from airframe and tail rotor effects. The roll damping from the main rotor comes indirectly through tilting of the rotor disk.

### 6.4.3 Linear Models Verification

The first step of the verification is to compare the linearized models, and especially the full-order linearized model, with flight test data. To provide an example of a verification process, the linearized models are compared to JUH-60A Black Hawk (Fig. 6.4) flight test data at 80 kts level flight. The comparison is done at 80 kts since flight test data is available to the authors only at suchthat condition. The flight test data was originally collected for the U.S. Army/NASA Rotorcraft Aircrew Systems Concepts Airborne Laboratory (RASCAL) program.



Figure 6.4: JUH-60A Black Hawk used in the U.S. Army/NASA Rotorcraft Aircrew Systems Concepts Airborne Laboratory (RASCAL) program.

Comparison with flight test data is performed to ensure that the simulation model is representative of an actual H-60 aircraft. Figure 6.5 shows a comparison of lateral and longitudinal on-axis frequency responses between flight test data and linearized models. For high coherence values (greater than 0.6 [Tis+17]) the frequency responses of the full-order linearized model generally match fairly well the flight test data. The frequency responses of the reduced-order models match closely the full-order model in the low frequency range. The 8-state model shows good accuracy up to about 4 rad/s. The 10-state model shows good accuracy up to about 10 rad/s. This is because the 10-state model incorporates the flapping states and therefore is able to predict the dynamics of the regressive flap mode. Both reduced-order models have reduced phase delay when compared to the full-order model and flight test data. This is due to the absence of states to model the actuator dynamics in the reduced order models. Further, the 8-state model has reduced phase delay when compared to the 10-state model. This is because the 8-state model lacks the rotor dynamics and is unable to predict the delay in the response caused by rotor flapping.

For frequencies corresponding with high coherence values, the magnitude and phase corresponding to the error of each on-axis frequency response with respect to the flight-test data are plotted to provide further insight on the similarities/discrepancies between the linearized simulation model and the model identified from JUH-60A flight test data (Fig. 6.6). The plot also includes the mismatch boundaries defined in MIL-STD-1797 [Ano97]. These boundaries represent the Maximum Unnoticeable Added Dynamics (MUAD) limits. When these limits are exceeded, a pilot can typically detect discrepancies between two aircraft modes being compared [Tis+17]. The linearized models roll rate response to lateral stick inputs, shown in Fig. 6.6a, falls within the MUAD boundaries at very low frequencies as well as frequencies greater than approximately 1 rad/s. Lateral flapping responses to lateral stick inputs, shown in Fig. 6.6b, fall within the MUAD boundaries for frequencies higher than approximately 2 rad/s. The pitch rate response to longitudinal cyclic inputs, shown in Fig. 6.6c, never falls within the MUAD boundaries, although it is close to the lower boundary for frequencies grater than 1 rad/s. The mismatch is due to a slight gain difference that can be easily compensated for. Notably, the phase error is within the boundaries across the frequency range of interest. On the other hand, the longitudinal cyclic response to longitudinal stick inputs, shown in Fig. 6.6d, indicates that this response falls within the boundaries across all frequencies of interest. It is worth noting

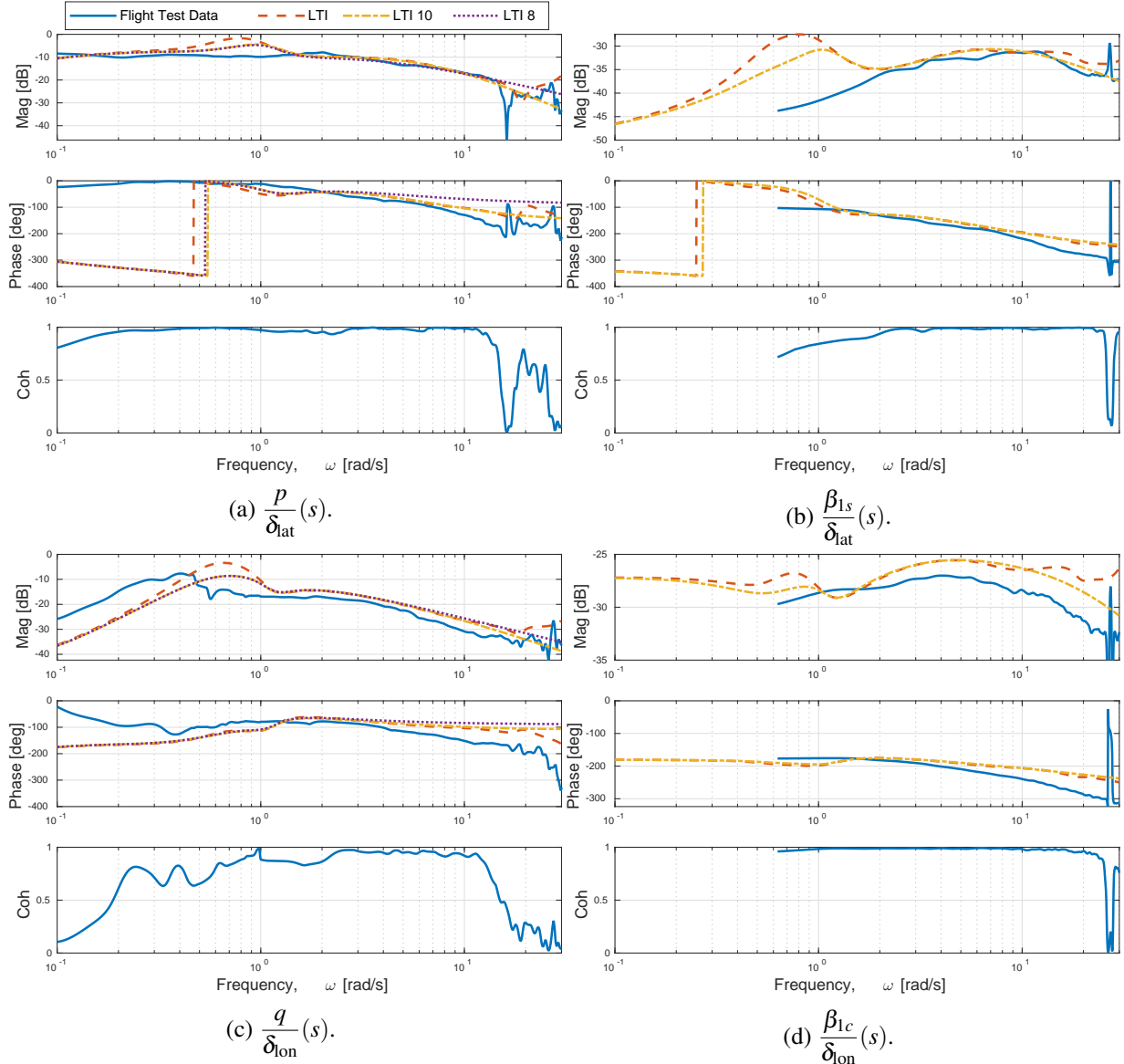


Figure 6.5: On-axis frequency responses: comparison between flight-test data and linearized models.

While the magnitude error can be significant and fall out of the boundaries, the phase error typically lies within the boundaries across all frequencies. Possible mismatch between the simulation model and identified data responses can be attributed to the fact that the simulation model is reflective of a general H-60 helicopter and was not tuned to be representative of a JUH-60A configuration. It is also worth noting that the full-order and 10-state models provide lower errors than the 8-state model for frequencies higher than approximately 4 rad/s. The error from the low-order models is also generally similar to that of the full-order system, indicating that the reduced-order models provide a reasonable approximation of the full-order linearized system.

Consider a cost function that quantifies the error between two frequency responses [TR12]:

$$J = \frac{20}{n_\omega} \sum_{\omega_1}^{\omega_{n_\omega}} W_g [W_g(|T_1| - |T_2|)^2 + W_p(\angle T_1 - \angle T_2)^2] \quad (6.58)$$

where:

- $n_\omega$  is the number of frequency points,
- $\omega_1$  and  $\omega_{n_\omega}$  are the upper and lower frequencies of fit,
- $T_1$  and  $T_2$  are the two frequency responses, and

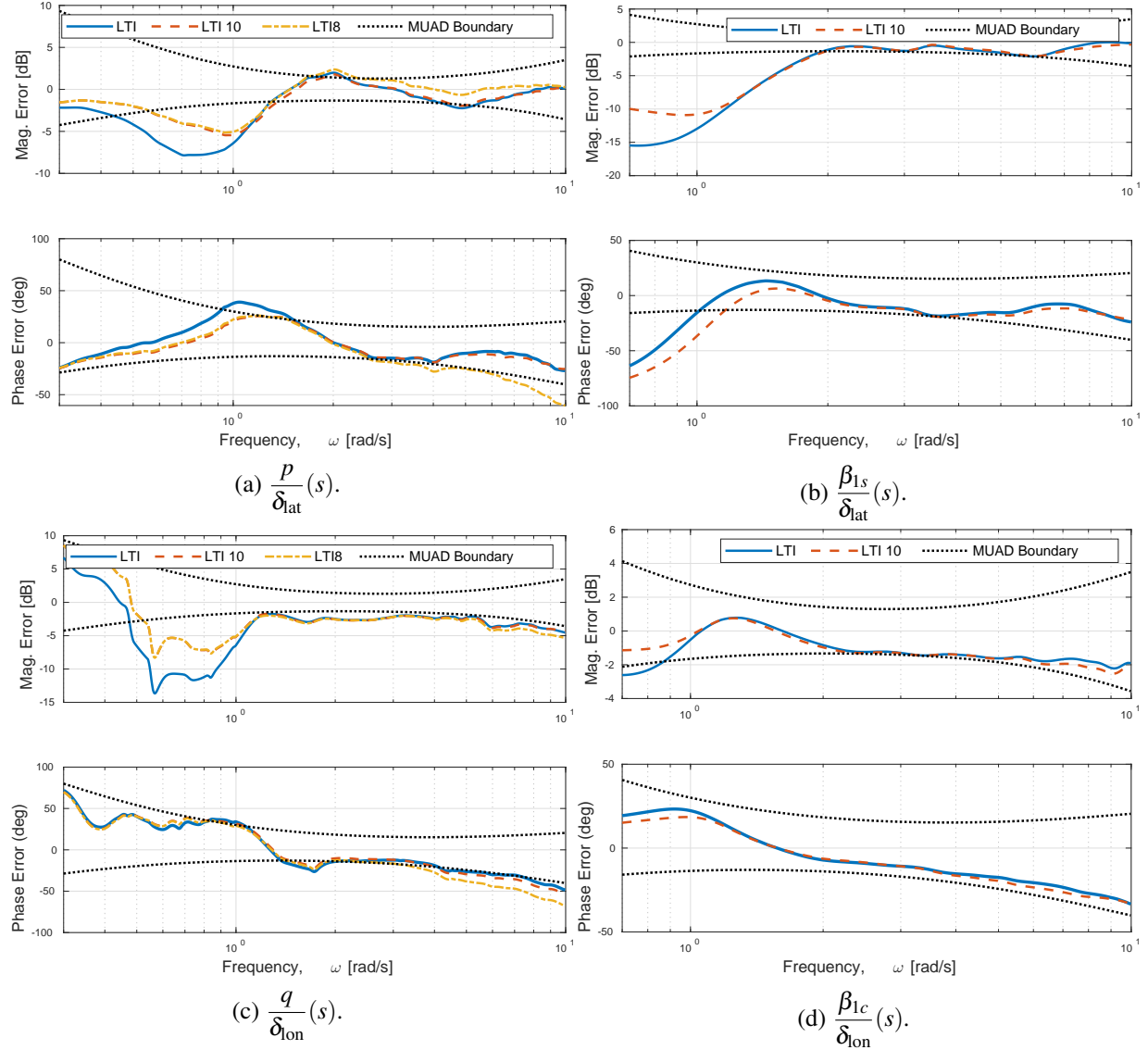


Figure 6.6: On-axis frequency responses: error between flight-test data and linearized models.

$W_\gamma$ ,  $W_g$ , and  $W_p$  are weighting functions.

More specifically,  $W_\gamma$  is a weighting function dependent on the value of the coherence function at each frequency point  $\omega_1, \omega_2, \dots, \omega_{n_\omega}$  and for each frequency response pair  $T_l$ :

$$W_\gamma(\omega) = \left[ 1.58 \left( 1 - e^{-\gamma_{xy}^2} \right) \right]^2 \quad (6.59)$$

where  $\gamma_{xy}^2$  is the coherence function, thereby emphasizing the most reliable data.  $W_g$  and  $W_p$  are the relative weights for magnitude and phase squared errors:

$$W_g = 1.0 \quad (6.60a)$$

$$W_p = 0.01745 \quad (6.60b)$$

This cost function is used to quantify the relative error between each on-axis frequency response of the two models in consideration. An average cost function across all cost functions for each individual frequency response of  $J \leq 100$  generally reflects an acceptable level of accuracy for flight dynamics modeling, whereas a cost function of  $J \leq 50$  can be expected to produce a model that is nearly indistinguishable from the original in the frequency and time domain. However, some of the individual cost functions can reach  $J \leq 200$  without resulting in a noticeable loss of overall predictive accuracy [TR12]. The individual cost functions

Table 6.1: Individual cost functions for the on-axis frequency responses of the full-order model as compared to the identified model from flight-test data.

| Frequency Response               | Frequency Range [rad/s] | Cost   |
|----------------------------------|-------------------------|--------|
| $p/\delta_{\text{lat}}$          | 0.3-10                  | 188.40 |
| $q/\delta_{\text{lon}}$          | 0.3-10                  | 577.17 |
| $\beta_{1s}/\delta_{\text{lat}}$ | 0.7-10                  | 667.38 |
| $\beta_{1c}/\delta_{\text{lon}}$ | 0.7-20                  | 143.11 |

Table 6.2: Individual cost functions for the on-axis frequency responses of the reduced-order models as compared to the full-order model.

| Frequency Response               | Frequency Range [rad/s] | Cost (LTI - LTI 8) | Cost (LTI - LTI 10) |
|----------------------------------|-------------------------|--------------------|---------------------|
| $p/\delta_{\text{lat}}$          | 0.3-10                  | 82.14              | 9.01                |
| $q/\delta_{\text{lon}}$          | 0.3-10                  | 164.02             | 19.30               |
| $\beta_{1s}/\delta_{\text{lat}}$ | 0.3-10                  | -                  | 65.42               |
| $\beta_{1c}/\delta_{\text{lon}}$ | 0.3-10                  | -                  | 5.24                |

corresponding to the comparison of the full-order model with the model identified from flight-test data are reported in Table 6.1 and substantiate the previous observations, *i.e.*, there is some mismatch between the simulation model and the flight-test data. Table 6.2 shows the cost function for the relative error between full-order and the reduced-order models. In this table, it is shown how both the 8- and 10-state models provide acceptable levels of accuracy compared to the full-order model. Additionally, the 10-state model is shown to provide a more accurate representation of the full-order model when compared to the 8-state model due to the inclusion of the flapping states. In fact, the 10-state model is nearly indistinguishable from the full-order model for frequencies up to 10 rad/s, whereas the accuracy of the 8-state model is limited up to 4 rad/s.

The fidelity of the reduced-order models with respect to the full-order model is also assessed by comparing their eigenvalues of these systems. While eigenvalues are discussed more in detail in the next chapter, it is still worthwhile to consider these quantities in the verification process. Figure 6.7 shows an enlarged eigenvalue plot. Many of the low frequency eigenvalues of reduced-order models are nearly overlaying the full-order model eigenvalues (Fig. 6.7a). The four integrator states at the origin disappear, because the associated states were removed, but this has no effect on the dynamics of interest (Fig. 6.7c). The most significant discrepancy is in the coupled roll mode / regressive flapping dynamics. The 8-state model has no flapping dynamics, so one real and two complex eigenvalues are replaced by a single real eigenvalue (Fig. 6.7b). The 10-state model has regressive flapping eigenvalues that are somewhat different from those of the full-order model. This is because there is some significant coupling between regressive flapping and aircraft roll dynamics. Nonetheless, both the 8- and 10-state model are not bad approximations.

## 6.5 Review of Numerical Integration Methods

Numerical integration is necessary to solve ordinary differential equations (ODEs) for which a closed-form solution does not exist. Generally, the equations of motion of a rotorcraft, may these equations correspond to the rigid-body dynamics only, to the coupled rigid-body and rotor dynamics, or to even higher-order models, do not have a closed-form solution. In this section, a select number of integration methods that are common in aerospace simulation is presented. To begin the review of numerical integration methods, consider a nonlinear time-invariant dynamics representative of the flight dynamics of a rotorcraft:

$$\dot{\mathbf{x}} = \mathbf{f}(\mathbf{x}, \mathbf{u}) \quad (6.61)$$

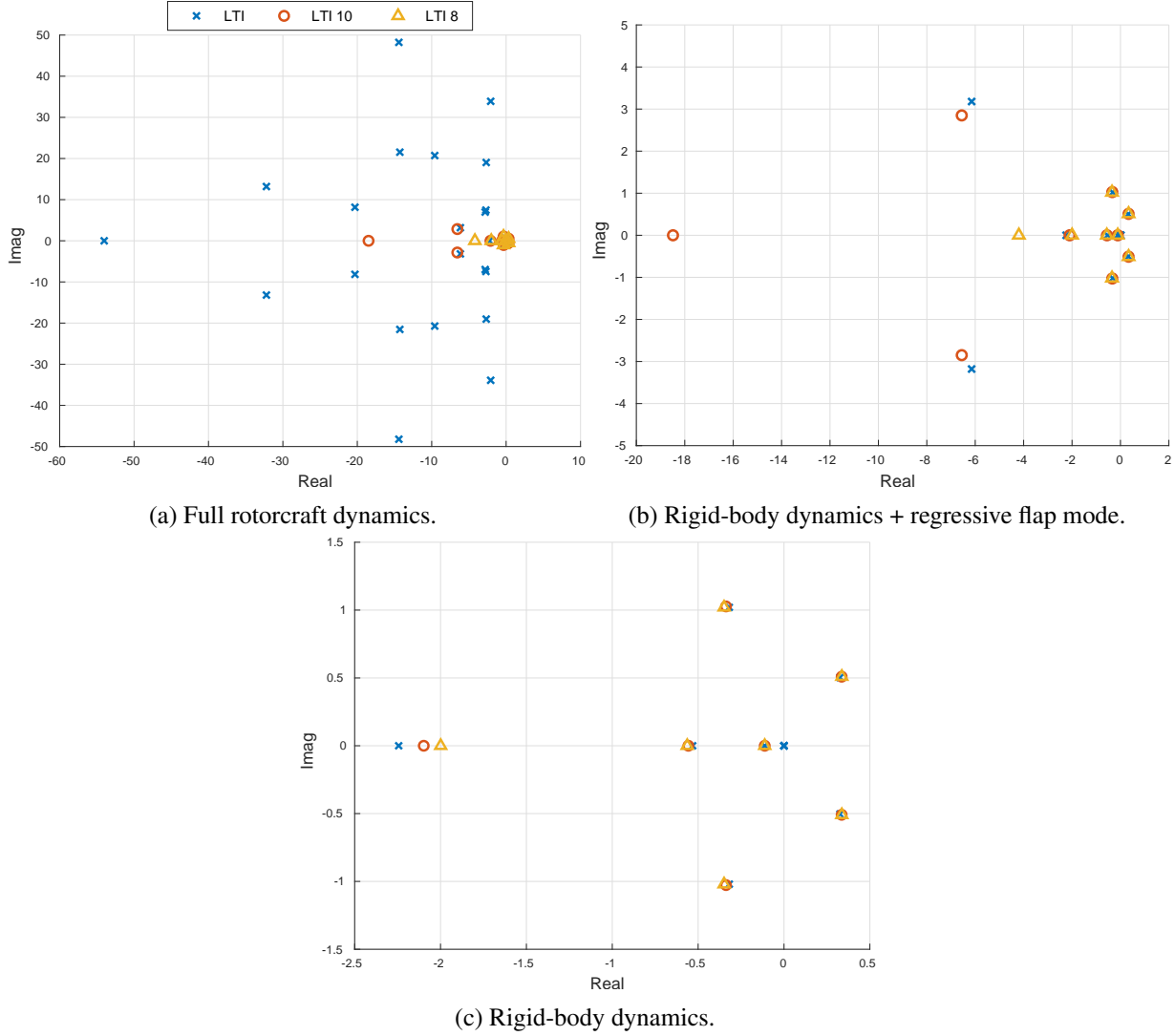


Figure 6.7: Eigenvalues of the linearized models.

where  $\mathbf{x} = \mathbf{x}(t) \in \mathcal{R}^n$  and  $\mathbf{u} = \mathbf{u}(t) \in \mathcal{R}^m$ . If  $\mathbf{f}$  is continuous with respect to time, then the solution satisfies:

$$\mathbf{x}(t) - \mathbf{x}_0 = \int_{t_0}^t \mathbf{f}(\mathbf{x}(\tau), \mathbf{u}(\tau)) d\tau \quad (6.62)$$

Numerical integration methods to approximate the integral above are discussed as follows.

### 6.5.1 Forward and Backward Euler

Suppose integration is performed in the time interval  $I = (t, t_0)$  and that the time interval is discretized in increments equal to  $h$ . Then, each time step can be written as  $t_n = t_0 + nh$ , where  $n = 1, \dots, N_h$ .  $N_h$  is the total number of time steps. Then, the system dynamics at time step  $n$  can be approximated by:

$$\dot{\mathbf{x}}_n = \mathbf{f}_n \approx \frac{\mathbf{x}_{n+1} - \mathbf{x}_n}{h} \quad (6.63)$$

where  $\mathbf{x}_n = \mathbf{x}(t_n)$ ,  $\mathbf{x}_{n+1} = \mathbf{x}(t_{n+1})$ ,  $f_n = (\mathbf{x}_n, \mathbf{u}_n)$ , and  $\mathbf{u}_n = \mathbf{u}(t_n)$ . Solving for the state vector at time step  $n+1$  yields:

$$\boxed{\mathbf{x}_{n+1} = \mathbf{x}_n + h\mathbf{f}_n} \quad (6.64)$$

This method has the following properties:

- One-step method:  $\forall n \geq 0$ ,  $\mathbf{x}_{n+1}$  depends only on  $\mathbf{x}_n$ .
- Explicit method:  $\mathbf{x}_{n+1}$  can be computed directly in terms of previous values of  $\mathbf{x}_k$ , for  $k \leq n$ .
- 1-stage method: Only requires a single evaluation of  $f$ .

### 6.5.2 Backward Euler

Consider the same setup as before. An alternative way to compute the state dynamics at time step  $t_{n+1}$  is:

$$\dot{\mathbf{x}}_{n+1} = \mathbf{f}_{n+1} \approx \frac{\mathbf{x} + n + 1 - \mathbf{x}_n}{h} \quad (6.65)$$

where  $\mathbf{f}_{n+1} = \mathbf{f}(\mathbf{x}_{n+1}, \mathbf{u}_{n+1})$  and  $\mathbf{u}_{n+1} = \mathbf{u}(t_{n+1})$ . Solving for the state vector at  $t_{n+1}$  yields:

$$\boxed{\mathbf{x}_{n+1} = \mathbf{x}_n + h\mathbf{f}_{n+1}} \quad (6.66)$$

The properties of this method are the following:

- One-step method.
- Implicit method: To compute  $\mathbf{x}_{n+1}$ , one needs  $\mathbf{f}_{n+1} = \mathbf{f}(\mathbf{x}_{n+1}, \mathbf{u}_{n+1})$ , which depends on  $\mathbf{x}_{n+1}$  itself. As such,  $\mathbf{x}_{n+1}$  must be solved for iteratively. For instance, one could use fixed-point iteration. Alternatively, one must already have an estimate of  $\mathbf{x}_{n+1}$ , perhaps found with another method. This is called a *predictor-corrector* approach. For instance, one could use forward Euler as a predictor step, then refine the estimate using backward Euler:

$$\tilde{\mathbf{x}}_{n+1} = \mathbf{x}_n + h\mathbf{f}(\mathbf{x}_n, \mathbf{u}_{n+1}), \quad \text{forward Euler (predictor)} \quad (6.67a)$$

$$\mathbf{x}_{n+1} = \mathbf{x}_n + h\mathbf{f}(\tilde{\mathbf{x}}_{n+1}, \mathbf{u}_{n+1}), \quad \text{backward Euler (corrector)} \quad (6.67b)$$

- 1-stage method.

### 6.5.3 Trapezoidal (or Crank-Nicholson)

Consider the same setup as for the previous methods. Another more robust scheme that uses more evaluations of the state dynamics  $\mathbf{f}$  is:

$$\frac{\mathbf{f}_n + \mathbf{f}_{n+1}}{2} = \frac{\mathbf{x}_{n+1} - \mathbf{x}_n}{h} \quad (6.68)$$

Solving for  $\mathbf{x}_{n+1}$  yields:

$$\boxed{\mathbf{x}_{n+1} = \mathbf{x}_n + \frac{h}{2}(\mathbf{f}_n + \mathbf{f}_{n+1})} \quad (6.69)$$

The method has the following properties:

- One-step method.
- Implicit method: To solve for  $\mathbf{x}_{n+1}$ , one needs  $\mathbf{f}_{n+1} = \mathbf{f}(\mathbf{x}_{n+1}, \mathbf{u}_{n+1})$ . Then, the following predictor-corrector approach could be used:

$$\tilde{\mathbf{x}}_{n+1} = \mathbf{x}_n + h\mathbf{f}(\mathbf{x}_n, \mathbf{u}_{n+1}), \quad \text{forward Euler (predictor)} \quad (6.70a)$$

$$\mathbf{x}_{n+1} = \mathbf{x}_n + \frac{h}{2}[\mathbf{f}_n + \mathbf{f}(\tilde{\mathbf{x}}_{n+1}, \mathbf{u}_{n+1})], \quad \text{trapezoidal (corrector)} \quad (6.70b)$$

- 2-stage method: Requires two evaluations of  $\mathbf{f}$ .

### 6.5.4 Heun

Combining forward Euler as a predictor step and trapezoidal (or Crank-Nicholson) as a corrector step, one obtains Heun's method:

$$\boxed{\mathbf{x}_{n+1} = \mathbf{x}_n + \frac{h}{2}[\mathbf{f}_n + \mathbf{f}(\mathbf{x}_n + h\mathbf{f}_n)]} \quad (6.71)$$

The properties are the following:

- One-step method.
- Explicit method.
- 2-stage method.

### 6.5.5 Runge-Kutta Fourth Order (RK4)

Runge-Kutta methods maintain a one-step structure but increase their accuracy at the price of an increase of functional evaluations at each time step. An example of fourth-order Runge-Kutta method is provided by the following four-state method:

$$\boxed{\mathbf{x}_{n+1} = \mathbf{x}_n + \frac{h}{2} (\mathbf{k}_1 + 2\mathbf{k}_2 + 2\mathbf{k}_3 + \mathbf{k}_4)} \quad (6.72)$$

where:

$$\mathbf{k}_1 = \mathbf{f}_n \quad (6.73a)$$

$$\mathbf{k}_2 = \mathbf{f} \left[ \mathbf{x}_n + \frac{h}{2} \mathbf{k}_1, \mathbf{u} \left( t_n + \frac{h}{2} \right) \right] \quad (6.73b)$$

$$\mathbf{k}_3 = \mathbf{f} \left[ \mathbf{x}_n + \frac{h}{2} \mathbf{k}_2, \mathbf{u} \left( t_n + \frac{h}{2} \right) \right] \quad (6.73c)$$

$$\mathbf{k}_4 = \mathbf{f} (\mathbf{x}_n + h\mathbf{k}_3, \mathbf{u}_{n+1}) \quad (6.73d)$$

The properties of this method are:

- One-step method.
- Explicit method.
- 4-stage method.

### 6.5.6 Runge-Kutta Fifth Order (RK5)

The fifth-order Runge-Kutta method presented here is taken from [Bou91]. The method is as follows:

$$\boxed{\mathbf{x}_{n+1} = \mathbf{x}_n + \frac{h}{90} (7\mathbf{k}_1 + 32\mathbf{k}_3 + 12\mathbf{k}_4 + 32\mathbf{k}_5 + 7\mathbf{k}_6)} \quad (6.74)$$

where:

$$\mathbf{k}_1 = \mathbf{f}_n \quad (6.75a)$$

$$\mathbf{k}_2 = \left[ \mathbf{x}_n + \frac{h}{4} \mathbf{k}_1, \mathbf{u} \left( t + \frac{h}{4} \right) \right] \quad (6.75b)$$

$$\mathbf{k}_3 = \left[ \mathbf{x}_n + \frac{h}{8} \mathbf{k}_1 + \frac{h}{8} \mathbf{k}_2, \mathbf{u} \left( t + \frac{h}{4} \right) \right] \quad (6.75c)$$

$$\mathbf{k}_4 = \left[ \mathbf{x}_n - \frac{h}{2} \mathbf{k}_2 + h\mathbf{k}_3, \mathbf{u} \left( t + \frac{h}{2} \right) \right] \quad (6.75d)$$

$$\mathbf{k}_5 = \left[ \mathbf{x}_n + \frac{3h}{16} \mathbf{k}_1 + \frac{9h}{16} \mathbf{k}_4, \mathbf{u} \left( t + \frac{h}{2} \right) \right] \quad (6.75e)$$

$$\mathbf{k}_6 = \left[ \mathbf{x}_n - \frac{3h}{7} \mathbf{k}_1 + \frac{2h}{7} \mathbf{k}_2 + \frac{12h}{7} \mathbf{k}_3 - \frac{12h}{7} \mathbf{k}_4 + \frac{8h}{7} \mathbf{k}_5, \mathbf{u}(t+h) \right] \quad (6.75f)$$

$$(6.75g)$$

The properties of this method are:

- One-step method.
- Explicit method.
- 5-stage method.

## Bibliography

[Ano97] Anon. *Flying qualities of piloting vehicles MIL-STD-1797A*. Technical report. Washington, DC: Department of Defense, 1997 (cited on page 151).

- [Bai41] F. J. Bailey. *A Simplified Theoretical Model of Determining the Characteristics of a Lifting Rotor in Forward Flight*. Technical report. NACA Report No. 716, 1941. (Cited on page 148).
- [Ben66] A. Ben-Israel. “A Newton-Raphson Method for the Solution of Systems of Equations”. In: *Journal of Mathematical Analysis and Applications* 15.2 (1966), pages 243–252 (cited on page 139).
- [Bou91] D. L. Boulet. “Methods of Orbit Determination for the Microcomputer”. In: Richmond, VA: Willmann-Bell, Inc., 1991 (cited on page 157).
- [FDF05] E. Frazzoli, M. A. Dahleh, and E. Feron. “Maneuver-Based Motion Planning for Nonlinear Systems With Symmetries”. In: *IEEE Transactions on Robotics* 21.6 (Dec. 2005), pages 1077–1091. DOI: <https://doi.org/10.1109/TRO.2005.852260> (cited on pages 138, 145).
- [Hor19] J. F. Horn. “Non-Linear Dynamic Inversion Control Design for Rotorcraft”. In: *Aerospace* 6.3 (2019). DOI: <https://doi.org/10.3390/aerospace6030038> (cited on page 148).
- [How80] J. J. Howlett. *UH-60A Black Hawk Engineering Simulation Program. Volume 1: Mathematical Model*. Technical report. NASA-CR-166309, 1980. (Cited on page 148).
- [KOS76] P. V. Kokotovic, R. E. O’Malley, and P. Sannuti. “Singular Perturbations and Order Reduction in Control Theory, an Overview”. In: *Automatica* 12.2 (1976), pages 123–132. DOI: [https://doi.org/10.1016/0005-1098\(76\)90076-5](https://doi.org/10.1016/0005-1098(76)90076-5) (cited on page 146).
- [PP80] D. M. Pitt and D. A. Peters. “Theoretical Prediction of Dynamic-Inflow Derivatives”. In: *Proceedings of the 6<sup>th</sup> European Rotorcraft and Powered Lift Aircraft Forum*. Bristol, England, September 16-19, 1980. (Cited on page 148).
- [Sae+19] U. Saetti et al. “Identification of Linear Time-Periodic Systems from Rotorcraft Flight Test Data”. In: *Journal of Guidance, Control, and Dynamics* 42.10 (2019), pages 2288–2296. DOI: <https://doi.org/10.2514/1.G004406> (cited on page 135).
- [TR12] M B Tischler and R K Remple. “Aircraft and Rotorcraft System Identification: Engineering Methods with Flight Test Examples”. In: 2nd edition. Reston, VA: American Institute of Aeronautics and Astronautics, 2012. Chapter 5, 13, 17 (cited on pages 152, 153).
- [Tis+17] M. B. Tischler et al. “Practical Methods for Aircraft and Rotorcraft Flight Control Design: An Optimization-Based Approach”. In: Reston, VA: American Institute of Aeronautics and Astronautics, 2017 (cited on page 151).



## 7. Stability and Response Analysis

### 7.1 Introduction

An overview of the basic terminology is provided below.

- **Stability:** The tendency of an aircraft to maintain or deviate from an established flight condition.
- **Control:** The ability of an aircraft to be maneuvered or steered from one flight condition to another.
- **Handling Qualities:** Used to designate those characteristics that are relevant to both stability and control.
- **Static Stability:** A stable aircraft has an initial tendency to return to a trim condition after a velocity or angular rate perturbation. An aircraft is statically unstable if it has an initial tendency to diverge from trim after being perturbed.
- **Dynamic Stability:** An aircraft is said dynamically stable if, following a velocity or angular rate perturbation, tends to settle back over time to the initial trim condition.

### 7.2 Static Stability

Static stability is measured in terms of moments generated due to perturbation in velocity components along the three translational body axes, typically due to gust disturbances. In general, rotorcraft static stability is described by the following stability derivatives:

- $M_u$ : longitudinal static stability with speed,  
 $M_w$ : longitudinal static stability with angle of attack ( $\alpha \approx w/V$ ),  
 $L_v$ : dihedral effect of static lateral stability, and  
 $N_v$ : weathercock stability or directional stability.

#### 7.2.1 Longitudinal Static Stability with Speed

Consider a helicopter in hover suddenly undergoing a headwind perturbation (Fig. 7.1a). The headwind causes the rotor to tilt back due to the difference of lift on the blades (also known as the *blow back effect*: recall the  $\approx 90$  deg lag between the maximum aerodynamic force and maximum flapping angle). A nose-up pitching moment is produced as a result (nose down moment for tail wind) about the CG (Fig. 7.1b). The moment produced is in a direction opposing the disturbance. Thus the main rotor contribution to longitudinal static stability is stabilizing, *i.e.*,  $M_u > 0$ . It is worth noting that in forward flight, contributions come also from the fuselage (unstable) and from the vertical tail (depends on whether the surface carries upload or download).

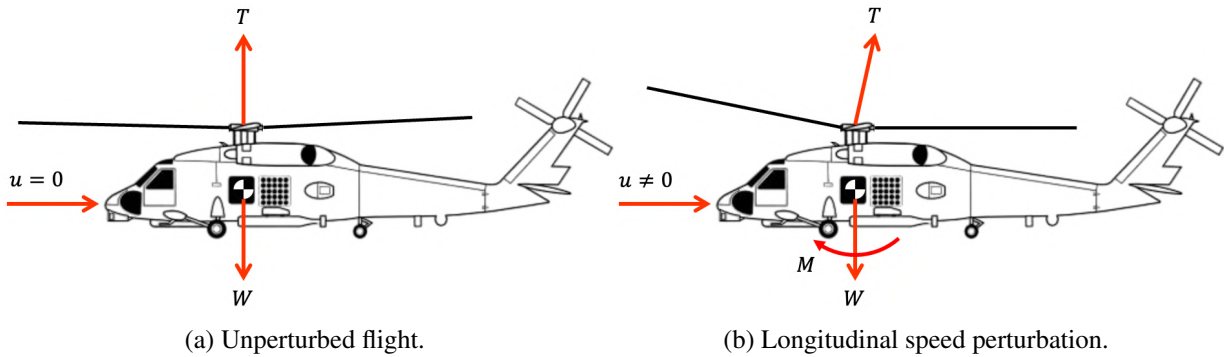


Figure 7.1: Hovering helicopter experiencing a sudden perturbation in longitudinal speed.

### 7.2.2 Longitudinal Static Stability with Angle of Attack

Consider a helicopter in hover suddenly undergoing an upward gust perturbation in the vertical speed (Fig. 7.2a). By neglecting the effect of the horizontal stabilizer (very small in hover), only an increment in thrust is produced due to the increased angle of attack at the blade element segments. No pitching moment is induced (Fig. 7.2b). Thus,  $M_w \approx 0$  or neutrally stable.

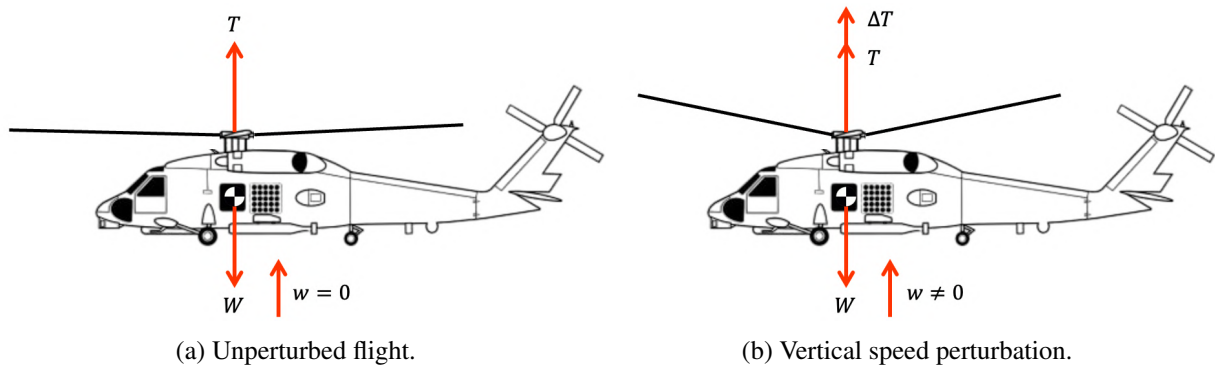


Figure 7.2: Hovering helicopter experiencing a sudden perturbation in vertical speed.

Consider now a helicopter in forward flight suddenly undergoing an upward gust perturbation (relative descent) (Fig. 7.3a). The change in vertical speed  $w$  results in a positive change in the blades angle of attack. The increased angle of attack of the blades on the advancing side makes the rotor tilt aft, causing a nose-up moment. The main rotor blow back reduces the inflow by reducing the rotor disk angle of attack (Fig. 3.16). The reduced inflow ratio causes the angle of attack of all blades to increase, given that:

$$\theta = \alpha + \phi = \text{const.} \quad (7.1)$$

A higher angle of attack on the advancing side causes the rotor to tilt aft even more, which causes a more nose-up moment (Fig. 7.3b). As such, the contribution to the angle of attack static stability is unstable, *i.e.*,  $M_w < 0$ . Note that the fuselage has a destabilizing effect whereas the horizontal tail provides a stabilizing moment (just like in fixed-wing aircraft).

### 7.2.3 Lateral Static Stability or Dihedral Effect

The dihedral effect refers to the roll moment resulting from sideslip:

$$L_v = \frac{\partial L}{\partial v} = V \frac{\partial L}{\partial \beta} = VL_\beta \quad (7.2)$$

where  $V = \sqrt{u^2 + v^2 + w^2}$  is the absolute speed and  $\beta \approx \frac{v}{V}$  is the sideslip angle. Consider a helicopter in hover suddenly undergoing a perturbation in lateral velocity (Fig. 7.4a). The side wind causes the main

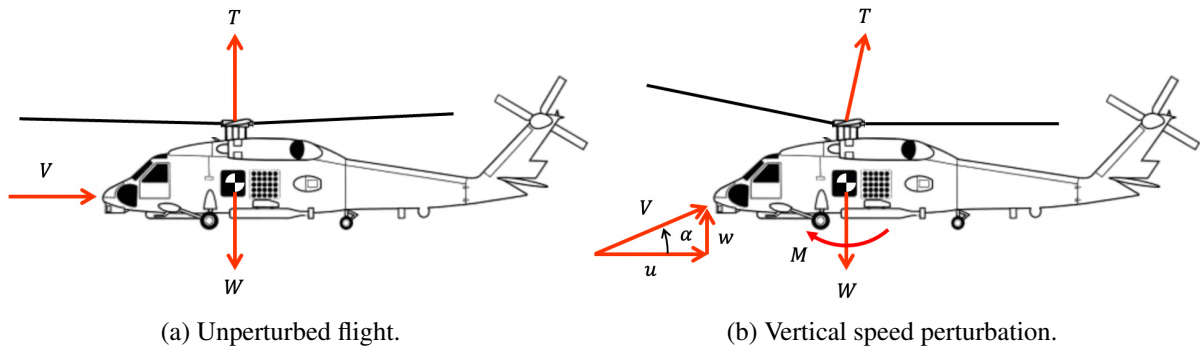


Figure 7.3: Helicopter in forward flight experiencing a sudden perturbation in longitudinal speed.

rotor to tilt port due to the difference in lift on the blades in the aft portion of the rotor. As a consequence, a right-wing-up rolling moment is produced (Fig. 7.4b). The moment produced is in the opposite direction of the disturbance, such that the main rotor contribution is statically stable, *i.e.*,  $L_v < 0$ . In forward flight, the vertical tail produces a relatively large force in sideslip. If the vertical tail center of pressure is above the CG, the vertical tail creates a stabilizing dihedral effect. If the vertical tail center of pressure is below the CG, the tail creates a destabilizing dihedral effect.

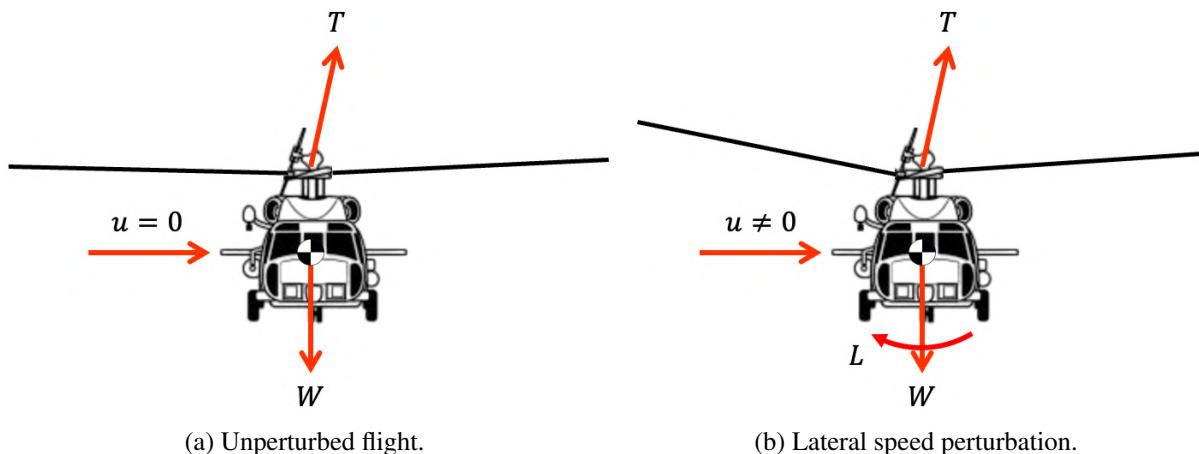


Figure 7.4: Hovering helicopter experiencing a sudden perturbation in lateral speed.

## 7.2.4 Directional Stability or Weathercock Stability

Directional or weathercock stability is a measure of the restoring yaw moment due to sideslip. The vertical tail generally has a stabilizing contribution (*i.e.*,  $N_v > 0$  for a vertical tail located aft of the CG) and is the main reason of why it is employed. The tail rotor also has a stabilizing contribution (*i.e.*,  $N_v > 0$ ) and is a major contribution in hover. Consider the case where a helicopter experiences a sudden (positive) gust in the lateral velocity (Fig. 7.5a). The side velocity increases the tail rotor inflow, which decreases its thrust. The decrease in thrust creates a yaw moment that reduces the lateral velocity (Fig. 7.5b).

## 7.3 Dynamic Stability

### 7.3.1 Review of Linear Systems Analysis

Consider a linear time-invariant (LTI) system in first-order form:

$$\dot{x} = Ax + Bu \quad (7.3)$$

where  $x \in \mathbb{R}^n$  is the state vector,  $u \in \mathbb{R}^m$  is the control vector. Additionally,  $A \in \mathbb{R}^{n \times n}$  is the system matrix,  $B \in \mathbb{R}^{n \times m}$  is the control matrix. Because the coefficient matrices are constant with time, a closed-form

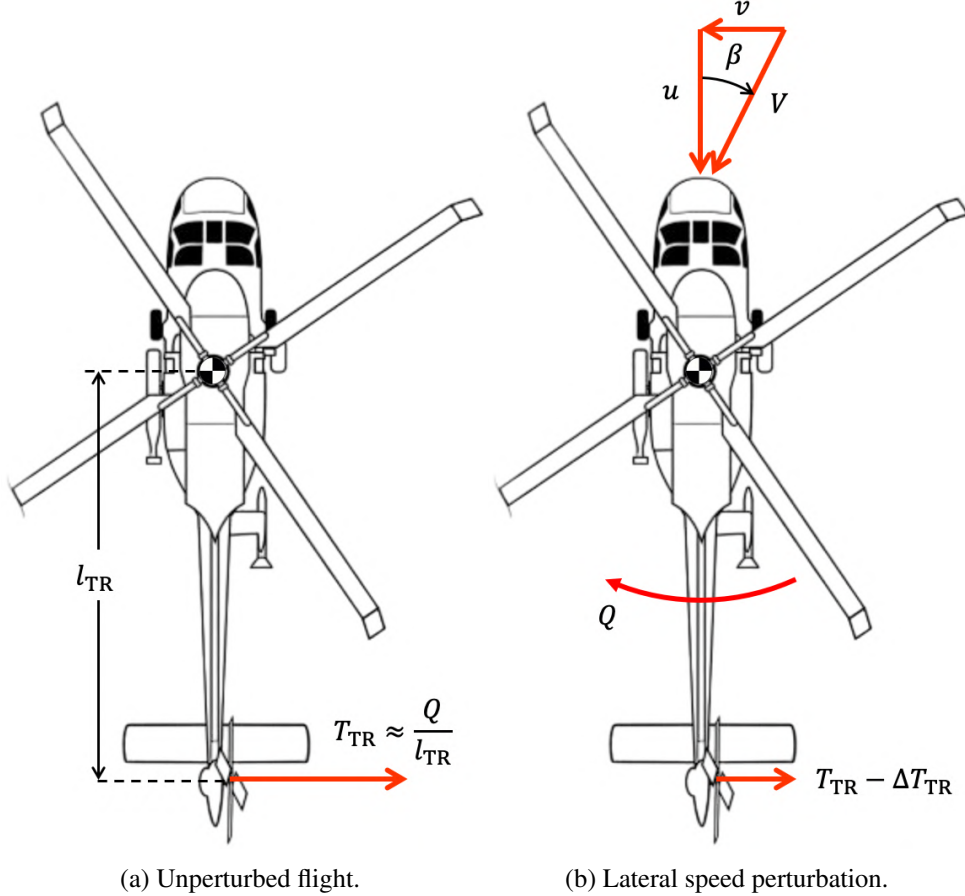


Figure 7.5: Hovering helicopter experiencing a sudden perturbation in lateral speed.

solution to a perturbation from initial conditions (*i.e.*, equilibrium) exists:

$$\mathbf{x}(t) = \underbrace{e^{\mathbf{A}t} \mathbf{x}_0}_{\text{Free response}} + \underbrace{\int_{t_0}^t e^{\mathbf{A}(t-\tau)} \mathbf{B} \mathbf{u}(\tau) d\tau}_{\text{Forced response}} \quad (7.4)$$

where:

$$e^{\mathbf{A}t} = \mathbf{I} + \mathbf{A}t + \frac{\mathbf{A}^2 t^2}{2!} + \frac{\mathbf{A}^3 t^3}{3!} + \dots \quad (7.5)$$

It is worth noting that  $e^{\mathbf{A}t}$  is known as the state transition matrix. Many ways exist to compute this matrix exponential. Nineteen (dubious) ways can be found in [MV78] and a twentieth in [MV03]. Out of this many ways, the popular approach used in dynamic systems analysis is to find a vector that decouples the  $\mathbf{A}$  matrix. To do so, consider the eigenvalue problem:

$$\mathbf{A} \mathbf{v}_i = \lambda_i \mathbf{v}_i, \quad i = 1, \dots, n \quad (7.6)$$

where  $\mathbf{v}_i$  is the  $i^{\text{th}}$  right (column) eigenvector and  $\lambda_i$  is the  $i^{\text{th}}$  eigenvalue. What the above equation means is that a certain combination of a vector  $\mathbf{v}_i$  and a scalar  $\lambda_i$  exists such that multiplying the matrix  $\mathbf{A}$  by such vector gives the same result as multiplying such vector by a scalar. Eigenvalues can be derived using the fact that the matrix  $(\mathbf{A} - \lambda_i \mathbf{I})$  is singular, which implies its determinant is zero:

$$(\mathbf{A} - \lambda_i \mathbf{I}) = \mathbf{0}, \quad \mathbf{v}_i \neq \mathbf{0} \quad \Rightarrow \quad |\mathbf{A} - \lambda_i \mathbf{I}| = 0 \quad (7.7)$$

This yields the *characteristic equation*, which defines the roots of the  $n^{\text{th}}$  order *characteristic polynomial*:

$$\lambda^n + c_{n-1}\lambda^{n-1} + c_{n-2}\lambda^{n-2} + \dots + c_1\lambda + c_0 = 0 \quad (7.8)$$

Eigenvectors are then solved by finding the null space of:

$$(\mathbf{A} - \lambda_i \mathbf{I}) \mathbf{v}_i = \mathbf{0} \quad (7.9)$$

Note that the eigenvector just defines a direction or subspace in  $\mathbb{C}^n$ . If  $\mathbf{v}_i \neq \mathbf{0}$  satisfies  $(\mathbf{A} - \lambda_i \mathbf{I}) \mathbf{v}_i = \mathbf{0}$ , any vector that is collinear with  $\mathbf{v}_i$  constitutes the same eigenvector, e.g.,  $(\mathbf{A} - \lambda_i \mathbf{I}) k\mathbf{v}_i = \mathbf{0}$  for any complex scalar  $k \neq 0$ ,  $k\mathbf{v}_i$  is the same eigenvector as  $\mathbf{v}_i$ . If  $\mathbf{A}$  has  $n$  distinct eigenvalues, then it will also have  $n$  distinct corresponding eigenvectors. Thus, the null space of  $(\mathbf{A} - \lambda_i \mathbf{I})$  will be defined by a single distinct vector  $\mathbf{v}_i$  for each eigenvalue. In that case, one can construct an invertible matrix whose columns are composed of the eigenvectors:

$$\mathbf{V} = [\mathbf{v}_1 \mid \mathbf{v}_2 \mid \cdots \mid \mathbf{v}_n] \quad (7.10)$$

The, it can be shown that both  $\mathbf{A}$  and its matrix exponential can be diagonalized as follows:

$$\mathbf{A} = \mathbf{V} \begin{bmatrix} \lambda_1 & & & 0 \\ & \lambda_2 & & \\ & & \ddots & \\ 0 & & & \lambda_n \end{bmatrix} \mathbf{V}^{-1} \quad (7.11a)$$

$$e^{\mathbf{A}t} = \mathbf{V} \begin{bmatrix} e^{\lambda_1 t} & & & 0 \\ & e^{\lambda_2 t} & & \\ & & \ddots & \\ 0 & & & e^{\lambda_n t} \end{bmatrix} \mathbf{V}^{-1} \quad (7.11b)$$

Effectively, an eigenvector decouples the matrix  $\mathbf{A}$ . If the matrix  $\mathbf{A}$  has  $n$  distinct eigenvalues, it implies that the characteristic polynomial can be factored as:

$$|\mathbf{A} - \lambda_i \mathbf{I}| = (\lambda - \lambda_1)(\lambda - \lambda_2) \cdots (\lambda - \lambda_n) \quad (7.12)$$

It is certainly possible that there are not  $n$  distinct eigenvalues, but instead some eigenvalues have *multiplicity*:

$$|\mathbf{A} - \lambda_i \mathbf{I}| = (\lambda - \lambda_1)(\lambda - \lambda_2) \cdots (\lambda - \lambda_j)^m \cdots (\lambda - \lambda_p) \quad (7.13)$$

where  $p < n$  and eigenvalue  $\lambda_j$  has multiplicity  $m$ . In this case, it is not necessarily possible to diagonalize  $\mathbf{A}$  and  $e^{\mathbf{A}t}$ , but the same basic transformation can be performed using generalized eigenvectors to construct the *Jordan canonical form*. This is a block diagonal form, with block, instead of pure diagonal elements,

corresponding to the repeated eigenvalues:

$$\mathbf{A} = \mathbf{V} \begin{bmatrix} \lambda_1 & & & & 0 \\ & \lambda_2 & & & \\ & & \ddots & & \\ & & & \lambda_j & 1 & 0 \\ & & & & \lambda_j & 1 \\ & & & & & \lambda_j \\ & & & & & \ddots \\ 0 & & & & & & \lambda_n \end{bmatrix} \mathbf{V}^{-1} \quad (7.14a)$$

$$e^{\mathbf{At}} = \mathbf{V} \begin{bmatrix} e^{\lambda_1 t} & & & & 0 \\ & e^{\lambda_2 t} & & & \\ & & \ddots & & \\ & & & e^{\lambda_j t} & te^{\lambda_j t} & \frac{t^2}{2!} e^{\lambda_j t} \\ & & & & e^{\lambda_j t} & te^{\lambda_j t} \\ & & & & & e^{\lambda_j t} \\ & & & & & \ddots \\ 0 & & & & & & e^{\lambda_n t} \end{bmatrix} \mathbf{V}^{-1} \quad (7.14b)$$

For most linear models of aircraft, any repeated eigenvalues are often associated with modes that can be decoupled from the aircraft model. Very often these repeated eigenvalues are at the origin of the complex plane ( $\lambda = 0$ ) and associated with simple integration of states, *e.g.*,

$$\Delta \dot{p}_N = \Delta V_T \quad (7.15a)$$

$$\Delta \dot{\psi} = r \quad (7.15b)$$

In some cases, there may be repeated eigenvalues associated with an aircraft component that is replicated multiple times, *e.g.*, same actuator properties used for multiple surfaces as shown in Fig. 7.6. In these cases, the repeated eigenvalues with multiplicity  $m$  usually have  $m$  distinct eigenvectors (*i.e.*, the *fully degenerate case*). In those cases, the  $\mathbf{A}$  matrix is still diagonalizable. It would be extremely rare for any of the fundamental modes of the aircraft dynamics to have repeated eigenvalues.

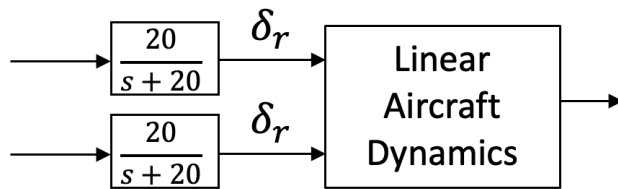


Figure 7.6: Repeated eigenvalues due to an aircraft component that is replicated multiple times.

Assuming a fully diagonalizable system:

$$\mathbf{x}(t) = \mathbf{V} \begin{bmatrix} \lambda_1 & & & & 0 \\ & \lambda_2 & & & \\ & & \ddots & & \\ 0 & & & & \lambda_n \end{bmatrix} \mathbf{V}^{-1} \mathbf{x}_0 + \int_{t_0}^t \mathbf{V} \begin{bmatrix} e^{\lambda_1 t} & & & & 0 \\ & e^{\lambda_2 t} & & & \\ & & \ddots & & \\ 0 & & & & e^{\lambda_n t} \end{bmatrix} \mathbf{V}^{-1} \mathbf{B} \mathbf{u}(\tau) d\tau \quad (7.16)$$

As discussed earlier,  $\mathbf{V}$  is constructed from the eigenvectors. It can also be shown that  $\mathbf{V}^{-1}$  is constructed from the left (line) eigenvectors:

$$\mathbf{V}^{-1} = [\mathbf{w}_1 \mid \mathbf{w}_2 \mid \cdots \mid \mathbf{w}_n]^T \quad (7.17)$$

where:

$$\mathbf{w}_i^T \mathbf{A} = \lambda_i \mathbf{w}_i^T, \quad \mathbf{w}_i \neq \mathbf{0} \quad (7.18)$$

The left eigenvectors  $\mathbf{w}_i$  are the eigenvectors of  $\mathbf{A}^T$ . Then, the following equation holds true:

$$e^{\mathbf{A}t} \mathbf{x}_0 = \sum_{i=1}^n \mathbf{w}_i \mathbf{x}_0 e^{\lambda_i t} \mathbf{v}_i \quad (7.19)$$

It follows that the response to initial conditions and non-zero input is now decomposed into a summation of responses of each mode:

$$\mathbf{x}(t) = \sum_{i=1}^n \mathbf{w}_i \mathbf{x}_0 e^{\lambda_i t} \mathbf{v}_i + \sum_{i=1}^n \mathbf{v}_i \int_{t_0}^t e^{\lambda_i(t-\tau)} \mathbf{w}_i \mathbf{B} \mathbf{u}(\tau) d\tau \quad (7.20)$$

The nature of the response of the system will depend on  $e^{\lambda_i t}$  and therefore on the eigenvalues  $\lambda_i$ . The eigenvalues (and eigenvectors) can be either real or complex. Real eigenvalues have the form  $\lambda_i = \sigma_i$  such that the free response becomes:

$$\mathbf{x}(t) = \sum_{i=1}^n \mathbf{A} e^{\lambda_i t} \quad (7.21)$$

For real eigenvalues, the mode response of each state is simply an exponential function and its properties are summarized as follows:

- **Real negative:** Eigenvalues of the form  $\lambda_i = \sigma_i$ ,  $\sigma_i < 0$  yield a subsidence mode (stable).
- **Real zero:** Eigenvalues of the form  $\lambda_i = \sigma_i$ ,  $\sigma_i = 0$  yield a neutrally stable response.
- **Real positive:** Eigenvalues of the form  $\lambda_i = \sigma_i$ ,  $\sigma_i > 0$  yield a divergence mode (unstable).

These behaviours are shown qualitatively in Fig. 7.7a. On the other hand, complex eigenvalues have the form  $\lambda_i = \sigma_i \pm i\omega_i$  such that the free response becomes:

$$\mathbf{x}(t) = \sum_{i=1}^n \mathbf{A} e^{\lambda_i t} \cos [\omega_i + \phi_i (\mathbf{x}_0)] \quad (7.22)$$

Note that complex eigenvalues always come in complex conjugate pairs. In either case, the stability of the response is dictated by the sign of the real part  $\sigma_i$ . Also note that all imaginary numbers vanish in the state response (this has to be the case, since the states are physical values). For the given mode, all states respond with the same frequency  $\omega$  and damping  $\sigma$ , but different amplitude  $A$  and phase  $\phi$ . For complex eigenvalues, the mode response of each state result in damped, divergent, or neutrally stable oscillations. The response properties are summarized as follows:

- **Complex pair with negative real part:** Eigenvalues of the form  $\lambda_i = \sigma_i \pm i\omega_i$ ,  $\sigma_i < 0$  yield a damped oscillation (stable).
- **Complex pair with zero real part:** Eigenvalues of the form  $\lambda_i = \sigma_i \pm i\omega_i$ ,  $\sigma_i = 0$  yield a neutrally stable oscillation.
- **Complex pair with positive real positive:** Eigenvalues of the form  $\lambda_i = \sigma_i \pm i\omega_i$ ,  $\sigma_i > 0$  yield a divergent oscillation (unstable).

These behaviours are shown qualitatively in Fig. 7.7b.

Not only the eigenvalues characterize the stability of the response, but also tell us the rate of subsidence or divergence, *e.g.*, the time to half/double amplitude:

$$t_{\text{half/double}} = \frac{\ln 2}{|\sigma|} \quad (7.23)$$

The denomination of this variable will depend on whether the response is stable (time to half amplitude) or unstable (time to double amplitude). Complex eigenvalues also tell us the frequency and period of oscillation

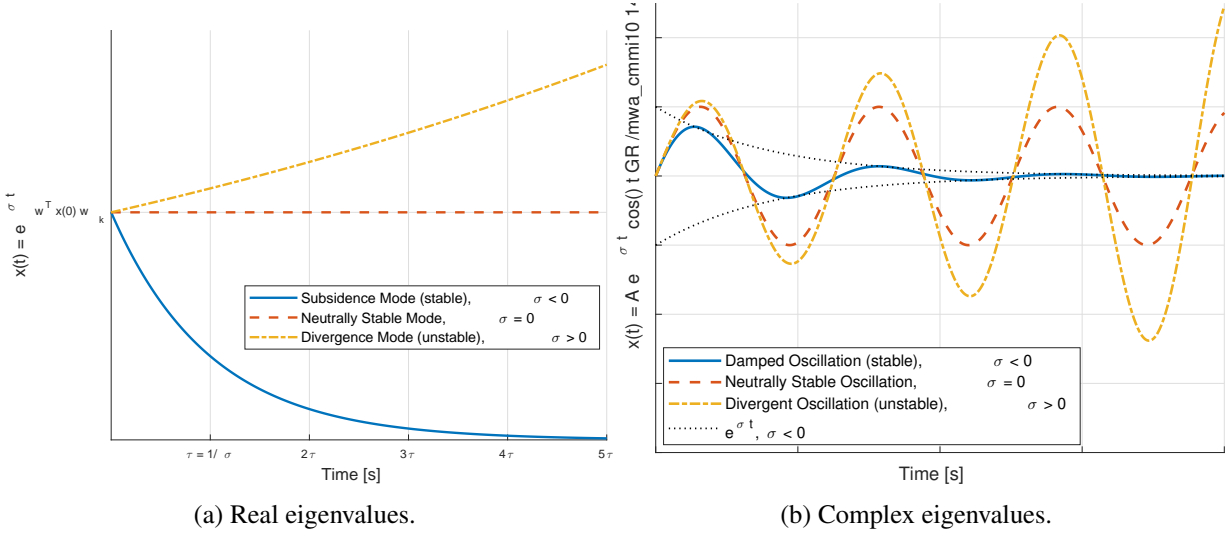


Figure 7.7: Nature of the linear system response.

of oscillatory modes:

$$T = \frac{2\pi}{\omega} \quad \text{period of oscillation} \quad (7.24a)$$

$$\omega_n = \sqrt{\sigma^2 + \omega^2} = |\lambda| \quad \text{natural (undamped) frequency} \quad (7.24b)$$

$$\zeta = \frac{|\sigma|}{\omega_n} \quad \text{damping ratio} \quad (7.24c)$$

The complex eigenvalues can be re-written in terms of these quantities as:

$$\lambda = \sigma \pm i\omega = -\zeta \omega_n \pm i\omega_n \sqrt{1 - \zeta^2} \quad (7.25)$$

Eigenvectors tell us the relative magnitude of the response observed in each state for a given mode. Note that eigenvectors have the same dimension as the state, and each component corresponds to the various states (in same order as with the state vector). Therefore the eigenvector has units – the same units as the state vector. Important to understand the difference between units of each state when analyzing the eigenvector. Eigenvectors also tell us the relative phase of the response of each state if the mode is oscillatory (complex), e.g.,

$$\mathbf{v}_i = \mathbf{u}_i + i\mathbf{w}_i = \begin{bmatrix} \vdots \\ M_k e^{\pm i\phi_k} \\ \vdots \\ M_l e^{\pm i\phi_l} \\ \vdots \end{bmatrix} \quad (7.26)$$

where  $M_k$  and  $\phi_k$  corresponds to the relative magnitude and phase of the response of state  $x_k(t)$ , whereas  $M_l$  and  $\phi_l$  corresponds to the relative magnitude and phase of the response of state  $x_l(t)$ . The relative magnitude can be calculated by  $\frac{M_l}{M_k}$  and the relative phase by  $\phi_l - \phi_k$ .

So far, the focus has been on the response to initial conditions. Let us now consider the forces response due to inputs:

$$\mathbf{x}(t) = \sum_{i=1}^n \mathbf{v}_i \int_{t_0}^t e^{\lambda_i(t-\tau)} \mathbf{w}_i \mathbf{B} \mathbf{u}(\tau) d\tau \quad (7.27)$$

The forced response of each mode:

$$x_i(t) = \mathbf{v}_i \int_{t_0}^t e^{\lambda_i(t-\tau)} \mathbf{w}_i^T \mathbf{B} \mathbf{u}(\tau) d\tau \quad (7.28)$$

is actually a convolution of the state transition matrix and a function proportional to the input signals:

$$x_i(t) = f(t) * g(t) \quad (7.29)$$

where  $f(t) = e^{\lambda_i t}$  and  $g(t) = \mathbf{w}_i^T \mathbf{B} \mathbf{u}(t)$ . Note that both of these are scalar functions. The convolution integral cannot be evaluated analytically except for very simple input signals. However, it tells us that the forced response will contain a transient response due to the modes and a steady-state response due to the input signal:

$$\mathbf{x}(t) = k_1 e^{\lambda_1 t} \mathbf{v}_1 + k_2 e^{\lambda_2 t} \mathbf{v}_2 + \cdots + k_n e^{\lambda_n t} \mathbf{v}_n + \text{steady-state response due to input} \quad (7.30)$$

In general, all modes will appear in the state response. However, there are special cases where certain modes will not appear in either the response to initial conditions or the forced response. For initial conditions, if  $(\mathbf{w}_i^T) = 0$ , then mode  $i$  will not appear in the response due to initial conditions  $\mathbf{x}_0$ . The left and right eigenvectors are orthogonal:

$$\mathbf{w}_i^T \mathbf{v}_j = \begin{cases} 0, & i \neq j \\ ||\mathbf{v}_j||_2^2, & i = j \end{cases} \quad (7.31)$$

Therefore, if  $\mathbf{x}_0 = k\mathbf{v}_i$  (the initial condition vector is collinear with an eigenvector), then all modes other than mode  $i$  will not appear in the state response. In simulation, it is possible to select initial conditions that isolate the response of a single mode. For a mode with a real eigenvalue just set the initial state vector to a multiple of the eigenvector. For a mode with complex eigenvalues, set the initial state vector to a multiple of the real part of the eigenvectors. This method is summarized as follows:

- To isolate the mode associated with eigenvalue  $\lambda_i = \sigma_i$ , set  $\mathbf{x}_0 = k\mathbf{v}_i$  such that:

$$\mathbf{x}(t) = k ||\mathbf{v}_i||_2^2 e^{\sigma_i t} \mathbf{v}_i \quad (7.32)$$

• To isolate the mode associated with complex eigenvalue  $\lambda_i = \sigma_i + i\omega_i$ , set  $\mathbf{x}_0 = k\mathbf{u}_i$ , where  $\mathbf{v}_i = \mathbf{u}_i \pm i\omega_i$ . Generally, it is not possible to isolate a mode using an input signal (forced response). This would require:

$$\mathbf{w}_i^T \mathbf{B} \mathbf{u} = 0 \quad (7.33)$$

for all modes other than the mode of interest. This is only possible if the aircraft is not under-actuated (the number of controls is at least equal to the number of states). This is very unusual. However, in practice we can find input signals that tend to excite some modes much more than others. This is needed in flight test, since we cannot set initial conditions in actual flight.

### 7.3.2 Linear Systems Analysis Tools in MATLAB®

Linear models can be analyzed in MATLAB® using the LTI system tools in the Control System Toolbox. First, it is necessary to construct a state-space object using the command:

```
sys=ss(A,B,C,D)
```

Then, the state-space system can be analyzed using a variety of LTI tools. Examples are provided below:

- `eig(sys)`: Eigenvalues of system. This is equivalent to `eig(A)`.
- `tzero(sys)`: Transmission zeros of system (MIMO transmission zeros).
- `pzmap(sys)`: Plots zeros and eigenvalues on complex plane.

One can also generate responses. By default, the following commands plot responses for every input-output combination (*i.e.*,  $m \times p$  plots):

- `step(sys)`: Unit step response.
- `impulse(sys)`: Unit impulse response.
- `bode(sys)`: Frequency response (magnitude and phase versus frequency).
- `initial(sys, x0)`: Response to initial conditions defined by state vector  $x_0$ .

Any operation with `sys(i, j)` will isolate results for single input  $j$  to single output  $i$ . Note that one can use output arguments to pull out data rather than generate plot, e.g.,

```
[y, t, x] = step(sys)
```

This syntax returns outputs, time, and states for a unit step response. One can also get a transfer function and a zero-pole-gain form of the system using the following commands:

```
sys_tf(sys)
sys_zpk=zpk(sys)
```

### 7.3.3 Decoupled Longitudinal and Lateral Dynamics

For the purpose of the analysis that follows, consider partitioning the 8-state model derived in the previous chapter into longitudinal and lateral components:

$$\begin{bmatrix} \dot{x}_{\text{lon}} \\ \dot{x}_{\text{lat}} \end{bmatrix} = \begin{bmatrix} \mathbf{A}_{\text{lon}} & \mathbf{A}_{12} \\ \mathbf{A}_{21} & \mathbf{A}_{\text{lat}} \end{bmatrix} \begin{bmatrix} x_{\text{lon}} \\ x_{\text{lat}} \end{bmatrix} + \begin{bmatrix} \mathbf{B}_{\text{lon}} \\ \mathbf{B}_{\text{lat}} \end{bmatrix} \begin{bmatrix} u_{\text{lon}} \\ u_{\text{lat}} \end{bmatrix} \quad (7.35)$$

where:

- $\mathbf{x}_{\text{lon}}^T = [u \ w \ q \ \theta]$  is the longitudinal state vector,
- $\mathbf{x}_{\text{lat}}^T = [v \ p \ r \ \phi]$  is the lateral state vector,
- $\mathbf{u}_{\text{lon}}^T = [\delta_{\text{lon}} \ \delta_{\text{col}}]$  is the longitudinal control input vector,
- $\mathbf{u}_{\text{lat}}^T = [\delta_{\text{lat}} \ \delta_{\text{ped}}]$  is the lateral control input vector,
- $\mathbf{A}_{\text{lon}}$  is the longitudinal dynamics system matrix,
- $\mathbf{A}_{\text{lat}}$  is the lateral dynamics system matrix,
- $\mathbf{B}_{\text{lon}}$  is the longitudinal dynamics control matrix,
- $\mathbf{B}_{\text{lat}}$  is the lateral dynamics control matrix, and
- $\mathbf{A}_{12}, \mathbf{A}_{21}$  are the coupling matrices.

Thus, the 8-state system is re-organized as:

$$\begin{bmatrix} \dot{u} \\ \dot{w} \\ \dot{q} \\ \dot{\theta} \\ \dot{v} \\ \dot{p} \\ \dot{r} \\ \dot{\phi} \end{bmatrix} = \begin{bmatrix} X_u & X_w - q_e & X_q - w_e & -g \cos \theta_e & X_v + r_e & X_p \\ Z_u + q_e & Z_w & Z_q + u_e & -g \sin \phi_e \sin \theta_e & Z_v - p_e & Z_p - v_e \\ M_u & M_w & M_q & 0 & M_v & M_p - 2p_e \frac{I_{xz}}{I_{yy}} - r_e \frac{(I_{xx} - I_{zz})}{I_{yy}} \\ 0 & 0 & \cos \phi_e & 0 & 0 & 0 \\ Y_u - r_e & Y_w + p_e & \bar{Y}_q & -g \sin \phi_e & \bar{Y}_v & \bar{Y}_p + w_e \\ L'_u & L'_w & L'_q + k_1 p_e - k_2 r_e & 0 & L'_v & L'_p + k_1 q_e \\ N'_u & N'_w & N'_q - k_1 r_e + k_3 p_e & 0 & N'_v & N'_p + k_3 q_e \\ 0 & 0 & \sin \phi_e \tan \theta_e & \psi_e \sec \theta_e & 0 & 1 \end{bmatrix} + \begin{bmatrix} X_r + v_e & 0 \\ Z_r & -g \sin \phi_e \cos \theta_e \\ M_r + 2r_e \frac{I_{xz}}{I_{yy}} - p_e \frac{(I_{xx} - I_{zz})}{I_{yy}} & 0 \\ -\sin \phi_e & -\psi_e \cos \theta_e \\ Y_r - u_e & g \cos \phi_e \cos \theta_e \\ L'_r - k_2 q_e & 0 \\ N'_r - k_1 q_e & 0 \\ \cos \phi_e \tan \theta_e & 0 \end{bmatrix} \begin{bmatrix} u \\ w \\ q \\ \theta \\ v \\ p \\ r \\ \phi \end{bmatrix} + \begin{bmatrix} X_{\delta_{\text{lon}}} & X_{\delta_{\text{col}}} & X_{\delta_{\text{lat}}} & X_{\delta_{\text{ped}}} \\ Z_{\delta_{\text{lon}}} & Z_{\delta_{\text{col}}} & Z_{\delta_{\text{lat}}} & Z_{\delta_{\text{ped}}} \\ M_{\delta_{\text{lon}}} & M_{\delta_{\text{col}}} & M_{\delta_{\text{lat}}} & M_{\delta_{\text{ped}}} \\ 0 & 0 & 0 & 0 \\ Y_{\delta_{\text{lon}}} & Y_{\delta_{\text{col}}} & Y_{\delta_{\text{lat}}} & Y_{\delta_{\text{ped}}} \\ L'_{\delta_{\text{lon}}} & L'_{\delta_{\text{col}}} & L'_{\delta_{\text{lat}}} & L'_{\delta_{\text{ped}}} \\ N'_{\delta_{\text{lon}}} & N'_{\delta_{\text{col}}} & N'_{\delta_{\text{lat}}} & N'_{\delta_{\text{ped}}} \\ 0 & 0 & 0 & 0 \end{bmatrix} \begin{bmatrix} \delta_{\text{lon}} \\ \delta_{\text{col}} \\ \delta_{\text{lat}} \\ \delta_{\text{ped}} \end{bmatrix}$$

(7.36)

The effect of the coupling matrices is significant in hover but less severe in forward flight. If one ignores the coupling effects, the system can be decoupled. While decoupling is a quite crude approximation in hover, a simplified decoupled system is still used herein for didactical purposes. The decoupled longitudinal dynamics is:

$$\begin{bmatrix} \dot{u} \\ \dot{w} \\ \dot{q} \\ \dot{\theta} \end{bmatrix} = \begin{bmatrix} X_u & X_w - q_e & X_q - w_e & -g \cos \theta_e \\ Z_u + q_e & Z_w & Z_q + u_e & -g \sin \phi_e \sin \theta_e \\ M_u & M_w & M_q & 0 \\ 0 & 0 & \cos \phi_e & 0 \end{bmatrix} \begin{bmatrix} u \\ w \\ q \\ \theta \end{bmatrix} + \begin{bmatrix} X_{\delta_{\text{lon}}} & X_{\delta_{\text{col}}} \\ Z_{\delta_{\text{lon}}} & Z_{\delta_{\text{col}}} \\ M_{\delta_{\text{lon}}} & M_{\delta_{\text{col}}} \\ 0 & 0 \end{bmatrix} \begin{bmatrix} \delta_{\text{lon}} \\ \delta_{\text{col}} \end{bmatrix} \quad (7.37)$$

The decoupled lateral dynamics is:

$$\begin{bmatrix} \dot{v} \\ \dot{p} \\ \dot{r} \\ \dot{\phi} \end{bmatrix} = \begin{bmatrix} Y_v & Y_p + w_e & Y_r - u_e & g \cos \phi_e \cos \theta_e \\ L'_v & L'_p + k_1 q_e & L'_r - k_2 q_e & 0 \\ N'_v & N'_p + k_3 q_e & N'_r - k_1 q_e & 0 \\ 0 & 1 & \cos \phi_e \tan \theta_e & 0 \end{bmatrix} \begin{bmatrix} v \\ p \\ r \\ \phi \end{bmatrix} + \begin{bmatrix} Y_{\delta_{\text{lat}}} & Y_{\delta_{\text{ped}}} \\ L_{\delta_{\text{lat}}} & L_{\delta_{\text{ped}}} \\ N_{\delta_{\text{lat}}} & N_{\delta_{\text{ped}}} \\ 0 & 0 \end{bmatrix} \begin{bmatrix} \delta_{\text{lat}} \\ \delta_{\text{ped}} \end{bmatrix} \quad (7.38)$$

To provide an example of the accuracy of the decoupled dynamics, the eigenvalues of the decoupled dynamics are compared to those of the 8-state model in hover and forward flight. Figure 7.8 shows the eigenvalues of these three models for a UH-60 helicopter. While the eigenvalues will be analyzed more in detail later in the chapter, it is clear that the eigenvalues of the decoupled dynamics offer an closer approximation in forward flight (Fig. 7.8b) than in hover (Fig. 7.8a).

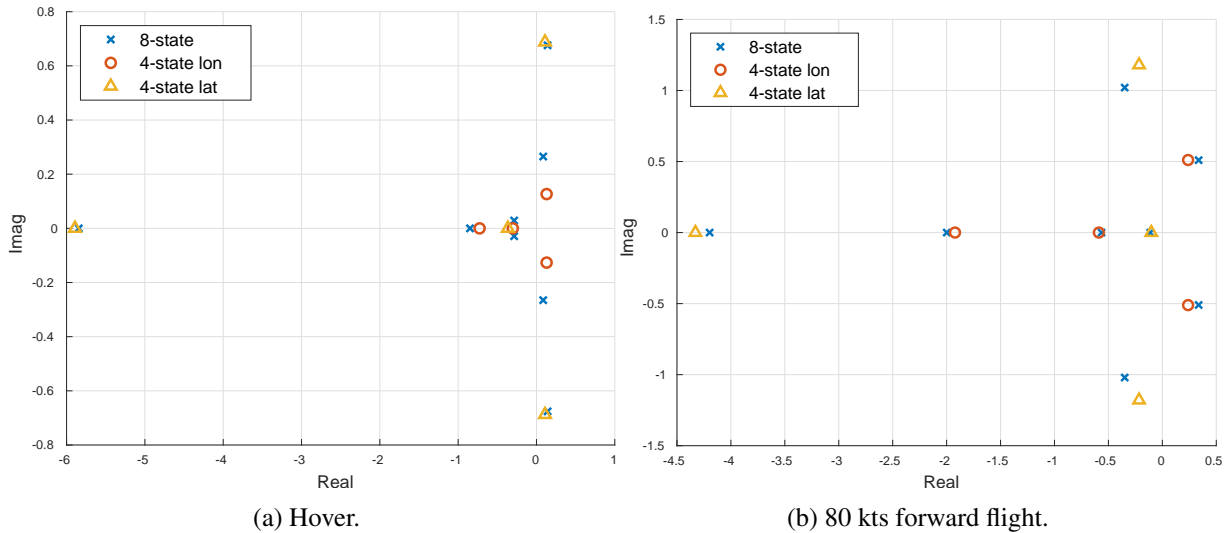


Figure 7.8: Comparison between the 8-state model eigenvalues with those of the decoupled longitudinal and lateral dynamics for a UH-60 helicopter.

### 7.3.4 Hover

In this section, it will be shown how the hover dynamics are really dominated by the main rotor and the tail rotor. The airframe aerodynamics have a small effect as the dynamic pressure is by definition very small, so lift and drag forces on the airframe components have only a small impact in hover.

#### Longitudinal-Heave Dynamic Stability

Consider making the following assumptions to simplify the decoupled longitudinal dynamics in Eq. (7.37) at hover:

- Obviously, the trim translational and angular velocities in hover are zero, such that  $u_e = w_e = q_e = 0$ .

- Typically, the trim roll and pitch attitudes at hover are small such that  $\sin \phi_e \approx \phi_e$ ,  $\sin \theta_e \approx \theta_e$ , and  $\cos \phi_e \approx \cos \theta_e \approx 1$ .
- $X_w \approx Z_{\delta_{\text{lon}}} \approx X_{\delta_{\text{col}}} \approx 0$ .
- $X_q$  and  $Z_q$  are not necessarily small, but from experience they have little impact on hover dynamics. As such, these stability derivatives can be assumed as zero.
- $M_w$  and  $M_{\delta_{\text{col}}}$  can be non-zero if the rotor is longitudinally offset from the CG, but they have little importance in hover. It is worth noting that  $M_w$ , becomes very significant in forward flight.
- $Z_u$  is the change in vertical force with forward speed. As airspeed increases or decreases, the rotor thrust will tend to increase due to the *translational lift effect*, i.e., the reduction of induced inflow with forward airspeed. However, the thrust always increases when translating away from hover, regardless of the direction in which the aircraft flies. So the linearization of this effect comes to zero.

These assumptions result in the following simplified decoupled longitudinal dynamics at hover:

$$\begin{bmatrix} \dot{u} \\ \dot{w} \\ \dot{q} \\ \dot{\theta} \end{bmatrix} = \begin{bmatrix} X_u & 0 & 0 & -g \\ 0 & Z_w & 0 & 0 \\ M_u & 0 & M_q & 0 \\ 0 & 0 & 1 & 0 \end{bmatrix} \begin{bmatrix} u \\ w \\ q \\ \theta \end{bmatrix} + \begin{bmatrix} X_{\delta_{\text{lon}}} & 0 \\ 0 & Z_{\delta_{\text{col}}} \\ M_{\delta_{\text{lon}}} & 0 \\ 0 & 0 \end{bmatrix} \begin{bmatrix} \delta_{\text{lon}} \\ \delta_{\text{col}} \end{bmatrix} \quad (7.39)$$

The diagonal terms in the system matrix (i.e.,  $X_u$ ,  $Z_w$ , and  $M_q$ ) dominate each respective equation and are called damping stability derivatives. These are typically negative. A more detailed description of each relevant longitudinal stability derivative is provided below:

- $X_u$ : As airspeed increases or decreases, the rotor will tend to experience longitudinal flapping (rotor blow back) such that the tilt of the rotor tip path plane generates a force in the opposite direction of the velocity.
- $M_u$ : The rotor blow back described above will also generate a pitching moment which will tend to pitch the aircraft nose up when it starts to move forward and nose down with rearward motion.
- $M_q$ : This is the pitch damping derivative. If the aircraft begins to rotate nose up or nose down, the gyroscopic precession of the rotor will cause longitudinal flapping that generates a moment that tends to resist the rotation.
- $Z_w$ : This is the heave damping derivative. If the aircraft translates up or down it changes the inflow to the main rotor, which will change the rotor thrust in such a way that it resists this motion.

The relevant longitudinal control derivatives are described as follows:

- $X_{\delta_{\text{lon}}}$ : A longitudinal cyclic input will cause longitudinal flapping that generates forward or aft force.
- $M_{\delta_{\text{lon}}}$ : This is the primary longitudinal control derivative. The flapping described above will likewise generate a pitching moment.
- $Z_{\delta_{\text{col}}}$ : This is the primary collective control derivative. Changes in collective pitch will change the rotor thrust.

By inspecting Eq. (7.39), we find that the vertical (or heave) dynamics ( $w$ ,  $\delta_{\text{col}}$ ) is decoupled from the longitudinal translation / pitch dynamics ( $u$ ,  $q$ ,  $\theta$ ,  $\delta_{\text{lon}}$ ). These two dynamics can therefore be separated in a first-order system representative of the heave dynamics, and a third-order system corresponding to the longitudinal translation / pitch dynamics:

$$\dot{w} = Z_w w + Z_{\delta_{\text{col}}}, \quad \text{vertical translation dynamics} \quad (7.40a)$$

$$\begin{bmatrix} \dot{u} \\ \dot{q} \\ \dot{\theta} \end{bmatrix} = \begin{bmatrix} X_u & 0 & -g \\ M_u & M_q & 0 \\ 0 & 1 & 0 \end{bmatrix} \begin{bmatrix} u \\ q \\ \theta \end{bmatrix} + \begin{bmatrix} X_{\delta_{\text{lon}}} \\ M_{\delta_{\text{lon}}} \\ 0 \end{bmatrix} \delta_{\text{lon}}, \quad \text{longitudinal translation / pitch dynamics} \quad (7.40b)$$

Consider the heave dynamics first. By applying the Laplace transform, Eq. (7.40a) can be transformed into the following transfer function representation:

$$\frac{w}{\delta_{\text{col}}}(s) = \frac{Z_{\delta_{\text{col}}}}{s - Z_w} = \frac{Z_{\delta_{\text{col}}}}{-Z_w \left( -1 \frac{1}{Z_w} s + 1 \right)} = \frac{-\frac{Z_{\delta_{\text{col}}}}{Z_w}}{-\frac{1}{Z_w} s + 1} = \frac{k_{\text{heave}}}{\tau_{\text{heave}} s + 1} \quad (7.41)$$

where  $k_{\text{heave}}$  is the heave control sensitivity and  $\tau_{\text{heave}}$  is the heave time constant. These quantities are found as:

$$k_{\text{heave}} = -\frac{Z_{\delta_{\text{col}}}}{Z_w} \quad (7.42\text{a})$$

$$\tau_{\text{heave}} = -\frac{1}{Z_w} \quad (7.42\text{b})$$

This is a first-order system with a pole at  $s = Z_w$ . As such, the system is stable for  $Z_w < 0$ , which is typically the case. The derivative  $Z_w$  is also known as *heave damping*. This mode of motion is called *heave subsidence*. The collective control axis is a Vertical Speed Command Response. If the damping derivative is too low, the sensitivity is high, but the time constant is long. This generally results in poor handling qualities. Larger time constant will feel like a Vertical Acceleration Command Response instead of Vertical Speed Command. On the other hand, if the damping is too high, the control sensitivity in the vertical axis can be too low. Consider a step input in the collective input of the form:

$$\delta_{\text{col}}(t) = \begin{cases} 0, & t < 0 \\ \Delta_{\text{col}}, & t \geq 0 \end{cases} \quad (7.43)$$

Then, the vertical speed response to a unit step input is:

$$w(t) = -\frac{Z_{\delta_{\text{col}}}}{Z_w} \left( 1 - e^{-\frac{t}{\tau_{\text{heave}}}} \right) \Delta_{\text{col}} \quad (7.44)$$

and is shown in Fig. 7.9. This figure shows that the unit step response converges to the control sensitivity value of  $k_{\text{heave}} = -\frac{Z_{\delta_{\text{col}}}}{Z_w}$  and that the response reaches steady state after approximately  $5\tau_{\text{heave}}$ .

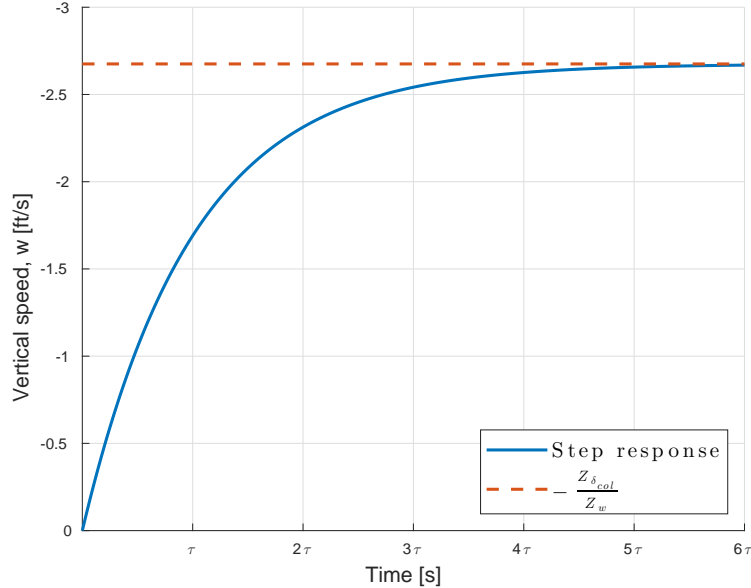


Figure 7.9: Vertical velocity response to a collective step input.

Consider now the longitudinal translation / pitch dynamics in Eq. (7.40b). Applying the Laplace transform to this equation yields the following equations:

$$su(s) = X_u u(s) - g\theta(s) + X_{\delta_{\text{lon}}} \delta_{\text{lon}}(s) \quad (7.45\text{a})$$

$$sq(s) = M_u u(s) + M_q q(s) + M_{\delta_{\text{lon}}} \delta_{\text{lon}} \quad (7.45\text{b})$$

$$s\theta(s) = q(s) \quad (7.45\text{c})$$

By substituting Eq. (7.45c) into Eq. (7.45b) and by re-arranging, one obtains:

$$(s - X_u) u(s) + g\theta(s) = X_{\delta_{\text{lon}}} \delta_{\text{lon}}(s) \quad (7.46a)$$

$$(-M_u) u(s) + (s^2 - M_q s) \theta(s) = M_{\delta_{\text{lon}}} \delta_{\text{lon}}(s) \quad (7.46b)$$

In matrix form:

$$\begin{bmatrix} s - X_u & g \\ -M_u & s^2 - M_q s \end{bmatrix} \begin{bmatrix} u(s) \\ \theta(s) \end{bmatrix} = \begin{bmatrix} X_{\delta_{\text{lon}}} \\ M_{\delta_{\text{lon}}} \end{bmatrix} \delta_{\text{lon}}(s) \quad (7.47)$$

Solving for the longitudinal speed and pitch attitude yields:

$$\begin{bmatrix} u(s) \\ \theta(s) \end{bmatrix} = \begin{bmatrix} s - X_u & g \\ -M_u & s^2 - M_q s \end{bmatrix}^{-1} \begin{bmatrix} X_{\delta_{\text{lon}}} \\ M_{\delta_{\text{lon}}} \end{bmatrix} \delta_{\text{lon}}(s) \quad (7.48)$$

$$= \frac{1}{s^3 - (X_u + M_q)s^2 + X_u M_q s + g M_u} \begin{bmatrix} s^2 - M_q s & -g \\ M_u & s - X_u \end{bmatrix} \begin{bmatrix} X_{\delta_{\text{lon}}} \\ M_{\delta_{\text{lon}}} \end{bmatrix} \delta_{\text{lon}}(s) \quad (7.49)$$

The resulting transfer functions from longitudinal cyclic stick to longitudinal speed and pitch attitude are:

$$\frac{u}{\delta_{\text{lon}}}(s) = \frac{X_{\delta_{\text{lon}}} s^2 - M_q X_{\delta_{\text{lon}}} s - g M_{\delta_{\text{lon}}}}{s^3 - (X_u + M_q)s^2 + X_u M_q s + g M_u} \quad (7.50a)$$

$$\frac{\theta}{\delta_{\text{lon}}}(s) = \frac{M_{\delta_{\text{lon}}} s + (M_u X_{\delta_{\text{lon}}} - X_u M_{\delta_{\text{lon}}})}{s^3 - (X_u + M_q)s^2 + X_u M_q s + g M_u} \quad (7.50b)$$

The stability of the longitudinal response is governed by a third-order characteristic equation, which is found by setting to zero the denominator of the transfer functions above the:

$$s^3 - (X_u + M_q)s^2 + X_u M_q s + g M_u = 0 \quad (7.51)$$

This characteristic equation is known as *hovering cubic*, and is common to every hovering vehicle (including flapping-wing hovering flyers such as birds or insects). Note that this expression only includes stability derivatives and no control derivatives. It is not possible to find a closed-form solution to this equation, but one can use the Routh-Hurwitz criterion to determine whether the dynamics are stable or not. The roots of the hovering cubic are of the form:

$$s^3 + as^2 + bs + c = 0 \quad (7.52)$$

The Routh-Hurwitz criterion necessary condition for stability is that all coefficients of the polynomial must be the same sign. This implies that they are all positive (since the first coefficient is 1), *i.e.*,  $a > 0$ ,  $b > 0$ , and  $c > 0$ . The sufficient condition for stability for a third-order system is  $ab - c > 0$ . The stability requirements can be summarized in terms of the stability derivatives:

$$a = -(X_u + M_q) > 0 \quad \checkmark \text{Typically met since } X_u, M_q < 0 \quad (7.53a)$$

$$b = X_u M_q \quad \checkmark \text{Typically met since } X_u, M_q < 0 \quad (7.53b)$$

$$c = g M_u > 0 \quad \checkmark \text{Typically met since } M_u > 0 \quad (7.53c)$$

$$ab - c > 0 \Leftrightarrow -(X_u + M_q) X_u M_q - g M_u > 0 \quad \text{Needs } M_u < \frac{-(X_u + M_q) X_u M_q}{g} \quad (7.53d)$$

The last criteria is often not met. The term on the right hand side is usually positive (again, because the damping derivatives are  $< 0$ ), but the  $M_u$  derivative is often too large to meet this requirement. It turns out that, for typical helicopters:

- One root is real, negative, and with large magnitude. This root corresponds to the *pitch subsidence* mode. The pitch subsidence mode is a heavily damped, short-period mode characterized by a first-order response.

- The other two roots are either real and negative or complex and unstable. These roots characterize the *longitudinal oscillation* mode, also known as *phugoid* mode. The phugoid mode is a long-period mode, usually oscillatory, and unstable. The location of the poles varies heavily with  $M_u$ . The mode is unstable largely due to the rotor blow back effect with longitudinal speed. This slow divergence is what makes rotorcraft so difficult to fly compared to fixed-wing aircraft. In fact, hands-off hovering is not possible as the pilot is required to actively regulate the longitudinal (and lateral) axis.

As such, the longitudinal translation / pitch response is dominated in the short-term by the stable pitch subsidence mode, whereas longer term, and in the longer term by a divergent oscillation corresponding to the phugoid mode. The phugoid mode can be described through a physical analogy. Consider a moving cart with the helicopter attached to it and free to pivot about its CG. The  $M_q$  and  $X_u$  derivatives provide damping to the system, but the  $M_u$  derivative can add energy, leading to instability if it is too large. This analogy is illustrated in Fig. 7.10.

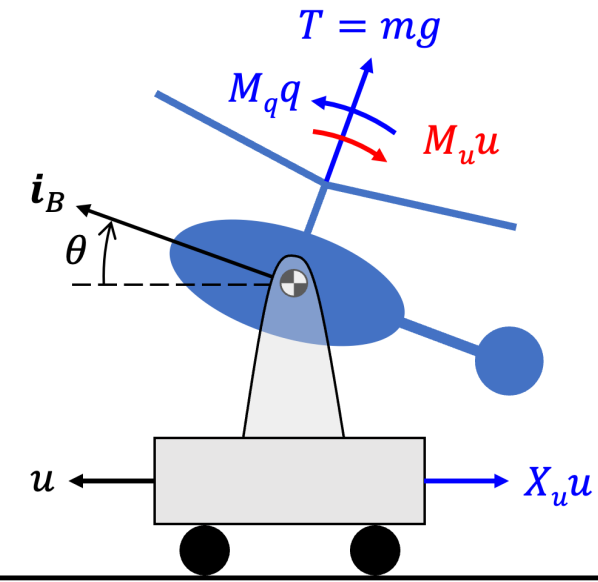


Figure 7.10: Physical analogy of the longitudinal hover oscillatory mode.

### Lateral-Directional Dynamic Stability

An important thing to note about hover is that the main rotor system is axis-symmetric. So it will behave the same way in sideward translation and roll as it does in longitudinal translation and pitch. Recall the hub-wind axes transformation for the main rotor model, such that the same equations could be used with the local in plane velocity coming from any direction. So we will see a lot of analogous behavior in lateral dynamics with a few key differences:

- The sign convention is different: positive roll attitude causes positive lateral velocity, whereas it is the opposite with pitch and longitudinal velocity. There is no difference in physics here, but in the equations some of the key terms have different signs.
- The tail rotor has significant effects in hover and causes some differences.
- The moments of inertia are often quite different in roll compared to pitch. For example on a UH-60 helicopter, the roll inertia is order of magnitude smaller than pitch inertia. This is conventional for conventional helicopters. For tilt-rotors (*e.g.*, XV-15) it can be very different – roll inertia is often the largest.

Consider the lateral-directional dynamics in Eq. (7.38). The following assumptions can be made with a reasonable level of accuracy in the hover flight condition:

- The trim and angular velocities in hover are zero, such that  $v_e = w_e = q_e = 0$ .
- Typically, the trim roll and pitch attitudes at hover are small such that  $\cos \phi_e \approx \cos \theta_e \approx 1$  and  $\tan \theta_e \approx \theta_e$ .
- $N'_v \approx 0$ . It is a fairly rough approximation to neglect this term. This is the directional stability term that will arise due to changes in inflow of the tail rotor in sideward flight. It will tend to have a positive

value such that it turns the aircraft into the relative air flow. However, it will still be neglected in this analysis to simplify the hover dynamics.

- $Y_r$ ,  $Y_p$ ,  $L'_r$  and  $N'_r$  are relatively small stability derivatives that have little impact on hover dynamics and can thus be assumed to be zero.
- $Y_{\delta_{ped}}$  and  $L'_{\delta_{ped}}$  have a significant value (due lateral force from the tail rotor), but they can be neglected to simplify hover dynamics.
- $N'_{\delta_{lat}}$  is not usually a significant control derivative and can be neglected.

These assumptions result in the following simplified decoupled lateral dynamics at hover:

$$\begin{bmatrix} \dot{v} \\ \dot{p} \\ \dot{r} \\ \dot{\phi} \end{bmatrix} = \begin{bmatrix} Y_v & 0 & 0 & g \\ L'_v & L'_p & 0 & 0 \\ N_v & 0 & N'_r & 0 \\ 0 & 0 & 1 & 0 \end{bmatrix} \begin{bmatrix} v \\ p \\ r \\ \phi \end{bmatrix} + \begin{bmatrix} Y_{\delta_{lat}} & 0 \\ L'_{\delta_{lat}} & 0 \\ 0 & N'_{\delta_{ped}} \\ 0 & 0 \end{bmatrix} \begin{bmatrix} \delta_{lat} \\ \delta_{ped} \end{bmatrix} \quad (7.54)$$

Like for the longitudinal-heave dynamics, the diagonal terms (*i.e.*, the damping derivatives  $Y_v$ ,  $L'_p$ , and  $N'_r$ ) dominate each respective equation. A summary of the relevant stability derivative is provided below:

- $Y_v$ : Analogous to  $X_u$ , as lateral airspeed increases or decreases, the rotor will tend to flap laterally (rotor blow back) generating a force in the opposite direction.
- $L'_v$ : The rotor blow back described above will also generate a rolling moment which will tend to roll the aircraft left when it starts to move to the right. This term is analogous to  $M_u$ , but because of differences in sign convention this the value is **negative instead of positive**.
- $L'_p$ : Roll damping, analogous to  $M_q$ .
- $N'_r$ : Yaw damping, this comes mainly from the tail rotor, tends to resist rotations in yaw.

The important control derivatives are  $Y_{\delta_{lat}}$ ,  $N_{\delta_{lat}}$ , and  $L'_{\delta_{ped}}$ . These are primary control derivative, very much analogous to the control derivatives kept in the longitudinal case.

Once again, by inspecting Eq. (7.54), the lateral dynamics are decoupled into a first-order system representative of the yaw dynamics and a the third-order system corresponding to the lateral translation / roll dynamics:

$$\dot{r} = N'_r r + N'_{\delta_{ped}}, \quad \text{directional dynamics} \quad (7.55a)$$

$$\begin{bmatrix} \dot{v} \\ \dot{p} \\ \dot{\phi} \end{bmatrix} = \begin{bmatrix} Y_u & 0 & g \\ L'_v & L'_p & 0 \\ 0 & 1 & 0 \end{bmatrix} \begin{bmatrix} v \\ p \\ \phi \end{bmatrix} + \begin{bmatrix} Y_{\delta_{lat}} \\ L'_{\delta_{lat}} \\ 0 \end{bmatrix} \delta_{lat}, \quad \text{lateral translation / roll dynamics} \quad (7.55b)$$

Consider the directional dynamics first. By applying the Laplace transform, Eq. (7.55a) is transformed into the following transfer function:

$$\frac{r}{\delta_{ped}}(s) = \frac{N_{\delta_{ped}}}{s - N_r} = \frac{N_{\delta_{ped}}}{-N_r \left( -1 \frac{1}{N_r} s + 1 \right)} = \frac{-\frac{N_{\delta_{ped}}}{N_r}}{-\frac{1}{N_r} s + 1} = \frac{k_{yaw}}{\tau_{yaw} s + 1} \quad (7.56)$$

where  $k_{yaw}$  is the yaw control sensitivity and  $\tau_{yaw}$  is the yaw time constant. These quantities are found as:

$$k_{yaw} = -\frac{N_{\delta_{ped}}}{N_r} \quad (7.57a)$$

$$\tau_{yaw} = -\frac{1}{N_r} \quad (7.57b)$$

Analogously to the heave dynamics (rotation about vertical axis instead of translation), this is a first-order system with a pole at  $s = N_r$ . As such, the system is stable for  $N_r < 0$ , which is typically the case. The derivative  $N_r$  is also known as *yaw damping*. This mode of motion is called *yaw subsidence*. Consider a step input in the pedals input of the form:

$$\delta_{ped}(t) = \begin{cases} 0, & t < 0 \\ \Delta_{ped}, & t \geq 0 \end{cases} \quad (7.58)$$

Then, the yaw rate response to a unit step input is:

$$r(t) = -\frac{N_{\delta_{ped}}}{N_r} \left( 1 - e^{-\frac{t}{\tau_{yaw}}} \right) \Delta_{ped} \quad (7.59)$$

and is analogous to that shown in Fig. 7.9. The unit step response converges to the control sensitivity value of  $k_{yaw} = -\frac{N_{\delta_{ped}}}{N_r}$  and that the response reaches steady state after approximately  $5\tau_{yaw}$ .

Consider now the lateral translation / roll dynamics in Eq. (7.55b). Applying the Laplace transform to this equation yields the following equations:

$$sv(s) = Y_v v(s) + g\phi(s) + Y_{\delta_{lat}} \delta_{lat}(s) \quad (7.60a)$$

$$sp(s) = L_v v(s) + L_p p(s) + L_{\delta_{lat}} \delta_{lat} \quad (7.60b)$$

$$s\theta(s) = q(s) \quad (7.60c)$$

By substituting Eq. (7.60c) into Eq. (7.60b) and by re-arranging, one obtains:

$$(s - Y_v) v(s) - g\phi(s) = Y_{\delta_{lat}} \delta_{lat}(s) \quad (7.61a)$$

$$(-L_v) u(s) + (s^2 - L_p s) \theta(s) = L_{\delta_{lat}} \delta_{lat}(s) \quad (7.61b)$$

In matrix form:

$$\begin{bmatrix} s - Y_v & -g \\ -L_v & s^2 - L_p s \end{bmatrix} \begin{bmatrix} v(s) \\ \phi(s) \end{bmatrix} = \begin{bmatrix} Y_{\delta_{lat}} \\ L_{\delta_{lat}} \end{bmatrix} \delta_{lat}(s) \quad (7.62)$$

Solving for the longitudinal speed and pitch attitude yields:

$$\begin{bmatrix} v(s) \\ \phi(s) \end{bmatrix} = \begin{bmatrix} s - Y_v & -g \\ -L_v & s^2 - L_p s \end{bmatrix}^{-1} \begin{bmatrix} Y_{\delta_{lat}} \\ L_{\delta_{lat}} \end{bmatrix} \delta_{lat}(s) \quad (7.63)$$

$$= \frac{1}{s^3 - (Y_v + L_p)s^2 + L_v L_p s - g L_v} \begin{bmatrix} s^2 - L_p s & g \\ L_v & s - Y_v \end{bmatrix} \begin{bmatrix} Y_{\delta_{lat}} \\ L_{\delta_{lat}} \end{bmatrix} \delta_{lat}(s) \quad (7.64)$$

The resulting transfer functions from longitudinal cyclic stick to longitudinal speed and pitch attitude are:

$$\frac{v}{\delta_{lat}}(s) = \frac{Y_{\delta_{lat}} s^2 - L_p Y_{\delta_{lat}} s + g L_{\delta_{lat}}}{s^3 - (Y_v + L_p)s^2 + Y_v L_p s - g L_v} \quad (7.65a)$$

$$\frac{\phi}{\delta_{lat}}(s) = \frac{L_{\delta_{lat}} s + (L_v Y_{\delta_{lat}} - Y_v L_{\delta_{lat}})}{s^3 - (Y_v + L_p)s^2 + Y_v L_p s - g L_v} \quad (7.65b)$$

The stability of the longitudinal response is governed by a third-order characteristic equation, which is found by setting to zero the denominator of the transfer functions above the:

$$s^3 - (Y_v + L_p)s^2 + Y_v L_p s - g L_v = 0 \quad (7.66)$$

This characteristic equation is the hovering cubic for the lateral axis. Like for the longitudinal dynamics, it is not possible to find a closed-form solution to this equation. Thus, the Routh-Hurwitz criterion is used to determine whether the dynamics are stable. The Routh-Hurwitz stability requirements are summarized as follows in terms of the stability derivatives:

$$a = -(Y_v + L_p) > 0 \quad \checkmark \text{Typically met since } Y_v, L_p < 0 \quad (7.67a)$$

$$b = Y_v L_p \quad \checkmark \text{Typically met since } Y_v, L_p < 0 \quad (7.67b)$$

$$c = -g L_v > 0 \quad \checkmark \text{Typically met since } L_v < 0 \quad (7.67c)$$

$$ab - c > 0 \Leftrightarrow -(Y_v + L_p) Y_v L_p + g L_v > 0 \quad \text{Needs } L_v < \frac{(Y_v + L_p) Y_v L_p}{g} \quad (7.67d)$$

In the case of the lateral-directional dynamics, the last criteria is sometimes met, but sometimes not. For most helicopters, the roll inertia is significantly lower than the pitch inertia. As a result, the roll damping is a lot larger than the pitch damping. This causes the term on the right to be more negative than the term on the left. This is the case for the UH-60. However, it is configuration dependent. It turns out that, for typical helicopters:

- One root is real, negative, and with large magnitude. This root corresponds to the *roll subsidence* mode. The roll subsidence mode is a heavily damped, short-period mode characterized by a first-order response.
- The other two roots are either real and negative or complex and unstable. These roots characterize the *lateral oscillation* mode. The lateral mode is a longer-period mode, usually oscillatory, and often unstable. The location of the poles varies heavily with  $L_v$ . Since for typical helicopters  $I_{xx} \ll I_{yy}$ , the lateral oscillatory mode tends to have higher frequency than the unstable longitudinal mode. Thus, lateral oscillations are more difficult to control as the smaller inertia leads to smaller period and damping ratio of the lateral mode. Since the pilot will have more difficulty in perceiving the roll motion and applying the appropriate cyclic stick inputs, the lateral oscillatory mode on helicopters with small lateral inertia will be more prone to pilot-induced oscillations (PIO) in hover. Of course, these considerations do not apply to tilt-rotors in that tilt-rotors have lateral moments of inertia that are typically similar, if not greater, than longitudinal moments of inertia, i.e.,  $I_{yy} \geq I_{xx}$ .

### 7.3.5 Forward Flight

In forward flight the stability and control derivatives change with speed, such that the eigenvalues and consequently the natural modes migrate. Eigenvalues migration with speed is shown in Fig. 7.11 for a UH-60 helicopter. This figure shows the major effects observed for conventional helicopters:

1. The lateral hover phugoid mode evolves into the Dutch roll mode as airspeed increases.
2. The heave subsidence and pitch subsidence modes coalesce to become the short period mode.
3. The roll subsidence mode decreases in frequency.
4. The longitudinal hover phugoid mode evolves into forward flight phugoid as airspeed increases.
5. The yaw subsidence mode becomes spiral mode.

Let us take a closer look to these new set of modes in forward flight.

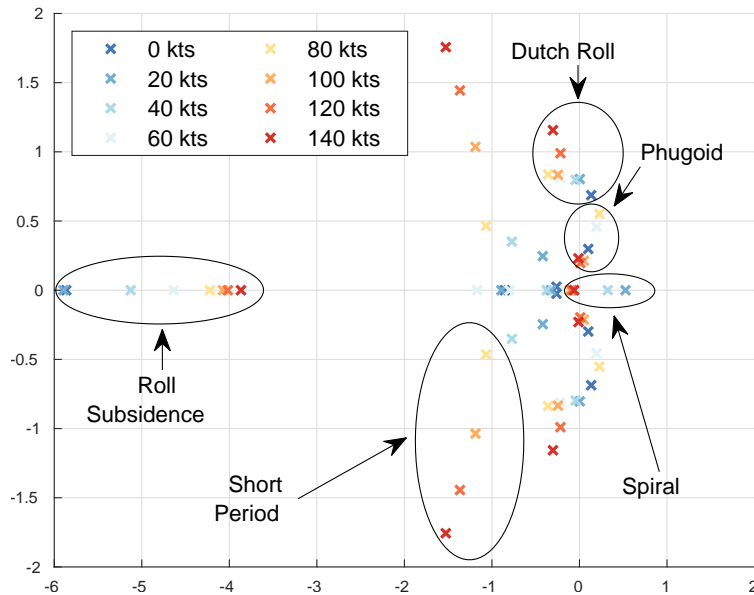


Figure 7.11: Eigenvalues migration with increasing speed for a UH-60 helicopter.

### Longitudinal-Heave Dynamic Stability

The dynamic stability analysis in forward flight starts with considering the decoupled 4-state residualized longitudinal dynamics in forward flight:

$$\begin{bmatrix} \dot{u} \\ \dot{w} \\ \dot{q} \\ \dot{\theta} \end{bmatrix} = \begin{bmatrix} X_u & X_w & X_q - w_e & -g \\ Z_u & Z_w & Z_q + u_e & 0 \\ M_u & M_w & M_q & 0 \\ 0 & 0 & 1 & 0 \end{bmatrix} \begin{bmatrix} u \\ w \\ q \\ \theta \end{bmatrix} + \begin{bmatrix} X_{\delta_{\text{lon}}} & X_{\delta_{\text{col}}} \\ Z_{\delta_{\text{lon}}} & Z_{\delta_{\text{col}}} \\ M_{\delta_{\text{lon}}} & M_{\delta_{\text{col}}} \\ 0 & 0 \end{bmatrix} \begin{bmatrix} \delta_{\text{lon}} \\ \delta_{\text{col}} \end{bmatrix} \quad (7.68)$$

Assume the inertial terms related to the pitch rate to be dominant (*i.e.*,  $X_q \ll w_e$  and  $Z_q \ll u_e$ ) and the  $X_w$  stability derivative to be negligible. Additionally, the control cross-coupling derivatives can be neglected to yield:

$$\begin{bmatrix} \dot{u} \\ \dot{w} \\ \dot{q} \\ \dot{\theta} \end{bmatrix} = \begin{bmatrix} X_u & 0 & -w_e & -g \\ Z_u & Z_w & u_e & 0 \\ M_u & M_w & M_q & 0 \\ 0 & 0 & 1 & 0 \end{bmatrix} \begin{bmatrix} u \\ w \\ q \\ \theta \end{bmatrix} + \begin{bmatrix} X_{\delta_{\text{lon}}} & 0 \\ 0 & Z_{\delta_{\text{col}}} \\ M_{\delta_{\text{lon}}} & 0 \\ 0 & 0 \end{bmatrix} \begin{bmatrix} \delta_{\text{lon}} \\ \delta_{\text{col}} \end{bmatrix} \quad (7.69)$$

To analyze the flight dynamics in forward flight, it is convenient to make a change in the state variable so that the angle of attack  $\alpha$  is used in place of the vertical speed  $w$  and the vertical velocity in the inertial frame  $V_z$  (rate of descent) is used in place of the pitch attitude  $\theta$ . Angle of attack and vertical velocity are defined as follows:

$$\alpha = \tan^{-1}\left(\frac{w}{u}\right) \quad (7.70a)$$

$$V_z = \dot{z} = w \cos \theta - u \sin \theta \quad (7.70b)$$

These equations are linearized as:

$$\Delta\alpha \approx \frac{w}{u} \quad (7.71a)$$

$$\Delta V_z \approx \Delta w - u_e \Delta \theta \quad (7.71b)$$

The change in state variables can be written in terms of a state transformation matrix:

$$\begin{bmatrix} u \\ V_z \\ \alpha \\ q \end{bmatrix} = \begin{bmatrix} 1 & 0 & 0 & 0 \\ 0 & 1 & 0 & -u_e \\ 0 & \frac{1}{u_e} & 0 & 0 \\ 0 & 0 & 1 & 0 \end{bmatrix} \begin{bmatrix} u \\ w \\ q \\ \theta \end{bmatrix} \Leftrightarrow \hat{\mathbf{x}}_{\text{lon}} = \mathbf{T} \mathbf{x}_{\text{lon}} \quad (7.72)$$

One can apply the similarity transformation on the state-space system much that:

$$\dot{\hat{\mathbf{x}}}_{\text{lon}} = \underbrace{(\mathbf{T} \mathbf{A}_{\text{lon}} \mathbf{T}^{-1})}_{\hat{\mathbf{A}}_{\text{lon}}} \hat{\mathbf{x}}_{\text{lon}} + \underbrace{(\mathbf{T} \mathbf{B}_{\text{lon}})}_{\hat{\mathbf{B}}_{\text{lon}}} \hat{\mathbf{u}}_{\text{lon}} \quad (7.73)$$

The transformed system partitions the longitudinal dynamics as:

$$\begin{bmatrix} \dot{u} \\ \dot{V}_z \\ \dot{\alpha} \\ \dot{q} \end{bmatrix} = \begin{bmatrix} X_u & \frac{g}{u_e} & -g & -w_e \\ Z_u & 0 & Z_\alpha & 0 \\ Z_u & 0 & \frac{Z_\alpha}{u_e} & 1 \\ u_e & 0 & u_e & M_q \\ M_u & 0 & M_\alpha & M_q \end{bmatrix} \begin{bmatrix} u \\ V_z \\ \alpha \\ q \end{bmatrix} + \begin{bmatrix} X_{\delta_{\text{lon}}} & 0 \\ 0 & Z_{\delta_{\text{col}}} \\ 0 & Z_{\delta_{\text{col}}} \\ M_{\delta_{\text{lon}}} & \frac{u_e}{u_e} \\ 0 & 0 \end{bmatrix} \begin{bmatrix} \delta_{\text{lon}} \\ \delta_{\text{col}} \end{bmatrix} \quad (7.74)$$

where  $Z_\alpha = Z_w u_e$  and  $M_\alpha = M_w u_e$ . One can now apply residualization to reduce the model by assuming a separation in time scale. It is reasonable to assume the pitch rate and angle of attack dynamics (associated with attitude dynamics) to be much faster than the airspeed and rate of descent (associated with trajectory dynamics). For the slow model, one can assume  $\alpha$  and  $q$  to reach steady-state quicker than  $u$  and  $V_z$ . As such, their dynamics can be set to zero:

$$\begin{bmatrix} \dot{\alpha} \\ \dot{q} \end{bmatrix} = \begin{bmatrix} Z_u \\ u_e \\ M_u \end{bmatrix} u + \begin{bmatrix} Z_\alpha & 1 \\ u_e & M_q \end{bmatrix} \begin{bmatrix} \alpha \\ q \end{bmatrix} + \begin{bmatrix} 0 & Z_{\delta_{\text{col}}} \\ M_{\delta_{\text{lon}}} & 0 \end{bmatrix} \begin{bmatrix} \delta_{\text{lon}} \\ \delta_{\text{col}} \end{bmatrix} \approx \mathbf{0} \quad (7.75)$$

The equation above constitutes an algebraic constraint on  $\alpha$  and  $q$  which can be substituted back into the original model to get a second-order system of the slow dynamics:

$$\begin{bmatrix} \dot{\alpha} \\ \dot{q} \end{bmatrix} = - \begin{bmatrix} Z_\alpha & 1 \\ \frac{u_e}{M_\alpha} & M_q \end{bmatrix}^{-1} \left( \begin{bmatrix} Z_u \\ \frac{u_e}{M_u} \end{bmatrix} u + \begin{bmatrix} 0 & \frac{Z_{\delta_{\text{col}}}}{u_e} \\ M_{\delta_{\text{ion}}} & 0 \end{bmatrix} \begin{bmatrix} \delta_{\text{ion}} \\ \delta_{\text{col}} \end{bmatrix} \right) \quad (7.76)$$

The slow dynamics in forward flight are governed by:

$$\begin{bmatrix} \dot{u} \\ \dot{V}_z \end{bmatrix} = \begin{bmatrix} X'_u & \frac{g}{u_e} \\ Z'_u & 0 \end{bmatrix} \begin{bmatrix} u \\ V_z \end{bmatrix} + \begin{bmatrix} X'_{\delta_{\text{ion}}} & X'_{\delta_{\text{col}}} \\ Z'_{\delta_{\text{ion}}} & Z'_{\delta_{\text{col}}} \end{bmatrix} \begin{bmatrix} \delta_{\text{ion}} \\ \delta_{\text{col}} \end{bmatrix} \quad (7.77)$$

where:

$$X'_u = X_u + \frac{g(M_q Z_u - M_u u_e) - w_e(M_\alpha Z_u - Z_\alpha M_u)}{(Z_\alpha M_q - M_\alpha u_e)} \quad (7.78a)$$

$$Z'_u = Z_u - \frac{Z_\alpha(M_q Z_u - M_u u_e)}{(Z_\alpha M_q - M_\alpha u_e)} \quad (7.78b)$$

$$X'_{\delta_{\text{ion}}} = X_{\delta_{\text{ion}}} - \frac{g u_e M_{\delta_{\text{ion}}}}{(Z_\alpha M_q - M_\alpha u_e)} \quad (7.78c)$$

$$X'_{\delta_{\text{col}}} = X_{\delta_{\text{col}}} - \frac{w_e M_q Z_{\delta_{\text{col}}}}{(Z_\alpha M_q - M_\alpha u_e)} \quad (7.78d)$$

$$Z'_{\delta_{\text{ion}}} = \frac{g Z_\alpha M_{\delta_{\text{ion}}}}{(Z_\alpha M_q - M_\alpha u_e)} \quad (7.78e)$$

$$Z'_{\delta_{\text{col}}} = Z_{\delta_{\text{col}}} - \frac{w_e M_\alpha Z_{\delta_{\text{col}}}}{(Z_\alpha M_q - M_\alpha u_e)} \quad (7.78f)$$

$$(7.78g)$$

This model will provide a reasonably good approximation of the *phugoid* dynamics of the rotorcraft in forward flight. The eigenvalues of these dynamics are governed by the characteristic equation:

$$\lambda^2 - X'_u \lambda - \frac{g Z'_u}{u_e} = 0 \quad (7.79)$$

The phugoid mode is governed by the modified speed damping  $X'_u$  and the modified lift-due-to-airspeed derivative  $Z'_u$ . The natural frequency and damping ratio are:

$$\omega_{n_{\text{PH}}} = \sqrt{-\frac{g Z'_u}{u_e}} \quad (7.80a)$$

$$\zeta_{n_{\text{PH}}} = -\frac{X'_u}{2\omega_{n_{\text{PH}}}} \quad (7.80b)$$

In a more crude phugoid approximation, one can assume the angle of attack not to vary in the phugoid mode, in which case the modified  $u$  derivatives are equivalent to the unmodified derivatives, *i.e.*,  $X'_u = X_u$  and  $Z'_u = Z_u$ . The speed damping comes primarily through drag force on both the airframe and rotor systems. For example, linearization of the drag forces:

$$X_{\text{airframe}} = -\frac{1}{2} \rho u^2 (C_D S)_{\text{airframe}} \quad (7.81)$$

results in:

$$(X_u)_{\text{airframe}} = -\rho u (C_D S)_{\text{airframe}} \quad (7.82)$$

Table 7.1: Comparison between the 8-state model, 4-state model, and mode approximations for the longitudinal dynamics of a UH-60 helicopter at 140 kts forward flight.

|                     | Short Period              | Phugoid      |                           |
|---------------------|---------------------------|--------------|---------------------------|
|                     | $\omega_{n_{SP}}$ [rad/s] | $\zeta_{SP}$ | $\omega_{n_{PH}}$ [rad/s] |
| 8-State Model       | 2.01                      | 0.879        | 0.116                     |
| 4-State Model       | 1.72                      | 0.756        | 0.0554                    |
| Mode Approximations | 1.72                      | 0.755        | 0.0541                    |

But note that rotor flapping and in-plane forces (*i.e.*, profile drag) are also a major factor for  $X_u$ . The lift-due-to-airspeed derivative  $Z_u$  comes from the rotor thrust increasing with forward speed due to changes in inflow. This can be negative due to reductions in induced inflow at low speed, but can turn positive in high-speed flight when the rotor tip path plane is tilted forward. The fast dynamics can also be extracted. These assume the slow states to remain constant:

$$\begin{bmatrix} \dot{\alpha} \\ \dot{q} \end{bmatrix} = \begin{bmatrix} Z_\alpha & 1 \\ u_e & M_q \\ M_\alpha & M_q \end{bmatrix} \begin{bmatrix} \alpha \\ q \end{bmatrix} + \begin{bmatrix} 0 & Z_{\delta_{\text{lon}}} \\ M_{\delta_{\text{lon}}} & 0 \end{bmatrix} \begin{bmatrix} \delta_{\text{lon}} \\ \delta_{\text{col}} \end{bmatrix} \quad (7.83)$$

The system matrix eigenvalues describe the short period mode stability:

$$\lambda_{SP}^2 - \left( \frac{Z_\alpha}{u_e} + M_q \right) \lambda_{SP} + \left( \frac{Z_\alpha M_q}{u_e} - M_\alpha \right) = 0 \quad (7.84)$$

The corresponding natural frequency and damping ratio are:

$$\omega_{n_{SP}} = \sqrt{\frac{Z_\alpha M_q}{u_e} - M_\alpha} \quad (7.85a)$$

$$\zeta_{n_{SP}} = -\frac{1}{2\omega_{n_{SP}}} \left( \frac{Z_\alpha}{u_e} + M_q \right) \quad (7.85b)$$

The transfer functions of the responses of the angle of attack to longitudinal and collective stick inputs are:

$$\frac{\alpha}{\delta_{\text{lon}}}(s) = \frac{M_{\delta_{\text{lon}}}}{s^2 - \left( \frac{Z_\alpha}{u_e} + M_q \right) s + \left( \frac{Z_\alpha M_q}{u_e} - M_\alpha \right)} \quad (7.86a)$$

$$\frac{\alpha}{\delta_{\text{col}}}(s) = \frac{M_q Z_{\delta_{\text{lon}}}}{s^2 - \left( \frac{Z_\alpha}{u_e} + M_q \right) s + \left( \frac{Z_\alpha M_q}{u_e} - M_\alpha \right)} \quad (7.86b)$$

A comparison between the 8-state model, 4-state model, and mode approximations shown in Table 7.1 for the UH-60 model at 140 kts. In this table, it is shown that there is significant error when going to the 4-state longitudinal model, indicating that cross-coupling effects are important. But closed form approximations of modes from the 4-state model are reasonable. The 8-state model, 4-state model, and mode approximations are also compared for the same helicopter model at 80 kts, as shown in Table 7.4. The 8-state model predicts an over damped short period mode (damping ratio  $> 1$  means there are two real eigenvalues). The mode approximation has complex eigenvalues but they very heavily damped and near the same frequency. The mode approximations predict the phugoid mode to be unstable and on the real axis. The natural frequency and damping ratio are actually imaginary values, but if we construct the roots of  $\lambda^2 + 2\omega_n \zeta \lambda + \omega_n^2$ , then we get the eigenvalues in the table. It is worth noting that eigenvalues of the phugoid mode can become very sensitive to variations in aircraft parameters.

The following conclusions can be reached for the stability analysis in forward flight:

Table 7.2: Comparison between the 8-state model, 4-state model, and mode approximations for the longitudinal dynamics of a UH-60 helicopter at 80 kts forward flight.

|                     | Short Period<br>$\omega_{n_{SP}}$ [rad/s] | $\zeta_{SP}$ | Phugoid<br>$\lambda_{PH_{1,2}}$ |        |
|---------------------|---|--------------|---------------------------------|--------|
| 8-State Model       | 1.28                                      | 1.074        | $-0.0341 \pm 0.0857i$           |        |
| 4-State Model       | 1.24                                      | 0.942        | $-0.0875$                       | 0.0593 |
| Mode Approximations | 1.24                                      | 0.945        | $-0.0809$                       | 0.0639 |

- The longitudinal modes of a rotorcraft in forward flight are the same as those of a fixed-wing aircraft, but variations in the modes with airspeed are different because the important forces are not all proportional to free-stream dynamic pressure.
- Significant non-linearity in the low- to high-speed transition region (20 to 60 knots) can cause rapid changes in modes as airspeed increases.
- The phugoid mode is typically characterized by low-frequency and lightly-damped oscillation in airspeed, pitch attitude, and altitude, which are easy to see in flight response. Frequency tends to decrease as airspeed increases.
- The short-period mode is characterized by high-frequency and heavily-damped oscillations in angle of attack and pitch angle. Pitch stiffness  $M_\alpha$  and pitch damping  $M_q$  are critical to the stability of this mode. The frequency tends to increase as airspeed increases and the horizontal stabilizer becomes more effective. It is generally hard to observe these oscillations in the time history of the aircraft's response (too damped).
- It is possible for either mode to become overdamped (*i.e.*, two negative real eigenvalues) or to exhibit static instability (*i.e.*, one positive real eigenvalue and one negative real eigenvalue).
- Mode approximations are not very accurate for some forward flight conditions. Cross-coupling effects, which are neglected in the approximations, can sometimes play an important factor.

Add eigenvalues plots for eigs derived with full-order model, 8-state, 4-state, and 2-state approximations.

### Lateral-Directional Dynamic Stability

Consider the decoupled 4-state lateral dynamics of Eq. (7.38) in forward flight with  $Y_p$  and  $Y_r$  dropped:

$$\begin{bmatrix} \dot{v} \\ \dot{p} \\ \dot{r} \\ \dot{\phi} \end{bmatrix} = \begin{bmatrix} Y_v & w_e & -u_e & g \\ L'_v & L'_p & L'_r & 0 \\ N'_v & N'_p & N'_r & 0 \\ 0 & 1 & 0 & 0 \end{bmatrix} \begin{bmatrix} v \\ p \\ r \\ \phi \end{bmatrix} + \begin{bmatrix} Y_{\delta_{lat}} & Y_{\delta_{ped}} \\ L'_{\delta_{lat}} & L'_{\delta_{ped}} \\ 0 & N'_{\delta_{ped}} \\ 0 & 0 \end{bmatrix} \begin{bmatrix} \delta_{lat} \\ \delta_{ped} \end{bmatrix} \quad (7.87)$$

One can apply a similar order reduction method as for the longitudinal dynamics in forward flight (see [Pad18]) to get closed form expressions for the natural modes. These closed form expressions are summarized as follows:

- Spiral mode:

$$\lambda_S \approx \frac{g(L'_v N'_r - N'_v L'_r)}{u_e (N'_v L'_p - N'_p L'_v) + g L'_v} \quad (7.88)$$

- Roll subsidence mode:

$$\lambda_R \approx L'_p \quad (7.89)$$

Table 7.3: Comparison between the 8-state model, 4-state model, and mode approximations for the lateral dynamics of a UH-60 helicopter at 140 kts forward flight.

|                     | Spiral<br>$\lambda_S$ | Roll Subsidence<br>$\lambda_R$ | Dutch Roll<br>$\omega_{n_{DR}}$ [rad/s] | $\zeta_{DR}$ |
|---------------------|-----------------------|--------------------------------|---|--------------|
| 8-State Model       | -0.0368               | -3.60                          | 2.05                                    | 0.0543       |
| 4-State Model       | -0.0371               | -4.14                          | 1.97                                    | 0.156        |
| Mode Approximations | 0.0309                | -3.93                          | 2.04                                    | 0.174        |

Table 7.4: Comparison between the 8-state model, 4-state model, and mode approximations for the lateral dynamics of a UH-60 helicopter at 80 kts forward flight.

|                     | Spiral<br>$\lambda_S$ | Roll Subsidence<br>$\lambda_R$ | Dutch Roll<br>$\omega_{n_{DR}}$ [rad/s] | $\zeta_{DR}$ |
|---------------------|-----------------------|--------------------------------|---|--------------|
| 8-State Model       | 0.0233                | -4.40                          | 1.45                                    | 0.180        |
| 4-State Model       | -0.0230               | -4.77                          | 1.43                                    | 0.196        |
| Mode Approximations | 0.0302                | -4.72                          | 1.44                                    | 0.190        |

- Dutch roll mode:

$$\omega_{n_{DR}}^2 \approx \frac{(u_e N'_v + \sigma_d L'_v)}{1 - \frac{\sigma_d L'_r}{L'_p u_e}} \quad (7.90a)$$

$$2\omega_{n_{DR}} \zeta_{DR} \approx \frac{- \left[ N'_r + Y_v + \sigma_d \left( \frac{L'_v}{u_e} - \frac{L'_v}{L'_p} \right) \right]}{1 - \frac{\sigma_d L'_r}{L'_p u_e}} \quad (7.90b)$$

where:

$$\sigma_d = \frac{g - N'_p u_e}{L'_p} \quad (7.91)$$

A comparison between the 8-state model, 4-state model, and mode approximations shown in Table 7.3 for the UH-60 model at 140 kts. In this table, it is shown that the 4-state model and mode approximation underpredict the Dutch roll mode damping. Sometimes, cross-coupling effects can degrade Dutch roll mode damping. Otherwise, the approximations are quite reasonable. The 8-state model, 4-state model, and mode approximations are also compared for the same helicopter model at 80 kts, as shown in Table 7.4. At 80 kts, the roll subsidence and Dutch roll modes are very well predicted by the mode approximations. On the other hand, the spiral mode switches signs when going to the decoupled 4-state model. This indicates that cross-coupling effects play a part in the unstable spiral mode. This is not too surprising, since spiral mode can cause an increase in airspeed.

Add eigenvalues plot.

### 7.3.6 Coupled Longitudinal-Lateral Dynamic Stability

If one desires to study the coupled longitudinal and lateral dynamic stability using the 8-state model, or even larger models, it may not be possible to differentiate the modes of motion introduced above just by looking at their eigenvalues. This is especially true for unconventional rotorcraft which may not have an eigenvalue structure similar to that presented above. In this case, it is useful to resort to eigenvector analysis to assess which eigenvalue corresponds to which mode. The first step to perform eigenvector analysis is to scale the system such that all units are comparable, *e.g.*, 1 ft is comparable with 1 deg, 1 ft/s is comparable with 1 deg/s, *etc.*. Because typically the Euler angles and angular rates are expressed in rad/s, the stability derivative

Table 7.5: 8-state model eigenvectors for a UH-60 helicopter at 80 kts forward flight.

| States   | Eigenvectors   |                       |                       |                       |                |  |
|----------|----------------|-----------------------|-----------------------|-----------------------|----------------|--|
|          | $\mathbf{v}_1$ | $\mathbf{v}_{2,3}$    | $\mathbf{v}_{4,5}$    | $\mathbf{v}_{6,7}$    | $\mathbf{v}_8$ |  |
| $u$      | -0.0053        | $0.0201 \mp 0.0206i$  | $-0.0524 \pm 0.0165i$ | $0.0024 \pm 0.3332i$  | 0.0581         |  |
| $v$      | -0.0546        | $0.4512 \pm 0.1921i$  | $-0.6575 \pm 0.0000i$ | $0.5569 \pm 0.0000i$  | 0.2348         |  |
| $w$      | -0.0851        | $0.6787 \pm 0.0000i$  | $-0.2995 \pm 0.1195i$ | $0.5105 \pm 0.1119i$  | 0.0001         |  |
| $p$      | -0.9554        | $-0.3280 \mp 0.0681i$ | $0.2635 \mp 0.3246i$  | $0.0296 \pm 0.1679i$  | -0.1151        |  |
| $q$      | 0.1394         | $-0.0987 \pm 0.1271i$ | $-0.0816 \mp 0.0792i$ | $0.1680 \pm 0.1486i$  | -0.0062        |  |
| $r$      | -0.0704        | $0.2527 \pm 0.0257i$  | $-0.1593 \pm 0.1812i$ | $-0.0100 \mp 0.1035i$ | 0.2216         |  |
| $\phi$   | 0.2272         | $0.2257 \pm 0.1611i$  | $-0.4293 \mp 0.1217i$ | $0.2703 \pm 0.0590i$  | 0.9375         |  |
| $\theta$ | -0.0327        | $0.1175 \mp 0.0684i$  | $-0.0395 \pm 0.1183i$ | $0.3336 \mp 0.1662i$  | 0.0150         |  |

units will have to be converted. As such, the  $\mathbf{A}$  matrix will have to be multiplied element wise by a scaling matrix. Suppose that the translational kinematics and dynamics states (*i.e.*,  $x$ ,  $y$ ,  $z$ ,  $u$ ,  $v$ , and  $w$ ) are given in ft/s whereas the angular kinematics and dynamics states (*i.e.*,  $\phi$ ,  $\theta$ ,  $p$ ,  $q$ , and  $r$ ) are given in rad/s. Then, the system matrix  $\mathbf{A}$  will have to be multiplied element wise by the following scaling matrix  $S$ :

$$\hat{\mathbf{A}} = S \odot \mathbf{A} \quad (7.92)$$

$$= \begin{bmatrix} 1 & 1 & 1 & \pi/180 & \pi/180 & \pi/180 & \pi/180 \\ 1 & 1 & 1 & \pi/180 & \pi/180 & \pi/180 & \pi/180 \\ 1 & 1 & 1 & \pi/180 & \pi/180 & \pi/180 & \pi/180 \\ 180/\pi & 180/\pi & 180/\pi & 1 & 1 & 1 & 1 \\ 180/\pi & 180/\pi & 180/\pi & 1 & 1 & 1 & 1 \\ 180/\pi & 180/\pi & 180/\pi & 1 & 1 & 1 & 1 \\ 180/\pi & 180/\pi & 180/\pi & 1 & 1 & 1 & 1 \\ 180/\pi & 180/\pi & 180/\pi & 1 & 1 & 1 & 1 \\ 180/\pi & 180/\pi & 180/\pi & 1 & 1 & 1 & 1 \end{bmatrix} \odot \mathbf{A} \quad (7.93)$$

where  $1 \text{ rad} = \frac{\pi}{180} \text{ deg}$ . Once this is done, the eigenvalues and eigenvectors of the  $\hat{\mathbf{A}}$  matrix can be computed. To assess the participation of each state to each mode, and the relative phasing between the states, it is convenient to compute the magnitude and phase of each eigenvector element. Consider the 8-state model corresponding to the UH-60 dynamics at 80 kts level flight. The  $\mathbf{A}$  matrix is scaled according to Eq. (7.92). The eigenvectors of the scaled matrix are reported in Table 7.5. The magnitude and phase of each eigenvector element is reported in Table 7.6. In this table, the states that participate to each mode most significantly can clearly be seen (highest participations underlined in the table). While it is trivial to classify the roll subsidence and spiral modes based on modal participation and eigenvalues (*e.g.*, the roll subsidence mode is a high-frequency mode with most of the participation coming from the roll rate, whereas the spiral mode is a low-frequency mode where the roll attitude has the highest contribution), the other modes are not necessarily trivial to identify as they now feature participation from off-axis states (*i.e.*, cross-coupling effects). This is particularly true for the short period and phugoid modes, which feature significant contributions from the lateral states. This is a major difference from fixed-wing aircraft, where these modes are almost entirely driven by longitudinal states. The eigenvalues and corresponding eigenvectors are reported in Table 7.7.

### 7.3.7 Example 1: Longitudinal Dynamics of a UH-60 Helicopter in Hover

Consider the decoupled 4-state longitudinal dynamics of a UH-60 helicopter at hover:

$$\begin{bmatrix} \dot{u} \\ \dot{w} \\ \dot{q} \\ \dot{\theta} \end{bmatrix} = \begin{bmatrix} -0.0261 & 0.0163 & 2.1589 & -32.1526 \\ 0.0111 & -0.3477 & 0.2881 & -1.0558 \\ 0.0109 & 0.0036 & -0.8136 & 0 \\ 0 & 0 & 0.9988 & 0 \end{bmatrix} \begin{bmatrix} u \\ w \\ q \\ \theta \end{bmatrix} + \begin{bmatrix} -0.1785 & 0.0953 \\ -0.0163 & -0.8984 \\ 0.0390 & -0.0015 \\ 0 & 0 \end{bmatrix} \begin{bmatrix} \delta_{\text{lon}} \\ \delta_{\text{col}} \end{bmatrix} \quad (7.94)$$

Table 7.6: Magnitude and phase of the 8-state model eigenvectors for a UH-60 helicopter at 80 kts forward flight.

| States   | Eigenvectors Magnitude and Phase |                                |                      |                                    |                      |                                    |                      |                                    |                  |                                |
|----------|----------------------------------|--------------------------------|----------------------|------------------------------------|----------------------|------------------------------------|----------------------|------------------------------------|------------------|--------------------------------|
|          | $ \mathbf{v}_1 $                 | $\angle \mathbf{v}_1$<br>[deg] | $ \mathbf{v}_{2,3} $ | $\angle \mathbf{v}_{2,3}$<br>[deg] | $ \mathbf{v}_{4,5} $ | $\angle \mathbf{v}_{4,5}$<br>[deg] | $ \mathbf{v}_{6,7} $ | $\angle \mathbf{v}_{6,7}$<br>[deg] | $ \mathbf{v}_8 $ | $\angle \mathbf{v}_8$<br>[deg] |
| $u$      | 0                                | 180                            | 0.03                 | -45                                | 0.06                 | 162                                | <u>0.33</u>          | 89                                 | 0                | 0                              |
| $v$      | 0.05                             | 180                            | <u>0.49</u>          | 23                                 | <u>0.66</u>          | 180                                | <u>0.56</u>          | 0                                  | 0.23             | 0                              |
| $w$      | 0.09                             | 180                            | <u>0.68</u>          | 0                                  | 0.32                 | 158                                | <u>0.52</u>          | 12                                 | 0                | 0                              |
| $p$      | <u>0.96</u>                      | 180                            | <u>0.34</u>          | 168                                | <u>0.42</u>          | -50                                | 0.17                 | 80                                 | 0.12             | 180                            |
| $q$      | 0.13                             | 0                              | 0.16                 | 127                                | 0.11                 | 135                                | 0.22                 | 41                                 | 0.01             | 180                            |
| $r$      | 0.07                             | 180                            | 0.25                 | 5.8                                | 0.24                 | 131                                | 0.1                  | -95                                | 0.22             | 0                              |
| $\phi$   | 0.23                             | 0                              | 0.28                 | 35                                 | <u>0.45</u>          | -164                               | 0.28                 | 12                                 | <u>0.94</u>      | 0                              |
| $\theta$ | 0.03                             | 180                            | 0.14                 | -30                                | 0.12                 | 108                                | <u>0.37</u>          | -26                                | 0.02             | 0                              |

Table 7.7: 8-state model eigenvectors for a UH-60 helicopter at 80 kts forward flight.

| Mode            | Eigenvalues     | Values                |
|-----------------|-----------------|-----------------------|
| Roll Subsidence | $\lambda_1$     | -4.2214               |
| Short Period    | $\lambda_{2,3}$ | $-1.0664 \pm 0.4646i$ |
| Dutch Roll      | $\lambda_{4,5}$ | $-0.3585 \pm 0.8370i$ |
| Phugoid         | $\lambda_{6,7}$ | $0.2277 \pm 0.5522i$  |
| Spiral          | $\lambda_8$     | -0.1112               |

The eigenvalues and corresponding modes are shown in Table 7.8. Notably, in this example, the unstable phugoid, pitch subsidence, and heave subsidence modes can clearly be seen. A good way to see the decoupling of the heave dynamics and the longitudinal dynamics, is to look at the transfer functions for particular input-output pairs. If certain transfer functions are shown in zero-pole-gain (zpk) form, then the approximate pole-zero cancellations will be apparent. This is the mathematical equivalent of approximate decoupling. Using MATLAB®, the coefficient matrices above can be transformed into a state-space system with the following command:

```
sys_lon = ss(Alon,Blon,eye(4),zeros(4,2))
```

Then, the zpk form of the vertical velocity response to collective can be found via:

```
sys_wdcol=sys_lon(2,2)
sys_wdcol=zpk(sys_wdcol)
```

By performing these commands, the zpk form form of the vertical velocity response to collective is:

$$\frac{w}{\delta_{\text{col}}}(s) = \frac{-0.7963(s+1.123)(s^2 - 0.2829s + 0.3112)}{(s+1.123)(s+0.3482)(s^2 - 0.2839 + 0.3151)} \quad (7.96)$$

$$\approx \frac{-0.7932}{s+0.3482} \quad (7.97)$$

The approximate pole-zero cancellations are apparent. A similar process can be performed for the longitudinal velocity response to longitudinal inputs via the following MATLAB® commands:

```
sys_udlon=sys_lon(1,1)
sys_wdlon=zpk(sys_udlon)
```

Table 7.8: Longitudinal-heave dynamics eigenvalues and corresponding modes for a UH-60 helicopter at hover.

| Eigenvalue      | Mode                   | Value                |
|-----------------|------------------------|----------------------|
| $\lambda_1$     | pitch subsidence       | -1.1230              |
| $\lambda_{2,3}$ | unstable hover phugoid | $0.1420 \pm 0.5431i$ |
| $\lambda_4$     | heave subsidence       | -0.3482              |

The resulting longitudinal velocity response to longitudinal inputs in zpk form is:

$$\frac{u}{\delta_{\text{lon}}}(s) = \frac{-0.17048(s+0.3478)(s^2 + 0.3362s + 7.112)}{(s+1.123)(s+0.3482)(s^2 - 0.2839s + 0.3151)} \quad (7.99)$$

$$\approx \frac{-0.17048(s^2 + 0.3362s + 7.112)}{(s+1.123)(s^2 - 0.2839s + 0.3151)} \quad (7.100)$$

Again, one can see the pole-zero cancellations. This time, the heave subsidence mode is cancelled such that the two remaining modes are the pitch subsidence and phugoid modes.

### 7.3.8 Example 2: Quadrotor Flight Dynamics at Hover

Consider the following dynamic model of a small-scale quadrotor at hover:

$$\begin{bmatrix} \dot{v} \\ \dot{p} \\ \dot{\phi} \\ \dot{u} \\ \dot{q} \\ \dot{\theta} \\ \dot{r} \\ \dot{\psi} \\ \dot{w} \end{bmatrix} = \begin{bmatrix} Y_v & 0 & g & 0 & 0 & 0 & 0 & 0 & 0 \\ L_v & L_p & 0 & 0 & 0 & 0 & 0 & 0 & 0 \\ \dot{\phi} & 0 & 1 & 0 & 0 & 0 & 0 & 0 & 0 \\ \dot{u} & 0 & 0 & 0 & X_u & 0 & -g & 0 & 0 \\ \dot{q} & 0 & 0 & 0 & M_u & M_q & 0 & 0 & 0 \\ \dot{\theta} & 0 & 0 & 0 & 0 & 1 & 0 & 0 & 0 \\ \dot{r} & 0 & 0 & 0 & 0 & 0 & N_r & 0 & 0 \\ \dot{\psi} & 0 & 0 & 0 & 0 & 0 & 1 & 0 & 0 \\ \dot{w} & 0 & 0 & 0 & 0 & 0 & 0 & Z_w & 0 \end{bmatrix} \begin{bmatrix} v \\ p \\ \phi \\ u \\ q \\ \theta \\ r \\ \psi \\ w \end{bmatrix} + \begin{bmatrix} 0 & 0 & 0 & 0 \\ L_{\delta_{\text{lat}}} & 0 & 0 & 0 \\ 0 & 0 & 0 & 0 \\ 0 & 0 & 0 & 0 \\ 0 & M_{\delta_{\text{lon}}} & 0 & 0 \\ 0 & 0 & 0 & 0 \\ 0 & 0 & N_{\delta_{\text{ped}}} & 0 \\ 0 & 0 & 0 & 0 \\ 0 & 0 & 0 & Z_{\delta_{\text{col}}} \end{bmatrix} \begin{bmatrix} \delta_{\text{lat}}(t - \tau_\phi) \\ \delta_{\text{lon}}(t - \tau_\theta) \\ \delta_{\text{ped}}(t - \tau_\psi) \\ \delta_{\text{col}}(t - \tau_z) \end{bmatrix} \quad (7.101)$$

where the stability and control derivatives, along with the on-axis time delays, were identified from flight test data [Sae+20]. The stability and control derivatives, and the time delays are shown reported in Table 7.9. The eigenvalues shown in Fig. 7.12 and reported in Table 7.10. The system is stable around the yaw and heave axes. The roll and pitch axes have one negative real eigenvalue and a pair of complex eigenvalues in the right half plane each, representing the classical hovering cubic dynamics present in all hovering vehicles [MAG73]. The real negative eigenvalues are the stable roll and pitch subsidence modes. The pairs of complex eigenvalues in the right half of the plane are the unstable oscillation modes in roll and pitch. The similarity between the eigenvalues in roll and pitch are due to the symmetry of the quadrotor's configuration about the roll and pitch axes. The slight differences may be due to the uneven distribution of the electronic components and sensors.

## 7.4 Stability with Feedback

This section will treat the behaviour of the rotorcraft with feedback control. The three major motivations for doing so are the following: (i) feedback control design is important for modern rotorcraft engineering, because so many rotorcraft now feature some type of Automatic Flight Control System (AFCS) that uses feedback; (ii) feedback control theory is also used to understand how a pilot controls a rotorcraft, and is therefore integral to understanding rotorcraft handling qualities; and (iii) most rotorcraft are inherently unstable over some portion of the flight envelope, so they must be stabilized either by a pilot or an AFCS (or sometimes both).

Table 7.9: Identified stability derivatives, control derivatives, and on-axis time delays [Sae+20].

| Parameter                 | Value                           | CR Bound [%] | Insensitivity [%] |
|---------------------------|---------------------------------|--------------|-------------------|
| $Y_v$                     | -0.3022 [1/s]                   | 6.107        | 1.825             |
| $L_v$                     | -0.8287 [rad/(ft s)]            | 5.943        | 1.580             |
| $L_p$                     | 0 [1/s]                         | -            | -                 |
| $L_{\delta_{\text{lat}}}$ | 33.514 [rad/(s <sup>2</sup> %)] | 3.297        | 1.144             |
| $\tau_\phi$               | 0.0565 [s]                      | 4.170        | 2.077             |
| $X_u$                     | -0.2568 [1/s]                   | 5.302        | 1.814             |
| $M_u$                     | 1.1257 [rad/(ft s)]             | 5.618        | 1.306             |
| $M_q$                     | 0 [1/s]                         | -            | -                 |
| $M_{\delta_{\text{lon}}}$ | 27.919 [rad/(s <sup>2</sup> %)] | 4.155        | 1.109             |
| $\tau_\theta$             | 0.0355 [s]                      | 10.73        | 5.321             |
| $N_r$                     | -0.5617 [1/s]                   | 25.19        | 9.713             |
| $N_{\delta_{\text{ped}}}$ | 6.0308 [rad/(s <sup>2</sup> %)] | 3.877        | 1.848             |
| $\tau_\psi$               | 0.0401 [s]                      | 7.023        | 2.452             |
| $Z_w$                     | -0.1734 [1/s]                   | 39.72        | 16.06             |
| $Z_{\delta_{\text{col}}}$ | -49.065 [ft/(s <sup>2</sup> %)] | 2.647        | 1.312             |
| $\tau_z$                  | 0.0389 [s]                      | 30.03        | 12.21             |

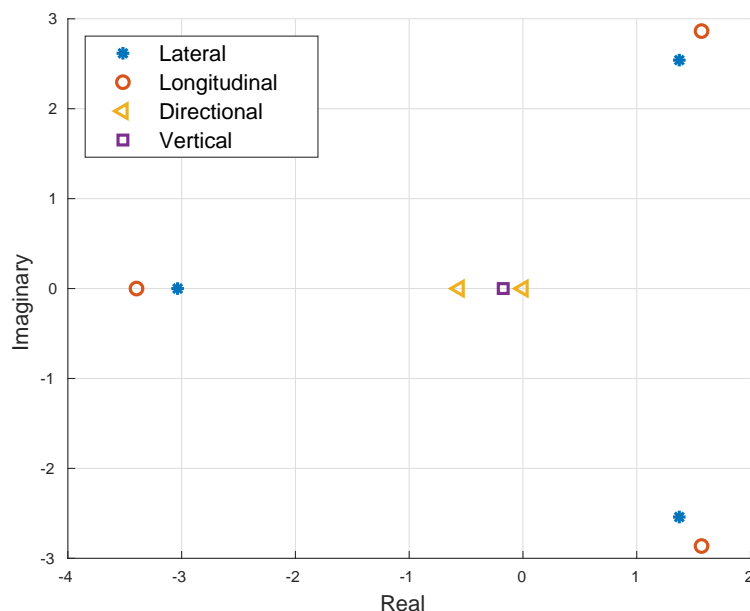


Figure 7.12: Eigenvalues of the quadrotor identified dynamics.

Table 7.10: Eigenvalues of the identified system.

| Eigenvalue      | Mode              | Value                |
|-----------------|-------------------|----------------------|
| $\lambda_{1,2}$ | roll oscillation  | $1.3948 \pm 2.5845i$ |
| $\lambda_3$     | roll subsidence   | -3.0919              |
| $\lambda_{4,5}$ | pitch oscillation | $1.5698 \pm 2.8634i$ |
| $\lambda_6$     | pitch subsidence  | -3.3964              |
| $\lambda_7$     | yaw subsidence    | -0.5616              |
| $\lambda_8$     | yaw integrator    | 0                    |
| $\lambda_9$     | heave subsidence  | -0.1734              |

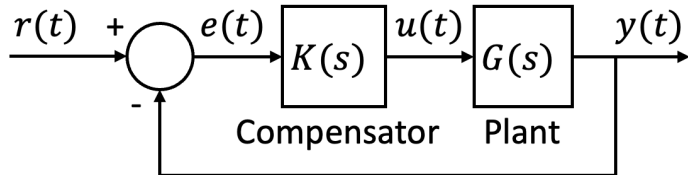


Figure 7.13: Standard structure of a feedback controller with compensation in the forward path.

### 7.4.1 Mathematical Overview

The structure of a typical feedback controller with compensation in the forward path is shown in Fig. 7.13. The helicopter dynamics are the plant. The signal  $r(t)$  is the reference command,  $e(t)$  is the tracking error,  $u(t)$  is the control input, and  $y(t)$  is the output. Signals can also be represented by their Laplace transforms:

$$R(s) = L[r(t)] \quad (7.102a)$$

$$E(s) = L[e(t)] \quad (7.102b)$$

$$U(s) = L[u(t)] \quad (7.102c)$$

$$Y(s) = L[y(t)] \quad (7.102d)$$

The compensator can be as simple as a gain, or can include some kind of internal dynamics, or even much more complex logic and non-linear dynamics. The focus will mainly be on linear control theory and linear feedback compensation that can be expressed in the form of either a state space system or a transfer function. Consider the components of the feedback system,  $K(s)$  and  $G(s)$ , as classical transfer functions.

The signals are related as follows:

$$Y(s) = G(s)U(s) \quad (7.103a)$$

$$U(s) = K(s)E(s) \quad (7.103b)$$

$$E(s) = R(s) - Y(s) \quad (7.103c)$$

The Closed Loop Transfer Function (CLTF),  $M(s)$ , can be derived as:

$$Y(s) = M(s)R(s) \quad (7.104)$$

where:

$$M(s) = [I + G(s)K(s)]^{-1} G(s)K(s) \quad (7.105)$$

In general, these can be MIMO transfer functions (transfer function matrices) and vector signals. However, we will mostly use SISO analysis:

$$\frac{Y}{R}(s) = M(s) = \frac{G(s)K(s)}{1 + G(s)K(s)} \quad (7.106)$$

The Open Loop Transfer Function (OLTF or just loop transfer function) is just the product of the plant and compensator:

$$\text{Loop Transfer Function} = G(s)K(s) \quad (7.107)$$

The closed loop poles are governed by the roots of:

$$1 + G(s)K(s) = 0 \quad (7.108)$$

Suppose the compensator is just a constant (or gain),  $K$ , we can look the variation in the poles with this parameter. This is a root locus:

$$1 + KG(s^*) = 0 \begin{cases} \text{Root Locus: values of } s^* \text{ for } K = 0 \rightarrow \infty \\ \text{Complementary Root Locus: values of } s^* \text{ for } K = -\infty \rightarrow 0 \end{cases} \quad (7.109)$$

The transfer functions are usually a ratio of a numerator polynomial,  $N(s)$ , and a denominator polynomial,  $D(s)$ :

$$1 + G(s)K = 1 + K \frac{N(s)}{D(s)} = 0 \quad \Rightarrow \quad D(s^*) + KN(s^*) = 0 \quad (7.110)$$

This implies that when  $K = 0$ , branches initiate at roots of  $D(s)$ , i.e. the open loop poles.

$$K = 0 \quad \Rightarrow \quad D(s^*) = 0 \quad (7.111)$$

And as  $K \rightarrow \infty$  branches either approach the roots of  $N(s)$ , the transmission zeros of the  $G(s)$ , or they run along asymptotes where the roots grow infinitely large.

$$\frac{1}{K}D(s^*) + N(s^*) = 0 \quad (7.112a)$$

$$K \rightarrow 0 \quad \Rightarrow \quad \begin{cases} N(s^*) = 0 \\ \text{or } |s^*| \rightarrow \infty \end{cases} \quad (7.112b)$$

Root loci can be generated in MATLAB® using the following commands:

- `rlocus(sys)`: Draws root locus and complementary root locus.
- `rltool(sys, 1)`: Interactive root locus with negative feedback and positive gain. It allows you to interactively change gain and move poles and zeros. It is generally more useful than `rlocus`.
- `rltool(sys, -1)`: Interactive root locus with negative feedback and negative gain (complementary root locus).
- `sisotool(sys)`: Like `rltool` but does a lot of other stuff.

Note that `sys` is the loop transfer function and not the closed loop transfer function. All of these tools require `sys` be Single Input / Single Output (SISO). Root loci usually have some branches that run off to infinitely large values, so selecting appropriate axis scales (zoom) is important.

## 7.4.2 Hover Stabilization

As discussed in Example 1, the UH-60 has an unstable mode in hover, related to the longitudinal hover phugoid mode in Eq. (7.50). Recall the longitudinal velocity response to longitudinal inputs in zpk form from Example 1:

$$\frac{u}{\delta_{\text{lon}}}(s) = \frac{-0.17048(s+0.3478)(s^2 + 0.3362s + 7.112)}{(s + 1.123)(s+0.3482)(s^2 - 0.2839s + 0.3151)} \quad (7.113)$$

$$\approx \frac{-0.17048(s^2 + 0.3362s + 7.112)}{(s + 1.123)(s^2 - 0.2839s + 0.3151)} \quad (7.114)$$

The roots of the second-order polynomial at the denominator are in the right-hand plane (RHP). Let us attempt to stabilize the phugoid mode with feedback. First, consider trying to stabilize via longitudinal speed feedback, as shown in Fig. 7.14. The plant is given by:

$$G(s) = \frac{u}{\delta_{\text{lon}}}(s) \approx \frac{X_{\delta_{\text{lon}}}s^2 - M_q X_{\delta_{\text{lon}}}s - gM_{\delta_{\text{lon}}}}{s^3 - (X_u + M_q)s^2 + X_u M_q s + gM_u} \quad (7.115)$$

The gain  $K$  is (s-%)/ft.

The first step is to trim the UH-60 simulation model and extract the decoupled 4-state model of the longitudinal dynamics. The transfer function from longitudinal inputs to longitudinal speed is pulled out using the following MATLAB® command:

```
G = sys_lon(1,1)
```

Then, `rltool` is applied assuming negative feedback and positive gain:

```
rltool(G)
```

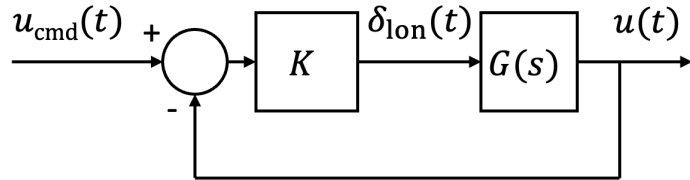


Figure 7.14: Phugoid mode stabilization with longitudinal speed feedback.

The resulting root locus is shown in Fig. 7.15a. Can The magenta squares can interactively be moved, which corresponds to changing the gain  $K$ . As  $K$  increases, the closed-loop poles approach zeros are move out along an asymptote. In this case there is a branch always in RHP, which is unstable! So, why can't the response be stabilized? In this case, a gain with the wrong sign is being used. In fact, a negative gain is needed. Recall that positive longitudinal cyclic ( $\delta_{\text{lon}} > 0$ ) leads to a nose-up change in the pitch attitude ( $\Delta\theta > 0$ ). This will tend to make the rotorcraft accelerate backwards, a negative change in longitudinal speed ( $\Delta u < 0$ ). Thus, the feedback control strategy will not work with a positive gain. Let us now try to use a negative gain:

$$\text{rltool}(G, -1) \quad \text{or} \quad \text{rltool}(-G) \quad (7.116)$$

The resulting root locus is shown in Fig. 7.15b. As shown in this figure, the response will stabilize with a gain  $K \lesssim -120$  (s-%)/ft. The root locus also shown that the heave mode pole does not move, and this is because of the approximate pole-zero cancellation. Note that the gain required to stabilize the response is extremely large – it would use full control through for less than 1 ft/s tracking error in velocity. Even if stabilized with extremely high gain, the closed-loop poles would have a pair of complex poles (oscillatory mode) with damping ratio of approximately 0.06 and frequency of 2.7 rad/sec. This is very poor damping. As such, feedback control via velocity feedback is not practical.

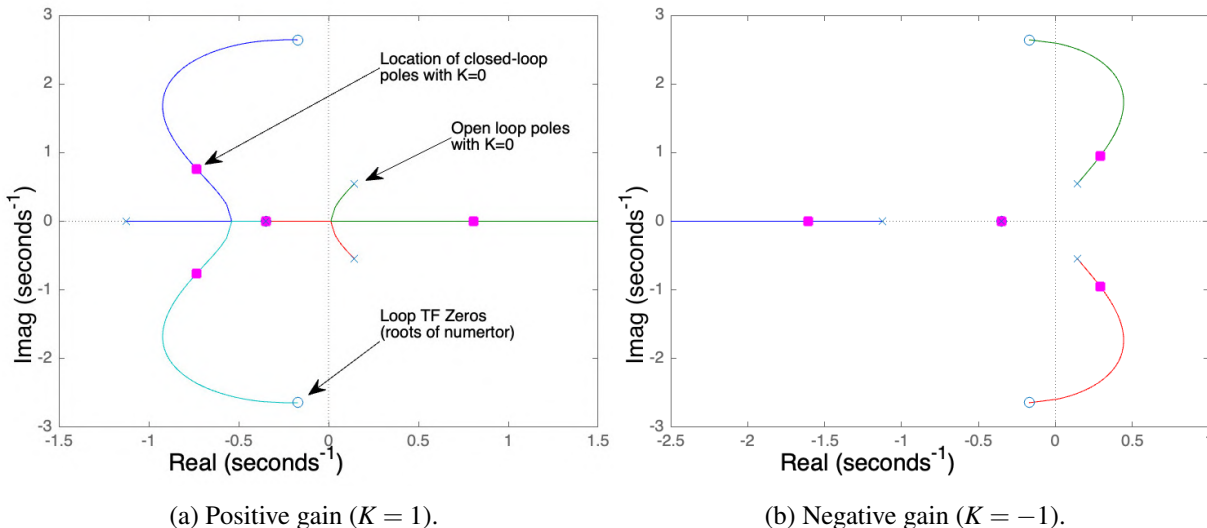


Figure 7.15: Root locus for the phugoid mode stabilization with longitudinal speed feedback.

Suppose now there is no AFCS and that the pilot acts as a feedback system. A pilot cannot control a rotorcraft using only compensation on position or velocity. In fact, the pilot needs to control attitude as well. Let us repeat the exercise by using pitch attitude feedback, as shown in the block diagram of Fig. 7.16. In this case, the plant is given by:

$$G(s) = \frac{\theta}{\delta_{\text{lon}}}(s) \approx \frac{M_{\delta_{\text{lon}}} s + (M_u X_{\delta_{\text{lon}}} - X_u M_{\delta_{\text{lon}}})}{s^3 - (X_u + M_q) s^2 + X_u M_q s + g M_u} \quad (7.117)$$

The gain  $K_\theta$  is in %/rad.

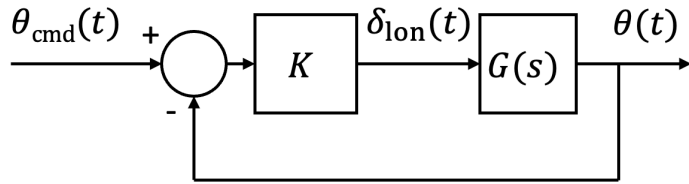


Figure 7.16: Phugoid mode stabilization with pitch attitude feedback.

The transfer function from longitudinal stick to pitch attitude can be found as follows:

$$G = \text{sys\_lon}(4, 1)$$

The root locus can then be found analogously to before, and is shown in Fig. 7.17. The maximum damping is achieved for a gain around  $K = 40\%/\text{rad}$  (or  $0.7\%/\text{deg}$ ). The closed-loop mode natural frequency corresponding to this gain is  $\omega_n = 1.17\text{ rad/s}$ , whereas the damping ratio is  $\zeta = 0.26$ . The damping ratio is still somewhat low.

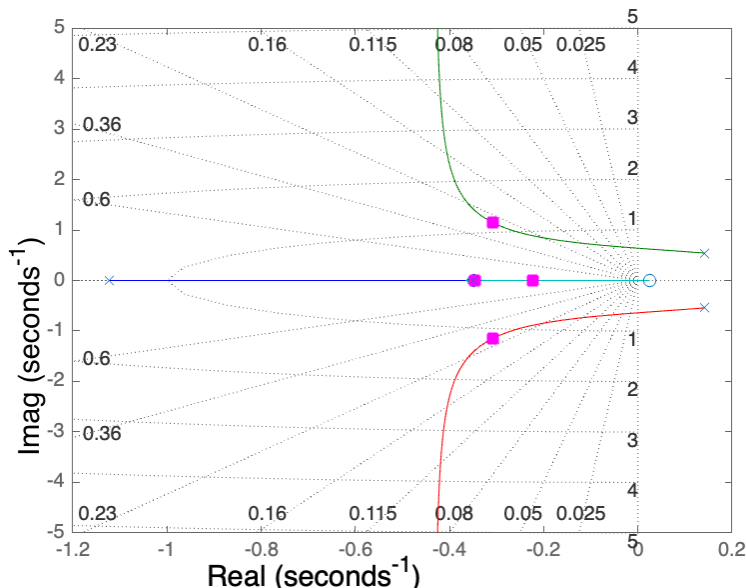


Figure 7.17: Phugoid mode stabilization with pitch attitude feedback ( $K = 40\%/\text{rad}$ ).

To add more damping, consider feeding back pitch rate as well. This could be achieved via the pilot (increases pilot workload), or via a type of AFCS called a Stability Augmentation System (SAS). In older rotorcraft, pitch and roll rate damping have also been enhanced by a type of mechanical feedback system – a stabilizer bar (shown in Fig. 7.18). The system with rate feedback can be represented as a multi-loop feedback system with *inner* and *outer* feedback loops, as shown in Fig. 7.19. In this block diagram, well known linearized kinematics of pitch attitude are used, *i.e.*,  $\dot{\theta} = q$ . Taking the Laplace transform yields  $s\Theta(s) = Q(s)$ . Reformulating this expression results in:

$$\frac{\Theta(s)}{Q(s)} = \frac{1}{s} \quad (7.118)$$

Also, the plant used in this block diagram is:

$$G(s) = \frac{q}{\delta_{\text{lon}}}(s) \quad (7.119)$$



Figure 7.18: Stabilizer bar for a UH-1 helicopter.

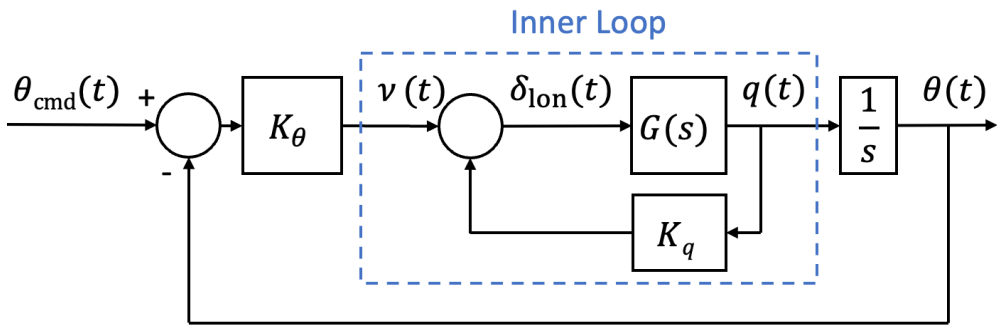


Figure 7.19: Phugoid mode stabilization with pitch attitude and rate feedback.

The closed-loop transfer function can be derived by first obtaining the transfer function from the input to the inner loop to the pitch rate:

$$\frac{Q}{v}(s) = \frac{G(s)}{1 + K_q G(s)} \quad (7.120)$$

Then, the transfer function from the pitch attitude tracking error to the tracking error is obtained:

$$\frac{\Theta}{E}(s) = \frac{K_\theta G(s)}{s[1 + K_q G(s)]} \quad (7.121)$$

The closed-loop transfer function is then found as:

$$\frac{\Theta}{\Theta_{cmd}}(s) = \frac{\frac{K_\theta G(s)}{s[1 + K_q G(s)]}}{1 + \frac{K_\theta G(s)}{s[1 + K_q G(s)]}} = \frac{K_\theta(s)G(s)}{s[1 + K_q G(s)] + K_\theta G(s)} \quad (7.122)$$

Because there are two gains that need to be tuned (*i.e.*,  $K_q$  and  $K_\theta$ ), classical root locus cannot be applied. Rather, successive loop closures can be applied, starting with the inner loop. The first loop closure involves pitch rate feedback. The root locus for the first loop closure can be found with:

```
rltool(sys_lon(3,1))
```

and is shown in Fig. 7.20a. The pitch rate gain  $K_q$  is tuned to decrease the instability of the hover phugoid mode with rate feedback. Note that it will not stabilize the poles, but will reduce frequency and decrease rate of divergence. A gain of  $K_q = 40$  (s-%)/rad is found to provide reasonable reduction in the rate of divergence. Consider now the system with the pitch rate feedback loop closed:

$$\frac{Q}{v}(s) = \frac{G(s)}{1 + K_q G(s)} \quad (7.123)$$

The MATLAB® command to create this transfer function (*i.e.*, the inner loop transfer function) is:

```
G_inner = feedback(sys_lon(3,1),40)
```

Then, the loop transfer function for pitch attitude feedback is found by multiplying by an integrator:

$$\frac{\Theta}{V}(s) = \frac{G(s)}{s[1 + K_q G(s)]} \quad (7.124)$$

The command to obtain this transfer function is:

```
H = tf(1,[1 0])*G_inner
```

Finally, the root locus is found via `rlocus(H)` and is shown in Fig. 7.20b. A pitch attitude gain of  $K_\theta = 40$  %/rad (or 0.7 %/deg) yields an oscillatory mode with natural frequency of  $\omega_n = 0.46$  rad/s and damping ratio  $\zeta = 0.91$ . As such, pitch rate and attitude feedback results in a more well-damped mode. The final closed-loop system is found by:

```
G_CL = feedback(40*H,1)
```

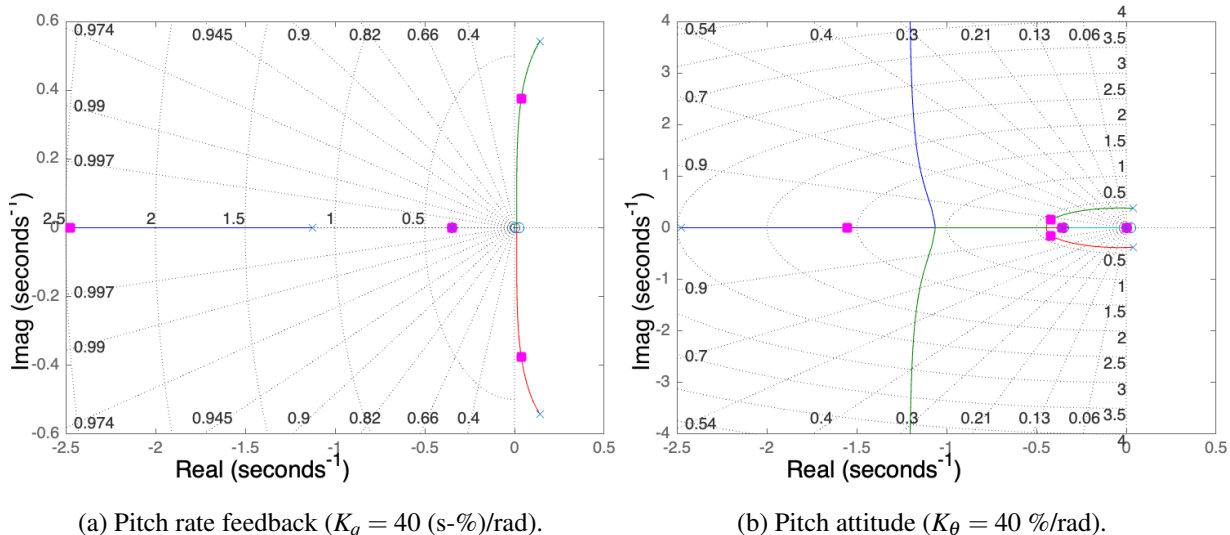


Figure 7.20: Root locus for the phugoid mode stabilization with pitch rate and attitude feedback.

## Bibliography

- [MAG73] D. T. McRuer, I. L. Ashkenas, and D. Graham. “Aircraft Dynamics and Automatic Control”. In: Princeton, NJ: Princeton University Press, 1973 (cited on page 184).
- [MV78] C. Moler and C. Val Loan. “Nineteen Dubious Ways to Compute the Exponential of a Matrix”. In: *SIAM Review* 20.4 (1978), pages 801–836. DOI: <https://doi.org/10.1137/1020098> (cited on page 162).
- [MV03] C. Moler and C. Val Loan. “Nineteen Dubious Ways to Compute the Exponential of a Matrix, Twenty-Five Years Later”. In: *SIAM Review* 45.1 (2003), pages 801–836. DOI: <https://doi.org/10.1137/1020098> (cited on page 162).
- [Pad18] G. D. Padfield. “Helicopter Flight Dynamics: Including a Treatment of Tiltrotor Aircraft”. In: 3rd edition. John Wiley Sons, 2018 (cited on page 180).
- [Sae+20] U. Saetti et al. “Handling-Qualities Perspective on Rotorcraft Load Alleviation Control”. In: *Journal of Guidance, Control, and Dynamics* (2020), pages 1–13. DOI: <https://doi.org/10.2514/1.G004965> (cited on pages 184, 185).





## 8. Flight Control Design

### 8.1 Introduction

Because of their unstable, high-order, and highly-coupled dynamics, rotorcraft are particularly prone to gust disturbances and therefore need flight control systems able to mitigate this deficiencies. Moreover, it is important that the closed-loop dynamics yield a simple, predictable response to commanded output that is common across helicopters. Model following control architectures such as Dynamic Inversion (DI) and Explicit Model Following (EMF) are especially well-suited for providing gust disturbance rejection. This is because their 2 degree-of-freedom (DoF) structure, with separate feed forward and feedback paths, allows to tune the rotorcraft response to gusts independently from responses to outer guidance/navigation loops. In contrast, in 1 DoF classic control methodologies, the responses to gusts and outer guidance/navigation loops cannot be independently tuned. A key aspect of both architectures is the reliance on model inversion to cancel the plant dynamics and track a desired reference model. EMF is essentially a linear design method that uses a simplified model inversion in the feed-forward path to follow the desired reference model, while feedback design is applied to the high-order linear plant models that are either identified from flight-test data or obtained from physics-based models via linearization schemes. Generally, both feed-forward inversion and feedback compensation needs to be scheduled with the flight condition to account variations in the flight dynamics. DI, on the other hand, inverts the plant model in its feedback linearization loop, which eliminates the need for gain scheduling. However, the plant model used for feedback linearization still needs to be scheduled with the flight condition. A typical multi-loop control scheme is shown in Fig. 8.1. This particular control scheme features an outer loop controller tracks longitudinal and lateral ground velocities commands in the heading frame and calculates the desired pitch and roll attitudes for the inner loop to track. The desired response type for the outer loop is Translational Rate Command (TRC). The inner loop achieves stability, disturbance rejection, and desired response characteristics about the roll, pitch, yaw, and heave axes. More specifically, an Attitude Command / Attitude Hold (ACAH) response is used for the roll and pitch axes, Rate Command / Attitude Hold (RCAH) is used for the yaw axis, and a TRC response is used for the heave axis.

### 8.2 Types of Stability and Control Augmentation

Rotorcraft feature different kind of stability and/or control augmentation systems. These systems are articulated below.

- **Stability Augmentation System (SAS):** A Stability Augmentation System is a flight control system that provides stability enhancements to the helicopter. It typically utilizes sensors, such as gyroscopes or accelerometers, to monitor the aircraft's motion and applies corrective control inputs to maintain stability. SAS can counteract off-axis disturbances, provide automatic stabilization during maneuvers, and enhance overall flight handling characteristics.

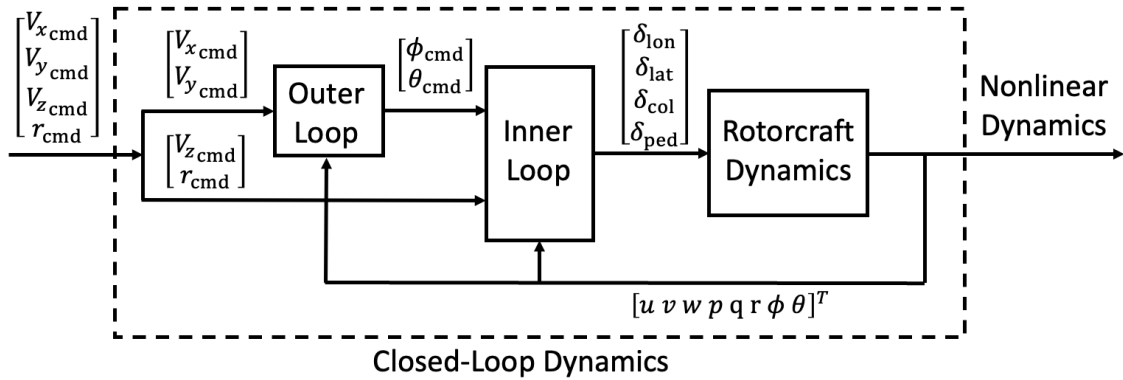


Figure 8.1: Schematic of the closed-loop helicopter dynamics.

- **Stability and Control Augmentation System (SCAS):** A Stability and Control Augmentation System goes beyond stability enhancements and also assists with controlling the helicopter's attitude and trajectory. SCAS combines stability augmentation with control inputs to improve the aircraft's handling, response, and maneuverability. It can help with automatic attitude control, attitude hold, and stabilization in various flight conditions.
- **Automatic Flight Control System (AFCS):** An Automatic Flight Control System is a comprehensive flight control system that provides both stability and active control augmentation. AFCS combines various sensors, control laws, and actuators to automate flight control tasks and reduce pilot workload. It includes features such as altitude hold, heading hold, navigation modes, autopilot functionality, and more. AFCS can assist with maintaining precise flight parameters, managing flight modes, and achieving accurate control responses.
- **Fly-by-Wire (FBW) System:** A Fly-by-Wire system replaces traditional mechanical linkages between the pilot's controls and the aircraft's control surfaces with an electronic interface. FBW systems use sensors to measure control inputs and aircraft parameters, and then transmit this information electronically to actuators that control the flight surfaces. FBW systems can incorporate stability augmentation, control laws, and flight envelope protection, resulting in enhanced flight control, stability, and safety.
- **Fly-by-Light (FBL) System:** Fly-by-Light is a variation of Fly-by-Wire control that employs optical fibers for signal transmission instead of traditional electrical wires. It offers advantages such as lighter weight, increased reliability, and better resistance to electromagnetic interference. FBL systems are typically used in advanced rotorcraft and provide similar benefits as FBW systems in terms of control augmentation and improved flight characteristics.

### 8.3 Frequency Domain Analysis

Before getting started with flight control design, it is beneficial to take a closer look at frequency domain analysis as it plays an important role in stability and control analysis, handling qualities, and feedback control of rotorcraft.

#### 8.3.1 Overview

Bode diagrams (frequency response of magnitude and phase plotted on a log scale) provide a broad amount of information on rotorcraft dynamics. Note that Bode diagrams use a logarithmic scale on the frequency axis (the x-axis) which allows to see dynamics across a wide range of frequencies (or time scales). The magnitude plot is expressed in decibels (dB), defined as  $20\log_{10}(X)$  which effectively makes it a logarithmic scale. The phase is plotted on a linear scale, traditionally in increments of 45 or 90 deg. Bode diagrams reveal resonant peaks associated with oscillatory modes (complex eigenvalues) as well as notches associated with complex zeros. Bode diagrams can also reveal the stability and relative stability of a system both with and without feedback. The reader is invited to consult supplementary notes that provide an overview on how different

parts of a linear system transfer function affect the shape of the Bode plot.

Consider a linear system driven by a sinusoidal input, as shown in Fig. 8.2. It can be shown that if the system is stable, then the steady-state response of the system will also be sinusoidal with the same frequency as the input but different amplitude and phase:

$$y(t) = MA \sin(\omega t + \phi) \quad (8.1)$$

where  $M$  is the magnitude (or gain) and  $\phi$  is the phase. If the input frequency is varied, the magnitude (or gain) and phase shift according to well known relationships:

$$M = |G(j\omega)| = \sqrt{a^2 + b^2} \quad (8.2a)$$

$$\phi = \angle G(j\omega) = \text{atan2}(b, a) \quad (8.2b)$$

where  $G(s)|_{s=j\omega} = a + jb$ .

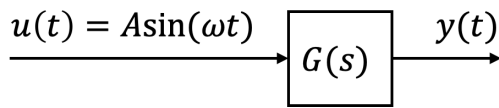


Figure 8.2: Linear system driven by a sinusoidal input.

### 8.3.2 Stability Margins

Consider a system with feedback, shown in Fig. 8.3. Using Nyquist stability theory, one can analyze the stability of the closed-loop system by looking at the Bode diagram of the open-loop system (*i.e.*, the Bode diagram of the *loop transfer function*). In addition, one can analyze the stability margins, *i.e.*, how much gain and phase shift are allowed before the closed loop system becomes unstable. The loop transfer function is given by  $G(s)K(s)$ .

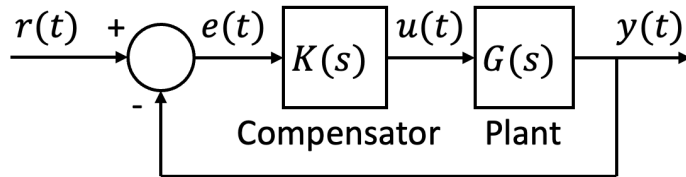


Figure 8.3: Linear system with feedback.

Consider the following linear system as an example:

$$G(s) = \left( \frac{\omega_{n_1}^2}{s^2 + 2\zeta_1\omega_{n_1} + \omega_{n_1}^2} \right) \left( \frac{\omega_{n_2}^2}{s^2 + 2\zeta_2\omega_{n_2} + \omega_{n_2}^2} \right) \quad (8.3)$$

where the natural frequencies are  $\omega_{n_1} = 5$  and  $\omega_{n_2} = 0.1$  whereas the damping ratios are  $\zeta_1 = 0.1$  and  $\zeta_2 = 0.3$ . Note that this system features two modes that are widely separated in frequency. The stability margins, *i.e.*, the gain margin (GM) and phase margin (PM), can be found in MATLAB® using the function:

`margin(G)`

and are shown in Fig. 8.4. The gain margin GM = 42.5 dB implies that the gain of the loop transfer function can be increased by up to 42.5 dB (equivalent to multiplying the gain by a factor of 133) and the closed-loop system will still be stable. A phase margin PM = 49.9 deg implies that a phase lag up to 49.9 deg at the gain crossover frequency can be added and the closed-loop system will still be stable.

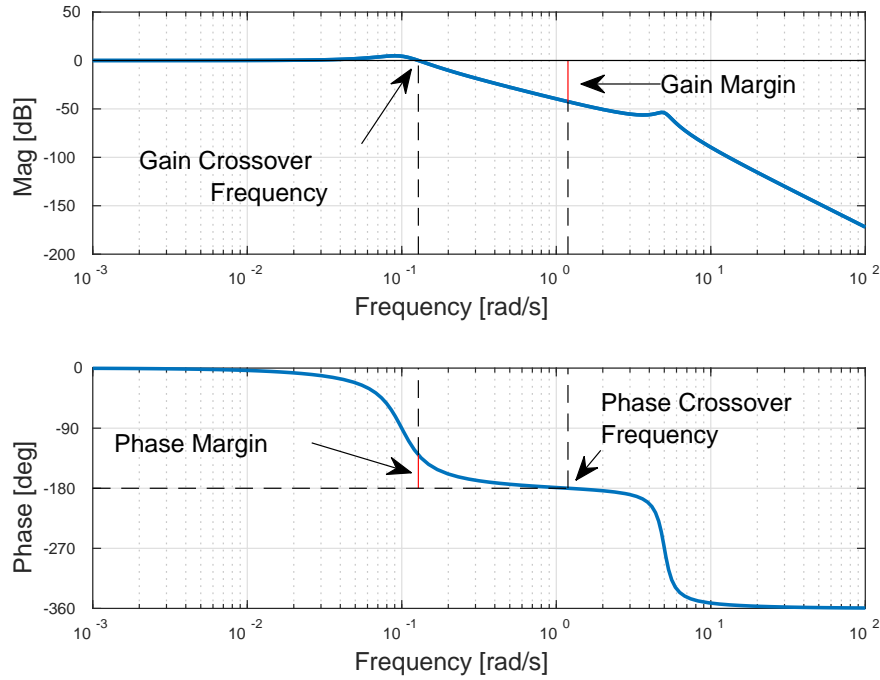


Figure 8.4: Gain and phase margins.

More in general, the stability margins provide a measure of robustness to the system. Suppose there is uncertainty in the form of:

$$K_u e^{-s \frac{\phi_u}{\omega_g}} \quad (8.4)$$

where  $K_u$  is the gain uncertainty, and  $\phi_u$  is the phase uncertainty. This uncertainty term is in series with the plant and compensator, as shown in Fig. 8.5. Then, the maximum value of  $\phi_u$  is  $PM/57.3$  deg (note the conversion to radians), and the maximum value of  $K_u$  is  $10^{(GM/20)}$  (note the conversion from dB to a gain amplification on a linear scale).

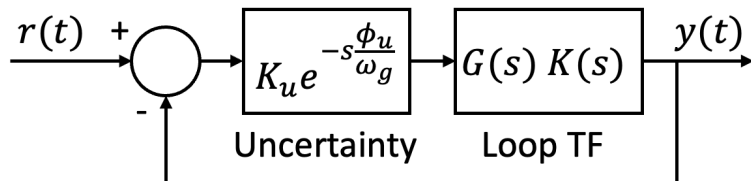


Figure 8.5: Closed-loop linear system with uncertainty.

## 8.4 Response Types

The basis upon which to build a flight control system is a linear model of the rotorcraft dynamics with the lowest possible order that is still representative of the relevant physics. For instance, the full-order dynamics (inclusive of rigid-body, flap, lead-lag, and inflow states) is too complex, whereas the 8-state residualized model representative of the rigid-body dynamics only is too simple as it does not predict the rotor delay in the dynamic response of the system. On the other hand, the 10-state model represents a good compromise in that it includes the rigid-body dynamics and the minimum number of rotor states to predict the response delay introduced by the rotor.

### 8.4.1 Angular Dynamics

#### Longitudinal

Consider the 10-state model derived in the earlier chapters. To further simplify it, one can decouple the longitudinal and lateral dynamics and truncate the velocity dynamics to focus on the angular rate dynamics. As such, the coupled pitch rate and longitudinal flapping dynamics is:

$$\begin{bmatrix} \dot{q} \\ \dot{\beta}_{1c} \end{bmatrix} = \begin{bmatrix} M_q & M_{\beta_{1c}} \\ 1 & -1/\tau_f \end{bmatrix} \begin{bmatrix} q \\ \beta_{1c} \end{bmatrix} + \begin{bmatrix} 0 \\ R_{\delta_{lon}} \end{bmatrix} \delta_{lon} \quad (8.5)$$

where  $M_q$  is pitch damping,  $M_{\beta_{1c}}$  is the pitching moment due to the longitudinal flapping motion, and  $R_{\delta_{lon}}$  is the change in longitudinal flapping angle due to longitudinal stick inputs. Additionally,  $\tau_f$  is the rotor flapping time constant and, for a UH-60 helicopter, is approximately  $\tau_f \approx 0.13$  seconds. Consider the the longitudinal flapping equation, apply the Laplace transform, and solve for longitudinal flapping to obtain:

$$\frac{\beta_{1c}}{\delta_{lon}}(s) = \frac{R_{\delta_{lon}}}{s + \frac{1}{\tau_f}} = \frac{\tau_f R_{\delta_{lon}}}{\tau_f s + 1} \approx \tau_f R_{\delta_{lon}} e^{-s\tau_f} \quad (8.6)$$

Substituting this equation in the pitch rate equation yields:

$$\dot{q} = M_q q + \underbrace{M_{\beta_{1c}} \tau_f R_{\delta_{lon}}}_{M_{\delta_{lon}}} e^{-s\tau_f} \delta_{lon} \quad (8.7)$$

By applying the Laplace transform, one obtains an approximate transfer function for the pitch rate response to longitudinal stick inputs:

$$\frac{q}{\delta_{lon}}(s) = \frac{M_{\delta_{lon}}}{s - M_q} e^{-s\tau_f} \quad (8.8)$$

It is clear that the pitch rate response to longitudinal stick inputs is described by a first-order system. Assume the following approximation for the pitch attitude  $\theta = \int q = \frac{1}{s}q$ . Then, the pitch attitude response to longitudinal stick inputs will be:

$$\frac{\theta}{\delta_{lon}}(s) = \frac{M_{\delta_{lon}}}{s(s - M_q)} e^{-s\tau_f} \quad (8.9)$$

Thus, the pitch attitude response to longitudinal stick inputs is described by a second-order system. Figure 8.6 shows the pitch rate and attitude frequency response to longitudinal stick inputs. The pitch rate response has first-order system characteristics with a flat amplitude at frequencies less than the break frequency  $\omega_b = -M_q$  and a -20 dB/decade slope at frequencies greater than the break frequency. On the other hand, the pitch attitude response has an initial -20 dB/decade slope that steepens to -40 dB/decade after  $\omega_b$ . It is also worth noting that the inclusion of the rotor delay  $\tau_f$  makes the phase of both pitch rate and attitude response roll off at high frequencies. These same concepts apply for the lateral and directional responses to the respective on-axis pilot control inputs.

#### Lateral

By following a similar procedure as above, the roll rate response to lateral stick inputs is:

$$\frac{p}{\delta_{lat}}(s) = \frac{L_{\delta_{lat}}}{s - L_p} e^{-s\tau_f} \quad (8.10)$$

and, like for the pitch rate response, is first order. The roll attitude response to lateral stick input is:

$$\frac{\phi}{\delta_{lat}}(s) = \frac{L_{\delta_{lat}}}{s(s - L_p)} e^{-s\tau_f} \quad (8.11)$$

and like the pitch rate response, is second order.

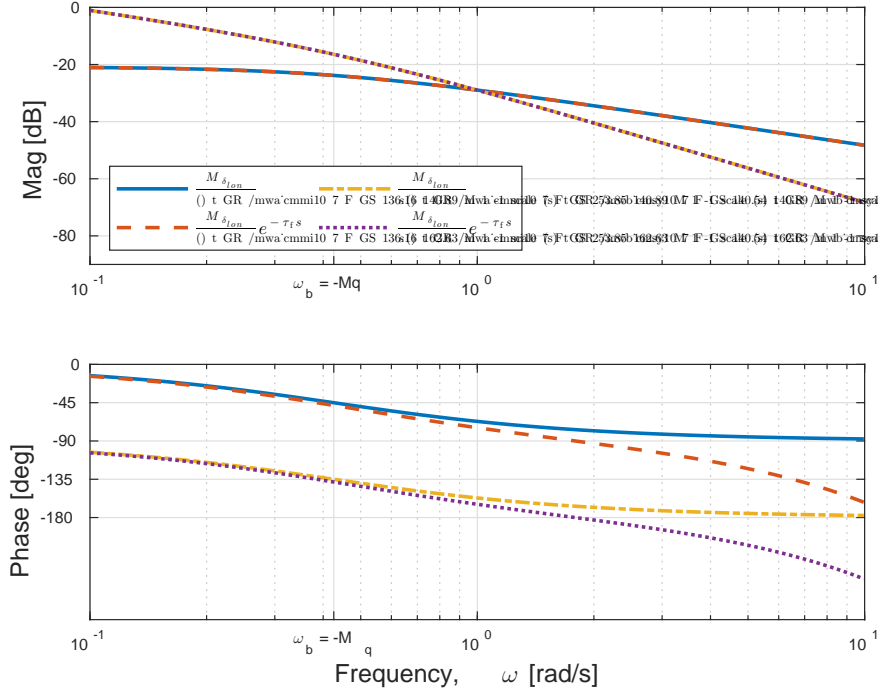


Figure 8.6: Pitch rate and attitude frequency response to longitudinal stick inputs.

### Directional

The yaw rate response to pedal inputs is:

$$\frac{r}{\delta_{ped}}(s) = \frac{N_{\delta_{ped}}}{s - N_r} e^{-s\tau_{TR}} \quad (8.12)$$

where  $\tau_{TR}$  is the delay associated with the tail rotor inflow response. Typically,  $\tau_{TR} \ll \tau_f$  such that  $\tau_{TR}$  be neglected in practice. The heading response to pedal stick input is:

$$\frac{\psi}{\delta_{ped}}(s) = \frac{N_{\delta_{ped}}}{s(s - N_r)} e^{-s\tau_{TR}} \quad (8.13)$$

### 8.4.2 Translational Dynamics

#### Longitudinal

Consider the following approximation of the decoupled of the longitudinal translation dynamics:

$$\dot{u} = X_u u - g\theta \quad (8.14)$$

where the vertical dynamics was ignored due to it being approximately decoupled from the forward translation and pitch dynamics. The control derivative  $X_{\delta_{lon}}$  was also neglected since its effect on speed compared to pitch attitude is low. Here, the pitch attitude is treated as an input to the system, *i.e.*, pitch attitude is used to control the longitudinal speed. By converting to the frequency domain using the Laplace transform one obtains:

$$\frac{u}{\theta}(s) = \frac{-g}{s - X_u} \quad (8.15)$$

By substituting Eq. (8.9) into the equation above, one obtains:

$$\frac{u}{\delta_{lon}}(s) = \left( \frac{-g}{s - X_u} \right) \left[ \frac{M_{\delta_{lon}}}{s(s - M_q)} e^{-s\tau_f} \right] \approx \frac{-gM_{\delta_{lon}}}{s - X_u} e^{-s(\tau_f + \tau_p)} \quad (8.16)$$

where  $\tau_p = -1/M_q$ . This approximation is justified by the fact that  $X_u \ll M_q$ , which means that the pitch attitude response is significantly faster than the forward velocity response and can thus be approximated with a transport delay. Thus, the longitudinal speed response to pitch attitude inputs is approximately a first-order system. Assume the following approximation for the pitch attitude  $x = \int u = \frac{1}{s}u$ . Then, the longitudinal position response to longitudinal stick inputs will be:

$$\frac{x}{\delta_{\text{lon}}}(s) = \frac{-gM_{\delta_{\text{lon}}}}{s(s-X_u)} e^{-s(\tau_f+\tau_p)} \quad (8.17)$$

It is apparent that the longitudinal position response to longitudinal stick inputs is a second order system.

### Lateral

Similarly, consider the following approximation for the lateral translation dynamics:

$$\dot{v} = Y_v v + g\phi \quad (8.18)$$

Here, the roll attitude is treated as an input to the system, *i.e.*, roll attitude is used to control the lateral speed. Converting this relationship to the frequency domain yields:

$$\frac{v}{\phi}(s) = \frac{g}{s - Y_v} \quad (8.19)$$

By substituting the roll attitude response to lateral stick inputs in the equation above, one obtains:

$$\frac{v}{\delta_{\text{lat}}}(s) = \left( \frac{g}{s - Y_v} \right) \left[ \frac{L_{\delta_{\text{lat}}}}{s(s-L_p)} e^{-s\tau_f} \right] \approx \frac{gL_{\delta_{\text{lat}}}}{s - Y_v} e^{-s(\tau_f+\tau_r)} \quad (8.20)$$

where  $\tau_r = -1/L_p$ . This approximation is justified by the fact that  $Y_v \ll L_p$ . Thus, the lateral speed response to roll attitude inputs is approximately a first-order system. Assume the following approximation for the roll attitude  $y = \int v = \frac{1}{s}v$ . Then, the lateral position response to lateral stick inputs will be:

$$\frac{y}{\delta_{\text{lat}}}(s) = \frac{gL_{\delta_{\text{lat}}}}{s(s-Y_v)} e^{-s(\tau_f+\tau_r)} \quad (8.21)$$

It is apparent that the lateral position response to lateral stick inputs is a second order system.

### Vertical

Consider an approximation for the vertical translation dynamics:

$$\dot{w} = Z_w w + Z_{\delta_{\text{col}}} \delta_{\text{col}} \quad (8.22)$$

Then, the transfer function from collective stick inputs to vertical velocity is:

$$\frac{w}{\delta_{\text{col}}}(s) = \frac{Z_{\delta_{\text{col}}}}{s - Z_w} \quad (8.23)$$

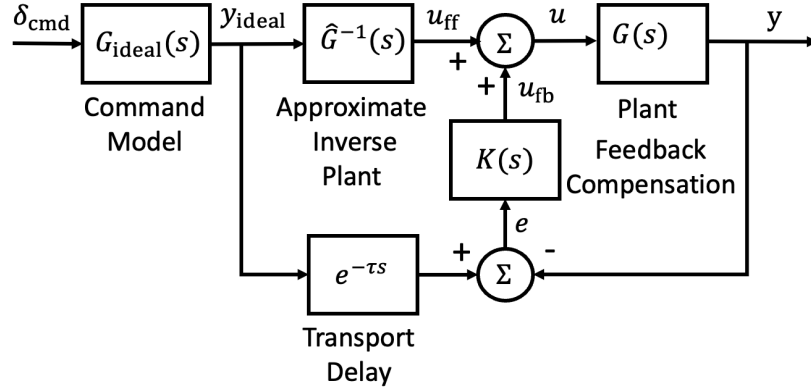
Thus, the vertical speed response to collective stick inputs is first order. Assume the following approximation for the roll attitude  $z = \int w = \frac{1}{s}w$ . Then, the vertical position response to collective stick inputs will be:

$$\frac{z}{\delta_{\text{col}}}(s) = \frac{Z_{\delta_{\text{col}}}}{s(s-Z_w)} \quad (8.24)$$

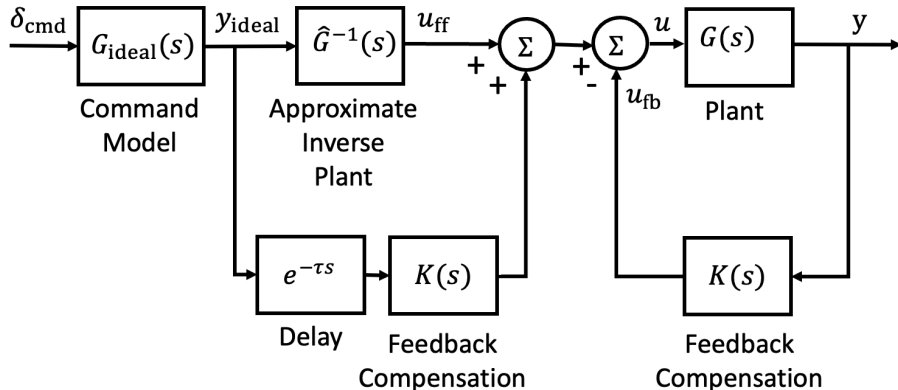
which is a second-order response.

## 8.5 Explicit Model Following

EMF is a popular control architecture in the helicopter community and across aerospace manufacturers. A general Explicit Model Following scheme for a SISO system is shown in Fig. 8.7a. The command model sets the desired dynamics of the closed-loop system. The approximate inverse plant generates the feed-forward actuator inputs which command the aircraft to approximately follow the command-model responses. Feedback compensation is used to minimize the error between the commanded response and actual aircraft response. Equivalent command delays are used to synchronize the commanded and measured responses in time. EMF naturally partitions the controller in a feed-forward and a feedback part. This allows the designer to easily tailor feed-forward compensation and have flexibility in the implementation of different feedback control strategies.



(a) Combined feed-forward and feedback loops.



(b) Separate feed-forward and feedback loops.

Figure 8.7: EMF block diagram.

### 8.5.1 RCAH EMF Controller

The EMF controller design starts with the ideal response, also known as command model or command filter. Because the natural response type of the pitch rate response is a first-order system response, then the ideal dynamics will also be a first-order system of the form:

$$\left( \frac{q}{\delta_{\text{lon}}} \right)_{\text{ideal}}(s) = \frac{k}{\tau s + 1} \quad (8.25)$$

where  $\tau$  is the ideal time constant and  $k$  is the ideal sensitivity. Note that  $k$  is the proportionality constant between the commanded pitch rate and the commanded longitudinal stick position. In general,  $\omega_b = 1/\tau$  (*i.e.*, the command filter break frequency) will have to be greater than the desired bandwidth of the closed-loop response. The natural time constant of the rotorcraft is:

$$\tau_{\text{natural}} \approx \frac{1}{|M_q|} \quad (8.26)$$

where  $M_q$  is taken from the 8-state residualized model. Thus, it is desirable for the ideal time constant to be faster than the natural one, formally  $\tau_{\text{ideal}} < \tau_{\text{natural}}$ . For reference, a UH-60 helicopter with Level 1 handling qualities (subject of the next chapter) as per ADS-33E-PRF [Ano00] will roughly have a pitch axis command filter break frequency of  $\omega_b = 4.5 \text{ rad/s}$  and a control sensitivity of approximately  $k = \frac{0.5\pi}{100} \text{ rad/(s-\%)}$  when the pilot stick inputs are expressed in %. Pitch rate and attitude ideal responses for different command filter time constants are shown in Fig. 8.8.

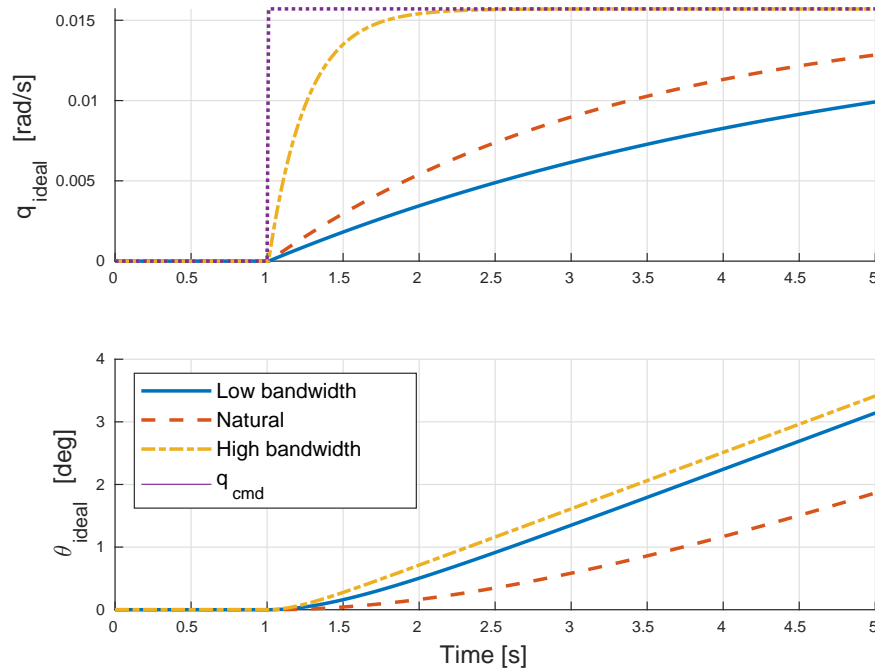


Figure 8.8: Pitch rate and attitude ideal response to a step input for varying command filter time constant.

The next step is the choice of the approximate inverse model. This model is based on the inverse of the pitch rate response in Eq. (8.8):

$$\left( \frac{q}{\delta_{\text{lon}}} \right)^{-1}(s) = \frac{s - M_q}{M_{\delta_{\text{lon}}}} e^{s\tau_f} \quad (8.27)$$

However, this transfer function is both improper (*i.e.*, the numerator has higher order than the denominator such that this transfer function requires unfiltered differentiation of a signal, which is not desirable) and non-causal (*i.e.*, its output or response at any time instant depends upon future values of the input) because of  $e^{s\tau_f}$ . Thus, the inverse model is chosen as:

$$\left( \frac{q}{\delta_{\text{lon}}} \right)^{-1}(s) = \frac{s - M_q}{M_{\delta_{\text{lon}}}} \quad (8.28)$$

and the ideal response  $q_{\text{ideal}}$  is delayed by  $e^{-s\tau_f}$  when compared to the actual response  $q$ . As such, the tracking error is defined as:

$$e = q_{\text{ideal}} e^{-s\tau_f} - q \quad (8.29)$$

If the inverse plant is perfect and if there are no other disturbances (*e.g.*, turbulence), then  $e = 0$  and:

$$\frac{q}{\delta_{\text{lon}_{\text{cmd}}}} = \frac{k}{\tau s + 1} e^{-s\tau_f} \quad (8.30)$$

Then, there would not be a need for a feedback loop. Obviously, there will be the need of a feedback loop given that the inverse plant is an approximate model and that rotorcraft are subject of disturbances like gusts,

turbulence, *etc.*. It is also worth noting that the inverse plant results in lead compensation of the feed-forward path and is thus put in series with the ideal response to form a *proper* such that:

$$\left( \frac{k}{\tau s + 1} \right) \left( \frac{s - M_q}{M_{\delta_{\text{lon}}}} \right) = k' \frac{\tau' s - 1}{\tau s + 1} \quad (8.31)$$

where  $k' = \frac{k M_q}{M_{\delta_{\text{lon}}}}$ ,  $\tau' = \frac{1}{|M_q|}$ , and  $\tau' > \tau$ . The frequency response of this transfer function is shown in Fig. 8.9.

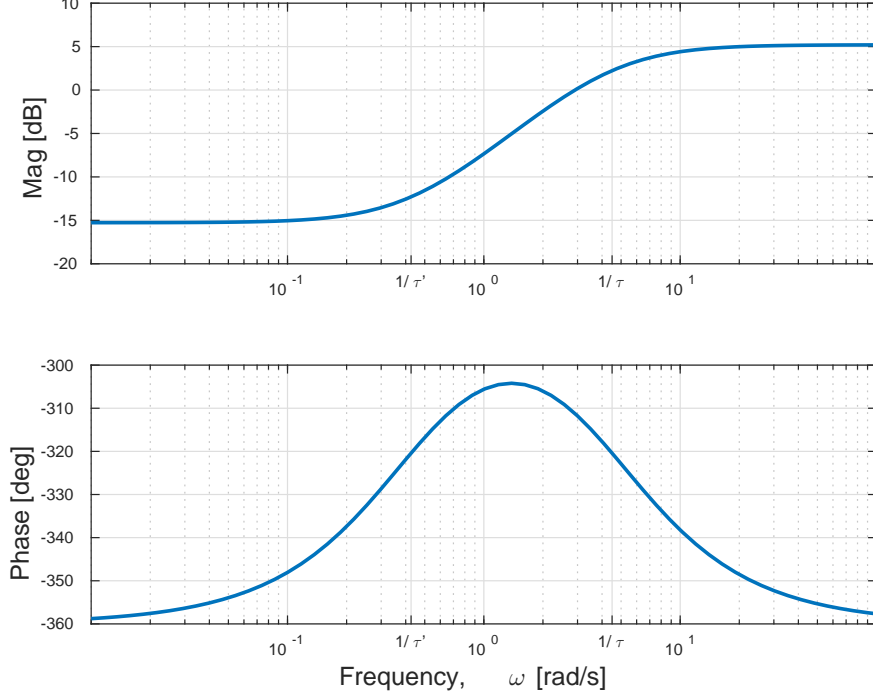


Figure 8.9: Lead compensation introduced by the inverse plant in the feed-forward path.

Because the feedback loop can be separated from the feed-forward path, feedback control design can be performed independently of the feed-forward path. Many strategies can be employed for control design, like pole placements, a Linear Quadratic Regulator (LQR), robust control theory ( $H_2$ ,  $H_\infty$ ), *etc.*. Here, an LQR compensator is used for simplicity. The cost function being minimized is:

$$J = \int_0^t [\hat{x}^T Q \hat{x} + u^T R u] d\tau \quad (8.32)$$

where  $\hat{x}$  is the state vector of the system used for the LQR design, and  $Q$  and  $R$  are the state and control weighting matrices. The weighting matrices can be designed according to Bryson's rule [Bry69]:

$$Q = \text{diag} \left[ \frac{\alpha_1^2}{(x_1)_{\max}^2} \dots \frac{\alpha_n^2}{(x_n)_{\max}^2} \right] \quad (8.33)$$

$$R = \rho \text{ diag} \left[ \frac{\beta_1^2}{(u_1)_{\max}^2} \dots \frac{\beta_m^2}{(u_m)_{\max}^2} \right] \quad (8.34)$$

where  $(x_i)_{\max}^2$  and  $(u_j)_{\max}^2$  are the largest desired response and input for that particular component of the output/input. Additionally,  $\sum_{i=1}^n \alpha_i^2 = 1$  and  $\sum_{j=1}^m \beta_j^2 = 1$  are used to add an additional relative weighting on the various components of the output/control input, and  $\rho$  is used as the relative weighting between the control and state penalties. It is suggested to set the penalties corresponding to the position and linear velocities states to 1 ft/s. On the other hand, the penalties corresponding to the angular states shall be set to the equivalent of 1 deg ( $\pi/180$  rad), with the exception of the penalties of integral of the attitude tracking

error (if any); these are found to require a significantly lower value than the equivalent of 1 deg [Sae+20]. The penalties corresponding to the controls are set to 1% (or 0.01).

Consider the case where only the pitch rate was fed back. Then,  $\hat{\mathbf{x}} = q$ ,  $\hat{\mathbf{u}} = \delta_{\text{lon}}$ , and the equation used for LQR design is simply:

$$\dot{q} = M_u q + M_{\delta_{\text{lon}}} \delta_{\text{lon}} \quad (8.35)$$

such that the system and control matrices used for the LQR design are  $\mathbf{A}_{\text{LQR}} = M_q$  and  $\mathbf{B}_{\text{LQR}} = M_{\delta_{\text{lon}}}$ . The LQR weighting matrices found with Bryson's rule become:

$$\mathbf{Q} = \text{diag} \left[ \frac{\alpha_q^2}{(q)_{\max}^2} \right] \quad (8.36a)$$

$$\mathbf{R} = \text{diag} \left[ \frac{\beta_{\delta_{\text{lon}}}^2}{(\delta_{\text{lon}})_{\max}^2} \right] \quad (8.36b)$$

The LQR gains can then be found with the MATLAB® function `lqr`. The resulting EMF RCAH control law with pitch rate only feedback is shown in Fig. 8.10a. Consider now the case where both pitch rate and attitude were fed back. Then,  $\hat{\mathbf{x}}^T = [q \ \theta]$ ,  $\hat{\mathbf{u}} = \delta_{\text{lon}}$ , and the equation used for LQR design becomes:

$$\begin{bmatrix} \dot{q} \\ \dot{\theta} \end{bmatrix} = \underbrace{\begin{bmatrix} M_q & 0 \\ 1 & 0 \end{bmatrix}}_{\mathbf{A}_{\text{LQR}}} \begin{bmatrix} q \\ \theta \end{bmatrix} + \underbrace{\begin{bmatrix} M_{\delta_{\text{lon}}} \\ 0 \end{bmatrix}}_{\mathbf{B}_{\text{LQR}}} \delta_{\text{lon}} \quad (8.37)$$

The LQR weighting matrices found with Bryson's rule become:

$$\mathbf{Q} = \text{diag} \left[ \frac{\alpha_q^2}{(q)_{\max}^2} \frac{\alpha_\theta^2}{(\theta)_{\max}^2} \right] \quad (8.38a)$$

$$\mathbf{R} = \text{diag} \left[ \frac{\beta_{\delta_{\text{lon}}}^2}{(\delta_{\text{lon}})_{\max}^2} \right] \quad (8.38b)$$

The LQR gains can then be found with the MATLAB® function `lqr`. The resulting EMF RCAH control law with pitch rate only feedback is shown in Fig. 8.10b.

### 8.5.2 ACAH EMF Controller

In Degraded Visual Environments (DVE) and other missions like shipboard landing operations, RCAH is not ideal for precision maneuvers at low speeds. For these particular flight conditions, ACAH response is better suited. ACAH response features a response to pilot stick inputs that is proportional to the rotorcraft attitude, unlike RCAH where pilot stick inputs result in a proportional angular rate response. Because it was shown that the natural response type of the pitch attitude response is a second-order system response, then the ideal dynamics will also be a second-order system of the form:

$$\left( \frac{\theta}{\delta_{\text{lon}}} \right)_{\text{ideal}} (s) = \frac{k\omega_n^2}{s^2 + 2\omega_n\zeta s + \omega_n^2} \quad (8.39)$$

where  $\omega_n$  is the ideal natural frequency and  $\zeta$  is the ideal damping ratio. Like for the RCAH EMF controller,  $k$  is the proportionality constant between the commanded pitch rate and the commanded longitudinal stick position. The choice of the natural frequency is similar to that of the EMF ACAH control law. Pitch attitude ideal responses for different command filter natural frequencies are shown in Fig. 8.11 for both the time domain (Fig. 8.11a) and the frequency domain (Fig. 8.11b). The ideal damping ratio is typically chosen as either  $\zeta = 0.707$  or as the critical damping ratio *i.e.*,  $\zeta = 1$ .

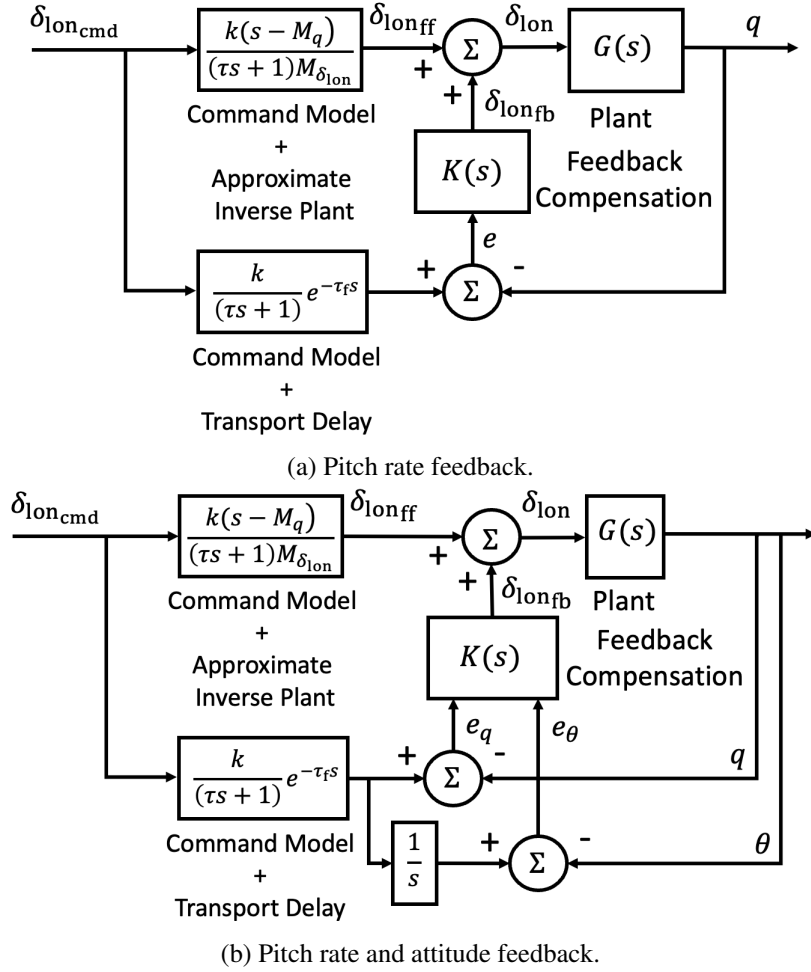


Figure 8.10: RCAH EMF controller.

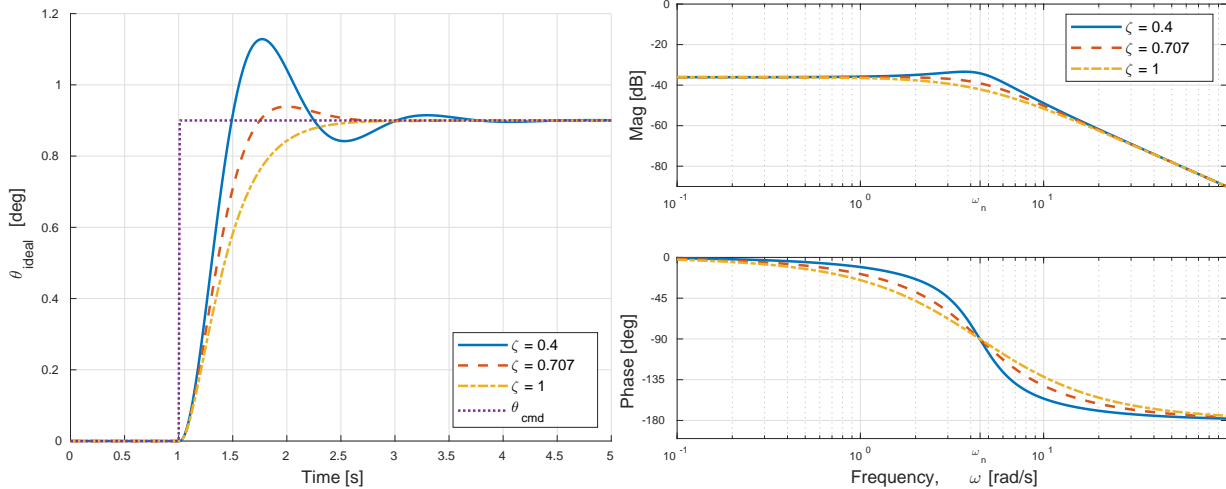


Figure 8.11: Pitch attitude ideal response to longitudinal stick inputs with varying command filter damping ratio.

The approximate inverse plant is chosen as the inverse of Eq. (8.9), *i.e.*,

$$\left( \frac{\beta_{1c}}{\delta_{\text{lon}}} \right)^{-1}(s) = \frac{s(s - M_q)}{M_{\delta_{\text{lon}}}} e^{s\tau_f} \quad (8.40)$$

Like for the EMF RCAH controller, this transfer function is non-causal (*i.e.*, its output or response at any time instant depends upon future values of the input) because of  $e^{s\tau_f}$ . Thus, the inverse model is chosen as:

$$\left( \frac{\beta_{1c}}{\delta_{\text{lon}}} \right)^{-1}(s) = \frac{s(s - M_q)}{M_{\delta_{\text{lon}}}} \quad (8.41)$$

and the ideal response  $\theta_{\text{ideal}}$  is delayed by  $e^{-s\tau_f}$  when compared to the actual response  $\theta$ . As such, the pitch rate and attitude tracking errors are:

$$e_q = q_{\text{ideal}} e^{-s\tau_f} - q \quad (8.42a)$$

$$e_\theta = \theta_{\text{ideal}} e^{-s\tau_f} - \theta \quad (8.42b)$$

Consider the case where pitch rate and attitude are fed back. Then,  $\hat{x}^T = [q \ \theta]$ ,  $\hat{u} = \delta_{\text{lon}}$ , and the equation used for LQR design becomes:

$$\begin{bmatrix} \dot{q} \\ \dot{\theta} \end{bmatrix} = \underbrace{\begin{bmatrix} M_q & 0 \\ 1 & 0 \end{bmatrix}}_{\mathbf{A}_{\text{LQR}}} \begin{bmatrix} q \\ \theta \end{bmatrix} + \underbrace{\begin{bmatrix} M_{\delta_{\text{lon}}} \\ 0 \end{bmatrix}}_{\mathbf{B}_{\text{LQR}}} \delta_{\text{lon}} \quad (8.43)$$

The LQR weighting matrices found with Bryson's rule become:

$$\mathbf{Q} = \text{diag} \left[ \frac{\alpha_q^2}{(q)_{\text{max}}^2} \frac{\alpha_\theta^2}{(\theta)_{\text{max}}^2} \right] \quad (8.44a)$$

$$\mathbf{R} = \text{diag} \left[ \frac{\beta_{\delta_{\text{lon}}}^2}{(\delta_{\text{lon}})_{\text{max}}^2} \right] \quad (8.44b)$$

The LQR gains can then be found with the MATLAB® function `lqr`. The resulting EMF ACAH control law with pitch rate only feedback is shown in Fig. 8.12a. Consider now the case where pitch rate, attitude, and integral error were fed back. Then,  $\hat{x}^T = [q \ \theta \ \int \theta]$ ,  $\hat{u} = \delta_{\text{lon}}$ , and the equation used for LQR design becomes:

$$\begin{bmatrix} \dot{q} \\ \dot{\theta} \\ \dot{\int \theta} \end{bmatrix} = \underbrace{\begin{bmatrix} M_q & 0 & 0 \\ 1 & 0 & 0 \\ 0 & 1 & 0 \end{bmatrix}}_{\mathbf{A}_{\text{LQR}}} \begin{bmatrix} q \\ \theta \\ \int \theta \end{bmatrix} + \underbrace{\begin{bmatrix} M_{\delta_{\text{lon}}} \\ 0 \\ 0 \end{bmatrix}}_{\mathbf{B}_{\text{LQR}}} \delta_{\text{lon}} \quad (8.45)$$

The LQR weighting matrices found with Bryson's rule become:

$$\mathbf{Q} = \text{diag} \left[ \frac{\alpha_q^2}{(q)_{\text{max}}^2} \frac{\alpha_\theta^2}{(\theta)_{\text{max}}^2} \frac{\alpha_{\int \theta}^2}{(\int \theta)_{\text{max}}^2} \right] \quad (8.46a)$$

$$\mathbf{R} = \text{diag} \left[ \frac{\beta_{\delta_{\text{lon}}}^2}{(\delta_{\text{lon}})_{\text{max}}^2} \right] \quad (8.46b)$$

The LQR gains can then be found with the MATLAB® function `lqr`. The resulting EMF ACAH control law with pitch rate only feedback is shown in Fig. 8.12b.

### 8.5.3 TRC EMF Controller

TRC allows the pilot to directly command forward speed or lateral speed, rather than controlling the aircraft's attitude or angular rates directly and translational velocity indirectly. What is controller here is the longitudinal velocity  $V_x$  in the heading frame. Because it was shown that the natural response type of longitudinal velocity response to pitch attitude is a first-order system response, then the ideal dynamics will also be a first-order system of the form:

$$\left( \frac{V_x}{\delta_{\text{lon}}} \right)_{\text{ideal}}(s) = \frac{k}{\tau s + 1} \quad (8.47)$$

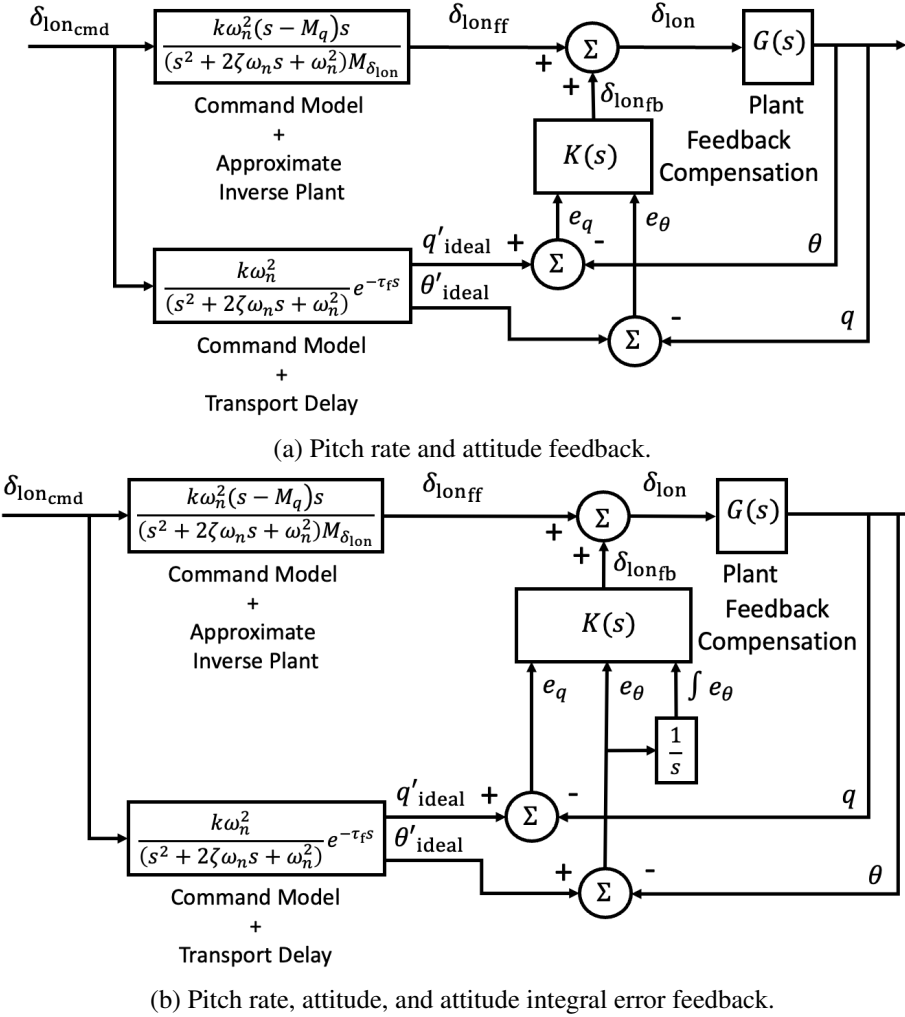


Figure 8.12: ACAH EMF controller.

where  $\tau$  is the ideal response time constant and  $k$  is the proportionality constant between the commanded longitudinal speed and the commanded longitudinal stick position. The break frequency (*i.e.*,  $\omega_b = 1/\tau$ ) must be chosen such that the frequency separation between the outer-velocity TRC loop and the inner-attitude ACAH loop is large enough not to have the two loops interact dynamically. Typically,  $\frac{1}{10}(\omega_n)_{\text{inner}} \leq (\omega_b)_{\text{outer}} \leq \frac{1}{5}(\omega_n)_{\text{inner}}$  [Tis+17]. The approximate inverse plant is chosen as the inverse of Eq. (8.15), *i.e.*,

$$\left(\frac{V_x}{\theta}\right)^{-1}(s) \approx \left(\frac{u}{\theta}\right)^{-1}(s) = \frac{s - X_u}{-g} \quad (8.48)$$

Consider the case where only the longitudinal velocity in the heading frame  $V_x$  was fed back. Then, the forward speed tracking error is defined as:

$$e_{V_x} = V_{x_{\text{ideal}}} e^{-s(\tau_f + \tau_p)} - V_x \quad (8.49)$$

To design an LQR compensator, consider using a system with state vector  $\hat{x} = V_x$ , control vector  $\hat{u} = \theta$ , and the following dynamics:

$$\dot{V}_x = X_u u - g\theta \quad (8.50)$$

such that the system and control matrices used for the LQR design are  $\mathbf{A}_{\text{LQR}} = X_u$  and  $\mathbf{B}_{\text{LQR}} = -g$ . The LQR weighting matrices found with Bryson's rule become:

$$\mathbf{Q} = \text{diag} \left[ \frac{\alpha_{V_x}^2}{(V_x)_{\max}^2} \right] \quad (8.51a)$$

$$\mathbf{R} = \text{diag} \left[ \frac{\beta_\theta^2}{(\theta)_{\max}^2} \right] \quad (8.51b)$$

The LQR gains can then be found with the MATLAB® function `lqr`. The resulting EMF RCAH control law with pitch rate only feedback is shown in Fig. 8.13a. Note that this TRC control law is an outer-velocity loop design around an inner ACAH pitch attitude loop. The ACAH pitch attitude loop is modified from the previous example to take as input commanded pitch attitude rather than longitudinal stick inputs. The modification consists of removing the inner loop command filter gain  $k$  or, equivalently, of setting it to  $k = 1$ .

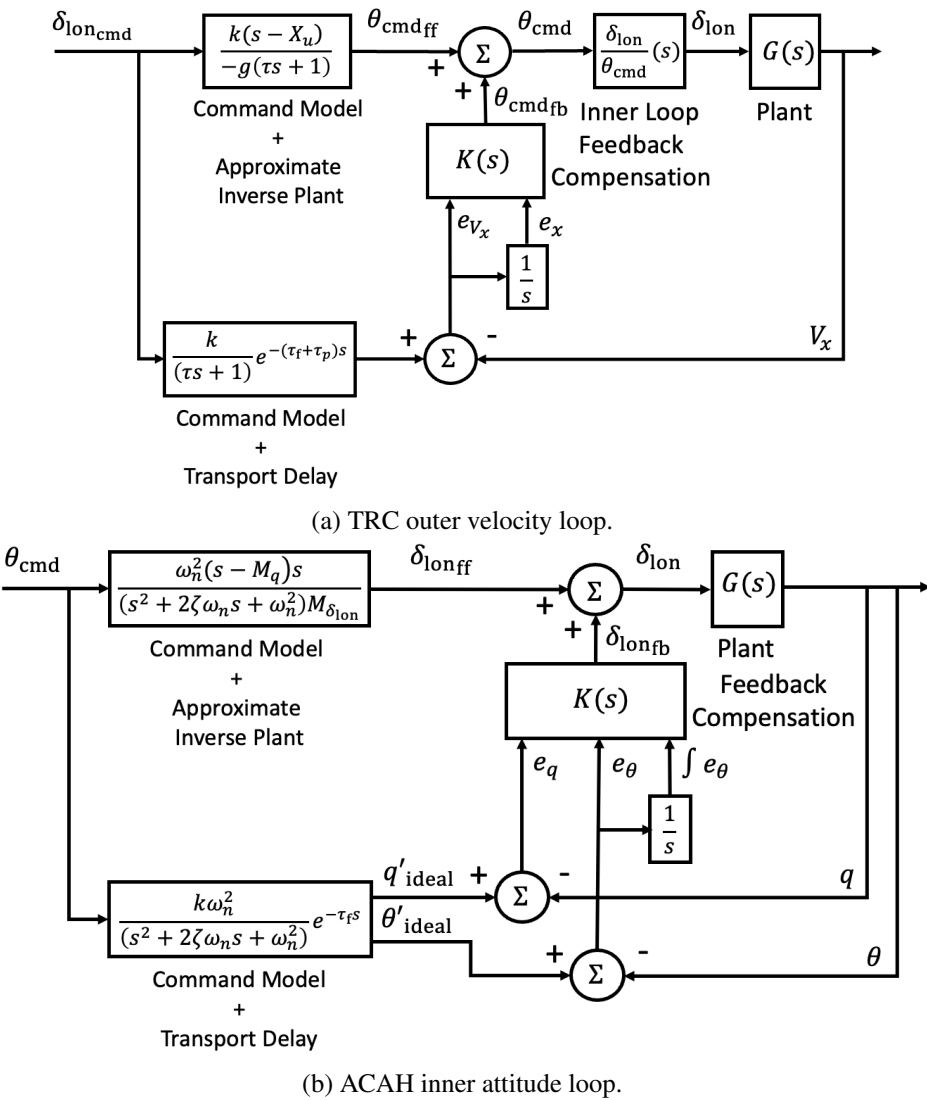


Figure 8.13: EMF TRC outer velocity loop coupled with an ACAH inner attitude loop.

#### 8.5.4 Example 1: UH-60 EMF SCAS

Figure 8.14 shows a RCAH SCAS developed for a UH-60 helicopter. This control law is designed to achieve RCAH response around the roll, pitch, and yaw axes. Differently from what was illustrated above, the LQR

compensator is designed based on the coupled rigid-body dynamics. The model used to obtain the LQR compensator is a modified version of the 8-state model where the translational velocity states are truncated and the heading is added to the state vector as the integral of the yaw rate. Thus, the vector of the model used for LQR design is  $\hat{x}^T = [p \ q \ r \ \phi \ \theta \ \psi]$  whereas the control vector is  $\hat{u}^T = [\delta_{\text{lat}} \ \delta_{\text{lon}} \ \delta_{\text{ped}}]$ . The gains are obtained in an analogous fashion as to the examples above. In addition, the control law features turn compensation and turn coordination blocks which will be discussed later in the chapter.

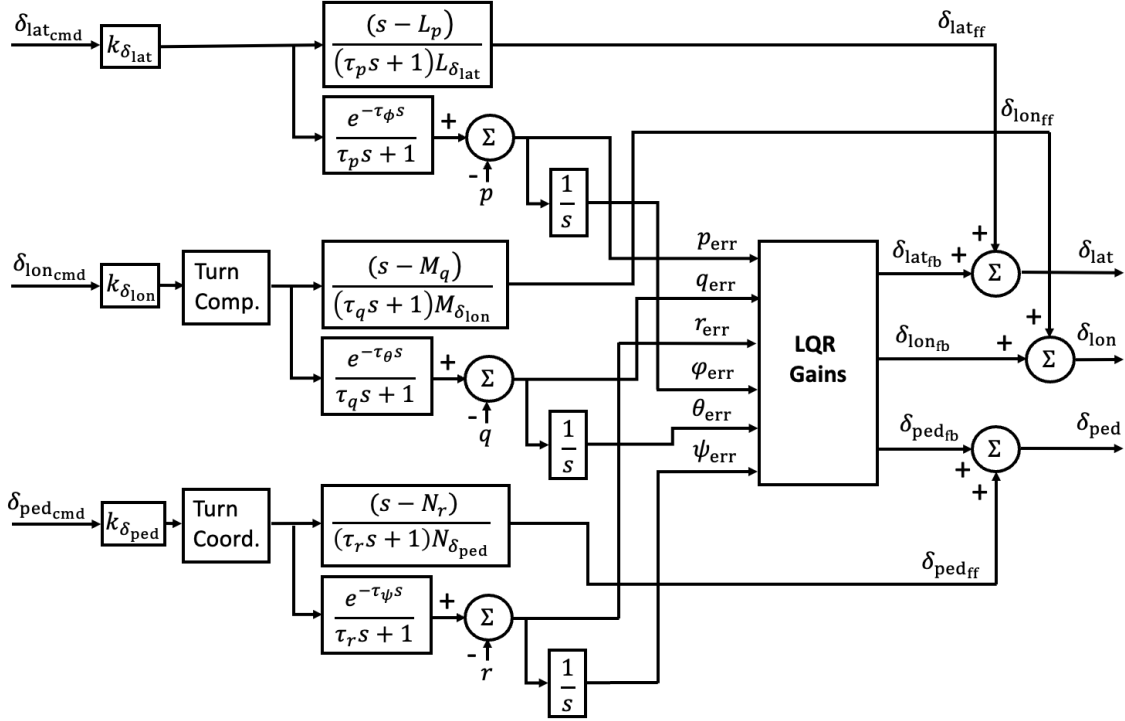


Figure 8.14: UH-60 RCAH SCAS.

### 8.5.5 Example 2: Quadrotor EMF AFCS

Figure 8.15 shows an EMF AFCS developed for a small-scale quadrotor unmanned aerial system (UAS) [Sae+20]. An EMF inner loop is designed to achieve stability, disturbance rejection, ACAH response about the roll and pitch axes, and RCAH response about the yaw axis, and TRC response about the heave axes. The inner loop is shown in Fig. 8.15a. LQR is used for stability and disturbance rejection. The state vector used to obtain the LQR gains is  $\hat{x}^T = [p \ \phi \ \int \phi \ q \ \theta \ \int \theta \ r \ \int r \ V_z \ z]$  whereas the control input vector is  $\hat{u}^T = [\delta_{\text{lat}} \ \delta_{\text{lon}} \ \delta_{\text{ped}} \ \delta_{\text{col}}]$ . The system and control matrices used for LQR design are:

$$\mathbf{A}_{\text{LQR}} = \begin{bmatrix} L_v & L_p & 0 & 0 & 0 & 0 & 0 & 0 & 0 \\ 0 & 1 & 0 & 0 & 0 & 0 & 0 & 0 & 0 \\ 0 & 0 & 1 & 0 & 0 & 0 & 0 & 0 & 0 \\ 0 & 0 & 0 & M_u & M_q & 0 & 0 & 0 & 0 \\ 0 & 0 & 0 & 0 & 1 & 0 & 0 & 0 & 0 \\ 0 & 0 & 0 & 0 & 0 & 1 & 0 & 0 & 0 \\ 0 & 0 & 0 & 0 & 0 & 0 & 1 & 0 & 0 \\ 0 & 0 & 0 & 0 & 0 & 0 & 0 & 1 & 0 \\ 0 & 0 & 0 & 0 & 0 & 0 & 0 & 0 & 1 \end{bmatrix}, \quad \mathbf{B}_{\text{LQR}} = \begin{bmatrix} L_{\delta_{\text{lat}}} & 0 & 0 & 0 \\ 0 & 0 & 0 & 0 \\ 0 & 0 & 0 & 0 \\ 0 & M_{\delta_{\text{lon}}} & 0 & 0 \\ 0 & 0 & 0 & 0 \\ 0 & 0 & 0 & 0 \\ 0 & 0 & N_{\delta_{\text{ped}}} & 0 \\ 0 & 0 & 0 & 0 \\ 0 & 0 & 0 & Z_{\delta_{\text{col}}} \\ 0 & 0 & 0 & 0 \end{bmatrix} \quad (8.52)$$

where the stability and control derivatives are obtained via parametric identification [Sae+20]. The EMF outer loop tracks forward and lateral velocities in the heading frame and is shown in Fig. 8.15b. LQR is used

independently on each axis for disturbance rejection. The system used to synthesize the gains for the forward speed is:

$$\begin{bmatrix} \dot{V}_x \\ \dot{x} \end{bmatrix} = \begin{bmatrix} X_u & 0 \\ 1 & 0 \end{bmatrix} \begin{bmatrix} V_x \\ x \end{bmatrix} + \begin{bmatrix} -g \\ 0 \end{bmatrix} \theta_{\text{cmd}} \quad (8.53)$$

where  $x$  is the longitudinal position in the heading frame. The system used to synthesize the gains for the lateral speed is:

$$\begin{bmatrix} \dot{V}_y \\ \dot{y} \end{bmatrix} = \begin{bmatrix} Y_v & 0 \\ 1 & 0 \end{bmatrix} \begin{bmatrix} V_y \\ y \end{bmatrix} + \begin{bmatrix} g \\ 0 \end{bmatrix} \phi_{\text{cmd}} \quad (8.54)$$

where  $y$  is the lateral position in the heading frame.

Figure 8.16 shows the closed-loop response to a lateral stick doublet for the EMF control law described, along with an approximately equivalent DI flight control law. More specifically, Fig. 8.16a shows how the controller tracks the commanded change in lateral speed, whereas Figs. 8.16b and 8.16c shows the angular and controls responses, respectively.

## 8.6 Dynamic Inversion

Dynamic inversion (DI) evolved into a popular flight control design method in the 1990s [EBS94], due to its capability to elegantly decouple the control compensation design from the variations in aircraft due to its capability to elegantly decouple the control compensation design from the variations in dynamics over a wide flight envelope. The method is based on feedback linearization, which was aircraft dynamics over a wide flight envelope. The method is based on feedback linearization, which first presented in the 1980's [JR80]. The method has been widely adopted for military fixed-wing aircraft [HR18] and is now well documented in textbooks [SL15]. Numerous extensions to DI have been developed over the past 30 years to overcome limitations in the design and to expand its applications, including to rotorcraft [Hor19]. Dynamic inversion design offers a desirable solution to rotorcraft flight control as it effectively decouples the plant model and effectively handles non-linearity. However, the method has limitations for rotorcraft due to the requirement for full-state feedback and issues with non-minimum phase zeros. However, reduced-order modeling was shown to alleviate the full-state feedback requirement [Hor19]. Non-linear dynamic inversion (NLDI), has the advantage of incorporating non-linear kinematics in the plant inversion, and can reduce complexity of the design by minimizing the need for individual gain tuning or gain scheduling. The most sophisticated NLDI controllers effectively contain a non-linear simulation model of the aircraft along with optimization solvers in the control algorithms and they eliminate the need for gain scheduling [HR18]. NLDI inverts model using feedback linearization [JR80], as opposed to the purely feed-forward inversion used in EMF. Feedback linearization requires full state feedback. For advanced aircraft, measurement and/or accurate estimation of the complete set of rigid body states is usually feasible. Thus, a six degree-of-and/or accurate estimation of the complete set of rigid body states is usually feasible. Thus, a six freedom (6 DOF) model can be used in the plant inversion.

The dynamic inversion control architecture as applied to a linear system is illustrated in Fig. 8.17. The key features are an inner feedback loop that achieves model inversion (*i.e.*, the cancellation of the plant non-linear plant inner feedback linearization); a command filter (also known as reference model or command model) that specifies desired response to pilot commands; and feedback compensation on the tracking error to govern disturbance rejection.

DI differs from EMF in that it uses feedback in plant inversion as opposed a plant cancelling transfer function in the feedforward path. Most published EMF designs use simplified single-input single-output (SISO) transfer functions for plant cancellation, separated into individual control axes (roll, pitch, yaw, and heave axes). DI uses state-space multi-input multi-output (MIMO) systems for the model inversion, which can be of any order as long as all states are available for feedback. MIMO versions of EMF have been proposed that use a MIMO transfer function in the inversion using so-called *decoupling numerators* [CTB94]. Both EMF and DI have issues when the plant model has transmission zeros in the right-half of the complex plane,

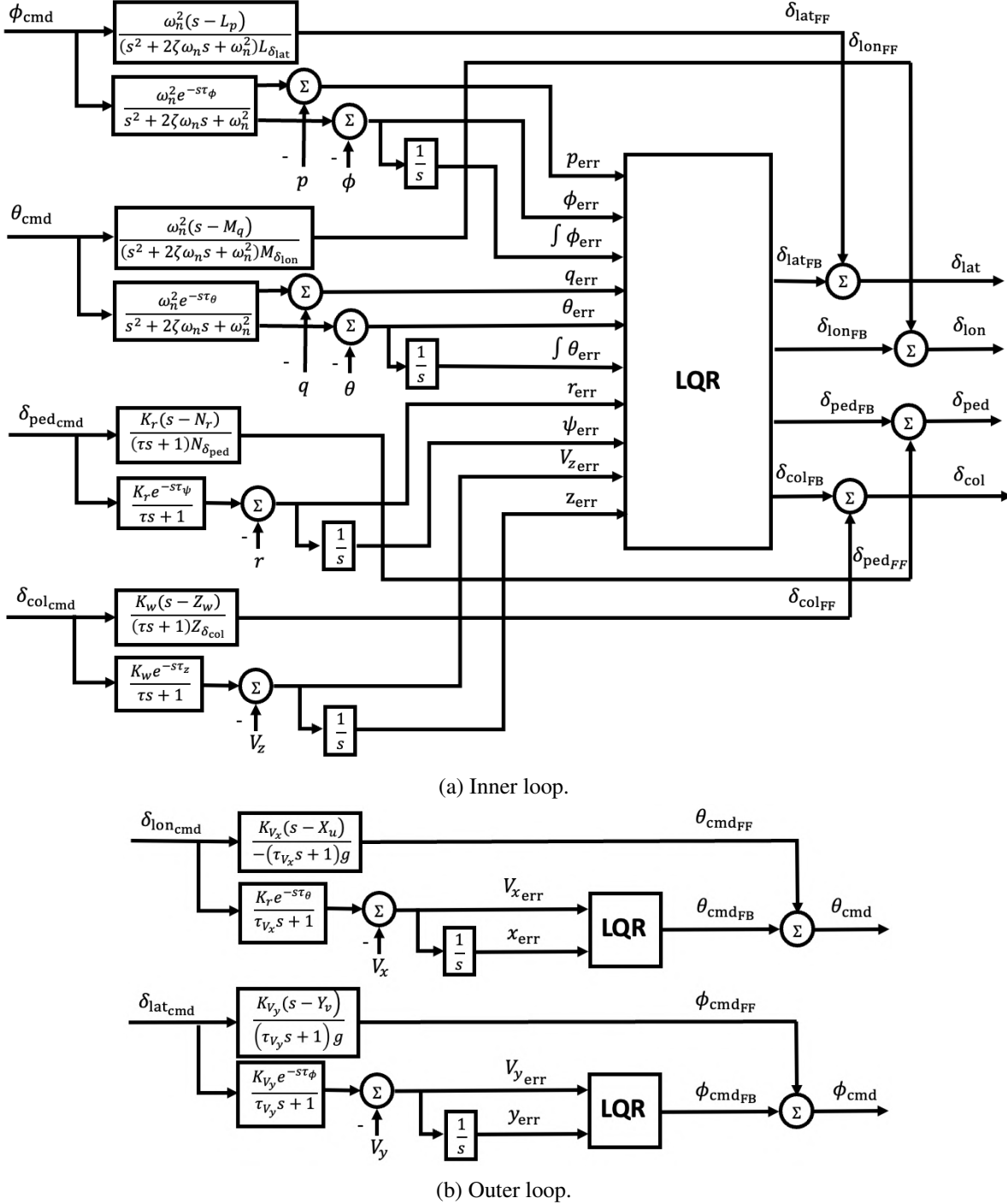


Figure 8.15: Quadrrotor EMF AFCS.

i.e., non-minimum phase (NMP) zeros. Clearly, when a transfer function with NMP zeros is inverted, it has unstable poles. Similarly, it is well known that the inversion in DI will also produce unstable modes corresponding to NMP zeros of the open loop plant model (as will be reviewed below). The DI design process is presented below for rotorcraft control design through a series of examples.

### 8.6.1 RCAH DI Controller

A single-loop DI control law is designed to achieve RCAH response in the pitch axis. Consider adopting the following approximate model of the aircraft dynamics system to design the control law:

$$\dot{q} = [M_q] q + [M_{\delta_{\text{lon}}}] \delta_{\text{lon}} \Leftrightarrow \dot{x}_{\text{DI}} = A_{\text{DI}} x_{\text{DI}} + B_{\text{DI}} u_{\text{DI}} \quad (8.55)$$

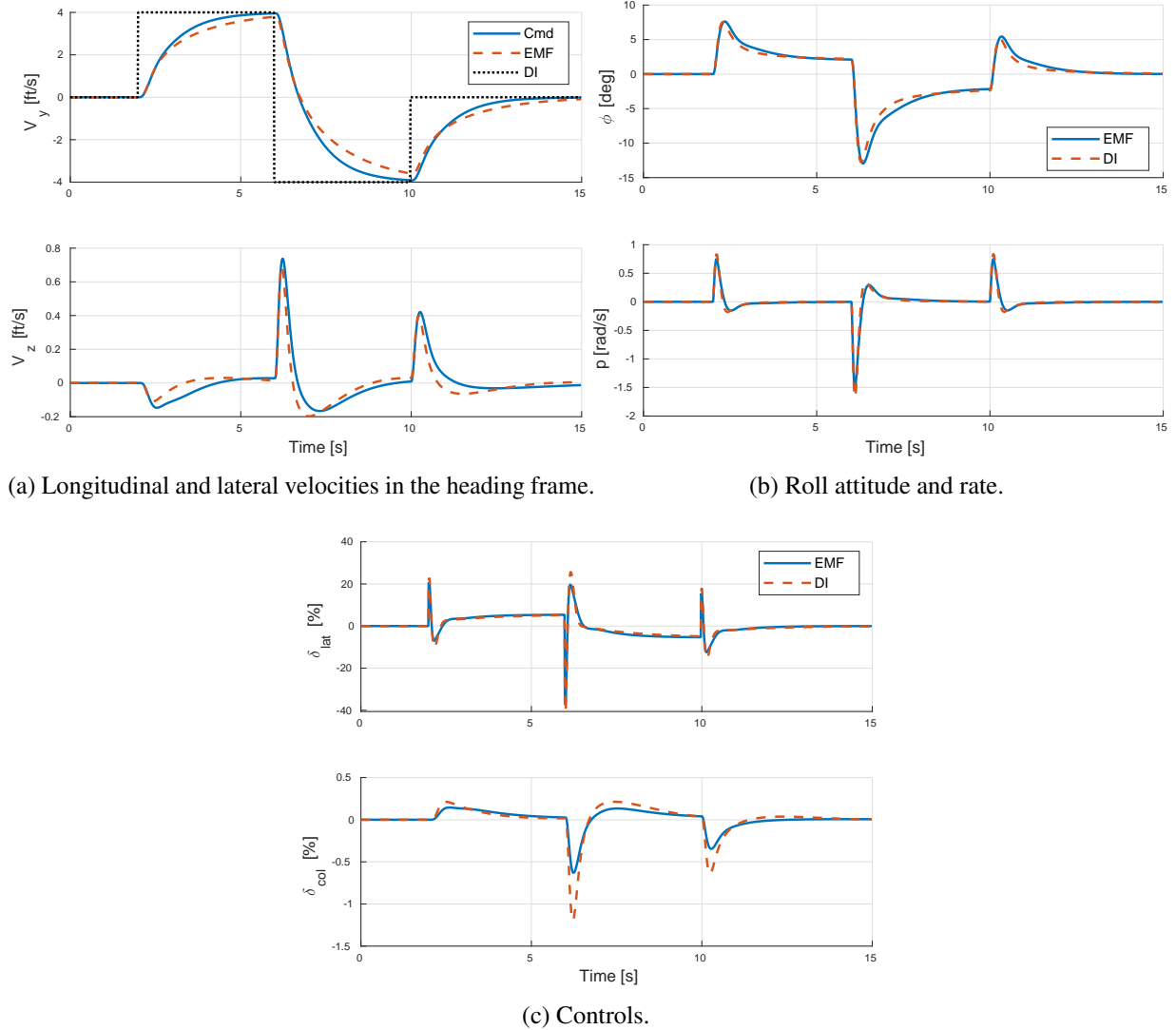


Figure 8.16: Closed-loop quadrotor response to a lateral stick doublet for approximately equivalent EMF and DI control laws.

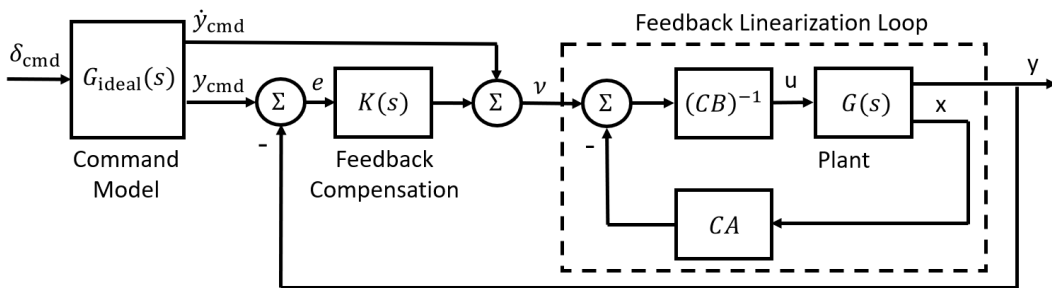


Figure 8.17: DI controller as applied to a linear system.

where the stability and control derivatives are pulled from the 8-state residualized model and can be scheduled with the flight condition. Additionally, the output equation is defined as:

$$q = [1] q \Leftrightarrow \mathbf{y}_{\text{DI}} = \mathbf{C}_{\text{DI}} \mathbf{x}_{\text{DI}} \quad (8.56)$$

corresponding to the controlled variables of the nonlinear system (*i.e.*, the aircraft dynamics). Consider differentiating the output equation once with respect to time to obtain:

$$\begin{aligned}\dot{q} &= \mathbf{C}_{\text{DI}} \dot{\mathbf{x}}_{\text{DI}} \\ &= \mathbf{C}_{\text{DI}} (\mathbf{A}_{\text{DI}} \mathbf{x}_{\text{DI}} + \mathbf{B}_{\text{DI}} \mathbf{u}_{\text{DI}}) \\ &= \mathbf{C}_{\text{DI}} \mathbf{A}_{\text{DI}} \mathbf{x}_{\text{DI}} + \mathbf{C}_{\text{DI}} \mathbf{B}_{\text{DI}} \mathbf{u}_{\text{DI}}\end{aligned}\quad (8.57)$$

The objective of the DI control law is that the output  $\mathbf{y}$  tracks a reference trajectory  $\mathbf{y}_{\text{cmd}}(t)$  given by  $\mathbf{y}_{\text{cmd}} = q_{\text{cmd}}$  with desired response characteristics. Because the pitch rate response to longitudinal stick inputs is first-order, the reference trajectory is fed through the first-order command filter of Eq. (8.25). The command filter is also used to extract the first derivative of the filtered reference trajectory for use in the proportional-integral (PI) compensator described below. The time constant of the ideal response is designed analogously to the EMF RCAH controller. PI compensation is used to reject external disturbances and to compensate for discrepancies between the approximate model used in this derivation and the actual bare-airframe dynamics of the aircraft. The resulting DI control law is found by solving for the control vector in Eq. (8.57), leading to:

$$\begin{aligned}\mathbf{u}_{\text{DI}} &= (\mathbf{C}_{\text{DI}} \mathbf{B}_{\text{DI}})^{-1} (\mathbf{v} - \mathbf{C}_{\text{DI}} \mathbf{A}_{\text{DI}} \mathbf{x}_{\text{DI}}) \\ &= \frac{1}{M_{\delta_{\text{lon}}}} (\mathbf{v} - M_q q)\end{aligned}\quad (8.58)$$

where  $\mathbf{v}$  is the pseudo-command vector. The pseudo-command vector is defined as:

$$\begin{aligned}\mathbf{v} &= \dot{q}_{\text{cmd}} + K_P \mathbf{e} + K_I \int_{t_0}^t \mathbf{e}(\tau) d\tau \\ &= \dot{q}_{\text{cmd}} + K_P e_q + K_I e_\theta\end{aligned}\quad (8.59)$$

where  $\mathbf{e} = \mathbf{y}_{\text{cmd}} - \mathbf{y}$  is the tracking error. The constants  $K_P$  and  $K_I$  identify the proportional and integral compensator gains, respectively. Note that the matrices  $(\mathbf{C}_{\text{DI}} \mathbf{B}_{\text{DI}})^{-1}$  and  $\mathbf{C}_{\text{DI}} \mathbf{A}_{\text{DI}}$  depend on the stability and control derivatives of the aircraft and thus on the flight condition. It follows that the control law could be scheduled with the flight condition. Should this be done, while the control law uses an approximate linearized aircraft model for inversion, scheduling effectively introduces nonlinearity in the control law such that it would effectively become NLDI. It can be demonstrated [SL15] that for a DI control law the output equation must be differentiated  $n$  times for the controls to appear explicitly in the output equation:

$$\mathbf{e}^{(n)} = \mathbf{y}_{\text{cmd}}^{(n)} - \mathbf{v} \quad (8.60)$$

As it turns out, translational and angular rates must only be differentiated once for this to happen. Consider substituting Eq. (8.59) into Eq. (8.60) to yield the error dynamics:

$$\dot{\mathbf{e}}(t) + K_P \mathbf{e}(t) + K_I \int_{t_0}^t \mathbf{e}(\tau) d\tau = \mathbf{0} \quad (8.61)$$

The gains are chosen such that the frequencies of the error dynamics are the same order of the command filter (*i.e.*, first order), ensuring that the bandwidth of the response to disturbances is comparable to that of an input from the pilot. Taking the Laplace transform yields:

$$\mathbf{e}(s) (s^2 + sK_P + K_I) = \mathbf{0} \quad (8.62)$$

To obtain gains that guarantee desired response, the error dynamics is set equal to the following system:

$$s^2 + 2\zeta\omega_n s + \omega_n^2 = 0 \quad (8.63)$$

yielding the following proportional and integral gains:

$$K_P = 2\zeta\omega_n \quad (8.64a)$$

$$K_I = \omega_n^2 \quad (8.64b)$$

The natural frequency is set to achieve the desired crossover frequency of the loop transfer function (*i.e.*, set equal to the break frequency of the ideal response  $\omega_n = \omega_b = 1/\tau$ ), while the damping ratio is usually selected to be provide critical damping (*i.e.*,  $\zeta = 1$ ). A block diagram of the DI flight control law is shown in Fig. 8.18. It is clear that feedback compensation does not depend on the plant and thus a single set of gains can be used across the flight envelope, while the approximate linearized model is what needs to be scheduled. This feature makes DI particularly attractive compared to EMF as it does not require gain scheduling, which can be time consuming.

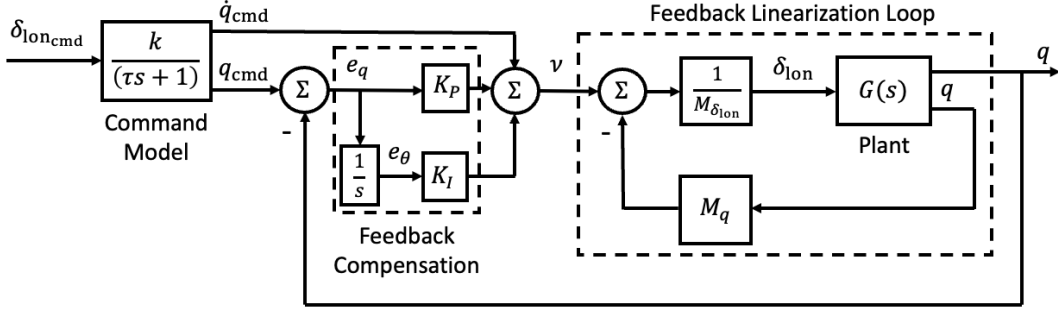


Figure 8.18: DI RCAH controller.

### 8.6.2 ACAH DI Controller

A single-loop DI control law is designed to achieve RACAH response in the pitch axis. Consider adopting the following approximate model of the aircraft dynamics system to design the control law:

$$\begin{bmatrix} \dot{q} \\ \dot{\theta} \end{bmatrix} = \begin{bmatrix} M_q & 0 \\ 1 & 0 \end{bmatrix} \begin{bmatrix} q \\ \theta \end{bmatrix} + \begin{bmatrix} M_{\delta_{\text{lon}}} \\ 0 \end{bmatrix} \delta_{\text{lon}} \Leftrightarrow \dot{x}_{\text{DI}} = \mathbf{A}_{\text{DI}} x_{\text{DI}} + \mathbf{B}_{\text{DI}} u_{\text{DI}} \quad (8.65)$$

where the stability and control derivatives are pulled from the 8-state residualized model and can be scheduled with the flight condition. Additionally, the output equation is defined as:

$$\theta = [0 \ 1] \begin{bmatrix} q \\ \theta \end{bmatrix} \Leftrightarrow y_{\text{DI}} = \mathbf{C}_{\text{DI}} x_{\text{DI}} \quad (8.66)$$

corresponding to the controlled variables of the nonlinear system (*i.e.*, the aircraft dynamics). Consider differentiating the output equation twice with respect to time to obtain:

$$\begin{aligned} \ddot{\theta} &= \mathbf{C}_{\text{DI}} \ddot{x}_{\text{DI}} \\ &= \mathbf{C}_{\text{DI}} (\mathbf{A}_{\text{DI}} \dot{x}_{\text{DI}}) \\ &= \mathbf{C}_{\text{DI}} [\mathbf{A}_{\text{DI}} (\mathbf{A}_{\text{DI}} x_{\text{DI}} + \mathbf{B}_{\text{DI}} u_{\text{DI}})] \\ &= \mathbf{C}_{\text{DI}} \mathbf{A}_{\text{DI}}^2 x_{\text{DI}} + \mathbf{C}_{\text{DI}} \mathbf{A}_{\text{DI}} \mathbf{B}_{\text{DI}} u_{\text{DI}} \end{aligned} \quad (8.67)$$

The objective of the DI control law is that the output  $y$  tracks a reference trajectory  $y_{\text{cmd}}(t)$  given by  $y_{\text{cmd}} = \theta_{\text{cmd}}$  with desired response characteristics. Because the pitch rate/attitude response to longitudinal stick inputs is first-order, the reference trajectory is fed through the first-order command filter of Eq. (8.39). The command filter is also used to extract the first and second derivative of the filtered reference trajectory for use in the proportional-integral-derivative (PID) compensator described below. The time constant of the ideal response is designed analogously to the EMF ACAH controller. PID compensation is used to reject external disturbances and to compensate for discrepancies between the approximate model used in this derivation and the actual bare-airframe dynamics of the aircraft. The resulting DI control law is found by solving for the

control vector in Eq. (8.67), leading to:

$$\begin{aligned}\mathbf{u}_{\text{DI}} &= (\mathbf{C}_{\text{DI}} \mathbf{A}_{\text{DI}} \mathbf{B}_{\text{DI}})^{-1} (\mathbf{v} - \mathbf{C}_{\text{DI}} \mathbf{A}_{\text{DI}}^2 \mathbf{x}_{\text{DI}}) \\ &= \left( [0 \ 1] \begin{bmatrix} M_q & 0 \\ 1 & 0 \end{bmatrix} \begin{bmatrix} M_{\delta_{\text{lon}}} \\ 0 \end{bmatrix} \right)^{-1} \left( \mathbf{v} - [0 \ 1] \begin{bmatrix} M_q & 0 \\ 1 & 0 \end{bmatrix}^2 \begin{bmatrix} q \\ \theta \end{bmatrix} \right) \\ &= \frac{1}{M_{\delta_{\text{lon}}}} \left( \mathbf{v} - [M_q \ 0] \begin{bmatrix} q \\ \theta \end{bmatrix} \right)\end{aligned}\quad (8.68)$$

where  $\mathbf{v}$  is the pseudo-command vector. The pseudo-command vector is defined as:

$$\begin{aligned}\mathbf{v} &= \ddot{\theta}_{\text{cmd}} + K_D \dot{\theta} + K_P \theta + K_I \int_{t_0}^t \mathbf{e}(\tau) d\tau \\ &= \ddot{\theta}_{\text{cmd}} + K_D e_q + K_P e_\theta + K_I \int_{t_0}^t e_\theta(\tau) d\tau\end{aligned}\quad (8.69)$$

where  $\mathbf{e} = \mathbf{y}_{\text{cmd}} - \mathbf{y}$  is the tracking error. The constants  $K_P$ ,  $K_I$ , and  $K_D$  identify the proportional, integral, and derivative compensator gains, respectively. Note that the matrices  $(\mathbf{C}_{\text{DI}} \mathbf{A}_{\text{DI}} \mathbf{B}_{\text{DI}})^{-1}$  and  $\mathbf{C}_{\text{DI}} \mathbf{A}_{\text{DI}}^2$  depend on the stability and control derivatives of the aircraft and thus on the flight condition. It can be demonstrated [SL15] that for a DI control law the output equation must be differentiated  $n$  times for the controls to appear explicitly in the output equation:

$$\mathbf{e}^{(n)} = \mathbf{y}_{\text{cmd}}^{(n)} - \mathbf{v} \quad (8.70)$$

As it turns out, attitude and position states must be differentiated twice for this to happen. Consider substituting Eq. (8.69) into Eq. (8.70) to yield the error dynamics:

$$\ddot{\mathbf{e}}(t) + K_D \dot{\mathbf{e}}(t) + K_P \mathbf{e}(t) + K_I \int_{t_0}^t \mathbf{e}(\tau) d\tau = \mathbf{0} \quad (8.71)$$

The gains are chosen such that the frequencies of the error dynamics are the same order of the command filter (*i.e.*, first order), ensuring that the bandwidth of the response to disturbances is comparable to that of an input from the pilot. Taking the Laplace transform yields:

$$\mathbf{e}(s) (s^3 + s^2 K_D + s K_P + K_I) = \mathbf{0} \quad (8.72)$$

To obtain gains that guarantee desired response, the error dynamics is set equal to the following system:

$$(s^2 + 2\zeta\omega_n s + \omega_n^2)(s + p) = 0 \quad (8.73)$$

yielding the following proportional and integral gains:

$$K_D = 2\zeta\omega_n + p \quad (8.74a)$$

$$K_P = 2\zeta\omega_n p + \omega_n^2 \quad (8.74b)$$

$$K_I = \omega_n^2 p \quad (8.74c)$$

The natural frequency is set to achieve the desired crossover frequency of the loop transfer function while the damping ratio is usually selected to be provide critical damping (*i.e.*,  $\zeta = 1$ ). The integrator pole  $p$  is usually chosen to be one-fifth of the natural frequency, corresponding to about one-fifth of the loop crossover frequency [Tis+17]. A block diagram of the DI flight control law is shown in Fig. 8.19. Also for the ACAH case, the feedback compensation does not depend on the plant and thus a single set of gains can be used across the flight envelope, while the approximate linearized model is what needs to be scheduled.

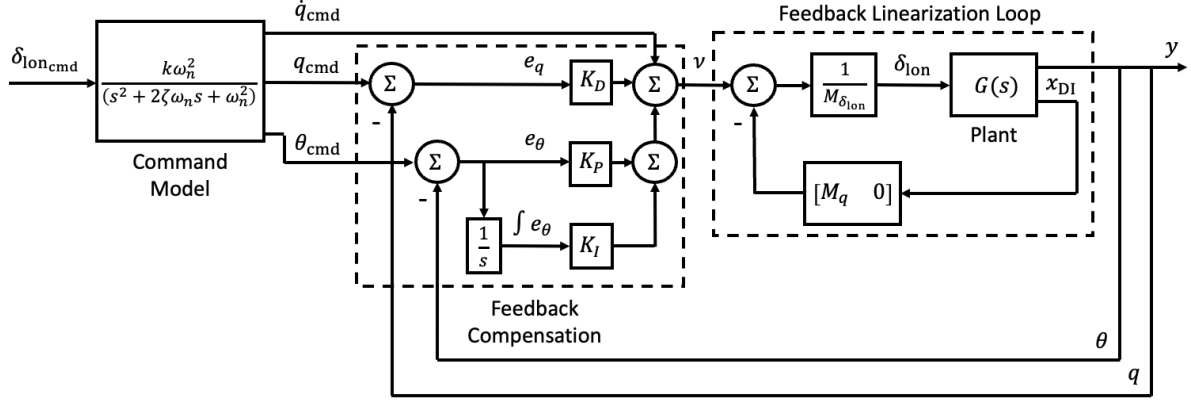


Figure 8.19: DI ACAH controller.

### 8.6.3 TRC DI Controller

A multi-loop DI control law is designed to achieve TRC response in the longitudinal speed and ACAH response in the pitch axis. Consider adopting the following approximate model of the aircraft dynamics system to design the control law:

$$\dot{u} = [X_u] u + [-g] \theta \Leftrightarrow \dot{x}_{\text{DI}} = \mathbf{A}_{\text{DI}} x_{\text{DI}} + \mathbf{B}_{\text{DI}} u_{\text{DI}} \quad (8.75)$$

where the stability derivative  $X_u$  is pulled from the 8-state residualized model and can be scheduled with the flight condition. Here, pitch attitude is used as an input to control longitudinal speed. Additionally, the output equation is defined as:

$$V_x = [1] u \Leftrightarrow y_{\text{DI}} = \mathbf{C}_{\text{DI}} x_{\text{DI}} \quad (8.76)$$

corresponding to the controlled variables of the nonlinear system (*i.e.*, the aircraft dynamics). The variable  $V_x$  is the longitudinal speed in the heading frame, described earlier. Consider differentiating the output equation once with respect to time to obtain:

$$\begin{aligned} \dot{V}_x &= \mathbf{C}_{\text{DI}} \dot{x}_{\text{DI}} \\ &= \mathbf{C}_{\text{DI}} (\mathbf{A}_{\text{DI}} x_{\text{DI}} + \mathbf{B}_{\text{DI}} u_{\text{DI}}) \\ &= \mathbf{C}_{\text{DI}} \mathbf{A}_{\text{DI}} x_{\text{DI}} + \mathbf{C}_{\text{DI}} \mathbf{B}_{\text{DI}} u_{\text{DI}} \end{aligned} \quad (8.77)$$

The objective of the DI control law is that the output  $\mathbf{y}$  tracks a reference trajectory  $\mathbf{y}_{\text{cmd}}(t)$  given by  $\mathbf{y}_{\text{cmd}} = V_{x_{\text{cmd}}}$  with desired response characteristics. Because the longitudinal speed response to longitudinal stick inputs is first-order, the reference trajectory is fed through the first-order command filter of Eq. (8.25). The command filter is also used to extract the first derivative of the filtered reference trajectory for use in the proportional-integral (PI) compensator described below. The time constant of the ideal response is designed analogously to the EMF TRC controller. The resulting DI control law is found by solving for the control vector in Eq. (8.77), leading to:

$$\begin{aligned} u_{\text{DI}} &= (\mathbf{C}_{\text{DI}} \mathbf{B}_{\text{DI}})^{-1} (\mathbf{v} - \mathbf{C}_{\text{DI}} \mathbf{A}_{\text{DI}} x_{\text{DI}}) \\ &= -\frac{1}{g} (\mathbf{v} - X_u u) \end{aligned} \quad (8.78)$$

where  $\mathbf{v}$  is the pseudo-command vector. The pseudo-command vector is defined as:

$$\begin{aligned} \mathbf{v} &= \dot{V}_{x_{\text{cmd}}} + K_P e + K_I \int_{t_0}^t e(\tau) d\tau \\ &= \dot{V}_{x_{\text{cmd}}} + K_P e_{V_x} + K_I e_x \end{aligned} \quad (8.79)$$

where  $\mathbf{e} = \mathbf{y}_{\text{cmd}} - \mathbf{y}$  is the tracking error. The constants  $K_P$  and  $K_I$  are designed similarly to the RCAH DI case. However, like for the TRC EMF case, the natural frequency of the outer loop should be chosen such that  $\frac{1}{10}(\omega_n)_{\text{inner}} \leq (\omega_b)_{\text{outer}} \leq \frac{1}{5}(\omega_n)_{\text{inner}}$  to guarantee the necessary frequency separation [Tis+17]. A block diagram of the DI flight control law is shown in Fig. 8.20, where Fig. 8.20a shows the TRC DI outer velocity loop, and Fig. 8.20b shows the inner attitude loop.

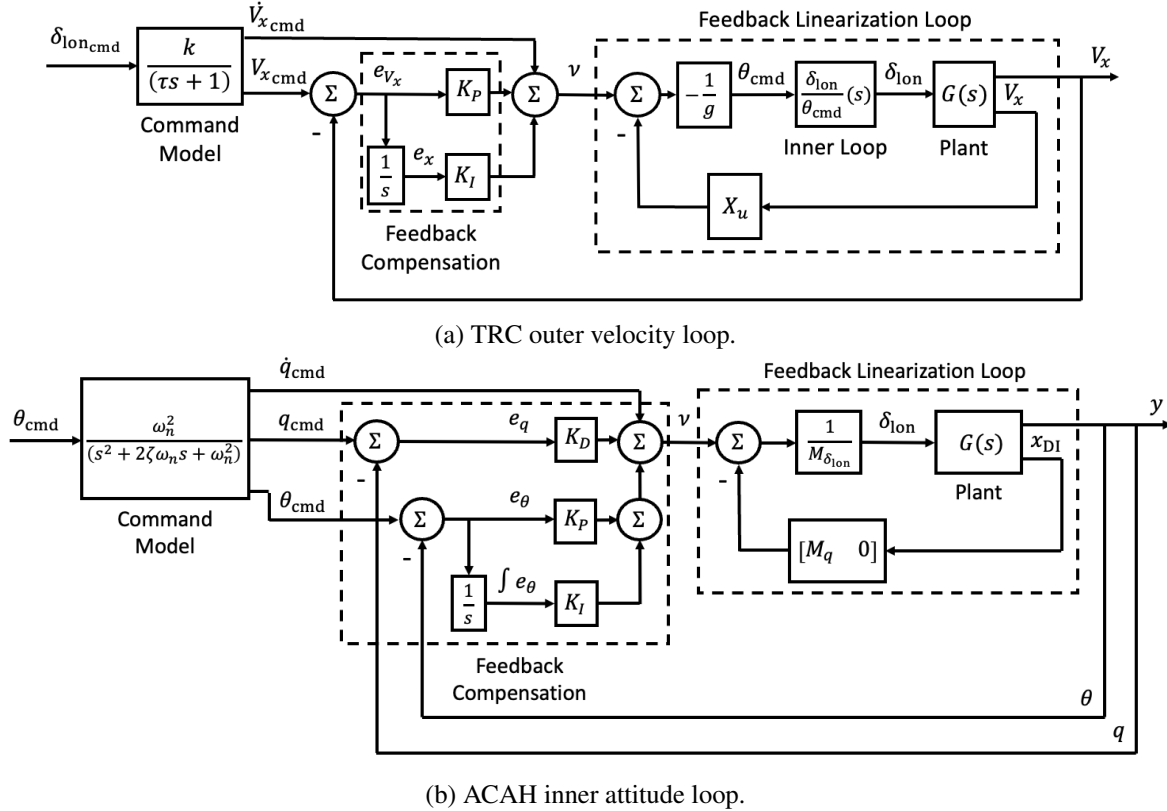


Figure 8.20: DI TRC outer velocity loop coupled with an ACAH inner attitude loop.

#### 8.6.4 Example 3: UH-60 DI AFCS

Consider the example where a multi-loop DI control law is designed to enable fully autonomous flight of the helicopter [Sae+22]. The outer loop controller tracks longitudinal and lateral ground velocities commands in the heading frame and calculates the desired pitch and roll attitudes for the inner loop to track. The desired response type for the outer loop is TRC. The inner loop achieves stability, disturbance rejection, and desired response characteristics about the roll, pitch, yaw, and heave axes. More specifically, an ACAH response is used for the roll, pitch, RCAH is used for the yaw axis, and a TRC response is used for the heave axis.

The very first step toward the development of this DI flight control law is to obtain linear models representative of the rotorcraft flight dynamics across the flight conditions of interest. For this reason, linear models are derived by trimming the rotorcraft at incremental speeds  $V$  in forward level flight and subsequently linearizing and residualizing about each trim condition:

$$\dot{\mathbf{x}} = \mathbf{A}(V)\mathbf{x} + \mathbf{B}(V)\mathbf{u} \quad (8.80)$$

where the coefficient matrices  $\mathbf{A}$  and  $\mathbf{B}$  are representative of the 8-state model described earlier and are functions of the total speed of the aircraft,  $V$ . The state vector of the linearized model used to design the inner loop is:

$$\hat{\mathbf{x}}^T = [u \ v \ w \ p \ q \ r \ \phi \ \theta] \quad (8.81)$$

Table 8.1: Inner loop command models parameters.

| Command                  | $\omega_n$ [rad/s] | $\zeta$ |
|--------------------------|--------------------|---------|
| Roll Attitude, $\phi$    | 4.5                | 0.7     |
| Pitch Attitude, $\theta$ | 4.5                | 0.7     |
| Yaw Rate, $r$            | 2.0                | -       |
| Vertical Position, $V_z$ | 1.0                | -       |

whereas the system and control matrices correspond to those of the 8-state model. Additionally, the following output vector is defined, corresponding to the controlled variables of the nonlinear system:

$$\mathbf{y}^T = [\phi \ \theta \ r \ V_z] \quad (8.82)$$

where  $V_z$  is the vertical speed in the heading frame (positive up). The output matrix that relates the state vector to the output vector:

$$\mathbf{C} = \begin{bmatrix} \mathbf{C}_1 \\ \mathbf{C}_2 \end{bmatrix} \quad (8.83)$$

where:

$$\mathbf{C}_1 = \begin{bmatrix} 0 & 0 & 0 & 0 & 0 & 0 & 1 & 0 \\ 0 & 0 & 0 & 0 & 0 & 0 & 0 & 1 \end{bmatrix} \quad (8.84a)$$

$$\mathbf{C}_2 = \begin{bmatrix} 0 & 0 & 0 & 0 & 0 & 1 & 0 & 0 \\ 0 & 0 & -1 & 0 & 0 & 0 & 0 & V \end{bmatrix} \quad (8.84b)$$

$\mathbf{C}_1$  corresponds to the roll and pitch attitudes whereas  $\mathbf{C}_2$  is related to the yaw rate and vertical speed. The matrix  $\mathbf{C}_2$  is a function of the total speed  $V$  and therefore requires scheduling. This partitioning is due to the fact that the output equations for  $\phi$  and  $\theta$  require being differentiated twice to have the control inputs appear explicitly in the output equation, while the same procedure requires being performed once for  $r$  and  $V_z$ :

$$\begin{bmatrix} \ddot{\phi} \\ \ddot{\theta} \\ \dot{r} \\ \dot{V}_z \end{bmatrix} = \begin{bmatrix} \mathbf{C}_1 \hat{\mathbf{A}}^2 \hat{\mathbf{x}} + \mathbf{C}_1 \hat{\mathbf{A}} \hat{\mathbf{B}} \mathbf{u} \\ \mathbf{C}_2 \hat{\mathbf{A}} \hat{\mathbf{x}} + \mathbf{C}_2 \hat{\mathbf{B}} \mathbf{u} \end{bmatrix} \quad (8.85)$$

The objective of the DI control law is that the output  $\mathbf{y}$  tracks a reference trajectory  $\mathbf{y}_{\text{cmd}}(t)$  given by:

$$\mathbf{y}_{\text{cmd}}^T = [\phi_{\text{cmd}} \ \theta_{\text{cmd}} \ r_{\text{cmd}} \ V_{z,\text{cmd}}] \quad (8.86)$$

with desired response characteristics. For this reason, the reference trajectory is fed through first- or second-order command models which dictate the desired response of the system. More specifically,  $\phi_{\text{cmd}}$  and  $\theta_{\text{cmd}}$  are fed through a second-order system, whereas  $r_{\text{cmd}}$  and  $V_{z,\text{cmd}}$  are fed through a first-order system. The command models are also used to extract the first and second derivatives of the filtered reference trajectory for use in the proportional-integral (PI) and proportional-derivative-integral (PID) compensators described below. Table 8.1 shows the values used for the parameters of the command models of the inner loop.

PI and PID compensation are used to reject external disturbances and to compensate for discrepancies between the approximate model used in this derivation and the actual bare-airframe dynamics of the aircraft. The resulting DI control law is found by solving for the control vector in Eq. (8.85), leading to:

$$\mathbf{u} = \begin{bmatrix} \mathbf{C}_1 \hat{\mathbf{A}} \hat{\mathbf{B}} \\ \mathbf{C}_2 \hat{\mathbf{B}} \end{bmatrix}^{-1} \left( \mathbf{v} - \begin{bmatrix} \mathbf{C}_1 \hat{\mathbf{A}}^2 \\ \mathbf{C}_2 \hat{\mathbf{A}} \end{bmatrix} \hat{\mathbf{x}} \right) \quad (8.87)$$

Table 8.2: Outer loop command models parameters.

| Command                   | $\omega_n$ [rad/s] | $\zeta$ |
|---------------------------|--------------------|---------|
| Longitudinal Speed, $V_x$ | 1                  | 0.7     |
| Lateral Speed, $V_y$      | 1                  | 0.7     |

where  $\mathbf{v}$  is the pseudo-command vector and  $\mathbf{e}$  is the error as defined respectively in Eqs. (8.88) and (??).

$$\begin{bmatrix} v_\phi \\ v_\theta \\ v_r \\ v_{V_z} \end{bmatrix} = \begin{bmatrix} \ddot{\phi}_{\text{cmd}} \\ \dot{\theta}_{\text{cmd}} \\ \dot{r}_{\text{cmd}} \\ \dot{V}_{z_{\text{cmd}}} \end{bmatrix} + \mathbf{K}_P \begin{bmatrix} e_\phi \\ e_\theta \\ e_r \\ e_{V_z} \end{bmatrix} + \mathbf{K}_D \begin{bmatrix} \dot{e}_\phi \\ \dot{e}_\theta \\ 0 \\ 0 \end{bmatrix} + \mathbf{K}_I \begin{bmatrix} \int e_\phi dt \\ \int e_\theta dt \\ \int e_r dt \\ \int e_{V_z} dt \end{bmatrix} \quad (8.88)$$

$$\mathbf{e} = \mathbf{y}_{\text{cmd}} - \mathbf{y}; \quad (8.89)$$

The 4-by-4 diagonal matrices  $\mathbf{K}_P$ ,  $\mathbf{K}_I$ , and  $\mathbf{K}_D$  identify the proportional, integral, and derivative gain matrices, respectively. Note that the coefficient matrices  $(\mathbf{C}_1 \hat{\mathbf{A}} \hat{\mathbf{B}})^{-1}$ ,  $\mathbf{C}_1 \hat{\mathbf{A}}^2$ ,  $(\mathbf{C}_2 \hat{\mathbf{B}})^{-1}$ , and  $\mathbf{C}_2 \hat{\mathbf{A}}$  are functions of the total velocity of the aircraft  $V$ . For this reason, from a practical standpoint, these matrices can be computed offline at incremental longitudinal speeds from 0 to 120 kts at, *e.g.*, 20 kts intervals and stored. When the linearized DI controller is implemented on the nonlinear aircraft dynamics, the coefficient matrices  $(\mathbf{C}_1 \hat{\mathbf{A}} \hat{\mathbf{B}})^{-1}$ ,  $\mathbf{C}_1 \hat{\mathbf{A}}^2$ ,  $(\mathbf{C}_2 \hat{\mathbf{B}})^{-1}$ , and  $\mathbf{C}_2 \hat{\mathbf{A}}$  are computed at each time step via interpolation based on the current total velocity  $V(t)$  and on the tabled stored offline. It is important to note that what is implemented on the nonlinear aircraft dynamics is linearized DI. However, because the coefficient matrices are scheduled with the longitudinal speed, where scheduling effectively introduces a nonlinear relation between the aircraft states and the feedback control input, the controller implemented is effectively nonlinear DI (NLDI) [Hor19]. A block diagram of the linearized DI flight control law is shown in Fig. 8.21a.

The objective of the outer loop is to track longitudinal and lateral velocities in the heading frame, such that the reference trajectory is given by:

$$\mathbf{y}_{\text{cmd}}^T = [V_{x_{\text{cmd}}} \ V_{y_{\text{cmd}}}] \quad (8.90)$$

The following approximate model of the longitudinal and lateral dynamics of the helicopter is used to derive the outer loop control law:

$$\underbrace{\begin{bmatrix} \dot{V}_x \\ \dot{V}_y \end{bmatrix}}_{\dot{x}} = \underbrace{\begin{bmatrix} X_u & 0 \\ 0 & Y_v \end{bmatrix}}_A \underbrace{\begin{bmatrix} V_x \\ V_y \end{bmatrix}}_x + \underbrace{\begin{bmatrix} -g & 0 \\ 0 & g \end{bmatrix}}_B \underbrace{\begin{bmatrix} \theta \\ \phi \end{bmatrix}}_u \quad (8.91a)$$

$$\underbrace{\begin{bmatrix} x \\ y \end{bmatrix}}_y = \underbrace{\begin{bmatrix} 0 & 1 & 0 & 0 \\ 0 & 0 & 0 & 1 \end{bmatrix}}_C \underbrace{\begin{bmatrix} V_x \\ x \\ V_y \\ y \end{bmatrix}}_x \quad (8.91b)$$

The command models for the longitudinal and lateral speed are first order. The natural frequencies and damping ratios are given in Table 8.2. Following a similar procedure to the inner loop yields to an outer control law of the form:

$$\mathbf{u} = (\mathbf{CAB})^{-1} (\mathbf{v} - \mathbf{CA}^2 \mathbf{x}) \quad (8.92)$$

Table 8.3: Inner loop disturbance rejection natural frequencies, damping ratios, and integrator poles.

|                | $\omega_n$ [rad/s] | $\zeta$ | p    |
|----------------|--------------------|---------|------|
| $\phi_{cmd}$   | 4.5                | 0.7     | 0.75 |
| $\theta_{cmd}$ | 4.5                | 0.7     | 0.75 |
| $r_{cmd}$      | 2                  | 0.7     | -    |
| $V_{z_{cmd}}$  | 1                  | 0.7     | -    |

Table 8.4: Outer loop disturbance rejection natural frequencies and damping ratios.

|               | $\omega_n$ [rad/s] | $\zeta$ |
|---------------|--------------------|---------|
| $V_{x_{cmd}}$ | 1                  | 0.7     |
| $V_{y_{cmd}}$ | 1                  | 0.7     |

The reference trajectory is subtracted from the output to find the error, which is compensated by a PI controller. The feed-forward signal is subsequently added, leading to the pseudo-control vector for the outer loop:

$$\begin{bmatrix} v_x \\ v_y \end{bmatrix} = \begin{bmatrix} \dot{V}_{x_{cmd}} \\ \dot{V}_{y_{cmd}} \end{bmatrix} + \mathbf{K}_P \begin{bmatrix} e_x \\ e_y \end{bmatrix} + \mathbf{K}_I \begin{bmatrix} \int e_x dt \\ \int e_y dt \end{bmatrix} \quad (8.93)$$

The DI outer loop block diagram is shown in Fig. 8.21b. Because this control law is designed to be suitable for both low- and high-speed flight, turn compensation and turn coordination as described later in the chapter are implemented. The PI/PID gains are designed according to the procedure described previously in the chapter. Table 8.3 and Table 8.4 show the natural frequencies, damping ratios, time constants, and the integrator pole values, respectively, for the inner and the outer loop. Tables 8.5 and 8.6 show the compensation gains for the inner and outer loops.

## 8.7 Feed-Forward Compensation

### 8.7.1 Turn Coordination

In forward flight, the centrifugal forces arising from turns are compensated by banking the helicopter - and thus the thrust vector - towards the center of the turn. This is effectively achieved by relating the commanded yaw rate to the absolute speed and bank angle of the rotorcraft. The turn coordination law is:

$$r'_{cmd} = \frac{g}{V} \sin \psi + r_{cmd} \quad (8.94)$$

and is implemented in the feed-forward path of the controller. Because rotorcraft operate at low speeds (*i.e.*, lower than 40 kts) as well as in relatively high-speed flight (*i.e.*, speeds greater than 60 kts), different control strategies are needed to control the yaw rate. Above 60 kts, turn coordination is used; below 40 kts no turn coordination (Ref. [Bla65]) is used; between 40 and 60 kts a blend between the two is used. These three

Table 8.5: Inner loop compensation gains.

|                | $K_P$  | $K_I$   | $K_D$ |
|----------------|--------|---------|-------|
| $\phi_{cmd}$   | 24.975 | 15.1875 | 7.05  |
| $\theta_{cmd}$ | 24.975 | 15.1875 | 7.05  |
| $r_{cmd}$      | 4      | 4       | 4     |
| $V_{z_{cmd}}$  | 2      | 1       | -     |

Table 8.6: Outer loop compensation gains.

|                   | $K_P$ | $K_I$  |
|-------------------|-------|--------|
| $V_{x\text{cmd}}$ | 1.5   | 0.5625 |
| $V_{y\text{cmd}}$ | 1.5   | 0.5625 |

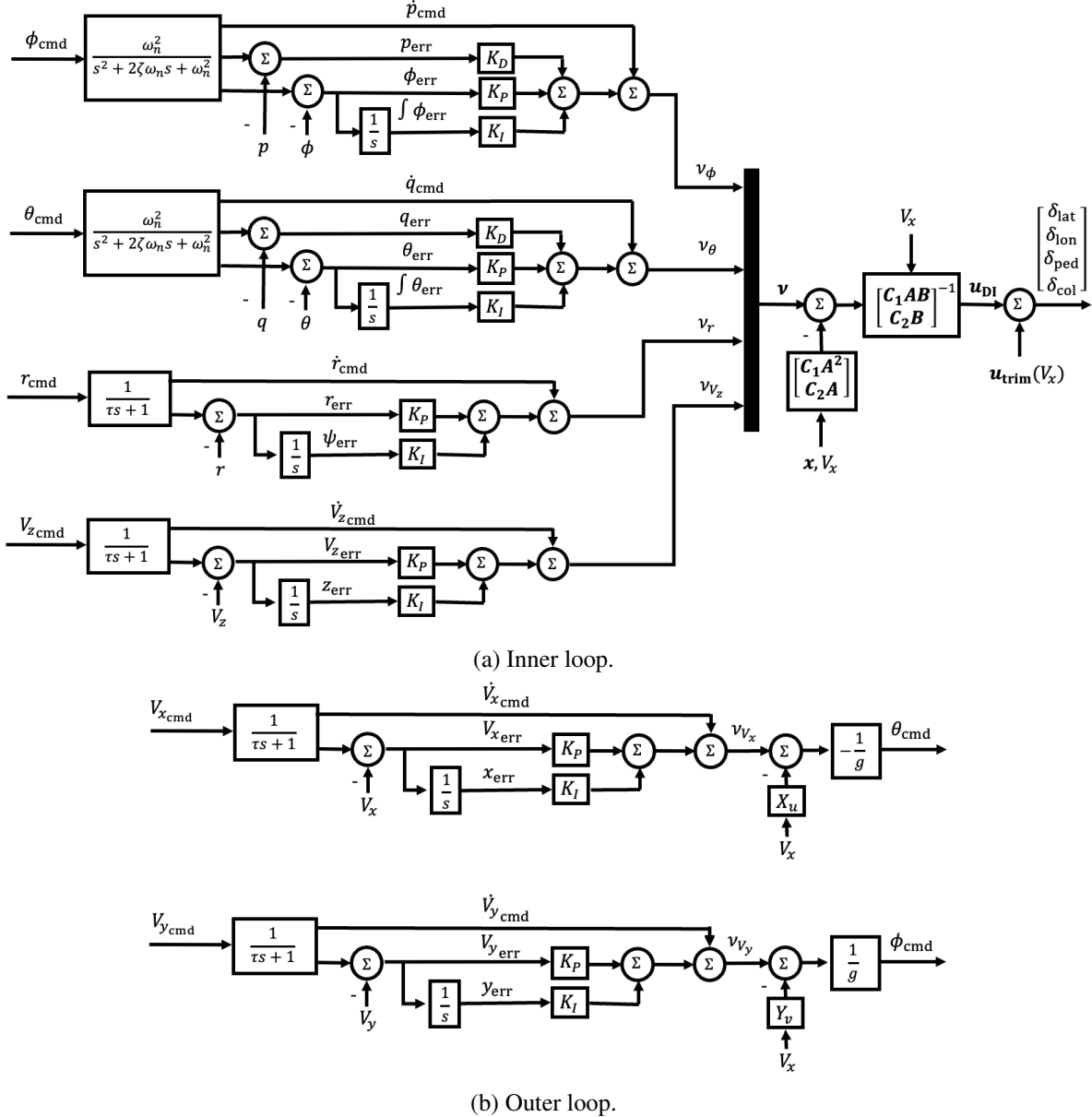


Figure 8.21: UH-60 DI AFCS.

control strategies are summarized as follows:

$$r'_{\text{cmd}} = \begin{cases} r_{\text{cmd}} & V < V_{\text{LS}} \\ r_{\text{cmd}} + \frac{g}{V} \sin \phi \left( \frac{V - V_{\text{LS}}}{V_{\text{HS}} - V_{\text{LS}}} \right) & V_{\text{LS}} \leq V < V_{\text{HS}} \\ r_{\text{cmd}} + \frac{g}{V} \sin \phi & V \geq V_{\text{HS}} \end{cases} \quad (8.95)$$

where  $V = \sqrt{u^2 + v^2 + w^2}$  is the total speed of the aircraft,  $V_{\text{LS}} = 40$  kts, and  $V_{\text{HS}} = 60$  kts.

### 8.7.2 Turn Compensation

Since the heave axis is left open loop, feedback compensation does not provide adjustments to potential losses in altitude during turns caused by rotating the thrust vector around the roll axis. This is why turn compensation is added to the feed-forward path of the controller. The turn compensation law relates the pitch rate with yaw rate and bank angle of the rotorcraft, and is given by:

$$q'_{\text{cmd}} = r \sin \phi + q_{\text{cmd}} \quad (8.96)$$

More information on the derivation of turn compensation and turn coordination are found in Ref. [Bla65]. As for turn coordination, turn compensation is only used in high-speed forward flight according to the following strategy:

$$q'_{\text{cmd}} = \begin{cases} q_{\text{cmd}} & V < V_{\text{LS}} \\ q_{\text{cmd}} + r \sin \phi \left( \frac{V - V_{\text{LS}}}{V_{\text{HS}} - V_{\text{LS}}} \right) & V_{\text{LS}} \leq V < V_{\text{HS}} \\ q_{\text{cmd}} + r \sin \phi & V \geq V_{\text{HS}} \end{cases} \quad (8.97)$$

## 8.8 Redundant Control Allocation

Rotorcraft like tiltrotors and compound rotorcraft feature auxiliary control surfaces and/or propulsion devices that make the number of control effectors greater than the number of the axes being controlled (roll, pitch, yaw, and heave). This is especially true for future-generation rotorcraft and UAM vehicles, featuring high levels of redundancy. As such, the AFCS must redistribute the control signal across the redundant control effectors intelligently depending on the flight condition/mission. Assume a simplified linearized state-space model is used for control design:

$$\dot{\mathbf{x}} = \mathbf{Ax} + \mathbf{Bu} \quad (8.98)$$

where  $\mathbf{x} \in \mathbb{R}^n$  is the reduced-order state vector representing the controllable degrees of freedom and  $\mathbf{u} \in \mathbb{R}^m$  is the control vector. For instance, this could be as simple as the roll, pitch, and yaw degrees of freedom, such that  $\mathbf{x}^T = [p \ q \ V_z \ r]$ . The control law prescribes the value of the forcing vector, denoted as  $\mathbf{d}$ , to achieve desired state response:

$$\mathbf{d} = \mathbf{Bu} \quad (8.99)$$

where  $\mathbf{B} \in \mathbb{R}^{n \times m}$ . If there happens to be the same number of actuators as the controlled degrees of freedom (*i.e.*,  $n = m$  such that  $\mathbf{B} \in \mathbb{R}^{n \times n}$  is square and thus invertible), which is typically the case for conventional helicopters, then a simple inverse of  $\mathbf{B}$  provides the control solution:

$$\mathbf{u} = \mathbf{B}^{-1} \mathbf{d} \quad (8.100)$$

Consider, however, a compound rotorcraft with  $p$  auxiliary control effectors:

$$\mathbf{u} = [\delta_{\text{lat}} \ \delta_{\text{lon}} \ \delta_{\text{ped}} \ \delta_{\text{ped}} \ \delta_{\text{aux}_1} \ \cdots \ \delta_{\text{aux}_m}] \quad (8.101)$$

such that the number of redundant control effectors is  $m = n + p$  and thus  $m > n$ . Because now  $\mathbf{B} \in \mathbb{R}^{n \times m}$  is wide, then there is a continuum of solutions that achieve the desired state response. One can solve using a weighted pseudo-inverse of  $\mathbf{B}$  [IJ15] such that:

$$\mathbf{u} = \mathbf{W}^{-1} \mathbf{B}_r^T (\mathbf{B}_r \mathbf{W}^{-1} \mathbf{B}_r^T)^{-1} \mathbf{d} \quad (8.102)$$

where  $\mathbf{W} \in \mathbb{R}^{m \times m}$  is a weighting matrix used to place different cost weightings on desired effectors. If the inverse exists, it can be shown that the control satisfies the desired constraint  $\mathbf{Bu} = \mathbf{d}$  while minimizing the

weighted norm of the control vector. Thus, it solves the constrained minimization problem:

$$\min_{\mathbf{u} \in \mathbb{R}^m} \frac{1}{2} \|\mathbf{W}\mathbf{u}\|_2^2 \quad (8.103)$$

$$\text{s.t. } \mathbf{B}\mathbf{u} = \mathbf{d} \quad (8.104)$$

$$\mathbf{d} \in \mathbb{R}^n \quad (8.105)$$

$$m < n \quad (8.106)$$

The weighting matrix can be tailored and scheduled with flight condition to achieve various goals for controller performance and robustness. The weighting matrix and the pseudo-inverse solution can also be modified to adapt to actuator faults, *i.e.*, control re-allocation, to provide load alleviation, *etc..* The state equation is re-written as:

$$\begin{aligned} \dot{\mathbf{x}} &= \mathbf{Ax} + \mathbf{B} [\mathbf{W}^{-1} \mathbf{B}^T (\mathbf{BW}^{-1} \mathbf{B}^T)^{-1}] \mathbf{d} \\ &= \mathbf{Ax} + \mathbf{BGd} \\ &= \mathbf{Ax} + \tilde{\mathbf{B}}\mathbf{d} \end{aligned} \quad (8.107)$$

where  $\mathbf{d} \in \mathbb{R}^m$  is the pseudo control vector, with one control per controlled axis,  $\mathbf{G} \in \mathbb{R}^{m \times n}$  is the ganging matrix, and  $\tilde{\mathbf{B}}$  is the modified control matrix. For the case in consideration, the pseudo control vector is:

$$\mathbf{d}^T = [\delta_{\text{lat}} \ \delta_{\text{lon}} \ \delta_{\text{col}} \ \delta_{\text{ped}}] \quad (8.108)$$

Note that the weighting matrix can be a diagonal matrix (*i.e.*, no cross-feed). In case all the control effectors are expressed using the same units and all the control effectors are given the same importance, the ganging matrix will be an identity matrix. On the other hand, if effectors were given a difference importance in different flight conditions (*e.g.*, a tiltrotor using differential collective pitch for roll attitude control in hover but using flaps in forward flight), then the weights would be different from one.

### 8.8.1 EMF Control Law with Redundant Control Allocation

This example illustrates the use of pseudo-inverse allocation within an EMF architecture. Consider the case where a moving horizontal tail, also known as stabilator, is used in pull/pushover maneuvers in forward flight in conjunction with longitudinal cyclic to alleviate the unsteady rotor loads. Then, an EMF RCAH flight control law is implemented which uses a pseudo-inverse strategy in the feed-forward patch and LQR architecture in the feedback path to re-allocate the signal to the stabilator. This way, feed-forward and feedback redundant control allocation is separate and can be designed independently to achieve maximum desired performance and load alleviation. The feed-forward is designed by pulling the control derivatives from  $\tilde{\mathbf{B}}$  (described above), rather than from  $\hat{\mathbf{B}}$ . For this reason, the inverse plant changes is approximated by the following first-order order transfer function:

$$\left( \frac{q}{\delta_{\text{lon}}} \right)^{-1} (s) = s - L_p \quad (8.109)$$

The weighting matrix  $\mathbf{W}$  can be adjusted to allocate more/less authority to each effector. Assuming only pitch rate is fed back, the LQR control law is designed using the following system:

$$\dot{q} = \underbrace{\mathbf{A}_{\text{LQR}}}_{\mathbf{A}_{\text{LQR}}} q + \underbrace{[M_{\delta_{\text{lon}}} \ M_{\delta_{\text{stb}}}]}_{\mathbf{B}_{\text{LQR}}} \begin{bmatrix} \delta_{\text{lon}} \\ \delta_{\text{ped}} \end{bmatrix} \quad (8.110)$$

The LQR weighting matrices found with Bryson's rule become:

$$\mathbf{Q} = \text{diag} \left[ \frac{\alpha_q^2}{(q)_{\max}^2} \right] \quad (8.111a)$$

$$\mathbf{R} = \text{diag} \left[ \frac{\beta_{\delta_{\text{lon}}}^2}{(\delta_{\text{lon}})_{\max}^2} \ \frac{\beta_{\delta_{\text{stb}}}^2}{(\delta_{\text{stb}})_{\max}^2} \right] \quad (8.111b)$$

The LQR gains can then be found with the MATLAB® function `lqr`. The weights  $\beta$  can be adjusted to provide more/less authority in feedback compensation to the stabilizer. The resulting flight control law is shown in Fig. 8.22.

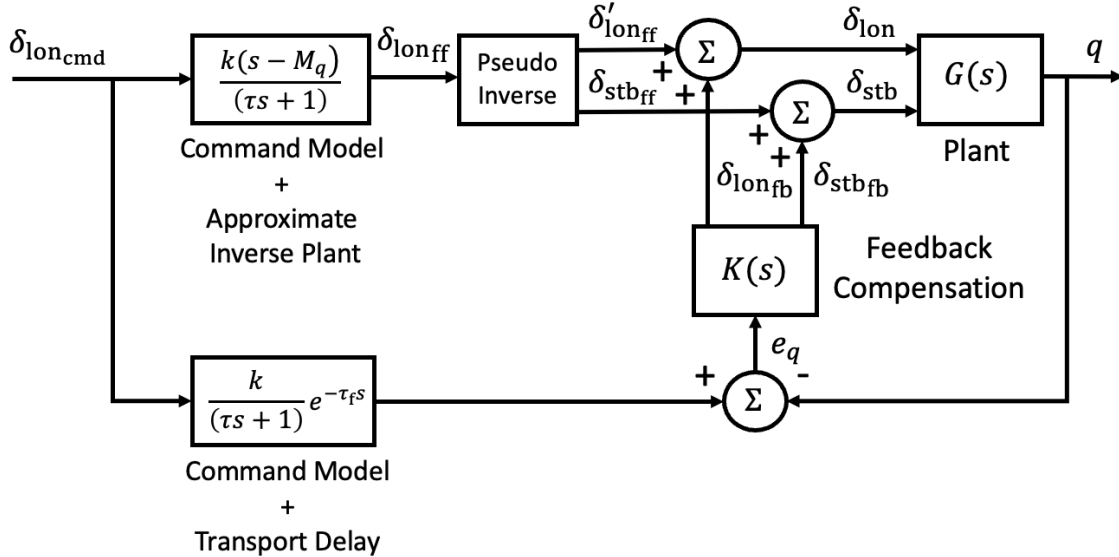


Figure 8.22: EMF control law with redundant control allocation.

### 8.8.2 DI Control Law with Redundant Control Allocation

To be finished.

### 8.8.3 Non-Minimum Phase Zeros

Both EMF and DI have issues when the plant model has transmission zeros in the right-half of the complex plane, *i.e.*, non-minimum phase (NMP) zeros. Clearly, when a transfer function with NMP zeros is inverted, it has unstable poles. Similarly, it is well known that the inversion in DI will also produce unstable modes corresponding to NMP zeros of the open loop plant model. For typical rotorcraft dynamics, multiple NMP zeros are quite prevalent in the full order dynamics but less common in the reduced order rigid body models. When NMP zeros do occur in the reduced order, they are generally benign (as they are small in magnitude) and can be handled by minor modifications to controlled variables or through outer control loops. Stability margin analysis with the full-order linear model coupled with the reduced order DI control law can be used to verify robust stability of the final design. As discussed earlier, the standard EMF design methods used in rotorcraft will place NMP zeros in the denominator of feed-forward inversion transfer function, resulting in an unstable controller. As shown in [SH15], the presence of NMP zeros can be particularly problematic when designing a MIMO EMF for rotorcraft using de-coupling numerators. In this approach, the NMP zeros are those of the individual SISO transfer functions in the MIMO transfer function matrix, and not the true transmission zeros of the MIMO transfer function. This increases the maximum number of transmission zeros from  $n$  to  $(n \times m \times m)$ . The problem of identifying and handling NMP zeros becomes amplified relative to the application of DI, which need only consider the true zeros of the MIMO system. Consider now the full- and reduced order (8 states) dynamics of a UH-60 simulation model at 80 kts. Figure 8.23 shows the pole-zero map for these models. Figure 8.23a shows how the full-order model exhibits three very high frequency NMP zeros. The reduced-order model poles and zeros are clustered at low frequency, corresponding to the rigid-body modes. Figure 8.23b offers a close up at the low-frequency and focuses on the rigid-body poles and nearby zeros. Note that the reduced-order model poles and zeros nearly overlay corresponding full-order model poles and zeros, with the exception of the poles with real parts around  $-3$ , where there is some discrepancy in damping. The full- and reduced-order models both have one very low frequency zero in the right half plane. As will be shown, this NMP zero will cause the controlled system to have a very

slow divergent mode when using a DI control law designed with the reduced-order model. This can be fixed through a small change in the controlled variable. The high-frequency zeros of the full-order system would be much more problematic, if one attempts to design DI with this high-order model. The numerical values for the poles and zeros of the full- and reduced-order system are provided in Tables 8.7 and 8.8.

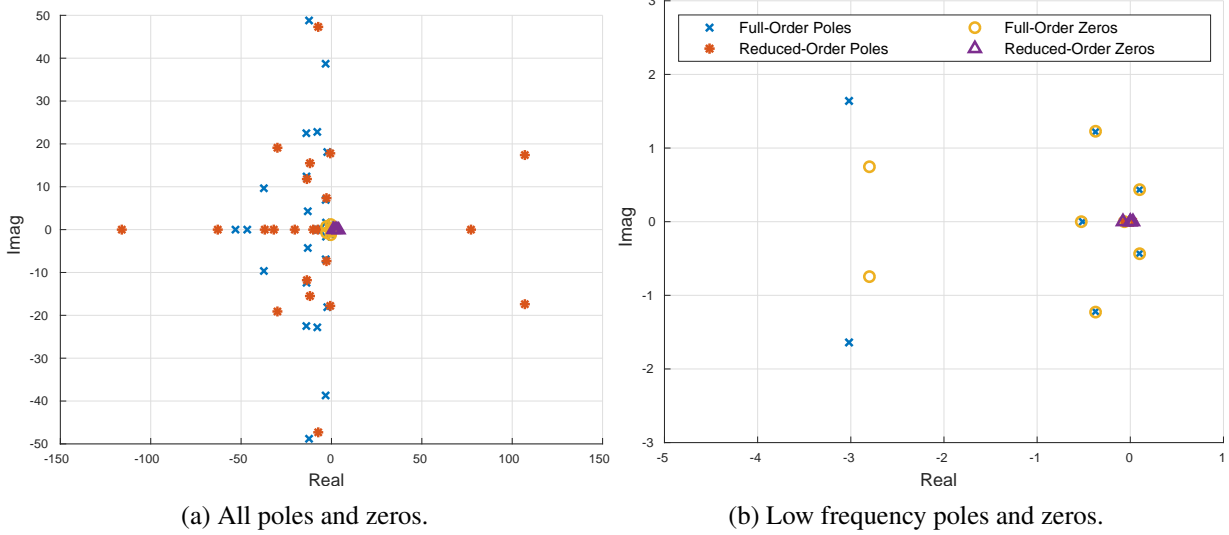


Figure 8.23: Pole-zero map of the full- and reduced-order linearized dynamics of a UH-60 at 80kts.

Recall the residualized dynamics of Eq. (6.39) and Eq. (6.41). Consider designing a DI control law based on these reduced-order dynamics. Then, the control law with the feedback linearization loop can be written as:

$$\mathbf{u}_{\text{DI}} = (\hat{\mathbf{C}}\hat{\mathbf{B}})^{-1} (\mathbf{v} - \hat{\mathbf{C}}\hat{\mathbf{A}}\mathbf{x}_s) \quad (8.112)$$

$$= [\mathbf{C}_s(\mathbf{B}_s - \mathbf{A}_{sf}\mathbf{A}_f^{-1}\mathbf{B}_f)]^{-1} [\mathbf{v} - \mathbf{C}_s(\mathbf{A}_s - \mathbf{A}_{sf}\mathbf{A}_f^{-1}\mathbf{A}_{fs})] \quad (8.113)$$

The resulting closed-loop linear system is:

$$\begin{bmatrix} \dot{\mathbf{x}}_s \\ \dot{\mathbf{x}}_f \end{bmatrix} = \begin{bmatrix} \left( \mathbf{A}_s - \mathbf{B}_s (\mathbf{C}_s \mathbf{B}_s - \mathbf{C}_s \mathbf{A}_{sf} \mathbf{A}_f^{-1} \mathbf{B}_f)^{-1} (\mathbf{C}_s \mathbf{A}_s - \mathbf{C}_s \mathbf{A}_{sf} \mathbf{A}_f^{-1} \mathbf{A}_{fs}) \right) & \mathbf{A}_{sf} \\ \left( \mathbf{A}_{fs} - \mathbf{B}_s (\mathbf{C}_s \mathbf{B}_s - \mathbf{C}_s \mathbf{A}_{sf} \mathbf{A}_f^{-1} \mathbf{B}_f)^{-1} (\mathbf{C}_s \mathbf{A}_s - \mathbf{C}_s \mathbf{A}_{sf} \mathbf{A}_f^{-1} \mathbf{A}_{fs}) \right) & \mathbf{A}_f \end{bmatrix} \begin{bmatrix} \mathbf{x}_s \\ \mathbf{x}_f \end{bmatrix} + \begin{bmatrix} \mathbf{B}_s (\mathbf{C}_s \mathbf{B}_s - \mathbf{C}_s \mathbf{A}_{sf} \mathbf{A}_f^{-1} \mathbf{B}_f)^{-1} \\ \mathbf{B}_f (\mathbf{C}_s \mathbf{B}_s - \mathbf{C}_s \mathbf{A}_{sf} \mathbf{A}_f^{-1} \mathbf{B}_f)^{-1} \end{bmatrix} \mathbf{v} \quad (8.114)$$

The system above represents the zero dynamics with feedback linearization, which is expected to be neutrally stable (one zero-valued eigenvalue for each controlled variable) if there are no NMP zeros. With simple proportional compensation on the controlled variables,

$$\mathbf{v} = -\mathbf{K}\mathbf{y} = -\mathbf{K}\mathbf{C}_s\mathbf{x}_s \quad (8.115)$$

the zero-input stability is governed by the following:

$$\begin{bmatrix} \dot{\mathbf{x}}_s \\ \dot{\mathbf{x}}_f \end{bmatrix} = \begin{bmatrix} \left( \mathbf{A}_s - \mathbf{B}_s (\mathbf{C}_s \mathbf{B}_s - \mathbf{C}_s \mathbf{A}_{sf} \mathbf{A}_f^{-1} \mathbf{B}_f)^{-1} (\mathbf{C}_s \mathbf{A}_s - \mathbf{C}_s \mathbf{A}_{sf} \mathbf{A}_f^{-1} \mathbf{A}_{fs}) \right) - \mathbf{B}_s (\mathbf{C}_s \mathbf{B}_s - \mathbf{C}_s \mathbf{A}_{sf} \mathbf{A}_f^{-1} \mathbf{B}_f)^{-1} \mathbf{K}\mathbf{C}_s & \mathbf{A}_{sf} \\ \left( \mathbf{A}_{fs} - \mathbf{B}_s (\mathbf{C}_s \mathbf{B}_s - \mathbf{C}_s \mathbf{A}_{sf} \mathbf{A}_f^{-1} \mathbf{B}_f)^{-1} (\mathbf{C}_s \mathbf{A}_s - \mathbf{C}_s \mathbf{A}_{sf} \mathbf{A}_f^{-1} \mathbf{A}_{fs}) \right) - \mathbf{B}_f (\mathbf{C}_s \mathbf{B}_s - \mathbf{C}_s \mathbf{A}_{sf} \mathbf{A}_f^{-1} \mathbf{B}_f)^{-1} \mathbf{K}\mathbf{C}_s & \mathbf{A}_f \end{bmatrix} \begin{bmatrix} \mathbf{x}_s \\ \mathbf{x}_f \end{bmatrix} \quad (8.116)$$

Table 8.7: Summary of eigenvalues at 80 kts forward flight, full- and reduced- order models.

| Mode                              | Full-Order Eigenvalues | Reduced-Order Eigenvalues |
|-----------------------------------|------------------------|---------------------------|
| Spiral                            | -0.0627                | -0.0627                   |
| Phugoid                           | $0.0977 \pm 0.433i$    | $0.100 \pm 0.435i$        |
| Dutch Roll                        | $-0.374 \pm 1.22i$     | $-0.373 \pm 1.228i$       |
| Coupled Roll / Pitch Short Period | $-3.019 \pm 1.64i$     | $-2.80 \pm 0.746i$        |
| Coupled Roll / Pitch Short Period | -0.512                 | -0.526                    |
| Roll / Regressive Flap            | -6.622                 |                           |
| Differential Lead-Lag             | $-3.20 \pm 6.93i$      |                           |
| Inflow Skew Distortion            | -7.96                  |                           |
| Regressing Flap                   | $-13.1 \pm 4.28i$      |                           |
| Collective Lead-Lag               | $-13.8 \pm 12.4i$      |                           |
| Regressing Lead-Lag               | $-2.33 \pm 18.1i$      |                           |
| Coning                            | $-7.85 \pm 22.8i$      |                           |
| Differential Flap                 | $-13.9 \pm 22.5i$      |                           |
| Cyclic Inflow                     | $-37.4 \pm 9.65i$      |                           |
| Progressing Lead-Lag              | $-3.23 \pm 38.7i$      |                           |
| Blade Twist                       | -46.6                  |                           |
| Tail Rotor Inflow                 | -53.1                  |                           |
| Progressing Flap                  | $-12.4 + 48.8i$        |                           |

Similar expressions can be derived with non-static compensation *e.g.*, integral and double-integral compensation) with the addition of controller states.

Now the feedback linearization loop is applied to the full- and reduced-order systems with no controlled variable feedback, *i.e.*,  $K(s) = 0$ . For the reduced-order model, one has a perfect inversion, and indeed there are four zero eigenvalues, and four eigenvalues identical to the zeros of the reduced-order model. For the full-order system with approximate feedback linearization, there are still four zero eigenvalues, as well as four eigenvalues slightly different from the zeros for the reduced order model (Table 8.8). In addition, there are several stable high-frequency modes. Note that the unstable eigenvalue increases with application of feedback linearization to the full-order model, but there are no large magnitude, unstable eigenvalues corresponding to the large NMP zeros of the full-order system. The eigenvalue at 0.123 is in fact manageable; its value is reduced with controlled variable feedback and then can be stabilized with outer loop control or pilot compensation. Application of this model results in a slow airspeed instability. A physical explanation is that if one constrains the pitch attitude of the rotorcraft, it will have no tendency to return to the trim airspeed. For the purpose of this example, the mode will be handled through output redefinition [RPT97]. Consider an example where the controlled variables are the roll, pitch, and yaw rates. Assume the DI control law to provide RCAH response. Then, a small component of forward speed is added to the pitch axis controlled variable:

$$\mathbf{y}^T = [p \ (q - 0.01u) \ r] \quad (8.117)$$

The change in controlled variables results in stable closed loop dynamics. In practice, the forward speed measurement is sent through a high-pass filter to avoid issue of defining perturbation from trim airspeed.

## Bibliography

- [Ano00] Anon. *Aeronautical design standard performance specification handling qualities requirements for military rotorcraft*. Technical report. Redstone Arsenal, AL: U.S. Army Aviation and Missile Command Aviation Engineering Directorate, 2000 (cited on page 201).

Table 8.8: Summary of transmission zeros at 80 kts forward flight, full- and reduced- order models, and along with eigenvalues of with feedback linearization loop closed. The underlined values indicate NMP zeros and corresponding unstable eigenvalues in the closed loop system.

| Zeros of Full-Order Open-Loop System | Zeros of Reduced-Order Open-Loop System | Eigenvalues of Full-Order System with Approximate Feedback Linearization | Eigenvalues of Reduced-Order System with Feedback Linearization | Zeros of Reduced-Order System with Output Redefinition |
|--------------------------------------|---|--|---|--|
| 0                                    | 0                                       | 0  | 0   | 0  |
| 0                                    | 0                                       | 0  | 0   | $-0.0536 \pm 0.591i$                                   |
| <u>0.0283</u>                        | <u>0.0283</u>                           | 0  | 0   | -0.0788  |
| -0.0788                              | -0.0788                                 | 0  | 0   |  |
| -7.48                                |   | 0  | 0   |  |
| -10.1                                |   | 0  | 0   |  |
| $-2.76 \pm 7.35i$                    |   | <u>0.123</u>   | <u>0.0283</u>   |  |
| $-13.6 \pm 11.8i$                    |   | $-0.0399 \pm 0.173i$   | -0.0788   |  |
| $-11.9 \pm 15.5i$                    |   | -0.166   |   |  |
| -20.3                                |   | -6.17  |   |  |
| $-0.675 \pm 17.8i$                   |   | $-3.15 \pm 7.25i$  |   |  |
| -31.9                                |   | $-15.1 \pm 5.29i$  |   |  |
| -36.9                                |   | $-13.8 \pm 12.4i$  |   |  |
| $-29.9 \pm 19.1i$                    |   | -7.59  |   |  |
| -62.9                                |   | $-8.51 \pm 22.5i$  |   |  |
| <u>77.2</u>                          |   | $-13.6 \pm 21.8i$  |   |  |
| -116                                 |   | $-37.4 \pm 9.32i$  |   |  |
| <u><math>107 \pm 17.4i</math></u>    |   | $-4.23 \pm 39.6i$  |   |  |
|                                      |   | -46.4  |   |  |
|                                      |   | -52.7  |   |  |
|                                      |   | $-12.9 \pm 49.0i$  |   |  |

- [Bla65] J. H. Blakelock. “Automatic Control of Aircraft and Missiles”. In: New York: John Wiley & Sons, 1965 (cited on pages 219, 221).
- [Bry69] A. E. Bryson. “Applied Optimal Control: Optimization, Estimation, and Control”. In: Waltham, Mass: Blaisdell Pub. Co, 1969 (cited on page 202).
- [CTB94] D. R. Catapang, M. B. Tischler, and D. J. Biezahl. “Robust Crossfeed Design for Hovering Rotorcraft”. In: *International Journal of Nonlinear Control* 4.1 (1994), pages 161–180. DOI: <https://doi.org/10.1002/rnc.4590040110> (cited on page 209).
- [EBS94] D. Enns, R. H. Bugaski, and G. Stein. “Dynamic inversion: An evolving methodology for flight control design”. In: *International Journal of Control* 59.1 (1994), pages 71–91. DOI: <https://doi.org/10.1080/00207179408923070> (cited on page 209).
- [HR18] J. J. Harris and Stanford J. R. “F-35 Flight Control Law Design, Development and Verification”. In: *Proceedings of the 2018 Aviation Technology, Integration, and Operations Conference, AIAA AVIATION Forum*. Atlanta, GA, June 2018. DOI: <https://doi.org/10.2514/6.2018-3516> (cited on page 209).
- [Hor19] J. F. Horn. “Non-Linear Dynamic Inversion Control Design for Rotorcraft”. In: *Aerospace* 6.3 (2019). DOI: <https://doi.org/10.3390/aerospace6030038> (cited on pages 209, 218).
- [IJ15] C Ivler and O Juhansz. “Evaluation of Control Allocation Techniques for a Medium Lift Tilt-Rotor”. In: *Proceedings of the 71<sup>st</sup> Annual Forum of the American Helicopter Society*. Virginia Beach, VA, May 2015 (cited on page 221).
- [JR80] B. Jacubczyk and W. Respindek. “On Linearization of Control Systems”. In: *Bulletin de l’Academie, Polonaise des Sciences* XXVIII.9-10 (1980) (cited on page 209).
- [RPT97] J. H. Ryu, C. S. Park, and M. J. Tahk. “Plant Inversion Control of Tail Controlled Missile”. In: *Proceedings of the AIAA Guidance, Navigation, and Control Conference*. New Orleans, LA, Aug. 1997. DOI: <https://doi.org/10.2514/6.1997-3766> (cited on page 225).
- [Sae+20] U. Saetti et al. “Handling-Qualities Perspective on Rotorcraft Load Alleviation Control”. In: *Journal of Guidance, Control, and Dynamics* (2020), pages 1–13. DOI: <https://doi.org/10.2514/1.G004965> (cited on pages 203, 208).
- [Sae+22] U. Saetti et al. “Dynamic Inversion-Based Flare Control Law for Autonomous Helicopter Autorotation”. In: *Proceedings of AIAA SCITECH Forum*. San Diego, CA, Jan. 2022. DOI: <https://doi.org/10.2514/6.2022-1645> (cited on page 216).
- [SH15] J. M. Spires and J. F. Horn. “Multi-Input Multi-Output Model-Following Control Design Methods for Rotorcraft”. In: *Proceedings of the 71<sup>st</sup> Annual Forum of the American Helicopter Society*. Virginia Beach, VA, May 2015 (cited on page 223).
- [SL15] B. L. Stevens and F. L. Lewis. “Aircraft Control and Simulation: Dynamics, Controls Design, and Autonomous Systems, Third Edition”. In: New York: John Wiley and Sons, Inc., 2015 (cited on pages 209, 212, 214).
- [Tis+17] M. B. Tischler et al. “Practical Methods for Aircraft and Rotorcraft Flight Control Design: An Optimization-Based Approach”. In: Reston, VA: American Institute of Aeronautics and Astronautics, 2017 (cited on pages 206, 214, 216).





## 9. Time-Periodic Systems Analysis

### 9.1 Introduction

So far, we have treated the helicopter flight dynamics as a time-invariant system. However, rotorcraft are in reality nonlinear time-periodic (NLTP) systems, where the periodicity is introduced by the periodicity of the main rotor that arises with forward speed due to lift asymmetry or with blade imbalance. It is worth noting that systems with periodic dynamics exist across multiple disciplines of engineering, with examples including bio-inspired robots (*e.g.*, insects, birds, fish), spacecraft, wind turbines, and jet engines. Whereas stability analysis of nonlinear time-invariant systems (NLTI) can be readily performed by checking whether the eigenvalues of the linearized dynamics about an equilibrium point lie in the left half of the complex plane, or by means of Lyapunov theory, stability analysis of NLTP systems is typically a more challenging task. This is because the solution (or equilibrium) of NLTP systems, in contrast to NLTI systems, may be represented by a periodic orbit rather than by a single point. As articulated in [MET20], two main approaches are typically adopted for determining the stability of NLTP systems: the first based on Floquet theory [Flo83] and the second based on averaging methods [SVM07]. Specifically, the first approach requires solving the dynamic equations to find the periodic orbit, linearizing the dynamic equations along the periodic orbit to obtain a linear time-periodic (LTP) system, and transforming the LTP system to a linear time-invariant (LTI) system: Floquet Decomposition. Hence, the stability of the system is assessed by checking whether the eigenvalues of the LTI system lie in the left half of the complex plane. The second approach exploits averaging methods to transform the NLTP system into an equivalent NLTI system in which the periodic orbit of the original system collapses to a single point in the state space. The stability of the NLTI system is then assessed via eigenvalue analysis of the linearized NLTI dynamics around equilibrium. In fact, the averaging theorem guarantees that exponential stability around the equilibrium point translates to stability of the periodic orbit for high-enough frequencies [SVM07]. These two main approaches to NLTP system stability analysis are shown qualitatively in Fig. 9.1.

Although the averaging approach is particularly popular in the design of vibrational control of mechanical systems [Bul02] because it avoids direct calculation of the periodic orbit, the Floquet-theory-based approach has gained more traction in the vertical flight domain, with specific applications to the dynamic analysis and control of rotorcraft. This is because in rotorcraft applications, LTP systems and their LTI reformulations are relevant to the prediction of vibratory/rotor loads and to the analysis and design of active rotor control systems. These active rotor control systems include, but are not limited to, higher-harmonic control (HHC) where the swashplate is actuated at higher harmonic frequencies, on-blade control (OBC) where HHC inputs are fed to actuators on each blade, and individual blade control (IBC) where each blade pitch angle is actuated independently. A comprehensive survey of these approaches and their history is found in [FM95]. Historically, these control laws were used toward the mitigation of compressibility effects on advancing

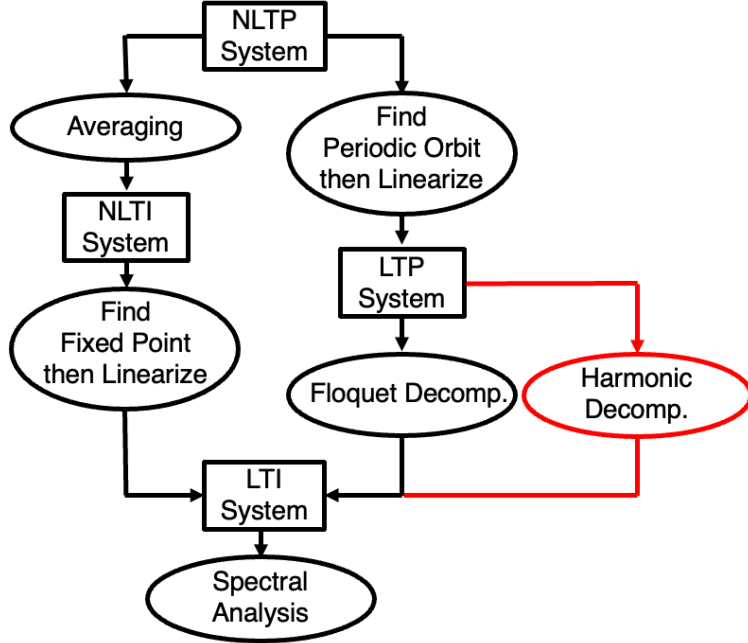


Figure 9.1: Illustration of the two main approaches to stability analysis of NLTP systems: averaging methods (left), Floquet theory (center), and harmonic decomposition (right) [MET20].

blades and reverse flow on retreating blades for improved rotor performance, control of individual blades that may be off-track, mitigation of undesired coupling between fuselage and rotor, reduction of trim and maneuver blade and rotor loads, and reduction of blade-vortex interaction noise; all of these while ensuring desired handling qualities. Further, LTI reformulations of LTP systems enabled to study the interference effects between HHC and the aircraft flight control system (AFCS) in maneuvering flight [Abr+11; CTC03; Lop+15; LP16; Pad+15]. Recently, LTI reformulations of LTP systems were employed in the design of load alleviation control (LAC) laws [SH20; Sae+20; SHS21] and in the prediction and avoidance of flight envelope limits [MP18; MP19]. In general, while averaged LTI models are sufficient for primary flight control design, LTP systems and their LTI reformulations are necessary for predicting and/or controlling the higher harmonics of the fuselage and rotor motion. The objective of this chapter is to summarize the relevant published research studies on the extraction of LTP systems and their LTI reformulations from rotorcraft physics-based models (*i.e.*, simulations).

## 9.2 Overview of Linear Time-Periodic Systems

This section aims at providing an introductory overview to the main properties of LTP systems. Specifically, the general forms (both state-space and input-output) for LTP systems will be first presented. Subsequently, the problem of studying stability of LTP systems will be considered.

### 9.2.1 State Space and Input-Output Representations

A basic classification of LTP systems is induced by the nature of the time variable, which will be denoted in any case with the letter  $t$ : in the *continuous-time* case  $t$  is real, while in the *discrete-time* case  $t$  is an integer. As is well known, state variables (denoted in the following with  $\mathbf{x}$ ) are internal variables which relate the input variables  $\mathbf{u}$  and the output variables  $\mathbf{y}$ . For systems of order  $n$  greater than 1 the state variables are arranged in a vector of dimension  $n$ . A general LTP state-space model can be written as the set of difference equations:

$$\mathbf{x}(t+1) = \mathbf{A}_d(t)\mathbf{x}(t) + \mathbf{B}_d(t)\mathbf{u}(t) \quad (9.1a)$$

$$\mathbf{y}(t) = \mathbf{C}_d(t)\mathbf{x}(t) + \mathbf{D}_d(t)\mathbf{u}(t) \quad (9.1b)$$

in discrete-time, or the set of differential equations:

$$\dot{\mathbf{x}}(t) = \mathbf{A}_c(t)\mathbf{x}(t) + \mathbf{B}_c(t)\mathbf{u}(t) \quad (9.2a)$$

$$\mathbf{y}(t) = \mathbf{C}_c(t)\mathbf{x}(t) + \mathbf{D}_c(t)\mathbf{u}(t) \quad (9.2b)$$

in continuous time. The matrices  $\mathbf{A}(\cdot)$ ,  $\mathbf{B}(\cdot)$ ,  $\mathbf{C}(\cdot)$  and  $\mathbf{D}(\cdot)$  are real matrices, of appropriate dimensions, which depend periodically on  $t$ :

$$\mathbf{A}(t+T) = \mathbf{A}(t) \quad (9.3a)$$

$$\mathbf{B}(t+T) = \mathbf{B}(t) \quad (9.3b)$$

$$\mathbf{C}(t+T) = \mathbf{C}(t) \quad (9.3c)$$

$$\mathbf{D}(t+T) = \mathbf{D}(t) \quad (9.3d)$$

The period of the system is defined as the smallest  $T$  for which these periodicity conditions hold, where  $T$  is an integer in the case of discrete time, while  $T$  is real in the case of continuous time. Note, in passing, that the state-space models introduced above may be generalized and extended in various ways, among which it is worth quoting the descriptor class of models [BC10], which occurs naturally as the result of the linearization of implicit nonlinear systems.

As for input-output representations, *i.e.*, direct time-domain relationships between the input and the output variables without any usage of intermediate variables, in discrete-time, they can be written, in the SISO case, in the form:

$$\begin{aligned} y(t) = & a_1(t)y(t-1) + a_2(t)y(t-2) + \cdots + a_{n_a}(t)y(t-n_a) + b_1(t)u(t-1) \\ & + b_2(t)u(t-2) + \cdots + b_{n_b}(t)u(t-n_b) \end{aligned} \quad (9.4)$$

where  $a_i(\cdot)$ ,  $i = 1, \dots, n_a$  and  $b_i(\cdot)$ ,  $i = 1, \dots, n_b$  are periodic real scalars (MIMO extensions can be obtained by replacing the  $a_i(\cdot)$  and  $b_i(\cdot)$  scalar functions with matrix functions of appropriate dimensions). As will be discussed later, discrete-time input-output models are mostly used in the framework of LTP model identification. Continuous-time input-output periodic models can be defined in a similar way, in terms of a differential equation, as follows:

$$\begin{aligned} y(t)^{(n_a)} = & a_1(t)y(t)^{(n_a-1)} + a_2(t)y(t)^{(n_a-2)} + \cdots + a_{n_a}(t)y(t) + b_1(t)u(t)^{(n_b-1)} \\ & + b_2(t)u(t)^{(n_b-2)} + \cdots + b_{n_b}(t)u(t) \end{aligned} \quad (9.5)$$

Finally, note that the realisation problem, *i.e.*, the problem of constructing a state space representation starting from an input-output model, is far from trivial in the LTP case and will not be discussed here (see, again, [BC10] for the LTP case and the more recent [Tot10] for a more general discussion in the framework of Linear Parameter-Varying (LPV) models).

## 9.2.2 Free Response and the Monodromy Matrix

The free response of a general linear time-varying (LTV) system, *i.e.*, the solution of the homogeneous equation

$$\mathbf{x}(t+1) = \mathbf{A}_d(t)\mathbf{x}(t) \quad (9.6)$$

in discrete-time or

$$\dot{\mathbf{x}}(t) = \mathbf{A}_c(t)\mathbf{x}(t) \quad (9.7)$$

in continuous-time starting from state  $\mathbf{x}(\tau)$  at time  $\tau$  can be always written as

$$\mathbf{x}(t) = \Phi_A(t, \tau)\mathbf{x}(\tau) \quad (9.8)$$

where the *transition matrix*  $\Phi_{\mathbf{A}}(t, \tau)$ , which is a matrix function of the two time indices  $t$  and  $\tau$ , is given by

$$\Phi_{\mathbf{A}_d}(t, \tau) = \mathbf{A}_d(t-1)\mathbf{A}_d(t-2)\cdots\mathbf{A}_d(\tau), \quad \Phi_{\mathbf{A}_d}(\tau, \tau) = \mathbf{I} \quad (9.9)$$

in discrete-time and by the solution of the matrix differential equation

$$\frac{\partial \Phi_{\mathbf{A}_c}(t, \tau)}{\partial t} = \mathbf{A}_c(t)\Phi_{\mathbf{A}_c}(t, \tau), \quad \Phi_{\mathbf{A}_c}(\tau, \tau) = \mathbf{I} \quad (9.10)$$

in continuous-time. As is clearly visible from  $\Phi_{\mathbf{A}_d}(\cdot, \cdot)$ , in the particular case of LTP systems the transition matrix turns out to be periodic with respect to shifts by  $T$  of both arguments, *i.e.*,

$$\Phi_{\mathbf{A}}(t+T, \tau+T) = \Phi_{\mathbf{A}}(t, \tau) \quad (9.11)$$

It can be shown that the transition matrix has the same property also in the continuous-time case.

### 9.2.3 Stability of LTP Systems

A generic LTV system is asymptotically stable if all free responses are bounded and vanish for  $t$  going to  $\infty$  and for any initial time. Given that, as discussed above,  $\mathbf{x}(t) = \Phi_{\mathbf{A}}(t, \tau)\mathbf{x}(\tau)$ , this is equivalent to

$$\lim_{t \rightarrow \infty} \Phi_{\mathbf{A}}(t, \tau) = 0, \quad \forall \tau \quad (9.12)$$

In the LTP case, the above condition can be written in a simpler form by introducing the so-called *monodromy matrix*, *i.e.*, the transition matrix over one period (at time  $\tau$ ):

$$\Psi_{\mathbf{A}}(\tau) = \Phi_{\mathbf{A}}(\tau+T, \tau) \quad (9.13)$$

The monodromy matrix  $\Psi_{\mathbf{A}}(\tau)$  is clearly periodic of period  $T$ , which leads to the following free response:

$$\mathbf{x}(\tau+T) = \Psi_{\mathbf{A}}(\tau)\mathbf{x}(\tau) \quad (9.14)$$

It follows that if one considers the sampling of the state defined as  $\mathbf{x}_{\tau}(k) = \mathbf{x}(\tau + kT)$ , its time evolution is governed by the time-invariant discrete-time equation

$$\mathbf{x}_{\tau}(k+1) = \Psi_{\mathbf{A}_d}(\tau)^k \mathbf{x}_{\tau}(k) \quad (9.15)$$

It is clear from the above equation that the eigenvalues of  $\Psi_{\mathbf{A}}(\tau)$  play a major role in the stability analysis of periodic systems. In the literature such eigenvalues are referred to as the *characteristic multipliers* of  $\mathbf{A}(\cdot)$ . Note that, although the monodromy matrix may depend upon  $\tau$ , the characteristic multipliers are constant. Moreover, while in continuous-time all characteristic multipliers are different from zero, a discrete-time system may exhibit null characteristic multipliers. This happens when at least one among matrices  $\mathbf{A}_d(i)$ ,  $i = 0, 1, \dots, T-1$  is singular, so that the system is nonreversible.

Consider now the particular case of LTI systems, seen as LTP systems of period  $T$ . Then the monodromy matrix takes the expression  $\Psi_{\mathbf{A}_d}(\tau) = \mathbf{A}_d^T$  in discrete time and  $\Psi_{\mathbf{A}_c}(\tau) = e^{\mathbf{A}_c T}$  in continuous time. Therefore, denoting by  $\lambda$  an eigenvalue of  $\mathbf{A}$ , the characteristic multipliers of a LTI system are given by  $e^{\lambda_c T}$  and  $\lambda_d^T$  in continuous-time and discrete-time, respectively. The monodromy matrix is the basic tool in the stability analysis of periodic systems. Indeed the free motion goes to zero asymptotically if and only if all characteristic multipliers have modulus less than one. Hence, a LTP system (in discrete or continuous-time) is asymptotically stable if and only if its characteristic multipliers belong to the open unit disk. It is important to underline that there is no direct relation between the eigenvalues of  $\mathbf{A}(\cdot)$  and system stability. In particular, it may well happen that all eigenvalues of  $\mathbf{A}(\cdot)$  belong to the stable region (*i.e.*, the left half plane in continuous-time and the unit disk in discrete-time) and nevertheless the system be unstable. Notable exceptions in continuous-time are slowly-varying matrices or high-frequency perturbed matrices (to which averaging may be applied).

Finally, note that stability conditions can be formulated in terms of Lyapunov equations. Not unlike the LTI case, in terms of a *Lyapunov equation*, i.e., in continuous-time

$$-\dot{\mathbf{P}}(t) = \mathbf{A}_c(t)^T \mathbf{P}(t) + \mathbf{P}(t) \mathbf{A}_c(t) + \mathbf{Q}(t) \quad (9.16)$$

where  $\mathbf{Q}(\cdot)$  is a periodic  $\mathbf{Q}(t+T) = \mathbf{Q}(t)$ ,  $\forall t$  and positive definite  $\mathbf{x}^T \mathbf{Q}(t) \mathbf{x} > 0$ ,  $\forall t$ ,  $\forall \mathbf{x} \neq 0$  matrix, it turns out that the continuous-time periodic system is stable if and only if the Lyapunov equation admits a (unique) periodic positive definite solution  $\mathbf{P}(\cdot)$ . An analogous result holds in discrete time, by making reference to

$$\mathbf{P}(t) = \mathbf{A}_d(t)^T \mathbf{P}(t+1) \mathbf{A}_d(t) + \mathbf{Q}(t), \quad (9.17)$$

where  $\mathbf{Q}(\cdot)$  is periodic and positive definite.

#### 9.2.4 Floquet Theory

Gaston Floquet, a French mathematician, was the first to formalized linear time-periodic systems in the late nineteenth century [DAn70; Flo83]. Indeed one of the long standing issues in periodic systems was whether it is possible to find a state-coordinate transformation leading to a periodic system with *constant* dynamic matrix. In this way the eigenvalues of such a dynamic matrix would determine the modes of the system (up to the state periodic transformation).

Floquet theory can be outlined as follows. If  $\mathbf{S}(\cdot)$  is a  $T$ -periodic invertible state-space transformation,  $\hat{\mathbf{x}}(t) = \mathbf{S}(t)\mathbf{x}(t)$ , then, in the new coordinates, the dynamic matrix  $\hat{\mathbf{A}}(t)$  is given by

$$\hat{\mathbf{A}}_d(t) = \mathbf{S}(t+1)\mathbf{A}_d(t)\mathbf{S}(t)^{-1} \quad (9.18)$$

in discrete-time, and

$$\hat{\mathbf{A}}_c(t) = \mathbf{S}(t)\mathbf{A}_c(t)\mathbf{S}(t)^{-1} + \dot{\mathbf{S}}(t)\mathbf{S}(t)^{-1} \quad (9.19)$$

in continuous-time. The Floquet problem is then to find  $\mathbf{S}(t)$  (if any) in order to obtain a constant dynamic matrix  $\hat{\mathbf{A}}(t) = \hat{\mathbf{A}}$ . In continuous-time it can be shown that such a transformation  $\mathbf{S}(\cdot)$  does exist and that  $\hat{\mathbf{A}}_c$  can be obtained by solving  $e^{\hat{\mathbf{A}}_c T} = \Psi_{\mathbf{A}_c}(\tau)$ , where  $\tau$  is any given time point. The appropriate ( $T$ -periodic) transformation  $\mathbf{S}(\cdot)$  is given by

$$\mathbf{S}(t) = e^{\hat{\mathbf{A}}_c(t-\tau)} \Phi_{\mathbf{A}_c}(\tau, t) \quad (9.20)$$

and satisfies the linear differential equation

$$\dot{\mathbf{S}}(t) = \hat{\mathbf{A}}_c \mathbf{S}(t) - \mathbf{S}(t) \mathbf{A}_c(t), \quad \mathbf{S}(\tau) = \mathbf{I}. \quad (9.21)$$

The discrete-time case is rather involved because of the possibility that the system is nonreversible. While the authors refer the interested reader to, e.g., [BC10] for details on the nonreversible case, note that in the reversible case the Floquet representation always exists and matrix  $\hat{\mathbf{A}}_d$  can be obtained by solving  $\hat{\mathbf{A}}_d^T = \Psi_{\mathbf{A}_d}(\tau) = \Phi_{\mathbf{A}_d}(\tau+T, \tau)$ . The transformation  $\mathbf{S}(\cdot)$  is given by

$$\mathbf{S}(t) = \hat{\mathbf{A}}_d^{t-\tau} \Phi_{\mathbf{A}_d}(t, \tau)^{-1} \quad (9.22)$$

$\mathbf{S}(\cdot)$  is periodic of period  $T$  and satisfies the linear difference equation

$$\mathbf{S}(t+1) = \hat{\mathbf{A}}_d \mathbf{S}(t) \mathbf{A}_d(t)^{-1}, \quad \mathbf{S}(\tau) = \mathbf{I}. \quad (9.23)$$

Whenever a Floquet representation exists, the eigenvalues of  $\hat{\mathbf{A}}$  are named *characteristic exponents*. In continuous-time, the correspondence between a characteristic multiplier  $z$  and a characteristic exponent  $s$  is the complex exponential map  $z = e^{sT}$ , from which it can be readily seen that the characteristic exponents are obtained from the corresponding multipliers through a complex logarithm and therefore are not uniquely defined (see, e.g., [Joh80] for details on the polydromy of continuous-time characteristic exponents and [PLA11] for the interpretation of these characteristic exponents). In discrete-time, on the other hand, the correspondence is  $z = s^T$ . Note that in this Subsection,  $z$  is used to indicate the characteristic multiplier. However, in later Sections,  $z$  is used as the  $z$ -transform variable, or as  $z = \psi/2$  in Eq. (9.40).

### 9.2.5 Time-Invariant Reformulations

It should be clear from the previous sections that on one hand the theory of LTP systems is significantly more complex than the corresponding one for LTI systems and that, on the other hand, a number of similarities and analogies do exist. In view of these considerations, the problem of finding a way to represent a LTP system using an equivalent LTI form has been studied extensively in the literature. Indeed using LTI reformulations one can leverage all the available results from the LTI case. Time-invariant reformulations have been developed in many different ways: in the frequency domain and in the time domain, acting on the input, state and output signals. Along the lines of [CCB04], as far as time-domain methods are concerned it is advisable to focus on discrete time, where the best known reformulations are named *time-lifted* and *cyclic* representations. The *frequency-lifted* representation, on the other hand, is developed in the frequency domain.

#### Lifted Reformulation

The *time-lifted reformulation* was originally proposed in [JM59] and [MB76]. The idea is to recall that as far as the free response is concerned if one samples the system state with sampling interval coincident with the system period  $T$ , one gets the time-invariant system  $\mathbf{x}(\tau + T) = \Psi_A(\tau)\mathbf{x}(\tau)$ . To take into account the effect of the input sequence and similarly relate the sampled state to the relevant outputs one can then organize the input and output signals in packed segments of subsequent intervals of length  $T$ , so as to form input and output vectors of enlarged dimensions. Precisely, considering the time instant  $\tau$  and introducing the *lifted* vectors of input and output signals given by

$$\tilde{\mathbf{u}}_\tau(k) = [\mathbf{u}(kT + \tau)^T \ \mathbf{u}(kT + \tau + 1)^T \ \dots \ \mathbf{u}(kT + \tau + T - 1)^T]^T \quad (9.24a)$$

$$\tilde{\mathbf{y}}_\tau(k) = [\mathbf{y}(kT + \tau)^T \ \mathbf{y}(kT + \tau + 1)^T \ \dots \ \mathbf{y}(kT + \tau + T - 1)^T]^T \quad (9.24b)$$

the lifted model is then given by

$$\mathbf{x}_\tau(k+1) = \mathbf{F}_\tau \mathbf{x}_\tau(k) + \mathbf{G}_\tau \tilde{\mathbf{u}}_\tau(k) \quad (9.25a)$$

$$\tilde{\mathbf{y}}_\tau(k) = \mathbf{H}_\tau \mathbf{x}_\tau(k) + \mathbf{E}_\tau \tilde{\mathbf{u}}_\tau(k) \quad (9.25b)$$

where the matrices in the state-space representation:  $\mathbf{F}_\tau \in R^{n \times n}$ ,  $\mathbf{G}_\tau \in R^{n \times mT}$ ,  $\mathbf{H}_\tau \in R^{pT \times n}$ ,  $\mathbf{E}_\tau \in R^{pT \times mT}$  are defined as:

$$\mathbf{F}_\tau = \Phi_{A_d}(\tau) \quad (9.26a)$$

$$\mathbf{G}_\tau = \begin{bmatrix} \Phi_{A_d}(\tau + T, \tau + 1)\mathbf{B}_d(\tau) & \Phi_{A_d}(\tau + T, \tau + 2)\mathbf{B}_d(\tau + 1) \\ \dots & \mathbf{B}_d(\tau + T - 1) \end{bmatrix} \quad (9.26b)$$

$$\begin{aligned} \mathbf{H}_\tau &= [\mathbf{C}_d(\tau)^T \ \Phi_{A_d}(\tau + 1, \tau)^T \mathbf{C}_d(\tau + 1)^T \ \dots \ \Phi_{A_d}(\tau + T - 1, \tau)^T \mathbf{C}_d(\tau + T - 1)^T]^T \\ \mathbf{E}_\tau &= \{(\mathbf{E}_\tau)_{ij}\}, \quad i, j = 1, 2, \dots, T \end{aligned} \quad (9.26c)$$

$$(\mathbf{E}_\tau)_{ij} = \begin{cases} 0 & i < j \\ \mathbf{D}_d(\tau + i - 1) & i = j \\ \mathbf{C}_d(\tau + i - 1)\Phi_{A_d}(\tau + i - 1, \tau + j)\mathbf{B}_d(\tau + j - 1) & i > j \end{cases} \quad (9.26d)$$

#### Cyclic Reformulation

In the *cyclic reformulation* (see [PV89] and [Fla91]), every signal in the state space representation is transformed into an enlarged signal. Considering a generic signal  $\mathbf{v}(t)$  of dimension  $q$ , the enlarged counterpart

is  $\bar{\mathbf{v}}_\tau(t)$  of dimension  $qT$ , defined as (given over one period starting from a given initial instant  $\tau$ ):

$$\bar{\mathbf{v}}_\tau(\tau) = \begin{bmatrix} \mathbf{v}(\tau) \\ 0 \\ \vdots \\ 0 \\ 0 \end{bmatrix}, \quad \bar{\mathbf{v}}_\tau(\tau+1) = \begin{bmatrix} 0 \\ \mathbf{v}(\tau+1) \\ 0 \\ \vdots \\ 0 \end{bmatrix}, \quad \bar{\mathbf{v}}_\tau(\tau+T-2) = \begin{bmatrix} 0 \\ 0 \\ \vdots \\ \mathbf{v}(\tau+T-2) \\ 0 \end{bmatrix} \quad (9.27\text{a-c})$$

$$\bar{\mathbf{v}}_\tau(\tau+T-1) = \begin{bmatrix} 0 \\ 0 \\ \vdots \\ 0 \\ \mathbf{v}(\tau+T-1) \end{bmatrix} \quad (9.27\text{d})$$

One can then relate the cyclic input to the cyclic state by means of a time-invariant state equation and the cyclic output to the cyclic state input via a time-invariant transformation, to obtain a  $nT$ -dimensional time-invariant system with  $mT$  inputs and  $pT$  outputs.

### Frequency-Lifted Reformulation

Finally, the *frequency-lifted reformulation* is based on the following considerations. Consider a discrete-time (vector) signal  $\mathbf{v}(t)$  and let  $\mathbf{V}(z)$  be its Z-transform. Now, one can associate with  $\mathbf{V}(z)$  the frequency augmented vector  $\mathbf{V}_f(z)$  as follows:

$$\mathbf{V}_f(z) = \begin{bmatrix} \mathbf{V}(z) \\ \mathbf{V}(ze^{\frac{2j\pi}{T}}) \\ \mathbf{V}(ze^{2\frac{2j\pi}{T}}) \\ \vdots \\ \mathbf{V}(ze^{(T-1)\frac{2j\pi}{T}}) \end{bmatrix} \quad (9.28)$$

By applying this procedure to the Z-transforms of the input and output signals of the periodic system, it is possible to establish an input-output correspondence described a matrix transfer function, see [ZZF96] for details. Such a transfer function is referred to as the frequency-lifted representation.

### Lifting and Cycling in Continuous Time

In continuous time, the above reformulations can be appropriately worked out as well leading to infinite-dimensional time-invariant systems. For instance, the time-lifted reformulation appears as in discrete-time, but now  $\mathbf{G}_\tau$ ,  $\mathbf{H}_\tau$  and  $\mathbf{E}_\tau$  are linear operators on/from Hilbert spaces. On this topic, the interested reader is referred to [Col91] and [BP92].

### Frequency-Domain Reformulation in Continuous Time

In 1990 a frequency response notion comparable to the classical LTI Bode gain and phase response was developed for continuous-time LTP systems at MIT. Wereley and Hall [HW90; WH90; WH91] gave fundamental contributions towards the development of a comprehensive open loop analysis theory for LTP systems, including a characterization of poles, transmission zeros and their directional properties, a generalized Nyquist criterion, and a comprehensive frequency domain interpretation. With reference to the time-invariant reformulation, recall that the fundamental notion behind the development of LTI systems is that a sinusoidal input with a given frequency is mapped by the LTI transfer function operator into a sinusoidal output of the same frequency, but with possibly a different amplitude and phase. In contrast, if a sinusoid is fed to an LTP system, multiple sinusoids may appear in the output at the input frequency plus or minus multiples of the fundamental frequency of the LTP system, each with possibly different amplitude and phase. Further, an infinite number of sinusoids may appear in the output of an LTP system at steady state. The transfer function for LTP systems that was developed, also known as harmonic transfer function,

maps periodic input signals to periodic output signals when the system is at steady state. Formally, consider a continuous-time linear periodic system:

$$\dot{\mathbf{x}}(t) = \mathbf{A}(t)\mathbf{x}(t) + \mathbf{B}(t)\mathbf{u}(t) \quad (9.29a)$$

$$\mathbf{y}(t) = \mathbf{C}(t)\mathbf{x}(t) + \mathbf{D}(t)\mathbf{u}(t) \quad (9.29b)$$

Each matrix can be expanded in a complex Fourier series:

$$\mathbf{A}(t) = \sum_{m=-\infty}^{\infty} \mathbf{A}_m e^{jm\Omega t} \quad (9.30)$$

and similarly for  $\mathbf{B}(t)$ ,  $\mathbf{C}(t)$  and  $\mathbf{D}(t)$ . The system can be analyzed in the frequency domain as follows. Introduce the class of *Exponentially Modulated Periodic* (EMP) signals [WH90]. The (complex) signal  $\mathbf{u}(t)$  is said to be EMP of period  $T$  and modulation  $s$  if:

$$\mathbf{u}(t) = \sum_{k=-\infty}^{\infty} \mathbf{u}_k e^{skt} = e^{st} \sum_{k=-\infty}^{\infty} \mathbf{u}_k e^{jk\Omega t} \quad (9.31)$$

where  $t \geq 0$ ,  $s_k = s + jk\Omega$ , and  $s$  is a complex scalar. The class of EMP signals is a generalization of the class of T-periodic signals, *i.e.*, of signals with period  $T$ : in fact, an EMP signal with  $s = 0$  is just an ordinary time-periodic signal. In particular, the class of EMP signals can be used to characterise the zeros of periodic systems in terms of their *blocking properties* [DFP98]: the system in Eq. (9.29) exhibits a zero in  $\sigma$  if and only if there exists a nonzero T-periodic vector  $\mathbf{p}(\cdot)$  such that the input  $\mathbf{u}(t) = \mathbf{p}(t)e^{\sigma(t-t_0)}$  produces  $\mathbf{y}(t) = 0$ ,  $\forall t \geq t_0$  for a suitable initial condition  $\mathbf{x}(t_0) = \mathbf{x}_0$ .

In much the same way as a time invariant system subject to a (complex) exponential input has an exponential steady-state response, a periodic system subject to an EMP input has an EMP steady-state response. In such a response, all signals of interest ( $\mathbf{x}$ ,  $\dot{\mathbf{x}}$ ,  $\mathbf{y}$ ) can be expanded as EMP signals. By deriving Fourier expansions for  $\mathbf{A}(t)$ ,  $\mathbf{B}(t)$ ,  $\mathbf{C}(t)$  and  $\mathbf{D}(t)$ , it is possible to prove that the EMP steady-state response of the system can be expressed as the infinite dimensional matrix equation with *constant* elements [WH90]:

$$s\mathcal{X} = (\mathcal{A} - \mathcal{N})\mathcal{X} + \mathcal{B}\mathcal{U} \quad (9.32a)$$

$$\mathcal{Y} = \mathcal{C}\mathcal{X} + \mathcal{D}\mathcal{U} \quad (9.32b)$$

where  $\mathcal{X}$ ,  $\mathcal{U}$  and  $\mathcal{Y}$  are doubly infinite vectors formed with the harmonics of  $\mathbf{x}$ ,  $\mathbf{u}$  and  $\mathbf{y}$  respectively, organized in the following fashion:

$$\mathcal{X}^T = [\cdots \mathbf{x}_{-2}^T \mathbf{x}_{-1}^T \mathbf{x}_0^T \mathbf{x}_1^T \mathbf{x}_2^T \cdots] \quad (9.33)$$

and similarly for  $\mathcal{U}$  and  $\mathcal{Y}$ .  $\mathcal{A}$ ,  $\mathcal{B}$ ,  $\mathcal{C}$  and  $\mathcal{D}$  are doubly infinite Toeplitz matrices formed with the harmonics of  $\mathbf{A}(\cdot)$ ,  $\mathbf{B}(\cdot)$ ,  $\mathbf{C}(\cdot)$  and  $\mathbf{D}(\cdot)$  respectively as follows:

$$\mathcal{A} = \begin{bmatrix} \ddots & \vdots & \vdots & \vdots & \vdots & \vdots \\ \cdots & \mathbf{A}_0 & \mathbf{A}_{-1} & \mathbf{A}_{-2} & \mathbf{A}_{-3} & \mathbf{A}_{-4} & \cdots \\ \cdots & \mathbf{A}_1 & \mathbf{A}_0 & \mathbf{A}_{-1} & \mathbf{A}_{-2} & \mathbf{A}_{-3} & \cdots \\ \cdots & \mathbf{A}_2 & \mathbf{A}_1 & \mathbf{A}_0 & \mathbf{A}_{-1} & \mathbf{A}_{-2} & \cdots \\ \cdots & \mathbf{A}_3 & \mathbf{A}_2 & \mathbf{A}_1 & \mathbf{A}_0 & \mathbf{A}_{-1} & \cdots \\ \cdots & \mathbf{A}_4 & \mathbf{A}_3 & \mathbf{A}_2 & \mathbf{A}_1 & \mathbf{A}_0 & \cdots \\ & \vdots & \vdots & \vdots & \vdots & \vdots & \ddots \end{bmatrix} \quad (9.34)$$

(and similarly for  $\mathcal{B}$ ,  $\mathcal{C}$  and  $\mathcal{D}$ ), where the submatrices  $\mathbf{A}_n$  in Eq. (9.34) are the coefficients of the Fourier expansion of matrix  $\mathbf{A}(t)$ , given in Eq. (9.30). Note that the expansions of the state space matrices can be also expressed in trigonometric form, recalling that<sup>1</sup>

$$\mathbf{A}_k = \frac{1}{2}(\mathbf{A}_{kc} - j\mathbf{A}_{ks}), \quad \mathbf{A}_{-k} = \frac{1}{2}(\mathbf{A}_{kc} + j\mathbf{A}_{ks}), \quad k = 1, 2, \dots \quad (9.35)$$

<sup>1</sup>Recall that the Fourier series can be rewritten in complex exponential form, *i.e.*,  $a(t) = a_0 + \sum_{k=1}^{\infty} (a_{nc} \cos n\omega t + a_{ns} \sin n\omega t) = \sum_{k=-\infty}^{\infty} a_k e^{jk\omega t}$ , with  $a_k = (a_{kc} - ja_{ks})/2$ , and  $a_{-k} = (a_{kc} + ja_{ks})/2$ ,  $k = 1, 2, \dots$

with  $A_0$  identical in Eq. (9.34). Similar relations hold for the harmonics of  $\mathbf{B}$ ,  $\mathbf{C}$ , and  $\mathbf{D}$ . The matrix  $\mathcal{N}$  is a block diagonal complex-valued matrix given by:

$$\mathcal{N} = \text{blkdiag}\{jn\Omega\mathbf{I}\} = j\Omega \begin{bmatrix} \ddots & \vdots & \vdots & \vdots & \vdots & \vdots \\ \cdots & -2\mathbf{I} & 0 & 0 & 0 & 0 & \cdots \\ \cdots & 0 & -\mathbf{I} & 0 & 0 & 0 & \cdots \\ \cdots & 0 & 0 & 0 & 0 & 0 & \cdots \\ \cdots & 0 & 0 & 0 & \mathbf{I} & 0 & \cdots \\ \cdots & 0 & 0 & 0 & 0 & 2\mathbf{I} & \cdots \\ \vdots & \vdots & \vdots & \vdots & \vdots & \vdots & \ddots \end{bmatrix} \quad (9.36)$$

where  $\mathbf{I}$  is the identity matrix of size equal to the number of states. From Eq. (9.32), one can define the *harmonic transfer function* (HTF) as the operator:

$$\mathcal{G}(s) = \mathcal{C}[s\mathcal{J} - (\mathcal{A} - \mathcal{N})]^{-1}\mathcal{B} + \mathcal{D}. \quad (9.37)$$

which relates the input harmonics and the output harmonics (contained in the infinite vectors  $\mathcal{U}$  and  $\mathcal{Y}$  respectively). Equation (9.37) is the extension to the case of periodic systems of the corresponding constant coefficient expression for the transfer function

$$\mathbf{G}(s) = \mathbf{C}[s\mathbf{I} - \mathbf{A}]^{-1}\mathbf{B} + \mathbf{D}. \quad (9.38)$$

Finally, note that the first correct formalization of poles, zeros, and transfer function for continuous-time periodic systems under a harmonic framework is to be attributed to Zhou and Hagiwara (see [Zho07] and references therein). It should be noted that notions for poles, zeros, and transfer function for discrete-time LTP systems had already been developed in the 80's at Politecnico di Milano and other Italian universities [BB85; BCS86; GL88].

The application of Floquet theory to the study of rotorcraft stability issues has been envisaged since the late 60's (see, *e.g.*, [Pet94] and the references therein for a discussion of efficient numerical methods to extract periodic stability characteristics from nonlinear rotorcraft models). In recent years, the problem of extracting complete LTP linearized models from nonlinear systems has been formulated along two different approaches. On one hand, it is possible to linearize the nonlinear helicopter model about a periodic trim condition in correspondence of many different values of rotor azimuth and collect the obtained LTI models into a LTP one. On the other hand, the application of model identification methods for LTP systems to the nonlinear model has been envisaged as an alternative approach. In both cases, eventually one has to consider the problem of approximating the obtained LTP models with LTI ones.

## 9.3 Extraction of LTP/LTI Systems from Simulation Models

### 9.3.1 Overview of Periodic Trim Methods

The very first step toward the approximation of the NLTP rotorcraft dynamics with LTP systems is the determination the periodic orbit about which the NLTP system is linearized, which involves computing the states and controls that result in a periodic equilibrium (*i.e.*, trimming a vehicle about a periodic orbit). Several solutions exist for trimming a vehicle about a periodic orbit and are described as follows.

#### Averaged Approximate Trim

Averaged approximate trim consists of finding a trim solution based on the averaged NLTP dynamics. Then, the periodic orbit is computed by integrating the NLTP dynamics over a single periodic orbit starting from the averaged solution. This approach was used in the recent studies on the AFCS/HHC interference [LP17; Lop+15; Pad+15; Pra+08] and on load alleviation control [SH20; Sae+20]. However, time marching the system starting from the averaged solution may lead to an inaccurate prediction of the vehicle's periodic response.

### Time Marching Trim

Time marching trim is a method for stable systems where the system is time marched until all transient dynamics die out and the solution reaches a periodic steady state. Once the trim solution is found, the periodic orbit itself is found by integrating the model over one periodic orbit. In the case where the periodic orbit is unstable, trajectories starting near the periodic orbit tend to diverge from it. Unfortunately, this is the case for most hovering vehicles because of their inherent and well-documented instability in hover [MAG73]. Moreover, this is especially true for helicopters because their dynamics are unstable not only in hover but also across most of their flight envelope (in particular, the phugoid mode is typically unstable as shown in [SH20] for the UH-60 helicopter).

### Autopilot Trim

This method utilizes a feedback controller to render the NLTP dynamics stable around the periodic orbit such that trajectories starting near the periodic orbit will approach the periodic orbit [PCF90; PKC84]. However, this approach is not always possible or convenient because it requires a relatively robust autopilot tailored to the configuration under analysis. Since autopilots are rarely available during the initial design or analysis stage when developing a new flight vehicle, the versatility of this method is limited. Further, the autopilot trim approach requires starting the system close enough to the periodic equilibrium for the closed-loop system to converge. However, the region of attraction of the periodic equilibrium may not be known with sufficient accuracy *a priori*.

### Periodic Shooting

Periodic shooting is an iterative solution strategy in which for any set of initial conditions the equations of motions are integrated over one rotor revolution. The errors at the beginning and end of the periodic orbit are subsequently minimized typically using a Newton-Raphson iteration [PI81]. Although this method proved successful in several instances [KCT93; Pet75; SP78], it only considers the case where a constant trim control vector is sought, which does not allow for the computation of a HHC open-loop control input *a priori* needed to constrain arbitrary state harmonics.

### Harmonic Balance

Harmonic balance is a powerful solution strategy in which the state vector is expressed as a sum of harmonic signals of the forcing frequency of the system, forming a set of  $n(2N + 1)$  equations, where  $n$  is the number of states and  $N$  is the number of harmonics to be balanced [GT12; LH11; WL15]. The periodic solution is found iteratively by setting the system dynamics zeroth harmonic to zero, and by exploiting the integral relations between the state harmonics. Although harmonic balance is a commonly-used method for computing periodic solutions in a variety of engineering applications – for instance, for rotating machinery see [GST07], or for computational fluid dynamics see [Da +13] – it enjoys less popularity in the rotorcraft field, where it was used only in a limited amount of studies [Eip16; PO75; WP78] most of which date prior to 1980. This scarce popularity is mostly due to the limitations in computing power available at that time, and to the lack of numerical methods to approximate LTP systems with higher-order LTI systems, which limited the application of the method to low-order models of the rotor dynamics alone. More specifically, the only available methods at the time were the Lyapunov-Floquet method [PS01] and frequency lifting methods [CCB04], which both suffered from the common disadvantage of a need for state transition matrices. In fact, the computation of state transition matrices can either be computationally intensive or numerically very sensitive to the number of terms used in analytical approximations that use Chebyshev polynomials.

### Modified Harmonic Balance

Recently, a modified harmonic balance algorithm was proposed in [SR21b] based on harmonic decomposition models [LP17; Lop+15]. While the algorithm is based on the overall architecture of harmonic balance, the algorithm introduces three major innovations compared to previous methods: (i) it does not rely on state transition matrices, (ii) it simultaneously solves for the approximate higher-order LTI dynamics about the periodic solution, and (iii) it can be used to compute the open-loop harmonic control inputs that attenuate arbitrary state harmonics. As such, the algorithm relaxes the computational disadvantages related to the computation of state transition matrices, Achilles' heel of conventional harmonic balance.

### 9.3.2 Early Efforts in the Approximation of the LTP Rotor Dynamics with High-Order LTI Models

To the best knowledge of the authors, the very first effort to approximate LTP systems with LTI models in the rotorcraft community is dated 1969 and is attributed to Crimi and Piarulli *et al.* [Cri69; PW70]. This study was motivated by the need to determine the aeroelastic stability of a rotor blade in forward flight. While the aeroelastic stability of a blade in hovering flight is a relatively straightforward problem, the study of rotor flutter in forward flight is fundamentally different because it involves equations of motion with periodic coefficients. Crimi and Piarulli *et al.* considered the bending flapping and torsional dynamics of a blade subjected to a free stream. In their approach, the blade coordinates are expressed in the rotating frame (*i.e.*, in a frame rigidly attached to the undeformed blade). The nonlinear system of equations of motion are given in terms of the  $N$  coupled modes of the free vibrations of the system:

$$\ddot{\zeta}_k + \bar{\omega}_k^2 \zeta_k = F_k(t), \quad k = 1, 2, \dots, N \quad (9.39)$$

where  $\bar{\omega}_k$  is the natural frequency of the  $k^{\text{th}}$  mode and  $F_k$  is the generalized force applied to the  $k^{\text{th}}$  mode. Since the generalized forces are nonlinear functions of the states and depend on the local angle of attack of each blade segment, which in terms depends on the azimuthal position of the blade, the generalized forces are expanded in a Taylor series around the nominal values of angle of attack and relative speed. The steady-state and terms higher than the first are subsequently discarded to lead to an LTP system given in second-order form:

$$\ddot{\zeta}_k + \bar{\omega}_k^2 \zeta_k - \sum_{n=1}^N \left[ G_{kn}(t) \zeta_n + H_{kn}(t) \dot{\zeta}_n \right] = 0, \quad k = 1, 2, \dots, N \quad (9.40)$$

where  $G_{kn}$  and  $H_{kn}$  are time-periodic coefficients relative to the linearized generalized forces. These equations are put in a somewhat more convenient form by defining an independent variable  $z$  that is effectively half of the azimuth angle of the blade  $\psi$ :

$$z = \frac{1}{2}\Omega t = \frac{1}{2}\psi \quad (9.41)$$

such that:

$$\frac{d^2 \zeta_m}{dz^2} + \sum_{n=1}^N \left( a_{mn} \frac{d\zeta_n}{dz} + b_{mn} \zeta_n \right) = 0, \quad m = 1, 2, \dots, N \quad (9.42)$$

where:

$$a_{mn} = -\frac{2}{\Omega} H_{mn} \quad (9.43a)$$

$$b_{mm} = -\frac{4}{\Omega^2} [\bar{\omega}_{mm}^2 - G_{mm}] \quad (9.43b)$$

$$a_{mn} = -\frac{4}{\Omega^2} G_{mn} \quad (9.43c)$$

and where  $\Omega = d\psi/dt$  is the angular speed of the rotor. The coefficients  $a_{mn}$  and  $b_{mn}$  are periodic functions with period  $\pi$  (*i.e.*, half a rotor revolution) such that:

$$a_{mn}(z + \pi) = a_{mn}(z) \quad (9.44a)$$

$$b_{mn}(z + \pi) = b_{mn}(z) \quad (9.44b)$$

The analysis proceeds with obtaining two related sets of equations by differentiating Eq. (9.101) multiple times and performing simple algebraic manipulations:

$$\frac{d^3 \zeta_m}{dz^3} + \sum_{n=1}^N \left( c_{mn} \frac{d\zeta_n}{dz} + d_{mn} \zeta_n \right) = 0, \quad m = 1, 2, \dots, N \quad (9.45a)$$

$$\frac{d^4 \zeta_m}{dz^4} + \sum_{n=1}^N \left( e_{mn} \frac{d\zeta_n}{dz} + f_{mn} \zeta_n \right) = 0, \quad m = 1, 2, \dots, N \quad (9.45b)$$

where  $c_{mn}$ ,  $d_{mn}$ ,  $e_{mn}$ , and  $f_{mn}$  are functions of  $a_{mn}$  and  $b_{mn}$ . Upon the application of Floquet theory, such that the solutions for each set of equations is assumed as a finite complex Fourier series,

$$\zeta_m = e^{iwz} \phi_m(z) = \sum_{k=-L}^L p_{mk} e^{(2k+\omega)z}, \quad m = 1, 2, \dots, N \quad (9.46)$$

the study shows how the solution of Eq. (9.101) is found by determining the  $2N$  common solutions between the  $3N$  and  $4N$  solutions of Eqs. (9.45a) and (9.45b), respectively. The solutions are practically found by solving for the unknown Fourier coefficients  $p_{mk}$  for each system.

This constituted a first successful attempt to study the aeroelastic stability of a blade by approximating its time-periodic coefficients with a finite series time-invariant coefficients. However, the computational limitations of the time prevented the analysis to be applied to more than three degrees of freedom. Further, the system considered was simple in the sense that it modeled the dynamics of the rotor only while disregarding the coupled fuselage-rotor dynamics.

### 9.3.3 T-Matrix

The classical formulation of HHC [Sha67] is based on the knowledge of the frequency response relating the higher-harmonics of the control inputs to the output measurements, which are typically the hub loads (rotor loads) and/or the fuselage accelerations (vibratory loads). This response model is the so-called “T-matrix” (or “transfer-matrix”). The  $T$ -matrices used in the formulation of HHC algorithms can be related to the elements of the HTF of the linearized helicopter models as follows.

It is worth noting that the rotor will be subject to a proper, steady-state higher-harmonic control input whenever the control vector  $\mathbf{u}$  is *constant*. This implies that in order to define the  $T$ -matrix for the helicopter, one only has to study the response of the periodic helicopter models to an EMP input with  $s = 0$ , *i.e.*, one has to compute the input/output operator  $\mathcal{G}(0)$ . Consider a generic LTP system and the constant input  $\mathbf{u}(t) = \mathbf{u}_0$ . The vector  $\mathcal{U}$  in the definition of the HTF corresponding to  $\mathbf{u}(t) = \mathbf{u}_0$  is given by:

$$\mathcal{U}^T = [\dots \ 0 \ 0 \ \mathbf{u}_0^T \ 0 \ 0 \ \dots] \quad (9.47)$$

and the steady state response  $\mathcal{Y}$  of the periodic system is given by:

$$\mathcal{Y} = \mathcal{G}(0) \mathcal{U} \quad (9.48)$$

with the “central” part of the infinite-dimensional operator  $\mathcal{G}(0)$  given by:

$$\mathcal{G}(0) = \begin{bmatrix} \mathbf{G}_{-2N,-2N} & \mathbf{G}_{-2N,-N} & \mathbf{G}_{-2N,0} & \mathbf{G}_{-2N,N} & \mathbf{G}_{-2N,2N} \\ \mathbf{G}_{-N,-2N} & \mathbf{G}_{-N,-N} & \mathbf{G}_{-N,0} & \mathbf{G}_{-N,N} & \mathbf{G}_{-N,2N} \\ \mathbf{G}_{0,-2N} & \mathbf{G}_{0,-N} & \mathbf{G}_{0,0} & \mathbf{G}_{0,N} & \mathbf{G}_{0,2N} \\ \mathbf{G}_{N,-2N} & \mathbf{G}_{N,-N} & \mathbf{G}_{N,0} & \mathbf{G}_{N,N} & \mathbf{G}_{N,2N} \\ \mathbf{G}_{2N,-2N} & \mathbf{G}_{2N,-N} & \mathbf{G}_{2N,0} & \mathbf{G}_{2N,N} & \mathbf{G}_{2N,2N} \end{bmatrix} \quad (9.49)$$

which yields:

$$\begin{bmatrix} \mathbf{y}_{-N} \\ \mathbf{y}_N \end{bmatrix} = \begin{bmatrix} \mathbf{G}_{-N,0} \\ \mathbf{G}_{N,0} \end{bmatrix} \mathbf{u}_0 \quad (9.50)$$

Converting the  $N_b/\text{rev}$  harmonics of the output from exponential to trigonometric form leads to<sup>2</sup>:

$$\begin{bmatrix} \mathbf{y}_{Nc} \\ \mathbf{y}_{Ns} \end{bmatrix} = 2 \begin{bmatrix} \text{Real}[\mathbf{G}_{N,0}] \\ \text{Imag}[\mathbf{G}_{N,0}] \end{bmatrix} \mathbf{u}_0 \quad (9.51)$$

<sup>2</sup>Note that  $\mathbf{G}_{-N,0}$  and  $\mathbf{G}_{N,0}$  are complex conjugates.

so that the  $T$ -matrix is given by:

$$\mathbf{T} = 2 \begin{bmatrix} \text{Real}[\mathbf{G}_{N,0}] \\ \text{Imag}[\mathbf{G}_{N,0}] \end{bmatrix} \quad (9.52)$$

From a practical point of view, the above theoretical analysis of the frequency response of periodic systems, and the corresponding definitions for the  $T$ -matrix relating selected input-output frequencies only, rely on the use of infinite dimensional matrices. When it comes to the numerical construction of the  $T$ -matrix, however, one has to resort to finite dimensional approximations of the system matrices  $\mathcal{A}$ ,  $\mathcal{B}$ ,  $\mathcal{C}$ , and  $\mathcal{D}$ , see [Lov+06] for details.

In other words, the  $T$ -matrix is the linear approximation of the  $N_b/\text{rev}$  vibratory response to the HHC input. Then, for instance, the necessary HHC input for vibration suppression can be obtained by means of optimal control and expressed in terms of the current output vector:

$$\mathbf{U}(t+1) = \mathbf{U}(t) - \mathbf{T}^\dagger \mathbf{Y}(t) \quad (9.53)$$

where  $\mathbf{U}$  and  $\mathbf{Y}$  are the finite-dimensional input and output vectors formed respectively with the harmonics of  $\mathbf{u}$  and  $\mathbf{y}$ . Additionally,  $\mathbf{T}^\dagger = (\mathbf{T}^T \mathbf{Q} \mathbf{T} + \mathbf{R})^{-1} \mathbf{T}^T \mathbf{Q}$  where  $\mathbf{Q}$  and  $\mathbf{R}$  are the optimal control weighting matrices. This approach to vibration suppression constitutes what is referred to as the  $T$ -matrix algorithm.

While the  $T$ -matrix approach paved the way for HHC, it only allowed for the derivation of these active vibration control laws in trim flight. It follows that to extend HHC to maneuvering flight, more powerful methodologies were needed.

### 9.3.4 Frequency and Time Lifting of Helicopter Models with HHC

In the early 2000's Lovera and Malpica *et al.* [Lov+06; Lov+07; Mal08] applied frequency-lifting and time-lifting methods for LTP systems to the closed-loop study of the coupled rigid-body/rotor dynamics subject to higher-harmonic control. More precisely, given the closed-loop dynamics of the helicopter subject to HHC, the problem of analysing the closed-loop stability can be studied either in continuous-time, by interconnecting a continuous-time model of the helicopter to a continuous-time equivalent model of the higher-harmonic controller, or in discrete-time, by interconnecting a discretized model of helicopter dynamics to a digital representation of the higher-harmonic controller. The former approach was studied in [Lov+06]: in the cited paper, first, continuous-time representations for MIMO HHC control laws (possibly involving different input-output harmonics) are derived; subsequently, closed-loop LTP representations are obtained and finally high-order LTI equivalent models are constructed, using the HTF. The latter approach, instead, was studied in [Lov+07], as follows:

1. Discrete-time models are obtained for each of the components of the control loop, including the dynamics of the helicopter, the hold circuit, and the harmonic analyzer;
2. A complete model is obtained for the series connection of the individual components; not surprisingly, this model is LTP;
3. A time-invariant reformulation of the complete model is obtained using the above-described theory of time-lifting of periodic systems, using the slower sampling rate (*i.e.*, that of the controller);
4. The overall closed-loop stability analysis is carried out in discrete-time.

The additional challenge from the modelling point of view is due to the fact that, besides the periodic nature of the dynamics of the helicopter, taking into account in detail the multirate nature of the HHC implementation ("fast" sampling of the acceleration measurements to estimate the vibration harmonics and "slow" update of the control harmonics) leads to additional periodicity in the analysis.

The discrete-time helicopter dynamic model is obtained from the linearized continuous-time model: the sampling frequency is the fastest of the two in the system, *i.e.*, that required to allow the reconstruction of the  $N_b/\text{rev}$  component of the accelerations of interest. To implement the HHC control algorithm, the  $N_b/\text{rev}$  components  $\tilde{\mathbf{y}}_{\text{HHC}}$  of the output accelerations are extracted from their time domain measurements  $\tilde{\mathbf{y}}_H$ . In each period, the information about  $\mathbf{y}_H$  is available starting from  $\eta = n_s/2 - 1 + Kn_s$ ,  $K = 1, 2, \dots$  but is provided as output only at  $\eta = (K + 1)n_s$ . The operation of the harmonic analyzer can be described mathematically by a linear time-periodic model with discrete time  $\eta$  and period  $n_s$ :

$$\tilde{\mathbf{x}}_F(\eta + 1) = \tilde{\mathbf{A}}_F(\eta)\tilde{\mathbf{x}}_F(\eta) + \tilde{\mathbf{B}}_F(\eta)\tilde{\mathbf{y}}_H(\eta) \quad (9.54a)$$

$$\tilde{\mathbf{y}}_{\text{HHC}}(\eta) = \tilde{\mathbf{C}}_F(\eta)\tilde{\mathbf{x}}_F(\eta) \quad (9.54b)$$

The matrices  $\tilde{\mathbf{A}}_F(\eta)$ ,  $\tilde{\mathbf{B}}_F(\eta)$  and  $\tilde{\mathbf{C}}_F(\eta)$  are defined in a way that reflects the various phases of the harmonic analysis that occur over one rotor revolution. The HHC control law can be written in state-space form as a linear time-invariant system

$$\tilde{\mathbf{x}}_C(k+1) = \tilde{\mathbf{A}}_C\tilde{\mathbf{x}}_C(k) + \tilde{\mathbf{B}}_C\tilde{\mathbf{y}}_{\text{HHC}}(k) \quad (9.55a)$$

$$\tilde{\mathbf{u}}_{\text{HHC}}(k) = \tilde{\mathbf{C}}_C\tilde{\mathbf{x}}_C(k) \quad (9.55b)$$

where:

$$\tilde{\mathbf{A}}_C = \mathbf{I} \quad (9.56a)$$

$$\tilde{\mathbf{B}}_C = -\{\mathbf{T}_C^T \mathbf{W} \mathbf{T}_C + \mathbf{R}\}^{-1} \mathbf{T}_C^T \mathbf{W} \quad (9.56b)$$

$$\tilde{\mathbf{C}}_C = \mathbf{I} \quad (9.56c)$$

The hold circuit is the interface between the controller and the helicopter. Since the controller operates at the discrete-time  $k$  (*i.e.*, once per revolution) while the helicopter model has been obtained at the discrete-time  $\eta$  (*i.e.*, once per sample needed to extract the N/rev harmonics), the controller provides a new value of the control variables only at  $\eta = kn_s$ ,  $k = 1, 2, \dots$ , and this output must be kept constant for the intervening samples  $kn_s \leq \eta < (k+1)n_s$ . Therefore, the model of the hold circuit is linear, discrete-time periodic, with discrete time  $\eta$  and period  $n_s$ .

The overall discrete HHC model, which relates the harmonics of the HHC input  $_{\text{HHC}}$  to the harmonics of the acceleration output  $\tilde{\mathbf{y}}_{\text{HHC}}$  can be obtained by connecting in series the harmonic analyzer, the discrete model for the response of the helicopter to HHC inputs, and that of the zero order hold. The model, with discrete-time  $\eta$ , is given by

$$\tilde{\mathbf{x}}_Z(\eta + 1) = \tilde{\mathbf{A}}_Z\tilde{\mathbf{x}}_Z(\eta) + \tilde{\mathbf{B}}_Z\tilde{\mathbf{u}}_{\text{HHC}}(\eta) \quad (9.57a)$$

$$\tilde{\mathbf{x}}_H(\eta + 1) = \tilde{\mathbf{A}}_H\tilde{\mathbf{x}}_H(\eta) + \tilde{\mathbf{B}}_H\tilde{\mathbf{C}}_Z\tilde{\mathbf{x}}_Z(\eta) + \tilde{\mathbf{B}}_H\tilde{\mathbf{D}}_Z\tilde{\mathbf{u}}_{\text{HHC}}(\eta) \quad (9.57b)$$

$$\tilde{\mathbf{x}}_F(\eta + 1) = \tilde{\mathbf{A}}_F\tilde{\mathbf{x}}_F(\eta) + \tilde{\mathbf{B}}_F\tilde{\mathbf{C}}_H\tilde{\mathbf{x}}_H(\eta) + \tilde{\mathbf{B}}_F\tilde{\mathbf{D}}_H\tilde{\mathbf{C}}_Z\tilde{\mathbf{x}}_Z(\eta) + \tilde{\mathbf{B}}_F\tilde{\mathbf{D}}_H\tilde{\mathbf{D}}_Z\tilde{\mathbf{u}}_{\text{HHC}}(\eta) \quad (9.57c)$$

$$\tilde{\mathbf{y}}_{\text{HHC}}(\eta) = \tilde{\mathbf{C}}_F\tilde{\mathbf{x}}_F(\eta) \quad (9.57d)$$

(the argument  $\eta$  in the matrices has been omitted for simplicity). This model cannot be connected directly to the HHC controller because its sampling rate is still different from that of the discrete HHC control law ( $n_s/\text{rev}$  vs.  $1/\text{rev}$ ). A combined model at the same sampling rate as the HHC controller can be obtained using the theory of time-invariant reformulations of linear time-periodic systems and, more precisely, through a time-lifted reformulation.

An in-depth analysis of the results of both approaches can be found in [Mal08].

### 9.3.5 Direct Derivation of High-Order LTI Models

In the early 2000's, Cheng *et al.* [CTC03] developed a numerical scheme to directly obtain a high-order LTI approximation of a NLTP system representative of a 4-bladed helicopter. This constituted the first successful attempt to approximate the coupled rigid-body/rotor dynamics, including the  $N_b/\text{rev}$  rotor loads, with a high-order LTI system. The study relies on the assumption that the rotor states, expressed in the body-fixed coordinate system, are comprised of an average and a  $4/\text{rev}$  portion; whereas the rigid-body states and inflow states are entirely described by their averaged dynamics over a rotor revolution. The form of the LTI system sought is the following:

$$\begin{bmatrix} \dot{\mathbf{x}}_{\text{ave}} \\ \dot{\mathbf{x}}_{4P} \end{bmatrix} = \begin{bmatrix} \mathbf{A}_{\text{ave}} & \mathbf{A}_{12} \\ \mathbf{A}_{21} & \mathbf{A}_{\text{HHC}} \end{bmatrix} \begin{bmatrix} \mathbf{x}_{\text{ave}} \\ \mathbf{x}_{4P} \end{bmatrix} + \begin{bmatrix} \mathbf{B}_{\text{ave}} & \mathbf{B}_{12} \\ \mathbf{B}_{21} & \mathbf{B}_{\text{HHC}} \end{bmatrix} \begin{bmatrix} \mathbf{u}_{\text{pilot}} \\ \mathbf{u}_{\text{HHC}} \end{bmatrix} \quad (9.58)$$

where  $\mathbf{x}_{\text{ave}}^T = [\mathbf{x}_B^T \mathbf{x}_{\text{MR}_{\text{ave}}}^T]$  is the average portion of the state vector containing the rigid-body and inflow states ( $\mathbf{x}_B$ ), and by the average portion of the main rotor states ( $\mathbf{x}_{\text{MR}_{\text{ave}}}$ ), and where  $\mathbf{x}_{4P}^T = [\mathbf{x}_{\text{MR}_{4c}}^T \mathbf{x}_{\text{MR}_{4s}}^T]$  contains the 4/rev components of the rotor states. Additionally,  $\mathbf{u}_{\text{pilot}}^T = [\delta_{\text{lat}} \delta_{\text{lon}} \delta_{\text{col}} \delta_{\text{ped}}]$  are the conventional pilot controls and  $\mathbf{u}_{\text{HHC}}^T = [\boldsymbol{\theta}_{3c} \boldsymbol{\theta}_{3s} \boldsymbol{\theta}_{4c} \boldsymbol{\theta}_{4s} \boldsymbol{\theta}_{5c} \boldsymbol{\theta}_{5s}]$  is the vector of higher-harmonic controls in the rotating frame. The submatrices  $\mathbf{A}_{\text{ave}}$  and  $\mathbf{A}_{21}$ , representing the influence of the average portion of the state vector on respectively the average and 4/rev portions of the state derivative vector, are obtained by means of finite difference. Specifically, each element of the average portion of the state vector is perturbed separately from the equilibrium (trim) condition, at incremental azimuthal steps over one rotor revolution, to obtain a set of matrices  $\mathbf{A}_F(\psi_i)$  (one per azimuthal step  $\psi_i$ ). The submatrix  $\mathbf{A}_{\text{ave}}$  was then obtained by averaging the matrices  $\mathbf{A}_F(\psi_i)$  over the number of azimuthal steps  $N_\psi$ . The submatrix  $\mathbf{A}_{21}$  is obtained by extracting the 4/rev cosine and sine harmonics through Fourier analysis:

$$\mathbf{A}_{F_{4c}} = \frac{2}{N_\psi} \sum_{i=1}^{N_\psi} \mathbf{A}_F(\psi_i) \cos 4\psi_i \quad (9.59a)$$

$$\mathbf{A}_{F_{4s}} = \frac{2}{N_\psi} \sum_{i=1}^{N_\psi} \mathbf{A}_F(\psi_i) \sin 4\psi_i \quad (9.59b)$$

such that  $\mathbf{A}_{21}^T = [\mathbf{A}_{F_{4c}}^T \mathbf{A}_{F_{4s}}^T]$ . The submatrices  $\mathbf{A}_{12}$  and  $\mathbf{A}_{\text{HHC}}$ , representing the influence of the 4/rev portion of the state vector on respectively the average and 4/rev portions of the state derivative vector, are also obtained by means of finite difference. However, rather than using a constant perturbation, the 4/rev portion of the state vector  $\mathbf{x}_{4P}$  is subjected to 4/rev perturbations both in the sine and cosine harmonics. This was done because the equations of motion of the helicopter were not expressed in 4/rev states, and therefore could not be directly perturbed. The procedure also accounted for the kinematic relationships between the rotor multi-blade coordinate rotor states. For instance, if the longitudinal flapping angle  $\beta_{1c}$  was perturbed by a constant  $\Delta\beta_{1c} \cos 4\psi_i$  at the azimuthal position  $\psi_i$ , then the longitudinal flapping angle derivative  $\dot{\beta}_{1c}$  must simultaneously be perturbed by a constant  $\frac{d}{dt}(\Delta\beta_{1c} \cos 4\psi_i) = -4\Omega\Delta\beta_{1c} \sin 4\psi_i$  to maintain kinematic consistency. Similarly to the procedure above, the set of matrices  $\mathbf{P}_F(\psi_i)$  thus obtained is averaged to find  $\mathbf{A}_{12}$ , whereas  $\mathbf{A}_{\text{HHC}}$  is obtained by extracting the 4/rev cosine and sine harmonics through Fourier analysis such that  $\mathbf{A}_{\text{HHC}}^T = [\mathbf{A}_{F_{4c}}^T \mathbf{A}_{F_{4s}}^T]$ . Because the higher-harmonic component of the input vector  $\mathbf{u}_{\text{HHC}}$  is expressed in term of its harmonics, the two portions of the control matrix ( $[\mathbf{B}_{\text{ave}} \mathbf{B}_{12}]$  and  $[\mathbf{B}_{21} \mathbf{B}_{\text{HHC}}]$ ) are readily obtained by following the same procedure used for  $\mathbf{A}_{\text{ave}}$  and  $\mathbf{A}_{21}$ . Obviously, the constant perturbations are applied to the control vector in this case.

The LTI model also included the output equation, which has the following form:

$$\begin{bmatrix} \mathbf{y}_{\text{ave}} \\ \mathbf{y}_{4P} \\ \mathbf{F}_{\text{ave}} \\ \mathbf{F}_{4P} \end{bmatrix} = \begin{bmatrix} \mathbf{I} & \mathbf{0} \\ \mathbf{0} & \mathbf{C}_{22} \\ \mathbf{C}_{31} & \mathbf{C}_{32} \\ \mathbf{C}_{41} & \mathbf{C}_{42} \end{bmatrix} \begin{bmatrix} \mathbf{x}_{\text{ave}} \\ \mathbf{x}_{4P} \end{bmatrix} + \begin{bmatrix} \mathbf{I} & \mathbf{0} \\ \mathbf{0} & \mathbf{C}_{22} \\ \mathbf{C}_{31} & \mathbf{C}_{32} \\ \mathbf{C}_{41} & \mathbf{C}_{42} \end{bmatrix} \begin{bmatrix} \mathbf{u}_{\text{pilot}} \\ \mathbf{u}_{\text{HHC}} \end{bmatrix} \quad (9.60)$$

where  $\mathbf{y}_{\text{ave}}$  is identical to  $\mathbf{x}_{\text{ave}}$ ,  $\mathbf{y}_{4P}$  is the 4/rev rotor state vector, and  $\mathbf{F}_{\text{ave}}$  and  $\mathbf{F}_{4P}$  are vectors containing the average and 4/rev hub loads. While the derivation of the coefficient matrices is similar to that of the state equations, it is worth noting that the coefficient matrix  $\mathbf{D}_{42}$  is equivalent to the  $T$ -matrix in typical HHC studies.

This study pioneered the use of higher-order state-space systems toward the design of a combined AFCS-HHC control laws that consider the coupling between the body states and the higher-frequency rotor response. Prior to this study, HHC/OBC/IBC synthesis was solely based on an update equation that linked the vibration harmonics to the HHC/OBC/IBC input through the  $T$ -matrix. Moreover, the  $T$ -matrix approach limited the synthesis of active vibration control laws to trim flight, whereas the introduction of these high-order state-space systems enabled the extension of active vibration control to maneuvering flight. Although the methodology successfully predicted the 4/rev component of the hub loads, the methodology did not include the harmonics higher than 4/rev, and was applied to a relatively simple 4-bladed helicopter model with rigid flap and lead-lag motions, and a single torsional mode. Further, the 4/rev component of the fuselage state, however small, was ignored.

### 9.3.6 Harmonic Decomposition: Second-Order Formulation

In the late 2000's Prasad *et al.* [Olc11; OP11; Pra+09; Pra+08] built upon Cheng's idea to use numerical perturbations to individual harmonic components of periodic states to develop a two-step procedure to compute high-order LTI models representative of the coupled rigid-body/rotor dynamics. First, a LTP model is extracted by linearizing the nonlinear dynamics of the helicopter about a periodic equilibrium at incremental azimuthal steps over one rotor revolution, as discussed in the previous section. Second, a harmonic decomposition is performed on the LTP system states to obtain an approximated high-order LTI model. The use of a LTP model as an intermediate step was motivated by the fact that the number of harmonic components of the rotor states to be retained in the derivation of a LTI model is typically not known *a priori*. Splitting the process in two steps guarantees that the LTP model accurately portrays the nonlinear system's behavior independently of the number of harmonics that are retained in the subsequent step of approximating the LTP system with a higher-order LTI model, which does not require perturbations. This way, LTI model matrices of various orders can be derived independently of the derivation of the LTP model. Step 1 starts with the assumption that the helicopter rigid-body/rotor dynamics can be described by the following nonlinear system:

$$\mathbf{f}(\mathbf{x}, \dot{\mathbf{x}}, \ddot{\mathbf{x}}, \mathbf{u}) = \mathbf{0} \quad (9.61)$$

where  $\mathbf{x}$  is the state vector and  $\mathbf{u}$  is the control vector. Let  $\mathbf{x}^*(\psi)$  and  $\mathbf{u}^*(\psi)$  represent a periodic solution of the system such that  $\mathbf{x}^*(\psi) = \mathbf{x}^*(\psi + 2\pi)$  and  $\mathbf{u}^*(t) = \mathbf{u}^*(\psi + 2\pi)$  where  $\psi$  is the main rotor azimuth angle in radians. It is convenient to note that  $\psi$  is equivalent to non-dimensional time, which can be related to dimensional time via the following relation:  $\psi = \Omega t$ , where  $\Omega$  is the main rotor angular speed in rad/s, and  $t$  is the dimensional time in seconds. Then, a linearization of Eq. (9.61) is found by considering the case of small disturbances about the periodic equilibrium:

$$\mathbf{x}(\psi) = \mathbf{x}^*(\psi) + \Delta\mathbf{x}(\psi) \quad (9.62a)$$

$$\mathbf{u}(\psi) = \mathbf{u}^*(\psi) + \Delta\mathbf{u}(\psi) \quad (9.62b)$$

and by expanding Eq. (9.61) into a Taylor series about the periodic equilibrium. After neglecting the terms of order higher than the second and with a few additional steps of algebraic manipulation, the following LTP system in second-order form can be obtained:

$$\ddot{\mathbf{x}} = -\mathbf{K}(\psi)\mathbf{x} - \mathbf{D}(\psi)\dot{\mathbf{x}} + \mathbf{G}(\psi)\mathbf{u} \quad (9.63)$$

where:

$$\mathbf{K}(\psi) = \left[ \frac{\partial \mathbf{f}}{\partial \ddot{\mathbf{x}}} \right]^{-1} \left[ \frac{\partial \mathbf{f}}{\partial \mathbf{x}} \right] \quad (9.64a)$$

$$\mathbf{D}(\psi) = \left[ \frac{\partial \mathbf{f}}{\partial \dot{\mathbf{x}}} \right]^{-1} \left[ \frac{\partial \mathbf{f}}{\partial \dot{\mathbf{x}}} \right] \quad (9.64b)$$

$$\mathbf{G}(\psi) = \left[ \frac{\partial \mathbf{f}}{\partial \mathbf{x}} \right]^{-1} \left[ \frac{\partial \mathbf{f}}{\partial \mathbf{u}} \right] \quad (9.64c)$$

The partial derivatives in Eq. (9.64) are evaluated along the periodic orbit such that the coefficient matrices of the LTP system in Eq. (9.63) are periodic with a fundamental period of  $T = \frac{2\pi}{\Omega}$  seconds, which corresponds to  $2\pi$  radians or one rotor revolution. The derivation of the LTP output equations follows a similar procedure to that of the state equations but is omitted for brevity.

In step 2, this LTP system is converted into an approximate higher-order LTI model by decomposing the state and control vectors into a finite number of harmonics via Fourier analysis:

$$\mathbf{x} = \mathbf{x}_0 + \sum_{n=1}^N \mathbf{x}_{nc} \cos n\psi + \mathbf{x}_{ns} \sin n\psi \quad (9.65a)$$

$$\mathbf{u} = \mathbf{u}_0 + \sum_{m=1}^M \mathbf{u}_{mc} \cos m\psi + \mathbf{u}_{ms} \sin m\psi \quad (9.65b)$$

The derivation continues by differentiating Eq. (9.65a) twice to obtain the first and second state derivative:

$$\dot{\mathbf{x}} = \dot{\mathbf{x}}_0 + \sum_{n=1}^N \mathbf{x}'_{nc} \cos n\psi + \mathbf{x}'_{ns} \sin n\psi \quad (9.66a)$$

$$\ddot{\mathbf{x}} = \ddot{\mathbf{x}}_0 + \sum_{n=1}^N \mathbf{x}''_{nc} \cos n\psi + \mathbf{x}''_{ns} \sin n\psi \quad (9.66b)$$

where:

$$\mathbf{x}'_{nc} = \dot{\mathbf{x}}_{nc} + n\Omega \mathbf{x}_{ns} \quad (9.67a)$$

$$\mathbf{x}'_{ns} = \dot{\mathbf{x}}_{ns} - n\Omega \mathbf{x}_{nc} \quad (9.67b)$$

$$\mathbf{x}''_{nc} = \ddot{\mathbf{x}}_{nc} + 2n\Omega \dot{\mathbf{x}}_{ns} - n^2 \Omega^2 \mathbf{x}_{nc} \quad (9.67c)$$

$$\mathbf{x}''_{ns} = \ddot{\mathbf{x}}_{ns} - 2n\Omega \dot{\mathbf{x}}_{nc} - n^2 \Omega^2 \mathbf{x}_{ns} \quad (9.67d)$$

Once Eqs. (9.65) and (9.66) are substituted in Eq. (9.63), the average state acceleration is obtained by averaging the state acceleration over one rotor revolution:

$$\begin{aligned} \bar{\mathbf{x}}_0 = \frac{1}{2\pi} \int_0^{2\pi} & \left[ -\mathbf{D}(\psi) \left( \dot{\mathbf{x}}_0 + \sum_{n=1}^N \mathbf{x}'_{nc} \cos n\psi + \mathbf{x}'_{ns} \sin n\psi \right) - \mathbf{K}(\psi) \left( \mathbf{x}_0 + \sum_{n=1}^N \mathbf{x}_{nc} \cos n\psi + \mathbf{x}_{ns} \sin n\psi \right) \right. \\ & \left. + \mathbf{G}(\psi) \left( \mathbf{u}_0 + \sum_{m=1}^M \mathbf{u}_{mc} \cos m\psi + \mathbf{u}_{ms} \sin m\psi \right) \right] d\psi \end{aligned} \quad (9.68)$$

Similarly, the  $i^{th}$  cosine and sine harmonics of the state acceleration are found in the following way:

$$\begin{aligned} \mathbf{x}''_{ic} = \frac{1}{\pi} \int_0^{2\pi} & \left[ -\mathbf{D}(\psi) \left( \dot{\mathbf{x}}_0 + \sum_{n=1}^N \mathbf{x}'_{nc} \cos n\psi + \mathbf{x}'_{ns} \sin n\psi \right) - \mathbf{K}(\psi) \left( \mathbf{x}_0 + \sum_{n=1}^N \mathbf{x}_{nc} \cos n\psi + \mathbf{x}_{ns} \sin n\psi \right) \right. \\ & \left. + \mathbf{G}(\psi) \left( \mathbf{u}_0 + \sum_{m=1}^M \mathbf{u}_{mc} \cos m\psi + \mathbf{u}_{ms} \sin m\psi \right) \right] \cos i\psi d\psi \end{aligned} \quad (9.69)$$

$$\begin{aligned} \mathbf{x}''_{is} = \frac{1}{\pi} \int_0^{2\pi} & \left[ -\mathbf{D}(\psi) \left( \dot{\mathbf{x}}_0 + \sum_{n=1}^N \mathbf{x}'_{nc} \cos n\psi + \mathbf{x}'_{ns} \sin n\psi \right) - \mathbf{K}(\psi) \left( \mathbf{x}_0 + \sum_{n=1}^N \mathbf{x}_{nc} \cos n\psi + \mathbf{x}_{ns} \sin n\psi \right) \right. \\ & \left. + \mathbf{G}(\psi) \left( \mathbf{u}_0 + \sum_{m=1}^M \mathbf{u}_{mc} \cos m\psi + \mathbf{u}_{ms} \sin m\psi \right) \right] \sin i\psi d\psi \end{aligned} \quad (9.70)$$

By exploiting the integral relations in Eq. (9.67) and with a few steps of algebraic manipulations, the zeroth and  $i^{th}$  cosine and sine harmonics of the state accelerations can be written as a function of the state and state velocity harmonics. These  $2n(2N+1)$  equations, where  $n$  is the dimension of the state vector and  $N$  is the number of the state harmonics retained, can be represented in matrix form by defining the augmented state and control vectors:

$$\mathbf{X}^T = [\mathbf{x}_0^T \ \mathbf{x}_{1c}^T \ \mathbf{x}_{1s}^T \ \dots \ \mathbf{x}_{Nc}^T \ \mathbf{x}_{Ns}^T \ \dot{\mathbf{x}}_0^T \ \dot{\mathbf{x}}_{1c}^T \ \dot{\mathbf{x}}_{1s}^T \ \dots \ \dot{\mathbf{x}}_{Nc}^T \ \dot{\mathbf{x}}_{Ns}^T] \quad (9.71a)$$

$$\mathbf{U}^T = [\mathbf{u}_0^T \ \mathbf{u}_{1c}^T \ \mathbf{u}_{1s}^T \ \dots \ \mathbf{u}_{Mc}^T \ \mathbf{u}_{Ms}^T] \quad (9.71b)$$

The resulting LTI model is defined as:

$$\dot{\mathbf{X}} = \begin{bmatrix} \mathbf{A}_{11} & \mathbf{A}_{12} \\ \mathbf{A}_{21} & \mathbf{A}_{22} \end{bmatrix} \mathbf{X} + \begin{bmatrix} \mathbf{B}_1 \\ \mathbf{B}_2 \end{bmatrix} \mathbf{U} \quad (9.72)$$

where:

$$\mathbf{A}_{11} = \mathbf{0}_{N \times N} \quad (9.73a)$$

$$\mathbf{A}_{12} = \mathbf{I}_{N \times N} \quad (9.73b)$$

$$\mathbf{B}_1 = \mathbf{0}_{N \times 1} \quad (9.73c)$$

and where closed-form expressions for the coefficient matrices  $\mathbf{A}_{21}$ ,  $\mathbf{A}_{22}$ , and  $\mathbf{B}_2$  can be found in [Pra+08]. A similar procedure is used to derive the LTI output equations but is omitted for brevity. The interested reader is invited to consult [Pra+08] for further detail.

The major advantage of this method compared to that of Cheng *et al.* [CTC03] is the ability to include an arbitrary number of harmonics in the high-order LTI system. Further, the harmonics that can be retained are not necessarily multiples of the number of blades per revolution. Although this numerical scheme was shown to improve computational speed by an order of magnitude when compared to previous algorithms from the literature, it relied on a second-order formulation of the original LTP system that can be problematic for degrees of freedom not explicitly represented in second-order form. In particular, this method showed limitations in predicting the effects of coupling harmonic terms for body, inflow, and rotor degrees of freedom.

### 9.3.7 Harmonic Decomposition: First-Order Formulation

A more general formulation that accurately captures the higher-harmonic dynamics relative to degrees of freedom not explicitly in second-order form was proposed by Lopez *et al.* starting from 2013 [Lopezz2; LP17; Lop+15]. This formulation retains the two-step approach of its predecessor but relies on a first-order representation of LTP systems. Step 1 starts with the assumption that the helicopter rigid-body/rotor dynamics can be described by the following nonlinear system:

$$\mathbf{f}(\mathbf{x}, \dot{\mathbf{x}}, \mathbf{u}) = \mathbf{0} \quad (9.74)$$

where  $\mathbf{x}$  is the state vector and  $\mathbf{u}$  is the control vector. Let  $\mathbf{x}^*(\psi)$  and  $\mathbf{u}^*(\psi)$  represent a periodic solution of the system such that  $\mathbf{x}^*(\psi) = \mathbf{x}^*(\psi + 2\pi)$  and  $\mathbf{u}^*(t) = \mathbf{u}^*(\psi + 2\pi)$  where  $\psi$  is the main rotor azimuth angle in radians. Then, a linearization of Eq. (9.74) is found by considering the case of small disturbances about the periodic equilibrium given in Eq. (9.62) and by expanding Eq. (9.74) into a Taylor series about the periodic equilibrium. After neglecting the terms of order higher than the second and with a few additional steps of algebraic manipulation, the following LTP system in first-order form can be derived:

$$\dot{\mathbf{x}} = \mathbf{F}(\psi)\mathbf{x} + \mathbf{G}(\psi)\mathbf{u} \quad (9.75)$$

where:

$$\mathbf{F}(\psi) = \left[ \mathbf{I} - \frac{\partial \mathbf{f}}{\partial \dot{\mathbf{x}}} \right]^{-1} \left[ \frac{\partial \mathbf{f}}{\partial \mathbf{x}} \right] \quad (9.76a)$$

$$\mathbf{G}(\psi) = \left[ \mathbf{I} - \frac{\partial \mathbf{f}}{\partial \dot{\mathbf{x}}} \right]^{-1} \left[ \frac{\partial \mathbf{f}}{\partial \mathbf{u}} \right] \quad (9.76b)$$

The partial derivatives in Eq. (9.76) are evaluated along the periodic orbit such that the coefficient matrices of the LTP system in Eq. (9.75) are periodic with a fundamental period of  $T = \frac{2\pi}{\Omega}$  seconds, which corresponds to  $2\pi$  radians or one rotor revolution. The derivation of the LTP output equations follows a similar procedure to that of the state equations but is omitted for brevity.

In step 2, this LTP system is converted into an approximate higher-order LTI model by decomposing the state and control vectors into a finite number of harmonics via Fourier analysis as it is done in Eq. (9.65). The derivation continues with the differentiation of Eq. (9.65a) to obtain the first state derivative, which is given in Eq. (9.66a). Once Eqs. (9.65), (9.66a) are substituted in Eq. (9.75), the average state derivative is obtained by averaging the state derivative over one rotor revolution:

$$\begin{aligned} \dot{\mathbf{x}}_0 = \frac{1}{2\pi} \int_0^{2\pi} & \left[ \mathbf{F}(\psi) \left( \mathbf{x}_0 + \sum_{n=1}^N \mathbf{x}_{nc} \cos n\psi + \mathbf{x}_{ns} \sin n\psi \right) \right. \\ & \left. + \mathbf{G}(\psi) \left( \mathbf{u}_0 + \sum_{m=1}^M \mathbf{u}_{mc} \cos m\psi + \mathbf{u}_{ms} \sin m\psi \right) \right] d\psi \quad (9.77) \end{aligned}$$

Similarly, the  $i^{th}$  cosine and sine harmonics of the state derivative are found in the following way:

$$\begin{aligned} \dot{\mathbf{x}}'_{ic} = \frac{1}{\pi} \int_0^{2\pi} \left[ \mathbf{F}(\psi) \left( \mathbf{x}_0 + \sum_{n=1}^N \mathbf{x}_{nc} \cos n\psi + \mathbf{x}_{ns} \sin n\psi \right) \right. \\ \left. + \mathbf{G}(\psi) \left( \mathbf{u}_0 + \sum_{m=1}^M \mathbf{u}_{mc} \cos m\psi + \mathbf{u}_{ms} \sin m\psi \right) \right] \cos i\psi d\psi \quad (9.78) \end{aligned}$$

$$\begin{aligned} \dot{\mathbf{x}}'_{is} = \frac{1}{\pi} \int_0^{2\pi} \left[ \mathbf{F}(\psi) \left( \mathbf{x}_0 + \sum_{n=1}^N \mathbf{x}_{nc} \cos n\psi + \mathbf{x}_{ns} \sin n\psi \right) \right. \\ \left. + \mathbf{G}(\psi) \left( \mathbf{u}_0 + \sum_{m=1}^M \mathbf{u}_{mc} \cos m\psi + \mathbf{u}_{ms} \sin m\psi \right) \right] \sin i\psi d\psi \quad (9.79) \end{aligned}$$

By exploiting the integral relations in Eqs. (9.67a) and (9.67b) and with a few steps of algebraic manipulations, the zeroth and  $i^{th}$  cosine and sine harmonics of the state derivative can be written as a function of the state harmonics. These  $n(2N+1)$  equations, where  $n$  is the dimension of the state vector and  $N$  is the number of the state harmonics retained, can be represented in matrix form by defining the augmented state and control vectors:

$$\mathbf{X}^T = [\mathbf{x}_0^T \ \mathbf{x}_{1c}^T \ \mathbf{x}_{1s}^T \ \dots \ \mathbf{x}_{Nc}^T \ \mathbf{x}_{Ns}^T] \quad (9.80a)$$

$$\mathbf{U}^T = [\mathbf{u}_0^T \ \mathbf{u}_{1c}^T \ \mathbf{u}_{1s}^T \ \dots \ \mathbf{u}_{Mc}^T \ \mathbf{u}_{Ms}^T] \quad (9.80b)$$

The resulting LTI model is defined as:

$$\dot{\mathbf{X}} = \mathbf{AX} + \mathbf{BU} \quad (9.81)$$

where closed-form expressions for the coefficient matrices can be found in [Lop+15]. A similar procedure is used to derive the LTI output equations but is omitted for brevity. The interested reader is invited to consult [Lop+15] for further detail.

This first-order formulation relaxed the shortcomings of the second-order formulation such that the effects of coupling harmonic terms for body, inflow, and rotor degrees of freedom are well-predicted. The methodology was successfully applied to a high-fidelity FLIGHTLAB® simulation model of a notional conventional utility helicopter representative of a UH-60. This model included flexible blades with representative in-plane, out-of-plane, and torsional bending modes, a six-state Peters-He inflow model, and nonlinear aerodynamic lookup tables for the airframe and rotor blade aerodynamic coefficients. This method constitutes the current state of the art in the approximation of NTLP rotorcraft models with higher-order LTI systems.

### 9.3.8 Recent Advancements in the Direct Derivation of High-Order LTI Models

Recently, Saetti *et al.* [SH23; SHB21] generalized the direct derivation of high-order LTI models method developed by Cheng *et al.* [CTC03] to an arbitrary number of harmonics, including those harmonics that are not multiples of the number of blades per rotor revolution (*i.e.*,  $N_b/\text{rev}$ ). The effort was motivated by the fact that, because in this method perturbations are given on a per-rotor-revolution basis rather than on a per-time-step basis, the perturbation scheme can be applied to those output measures that require the solution of partial differential equations (PDE's). In fact, the method was used to obtain time-invariant, linearized output equations of the aerodynamically-generated noise of a helicopter, which involves the numerical solution of the Ffowcs Williams-Hawkins equation (or its reformulations) [Bre94] and requires at least  $1/N_b$  rotor revolutions to be computed. This is articulated in the following steps:

1. Find the periodic equilibrium over one rotor revolution of the rotorcraft flight dynamics only. To achieve this, the modified harmonic balance scheme of [SR21b] was used to yield the periodic solution  $\mathbf{x}^*(t)$  and  $\mathbf{u}^*(t)$  at the desired flight condition.

2. Run a flight dynamics simulation without integrating the states but forcing them to follow the periodic trajectory above while recording data needed for the aeroacoustic calculations. Then, perturbations are applied to each of the coefficients of the periodic state and control trajectory (*i.e.*,  $\mathbf{x}_0^*$ ,  $\mathbf{x}_{1c}^*$ ,  $\mathbf{x}_{1s}^*$ , ...,  $\mathbf{x}_{Nc}^*$ ,  $\mathbf{x}_{Ns}^*$ , and  $\mathbf{u}_0^*$ ,  $\mathbf{u}_{1c}^*$ ,  $\mathbf{u}_{1s}^*$ , ...,  $\mathbf{u}_{Mc}^*$ ,  $\mathbf{u}_{Ms}^*$ ) one by one. The duration of each perturbation is one rotor revolution. The perturbations are applied first in the positive then in the negative direction. Store the time history of the data necessary for the aeroacoustic calculations.
3. Obtain the perturbation time history of the chosen output, where the output has dimension  $\mathbf{y} \in \mathbb{R}^l$ . In the case of aeroacoustic measures, the data is processed with an aeroacoustic solver to obtain the perturbation time history of the chosen composite acoustic measure (*e.g.*, acoustic pressure).
4. Compute the time-varying partial derivatives using central difference approximations. The derivative corresponding to the  $i^{th}$  output relative to the perturbation in the  $j^{th}$  element of the augmented state vector of Eq. (9.80a):

$$\frac{\partial y_i}{\partial X_j}(\psi) = \frac{1}{2\Delta X_j} [y_{ij}^+(\psi) - y_{ij}^-(\psi)] \quad (9.82)$$

where  $\Delta X_j$  is the size of the perturbation in the  $j^{th}$  augmented state vector. These derivatives together constitute an interim time-periodic matrix  $\hat{\mathbf{P}}(\psi) \in \mathbb{R}^{l \times n(2N+1)}$ . Similarly, the partial derivatives computed from the perturbations in the augmented control vector of Eq. (9.80b) form an interim time-periodic matrix  $\hat{\mathbf{Q}}(\psi) \in \mathbb{R}^{l \times m(2M+1)}$ .

5. Perform a Fourier decomposition of each element of the interim matrices  $\hat{\mathbf{P}}(\psi)$  and  $\hat{\mathbf{Q}}(\psi)$ :

$$\hat{\mathbf{P}} = \hat{\mathbf{P}}_0 + \sum_{k=1}^L \hat{\mathbf{P}}_{lc} \cos k\psi + \hat{\mathbf{P}}_{ls} \sin k\psi \quad (9.83a)$$

$$\hat{\mathbf{Q}} = \hat{\mathbf{Q}}_0 + \sum_{k=1}^L \hat{\mathbf{Q}}_{lc} \cos k\psi + \hat{\mathbf{Q}}_{ls} \sin k\psi \quad (9.83b)$$

Then, the high-order time-invariant output and feedthrough matrices  $\mathbf{C}$  and  $\mathbf{D}$  are given by:

$$\mathbf{C}_p^T = [\hat{\mathbf{P}}_0^T \hat{\mathbf{P}}_{1c}^T \hat{\mathbf{P}}_{1s}^T \dots \hat{\mathbf{P}}_{Lc}^T \hat{\mathbf{P}}_{Ls}^T] \quad (9.84a)$$

$$\mathbf{D}_p^T = [\hat{\mathbf{Q}}_0^T \hat{\mathbf{Q}}_{1c}^T \hat{\mathbf{Q}}_{1s}^T \dots \hat{\mathbf{Q}}_{Lc}^T \hat{\mathbf{Q}}_{Ls}^T] \quad (9.84b)$$

It is worth noting that Step 2 and 3 require performing  $n_p = 2n_\psi[n(2N+1) + m(2M+1)]$  evaluations of the rotorcraft flight dynamics and aeroacoustics, where  $n_\psi$  is the number of azimuthal steps. Or, equivalently,  $n_{rev} = 2[n(2N+1) + m(2M+1)]$  rotor revolutions are required for the output linearization.

While the methodology was only developed to obtain high-order LTI output equations as the vehicle dynamics was still derived through harmonic decomposition, it is straightforward to extend the methodology to obtain high-order LTI equations for system's dynamics. In fact, one would simply need to substitute the perturbation time history of the output vector in Eq. (9.82) with that of the state vector and repeat Steps 4 and 5 to obtain the system and output matrices  $\mathbf{A}$  and  $\mathbf{B}$  of the same form of Eq. (9.81). The methodology was applied to a relatively complex helicopter model including the periodic rigid-body and rotor dynamics to derive high-order LTI models suitable for vibration and acoustic predictions. The application of the methodology toward the approximation of the time-periodic main rotor forces and moments yielded nearly identical results to those obtained with harmonic decomposition.

## 9.4 Deeper Dive into Harmonic Balance and Harmonic Decomposition

### 9.4.1 Periodic Trim Problem Definition

Consider a nonlinear time-periodic (NLTP) system in first-order form:

$$\dot{\mathbf{x}} = \mathbf{f}(\mathbf{x}, \mathbf{u}, t) \quad (9.85)$$

where  $\mathbf{x}(t) \in \mathbb{R}^n$  is the state vector,  $\mathbf{u}(t) \in \mathbb{R}^m$  is the input vector, and  $t$  is time. The nonlinear function  $\mathbf{f}$  is  $T$ -periodic in  $t$  such that:

$$\mathbf{f}(\mathbf{x}, \mathbf{u}, t) = \mathbf{f}(\mathbf{x}, \mathbf{u}, t + T) \quad (9.86)$$

Let  $\mathbf{x}^*(t)$  and  $\mathbf{u}^*(t)$  represent a periodic solution of the system such that  $\mathbf{x}^*(t) = \mathbf{x}^*(t + T)$  and  $\mathbf{u}^*(t) = \mathbf{u}^*(t + T)$ . Then, the balance problem is stated as follows: determine  $\mathbf{x}^*(t)$  and  $\mathbf{u}^*(t)$  such that:

$$\dot{\mathbf{x}}^* = \mathbf{f}(\mathbf{x}^*, \mathbf{u}^*, t) \quad (9.87)$$

where  $\dot{\mathbf{x}}^*(t) = \dot{\mathbf{x}}^*(t + T)$ . In other words, the balance problem consists of determining the periodic state and control vectors such that the system dynamics are periodic.

### 9.4.2 Modified Harmonic Balance

Assume that the fundamental period  $T$  of the nonlinear time-periodic system is known. The proposed algorithm is iterative in nature, in that a candidate solution is refined over a series of computational steps until a convergence criteria is reached. Consider the candidate periodic solution at iteration  $k$  of the algorithm:  $\mathbf{x}_k^*(t)$  and  $\mathbf{u}_k^*(t)$ . One iteration of the algorithm begins with approximating the candidate periodic solution using a Fourier series with a finite number of harmonics:

$$\mathbf{x}_k^* = \mathbf{x}_{k_0}^* + \sum_{i=1}^N \mathbf{x}_{k_{ic}}^* \cos\left(\frac{2\pi i t}{T}\right) + \mathbf{x}_{k_{is}}^* \sin\left(\frac{2\pi i t}{T}\right) \quad (9.88a)$$

$$\mathbf{u}_k^* = \mathbf{u}_{k_0}^* + \sum_{j=1}^M \mathbf{u}_{k_{jc}}^* \cos\left(\frac{2\pi j t}{T}\right) + \mathbf{u}_{k_{js}}^* \sin\left(\frac{2\pi j t}{T}\right) \quad (9.88b)$$

where the Fourier coefficients are given by:

$$\mathbf{x}_{k_0}^* = \frac{1}{T} \int_0^T \mathbf{x}_k^* d\tau \quad (9.89a)$$

$$\mathbf{x}_{k_{ic}}^* = \frac{2}{T} \int_0^T \mathbf{x}_k^* \cos\left(\frac{2\pi i \tau}{T}\right) d\tau \quad (9.89b)$$

$$\mathbf{x}_{k_{is}}^* = \frac{2}{T} \int_0^T \mathbf{x}_k^* \sin\left(\frac{2\pi i \tau}{T}\right) d\tau \quad (9.89c)$$

$$\mathbf{u}_{k_0}^* = \frac{1}{T} \int_0^T \mathbf{u}_k^* d\tau \quad (9.90a)$$

$$\mathbf{u}_{k_{jc}}^* = \frac{2}{T} \int_0^T \mathbf{u}_k^* \cos\left(\frac{2\pi j \tau}{T}\right) d\tau \quad (9.90b)$$

$$\mathbf{u}_{k_{js}}^* = \frac{2}{T} \int_0^T \mathbf{u}_k^* \sin\left(\frac{2\pi j \tau}{T}\right) d\tau \quad (9.90c)$$

The candidate periodic solution is re-written in terms of its respective Fourier coefficients:

$$\mathbf{X}_k^{*T} = [\mathbf{x}_{k_0}^{*T} \mathbf{x}_{k_{1c}}^{*T} \mathbf{x}_{k_{1s}}^{*T} \dots \mathbf{x}_{k_{Nc}}^{*T} \mathbf{x}_{k_{Ns}}^{*T}] \quad (9.91a)$$

$$\mathbf{U}_k^{*T} = [\mathbf{u}_{k_0}^{*T} \mathbf{u}_{k_{1c}}^{*T} \mathbf{u}_{k_{1s}}^{*T} \dots \mathbf{u}_{k_{Nc}}^{*T} \mathbf{u}_{k_{Ns}}^{*T}] \quad (9.91b)$$

Since the balance problem simultaneously solves for the periodic solution and the necessary control inputs that ensure it, the harmonic realization of the candidate periodic solution of Eq. (9.91a) is augmented with the harmonic realization of the candidate control inputs of Eq. (9.91b) to form the vector of unknowns at iteration  $k$ :

$$\boldsymbol{\Theta}_k^T = [\mathbf{X}_k^{*T} \mathbf{U}_k^{*T}] \quad (9.92)$$

where  $\Theta_k \in \mathbb{R}^{n(2N+1)+m(2M+1)}$ .

Next, the state derivative vector calculated along the candidate periodic solution over a single periodic orbit is decomposed into a finite number of harmonics via Fourier analysis:

$$\dot{\mathbf{x}}_k^* = \dot{\mathbf{x}}_{k_0}^* + \sum_{i=1}^N \dot{\mathbf{x}}_{k_{ic}}^* \cos\left(\frac{2\pi i t}{T}\right) + \dot{\mathbf{x}}_{k_{is}}^* \sin\left(\frac{2\pi i t}{T}\right) \quad (9.93)$$

where the state derivative Fourier coefficients are:

$$\dot{\mathbf{x}}_{k_0}^* = \frac{1}{T} \int_0^T \mathbf{f}(\mathbf{x}_k^*, \mathbf{u}_k^*, \tau) d\tau \quad (9.94a)$$

$$\dot{\mathbf{x}}_{k_{ic}}^* = \frac{2}{T} \int_0^T \mathbf{f}(\mathbf{x}_k^*, \mathbf{u}_k^*, \tau) \cos\left(\frac{2\pi i \tau}{T}\right) d\tau \quad (9.94b)$$

$$\dot{\mathbf{x}}_{k_{is}}^* = \frac{2}{T} \int_0^T \mathbf{f}(\mathbf{x}_k^*, \mathbf{u}_k^*, \tau) \sin\left(\frac{2\pi i \tau}{T}\right) d\tau \quad (9.94c)$$

Note that the number of state derivative harmonics that are retained in Eq. (9.93) is equal to the number of state harmonics retained in Eq. (9.88a) (*i.e.*,  $N$ ). Consider differentiating the candidate periodic solution of Eq. (9.88a):

$$\dot{\mathbf{x}}_k^* = \underbrace{\frac{d}{dt}(\mathbf{x}_{k_0}^*)}_{\dot{\mathbf{x}}_{k_0}^*} + \sum_{i=1}^N \underbrace{\left[ \frac{d}{dt}(\mathbf{x}_{k_{ic}}^*) + \frac{2\pi i}{T} \mathbf{x}_{k_{is}}^* \right]}_{\dot{\mathbf{x}}_{k_{ic}}^*} \cos\left(\frac{2\pi i t}{T}\right) + \underbrace{\left[ \frac{d}{dt}(\mathbf{x}_{k_{is}}^*) - \frac{2\pi i}{T} \mathbf{x}_{k_{ic}}^* \right]}_{\dot{\mathbf{x}}_{k_{is}}^*} \sin\left(\frac{2\pi i t}{T}\right) \quad (9.95)$$

Since at equilibrium the Fourier coefficients of the system dynamics are constant (*i.e.*, their time derivative is zero), the following integral relations are true:

$$\dot{\mathbf{x}}_0^* = \mathbf{0} \quad (9.96a)$$

$$\dot{\mathbf{x}}_{ic}^* = \frac{2\pi i}{T} \mathbf{x}_{is}^* \quad (9.96b)$$

$$\dot{\mathbf{x}}_{is}^* = -\frac{2\pi i}{T} \mathbf{x}_{ic}^* \quad (9.96c)$$

A total of  $n(2N+1)$  constraints are formed by requiring that the state derivative Fourier coefficients in Eq. (9.94) and the state Fourier coefficients in Eq. (9.89) satisfy the integral relations in Eq. (9.96). This leads to the definition of the error vector at the iteration  $k$  as:

$$\mathbf{e}_k^T = \mathbf{W} \left[ (\dot{\mathbf{x}}_{k_0}^*)^T \left( \dot{\mathbf{x}}_{k_{ic}}^* - \frac{2\pi i}{T} \mathbf{x}_{k_{is}}^* \right)^T \left( \dot{\mathbf{x}}_{k_{is}}^* + \frac{2\pi i}{T} \mathbf{x}_{k_{ic}}^* \right)^T \right] \quad (9.97)$$

where  $\mathbf{e}_k \in \mathbb{R}^{n(2N+1)}$  and  $\mathbf{W} \in \mathbb{R}^{n(2N+1) \times n(2N+1)}$  is a diagonal scaling matrix to make all elements of the error vector approximately the same order of magnitude (*e.g.*, 1 deg error is equivalent to 1 ft error).

Next, the NLTP system is linearized at incremental time steps along the candidate periodic solution. Consider the case of small disturbances:

$$\mathbf{x} = \mathbf{x}_k^* + \Delta \mathbf{x} \quad (9.98a)$$

$$\mathbf{u} = \mathbf{u}_k^* + \Delta \mathbf{u} \quad (9.98b)$$

where  $\Delta \mathbf{x}$  and  $\Delta \mathbf{u}$  are the state and control perturbation vectors from the candidate periodic solution. A Taylor series expansion is performed on the state derivative vector. Neglecting terms higher than first order results in the following equation:

$$\mathbf{f}(\mathbf{x}_k^* + \Delta \mathbf{x}, \mathbf{u}_k^* + \Delta \mathbf{u}, t) = \mathbf{f}(\mathbf{x}_k^*, \mathbf{u}_k^*, t) + \mathbf{F}_k(t) \Delta \mathbf{x} + \mathbf{G}_k(t) \Delta \mathbf{u} \quad (9.99)$$

where:

$$\mathbf{F}_k(t) = \frac{\partial \mathbf{f}(\mathbf{x}, \mathbf{u})}{\partial \mathbf{x}} \Big|_{\mathbf{x}_k^*, \mathbf{u}_k^*} \quad (9.100a)$$

$$\mathbf{G}_k(t) = \frac{\partial \mathbf{f}(\mathbf{x}, \mathbf{u})}{\partial \mathbf{u}} \Big|_{\mathbf{x}_k^*, \mathbf{u}_k^*} \quad (9.100b)$$

Note that the state-space matrices in (9.100a) and (9.100b) have time-periodic coefficients such that  $\mathbf{F}_k(t) = \mathbf{F}_k(t+T)$  and  $\mathbf{G}_k(t) = \mathbf{G}_k(t+T)$ . Equation (9.99) yields a linear time-periodic (LTP) approximation of the NLTP system of Eq. (9.85) as follows:

$$\Delta \dot{\mathbf{x}} = \mathbf{F}_k(t) \Delta \mathbf{x} + \mathbf{G}_k(t) \Delta \mathbf{u} \quad (9.101)$$

Hereafter, the notation is simplified by dropping the  $\Delta$  in front of the linearized perturbation state and control vectors while keeping in mind that these vectors represent perturbations from a periodic equilibrium. Next, the state and output vectors of the LTP systems are decomposed into a finite number of harmonics via Fourier analysis:

$$\mathbf{x} = \mathbf{x}_0 + \sum_{i=1}^N \mathbf{x}_{ic} \cos\left(\frac{2\pi i t}{T}\right) + \mathbf{x}_{is} \sin\left(\frac{2\pi i t}{T}\right) \quad (9.102a)$$

$$\mathbf{u} = \mathbf{u}_0 + \sum_{j=1}^M \mathbf{u}_{jc} \cos\left(\frac{2\pi j t}{T}\right) + \mathbf{u}_{js} \sin\left(\frac{2\pi j t}{T}\right) \quad (9.102b)$$

Note that the number of state harmonics retained in Eq. (9.102a) is the same as in Eqs. (9.88a) and (9.93) (*i.e.*,  $N$ ), whereas the number of control input harmonics retained in Eq. (9.102b) is the same as in Eq. (9.88b). As shown in [LP17], the LTP model can be approximated by a higher-order linear time-invariant (LTI) model in first-order form through the harmonic decomposition methodology:

$$\dot{\mathbf{X}} = \mathbf{A}_k \mathbf{X} + \mathbf{B}_k \mathbf{U} \quad (9.103)$$

where the augmented state and control vectors are:

$$\mathbf{X}^T = [\mathbf{x}_0^T \ \mathbf{x}_{1c}^T \ \mathbf{x}_{1s}^T \ \dots \ \mathbf{x}_{Ns}^T] \quad (9.104a)$$

$$\mathbf{U}^T = [\mathbf{u}_0^T \ \mathbf{u}_{1c}^T \ \mathbf{u}_{1s}^T \ \dots \ \mathbf{u}_{Mc}^T \ \mathbf{u}_{Ms}^T] \quad (9.104b)$$

and where  $\mathbf{A}_k \in \mathbb{R}^{n(2N+1) \times n(2N+1)}$  and  $\mathbf{B}_k \in \mathbb{R}^{n(2N+1) \times m(2M+1)}$  are the linear time-invariant system and control matrices. These are given by:

$$\mathbf{A}_k = \begin{bmatrix} \mathbf{F}_{k_{0,0}} & \mathbf{F}_{k_{0,1c}} & \mathbf{F}_{k_{0,1s}} & \cdots & \mathbf{F}_{k_{0,Nc}} & \mathbf{F}_{k_{0,Ns}} \\ \mathbf{F}_{k_{1c,0}} & \mathbf{F}_{k_{1c,1c}} & -\frac{2\pi}{T} + \mathbf{F}_{k_{1c,1s}} & \cdots & \mathbf{F}_{k_{1c,Nc}} & \mathbf{F}_{k_{1c,Ns}} \\ \mathbf{F}_{k_{1s,0}} & \frac{2\pi}{T} + \mathbf{F}_{k_{1s,1c}} & \mathbf{F}_{k_{1s,1s}} & \cdots & \mathbf{F}_{k_{1s,Nc}} & \mathbf{F}_{k_{1s,Ns}} \\ \vdots & \vdots & \vdots & \ddots & \vdots & \vdots \\ \mathbf{F}_{k_{Nc,0}} & \mathbf{F}_{k_{Nc,1c}} & \mathbf{F}_{k_{Nc,1s}} & \cdots & \mathbf{F}_{k_{Nc,Nc}} & -\frac{2\pi N}{T} + \mathbf{F}_{k_{Nc,Ns}} \\ \mathbf{F}_{k_{Ns,0}} & \mathbf{F}_{k_{Ns,1c}} & \mathbf{F}_{k_{Ns,1s}} & \cdots & \frac{2\pi N}{T} + \mathbf{F}_{k_{Ns,Nc}} & \mathbf{F}_{k_{Ns,Ns}} \end{bmatrix} \quad (9.105a)$$

These matrices are used to define the Jacobian matrix of the harmonic balancing algorithm at iteration  $k$ :

$$\mathbf{J}_k = [\mathbf{A}_k \ \mathbf{B}_k] \quad (9.106)$$

where  $\mathbf{J}_k \in \mathbb{R}^{n(2N+1) \times [n(2N+1)+m(2M+1)]}$ .

The Jacobian matrix is used in each algorithm iteration to compute a candidate periodic solution and controls update (*i.e.*, the vector of unknowns) given the error vector at that iteration via a Newton-Raphson scheme [Ypm95]. It is clear that the Jacobian matrix is not square because the number of constraints in Eq. (9.96) is less than the number of unknowns in Eq. (9.92). In fact, the number of constraints is  $n(2N+1)$

whereas the number of unknowns is  $n(2N + 1) + m(2M + 1)$ . This leads to an under-determined problem which does not have a unique solution. To make the problem square such that the solution is unique,  $m(2M + 1)$  conditions have to be specified. These are the trim conditions. Because typical periodically-forced flight vehicles such as helicopters only utilize control input bandwidths significantly lower than the forcing frequency, one can safely assume the control input harmonics higher than the zeroth to be zero. This corresponds to imposing  $2Mm$  conditions, which brings down the number of unknowns to  $n(2N + 1) + m$ . It follows that  $m$  conditions still need to be specified. Note that if the  $m$  inputs are given and the corresponding equilibrium solution is required, then the problem in consideration becomes a closed system. On the other hand, in the case where one or more (possibly all) of the  $m$  control inputs is unknown, then each input is used to ensure some desired condition (e.g., trim equation). For periodically-forced aerospace vehicles for which the vehicle dynamics are invariant with respect to position and heading, the zeroth harmonic of the position and heading can be arbitrarily assigned and removed from the vector of unknowns. Since these vehicles typically employ control about four axes (*i.e.*, roll, pitch, yaw, and heave) leading to four control inputs, fixing the three components of the zeroth harmonic of the position ( $x_0, y_0, z_0$ ) and heading ( $\psi_0$ ) at equilibrium leads to a square problem. Hence, Newton Raphson is used to find a candidate periodic solution update (in harmonic form):

$$\hat{\Theta}_{k+1} = \hat{\Theta}_k - \hat{\mathbf{J}}_k^{-1} \mathbf{e}_k \quad (9.107)$$

where  $\hat{\Theta}_k$  and  $\hat{\mathbf{J}}_k$  are the vector of unknowns and the Jacobian matrix deprived of the unknowns that were fixed, respectively. As a final step, the new candidate periodic solution is reconstructed in the time domain:

$$\mathbf{x}_{k+1}^* = \mathbf{x}_{k+10}^* + \sum_{i=1}^N \mathbf{x}_{k+1ic}^* \cos\left(\frac{2\pi it}{T}\right) + \mathbf{x}_{k+1is}^* \sin\left(\frac{2\pi it}{T}\right) \quad (9.108a)$$

$$\mathbf{u}_{k+1}^* = \mathbf{u}_{k0}^* + \sum_{j=1}^M \mathbf{u}_{k+1jc}^* \cos\left(\frac{2\pi jt}{T}\right) + \mathbf{u}_{k+1js}^* \sin\left(\frac{2\pi jt}{T}\right) \quad (9.108b)$$

The next iteration of the algorithm then proceeds with this new candidateF solution, starting from Eqs. (9.88a) and (9.88b). The algorithm is stopped when  $\|\mathbf{e}_k\|_\infty$  becomes less than an arbitrary tolerance. It is worth noting that the algorithm requires a first guess of the periodic solution over one periodic orbit. A flowchart of the algorithm is shown in Fig. 9.2.

An added benefit of the algorithm is that, to update the solution, a higher-order LTI approximation of the NLTP system is computed at each iteration along the candidate periodic solution. Thus, the algorithm not only solves for the periodic solution of NLTP systems, but also simultaneously constructs a higher-order LTI approximation of the NLTP system. The higher-order LTI system can readily be used for stability analysis, feedback control design, or in the prediction of loads and vibrations (see, *e.g.*, [LP17; SH16]).

### 9.4.3 Modal Participation Factors

Modal participation factors are a useful tool for quantifying the influence of higher harmonics on the dynamics of time-periodic systems. Modal participation factors describe the modal participation of each state to each mode through the relative magnitude of the harmonic components of each state. Recently, it has been shown that modal participation factors can be computed directly from harmonic decomposition models through the following procedure [LP16]:

1. Solve for the eigenvalues and eigenvectors of the high-order LTI system matrix  $\mathbf{A}$  in Eq. (6.9a). The eigenvector corresponding to the  $k^{th}$  mode will be in the form:

$$\mathbf{X}_k^T = [\mathbf{x}_{k,0}^T \mathbf{x}_{k,1c}^T \mathbf{x}_{k,1s}^T \dots \mathbf{x}_{k,Nc}^T \mathbf{x}_{k,Ns}^T] \quad (9.109)$$

where  $\mathbf{x}_{k,0}$  is the zeroth harmonic component, and  $\mathbf{x}_{k,nc}$  and  $\mathbf{x}_{k,ms}$  are respectively the  $n^{th}$  cosine and sine components of the periodic eigenvector corresponding to the  $k^{th}$  mode. The eigenvalues of the  $\mathbf{A}$  matrix are equivalent to the Floquet exponents of the LTP system.

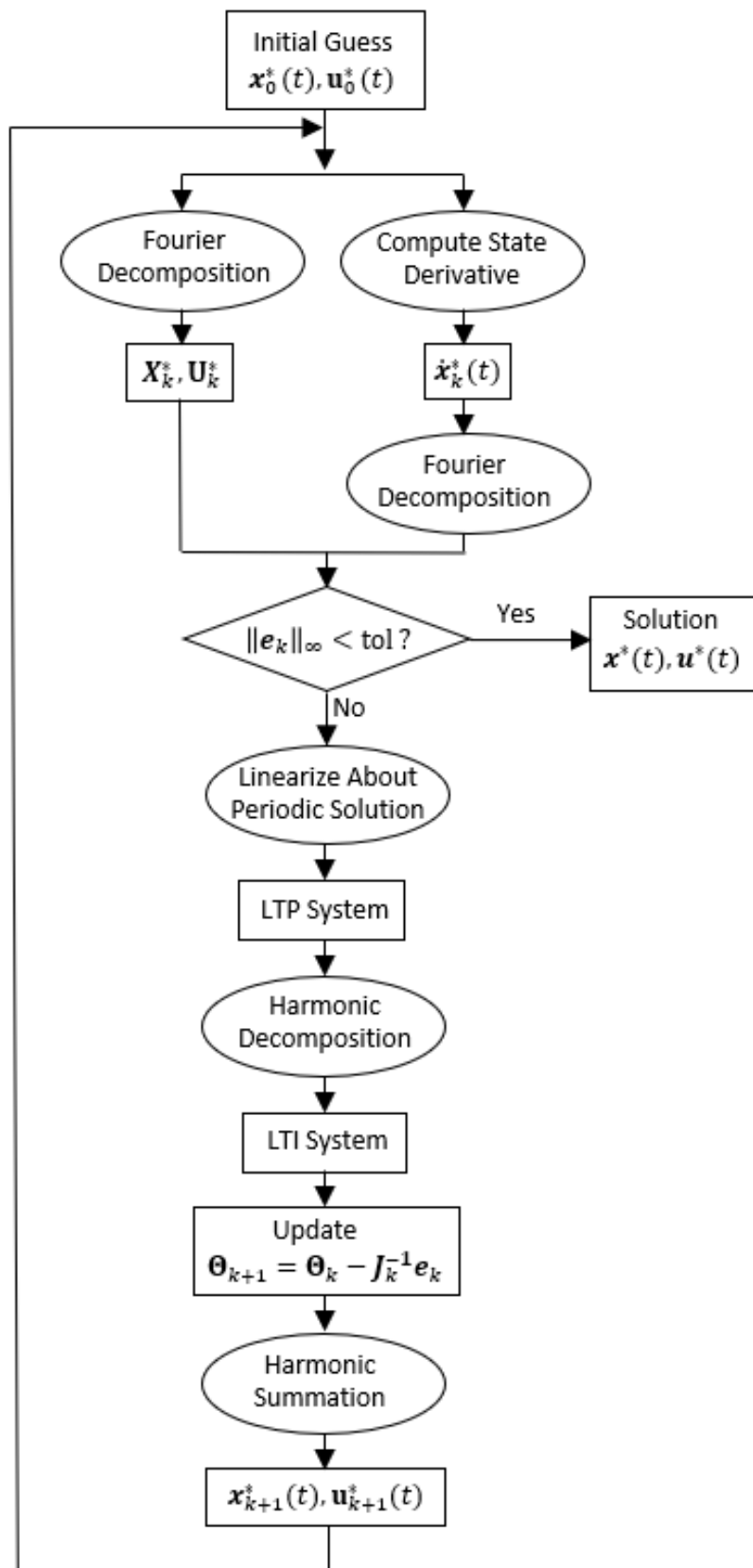


Figure 9.2: Harmonic balance algorithm flowchart.

2. Convert the LTI eigenvector harmonic states from real-trigonometric Fourier coefficients to complex-exponential Fourier coefficients as follows:

$$c_{j,k,0} = x_{j,k,0} \quad (9.110a)$$

$$c_{j,k,+n} = \frac{x_{j,k,nc} - ix_{j,k,ns}}{2} \quad (9.110b)$$

$$c_{j,k,-n} = \frac{x_{j,k,nc} + ix_{j,k,ns}}{2} \quad (9.110c)$$

where  $x_{j,k,0}$ ,  $x_{j,k,nc}$ , and  $x_{j,k,ns}$  are respectively the zeroth,  $n^{th}$  cosine, and  $n^{th}$  sine real-trigonometric harmonic LTI eigenvector elements corresponding to the  $j^{th}$  LTP system state and  $k^{th}$  mode.

3. Compute the modal participation factors by normalizing the modal participation with respect to the sum of the magnitudes of all harmonic components for each particular state and mode:

$$\phi_{j,k,n} = |c_{j,k,n}| \left( \sum_{i=-N}^N |c_{j,k,i}| \right)^{-1} \quad (9.111)$$

where  $N$  is the number of state harmonics retained when performing harmonic decomposition.

It is worth noting that those LTI system modes corresponding to eigenvalues with imaginary parts between  $\pm\omega/2$  are referred to as the base modes. Only the base modes are needed to completely describe the system with the understanding that higher-frequency modes simply shift the naming of harmonics and do not affect the actual modal participation content.

#### 9.4.4 Example 1: Vibrational Stabilization of an Inverted Pendulum

The harmonic decomposition methodology is explained through a simple example involving an inverted pendulum with a vibrating suspension point, shown in Fig. 9.3. Consider the dynamics of such pendulum:

$$L\ddot{\theta} - (g + A)\theta = 0 \quad (9.112)$$

where  $L$  is the pendulum length,  $A$  the acceleration resulting from the periodic displacement of the point of suspension, and  $g$  is the gravitational acceleration. Assume that the displacement of the point of suspension is given by:

$$D = a \sin \psi \quad (9.113)$$

where  $\psi = \Omega t$ . Then, the acceleration  $A$  of the suspension point is:

$$A = \ddot{D} = -a\Omega^2 \sin \psi \quad (9.114)$$

The system in Eq. (9.141) can be reformulated as a system of ordinary differential equations (ODEs) such that:

$$\dot{\mathbf{x}} = \begin{bmatrix} 0 & \frac{g}{L} - \frac{a}{L}\Omega^2 \sin \psi \\ 0 & 1 \end{bmatrix} \mathbf{x} = \mathbf{F}(\psi) \mathbf{x} \quad (9.115)$$

where  $\mathbf{x}^T = [\dot{\theta} \ \theta]$ . Note that  $\mathbf{F}(\psi) = \mathbf{F}(\psi + \Omega T)$ , where  $T = 2\pi/\Omega$ . Thus, the system in Eq. (9.115) is a linear time-periodic (LTP) system.

Consider now decomposing the state vector into harmonics of the fundamental frequency  $\Omega$ , such that:

$$\mathbf{x} = \mathbf{x}_0 + \sum_{n=1}^N [\mathbf{x}_{nc} \cos(n\psi) + \mathbf{x}_{ns} \sin(n\psi)] \quad (9.116)$$

Then, it can be shown [Lop16; LP17] that the system in Eq. (9.115) is approximated with a higher-order linear time-invariant (LTI) system of the form:

$$\dot{\mathbf{X}} = \mathbf{AX} \quad (9.117)$$

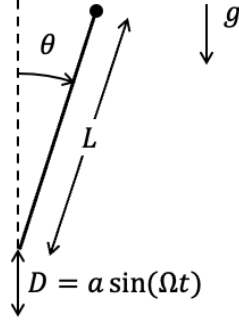


Figure 9.3: Inverted pendulum with the point of suspension being vibrated.

where  $\mathbf{X}^T = [\mathbf{x}_0^T \ \mathbf{x}_{1c}^T \ \mathbf{x}_{1s}^T \ \dots \ \mathbf{x}_{Nc}^T \ \mathbf{x}_{Ns}^T]$  is the augmented state vector and:

$$\mathbf{A} = \begin{bmatrix} \mathbf{H}_{0F} & \mathbf{H}_{0F^{1c}} & \mathbf{H}_{0F^{1s}} & \cdots & \mathbf{H}_{0F^{Nc}} & \mathbf{H}_{0F^{Ns}} \\ \mathbf{H}_{1cF} & \mathbf{H}_{1cF^{1s}} & -\Omega + \mathbf{H}_{1cF^{1s}} & \cdots & \mathbf{H}_{1cF^{Nc}} & \mathbf{H}_{1cF^{Ns}} \\ \mathbf{H}_{1sF} & \Omega + \mathbf{H}_{1sF^{1s}} & \mathbf{H}_{1sF^{1s}} & \cdots & \mathbf{H}_{1sF^{Nc}} & \mathbf{H}_{1sF^{Ns}} \\ \vdots & \vdots & \vdots & \ddots & \vdots & \vdots \\ \mathbf{H}_{NcF} & \mathbf{H}_{NcF^{1s}} & \mathbf{H}_{NcF^{1s}} & \cdots & \mathbf{H}_{NcF^{Nc}} & -N\Omega + \mathbf{H}_{NcF^{Ns}} \\ \mathbf{H}_{NsF} & \mathbf{H}_{NsF^{1s}} & \mathbf{H}_{NsF^{1s}} & \cdots & N\Omega + \mathbf{H}_{NsF^{Nc}} & \mathbf{H}_{NsF^{Ns}} \end{bmatrix} \quad (9.118)$$

The  $\mathbf{A}$  matrix coefficients are given by:

$$\mathbf{H}_{0M} = \frac{1}{2\pi} \int_0^{2\pi} \mathbf{F}(\psi) d\psi \quad (9.119a)$$

$$\mathbf{H}_{icM} = \frac{1}{\pi} \int_0^{2\pi} \mathbf{F}(\psi) \cos(n\psi) d\psi \quad (9.119b)$$

$$\mathbf{H}_{isM} = \frac{1}{\pi} \int_0^{2\pi} \mathbf{F}(\psi) \sin(n\psi) d\psi \quad (9.119c)$$

$$\mathbf{H}_{0F^{nc}} = \frac{1}{2\pi} \int_0^{2\pi} \mathbf{F}^{nc}(\psi) d\psi \quad (9.119d)$$

$$\mathbf{H}_{icF^{nc}} = \frac{1}{\pi} \int_0^{2\pi} \mathbf{F}^{nc}(\psi) \cos(n\psi) d\psi \quad (9.119e)$$

$$\mathbf{H}_{isF^{nc}} = \frac{1}{\pi} \int_0^{2\pi} \mathbf{F}^{nc}(\psi) \sin(n\psi) d\psi \quad (9.119f)$$

$$\mathbf{H}_{0F^{ns}} = \frac{1}{2\pi} \int_0^{2\pi} \mathbf{F}^{ns}(\psi) d\psi \quad (9.119g)$$

$$\mathbf{H}_{icF^{ns}} = \frac{1}{\pi} \int_0^{2\pi} \mathbf{F}^{ns}(\psi) \cos(n\psi) d\psi \quad (9.119h)$$

$$\mathbf{H}_{isF^{ns}} = \frac{1}{\pi} \int_0^{2\pi} \mathbf{F}^{ns}(\psi) \sin(n\psi) d\psi \quad (9.119i)$$

where:

$$\mathbf{F}^{nc}(\psi) = \mathbf{F}(\psi) \cos \psi \quad (9.120a)$$

$$\mathbf{F}^{ns}(\psi) = \mathbf{F}(\psi) \sin \psi \quad (9.120b)$$

Because the periodicity in Eq. (9.115) is limited to frequencies of one per forcing cycle, it is sufficient to retain up to the first harmonic in the harmonic decomposition of state vector in Eq. (9.116). By doing so, the

LTP system in Eq. (9.115) is transformed into an equivalent LTI system with a system matrix:

$$\mathbf{A} = \begin{bmatrix} 0 & \frac{g}{L} & 0 & 0 & 0 & \Omega^2 \frac{a}{2L} \\ 1 & 0 & 0 & 0 & 0 & 0 \\ 0 & 0 & 0 & \frac{g}{L} & -\Omega & 0 \\ 0 & 0 & 1 & 0 & 0 & -\Omega \\ 0 & \Omega^2 \frac{a}{L} & \Omega & 0 & 0 & \frac{g}{L} \\ 0 & 0 & 0 & \Omega & 1 & 0 \end{bmatrix} \quad (9.121)$$

and where  $\mathbf{x}^T = [\dot{\theta}_0 \ \theta_0 \ \dot{\theta}_{1c} \ \theta_{1c} \ \dot{\theta}_{1s} \ \theta_{1s}]$  is the augmented state vector. The stability of the system will be determined by the eigenvalues of the  $\mathbf{A}$  matrix. The eigenvalues are given by:

$$\lambda_{1,2} = \pm c_1 \quad (9.122a)$$

$$\lambda_{3,4} = \pm c_2 \quad (9.122b)$$

$$\lambda_{5,6} = \pm \sqrt{c_3 + c_4 - \frac{c_5}{c_3}} \quad (9.122c)$$

where:

$$c_1 = \sqrt{c_4 - \frac{c_3}{2} + \frac{c_5}{2c_3} - \frac{1}{2}\sqrt{3} \left( c_3 \frac{c_5}{c_3} i \right)} \quad (9.123a)$$

$$c_2 = \sqrt{c_4 - \frac{c_3}{2} + \frac{c_5}{2c_3} + \frac{1}{2}\sqrt{3} \left( c_3 \frac{c_5}{c_3} i \right)} \quad (9.123b)$$

$$c_3 = \left\{ c_6 + \sqrt{\left[ c_6 + \frac{(6L^2 g - 4L^3 \Omega^2)^3}{216L^9} - c_7 \right]^2 + c_5^3} + \frac{(6L^2 g - 4L^3 \Omega^2)^3}{216L^9} - c_7 \right\}^{1/3} \quad (9.123c)$$

$$c_4 = \frac{6L^2 g - 4L^3 \Omega^2}{6L^3} \quad (9.123d)$$

$$c_5 = \frac{2L^3 \Omega^4 - L\Omega^4 a^2 + 6Lg^2}{6L^3} - \frac{(6L^2 g - 4L^3 \Omega^2)^2}{36L^6} \quad (9.123e)$$

$$c_6 = \frac{2L^2 \Omega^4 g - L\Omega^6 a^2 + 4L\Omega^2 g^2 - \Omega^4 a^2 g + 2g^3}{4L^3} \quad (9.123f)$$

$$c_7 = \frac{(6L^2 g - 4L^3 \Omega^2)(2L^3 \Omega^4 - L\Omega^4 a^2 + 6Lg^2)}{24L^6} \quad (9.123g)$$

It can be shown [Levi1995] that the inverted pendulum is strongly stable (*i.e.*, stable for a high-enough forcing frequency) if:

$$a < \frac{\pi^2}{32} L \quad (9.124)$$

Consider an inverted pendulum where  $g = 9.81 \text{ m/s}^2$ ,  $L = 1 \text{ m}$ , and  $a = \frac{1}{2} \left( \frac{\pi^2}{32} L \right)$ . Then, this pendulum will be stable for forcing frequencies  $\Omega \gtrapprox 40.59 \text{ rad/s}$ . For instance, the eigenvalues for the case where  $\Omega = 0 \text{ rad/s}$  (*i.e.*, no periodic forcing) are:

$$\lambda_1 = 3.1321, \quad \lambda_2 = -3.1321 \quad (9.125)$$

whereas the eigenvalues for the case where  $\Omega = 50 \text{ rad/s}$  are:

$$\lambda_{1,2} = \pm 4.5314i, \quad \lambda_{3,4} = \pm 47.4166i, \quad \lambda_{5,6} = \pm 51.9779i \quad (9.126)$$

The order of the system in Eq. (9.117) can be reduced by assuming that some fast states converge to a steady state quicker than some other slower states Kokotovic. As such, the augmented state vector in partitioned into fast and slow components:

$$\mathbf{X}^T = [\mathbf{X}_s^T \mathbf{X}_f^T] \quad (9.127)$$

Then, the system in Eq. (9.117) can be written as:

$$\begin{bmatrix} \dot{\mathbf{X}}_s \\ \dot{\mathbf{X}}_f \end{bmatrix} = \begin{bmatrix} \mathbf{A}_s & \mathbf{A}_{sf} \\ \mathbf{A}_{fs} & \mathbf{A}_f \end{bmatrix} \begin{bmatrix} \mathbf{X}_s \\ \mathbf{X}_f \end{bmatrix} \quad (9.128)$$

By neglecting the dynamics of the fast states (*i.e.*,  $\dot{\mathbf{X}}_f = 0$ ) and performing a few algebraic manipulations, the equations for a reduced-order system with the state vector composed of the slow states are:

$$\dot{\mathbf{X}}_s = \hat{\mathbf{A}}\mathbf{X}_s \quad (9.129)$$

where:

$$\hat{\mathbf{A}} = \mathbf{A}_s - \mathbf{A}_{sf}\mathbf{A}_f^{-1}\mathbf{A}_{fs} \quad (9.130)$$

In this study, the slow states are chosen as the zeroth harmonic states, whereas the fast states are taken as the higher harmonics:

$$\mathbf{X}_s = \mathbf{x}_0 \quad (9.131a)$$

$$\mathbf{X}_f^T = [\mathbf{x}_{1c}^T \mathbf{x}_{1s}^T] \quad (9.131b)$$

Then,

$$\mathbf{A}_s = \begin{bmatrix} 0 & \frac{g}{L} \\ 1 & 0 \end{bmatrix}, \quad \mathbf{A}_{sf} = \begin{bmatrix} 0 & 0 & 0 & \Omega^2 \frac{a}{2L} \\ 0 & 0 & 0 & 0 \end{bmatrix}, \quad \mathbf{A}_f = \begin{bmatrix} 0 & \frac{g}{L} & -\Omega & 0 \\ 1 & 0 & 0 & -\Omega \\ \Omega & 0 & 0 & \frac{g}{L} \\ 0 & \Omega & 1 & 0 \end{bmatrix}, \quad \mathbf{A}_{fs} = \begin{bmatrix} 0 & 0 \\ 0 & 0 \\ 0 & \Omega^2 \frac{a}{L} \\ 0 & 0 \end{bmatrix} \quad (9.132a-d)$$

Based on this setup, the reduced-order system matrix is:

$$\hat{\mathbf{A}} = \begin{bmatrix} 0 & \frac{g}{L} - \frac{\Omega^4 a^2}{2L(L\Omega^2 + g)} \\ 1 & 0 \end{bmatrix} \quad (9.133)$$

The eigenvalues of this matrix are:

$$\lambda_{1,2} = \pm \frac{\sqrt{2}\sqrt{-\Omega^4 a^2 + 2L\Omega^2 g + 2g^2}}{2\sqrt{L}\sqrt{L\Omega^2 + g}} \quad (9.134)$$

Setting  $\text{Re}(\lambda_{1,2}) = 0$ , solving for  $\Omega$ , and discarding any non-physical solution yields:

$$\begin{aligned} \Omega &= \pm \frac{1}{a} \sqrt{Lg + \sqrt{L^2 g^2 + 2a^2 g^2 + a^2}} \\ &\approx 28.89 \text{ rad/s} \end{aligned} \quad (9.135)$$

Note that this is only an approximation to the minimum frequency that yields neutral stability. In fact, as shown above, this frequency is  $\Omega \approx 40.59 \text{ rad/s}$ .

### 9.4.5 Example 2: Periodic Trim of the Vertical Dynamics of Flapping-Wing Vehicle

Despite apparent differences in shape and dimension, the dynamics of flapping-wing flyers/MAVs is mathematically similar to those of rotary-wing vehicles such as helicopters. In fact, the dynamics of flapping flight is described by NLTP systems of the coupled rigid-body and complex interactional aerodynamics between the wings, body, and the self-induced wake, similarly to helicopters. However, the relative importance of the time-periodic dynamics (*i.e.*, those dynamics with natural frequencies that are multiples of the fundamental frequency of the system) and the overall dynamics of the system (*i.e.*, averaged + time-periodic dynamics) is significantly higher for flapping-wing MAVs than it is for helicopters – approximately 7% for helicopters [Sae+19] and up to 50% for flapping-wing MAVs [HSP22; SR21a; SR]. This example considers the vertical flight dynamics of flapping-wing vehicles, as opposed to helicopters, due to its simplicity and yet representativeness of time-periodic phenomena.

Consider the NLTP vertical dynamics of a hovering flapping-wing micro-aerial-vehicle (FWMAV) derived in [HT16]:

$$\begin{bmatrix} \dot{z} \\ \dot{\phi} \\ \dot{w} \\ \ddot{\phi} \end{bmatrix} = \begin{bmatrix} w \\ \dot{\phi} \\ g - k_{d_1}|\dot{\phi}|w - k_L\dot{\phi}^2 \\ -k_{d_2}|\dot{\phi}|\dot{\phi} - k_{d_3}w\dot{\phi} \end{bmatrix} + \begin{bmatrix} 0 \\ 0 \\ 0 \\ \frac{1}{I_F} \cos(\omega t) \end{bmatrix} U \quad (9.136)$$

where  $z$  is the vertical position (positive down),  $\phi$  is the wing flapping angle,  $w$  is the vertical speed. The coefficient  $g$  is the gravitational acceleration whereas  $k_{d_1}$ ,  $k_{d_2}$ ,  $k_{d_3}$ , and  $k_L$  are constant parameters. In addition,  $I_F$  is the flapping moment of inertia,  $\omega$  is the flapping frequency, and  $U$  is the amplitude of the flapping control input torque. The state vector is  $\mathbf{x}^T = [z \ \phi \ w \ \dot{\phi}]$  and the control vector is  $\mathbf{u} = U$ . The state vector has dimension  $n = 4$  and the control vector has dimension  $m = 1$ . The system parameters are given for a hawk moth in [HT16] and provided in Table 9.1.

Table 9.1: Vertical dynamics parameters of a FWMAV representative of a hawk moth [HT16].

| Parameter | Numerical Value | Units             |
|-----------|-----------------|-------------------|
| $k_{d_1}$ | 0.0353739       | -                 |
| $k_{d_2}$ | 0.333915        | -                 |
| $k_{d_3}$ | 16.5766         | 1/m               |
| $k_L$     | 0.000621676     | m                 |
| $I_F$     | 0.0353739       | kg·m <sup>2</sup> |
| $\omega$  | 165.2478        | rad/s             |
| $g$       | 9.80665         | m/s <sup>2</sup>  |

An approximate periodic solution is sought to provide insights on the minimum number of harmonics to be retained in the harmonic balance solution. Figure 9.4 (dashed line) shows the approximate solution found by time marching the system dynamics over one fundamental period (*i.e.*,  $T = 2\pi/\omega$ ) starting from the equilibrium control input and initial wing flapping angles suggested in [HT16]. In this figure, the vertical position  $z$  and vertical velocity  $w$  are shown to vary 2-times-per-revolution (or 2/rev), whereas the flapping angle  $\phi$  and the flapping angular speed  $\dot{\phi}$  vary 1-time-per-revolution (or 1/rev). Based on these indications, state harmonics up to the second are retained in the harmonic balance algorithm (*i.e.*,  $N = 2$ ). On the other hand, because the periodicity of the control input (*i.e.*, the first cosine harmonic of the flapping torque) is incorporated in the system dynamics, only the zeroth harmonic is retained for the control input (*i.e.*,  $M = 0$ ). As such, the vector of  $n(2N + 1) + m(2M + 1) = 21$  unknowns is:

$$\Theta^T = \underbrace{[z_0 \ \phi_0 \ w_0 \ \dot{\phi}_0]}_{0^{\text{th}} \text{state harmonic}} \underbrace{[z_{1c} \ \phi_{1c} \ w_{1c} \ \dot{\phi}_{1c}]}_{1^{\text{st}} \text{state harmonic}} \underbrace{[z_{1s} \ \phi_{1s} \ w_{1s} \ \dot{\phi}_{1s}]}_{2^{\text{nd}} \text{state harmonic}} \underbrace{[z_{2c} \ \phi_{2c} \ w_{2c} \ \dot{\phi}_{2c}]}_{0^{\text{th}} \text{control harmonic}} \underbrace{[z_{2s} \ \phi_{2s} \ w_{2s} \ \dot{\phi}_{2s}]}_{\dots} \underbrace{U_0}_{\dots} \quad (9.137)$$

whereas the  $n(2N + 1) = 20$  constraints are:

$$[\dot{z}_0 \dot{\phi}_0 \dot{w}_0 \ddot{\phi}_0]^T = \mathbf{0} \quad (9.138a)$$

$$[\dot{z}_{1c} \dot{\phi}_{1c} \dot{w}_{1c} \ddot{\phi}_{1c}]^T - \omega [z_{1s} \phi_{1s} w_{1s} \dot{\phi}_{1s}]^T = \mathbf{0} \quad (9.138b)$$

$$[\dot{z}_{1s} \dot{\phi}_{1s} \dot{w}_{1s} \ddot{\phi}_{1s}]^T + \omega [z_{1c} \phi_{1c} w_{1c} \dot{\phi}_{1c}]^T = \mathbf{0} \quad (9.138c)$$

$$[\dot{z}_{2c} \dot{\phi}_{2c} \dot{w}_{2c} \ddot{\phi}_{2c}]^T - 2\omega [z_{2s} \phi_{2s} w_{2s} \dot{\phi}_{2s}]^T = \mathbf{0} \quad (9.138d)$$

$$[\dot{z}_{2s} \dot{\phi}_{2s} \dot{w}_{2s} \ddot{\phi}_{2s}]^T + 2\omega [z_{2c} \phi_{2c} w_{2c} \dot{\phi}_{2c}]^T = \mathbf{0} \quad (9.138e)$$

Because there are 21 unknowns and only 20 constraints, one unknown must be fixed and removed from the problem. Because the dynamics of the FWMAV are invariant with respect to position and heading [FDF05] (that is, if it is assumed that the air density does not depend on vertical position), the zeroth harmonic of the vertical position is set to an arbitrary value and removed from the unknowns, leading to a square problem. Here, the desired zeroth harmonic of the vertical position is set to zero (*i.e.*,  $z_0 = 0$ ).

In this example, the periodic solution is discretized with a time step of  $dt = T/n_t$ , where the number of evenly-spaced time steps is  $n_t = 360$ . The first guess is chosen as the combination of the the approximate periodic solution found via time marching and the control input that was used to compute it, which was taken from [HT16]:

$$\mathbf{u}_0^*(t) = 1.058 \sqrt{\frac{2gI_F^2\omega^2}{k_L}} \quad (9.139)$$

This was derived using a third-order averaging scheme in [HT16]. Based on this setup, the modified harmonic balance algorithm is used to refine the initial guess and to compute the approximate LTI dynamics about the refined solution. The numerical solution thus obtained is shown in Fig. 9.4 using an absolute error tolerance of  $1e-7$ . The control input corresponding to the refined solution is:

$$\mathbf{u}^*(t) = 1.0468 \sqrt{\frac{2gI_F^2\omega^2}{k_L}} \quad (9.140)$$

Note that the control input in the equation above is put into a form compatible with how the trim control input is expressed in [HT16] for validation.

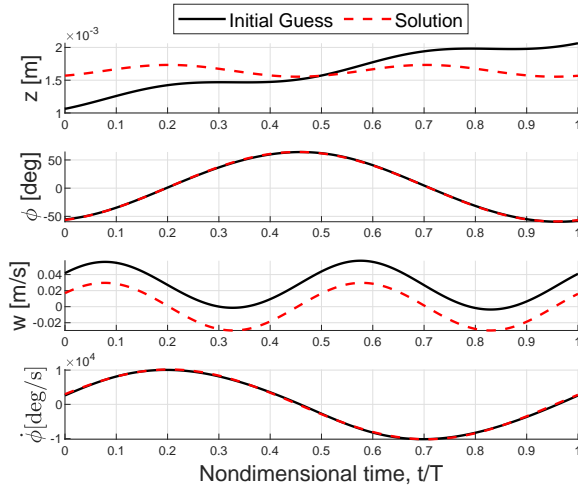


Figure 9.4: Comparison between the numerical solution and initial guess of the periodic motion of a flapping-wing micro aerial vehicle.

To validate the results obtained with the modified harmonic balance algorithm, the response of the harmonic decomposition model is compared to that of the NLTP dynamics following a doublet in the

control input. Figure 9.5 shows a close match between the higher-order LTI system response and that of the NLTP dynamics. This result indicates that the NLTP vertical dynamics of a FWMAV can successfully be approximated by a harmonic decomposition model.

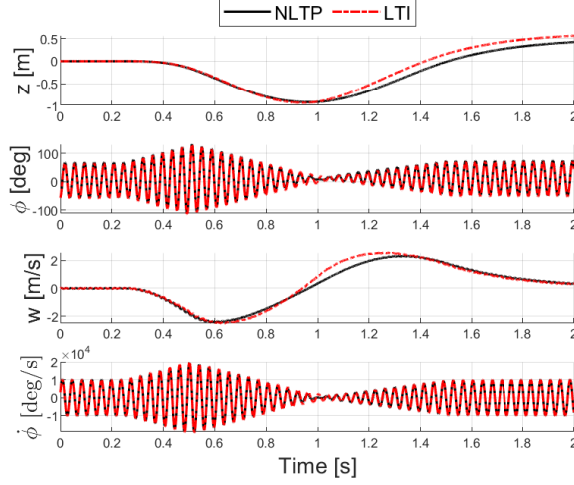


Figure 9.5: Response of the NLTP vertical dynamics of a FWMAV compared to that of its higher-order LTI approximation following a control input doublet.

The base eigenvalues of the high-order LTI model are compared with those of the averaged dynamics. The averaged dynamics are found by retaining only the zeroth state harmonic when performing harmonic decomposition. As such, the average dynamics are given by a 4-state system and do not contain any information about the higher-harmonics of the original system. The eigenvalues of these systems are shown qualitatively in Fig. 9.17a and quantitatively in Table 9.2. As shown in these results, when compared to the high-order LTI dynamics, the averaged dynamics predicts a lower-frequency base eigenvalue associated with the flap mode, and a higher-frequency eigenvalue associated with the heave subsidence mode. However, the mismatch between the base eigenvalues of the high-order LTI and the eigenvalues of the averaged dynamics is fairly small. Based on spectral analysis only, it is not possible to reach any conclusion on the suitability of the averaged dynamics for describing the overall vertical dynamics of flapping-wing flight. This necessitates a comparison of the dynamics of the two models using modal participation factors.

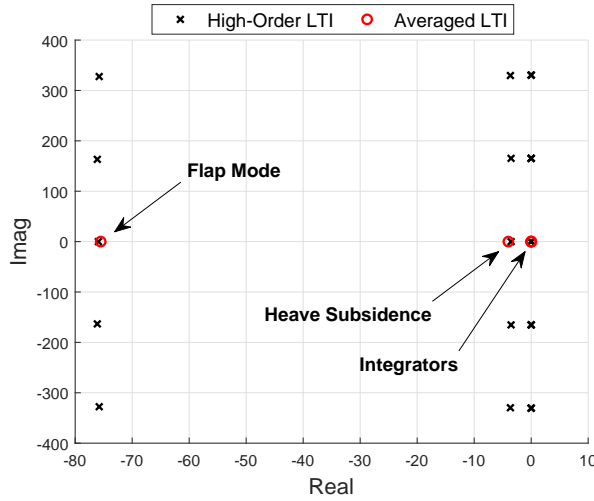


Figure 9.6: Comparison between the eigenvalues of the high-order approximate LTI dynamics and the averaged LTI dynamics.

The modal participation factors are computed for the high-order LTI system with the states corresponding to vertical position, flapping angle, and their harmonics removed. This is done to simplify the analysis as the

Table 9.2: Vertical dynamics base eigenvalues.

| LTI System | $\lambda_1$ | $\lambda_2$ | $\lambda_3$ | $\lambda_4$ |
|------------|-------------|-------------|-------------|-------------|
| High-Order | -75.93      | -3.53       | 0.00        | 0.00        |
| Averaged   | -75.00      | -4.00       | 0.00        | 0.00        |

vertical position and flapping angle are simply described by integral relationships and thus do not affect the dynamics of the system. Figure 9.7 shows the modal participation factors for the vertical speed and flapping speed states to the flap and heave modes. Specifically, Fig. 9.7a shows that the vertical speed contributes to the flap mode almost entirely with its first harmonic, whereas it contributes to the heave mode almost exclusively through its zeroth harmonic. Figure 9.7b suggests that the flapping speed contributes to the flap mode about 86% through its zeroth harmonic, and the remaining 14% through its second harmonic. Higher harmonics were not modeled because the trim solution did not indicate the existence of any harmonic greater than 2/rev, as explained in the previous sections. As such, any contributions from harmonics higher than the second are assumed to be negligible compared to the zeroth, first, and second. In addition, this figure shows that the flapping speed contributes to the heave mode solely through its first harmonic.

This analysis suggests that the vertical and flapping speed states contribute to the overall vertical dynamics of the flapping-wing MAV significantly through their higher harmonics. Thus, it is necessary to include higher-harmonic states (in particular, the 1/rev harmonic) in the LTI approximations of the NLTP vertical flight dynamics for these approximations to be accurate. As such, the averaged dynamics alone are not suitable for describing the NLTP vertical dynamics.

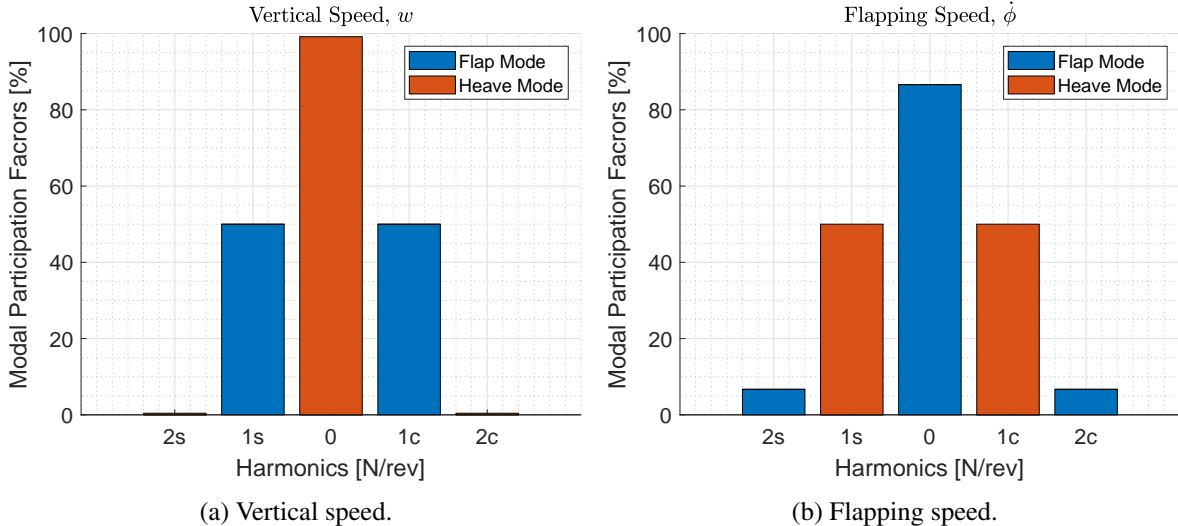


Figure 9.7: Modal participation factors for the vertical dynamics of a hawk moth in hover.

#### 9.4.6 Example 3: Periodic Trim of the Longitudinal Dynamics of Flapping-Wing Vehicle

Consider now a more complex NLTP model representing the longitudinal dynamics of a FWMAV from [Tah+15]:

$$\begin{bmatrix} \dot{x} \\ \dot{z} \\ \dot{u} \\ \dot{w} \\ \dot{q} \\ \dot{\theta} \end{bmatrix} = \begin{bmatrix} u \cos \theta + w \sin \theta \\ -u \sin \theta + w \cos \theta \\ -qw - g \sin \theta \\ qu + g \cos \theta \\ 0 \\ q \end{bmatrix} + \begin{bmatrix} 0 \\ 0 \\ X_0 \\ Z_0 \\ M_0 \\ 0 \end{bmatrix} + \begin{bmatrix} 0 & 0 & 0 & 0 & 0 & 0 \\ 0 & 0 & 0 & 0 & 0 & 0 \\ 0 & 0 & X_u & X_w & X_q & 0 \\ 0 & 0 & Z_u & Z_w & Z_q & 0 \\ 0 & 0 & M_u & M_w & M_q & 0 \\ 0 & 0 & 0 & 0 & 0 & 0 \end{bmatrix} \begin{bmatrix} x \\ z \\ u \\ w \\ q \\ \theta \end{bmatrix} \quad (9.141)$$

were  $x$  and  $z$  are the longitudinal and vertical position in the inertial frame,  $u$  and  $w$  are the longitudinal and vertical velocities in the body-fixed frame,  $q$  is the pitch rate, and  $\theta$  is the pitch attitude. Assuming a horizontal stroke plane, the forces and moments that are independent of the system's states are parametrized by the back-and-forth flapping motion  $\phi(t)$  and a piecewise constant variation in the wing pitch angle  $\eta(t)$  [Tah+15]:

$$X_0 = -2 \frac{K_{21}}{m} \dot{\phi} |\dot{\phi}| \cos \phi \sin^2 \eta \quad (9.142a)$$

$$Z_0 = -\frac{K_{21}}{m} \dot{\phi} |\dot{\phi}| \sin 2\eta \quad (9.142b)$$

$$M_0 = 2\dot{\phi} |\dot{\phi}| \left[ \frac{K_{22}}{I_y} \Delta\hat{x} \cos \phi + \frac{K_{21}}{I_y} x_h \cos \eta + \frac{K_{31}}{I_y} \sin \phi \cos \eta \right] \quad (9.142c)$$

In the equations above,  $x_h$  is the distance between the vehicle center of gravity and the root of the wing hinge line (see Fig. 9.8) and  $\Delta\hat{x}$  is the chordwise distance between the center of pressure and the root of the wing hinge line. Additionally,  $K_{mn} = \frac{1}{4} \rho C_{L\alpha} I_{mn}$  where  $\rho$  is air density,  $C_{L\alpha}$  is the three-dimensional lift curve slope of the wing, and  $I_{mn}$  are the moments of the wing chord distribution. The lift curve slope of the wing is given by:

$$C_{L\alpha} = \frac{\pi AR}{2 \left[ 1 + \sqrt{\left( \frac{\pi AR}{a_0} \right)^2 + 1} \right]} \quad (9.143)$$

where  $AR$  is the wing aspect ratio and  $a_0$  is the lift-curve slope of the airfoil section [THN14]. By definition, the aspect ratio is given by the ratio between the wing surface and the mean chord  $S/\bar{c}$ . The moments of the wing chord distribution are given by:

$$I_{mn} = \int_0^R r^m c^n(r) dr \quad (9.144)$$

where  $R$  is the wing radius and  $c(r)$  is the chord distribution [WW10]. The chord distribution is given by:

$$c(r) = \frac{\bar{c}}{\beta} \left( \frac{r}{R} \right)^{\alpha-1} \left( 1 - \frac{r}{R} \right)^{\gamma-1} \quad (9.145)$$

where:

$$\alpha = \hat{r}_1 \left[ \frac{\hat{r}_1(1-\hat{r}_1)}{\hat{r}_2^2 - \hat{r}_1^2} - 1 \right] \quad (9.146a)$$

$$\gamma = (1-\hat{r}_1) \left[ \frac{\hat{r}_1(1-\hat{r}_1)}{\hat{r}_2^2 - \hat{r}_1^2} - 1 \right] \quad (9.146b)$$

$$\beta = \int_0^1 \hat{r}^{\alpha-1} (1-\hat{r})^{\gamma-1} d\hat{r} \quad (9.146c)$$

The time-varying stability derivatives are given by:

$$X_u = -4 \frac{K_{11}}{m} |\dot{\phi}| \cos^2 \phi \sin^2 \eta \quad (9.147a)$$

$$X_w = -\frac{K_{11}}{m} |\dot{\phi}| \cos \phi \sin 2\eta \quad (9.147b)$$

$$X_q = \frac{K_{21}}{m} |\dot{\phi}| \sin \phi \cos \phi \sin 2\eta - x_h X_w \quad (9.147c)$$

$$Z_u = 2X_w \quad (9.147d)$$

$$Z_w = -2 \frac{K_{11}}{m} |\dot{\phi}| \cos^2 \eta \quad (9.147e)$$

$$Z_q = 2 \frac{K_{21}}{m} |\dot{\phi}| \sin \phi \cos^2 \eta - \frac{K_{\text{rot}12}}{m} \dot{\phi} \cos \phi - x_h Z_w \quad (9.147f)$$

$$M_u = 4 \frac{K_{12}\Delta\hat{x}}{I_y} |\dot{\phi}| \cos^2 \phi \sin \eta + \frac{m}{I_y} (2X_q - x_h Z_u) \quad (9.147g)$$

$$M_w = 2 \frac{K_{12}\Delta\hat{x}}{I_y} |\dot{\phi}| \cos \phi \cos \eta + 2 \frac{K_{21}}{m} |\dot{\phi}| \sin \phi \cos^2 \eta - \frac{mx_h}{I_y} Z_w \quad (9.147h)$$

$$\begin{aligned} M_q = & -2 \frac{\Delta\hat{x}}{I_y} |\dot{\phi}| \cos \phi \cos \eta (K_{12}x_h + K_{22} \sin \phi) + \frac{1}{I_y} \dot{\phi} \cos \phi (K_{\text{rot}13}\Delta\hat{x} \cos \phi \cos \eta + K_{\text{rot}22} \sin \phi) \\ & - \frac{2}{I_y} |\dot{\phi}| \cos^2 \eta \sin \phi (K_{21}x_h + K_{31} \sin \phi) - \frac{K_v \mu_1 \omega}{2\pi I_y} \cos^2 \phi - \frac{mx_h}{I_y} Z_q \end{aligned} \quad (9.147i)$$

where  $K_{\text{rot}} = \pi \rho (\frac{1}{2} - \Delta\hat{x}) I_{mn}$ ,  $K_v = \frac{\pi}{16} \rho I_{04}$ , and  $\mu_1$  depends on the viscosity of the fluid.

As suggested in [Opp+14; Opp+15; SOD10; Tah+15], a triangular waveform is used for the flapping motion:

$$\phi(t) = \begin{cases} \Phi_0 + \frac{4\Phi}{T} \left( t - \frac{T}{4} \right) & 0 \leq t < \frac{T}{2} \\ \Phi_0 - \frac{4\Phi}{T} \left( t - \frac{3T}{4} \right) & \frac{T}{2} \leq t < T \end{cases} \quad (9.148)$$

where  $\Phi_0$  is an offset angle and  $\Phi$  is the amplitude of the flapping motion. The wing pitching motion is assumed piecewise constant and is given by:

$$\eta(t) = \begin{cases} \alpha_d & 0 \leq t < \frac{T}{2} \\ \pi - \alpha_u & \frac{T}{2} \leq t < T \end{cases} \quad (9.149)$$

where  $\alpha_d$  and  $\alpha_u$  are, respectively, the downstroke and upstroke angles of attack. In general, these two moments are different and will generate a net pitching moment if there is an offset between the CG and the hinge line of the wings (*i.e.*,  $x_h \neq 0$ ). In this study, it is assumed that  $x_h = 0$  and  $\alpha_d = \alpha_u = \alpha_m$  (*i.e.*, symmetric pitching motion). As a result, the pitching moment necessary for equilibrium will be generated by other mechanisms. For instance, setting  $\Phi_0 \neq 0$  introduces an asymmetric flapping motion such that an offset, typically known as wing bias, is created between the wing center of pressure averaged over one period and the CG, thus generating a pitching moment [DOS10; ODS11; ODS10]. As such,  $\Phi_0$  is used to introduce a change in pitching attitude or horizontal velocity of the FWMAV, analogously to cyclic pitch in a helicopter rotor. A similar analogy can be made between the flapping amplitude  $\Phi$  and the collective pitch of a helicopter, which are both used to control the heave motion [PL21]. The periodic equilibrium of the FWMAV both at hover and in forward flight can therefore be found by determining suitable values for  $\Phi$  and  $\Phi_0$ , and thus the control vector is chosen as  $\mathbf{u}^T = [\Phi \Phi_0]$ . As such, the state vector (from Eq. 9.141) has dimension  $n = 6$  and the control vector has dimension  $m = 2$ .

The base parameters used in this analysis are reported in Table 9.3 and partially taken from [THN14]. A periodic solution is sought for the case where the hinge line is aligned with the center of mass (*i.e.*,  $x_h = 0$ )

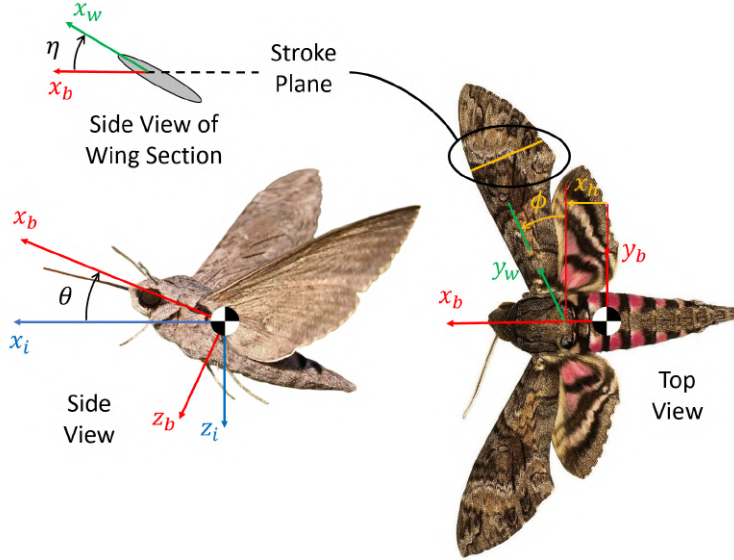


Figure 9.8: Schematic diagram of a hovering FWMAV (recreated from [Tah+15]).

and the flapping motion is not necessarily symmetric (*i.e.*,  $\Phi_0 \neq 0$ ). As an initial guess for the modified harmonic balance algorithm, the controls are chosen as  $\Phi = 60.5$  deg and  $\Phi_0 = 0$  deg and the states are initialized to a constant value of zero across the fundamental period. The control values are taken from [Tah+15]. As was done for the vertical dynamics, the state and control harmonics retained in the modified harmonic balance algorithm are, respectively, up to the second and the zeroth order (*i.e.*,  $N = 2$  and  $M = 0$ ). It follows that the vector of  $n(2N + 1) + m(2M + 1) = 32$  unknowns is:

$$\Theta^T = [\mathbf{x}_0^T \mathbf{x}_{1c}^T \mathbf{x}_{1s}^T \mathbf{x}_{2c}^T \mathbf{x}_{2s}^T \mathbf{u}_0^T] \quad (9.150)$$

The  $n(2N + 1) = 30$  constraints are given by the integral relations. Note that, if trim in forward flight was sought rather than at hover, the zeroth harmonic of the derivative of the longitudinal position state  $x$  would be set to the desired forward speed. Because there are  $m(2M + 1) = 2$  unknowns more than there are constraints, the zeroth harmonics of the position states  $x$  and  $z$ , denoted as  $x_0$  and  $y_0$ , are removed from the problem and set to arbitrary values. This choice is justified by the fact that the zeroth harmonic of the position does not affect the dynamics of the FWMAV. This way, the number of unknowns decreases to 30 such that the problem is square. The modified vector of unknowns is denoted as,

$$\hat{\Theta}^T = [\hat{\mathbf{x}}_0^T \mathbf{x}_{1c}^T \mathbf{x}_{1s}^T \mathbf{x}_{2c}^T \mathbf{x}_{2s}^T \mathbf{u}_0^T] \quad (9.151)$$

where  $\hat{\mathbf{x}}_0$  is the zeroth-harmonic state vector without the position states included. In this example, the number of time steps is chosen as  $n_t = 360$ . Figure 9.9 shows the periodic angular rates obtained with the proposed algorithm using an absolute error tolerance of  $1e-7$ . The periodic equilibrium obtained is similar to that shown in [TWH16] in the harmonic content of each state and in the state oscillation magnitudes. However, some differences in the shape of the periodic orbit, especially for the pitch rate and longitudinal speed, are evident. These differences are likely caused by the fact that the periodic equilibrium shown in [TWH16] is obtained using a higher-order model that includes the flapping dynamics. Nonetheless, the agreement between the periodic equilibria computed here and that found in [TWH16] is quite favorable. The trim control inputs corresponding to the periodic equilibrium in Fig. 9.9 are  $\Phi = 77.83$  deg and  $\Phi_0 = -1.70$  deg. This trim flapping amplitude is larger than the observed flapping amplitude for hawk moths, which is 60.5 deg [Tah+15].

To validate the approximate LTI dynamics obtained with the modified harmonic balance algorithm, the response of the high-order LTI system is compared to that of the NLTP dynamics following a doublet in the flapping amplitude. As shown in Fig. 9.10, the LTI response matches closely that of the NLTP dynamics for the first second of the simulation, whereas discrepancies in the longitudinal position, longitudinal speed, and

Table 9.3: Longitudinal dynamics parameters of a FWMAV representative of a hawk moth (partially taken from [THN14]).

| Parameter       | Numerical Value        | Units             |
|-----------------|------------------------|-------------------|
| $R$             | $5.19 \times 10^{-4}$  | m                 |
| $\bar{c}$       | $1.83 \times 10^{-4}$  | m                 |
| $S$             | $947.8 \times 10^{-6}$ | $\text{m}^2$      |
| $a_0$           | $2\pi$                 | 1/rad             |
| $m$             | $1.648 \times 10^{-6}$ | kg                |
| $r_h$           | 0                      | m                 |
| $\Delta\hat{x}$ | 0.05                   | -                 |
| $\hat{r}_1$     | 0.44                   | -                 |
| $\hat{r}_2$     | 0.525                  | -                 |
| $I_y$           | $2.08 \times 10^{-7}$  | kg-m <sup>2</sup> |
| $\mu_1$         | 0.2                    | -                 |
| $\omega$        | 165.2478               | rad/s             |
| $g$             | 9.80665                | m/s <sup>2</sup>  |
| $\alpha_m$      | 26.75                  | deg               |

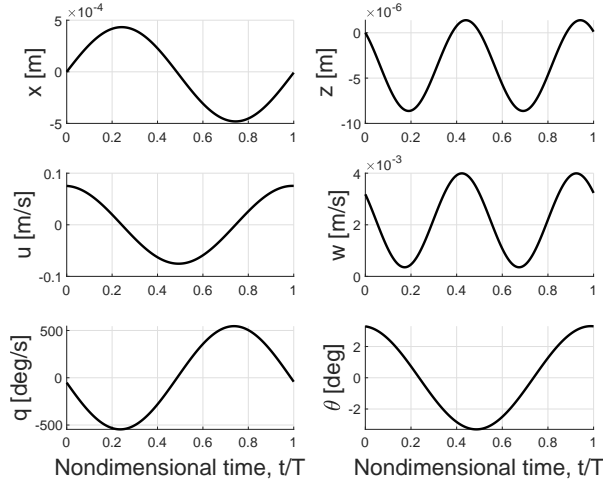


Figure 9.9: Periodic orbit for the longitudinal dynamics of a hawk moth at hover.

pitch attitude arise after the second second or, equivalently, after approximately 26 wingbeats. This may be due to the fact that the relatively large control input doublet in the flapping amplitude (20% of the trim control input) triggers some nonlinear behavior after many wingbeats. Nonetheless, the high-order LTI dynamics is shown to provide a good approximation to the NLTP dynamics.

The base eigenvalues of the high-order LTI model are compared with the eigenvalues of the averaged and residualized dynamics. The residualized dynamics are obtained by neglecting the dynamics of the higher harmonic states, thus yielding a 6-state system via singular perturbation theory. On the other hand, the averaged dynamics are found by truncating the higher-harmonic states while retaining the zeroth-harmonic states. It follows that the average dynamics will be a 6-state system as well. The eigenvalues of these systems are shown qualitatively in Fig. 9.11 and quantitatively in Table 9.4. Note that the longitudinal and vertical position integrators are omitted from the table. It is observed that the eigenvalues of the residualized dynamics match the base eigenvalues of the high-order LTI quite well. Notably, both sets of eigenvalues predict a stable pitch oscillation mode, which is a result that was recently observed in the literature [Tah+15]. Conversely, in addition to largely under-predicting the eigenvalue for the pitch subsidence mode, the averaged dynamics

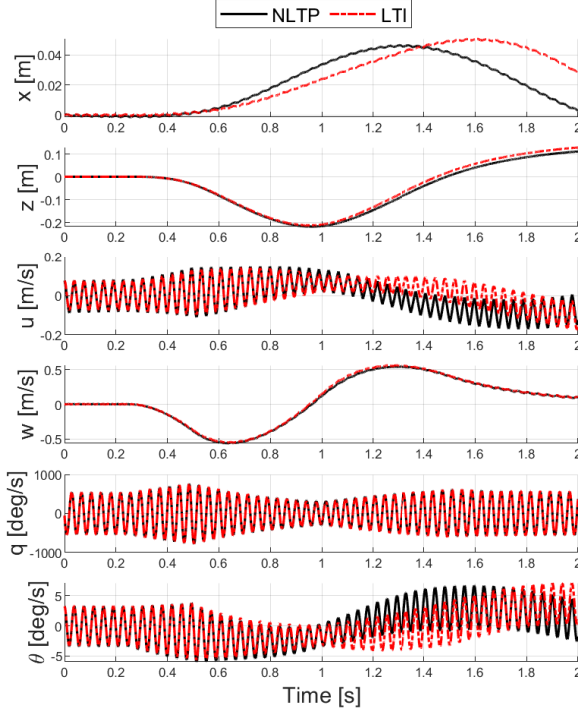


Figure 9.10: Response of the NLTP longitudinal dynamics of the hawk moth compared to that of its higher-order LTI approximation following a flapping amplitude doublet.

predict an unstable pitch oscillation mode. As such, these results indicate that the averaged dynamics are not sufficient to fully describe the longitudinal dynamics of hovering flapping-wing flyers. Additionally, the analysis suggests that the higher harmonics induce a mechanism that stabilizes the dynamics at hover.

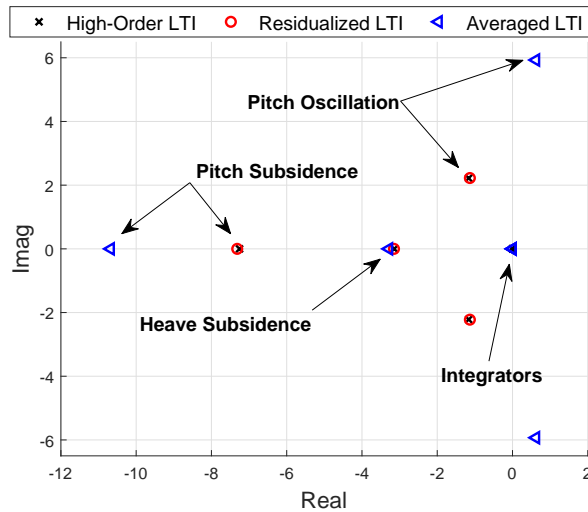


Figure 9.11: Comparison between the eigenvalues of the high-order LTI, residualized, and averaged longitudinal dynamics.

To investigate in more detail this vibrational stabilization mechanism, consider the following form for the

Table 9.4: Longitudinal dynamics base eigenvalues.

| LTI System   | $\lambda_1$ | $\lambda_2$ | $\lambda_{3,4}$   |
|--------------|-------------|-------------|-------------------|
| High-Order   | -7.25       | -3.14       | $-1.16 \pm 2.22i$ |
| Residualized | -7.32       | -3.15       | $-1.13 \pm 2.22i$ |
| Averaged     | -10.68      | -3.28       | $0.62 \pm 5.96i$  |

Table 9.5: Stability derivatives for the longitudinal averaged and residualized dynamics.

| Derivative | Averaged | Residualized | Units                             |
|------------|----------|--------------|-----------------------------------|
| $X_u$      | -4.46    | -4.44        | kg/s                              |
| $Z_w$      | -3.29    | -3.15        | kg/s                              |
| $M_u$      | 38.74    | 4.66         | kg-m/s                            |
| $M_q$      | -4.98    | -5.14        | kg-m <sup>2</sup> /s              |
| $M_\theta$ | 0        | 0.03         | kg-m <sup>2</sup> /s <sup>2</sup> |

system matrix for the averaged and residualized dynamics with the position states removed:

$$\mathbf{A} = \begin{bmatrix} X_u & 0 & 0 & -g \\ 0 & Z_w & 0 & 0 \\ M_u & 0 & M_q & M_\theta \\ 0 & 0 & 1 & 0 \end{bmatrix} \quad (9.152)$$

The numerical values of the stability derivatives derived from Eq. (9.152) corresponding to the longitudinal hovering cubic and heave dynamics are reported in Table 9.5 for the averaged and residualized systems. As observed in [Tah+15], due to the high-amplitude, high-frequency, periodic forcing, the residualized system gains pitch damping ( $M_q$ ) and some pitch stiffness ( $M_\theta$ ) when compared to the average model. On the other hand, the higher harmonics cause a significant reduction in speed stability ( $M_u$ ) and a slight reduction in the longitudinal and heave damping ( $X_u$  and  $Z_w$ ). Based on this analysis, the higher harmonics induce a stabilization mechanism that increases the pitch damping and stiffness while reducing speed stability. This results in stabilization of the pitch oscillation mode and in a pitch subsidence mode with a lower frequency, which overall yields a stable hovering cubic. The heave dynamics remain largely unaffected. This further substantiates the results of [Tah+15], which were obtained via high-order averaging, and that predicted that periodic forcing at a high enough frequency and amplitude may stabilize the flight modes of a hovering vehicle. Moreover, these results show that the proposed approach is successful in predicting behaviors that were only observed using higher-order averaging.

The modal participation factors are computed for the high-order LTI system with the states corresponding to vertical position, longitudinal position, and their harmonics removed. This is done to simplify the analysis as the longitudinal and vertical position are simply described by integral relationships and thus do not affect the dynamics of the system. Figure 9.12 shows the modal participation factors for the longitudinal dynamics of a hawk moth in hover. The following observations can be made:

- Figure 9.12a shows that the longitudinal speed contributes to the heave subsidence mode exclusively through its first harmonic, whereas it contributes to the pitch oscillation and pitch subsidence modes solely through its zeroth harmonic.
- Figure 9.12b suggests that the vertical speed contributes to the heave subsidence mode exclusively through its zeroth harmonic, whereas it contributes to the pitch oscillation and pitch subsidence modes solely through its first harmonic.
- Figure 9.12c indicates that the pitch rate contributes to the heave subsidence mode solely through its first harmonic. On the other hand, it contributes to the pitch oscillation mode roughly 45% through its zeroth harmonic, and the remaining 55% through its second harmonic. The opposite is true for the pitch subsidence mode, to which the pitch rate contributes 55% through its zeroth harmonic, and 45% through its second harmonic.

4. Figure 9.12d shows how the pitch attitude contributes to the heave subsidence mode almost entirely with its first harmonic, while it contributes to the pitch oscillation and pitch subsidence modes solely through its zeroth harmonic.

As in the case of the vertical dynamics, the modal participation analysis suggests that the longitudinal dynamics are heavily affected by the higher harmonics. It follows that these harmonics must be included in linear models for these approximations to be accurate representations of the NLTP dynamics. Furthermore, the modal participation analysis provides valuable insight into how each mode of motion depends on the higher harmonics of the system. To the authors' knowledge, this constitutes the first time that this type of model participation analysis has been performed on the NLTP dynamics of flapping-wing flight.

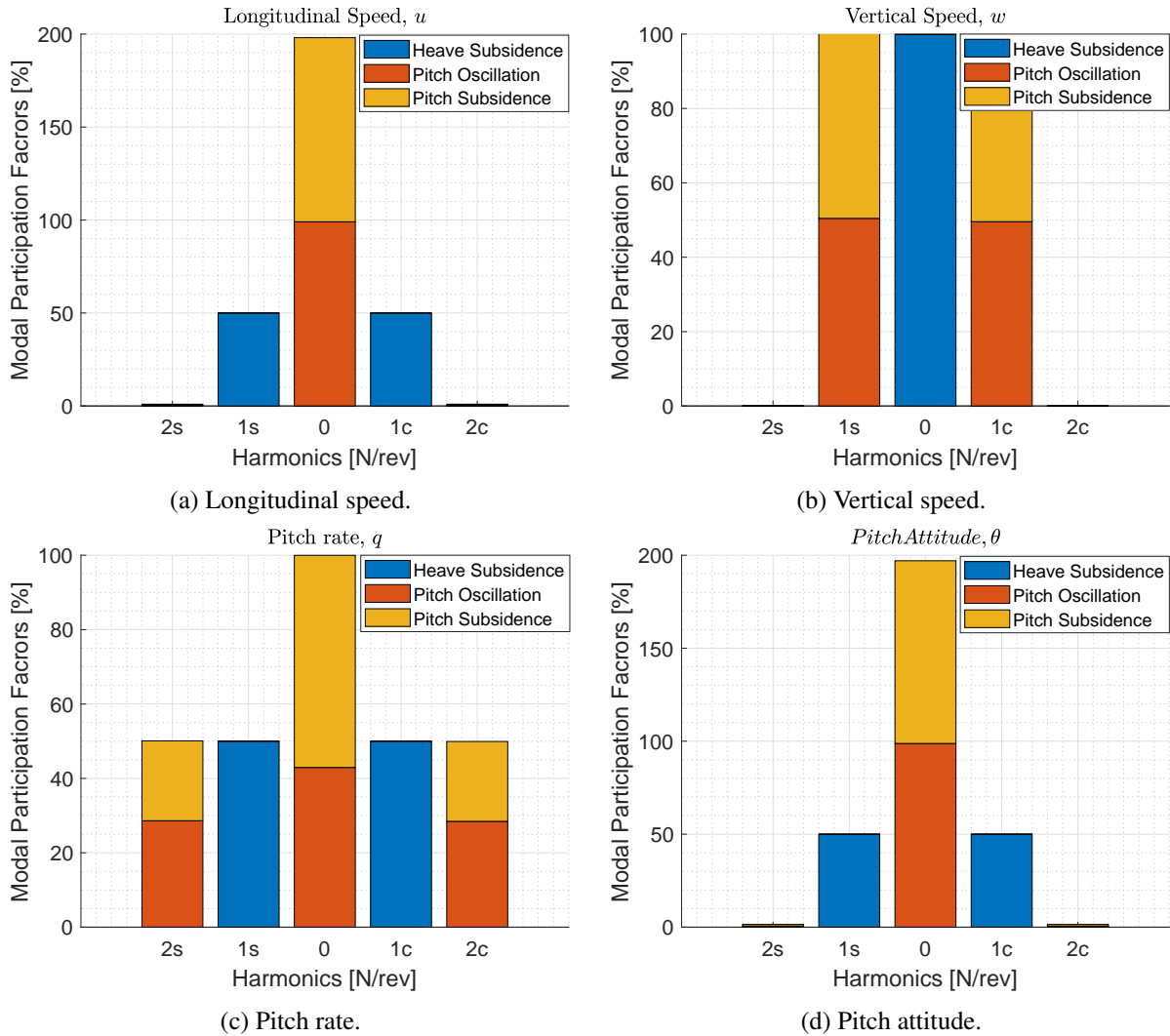


Figure 9.12: Modal participation factors for the longitudinal dynamics of a hawk moth at hover.

#### 9.4.7 Example 4: Periodic Trim of a Helicopter

Consider now a more complex example involving the flight dynamics of a helicopter in forward flight. The dynamics of helicopters in forward flight are dominated by harmonics with frequencies that are multiples of the number of blades per revolution (or  $N_b/\text{rev}$ ) [Joh80]. This is because the main rotor aerodynamic forces and moments are periodic with respect to the main rotor azimuth angle  $\psi$ , which is related to time through  $\psi = \Omega t$ , where  $\Omega$  is the angular speed of the main rotor. Under the assumption that the angular speed of the main rotor is constant, the fundamental period of the helicopter flight dynamics is defined as  $T = 2\pi/\Omega$ . For instance, the nominal angular speed of the main rotor for the UH-60 is  $\Omega = 27 \text{ rad/s}$  and thus the fundamental period is approximately  $T = 0.23 \text{ seconds}$ . In this work, the helicopter model used

to simulate the system dynamics is a Julia [Bez+17] implementation of a variant of the General Helicopter (GenHel) flight dynamics simulation (Refs. [Hor19; How80]) representative of a utility helicopter similar to a UH-60. The model contains a 6-degree-of-freedom rigid-body dynamic model of the fuselage, nonlinear aerodynamic lookup tables for the fuselage, rotor blades, and empennage, rigid flap and lead-lag rotor blade dynamics, a three-state Pitt-Peters inflow model [PP80], and a Bailey tail rotor model [Bai41]. The state vector is:

$$\mathbf{x}^T = [u \ v \ w \ p \ q \ r \ \phi \ \theta \ \psi \ x \ y \ z \ \beta_0 \ \beta_{1c} \ \beta_{1s} \ \beta_{0D} \ \dot{\beta}_0 \ \dot{\beta}_{1c} \ \dot{\beta}_{1s} \ \dot{\beta}_{0D} \ \zeta_0 \ \zeta_{1c} \ \zeta_{1s} \ \zeta_{0D} \ \dot{\zeta}_0 \ \dot{\zeta}_{1c} \ \dot{\zeta}_{1s} \ \dot{\zeta}_{0D} \ \lambda_0 \ \lambda_{1c} \ \lambda_{1s} \ \lambda_{0T}] \quad (9.153)$$

where:

$u, v, w$  are the longitudinal, lateral, and vertical velocities in the body-fixed frame,

$p, q, r$  are the roll, pitch, and yaw rates,

$\phi, \theta, \psi$  are the Euler angles,

$x, y, z$  are the positions in the North-East-Down (NED) frame,

$\beta_0, \beta_{1c}, \beta_{1s}, \beta_{0D}$  are the flapping angles in multi-blade coordinates,

$\zeta_0, \zeta_{1c}, \zeta_{1s}, \zeta_{0D}$  are the lead-lag angles in multi-blade coordinates,

$\lambda_0, \lambda_{1c}, \lambda_{1s}$ , are the main rotor induced inflow ratio harmonics, and

$\lambda_{0T}$  is the tail rotor induced inflow ratio.

The control vector is:

$$\mathbf{u}^T = [\delta_{\text{lat}} \ \delta_{\text{lon}} \ \delta_{\text{col}} \ \delta_{\text{ped}}] \quad (9.154)$$

where  $\delta_{\text{lat}}$  and  $\delta_{\text{lon}}$  are the lateral and longitudinal cyclic inputs,  $\delta_{\text{col}}$  is the collective input, and  $\delta_{\text{ped}}$  is the pedal input. It follows that the state vector has dimension  $n = 32$  and the control vector has dimension  $m = 4$ .

The objective is to find the periodic solution for the state vector in level forward flight at a forward speed of  $\dot{x} = 80$  kts with constant control setting. The choice of 80 kts level flight is justified by the fact that readily-available flight test data exists at this particular flight condition such that comparisons can be made with the numerical solution. It is worth noting that the flight dynamics of the UH-60 in this particular flight condition are unstable [Sae+19] and it is therefore not possible to find an approximate periodic solution by simulating the system long enough for it to reach steady state (unless a feedback controller is implemented). Since the helicopter under consideration has four rotor blades, the first four state harmonics are retained in the numerical solution of the periodic motion ( $N = 4$ ). Only the zeroth harmonic is retained for the control input ( $M = 0$ ). The vector of  $n(2N + 1) + m(2M + 1) = 292$  unknowns is:

$$\hat{\Theta}^T = [\mathbf{x}_0^T \ \mathbf{x}_{1c}^T \ \mathbf{x}_{1s}^T \ \dots \ \mathbf{x}_{Nc}^T \ \mathbf{x}_{Ns}^T \ \mathbf{u}_0^T] \quad (9.155)$$

The  $n(2N + 1) = 288$  constraints are given by Eq. (9.96), with the exception of the zeroth harmonic of the derivative of the  $x$  position state which is set to the desired forward speed (i.e.  $\dot{x}_0 = 80$  kts). Because there are  $m(2M + 1) = 4$  unknowns more than there are constraints, the zeroth harmonics of the position states ( $x, y, z$ ) and yaw angle  $\psi$ , denoted as  $x_0, y_0, z_0$ , and  $\psi_0$ , are removed from the problem and set to arbitrary values. This choice is justified by the fact that the zeroth harmonic of the position and yaw angle do not affect the dynamics of the helicopter. This way, the number of unknowns decreases to 288 such that the problem is square. The modified vector of unknowns is denoted as,

$$\hat{\Theta}^T = [\hat{\mathbf{x}}_0^T \ \mathbf{x}_{1c}^T \ \mathbf{x}_{1s}^T \ \dots \ \mathbf{x}_{Nc}^T \ \mathbf{x}_{Ns}^T \ \mathbf{u}_0^T] \quad (9.156)$$

where  $\hat{\mathbf{x}}_0$  is the zeroth-harmonic state vector without the position and yaw angle states included. In this example, the number of time steps is chosen as  $n_t = 360$ . The initial guess of the algorithm is found by trimming the helicopter at incremental time instants (as if it was a NLTI system) over one rotor revolution using standard NLTI trimming techniques, and averaging the trim solution thus found. Figure 9.13 shows the periodic angular rates obtained with the proposed algorithm (solid line) using an error tolerance of  $1e-7$ . As expected, since the helicopter in consideration has four main rotor blades with equal mass and since the state

harmonics retained in the solution are four, the higher-harmonic content of the periodic solution is limited to the fourth sine and cosine harmonics. Additional harmonics which are multiples of four (i.e. 8/rev, 12/rev, 16/rev, etc.) can readily be captured by increasing the number of state harmonics retained in the solution (i.e.  $N = 8$ ,  $N = 12$ ,  $N = 16$ , etc.). It should be noted that the algorithm is able to capture harmonics in the periodic solution that are not only multiples of the  $N_b/\text{rev}$  harmonics. For instance, if one rotor blade had a different mass with respect to the others such that the rotor was imbalanced, then the algorithm would capture the 1/rev component in the resulting periodic solution, provided that the first harmonic is retained in the solution.

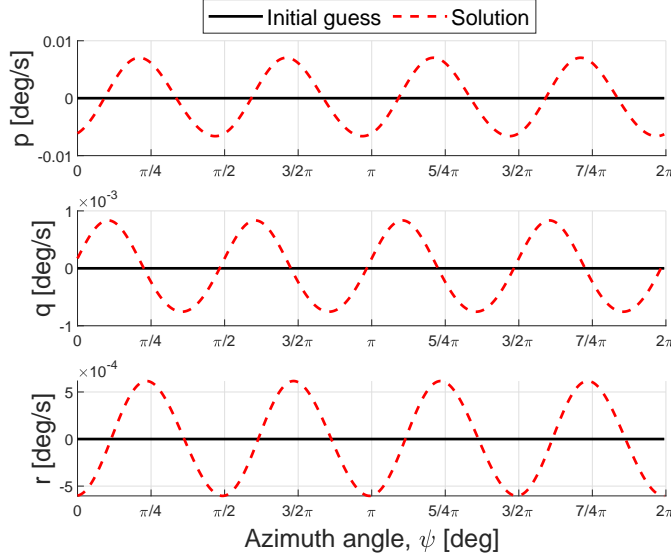


Figure 9.13: Comparison between the numerical solution and initial guess of the angular rates periodic motion of a helicopter.

To validate the results, the vertical acceleration is computed along the periodic solution and compared with flight test data of the U.S. Army Rotorcraft Aircrew System Concepts Airborne Laboratory (RASCAL) JUH-60A helicopter as shown in Fig. 9.14. This figure shows good agreement between the numerical solution of the periodic motion and the flight test data. Particularly, the phase of the 4/rev component of the vertical acceleration closely matches that of the flight test data, whereas the amplitude of the signal is slightly under-predicted. This may be due to limitations of the flight dynamics model, specifically the use of a low-order inflow model and reliance on only the rigid flap and lead-lag motions.

As was done for the FWMAV example, a second solution is computed starting from a very rough guess of the trim states and controls to test the convergence properties and robustness of the algorithm. Specifically, the initial state vector is the vector of zeros with the exception of the body-frame forward speed component, average main rotor inflow ratio, and tail rotor inflow ratio which are initialized respectively to  $u = 80$  kts,  $\lambda_0 = 0.05$ , and  $\lambda_{0T} = 0.05$ . The controls are initialized to a constant value of 50% for each input. Figure 9.15 shows the infinity norm of the iteration error versus the number of iterations for this case (dashed line) and the previous example (solid line). As in the FWMAV example, Fig. 9.15 shows that while the convergence rate remains the same, the solution starting from an initial guess that is farther from the periodic equilibrium takes more iterations to reach the desired error tolerance. It is worth noting that the solution still converges even from a very poor initial guess. Furthermore, both solutions are reached with initial guesses that do not contain information about the harmonic content of the periodic solution. Using a hybrid MATLAB®-Julia implementation of the algorithm on the same computer used for the FWMAV example, the algorithm takes on average 40 seconds per iteration. It follows that the approximate computation time associated with the solutions in Fig. 9.15 is 4 and 6 minutes, respectively. The increased runtime compared to that of the FWMAV example can be explained by the more complex and higher-order dynamics of the helicopter model with respect to that of the FWMAV.

An example use case of the algorithm lies in its ability to compute the necessary higher harmonic control

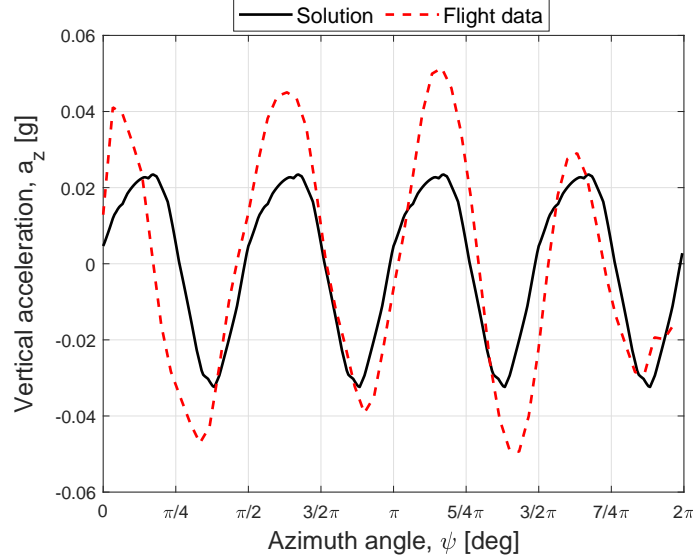


Figure 9.14: Comparison of the vertical acceleration along the periodic solution obtained numerically with RASCAL JUH-60A flight-test data at 80 kts level flight.

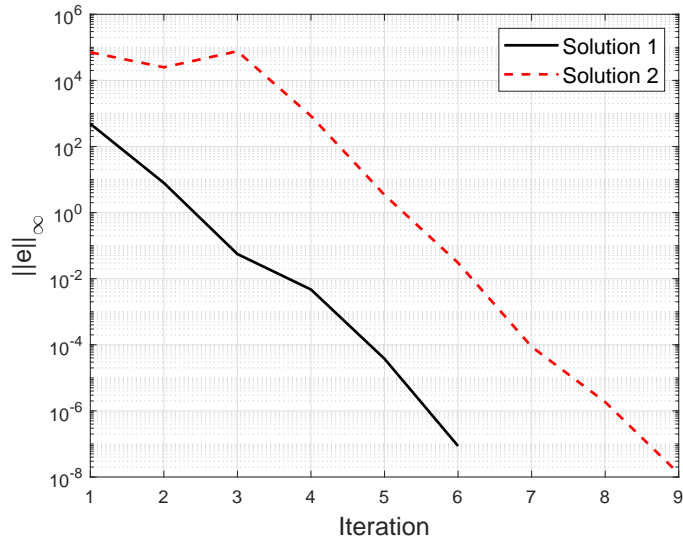


Figure 9.15: Iteration error vs. number of iterations for numerical solutions based on different initial guesses.

inputs for the helicopter to constrain arbitrary state harmonics. Consider the example in which the desired higher-harmonics of the position and heading are zero (i.e. no vibrations at the center of gravity). In this case, it is necessary to retain up to the fourth state and control harmonics in the numerical solution ( $N = 4$  and  $M = 4$ ). The vector of  $n(2N + 1) + m(2M + 1) = 324$  unknowns is:

$$\Theta^T = [\mathbf{x}_0^T \ \mathbf{x}_{1c}^T \ \mathbf{x}_{1s}^T \ \dots \ \mathbf{x}_{Nc}^T \ \mathbf{x}_{Ns}^T \ \mathbf{u}_0^T \ \mathbf{u}_{1c}^T \ \mathbf{u}_{1s}^T \ \dots \ \mathbf{u}_{Mc}^T \ \mathbf{u}_{Ms}^T] \quad (9.157)$$

The  $n(2N + 1) = 288$  constraints are given by Eq. (9.96), with the exception of the zeroth harmonic of  $\dot{x}$  which is set to the desired longitudinal speed of 80 kts. Because there are  $m(2M + 1) = 36$  more unknowns than constraints, all the harmonics of  $x$ ,  $y$ ,  $z$ , and  $\psi$  are set to zero and removed from the problem. This way, the number of unknowns decreases to 288 such that the problem is square. The periodic control solution obtained from the algorithm, which corresponds to the desired HHC input, is shown in Fig. 9.16. These are the desired control inputs that an HHC control law should exert to eliminate vibrations about the center of gravity. As a result, if the system is linearized around the periodic solution thus found, these linear

dynamics will correspond to the linear dynamics of the helicopter augmented with the HHC law which provides these open-loop control inputs. This example demonstrates a powerful application of the proposed solution algorithm, namely, that it can be used to derive open-loop control inputs for periodic systems that eliminate some harmonic content in the system response.

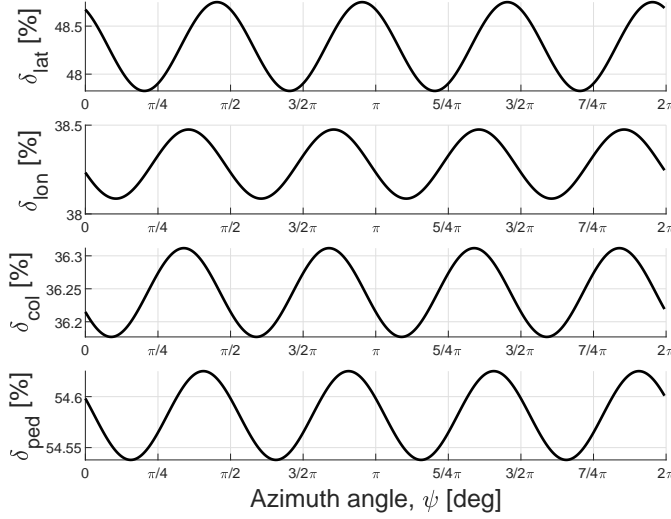


Figure 9.16: Desired control inputs that an HHC control law should exert to eliminate vibrations at the center of gravity.

#### 9.4.8 Example 5: Vibrational Stabilization Effects in Rotorcraft Flight Dynamics

This example is motivated by the fact that eigenvalues of the rotorcraft flight dynamics identified from flight test often differ from those computed with physics-based simulations, and that some commonly observed mismatches may be ascribed to vibrational stability effects due to rotor blade imbalance or other periodic disturbance on the rotorcraft. Consider now an example involving the flight dynamics of a helicopter. Since helicopters are subjected to a variety of vibrations, it is feasible that vibrational effects might affect their stability characteristics. Traditionally, linear time invariant models of helicopter flight dynamics neglect vibrational effects, but through the use of Harmonic Decomposition [LP17] time periodic terms can be retained in the LTI models. The non-linear flight dynamics are modeled using PSUHeloSim [Hor19], a MATLAB® implementation of the General Helicopter (GenHel) flight dynamics simulation model (Ref. GenHel) with improved rotor, trimming, and linearization routines. PSUHeloSim is representative of a utility helicopter similar to a UH-60. The model contains a 6-degree-of-freedom rigid-body dynamic model of the fuselage, nonlinear aerodynamic lookup tables for the fuselage, rotor blades, and empennage, rigid flap and lead-lag rotor blade dynamics, a three-state Pitt-Peters inflow model (Ref. Pitt), and a Bailey tail rotor model (Ref. Bailey). The state vector is:

$$\mathbf{x}^T = \left[ u \ v \ w \ p \ q \ r \ \phi \ \theta \ \psi \ x \ y \ z \ \beta_0 \ \beta_{1c} \ \beta_{1s} \ \beta_{0D} \ \dot{\beta}_0 \ \dot{\beta}_{1c} \ \dot{\beta}_{1s} \ \dot{\beta}_{0D} \ \zeta_0 \ \zeta_{1c} \ \zeta_{1s} \ \zeta_{0D} \ \dot{\zeta}_0 \ \dot{\zeta}_{1c} \ \dot{\zeta}_{1s} \ \dot{\zeta}_{0D} \ \lambda_0 \ \lambda_{1c} \ \lambda_{1s} \ \lambda_{0T} \right] \quad (9.158)$$

where:

$u, v, w$  are the longitudinal, lateral, and vertical velocities in the body-fixed frame,

$p, q, r$  are the roll, pitch, and yaw rates,

$\phi, \theta, \psi$  are the Euler angles,

$x, y, z$  are the positions in the North-East-Down (NED) frame,

$\beta_0, \beta_{1c}, \beta_{1s}, \beta_{0D}$  are the flapping angles in multi-blade coordinates,

$\zeta_0, \zeta_{1c}, \zeta_{1s}, \zeta_{0D}$  are the lead-lag angles in multi-blade coordinates,

$\lambda_0$ ,  $\lambda_{1c}$ ,  $\lambda_{1s}$ , are the main rotor induced inflow ratio harmonics, and  $\lambda_{0T}$  is the tail rotor induced inflow ratio.

The control vector is:

$$\mathbf{u}^T = [\delta_{\text{lat}} \ \delta_{\text{lon}} \ \delta_{\text{col}} \ \delta_{\text{ped}}] \quad (9.159)$$

where  $\delta_{\text{lat}}$  and  $\delta_{\text{lon}}$  are the lateral and longitudinal cyclic inputs,  $\delta_{\text{col}}$  is the collective input, and  $\delta_{\text{ped}}$  is the pedal input.

In general, the flight dynamics of this model are non-linear time-periodic (NLTP), such that:

$$\dot{\mathbf{x}} = \mathbf{f}(\mathbf{x}, \mathbf{u}, \psi) \quad (9.160)$$

Blade imbalance is modeled by assuming one of the four rotor blades to have a different mass with respect to the others. Given this difference in mass, first and second flapping moments are varied accordingly. Because blade imbalance results in a periodic forcing at one-per-rotor-revolution (1/rev), trim at hover will no longer be represented a single point in the state space but rather by a periodic orbit such that the trim state and control vectors are  $\mathbf{x}^*(\psi) = \mathbf{x}^*(\psi + \Omega T)$  and  $\mathbf{u}^*(\psi) = \mathbf{u}^*(\psi + \Omega T)$ . To solve for this periodic orbit, the modified harmonic balance algorithm of Ref. SaettiJGCD2021 is used. Next, the flight dynamics are linearized about this periodic orbit to yield an LTP system. The LTP system is approximated with a higher-order LTI system by retaining up to the first harmonic of the fundamental frequency (*i.e.*, the angular speed of the main rotor  $\Omega$ ). The order of the higher-order LTI model is subsequently reduced by assuming that the fast states reach steady-state quicker than the remaining slower states, where the fast and slow states are chosen as:

$$\mathbf{X}_s = \mathbf{x}_{F_0} \quad (9.161a)$$

$$\mathbf{X}_f^T = [\mathbf{x}_{R_0}^T \ \mathbf{x}_{R_{1c}}^T \ \mathbf{x}_{R_{1s}}^T] \quad (9.161b)$$

where:

$$\mathbf{x}_F^T = [u \ v \ w \ p \ q \ r \ \phi \ \theta] \quad (9.162a)$$

$$\mathbf{x}_R^T = [\beta_0 \ \beta_{1c} \ \beta_{1s} \ \beta_{0D} \ \dot{\beta}_0 \ \dot{\beta}_{1c} \ \dot{\beta}_{1s} \ \dot{\beta}_{0D} \ \zeta_0 \ \zeta_{1c} \ \zeta_{1s} \ \zeta_{0D} \ \dot{\zeta}_0 \ \dot{\zeta}_{1c} \ \dot{\zeta}_{1s} \ \dot{\zeta}_{0D} \ \lambda_0 \ \lambda_{1c} \ \lambda_{1s} \ \lambda_{0T}] \quad (9.162b)$$

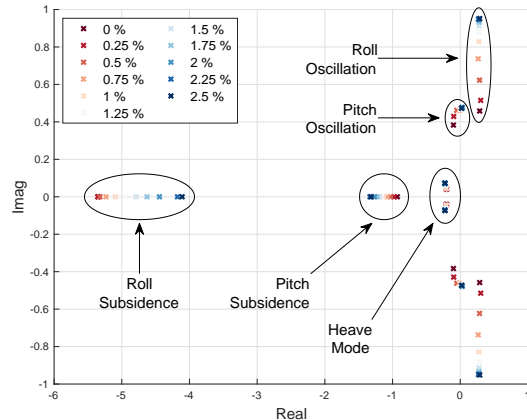
The effect of blade imbalance on the flight dynamics stability can be checked via spectral analysis of the reduced-order system thus obtained. Figure 9.17 shows the eigenvalues of the rigid-body dynamics for blade imbalance varying from zero to 2.5% of the total mass of the blade. The following observations can be made:

1. Frequency of the roll subsidence mode decreases for increasing imbalance (pole moves toward the origin).
2. Frequency of the pitch subsidence mode increased for increasing imbalance (pole moves away from the origin).
3. Damping of the oscillatory roll mode decreases whereas its frequency increases.
4. Damping of the roll oscillatory roll mode decreases and frequency increases.
5. Poles of the heave mode are relatively unaffected compared to the other modes.

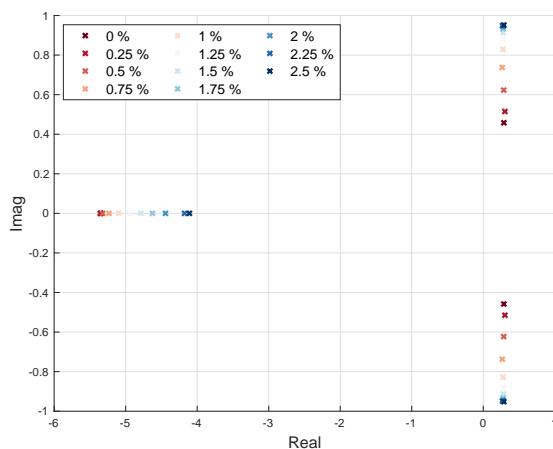
Figure 9.18 shows the lateral (Fig. 9.18a) and longitudinal (Fig. 9.18b) stability derivatives for varying blade imbalance. While  $L_p$  increases for increasing blade imbalance,  $M_q$  decreases, which suggests that vibrations induced by blade imbalance affect the roll and pitch dynamics in opposite ways. These preliminary results indicate that, indeed, rotor blade imbalance affects the eigenvalues of a rotorcraft at hover. Thus, eigenvalues identified for a helicopter with an imbalanced rotor may differ from those obtained from simulations where the rotor is perfectly balanced.

## Bibliography

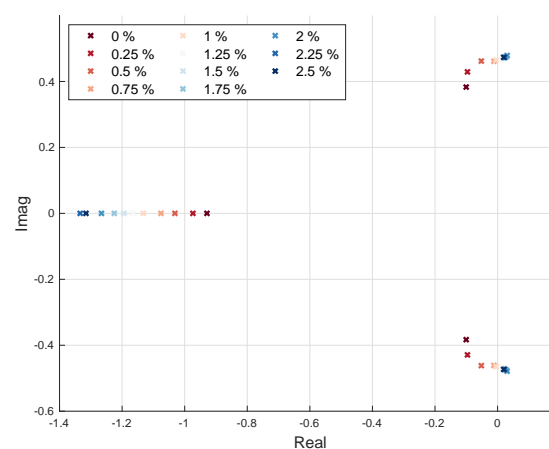
- [Abr+11] M D Abraham et al. “Integrated Design of AFCS and HHC for Rotorcraft Vibration Reduction using Dynamic Crossfeed”. In: *Proceedings of the 67<sup>th</sup> Annual Forum of the American Helicopter Society*. Virginia Beach, VA, May 2011 (cited on 230).



(a) Rigid-body dynamics.

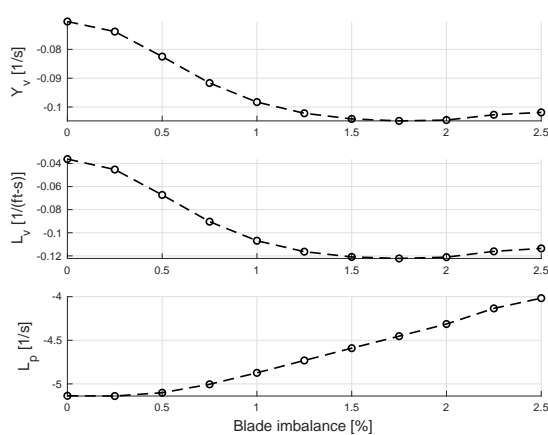


(b) Lateral dynamics hovering cubic.

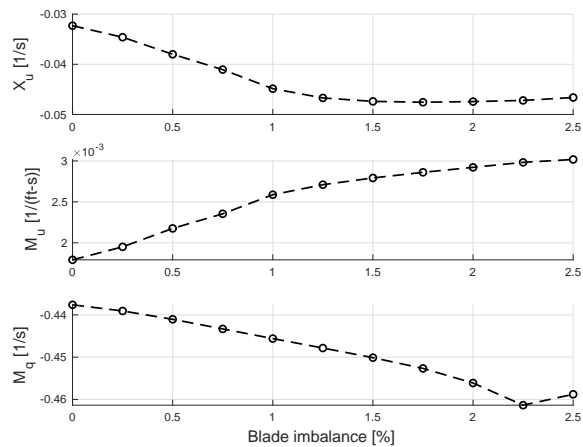


(c) Longitudinal dynamics hovering cubic.

Figure 9.17: Hover eigenvalues for varying blade imbalance.



(a) Lateral stability derivatives.



(b) Longitudinal stability derivatives.

Figure 9.18: Hover stability derivatives for varying blade imbalance.

[Bai41] F. J. Bailey. *A Simplified Theoretical Model of Determining the Characteristics of a Lifting Rotor in Forward Flight*. Technical report. NACA Report No. 716, 1941. (Cited on page 269).

- [BP92] B. A. Bamieh and J. B. Pearson. “A general framework for linear periodic systems with application to  $H_\infty$  sampled-data control”. In: *IEEE Transactions on Automatic Control* 37.4 (1992), pages 418–435. DOI: 10.1109/9.126576 (cited on page 235).
- [Bez+17] J. Bezanson et al. “Julia: A Fresh Approach to Numerical Computing”. In: *SIAM Review* 59.1 (2017), pages 65–98. DOI: <https://doi.org/10.1137/141000671> (cited on page 269).
- [BB85] S. Bittanti and P. Bolzern. “Stabilizability and detectability of linear periodic systems”. In: *System & Control Letters* 6.2 (July 1985), pages 141–145. DOI: 10.1016/0167-6911(85)90083-0 (cited on page 237).
- [BC10] S. Bittanti and P. Colaneri. *Periodic Systems: Filtering and Control*. Springer, 2010 (cited on pages 231, 233).
- [BCS86] P. Bolzern, P. Colaneri, and R. Scattolini. “Zeros of Discrete-Time Linear Periodic Systems”. In: *IEEE Transactions on Automatic Control* 31.11 (Nov. 1986), pages 1057–1058. DOI: 10.1109/TAC.1986.1104172 (cited on page 237).
- [Bre94] K. S. Brentner. “A New Algorithm for Computing Acoustic Integrals”. In: *Proceedings of IMACS 14<sup>th</sup> World Congress on Computational and Applied Mathematics*. Atlanta, GA, July 1994, pages 592–595 (cited on page 247).
- [Bul02] F. Bullo. “Averaging and Vibrational Control of Mechanical Systems”. In: *SIAM Journal on Control and Optimization* 41.2 (2002), pages 542–562. DOI: <https://doi.org/10.1137/S0363012999364176> (cited on page 229).
- [CTC03] R P Cheng, M B Tischler, and R Celi. “A High-Order, Time Invariant Linearized Model for Application to HHC/AFCS Interaction Studies”. In: *Proceedings of the 59<sup>th</sup> Annual Forum of the American Helicopter Society*. Phoenix, AZ, May 6-8, 2003. (Cited on pages 230, 242, 246, 247).
- [CCB04] P Colaneri, R. Celi, and S. Bittanti. “Constant Coefficient Representation of Discrete Periodic Linear Systems”. In: *Proceedings of the 4<sup>th</sup> Decennial Specialists’ Conference on Aeromechanics*. San Francisco, CA, Jan 21-24, 2004. (Cited on pages 234, 238).
- [Col91] P. Colaneri. “Hamiltonian matrices for lifted systems and periodic Riccati equations in  $H_2/H_\infty$  analysis and control”. In: *Proceedings of the 30<sup>th</sup> IEEE Conference on Decision and Control*. Brighton, UK, Dec. 1991. DOI: 10.1109/CDC.1991.261749 (cited on page 235).
- [Cri69] P Crimi. *A Method for Analyzing the Aeroelastic Stability of a Helicopter Rotor in Forward Flight*. Technical report. Washington, DC: NASA CR-1332, 1969 (cited on page 239).
- [DAn70] H. D’Angelo. *Linear time-varying systems: analysis and synthesis*. Allyn and Bacon, 1970 (cited on page 233).
- [Da +13] A. Da Ronch et al. “Linear Frequency Domain and Harmonic Balance Predictions of Dynamic Derivatives”. In: *Journal of Aircraft* 50.3 (May 2013), pages 694–707. DOI: 10.2514/1.C031674 (cited on page 238).
- [DFP98] G. De Nicolao, G. Ferrari-Trecate, and S. Pinzoni. “Zeros of continuous-time linear periodic systems”. In: *Automatica* 34.12 (Dec. 1998), pages 1651–1655. DOI: 10.1016/S0005-1098(98)80023-X (cited on page 236).
- [DOS10] D. B. Doman, M. W. Oppenheimer, and D. O. Sighorsson. “Dynamics and Control of a Biomimetic Vehicle Using Biased Wingbeat Forcing Functions Part II – Controller”. In: *AIAA 2010-1024, 48<sup>th</sup> AIAA Aerospace Sciences Meeting*. Orlando, FL, Jan. 2010. DOI: <https://doi.org/10.2514/6.2010-1024> (cited on page 263).
- [Eip16] A. Eipe. “Effect of Blade Flexibility, Structural Parameters, and Trim Conditions on Rotor Loads”. PhD thesis. St. Louis, MO: Washington University, 2016 (cited on page 238).

- [Fla91] D.S. Flamm. “A new shift-invariant representation for periodic systems”. In: *Systems and Control Letters* 17.1 (July 1991), pages 9–14. DOI: 10.1016/0167-6911(91)90093-T (cited on page 234).
- [Flo83] G. Floquet. “Sur les équations différentielles linéaires à coefficients périodiques”. fr. In: *Annales scientifiques de l’École Normale Supérieure* 2.12 (1883), pages 47–88. DOI: <https://doi.org/10.24033/asens.220> (cited on pages 229, 233).
- [FDF05] E. Frazzoli, M. A. Dahleh, and E. Feron. “Maneuver-Based Motion Planning for Nonlinear Systems With Symmetries”. In: *IEEE Transactions on Robotics* 21.6 (Dec. 2005), pages 1077–1091. DOI: <https://doi.org/10.1109/TRO.2005.852260> (cited on page 259).
- [FM95] P P Friedmann and T A Millot. “Vibration Reduction in Rotorcraft Using Active Control: A Comparison of Various Approaches”. In: *Journal of Guidance, Control, and Dynamics* 18.4 (1995), pages 664–673. DOI: 10.2514/3.21445 (cited on page 229).
- [GL88] O. M. Grasselli and S. Longhi. “Zeros and Poles of Linear Periodic Multivariable Discrete-Time Systems”. In: *Circuits, Systems and Signal Processing* 7.3 (Sept. 1988), pages 361–380. DOI: 10.1007/BF01599976 (cited on page 237).
- [GST07] M. Guskov, J. J. Sinou, and F. Thouvezel. “Multi-Dimensional Harmonic Balance Applied to Rotor Dynamics”. In: *Proceedings of the ASME 2007 International Design Engineering Technical Conferences & Computers and Information in Engineering Conference*. Las Vegas, NV, September 4-7, 2007. (Cited on page 238).
- [GT12] M. Guskov and F. Thouvezel. “Harmonic Balance-Based Approach for Quasi-Periodic Motions and Stability Analysis”. In: *Journal of Vibration and Acoustics* 134.3 (June 2012). DOI: 10.1115/1.4005823 (cited on page 238).
- [HW90] Steven R Hall and Norman M Wereley. “Generalized Nyquist Stability Criterion for Linear Time Periodic Systems”. In: *Proceedings of the 1990 American Control Conference*. San Diego, CA, May 1990. DOI: 10.23919/ACC.1990.4790991 (cited on page 235).
- [HT16] A. M. Hassan and H. E. Taha. “Higher-Order Averaging Analysis of the Nonlinear Time-Periodic Dynamics of Hovering Insects/Flapping-Wing Micro-Air-Vehicles”. In: *Proceedings of the 55<sup>th</sup> Conference on Decision and Control*. Las Vegas, NV, December 12-14, 2016. DOI: <https://doi.org/10.1109/CDC.2016.7799424> (cited on pages 258, 259).
- [HSP22] M. A. Hayajneh, U. Saetti, and J. V. R. Pradad. “Identification of High-Order Linear Time-Invariant Models From Periodic Nonlinear System Responses”. In: *Proceedings of the VFS Aeromechanics for Advanced Vertical Flight Technical Meeting*. San Jose, CA, Jan. 2022 (cited on page 258).
- [Hor19] J. F. Horn. “Non-Linear Dynamic Inversion Control Design for Rotorcraft”. In: *Aerospace* 6.3 (2019). DOI: <https://doi.org/10.3390/aerospace6030038> (cited on pages 269, 272).
- [How80] J. J. Howlett. *UH-60A Black Hawk Engineering Simulation Program. Volume 1: Mathematical Model*. Technical report. NASA-CR-166309, 1980. (Cited on page 269).
- [Joh80] W Johnson. “Helicopter Theory”. In: Princeton, NJ: Princeton University Press, 1980 (cited on pages 233, 268).
- [JM59] E.I. Jury and F.J. Mullin. “The analysis of sampled-data control systems with a periodic time-varying sampling rate”. In: *IRE Transactions on Automatic Control* AC-24.1 (May 1959), pages 15–21. DOI: 10.1109/TAC.1959.6429398 (cited on page 234).
- [KCT93] F. D. Kim, R. Celi, and M. B. Tischler. “Forward Flight Trim and Frequency Response Validation of a Helicopter Simulation Model”. In: *Journal of Aircraft* 30.6 (1993), pages 854–863. DOI: 10.2514/3.46427 (cited on page 238).
- [Lop16] M J S Lopez. “LINEAR TIME INVARIANT APPROXIMATIONS OF LINEAR TIME PERIODIC SYSTEMS FOR INTEGRATED FLIGHT AND VIBRATION CONTROL”. PhD thesis. Atlanta, GA: Georgia Institute of Technology, May, 2016. (Cited on page 254).

- [LP17] M. Lopez and J. V. R. Prasad. “Linear Time Invariant Approximations of Linear Time Periodic Systems”. In: *Journal of the American Helicopter Society* (62, 012006 (2017)). DOI: 10.4050/JAHS.62.012006 (cited on pages 237, 238, 246, 251, 252, 254, 272).
- [Lop+15] M. J. S. Lopez et al. “Simulating HHC/AFCS Interaction and Optimized Controllers using Piloted Maneuvers”. In: *Proceedings of the 71<sup>st</sup> Annual Forum of the American Helicopter Society*. Virginia Beach, VA, May 5-7, 2015 (cited on pages 230, 237, 238, 246, 247).
- [LP16] Mark J. S. Lopez and J. V. R. Prasad. “Estimation of Modal Participation Factors of Linear Time Periodic Systems Using Linear Time Invariant Approximations”. In: *Journal of the American Helicopter Society* 61.4 (Oct. 2016), pages 1–4. DOI: <https://doi.org/10.4050/JAHS.61.045001> (cited on pages 230, 252).
- [Lov+06] M. Lovera et al. “Closed-loop aeromechanical stability of hingeless rotor helicopters with Higher Harmonic Control”. In: *Journal of Guidance, Control, and Dynamics* 29.1 (Jan. 2006), pages 179–189. DOI: 10.2514/1.7949 (cited on page 241).
- [Lov+07] M. Lovera et al. “Discrete-time, closed-loop aeromechanical stability analysis of helicopters with Higher Harmonic Control”. In: *Journal of Guidance, Control, and Dynamics* 30.5 (2007), pages 1249–1260. DOI: 10.2514/1.13874 (cited on page 241).
- [LH11] A. C. J Luo and J. Huang. “Approximate solutions of periodic motions in nonlinear systems via a generalized harmonic balance”. In: *Journal of Vibration and Control* 18.11 (Oct. 2011), pages 1661–1674. DOI: 10.1177/1077546311421053 (cited on page 238).
- [MET20] M. Maggia, S. A. Eisa, and H. E. Taha. “On higher-order averaging of time-periodic systems: reconciliation of two averaging techniques”. In: *Nonlinear Dynamics* 99 (2020), pages 813–836. DOI: <https://doi.org/10.1007/s11071-019-05085-4> (cited on pages 229, 230).
- [Mal08] C. Malpica. “Contributions to the dynamics of helicopters with active rotor control”. PhD thesis. College Park, MD: University of Maryland, 2008 (cited on pages 241, 242).
- [MP18] C. E. Mballo and J V R Prasad. “A Real Time Scheme for Rotating System Component Load Estimation Using Fixed System Measurements”. In: *Proceedings of the 74<sup>th</sup> Annual Forum of the Vertical Flight Society*. Phoenix, AZ, May 2018 (cited on page 230).
- [MP19] C. E. Mballo and J V R Prasad. “Real Time Rotor Component Load Limiting via Model Predictive Control”. In: *Proceedings of the 75<sup>th</sup> Annual Forum of the Vertical Flight Society*. Philadelphia, PA, May 2019 (cited on page 230).
- [MAG73] D. T. McRuer, I. L. Ashkenas, and D. Graham. “Aircraft Dynamics and Automatic Control”. In: Princeton, NJ: Princeton University Press, 1973 (cited on page 238).
- [MB76] R. A. Meyer and C.S. Burrus. “Design and implementation of multirate digital filters”. In: *IEEE Transactions on Acoustics, Speech and Signal Processing* 24.1 (Feb. 1976), pages 53–58. DOI: 10.1109/TASSP.1976.1162760 (cited on page 234).
- [Olc11] F E Olcer. “Linear Time Invariant Models for Integrated Flight and Rotor Control”. PhD thesis. Atlanta, GA: Georgia Institute of Technology, 2011 (cited on page 244).
- [OP11] F E Olcer and J V R Prasad. “A Methodology for Evaluation of Coupled Rotor-Body Stability Using Reduced Order Linear Time Invariant (LTI) Models”. In: *Proceedings of the 67<sup>th</sup> Annual Forum of the American Helicopter Society*. Virginia Beach, VA, May 2011 (cited on page 244).
- [ODS11] M. W. Oppenheimer, D. B. Doman, and Sighorsson. “Dynamics and Control of a Biomimetic Vehicle Using Biased Wingbeat Forcing Functions”. In: *Journal of Guidance, Control, and Dynamics* 34.1 (2011), pages 204–217. DOI: <https://doi.org/10.2514/1.49735> (cited on page 263).
- [ODS10] M. W. Oppenheimer, D. B. Doman, and D. O. Sighorsson. “Dynamics and Control of a Biomimetic Vehicle Using Biased Wingbeat Forcing Functions Part I – Aerodynamic Model”. In: *AIAA 2010-1023, 48<sup>th</sup> AIAA Aerospace Sciences Meeting*. Orlando, FL, Jan. 2010. DOI: <https://doi.org/10.2514/6.2010-1023> (cited on page 263).

- [Opp+14] M. W. Oppenheimer et al. “Quarter Cycle Modulation of a Minimally Actuated Biomimetic Vehicle”. In: *AIAA 2014-1467, AIAA SciTech Forum*. National Harbor, MD, Jan. 2014. DOI: <https://doi.org/10.2514/1.G000548> (cited on page 263).
- [Opp+15] M. W. Oppenheimer et al. “Control of a Minimally Actuated Biometric Vehicle Using Quarter-Cycle Wingbeat Modulation”. In: *Journal of Guidance, Control, and Dynamics* 38.7 (2015), pages 1187–1196. DOI: <https://doi.org/10.2514/1.G000548> (cited on page 263).
- [Pad+15] A. K. Padthe et al. “Analysis of High Fidelity Reduced-Order Linearized Time-Invariant Helicopter Models for Integrated Flight and On-Blade Control Applications”. In: *Proceedings of the 41<sup>st</sup> European Rotorcraft Forum*. Munich, Germany, Sep 1-4, 2015 (cited on pages 230, 237).
- [PS01] R. Pandyan and S. C. Sinha. “Time-Varying Controller Synthesis for Nonlinear Systems subjected to Periodic Parametric Loading”. In: *Journal of Vibration and Control* 7.1 (Jan. 2001), pages 73–90. DOI: [10.1177/107754630100700105](https://doi.org/10.1177/107754630100700105) (cited on page 238).
- [PV89] B. Park and E.I. Verriest. “Canonical forms for discrete-linear periodically time-varying systems and a control application”. In: *Proceedings of the 28<sup>th</sup> IEEE Conference on Decision and Control*. Tampa, FL, Dec. 1989, pages 1220–1225. DOI: [10.1109/CDC.1989.70329](https://doi.org/10.1109/CDC.1989.70329) (cited on page 234).
- [PL21] M. Passaro and M. Lovera. “LPV model identification of a flapping wing MAV”. In: *Proceedings of the 4<sup>th</sup> IFAC Workshop on Linear Parameter Varying Systems*. Milan, Italy, July 2021 (cited on page 263).
- [PLA11] D A Peters, S M Lieb, and L A Ahaus. “Interpretation of Floquet Eigenvalues and Eigenvectors for Periodic Systems”. In: *Journal of the American Helicopter Society* 56.3 (2011), pages 1–11. DOI: [10.4050/JAHS.56.032001](https://doi.org/10.4050/JAHS.56.032001) (cited on page 233).
- [Pet94] D. Peters. “Fast Floquet Theory and Trim for Multi-bladed Rotorcraft”. In: *Journal of the American Helicopter Society* 39.4 (Oct. 1994), pages 82–89. DOI: [10.4050/JAHS.39.82](https://doi.org/10.4050/JAHS.39.82) (cited on page 237).
- [Pet75] D. A. Peters. “Flap-Lag Stability of Helicopter Rotor Blades in Forward Flight”. In: *Journal of the American Helicopter Society* 20.4 (Oct. 1975), pages 2–13. DOI: [10.4050/JAHS.20.4.2](https://doi.org/10.4050/JAHS.20.4.2) (cited on page 238).
- [PCF90] D. A. Peters, M. Chouchane, and M. Fulton. “Helicopter Trim with Flap-Lag-Torsion and Stall by an Optimized Controller”. In: *Journal of Guidance, Control, and Dynamics* 13.5 (1990), pages 824–834. DOI: [10.2514/3.25408](https://doi.org/10.2514/3.25408) (cited on page 238).
- [PI81] D. A. Peters and A. P. Izadpanah. “Helicopter Trim by Periodic Shooting with Newton-Raphson Iteration”. In: *Proceedings of the 37<sup>th</sup> Annual Forum of the American Helicopter Society*. New Orleans, LA, May 17-20, 1981. (Cited on page 238).
- [PKC84] D. A. Peters, B. S. Kim, and H. S. Chen. “Calculation of Trim Settings of a Helicopter Rotor by an Optimized Automatic Controller”. In: *Journal of Guidance, Control, and Dynamics* 7.1 (1984), pages 85–91. DOI: [10.2514/3.8549](https://doi.org/10.2514/3.8549) (cited on page 238).
- [PO75] D. A. Peters and R. A. Ormiston. *Flapping Response Characteristics of Hingless Rotor Blades by a Generalized Harmonic Balance Method*. Technical report. NASA TN D-7856, 1975. (Cited on page 238).
- [PW70] V J Piarulli and R P White. *A Method for Determining the Characteristic Functions Associated with the Aeroelastic Instabilities of Helicopter Rotor Blades in Forward Flight*. Technical report. Washington, DC: NASA CR-1577, 1970 (cited on page 239).
- [PP80] D. M. Pitt and D. A. Peters. “Theoretical Prediction of Dynamic-Inflow Derivatives”. In: *Proceedings of the 6<sup>th</sup> European Rotorcraft and Powered Lift Aircraft Forum*. Bristol, England, September 16-19, 1980. (Cited on page 269).
- [Pra+09] J V R Prasad et al. “Linear Time Invariant Models for Integrated Flight and Rotor Control”. In: *Proceedings of the 35<sup>th</sup> European Rotorcraft Forum*. Hamburg, Germany, Sept. 2009 (cited on page 244).

- [Pra+08] J. V. R. Prasad et al. “Linear Models for Integrated Flight and Rotor Control”. In: *Proceedings of the 34<sup>th</sup> European Rotorcraft Forum*. Liverpool, UK, Sept. 2008 (cited on pages 237, 244, 246).
- [SH16] U Saetti and J F Horn. “Use of Harmonic Decomposition Models in Rotorcraft Flight Control Design with Alleviation of Vibratory Loads”. In: *Proceedings of the 72<sup>nd</sup> Annual Forum of the American Helicopter Society*. West Palm Beach, FL, May 2016 (cited on page 252).
- [SH20] U. Saetti and J. F. Horn. “Load Alleviation Flight Control Design using High-Order Dynamic Models”. In: *Journal of the American Helicopter Society* 65.3 (2020). DOI: <https://doi.org/10.4050/JAHS.65.032009> (cited on pages 230, 237, 238).
- [SH23] U. Saetti and J. F. Horn. “Linear Time-Invariant Approximations of Nonlinear Time-Periodic Systems”. In: *Journal of the American Helicopter Society* 68.1 (2023), pages 1–10. DOI: <https://doi.org/10.4050/JAHS.68.012006> (cited on page 247).
- [SHB21] U. Saetti, J. F. Horn, and K. S. Brentner. “Linear Time-Invariant Models of Rotorcraft Flight Dynamics, Vibrations, and Acoustics”. In: *Proceedings of the 77<sup>th</sup> Annual Forum of the Vertical Flight Society*. Virtual, May 2021 (cited on page 247).
- [SR21a] U. Saetti and J. D. Rogers. “Linear Time-Invariant Models of the Dynamics of Flapping-Wing Flight”. In: *Proceedings of the 77<sup>th</sup> Annual Forum of the Vertical Flight Society*. Virtual, May 2021 (cited on page 258).
- [SR21b] U. Saetti and J. D. Rogers. “Revisited Harmonic Balance Trim Solution Method for Periodically-Forced Aerospace Vehicles”. In: *Journal of Guidance, Control, and Dynamics* 44.5 (May 2021), pages 1008–1017. DOI: 10.2514/1.G005553 (cited on pages 238, 247).
- [SR] U. Saetti and J. D. Rogers. “Harmonic Decomposition Models of Flapping-Wing Flight for Stability Analysis and Control Design”. In: *Journal of Guidance, Control, and Dynamics* Accepted for Publication () (cited on page 258).
- [Sae+19] U. Saetti et al. “Identification of Linear Time-Periodic Systems from Rotorcraft Flight Test Data”. In: *Journal of Guidance, Control, and Dynamics* 42.10 (2019), pages 2288–2296. DOI: <https://doi.org/10.2514/1.G004406> (cited on pages 258, 269).
- [Sae+20] U. Saetti et al. “Handling-Qualities Perspective on Rotorcraft Load Alleviation Control”. In: *Journal of Guidance, Control, and Dynamics* (2020), pages 1–13. DOI: <https://doi.org/10.2514/1.G004965> (cited on pages 230, 237).
- [SVM07] J. A. Sanders, F. Verhulst, and J. Murdock. “Averaging Methods in Nonlinear Dynamical Systems”. In: Princeton, NJ: Springer, 2007. Chapter Averaging: the periodic case. DOI: <https://doi.org/10.1007/978-0-387-48918-6> (cited on page 229).
- [SHS21] M. Scaramal, J. F. Horn, and U. Saetti. “Load Alleviation Control using Dynamic inversion with Direct Load Feedback”. In: *Proceedings of the 77<sup>th</sup> Annual Forum of the Vertical Flight Society*. Virtual, May 2021 (cited on page 230).
- [SP78] D. P. Schrage and D. A. Peters. “Effect of Structural Coupling Parameters on the Flap-Lag Forced Response of a Rotor Blade in Forward Flight Using Floquet Theory”. In: *Proceedings of the 4<sup>th</sup> European Rotorcraft and Powered Lift Aircraft Forum*. Stresa, Italy, September 13–15, 1978. (Cited on page 238).
- [Sha67] J Shaw. “Higher Harmonic Blade Pitch Control for Helicopter Vibration Reduction: a Feasibility Study”. Master’s thesis. Cambridge, MA: Massachusetts Institute of Technology, 1967 (cited on page 240).
- [SOD10] D. O. Sighorsson, M. W. Oppenheimer, and D. B. Doman. “Flapping-Wing Micro-Air-Vehicle Control Employing Triangular Waves Strokes and Cycle Averaging”. In: *AIAA 2010-7553, AIAA Guidance, Navigation, and Control Conference*. Toronto, Ontario, Canada, Aug. 2010. DOI: <https://doi.org/10.2514/6.2010-7553> (cited on page 263).

- [TWH16] E. H. Taha, C. A. Woosley, and M. R. Hajj. “Geometric Control Approach to Longitudinal Stability of Flapping Flight”. In: *Journal of Guidance, Control, and Dynamics* 39.2 (Feb. 2016), pages 214–226. DOI: <https://doi.org/10.2514/1.G001280> (cited on page 264).
- [THN14] H. E. Taha, M. R. Hajj, and A. H. Nayfeh. “Longitudinal Flight Dynamics of Hovering MAVs/Insects”. In: *Journal of Guidance, Control, and Dynamics* 37.3 (2014), pages 970–978. DOI: <https://doi.org/10.2514/1.62323> (cited on pages 262, 263, 265).
- [Tah+15] H. E. Taha et al. “The Need for Higher-Order Averaging in the Stability Analysis of Hovering, Flapping-Wing Flight”. In: *Bioinspiration & Biomimetics* 10.1 (2015), pages 1–15. DOI: <https://doi.org/10.1088/1748-3190/10/1/016002> (cited on pages 261–265, 267).
- [Tot10] R. Toth. *Modeling and Identification of Linear Parameter-Varying Systems*. Springer, 2010 (cited on page 231).
- [WL15] Y. Wang and Z. Liu. “A Matrix-Based Computational Scheme of Generalized Harmonic Balance Method for Periodic Solutions of Nonlinear Vibratory Systems”. In: *Journal of Applied Nonlinear Dynamics* 4.4 (Oct. 2015), pages 379–389. DOI: 10.5890/JAND.2015.11.005 (cited on page 238).
- [WP78] F. S. Wei and D. A. Peters. “Lag Damping in Autorotation by a Perturbation Method”. In: *Proceedings of the 34<sup>th</sup> Annual Forum of the American Helicopter Society*. Washington, DC, May 15–17, 1978. (Cited on page 238).
- [WH90] Norman M Wereley and Steven R Hall. “Frequency Response of Linear Time Periodic Systems”. In: *Proceedings of the 29<sup>th</sup> IEEE Conference on Decision and Control*. Honolulu, HI, Dec. 1990. DOI: 10.1109/CDC.1990.203516 (cited on pages 235, 236).
- [WH91] Norman M Wereley and Steven R Hall. “Linear Time Periodic Systems: Transfer Function, Poles, Transmission Zeroes and Directional Properties”. In: *Proceedings of the 1991 American Control Conference*. Boston, MA, June 1991. DOI: 10.23919/ACC.1991.4791563 (cited on page 235).
- [WW10] J. P. Whitney and R. J. Wood. “Aeromechanics of passive rotation in flapping flight”. In: *Journal of Fluid Mechanics* 60 (2010), pages 197–220. DOI: <https://doi.org/10.1017/S002211201000265X> (cited on page 262).
- [Ypm95] T. J. Ypma. “Historical Development of the Newton–Raphson Method”. In: *SIAM Review* 37.4 (1995), pages 531–551. DOI: <https://doi.org/10.1137/1037125> (cited on page 251).
- [ZZF96] C. Zhang, J. Zhang, and K. Furuta. “Performance analysis of periodically time-varying controllers”. In: *Proceedings of the 13<sup>th</sup> IFAC World Congress*. San Francisco, CA, June 1996, pages 207–212. DOI: 10.1016/S1474-6670(17)57905-7 (cited on page 235).
- [Zho07] J. Zhou. “A Harmonic Framework for Controllability in Linear Continuous-Time Periodic Systems”. In: *SIAM Journal on Control and Optimization* 46.2 (Apr. 2007), pages 630–654. DOI: 10.1137/050639934 (cited on page 237).